Deeply Virtual Compton Scattering and the HERMES-Recoil-Detector

Den Naturwissenschaftlichen Fakultäten
der Friedrich-Alexander-Universität Erlangen-Nürnberg
zur
Erlangung des Doktorgrades

vorgelegt von
Bernhard Krauß

aus Nürnberg

Als Dissertation genehmigt von den Naturwissen-
schaftlichen Fakultäten der Universität Erlangen-Nürnberg

Tag der mündlichen Prüfung :	4. 2. 2005
Vorsitzender der Promotionskommission:	Prof. Dr. D.-P. Häder
Erstberichterstatter:	Prof. Dr. K. Rith
Zweitberichterstatter:	Prof. Dr. E. Kinney
Drittberichterstatter:	Prof. Dr. D. Müller

Contents

1. Introduction

Originally the HERMES experiment at the HERA accelerator (DESY, Hamburg) was designed to study the spin structure of the nucleon by inclusive and semi-inclusive lepton-nucleon scattering using a polarised beam of 27.5 GeV and a polarised gas target. Meanwhile it has been found that the same experimental apparatus also allows to focus on other topics like nuclear attenuation or exotic mesons; one important discovery was the first observation of an indication for Deeply Virtual Compton Scattering in 2001 [HERMES01a, HERMES02, HERMES03b].

Deeply Virtual Compton scattering (DVCS) denotes exclusive production of high energy photons, where in contrast to Bremsstrahlung the photon is not emitted by the lepton but by one of the quarks inside the nucleon. For a certain reaction kinematics, numerical estimates for this process were given by Ji [Ji98] and others in 1998. However, the story of DVCS is much longer. After the first quantum mechanical calculations of Bremsstrahlung by Bethe and Heitler in 1934 [BH34], Mo and Tsai published a fully field-theoretical calculation in 1969 [MT69], in which they stated that apart from some calculable features at high lepton energies there would be a competing photon production mechanism due to the hadronic state. They also noted that this other process is directly linked with the understanding of nuclear structure and that such knowledge was not available at that time.

Recently this understanding of nuclear structure has been manifesting itself with the invention of the Generalised Parton Distributions (GPDs). Although the concept of "interpolating functions" had been introduced earlier [DMR$^+$88], it took about 10 years to realize that the GPDs have very important consequences. On the one hand they contain the existing knowledge about the nucleon form factors as well as the conventional parton distributions. On the other hand they can be used to describe many other scattering processes [GPV01, HERMES00] apart from DVCS and finally there exists a relation to the total angular momentum of the quarks inside the nucleon. At the moment there are only very few ideas how to measure this important quantity and driven by this interest several other experiments have successfully searched for DVCS, e.g. the CLAS [CLAS01] experiment at somewhat lower beam energies or H1 [H101] and ZEUS [ZEUS03] at quite different kinematics. Several future experiments (e.g. [A$^+$04]) are motivated by the GPDs.

It is also possible to extend the theoretical framework of GPDs to nuclear targets in order to learn more about nuclear structure. An obvious candidate for this is the deuteron; due to its spin-1 character, the theoretical formalism gets more complicated, but nevertheless theoretical predictions exist [KM03]. Calculations for HERMES energies are usually made for asymmetries in the cross-section that arise from an interference of the amplitudes of Bremsstrahlung and DVCS.

The aim of this thesis was to study and extract all possible asymmetries that are accessible with the HERMES experiment for a longitudinally polarised deuterium target. In order to detect and isolate exclusive BH/DVCS, strong requirements on the detector resolution and stability have to be fulfilled. Hence some part of this thesis deals with consistency checks of the hardware response (chapter 5). In addition a Monte Carlo generator was written (chapter 4) in order to confirm a quantitative agreement of theoretical predictions and the observed data. Due to the limited statistics and the multidimensional shape of the asymmetries the best extraction procedure had to be looked for (chapter 6) and its expected accuracy and limits had to be studied before the final results could be obtained (chapter 7).

One constraint remains for the performance of HERMES in terms of DVCS: It is not completely possible to ensure exclusivity of the observed data sample and at the moment a non-negligible background contamination exists that is difficult to correct for. Hence it was decided to construct a new detector, the HERMES recoil detector, to identify the recoiling low momentum proton that is typical of DVCS on hydrogen. A major part of this thesis was dedicated to the design of this detector and projections for its performance. The results of this work are shown in chapters 8 and 9. As part of this task, testbeam experiments related to the silicon subdetector were carried out and the results are also shown in chapter 9. In addition, the Erlangen group took over the responsibility for purchasing and testing the silicon sensors. Extensive tests of their performance were made and the results are summarised in appendix A. The recoil detector will be installed in the HERMES experiment in 2005 and will certainly turn out to be useful for many other physics processes than DVCS.

2. Deeply Virtual Compton Scattering and Generalised Parton Distributions

2.1. Kinematical Definitions

Before discussing the theoretical framework that has been worked out for Deeply Virtual Compton Scattering and related processes, a number of definitions and restrictions have to be provided. The kinematics of the reactions is governed by the same variables that are conventionally used to describe deep inelastic lepton nucleon scattering (DIS). Hence it is useful to explain this process first.

In DIS the scattering of a high-energy electron on a nucleon is considered as shown in figure 2.1: An electron of 4-momentum $\mathbf{k}$ emits a virtual photon with 4-momentum $\mathbf{q}$. This is absorbed by a nucleon N which subsequently fragments into the hadronic final state X.

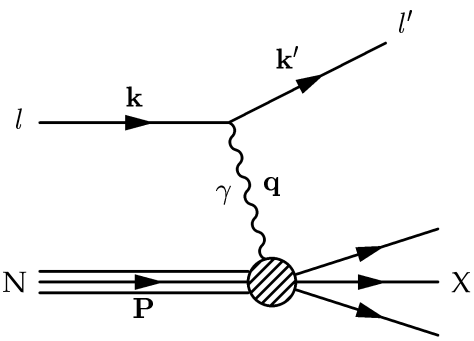

Figure 2.1.: Deep inelastic scattering: The incident lepton l scatters on a nucleon N which breaks up into the hadronic final state X.

Although in the experiment the specification of the initial lepton and nucleon momentum vectors fixes the reference system, the scattering kinematics can more generally be expressed in terms of Lorentz-invariant quantities. In this way a simple comparison e.g. between electron-proton-colliders and fixed target experiments is possible. In principle only 3 variables are required, however a fourth one is usually added:

$$s \equiv (\mathbf{k}+\mathbf{P})^2, \quad (2.1)$$
$$q^2 \equiv -Q^2 = \left(\mathbf{k}-\mathbf{k}'\right)^2 < 0, \quad (2.2)$$
$$W^2 \equiv (\mathbf{P}+\mathbf{q})^2, \quad (2.3)$$
$$\nu \equiv \frac{\mathbf{P}\cdot\mathbf{q}}{M}. \quad (2.4)$$

s is the total available centre of mass energy squared, q^2 denotes the 4-momentum transfer by the virtual photon, W^2 is the square of the invariant mass of the hadronic final state X. There is no general Lorentz-invariant interpretation of ν. However for a fixed-target experiment like HERMES the nucleon N is at rest and in this reference frame one obtains:

$$s = 2ME + M^2, \quad (2.5)$$
$$Q^2 = 4EE' \sin^2\frac{\theta_e}{2}, \quad (2.6)$$
$$W^2 = M^2 + 2M\nu - Q^2, \quad (2.7)$$
$$\nu = E - E'. \quad (2.8)$$

E and E' denote the energies of the initial and scattered lepton respectively, θ_e is the scattering angle of the lepton with respect to the beam direction and M is the rest mass of the nucleon N. In this reference frame ν is simply the energy loss of the scattered lepton.

In addition to these quantities, two other dimensionless variables are usually introduced because they turn out to be convenient in terms of interpretation:

$$x_B = \frac{Q^2}{2\mathbf{P}\cdot\mathbf{q}} = \frac{Q^2}{2M\nu} = \frac{Q^2}{Q^2+W^2-M^2} \quad (2.9)$$

and

$$y = \frac{\mathbf{P}\cdot\mathbf{q}}{\mathbf{P}\cdot\mathbf{k}} = \frac{\nu}{E}. \quad (2.10)$$

For both variables the allowed region is:

$$0 < x_B, y \leq 1. \quad (2.11)$$

In the case of DIS, x_B can be interpreted as the fraction of the 4-momentum of the nucleon that is carried by the struck quark. In the case of DVCS, Bremsstrahlung and almost all other cases discussed in this thesis, the meaning of x_B is more obscure. y has no special meaning in the DIS picture but is useful to describe Bremsstrahlung (cf. [Par00]). It is important to note that all the variables Q^2, W^2, ν, x_B and y are purely inclusive, i.e. they are fully determined by the kinematics of the outgoing lepton, even if the Feynman diagram belonging to the considered reaction is of a completely different kind than shown in figure 2.1.

In order to describe exclusive meson production or DVCS more variables are required to deal with a 3-particle final state. This is shown in figure 2.2. Again the incoming lepton emits a virtual photon with 4-momentum $\mathbf{q}$. However this time the photon interacts with some object O that is emitted by the nucleon and a meson or a real photon m with mass m_m and 4-momentum $\mathbf{v}$ is created. The 4-momentum transfer to the nucleon is denoted as Δ and often the variable t is introduced as the square of it:

$$\Delta \equiv \mathbf{P}' - \mathbf{P}, \tag{2.12}$$
$$t \equiv \Delta^2 < 0. \tag{2.13}$$

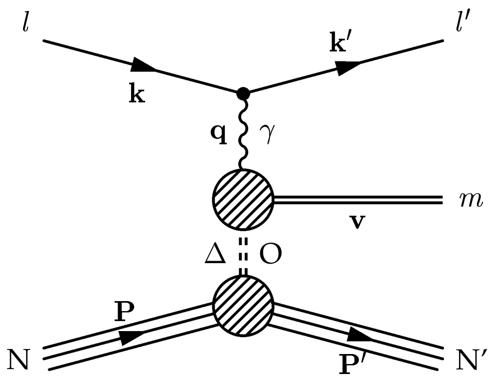

Figure 2.2.: Exclusive meson/photon production: A virtual photon is emitted by the lepton, interacts with the object O that is emitted by the nucleon and changes it into a nucleon or resonance N'.

The value of the variable t is always negative. If the mass of the nucleon is unchanged, this is easily seen in the rest frame of the nucleon N :

$$t = 2M(M - E_{N'}). \tag{2.14}$$

If the mass changes from M to M', it is more difficult to prove that t is negative. In this case t can be written as

$$t = M'^2 + M^2 - 2ME_{N'} \tag{2.15}$$

in the rest frame of the nucleon N. The calculation of the allowed range in t can be made in the centre of mass system [Par00]. For given values of m_m, M', Q^2 and W^2 the exact limits $t_{0,1}$ for the quantity t are given by

$$t_{0,1} = (E_{N,cm} - E_{N',cm})^2 - (p_{N,cm} \mp p_{N',cm})^2, \tag{2.16}$$

where

$$E_{N,cm} = \frac{W^2 + M^2 + Q^2}{2\sqrt{W^2}}, \qquad E_{N',cm} = \frac{W^2 + M'^2 - m_m^2}{2\sqrt{W^2}}. \tag{2.17}$$

The corresponding momenta $p_{N,cm}$ and $p_{N',cm}$ are obtained from the known energy-momentum relationship. The allowed range is $t_1 < t < t_0$. Often t_0 is called t_{min}, because $|t_0|$ is the minimum allowed value of $|t|$. However this is a bit misleading and hence in all following discussions the name t_0 will be used.

From these equations it can be shown that $t_0 = 0$ for all values of M' and W^2 if $m_m = Q^2 = 0$. In addition it can be shown that t_0 decreases monotonously with increasing Q^2 for all values of the other variables and that it also decreases with increasing m_m for all values of the other variables. Consequently t_0 is always negative and can never be zero if $Q^2 > 0$.

For illustration the values of t_0 and t_1 depending on W^2 and Q^2 are plotted in figures 2.3 and 2.4. Figure 2.3 shows the elastic process in which a photon is produced, while the values in figure 2.4 are calculated for photon production with simultaneous excitation of the nucleon into a $\Delta(1232)$. As can be seen t_0 decreases with increasing mass of the final state nucleon if $Q^2 > 0$. The limit t_1 is of no further importance, as it is far outside the region of interest for DVCS.

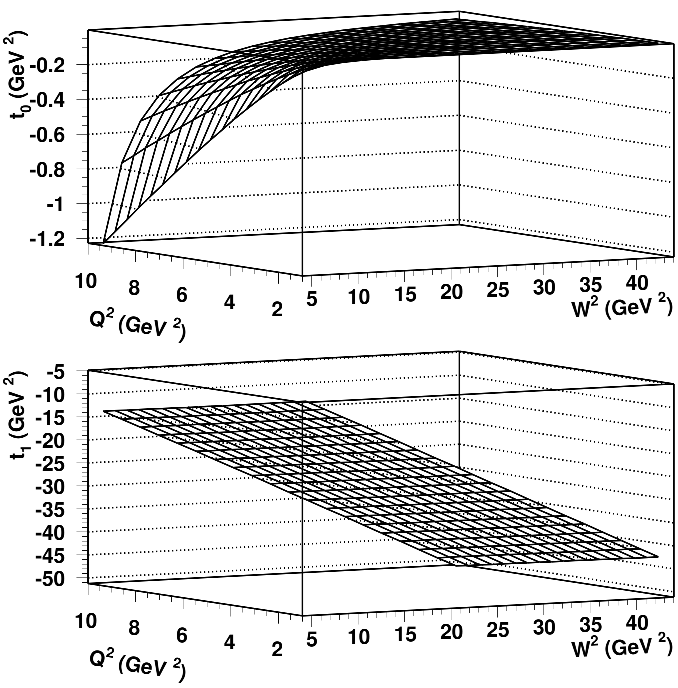

Figure 2.3.: t_0(top) and t_1(bottom) for the case of elastic single photon production.

Although all particle energies are now fixed by knowing x_B, Q^2 and t, one additional variable is needed to describe the directions of motion of the final state particles relative to each other. Usually the angle ϕ is chosen, which is the angle between the scattering plane and the photon/meson production plane as shown in figure 2.5. The allowed values of ϕ are $-\pi < \phi < \pi$; under parity transformation it behaves like $\phi \to -\phi$. Furthermore ϕ is invariant under Lorentz boosts along the direction of the virtual photon. Hence the same value will be obtained in the rest frame of the nucleon as in the centre of mass system (cms) of the nucleon and the virtual photon.

Using these quantities, all non-trivial information of a cross-section with a 3-particle final

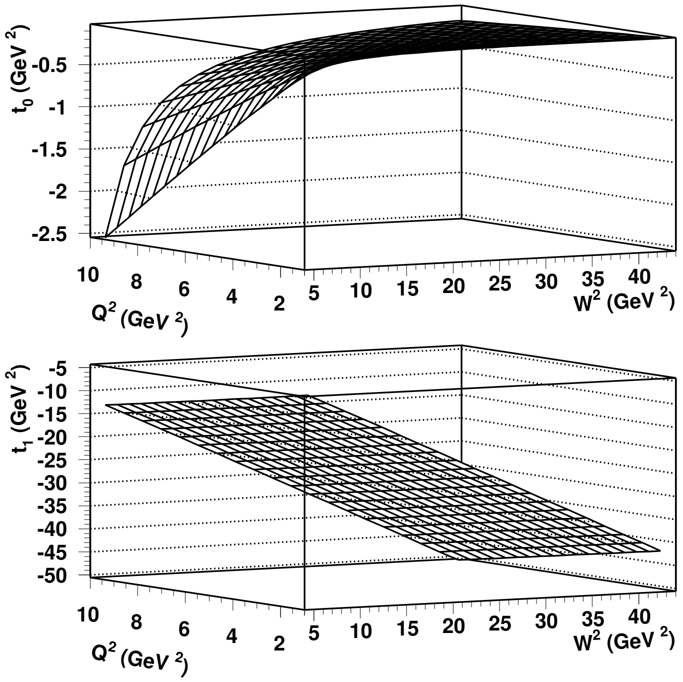

Figure 2.4.: t_0(top) and t_1(bottom) for the case of single photon production with excitation of a $\Delta(1232)$ resonance.

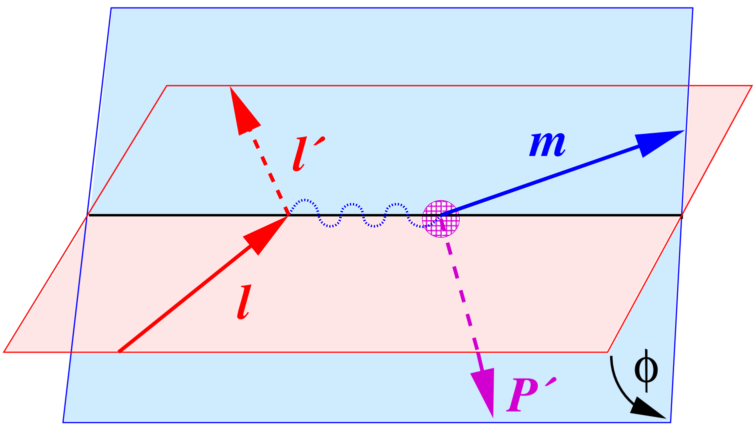

Figure 2.5.: Definition of the angle ϕ between scattering plane and meson (photon) production plane. Also different definitions are used in literature.

state is contained in the four-times differential quantity

$$\frac{d\sigma}{dx_B\, dQ^2\, dt\, d\phi}.$$

Especially for Bremsstrahlung the cross-section

$$\frac{d\sigma}{dE'\, d\Omega_{l'}\, d\Omega_m}$$

is often given instead, where the solid angle is used for the direction of the lepton ($\Omega_{l'}$) and the direction of the meson/photon (Ω_m). The transformation for the elastic Bremsstrahlung is

$$\frac{d\sigma}{dx_B\, dQ^2\, dt\, d\phi} = \frac{d\sigma}{dE'\, d\Omega_{l'}\, d\Omega_m} \cdot \frac{2\pi y^2}{1-y} \cdot \frac{W^2 - M^2}{4Q^2 E_\gamma^2 \sqrt{\nu^2 + Q^2}}, \tag{2.18}$$

where E_γ denotes the energy of the photon.

In addition to the kinematical variables that are really required to define the kinematics of interest, it is often useful to introduce some angles in the lab-system: While θ_e is the polar angle between the scattered lepton and the beam, ϕ_e is the azimuthal angle of the lepton around the beam. The same angles will be used for the photon (θ_γ, ϕ_γ) and the proton (θ_p, ϕ_p).

For nuclear targets the definitions of the kinematical variables have to be extended. If the nucleus does not break up during interaction, it can essentially be treated as a heavy nucleon and in the calculation of the inclusive kinematical quantities the mass M is replaced by the mass M_A of the nucleus. The two new nuclear variables will be denoted as x_A and W_A^2.

On the other hand if the nucleus breaks up, quasi-elastic scattering can take place in which only one nucleon is affected and removed from the nucleus. Neglecting Fermi motion, binding energies and more subtle effects like nuclear shadowing, the hit nucleon can be considered as a quasi-free particle at rest and the variables x_B and W^2 are again more or less well-defined. As soon as binding effects are taken into account, it is not possible to retrieve the exact values of x_B or W^2. Even the simple spectator model (section 4.3) would at least require a measurement of the momentum vector of the remaining nucleus.

In the HERMES experiment mixed data-samples are studied and both sets of variables - as calculated from the lepton and photon kinematics - are used alternatively.

2.2. Lightcone Coordinates

For the calculation of high-energy electron-proton cross-sections it is often useful to transform the problem to a special reference frame: First a Lorentz-transformation is applied such that the virtual photon and the nucleon only move along the z-axis. The nucleon moves towards the positive z-direction and the photon moves towards the negative z-direction as shown in figure 2.6. This can e.g. be the cms of the two particles.

Two special vectors are of importance in the case of exclusive photon-/meson-production: The vector Δ as defined before and the vector $\bar{P} = \frac{1}{2}(P+P')$ which is the average 4-momentum of the initial and final state nucleon. To be more precise in the calculation of exclusive cross-sections it is usually required that $\bar{P}$ instead of P is collinear with the virtual photon. Then the transformation to the lightcone system for an arbitrary 4-vector $\mathbf{a}$ is defined by

$$a^+ = \frac{1}{\sqrt{2}}(a^0 + a^3), \tag{2.19}$$

$$a^- = \frac{1}{\sqrt{2}}(a^0 - a^3), \tag{2.20}$$

$$\vec{a}_\perp = (a^1, a^2). \tag{2.21}$$

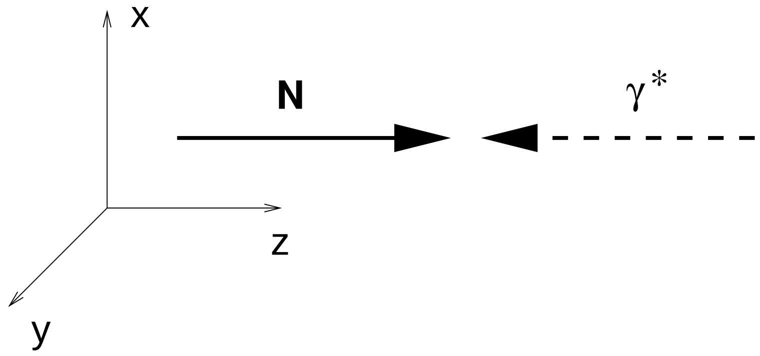

Figure 2.6.: Reference system for lightcone coordinates: It is chosen such that the nucleon and the virtual photon move along the z-axis towards a head-on collision with each other.

For the position vector $\mathbf{y}$, y^+ takes over the meaning of "lightcone time" and y^- is called "lightcone distance". The component k^+ derived from a 4-momentum vector $\mathbf{k}$ is called "lightcone momentum". For fast particles moving towards the positive z-direction k^+ is large, while k^- is small. All transverse momentum components are usually assumed to be small, too, such that the lightcone momentum vector is dominated by one component. The same method can also be applied to obtain γ^+ and γ^- from the Dirac-matrices γ^i or to create a lightcone tensor operator $\sigma^{+,i}$ by transformation with respect to the first index.

Lightcone coordinates have the following properties:

- For boosts along the z-axis with a relative velocity v, the components transform like

$$k^+ \to \gamma(1-\beta)k^+, \qquad k^- \to \gamma(1+\beta)k^-, \tag{2.22}$$

  where $\beta = \frac{v}{c}$ and $\gamma = \frac{1}{\sqrt{1-\beta^2}}$.

  The product $k^+k'^-$ is invariant for two momentum vectors k and k' pointing towards the positive z-direction.

- The following definitions are required for consistency:

$$\mathbf{v}\cdot\mathbf{w} = v^+w^- + v^-w^+ - \vec{v}_\perp\vec{w}_\perp, \tag{2.23}$$

$$\int d^4y = \int dy^-\, dy^+\, d^2\vec{y}_\perp, \tag{2.24}$$

$$\partial^+ = \frac{\partial}{\partial y^-}. \tag{2.25}$$

- The coordinates are chosen to simplify the calculus; one trivial example is the 1-dimensional wave-equation:

$$(\partial_t^2 - \partial_z^2)f(t,z) = 2\partial^+\partial^- f(y^+,y^-) = 0. \tag{2.26}$$

  The solution is obviously $f = g(y^+) + h(y^-)$ with two arbitrary functions g and h.

Using this transformation a skewedness variable ξ can then be defined as:

$$\xi = -\frac{1}{2}\frac{\Delta^+}{\bar{P}^+}, \tag{2.27}$$

which is obviously invariant under Lorentz-boosts along the z-axis. In the limit of $|t| \ll Q^2$ it simplifies to $\xi \approx \frac{x_B}{2-x_B}$. Due to the allowed values of x_B this implies also $0 < \xi < 1$. Until now all discussions have been valid for any final state consisting of 3 particles.

2.3. Hard Exclusive Reactions and GPDs

At HERMES "Hard exclusive reactions" are a subsample of possible DIS processes (apart from the BH process which is a higher order QED-process). "Exclusive" means that the final state may only consist of three particles: the scattered lepton, a - possibly exited - nucleon and a meson or photon. "Hard" means that a hard scale has to be present in the reaction kinematics. At HERMES the hard scale is usually given by $Q^2 \gg M^2$, but depending on the process the hard scale can also be given by t; for heavy vector mesons like the J/Ψ the meson mass can also enter into the effective scale [ALR97]. The hard scale is required in order to allow a formal treatment within the framework of perturbative QCD and thus it allows to resolve the nuclear structure into single quarks and gluons.

Hard exclusive reactions can be described by the so-called handbag diagram, as shown in figure 2.7 for DVCS: A quark with plus-momentum $(x + \xi)\bar{P}^+$ is taken out of the nucleon, it interacts with the virtual photon, emits a real photon and returns to the nucleon with plus-momentum $(x - \xi)\bar{P}^+$, while possibly exciting it into a resonant state. In this way the plus-momentum $\Delta^+ = -2\xi\bar{P}^+$ is transfered to the nucleon as was ensured by the definition of ξ. The quark-loop momentum $k^+ = x\bar{P}^+$ is naturally unobservable from outside. x is bounded by $-1 < x < 1$, where the negative x-region denotes antiquarks.

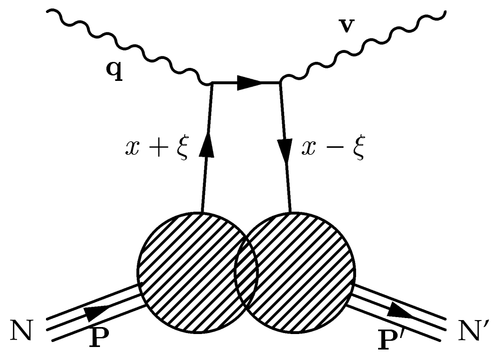

Figure 2.7.: Deeply Virtual Compton Scattering: The virtual photon interacts with a quark that has been taken out of the nucleon. After a real photon has been emitted, a quark returns to the nucleon and may excite a resonant state.

Obviously the handbag digram is not a usual Feynman graph. The reason for this is that the initial and final quarks are by no means free particles. Hence, in order to calculate the cross-section of such a process, the matrix element of a well-defined operator has to be known. The operator is sandwiched between the complex multi-particle quantum states of the incoming and outgoing nucleon. This is symbolised by the big shaded blob. On the light cone the relevant matrix elements for the elastic process ($N = N'$) can be written as

$$M_{\alpha,\beta} = \frac{\bar{P}^+}{2\pi} \int dy^- \; e^{ik^+y^-} \langle P'|\bar{\psi}_\alpha(-\frac{y^-}{2})\psi_\beta(\frac{y^-}{2})|P\rangle \;|_{y^+=\vec{y}_\perp=0} \; . \tag{2.28}$$

In this notation [Ji98] a Fourier-integral transforms the position dependent matrix-element into momentum space (for one coordinate). Instead of using indices α and β the matrix-elements can also be written as $\propto \langle P'|\bar{\psi}(-\frac{y^-}{2})O\psi(\frac{y^-}{2})|P\rangle \;|_{y^+=\vec{y}_\perp=0}$ where O symbolises a number of different matrix-operators. Sometimes a gauge link $P\;\exp(ig\int dx^\mu\; A_\mu)$ is included in the matrix element to deal with a general colour gauge, but this reduces to 1 for the axial-gauge. Similar matrix elements can be defined for gluons.

To twist-2 accuracy the matrix-elements can be parametrised as

$$\begin{aligned} M_{\alpha,\beta} \;\; = \;\; & \frac{1}{4}\{(\gamma^-)_{\alpha\beta}[H^q(x,\xi,t)\bar{N}(P')\gamma^+N(P) \\ & +E^q(x,\xi,t)\bar{N}(P')i\sigma^{+\kappa}\frac{\Delta_\kappa}{2M}N(P)] \\ & +(\gamma_5\gamma^-)_{\alpha\beta}[\tilde{H}^q(x,\xi,t)\bar{N}(P')\gamma^+\gamma_5 N(P) \\ & +\tilde{E}^q(x,\xi,t)\bar{N}(P')\gamma_5\frac{\Delta^+}{2M}N(P)], \end{aligned} \tag{2.29}$$

where $N(P)$ and $N(P')$ are the nucleon spinors. Four different GPDs are required that correspond to different transitions between the nucleon states. H denotes a vector transition, E a tensor transition, $\tilde{H}$ an axial-vector transition and $\tilde{E}$ a pseudoscalar transition. Since all possible observables are encoded in the matrix elements, the measurement of all GPDs implies the measurement of a complete set of observables at the twist-2 level.

These matrix elements are not only encountered in the definition of the GPDs. They are also needed if one tries to formulate the leading twist structure functions F_1 and g_1 in terms of hard and soft subprocesses [Hoy02]: Due to the optical theorem, the cross-section for all possible final states in DIS can be related to the imaginary part of the forward Compton scattering amplitude at $t = \xi = 0$, where the initial state is identical to the final state. In this way DIS can be related to the right-hand diagram in figure 2.8, while DVCS is related to the left-hand diagram.

The connection between the GPDs and the inclusive structure functions is recovered in the limit of $\xi = 0$ and $t = 0$, where the following relations hold for quarks of the flavour q:

$$H^q = \begin{cases} q(|x|) & \text{for}\, x > 0 \\ -\bar{q}(|x|) & \text{for}\, x < 0 \end{cases} , \tag{2.30}$$

$$\tilde{H}^q = \begin{cases} \Delta q(|x|) & \text{for}\, x > 0 \\ \Delta\bar{q}(|x|) & \text{for}\, x < 0 \end{cases} . \tag{2.31}$$

The GPDs E and $\tilde{E}$ are not observable in DIS, as the corresponding kinematical terms in $M_{\alpha,\beta}$ vanish in this limit.

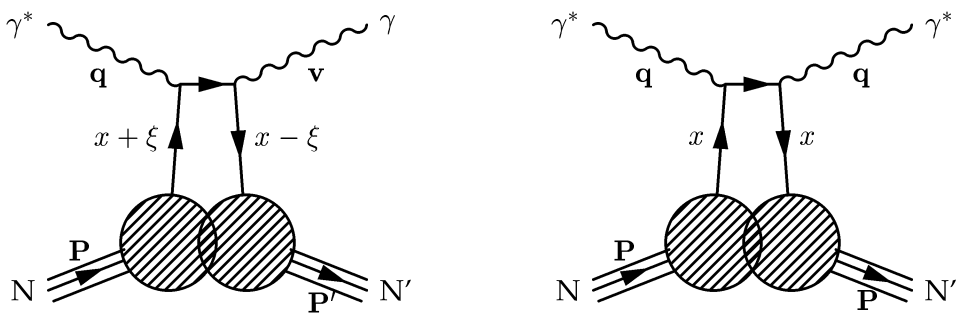

Figure 2.8.: Comparison of DVCS (left) and DIS (right): For DIS the same matrix element of the nucleon is evaluated, but only at $t = \xi = 0$ and $x = x_B$.

In addition there exist relations to the formfactors of the nucleon:

$$\int_{-1}^{+1} dx\, H^q(x,\xi,t) = F_1^q(t), \tag{2.32}$$

$$\int_{-1}^{+1} dx\, E^q(x,\xi,t) = F_2^q(t), \tag{2.33}$$

$$\int_{-1}^{+1} dx\, \tilde{H}^q(x,\xi,t) = g_A^q(t), \tag{2.34}$$

$$\int_{-1}^{+1} dx\, \tilde{E}^q(x,\xi,t) = h_A^q(t). \tag{2.35}$$

where the quantities F_1^q and F_2^q can be derived from the known Dirac and Pauli formfactors of the proton (p) and the neutron (n) using isospin-symmetry:

$$F_1^{u/p} = 2F_1^p + F_1^n + F_1^s, \tag{2.36}$$

$$F_1^{d/p} = 2F_1^n + F_1^p + F_1^s. \tag{2.37}$$

F_1^s is an additional strange form-factor which is often neglected due to the dominance of the valence quarks. The formfactors $g_A^q(t)$ and $h_A^q(t)$ can be studied in weak reactions. E.g. $g_A^u(t)$ can be obtained from the isovector and isoscalar formfactors $g_A(t)$ and $g_A^0(t)$ using the relation

$$g_A^u(t) = \frac{1}{2}g_A(t) + \frac{1}{2}g_A^0(t). \tag{2.38}$$

$g_A(t)$ is experimentally known [A199] with a value of $g_A(0) \approx 1.267$ [GPV01, A+87] from neutron β-decay. More information on these formfactors can be found in reference [C+93].

In summary this means that the existing knowledge to confine the GPD H is the best, while for the other GPDs only partial knowledge exists if hard exclusive reactions are not considered. At the same time H is the dominant GPD when measuring DVCS on the proton.

More complicated restrictions to the GPDs exist as well: it can be shown that polynomiality has to be fulfilled. The Mellin moments of the functions H and E are required to allow the following decomposition, where the t-dependence of all functions has been omitted for reasons of better readability:

$$\int_{-1}^{1} dx\, x^n\, H^q(x,\xi) \;=\; h_0^{q,n} + h_2^{q,n}\xi^2 + \cdots + h_{n+1}^{q,n}\xi^{n+1}, \tag{2.39}$$

$$\int_{-1}^{1} dx\, x^n\, E^q(x,\xi) \;=\; e_0^{q,n} + e_2^{q,n}\xi^2 + \cdots + e_{n+1}^{q,n}\xi^{n+1}, \tag{2.40}$$

with the additional requirement that

$$e_{n+1}^{q,n} = -h_{n+1}^{q,n}. \tag{2.41}$$

The most trivial way to fulfil this is to let all functions $h_i^{q,n}$ and $e_i^{q,n}$ vanish. This would mean that there is no dependence of the GPDs on ξ at all, such that there are no skewing effects. There is a different more universal way to construct GPDs with this requirement, which will be introduced in the following section.

The GPDs are defined in two very different regions. One region is the region with $\xi < x < 1$ or $-1 < x < -\xi$ where a quark or antiquark, respectively, shows up in the loop of the handbag-diagram. Here the GPDs behave like ordinary quark distributions and also their evolution in Q^2 [BR97] is similar to the quark distributions [AP77]; hence this region is called DGLAP-region (named after Dokshitzer, Gribov, Lipatov, Altarelli and Parisi).

In the ERBL-region (Efremov-Radyushkin-Brodsky-Lepage), which means $-\xi < x < \xi$, the evolution is different [BFM00, BR97]. Here the handbag-diagram is deformed, as the nucleon effectively emits a quark-antiquark-pair. During evolution to higher values of Q^2 more and more quarks move from the DGLAP into the ERBL region.

One of the main interests in the GPDs is their relation to the total angular momentum J^q carried by quarks in the nucleon. This is formulated by Ji's sumrule:

$$\int_{-1}^{+1} dx\, x(H^q(x,\xi) + E^q(x,\xi)) = 2J^q, \tag{2.42}$$

which is only valid for $t = 0$ [Ji98]. Together with the knowledge of the fraction of the nucleon spin which can be attributed to the spins of the quarks, this would allow access to their orbital angular momentum. At the moment non-zero values for the Sivers effect measured at Hermes [HERMES04b] indicate that there is indeed some non-zero orbital angular momentum although the Sivers effect does not yet allow to quantify it.

Apart from this aim, many other suggestions have been made to interpret the knowledge contained in the GPDs. For example the transverse distribution of quarks inside the nucleon can be extracted, such that a two-dimensional picture of the nucleon can be produced [Bur03]. It is also possible to introduce a gravitational interpretation: The GPDs are linked to the energy-momentum tensor and hence they are by general relativity related to the gravitational properties of the nucleon [BDH01].

Finally also hydrodynamical interpretations are possible in which the internal pressure or the surface tension of a nucleon/nucleus is derived from the GPDs [Pol03]. This multitude of possibilities is impressive, but the proof is still missing that the GPDs can be extracted at all in each point in x, ξ and t using all possible experiments on hard exclusive reactions. So far only one method based on the Q^2-evolution of DVCS has been suggested [Fre99] and at present mainly the verification or falsification of particular GPD-models is attempted in experiments. Only for the special case of $x = \xi$ an extraction may be possible [KN02a] even if a limited range in Q^2 is available.

2.4. Parametrisations of the GPDs

A multitude of different GPD-models are available. One class of models consists of simple 3-dimensional functions that fulfil at least some of the discussed requirements [VGG00, VGG99, KM03, KN02b]. In addition there are attempts to use existing models for the structure of the nucleon to derive the corresponding values of the GPDs. This was e.g. done for the MIT-bag-model [JMS97] or the chiral quark-soliton model [DP00]. Finally ideas exist to extrapolate structure functions to GPDs as in the aligned jet model [FMS03] or the model proposed in reference [GBMR99].

One hard exclusive process that has already been studied for a very long time is the exclusive production of π^+ on a hydrogen-target [B$^+$78a]. This process was of interest as the pion-cloud of the nucleon was considered to be the best supplier for pions at rest. It is known that there is a significant pion-pole-contribution at low values of t, which corresponds to the pion-cloud picture. This knowledge constraints the formfactor $h_a^q(t)$ and the GPD $\tilde{E}$ for the relevant kinematics. Hence this contribution is present in all models.

The most direct GPD-model was introduced by Vanderhaeghen, Guichon and Guidal in 1999 [VGG99]:

$$H^{u/p} = u(x)\frac{1}{2}F_1^{u/p}(t), \tag{2.43}$$

$$H^{d/p} = d(x)F_1^{d/p}(t), \tag{2.44}$$

$$\tilde{H}^{u/p} = \Delta u_v(x)\frac{g_A^{u/p}(t)}{g_A^{u/p}(0)}, \tag{2.45}$$

$$\tilde{H}^{d/p} = \Delta d_v(x)\frac{g_A^{d/p}(t)}{g_A^{d/p}(0)}, \tag{2.46}$$

$$E^{u/p} = u(x)\frac{1}{2}F_2^{u/p}(t), \tag{2.47}$$

$$E^{d/p} = d(x)F_2^{d/p}(t), \tag{2.48}$$

$$\tilde{E}^{u/p} = \frac{1}{2}\theta\left(1-\frac{x^2}{\xi^2}\right)\frac{(2M)^2 g_A(0)}{-t+m_\pi^2}\frac{1}{\xi}\frac{3}{4}\left(1-\left(\frac{x}{\xi}\right)^2\right), \tag{2.49}$$

$$\tilde{E}^{d/p} = -\frac{1}{2}\theta\left(1-\frac{x^2}{\xi^2}\right)\frac{(2M)^2 g_A(0)}{-t+m_\pi^2}\frac{1}{\xi}\frac{3}{4}\left(1-\left(\frac{x}{\xi}\right)^2\right). \tag{2.50}$$

Any contributions from strange quarks as well as the contributions of the sea-quarks to $\Delta q(x)$ are neglected. The GPD $\tilde{E}$ is only non-zero in the ERBL-region, as suggested by the pion-cloud picture. Obviously this ansatz for the GPDs fulfils all requirements mentioned before. An example of the function $H^{d/p}$ according to this model is shown in figure 2.9.

A different approach is possible that ensures polynomiality of H and E by using the double-distribution formalism as suggested by Radyushkin. In this way the polynomiality condition is automatically satisfied even with a non-vanishing dependence on ξ (cf. figure 2.9).

Using the profile function

$$h(\beta,\alpha) = \frac{\Gamma(3b+2)}{2^{2b+1}\Gamma^2(b+1)}\frac{[(1-|\beta|)^2-\alpha^2]^b}{(1-|\beta|)^{2b+1}} \tag{2.51}$$

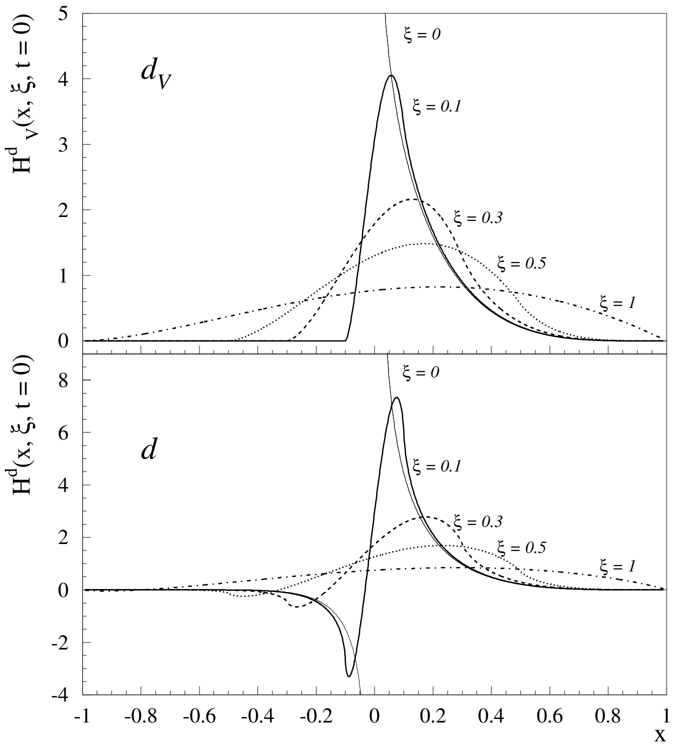

Figure 2.9.: The GPD $H^{d/p}$ for various values of ξ (taken from reference [VGG99]). For $\xi \neq 0$ the double-distribution formalism with $b = 1$ is used according to equations 2.52 to 2.54.

with an arbitrary parameter $b > 0$ the skewed (i.e. ξ-dependent) GPDs can be written in terms of the unskewed ones as

$$H^{q/p}_{DD}(x,\xi,t) = \int_{-1}^{1} d\beta \int_{-1+|\beta|}^{1-|\beta|} d\alpha\delta(x-\beta-\alpha\xi)h(\beta,\alpha)H^{q/p}(x,\xi,t), \tag{2.52}$$

$$\tilde{H}^{q/p}_{DD}(x,\xi,t) = \int_{-1}^{1} d\beta \int_{-1+|\beta|}^{1-|\beta|} d\alpha\delta(x-\beta-\alpha\xi)h(\beta,\alpha)\tilde{H}^{q/p}(x,\xi,t), \tag{2.53}$$

$$E^{q/p}_{DD}(x,\xi,t) = \int_{-1}^{1} d\beta \int_{-1+|\beta|}^{1-|\beta|} d\alpha\delta(x-\beta-\alpha\xi)h(\beta,\alpha)E^{q/p}(x,\xi,t). \tag{2.54}$$

Since the pion pole contribution to $\tilde{E}$ has an intrinsic dependence on ξ no changes are made for this GPD. For the other GPDs also the t-dependence is quite unclear: Some authors suggest a Regge-inspired ansatz instead of the formfactors used here. It is also not expected that the dependence on t factorises at all at large values of t; there may even be a different t-dependence for valence quarks and sea-quarks. But these statements are in general true for all present models.

Only after some time it was noticed that although the double-distribution formalism fulfils the polynomiality condition, the highest allowed coefficients $h^{q,n}_{n+1}$ and $e^{q,n}_{n+1}$ are automatically set to zero. These coefficients can be reobtained by introducing the so-called D-term $D^q(\frac{x}{\xi})$ into the double distribution formalism; it is an odd function that only contributes to the GPDs E^q and H^q:

$$H^{q/p}_{DT}(x,\xi,t) \quad = \quad H^{q/p}_{DD}(x,\xi,t) + \theta\left(1-\frac{x^2}{\xi^2}\right) D^q\left(\frac{x}{\xi}\right), \tag{2.55}$$

$$E^{q/p}_{DT}(x,\xi,t) \quad = \quad E^{q/p}_{DD}(x,\xi,t) - \theta\left(1-\frac{x^2}{\xi^2}\right) D^q\left(\frac{x}{\xi}\right). \tag{2.56}$$

For any value of ξ and t this leads to

$$e^{q,n}_{n+1} = -h^{q,n}_{n+1} = \int_{-1}^{1} dz\, z^n D^q(z). \tag{2.57}$$

The D-term is essentially unknown; calculations within the chiral quark-soliton model predict that $D^u(z) \approx D^d(z)$ and hence the D-term can be reduced to the quantity

$$D^q(z) = \frac{1}{2} D(z), \tag{2.58}$$

where the number of active flavours (i.e. 2) gives the denominator. A parametrisation of the D-term obtained from the chiral quark-soliton model is given in [GPV01] for $t = 0$:

$$D(z) = (1-z^2)[-4.0C_1^{3/2}(z) - 1.2C_3^{3/2}(z) - 0.4C_5^{3/2}(z) + \ldots]. \tag{2.59}$$

In this equation the Gegenbauer-polynomials are

$$C_0^{(\lambda)}(z) \quad = \quad 1, \tag{2.60}$$

$$C_1^{(\lambda)}(z) \quad = \quad 2\lambda z, \tag{2.61}$$

$$C_2^{(\lambda)}(z) \quad = \quad -\lambda + 2\lambda(1+\lambda)z^2, \tag{2.62}$$

with the recurrence relation

$$nC_n^{(\lambda)}(z) = 2(n+\lambda-1)zC_{n-1}^{(\lambda)}(z) - (n+2\lambda-2)C_{n-2}^{(\lambda)}(z). \tag{2.63}$$

The chiral quark soliton model implies a very low scale of about $\mu^2 \approx 0.36$ GeV^2. Evolution to the typical scale at HERMES of about $Q^2 \approx 4$ GeV^2 can reduce the absolute value of the Gegenbauer-coefficients by more than 25%. But this depends also on the treatment of unknown gluon contributions during evolution [BMK02].

As the D-term exists only in the ERBL-region, it does not contribute in the forward limit $\xi \to 0$. In addition the D-term as an odd function drops out when integrating over x, hence also the t-dependence of the D-term is unconstraint by the nucleon formfactors. It was argued that the D-term is needed to produce a sizable beam-charge-asymmetry in DVCS [GPV01], but other authors obtain similar effects by using different t-dependences for valence quarks and sea-quarks [Mül03]. In the sum $H^q + E^q$ (cf. Ji's sumrule) the D-term drops out; as this combination is not accessible in the usual observables, the D-term will still be needed to understand the experimental results.

2.5. Non-standard GPDs

So far the discussion of the GPDs was focused on flavour-diagonal GPDs, as in DVCS the returning quark naturally has to be of the same flavour as the emitted quark. However, especially in hard exclusive production of charged mesons it is obvious that this is not the general case. As long as u and d-quarks are exchanged with each other there is no difficulty, as the occurring matrix elements can be related to flavour-diagonal matrix-elements by $SU(2)_f$ symmetry [FPPS99]. For example this implies the relation

$$\langle n|\bar{d}u|p\rangle = \langle p|\bar{u}u|p\rangle - \langle p|\bar{d}d|p\rangle \tag{2.64}$$

which determines the creation of a $u\bar{d}$ state from the proton (spin indices have been omitted). This is the reason, why hard exclusive electroproduction of light mesons can be related to various flavour-combinations of the different GPDs.

This situation changes if the meson contains a strange quark. Although it may still be possible to use $SU(3)_f$ relations to derive the flavour non-diagonal GPDs in terms of the flavour diagonal ones, here the GPDs for the strange quark cannot be set to zero as done in the above mentioned models. On the other hand due to $SU(3)_f$ breaking effects ($\propto m_s$) additional unknown functions may enter that are not related to the flavour-diagonal GPDs of the proton [GPV01].

A different situation is encountered for decuplet baryons in the final state. Even if the transition is flavour-diagonal, the final state nucleon has more degrees of freedom due to its spin of 3/2. In total 6 GPDs H_M, H_E, H_C, C_1, C_2 and C_3 are required for each flavour, where the later 3 GPDs are quark-helicity dependent. In the limit of a large number of colours N_c only three of these GPDs are non-zero and furthermore related to nucleon GPDs [GPV01]:

$$H_M(x,\xi,t) = \frac{2}{\sqrt{3}}[E^u(x,\xi,t) - E^d(x,\xi,t)], \tag{2.65}$$

$$C_1(x,\xi,t) = \sqrt{(}3)[\tilde{H}^u(x,\xi,t) - \tilde{H}^d(x,\xi,t)], \tag{2.66}$$

$$C_2(x,\xi,t) = \frac{\sqrt{3}}{4}[\tilde{E}^u(x,\xi,t) - \tilde{E}^d(x,\xi,t)]. \tag{2.67}$$

Models for these GPDs are important to clarify the background situation in all present experiments [GMV03]. Obviously this method can be extended to other nucleon- or Delta-resonances as well, however a full decomposition into nucleon resonances with different quantum numbers is required.

Close to single-pion production threshold the $N \to N\pi$ transition GPDs can be expressed in terms of nucleon and pion GPDs. In this region chiral perturbation is applicable.

It has been mentioned that the evolution of the GPDs is subject to gluon-contributions. This happens in a similar way as in the scaling-violations for the inclusive structure functions $F_1(x_B)$ and $g_1(x_B)$. At twist 2 level there are 4 Generalised Gluon distributions that can be defined as matrix elements involving the gluon field strength tensor in a similar way as done for the quarks. The nucleon helicity conserving Generalised Gluon Distributions (GGDs) are called $H^g(x,\xi,t), E^g(x,\xi,t)$, the helicity-flip GGDs are called $\tilde{H}^g(x,\xi,t)$ and $\tilde{E}^g(x,\xi,t)$. In the limit of $\xi = 0$ and $t = 0$ the functions H^g and $\tilde{H}^g$ are related to the forward gluon distributions

Table 2.1.: Leading twist GPDs for nuclear targets.

Spin	Targets	GPDs
0	π, ^{4}He, ^{20}Ne	H
$\frac{1}{2}$	p, n	$H, \tilde{H}, E, \tilde{E}$
1	^{2}D	$H_1, H_2, H_3, H_4, H_5, \tilde{H}_1, \tilde{H}_2, \tilde{H}_3, \tilde{H}_4,$

by

$$H^g(x,0,0) = g(x), \tag{2.68}$$
$$\tilde{H}^g(x,0,0) = -x\Delta g(x). \tag{2.69}$$

Apart from the indirect effect in the evolution equations, the GGDs can enter directly in the production of vector-mesons. In the region of small values of x_B, where this contribution becomes important, it is often assumed that skewing effects can be neglected. Hence model calculations [FKS96] are often directly referring to the forward gluon distributions.

The treatment of all processes as described until now is only valid on the level of a Twist-2 calculation (i.e. order of $(1/Q)^0$). At order $(1/Q)$ eight additional GPDs contribute that arise for each quark-flavour. Using the notation of [BMK02] they are called $H^3_+, E^3_+, \tilde{H}^3_-, \tilde{E}^3_-, \tilde{H}^3_+, \tilde{E}^3_+, H^3_-$ and E^3_-. Each of these GPDs "$F^3_\pm$" can be split into a part that is fully determined by the twist-2 GPDs (Wandzura-Wilczek part) and a genuine twist-3 part that is related to antiquark-gluon-quark correlations:

$$F^3_\pm = F^{WW}_\pm + F^{qGq}_\pm. \tag{2.70}$$

Estimates within the instanton model of the QCD-vacuum suggest that the genuine twist-3 part is much smaller than the twist-2 induced contributions. Hence in the Wandzura-Wilczek-approximation the part arising from the distribution $F^{qGq}_\pm$ is neglected; the quality of this approximation has turned out to be very good in the measurements of the structure function g_2 [E15503].

In addition to these quark-GPDs an additional contribution from the gluons is possible at twist-3-level. This "gluon transversity" can be parametrised in terms of 4 functions $H_T, E_T, \tilde{H}_T$ and $\tilde{E}_T$. Their behaviour is at the moment completely unconstrained.

2.6. GPDs for Deuterium and other Nuclear Targets

Some modifications have to be made in the case of nuclear targets. In many cases nuclear targets have spin quantum numbers much larger than $\frac{1}{2}$. Until now GPDs have explicitly been introduced only for targets with spin 0, $\frac{1}{2}$ and 1. They are listed in table 2.1.

In this case it is always assumed that the nucleus does not break up during interaction. Also excited states of the nucleus should not appear in the final state as otherwise transition GPDs like for $p \to \Delta$ will be required.

Since the data analysis will later deal with deuterium data, the following discussion will focus only on this nucleus. A GPD-model for the deuteron has been explicitly worked out by Müller and Kirchner [KM03]. As in the case of hydrogen the model has to fulfil certain boundary conditions. First of all the symmetry of the GPDs is known: The GPDs H_1, H_2, H_3, H_5, $\tilde{H}_1$, $\tilde{H}_2$ and $\tilde{H}_4$ are symmetric in x, while the GPDs H_4 and $\tilde{H}_3$ are antisymmetric. In addition they can be related to the formfactors of the deuteron in the following way:

$$\sum_q e_q \int_{-1}^{1} dx H_k^{q,D}(x, \xi_A, t, Q^2) = G_k(t) \qquad \text{for } k = 1 \ldots 3, \tag{2.71}$$

$$\int_{-1}^{1} dx H_k^{q,D}(x, \xi_A, t, Q^2) = 0 \qquad \text{for } k = 4, 5, \tag{2.72}$$

where ξ_A is defined by

$$\xi_A \approx \frac{x_A}{2 - x_A} \tag{2.73}$$

in analogy to the definition of ξ.

The formfactors G_1, G_2 and G_3 used in this notation can be derived from the charge formfactor G_E, the magnetic formfactor G_M and the electrical quadrupole formfactor G_C of the deuteron. While G_E and G_M can be measured in the scattering of electrons off unpolarised deuterium, the formfactor G_C is only accessible if the target is polarised. There have also been many other suggestions how to define formfactors for the deuteron (cf. [AKP01, KS95, KM03]).

The 3 formfactors G_1, G_2 and G_3 are shown in figure 2.10. The following normalisation is used:

$$G_1(0) = 1, \tag{2.74}$$

$$G_2(0) = \mu_D, \tag{2.75}$$

$$G_3(0) = \mu_D + Q_D - 1, \tag{2.76}$$

where μ_D denotes the magnetic moment and Q_D the electrical quadrupole moment of the deuteron.

Nothing is experimentally known about the axial formfactors $\tilde{G}_1$ and $\tilde{G}_2$, but still the following relation has to be fulfilled:

$$\sum_q e_q \int_{-1}^{1} dx \tilde{H}_k^{q,D}(x, \xi_A, t, Q^2) = \tilde{G}_k(t) \qquad \text{for } k = 1, 2, \tag{2.77}$$

$$\int_{-1}^{1} dx \tilde{H}_3^{q,D}(x, \xi_A, t, Q^2) = 0. \tag{2.78}$$

In addition the forward limit of the GPDs H_1, H_5 and $\tilde{H}_1$ is known:

$$H_1^{q,D}(x, 0, 0) = q^D(x), \tag{2.79}$$

$$H_5^{q,D}(x, 0, 0) = \delta q^D(x), \tag{2.80}$$

$$\tilde{H}_1^{q,D}(x, 0, 0) = \Delta q^D(x), \tag{2.81}$$

where q^D and Δq^D are the usual parton distributions and quark helicity distributions, respectively, and δq^D can be written as

$$\delta q^D(x) = q^0(x) - \frac{1}{2}\{q^+(x) + q^-(x)\} \tag{2.82}$$

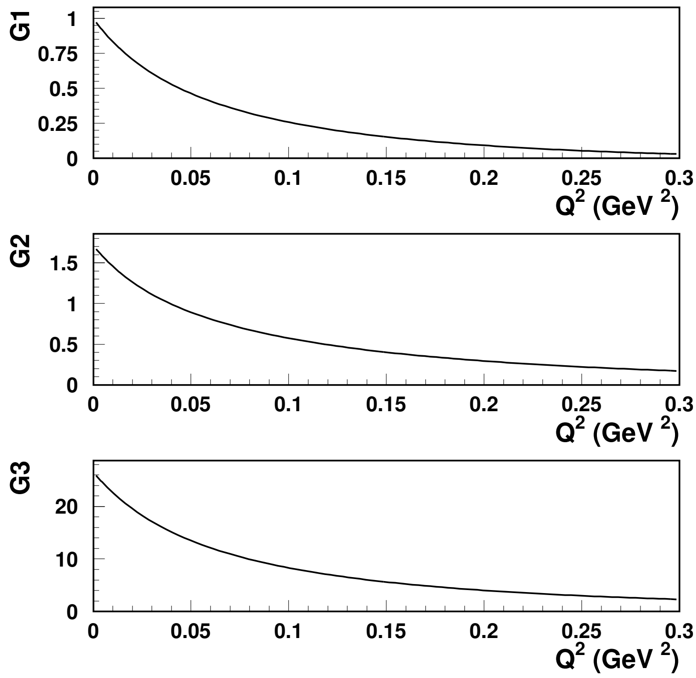

Figure 2.10.: Formfactors G_1, G_2 and G_3 of the deuteron according to the parametrisation given in [KS95] and the notation of [KM03].

in terms of the quark densities for the 3 possible spin states of the target nucleus. $\delta q^D(c)$ should not be confused with the transverse parton distributions that are often denoted as $\delta q(x)$. The following convention applies for the treatment of antiquarks:

$$\bar{q}^D(x) = -q^D(-x), \tag{2.83}$$

$$\delta\bar{q}^D(x) = -\delta q^D(-x), \tag{2.84}$$

$$\Delta\bar{q}^D(x) = \Delta q^D(-x). \tag{2.85}$$

δq^D can have a non-zero value due to shadowing/anti-shadowing effects and is related to b_1 of the nucleon by $b_1 = \sum_q e_q^2 \delta q^D$. Measurements of this structure function at HERMES indicate that b_1 is small in the valence region and rises towards low values of x_B [HERMES]. For the typical x_B region that can be observed in exclusive reactions at HERMES it may be a good approximation to set $\delta q^D = 0$ and thus $H_5^{q,D} = 0$.

In order to relate the deuteron parton and gluon distributions of the kind H_1^D to the GPDs of the proton, the following ansatz can be used:

$$\begin{aligned} H_1^{u_{val},D}(x,\xi_A,t) &= F^{u_{val},D}(t)\left|\frac{dx_N}{dx}\right|\theta(1-x_N^2)\times \\ & [H^{u_{val}}+H^{d_{val}}](x_N,\xi_N,t=0), \quad (2.86)\\ H_1^{d_{val},D}(x,\xi_A,t) &= F^{d_{val},D}(t)\left|\frac{dx_N}{dx}\right|\theta(1-x_N^2)\times \\ & [H^{d_{val}}+H^{u_{val}}](x_N,\xi_N,t=0), \quad (2.87)\\ H_1^{i_{sea},D}(x,\xi_A,t) &= F^{sea,D}(t)\left|\frac{dx_N}{dx}\right|\theta(1-x_N^2)2H^{i_{sea}}(x_N,\xi_N,t=0), \quad (2.88)\\ H_1^{g,D}(x,\xi_A,t) &= F^{g,D}(t)\left|\frac{dx_N}{dx}\right|\theta(1-x_N^2)2H^{g}(x_N,\xi_N,t=0), \quad (2.89)\end{aligned}$$

where in this model the valence-quark distributions $H_1^{u_{val},D}(x,\xi_A,t)$ and the sea-quark distributions $H_1^{i_{sea},D}(x,\xi_A,t)$ with $i=u,d$ are considered separately. The analogous relation can be used to obtain $\tilde{H}_1^{i,D}(x,\xi_A,t)$ from $\tilde{H}^i(x,\xi,t)$. x_N is defined as

$$x_N = \frac{2x}{1-\xi_A} \quad (2.90)$$

and ξ_N is defined as

$$\xi_N = \frac{2\xi_A}{1-\xi_A}. \quad (2.91)$$

This notation is consistent with the definitions of reference [KM03] expect for the replacements $\eta \to -\xi_A$ and $\eta_N \to -\xi_N$. The GPDs are defined as functions of ξ_A instead of $\eta = -\xi_A$ to conform to the usual definitions for the proton GPDs.

In addition to H_5 the GPD H_3 probes the binding force of the deuteron. Very different models are possible: H_3 can be equal to zero (as assumed above) but also be as big as H_1. All other GPDs are essentially unconstrained but can be set to zero as their contribution to the DVCS amplitude is kinematically suppressed.

There are also other GPD models for the deuteron [CP04]. In addition the GPDs of heavy spinless nuclei have been derived in [GS03].

2.7. Exclusive Meson Production

At HERMES energies the cross-sections for hard exclusive production of light mesons can be calculated using the GPDs. It was shown by Collins et al. [Col98] that the process factorises into a combination of GPDs that is denoted as $F(x,\xi,t,\mu)$, a hard scattering amplitude $\mathrm{H}(\mathrm{x},\xi,\mathrm{Q}^2,\mu)$ to be determined in pQCD and the meson distribution amplitude (DA) denoted as $\Phi(z,\mu)$. One handbag graph for this process is shown in figure 2.11(left); it is usually referred to as Quark-Exchange Mechanism (QEM) and is expected to dominate at HERMES kinematics. Due to the factorisation theorem the amplitude of this process is obtained in the following way:

$$\mathcal{M} \propto \sum_i \int_0^1 dz \int_{-1}^{+1} dx\, F_i(x,\xi,t,\mu)\mathrm{H_i}(\mathrm{x},\xi,\mathrm{Q}^2,\mu)\Phi(\mathrm{z},\mu). \quad (2.92)$$

The leading twist distribution amplitude $\Phi(z,\mu)$ describes the probability amplitude to create a meson from the QCD-vacuum if a quark-antiquark-pair with relative momentum fractions z and $1-z$ has been generated by some process [BBKT98]. $\Phi(z,\mu)$ as well as $F(x,\xi,t,\mu)$ depend on the hard scale μ. This is usually identified with $\sqrt{Q^2}$ but due to the additionally exchanged gluon this need not be the best choice. As the 4-momentum transfer of the gluon is not controlled by external kinematical variables, it can be much smaller than $\sqrt{Q^2}$. Hence, next-to-leading order corrections can be sizable and uncertainties may arise [BM01]. For vector mesons an additional contribution is possible from the Perturbative Two-Gluon Exchange Mechanism (PTGEM), which is also shown in figure 2.11(right). At HERMES kinematics this process is predicted to give a small contribution for the light vector-mesons which contain only u- and d-quarks. PTGEM is often identified with Pomeron exchange and governs the production of vectormesons at the HERA collider experiments [H100].

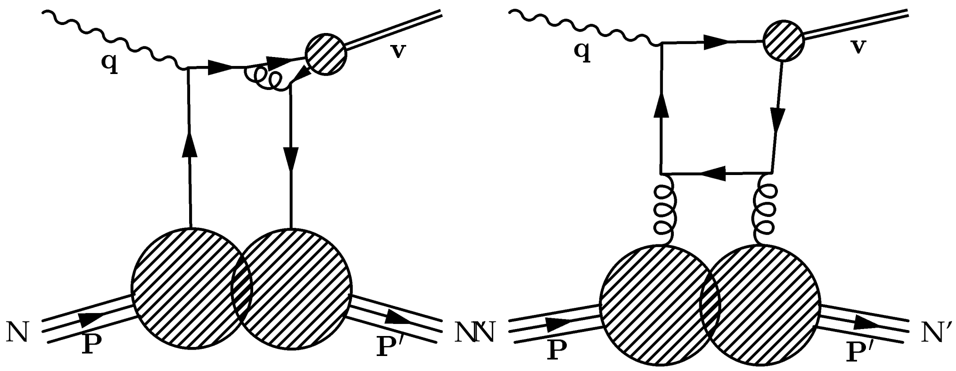

Figure 2.11.: Handbag diagrams for exclusive meson production: The virtual photon couples to a quark that is either directly emitted by the nucleon (Quark-Exchange Mechanism, left) or is created from the vacuum by coupling to gluons from the nucleon (Perturbative Two-Gluon Exchange Mechanism). Finally a meson m is formed; again the blob represents a non perturbative object $\Phi(z,\mu)$ and not a usual vertex.

The combinations of GPDs that enter in $F(x,\xi,t)$ for the individual meson production process are given in table 2.2. In addition the table contains parametrisations of the meson distribution amplitudes according to reference [GPV01]. The production of η-mesons involves strangeness and can also be related to GPDs if the axial anomaly is neglected [GPV01].

In all meson production processes the leading twist contribution corresponds to the absorption of virtual photons with longitudinal polarisation. Only in this case factorisation was proven to work and only in this case the cross-section is predicted to depend on twist-2 GPDs. In the case of vector-mesons one can exploit the self-analysing decay into spinless pions to obtain the polarisation of the vector-meson. Assuming s-channel helicity conservation (which was shown to work also at HERMES energies [Tyt01]) the helicity of the ρ^0 is almost entirely given by the helicity of the virtual photon, such that the contribution $\sigma_L(\gamma^* p \to \rho^0 p)$ can be obtained from the total cross-section. The ratio $R = \frac{\sigma_L}{\sigma_T}$ for ρ^0-production has been measured within a wide range in Q^2 [H100].

In the case of pion-production there is no such possibility. In principle a full Rosenbluth separation of σ_L and σ_T has to be done, but this would require different beam-energies with

Table 2.2.: GPD-combinations and Distribution amplitudes for the hard exclusive production of mesons presently studied at HERMES . In the given GPD-combinations H can be replaced by E and $\tilde{H}$ by $\tilde{E}$ to obtain the second combination that enters in $F(x,\xi,t)$.

Process	GPDs	DA
$p \to p\pi^0$	$e_u\tilde{H}^u - e_d\tilde{H}^d$	0.0924 GeV $\cdot 6\sqrt{2}z(1-z)$
$p \to n\pi^+$	$\tilde{H}^u - \tilde{H}^d$	0.0924 GeV $\cdot 6\sqrt{2}z(1-z)$
$p \to p\omega^0$	$e_uH^u + e_dH^d$	0.195 GeV $\cdot 6z(1-z)$
$p \to p\rho^0$	$e_uH^u - e_dH^d$	0.216 GeV $\cdot 6z(1-z)$
$p \to n\rho^+$	$H^u - H^d$	0.216 GeV $\cdot 6z(1-z)$

enough overlap in the observed kinematics. Especially at HERMES this is not possible. On the other hand the cross-section for transversely polarised photons is classified as twist-3 and consequently suppressed by one order of $1/Q$.

For all meson production processes rather high values of $Q^2 > 10$ GeV^2 are usually suggested in order to have sufficient virtuality of the exchanged gluon. These values are typically not reached at HERMES kinematics. As a solution it was proposed to use ratios of meson-production cross-sections. For example it was predicted [GPV01] that

$$\frac{\sigma_\eta}{\sigma_{\pi_0}} \approx \frac{2}{3} \cdots \frac{4}{5}. \tag{2.93}$$

In such ratios "precocious scaling" is expected to set in even at comparatively low values of Q^2. The experimental problem in this case is related to the different meson masses as well as to the fact that e.g. the ω^0 decays predominantly into a 4 particle final state (including 2 photons), while the ρ^0 only decays into two charged pions. Consequently the spectrometer acceptance can be very different as the spectrometer is not covering 4π in solid angle and very precise extrapolations would be required.

Also the measurement of kinematical dependencies of cross-sections is difficult due to the restricted phase-space. Although there are a number of meson production models that allow perfect fits inside the HERMES acceptance, the quality outside of the acceptance is unknown. E.g for exclusive π^+ production even a parametrisation of the type

$$\frac{d\sigma}{dx_B\, dQ^2\, dt} \propto \frac{1}{Q^4} e^{bt} \tag{2.94}$$

is rather successful. In the case of ρ^0-production also a generator that is based on pure gluon-exchange ([ALR97]) can reproduce the shape of the distributions, although the total predicted cross-section can be off by orders of magnitude.

2.8. Deeply Virtual Compton Scattering

Deeply Virtual Compton Scattering is in a way the cleanest process to study GPDs. On one hand no additional gluon exchange is needed and also no second non-perturbative object like the DA is required to describe the cross-section. On the other hand it is easier to ensure exclusivity of the reaction due to the interference with the Bethe-Heitler-process (BH). This fact will be discussed in more detail in the following two sections.

The Compton amplitude can be written as the sum of the amplitude $\mathcal{M}_{DVCS,f}$, for which the real photon is emitted by the quark after it has absorbed the virtual photon, and the amplitude $\mathcal{M}_{DVCS,i}$, for which the real photon is emitted first [VGG99]. The mathematical structure of both terms is similar and hence only $\mathcal{M}_{DVCS,f}$ will be discussed in more detail, while $\mathcal{M}_{DVCS,i}$ will be denoted by "crossed graph".

The expression for the Compton amplitude is (cf. also [Ji97]):

$$\begin{aligned}\mathcal{M} &= \mathcal{M}_{DVCS,f} + \mathcal{M}_{DVCS,i} \\ &= \sum_q \int \frac{d^4k}{(2\pi)^4}[(-ie\,e_q)\gamma^\nu \epsilon'^*_\nu i\frac{(\not{k}+\not{q})+m_q}{(k+q)^2-m_q^2+i\epsilon}(-ie\,e_q)\gamma^\mu\epsilon_\mu]_{\beta,\alpha} \\ &\quad \times\langle p's'|i\int d^4z\, e^{ikz}T\bar{q}_\beta(0)q_\alpha(z)|ps\rangle + \text{crossed graph} \qquad (2.95)\end{aligned}$$

where

- the sum is taken over all flavours q with fractional charge e_q,
- k is in this case the quark loop momentum,
- q is the 4-momentum of the virtual photon,
- $(-ie\,e_q)\gamma^\nu\epsilon'^*_\nu$ is the vertex factor for the virtual photon with polarisation vector ϵ'^* coupling to the quark,
- $i\frac{(\not{k}+\not{q})+m_q}{(k+q)^2-m_q^2+i\epsilon}$ is the quark propagator,
- $(-ie\,e_q)\gamma^\nu\epsilon_\nu$ is the vertex factor for the real photon with polarisation ϵ,
- $\langle p's'|i\int d^4z\, e^{ikz}T\bar{q}_\beta(0)q_\alpha(z)|ps\rangle$ is the soft matrix element (including the time-ordering operator T) that can then be expressed in terms of the GPDs.

In leading twist the result can be expressed in terms of the 4 GPDs $H, E, \tilde{H}$ and $\tilde{E}$. Again the process factorises into a soft part described by the GPDs and the hard part of the quark-photon interaction, which is calculable in perturbative field theory. The validity of this factorisation theorem was proven by Collins [CF99] in 1998.

Due to this factorisation, the amplitude of this process is very similar to the invariant amplitude that is obtained in the derivation of the Klein-Nishina formula for the Compton effect [AH89]:

$$\mathcal{M} = e^2\epsilon'^*_\nu\epsilon'_\mu\bar{u}'\gamma^\nu\frac{(\not{k}+\not{q})+m_e}{(k+q)^2-m_e^2+i\epsilon}\gamma^\mu u + \text{crossed graph}, \qquad (2.96)$$

where k is the lepton 4-momentum and q the 4-vector of the real photon. u and u' denote the spinors of the incoming and outgoing lepton. As these spinors are fixed from outside, neither the unknown matrix-element nor the integral over the loop-momentum is required. This process is then exactly calculable in QED.

In the case of DVCS the final result can be expressed in terms of the 4 Compton formfactors of the nucleon. Each formfactor is a complex function that depends on the sum over all quark flavours of the related GPD. The Compton formfactors for the proton are denoted as $\mathcal{H}, \mathcal{E}, \tilde{\mathcal{H}}$ and $\tilde{\mathcal{E}}$ and can be calculated as:

$$\Im\mathfrak{m}\mathcal{H} = -\pi \sum_q e_q^2 (H^q(\xi,\xi,t) - H^q(-\xi,\xi,t)), \tag{2.97}$$

$$\Im\mathfrak{m}\tilde{\mathcal{H}} = -\pi \sum_q e_q^2 (\tilde{H}^q(\xi,\xi,t) + \tilde{H}^q(-\xi,\xi,t)), \tag{2.98}$$

$$\Re\mathfrak{e}\mathcal{H} = \sum_q e_q^2 \left[\mathcal{P} \int_{-1}^{+1} H^q(x,\xi,t)(\frac{1}{x-\xi} + \frac{1}{x+\xi})\, dx \right], \tag{2.99}$$

$$\Re\mathfrak{e}\tilde{\mathcal{H}} = \sum_q e_q^2 \left[\mathcal{P} \int_{-1}^{+1} \tilde{H}^q(x,\xi,t)(\frac{1}{x-\xi} - \frac{1}{x+\xi})\, dx \right], \tag{2.100}$$

where $\mathcal{P}$ denotes Cauchy's principle value.

The results for $\mathcal{E}$ and $\tilde{\mathcal{E}}$ depend on E and $\tilde{E}$ in the same way. At leading twist the unpolarised lepto-production cross-section for DVCS is then proportional to the following combination of formfactors:

$$c_{0,up}^{DVCS} = 2(2-2y+y^2)\mathcal{C}_{up}^{DVCS}, \tag{2.101}$$

$$\begin{aligned} \mathcal{C}_{up}^{DVCS} = {} & \frac{1}{(2-x_B)^2}\{4(1-x_B)(\mathcal{H}\mathcal{H}^* + \tilde{\mathcal{H}}\tilde{\mathcal{H}}^*) - x_B^2(\mathcal{H}\mathcal{E}^* + \mathcal{E}\mathcal{H}^* + \tilde{\mathcal{H}}\tilde{\mathcal{E}}^* + \tilde{\mathcal{E}}\tilde{\mathcal{H}}^*) - \\ & (x_B^2 + (2-x_B)^2 \frac{t}{4M^2})\mathcal{E}\mathcal{E}^* - x_B^2 \frac{t}{4M^2}\tilde{\mathcal{E}}\tilde{\mathcal{E}}^*\}. \end{aligned} \tag{2.102}$$

Naturally $\sigma \propto |\mathcal{M}|^2$ such that quantities of the kind $\mathcal{F}\mathcal{F}^*$ appear in the result. The problem with this fact is, that e.g. in the product $\mathcal{H}\mathcal{H}^*$ the real part of the formfactor, which is obtained from an integral of $\sum_q H^q(x,\xi,t)$ over x, is mixed with the imaginary part of the formfactor, that is obtained from $\sum_q H^q(x,\xi,t)$ at $x=\xi$. This makes it difficult to extract any knowledge about the GPDs by measuring $\mathcal{C}_{up}^{DVCS}$ or its target polarisation dependent counterparts.

The situation gets even more complicated if higher twist contributions are included. At leading twist there is no explicit dependence of the cross-section on the angle ϕ such that the cross-section is radially symmetric with respect to the direction of the vector q. Moreover the cross-section does not depend on the polarisation of the lepton beam. This is changed when the twist-3 contributions are included. In this case the cross-section for an unpolarised target receives a $\sin(\phi)$ moment that depends on the lepton helicity. This moment as well as the $\cos(\phi)$ moment depend on the "ordinary twist-3" contribution in equation 2.70, while an additional $\cos(2\phi)$ moment also receives contributions from gluon transversity that is also classified as twist-3. As only the combination $F_+^3 - F_-^3$ of twist-3 GPDs enters in the DVCS amplitudes, this means that up to twist-3 there are 12 independent Compton Form-Factors to be measured.

In the case of nuclear targets, only the scalar target has been explicitly worked out to twist-3 accuracy. In this case one additional GPD enters to describe the quark-gluon-antiquark-correlations. For spin 1 targets only the leading twist calculations have been done so far. The expressions get lengthy and can be looked up in reference [KM03].

2.9. Bremsstrahlung

As has been mentioned Bremsstrahlung is a different process that leads to the same final state as DVCS, but in this case the photon is emitted by the scattered electron. Following the notation from reference [E+01] this is due to the four Feynman diagrams shown in figure 2.12. The amplitudes $\mathcal{M}_{ei}$ and $\mathcal{M}_{ef}$ correspond to initial state radiation and final state radiation from the lepton, respectively; $\mathcal{M}_{pi}$ and $\mathcal{M}_{pf}$ denotes initial and final state radiation by the nucleon. For the first 2 amplitudes the situation is clear, since the electromagnetic vertex of the nucleon can be strictly expressed in terms of a vertex factor, that suppresses the process at large values of $|t|$:

$$\Gamma^{\mu}(\mathbf{q}) = F_1(q^2)\gamma^{\mu} + \frac{1}{2M}F_2(q^2)i\sigma^{\mu\nu}q_{\nu}, \tag{2.103}$$

where F_1 denotes the Dirac-formfactor and F_2 the Pauli-formfactor. Using the lepton spinor u, the Nucleon spinor N and the photon polarisation vector ϵ the first 2 amplitudes are then:

$$\mathcal{M}_{ei} = i\bar{u}(k')\gamma^{\mu}\left[\frac{i(\not{k}-\not{v})+m_e}{(k-v)^2-m_e^2}\right]e\gamma^{\nu}\epsilon_{\nu}u(k)\frac{e^2}{t}\bar{N}(P')\Gamma_{\mu}(\Delta)N(P), \tag{2.104}$$

$$\mathcal{M}_{ef} = i\bar{u}(k')e\gamma^{\nu}\epsilon_{\nu}\left[\frac{i(\not{k}'+\not{v})+m_e}{(k'+v)^2-m_e^2}\right]\gamma^{\mu}u(k)\frac{e^2}{t}\bar{N}(P')\Gamma_{\mu}(\Delta)N(P) \tag{2.105}$$

with the 4-vectors defined in section 2.1.

At HERMES energies the lepton mass m_e can be neglected. In this case the quantities P_1 and P_2 are defined from the denominators of the lepton propagators according to $(k-v)^2 \equiv Q^2P_1$ and $(k'+v)^2 = (k-\Delta)^2 \equiv Q^2P_2$, respectively. Obviously the propagators can cause a divergence in the cross-section if $\mathbf{v}$ is collinear with either $\mathbf{k}$ or $\mathbf{k}'$. These are the domains, where the cross-section is dominated by one of these processes.

On the other hand there is the additional propagator of the virtual photon, such that both terms depend on $\frac{1}{t}$. Also the formfactors are at their maximum for $t \to 0$, hence an additional peak will show up at low values of $|t|$. This is the reason, why the BH cross-section peaks along the direction of the vector $\vec{q}$ although this direction does not coincide with the direction of a virtual photon as in DVCS. The full calculation shows that lepton energies much larger than the nucleon mass are required to produce a clear enhancement. Under these conditions the results of calculations in terms of peaking approximations for initial and final state radiation are wrong as soon as $t \to 0$.

The two other processes are more problematic. The graphs do not really tell which kind of intermediate state propagates between the two photons coupling to the nucleon. Without any special knowledge about the possible hadronic excitation the first (but not necessarily correct) ansatz would be to treat the proton as an elementary fermion with the usual vertex factor Γ:

$$\mathcal{M}_{pi} = i\bar{N}(P')\Gamma^{\mu}(q)\left[\frac{i(\not{P}-\not{v})+M}{(P-v)^2-M^2}\right](-e)\Gamma^{\nu}(v)\epsilon_{\nu}N(P)\frac{e^2}{q^2}\bar{u}(k')\gamma_{\mu}u(k), \tag{2.106}$$

$$\mathcal{M}_{pf} = i\bar{N}(P')(-e)\Gamma^{\nu}(v)\epsilon_{\nu}\left[\frac{i(\not{P}'+\not{v})+M}{(P'+v)^2-M^2}\right]\Gamma^{\mu}(q)N(P)\frac{e^2}{q^2}\bar{u}(k')\gamma_{\mu}u(k). \tag{2.107}$$

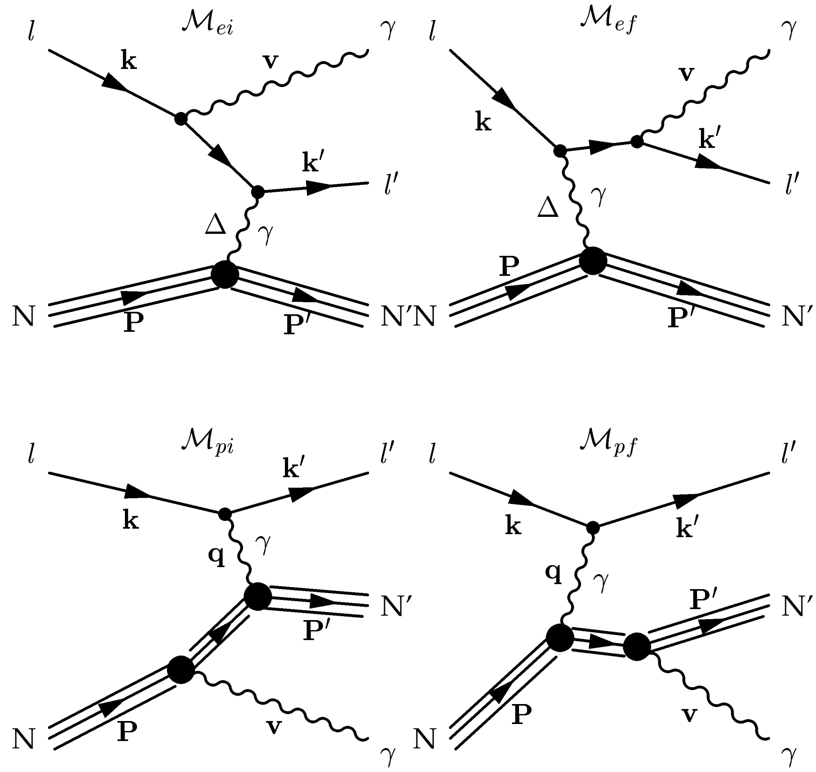

Figure 2.12.: Bethe-Heitler process: The 4 shown diagrams contribute to the Bethe-Heitler process: The amplitude $\mathcal{M}_{ei}$ correspond to initial state radiation from the lepton, $\mathcal{M}_{ef}$ is final state radiation, $\mathcal{M}_{pi}$ is initial state radiation by the nucleon and $\mathcal{M}_{pf}$ is final state radiation by the nucleon.

In addition the same approach can be made for higher order diagrams in which 2 virtual photons are exchanged instead of one. These contributions are necessary to cure the infrared divergence for $Q^2 \to 0$ (for technical details see [E$^+$01]).

Although it can be argued that the given amplitudes for photon emission by the nucleon should be valid for low values of W^2 it has been noticed recently that modifications to this leading order behaviour occur due to the generalised polarisabilities of the nucleon. It was shown that below pion emission threshold an additional non-Born type amplitude arises that can be parametrised in terms of 6 of these Q^2-dependent functions [V$^+$00]. The process is known as Virtual Compton Scattering (VCS) and has been extensively studied at MAMI [VCS00].

In the kinematic domain of DVCS the contribution of these processes, in which an intermediate proton propagates, is strongly suppressed. On the one hand the requirement of $W^2 > 4$ GeV implies a proton for the graph $\mathcal{M}_{pf}$ that is far off-shell, such that the proton propagator gets small. On the other hand the propagator of the virtual photon is $\frac{1}{Q^2}$ for both amplitudes $\mathcal{M}_{pi}$ and $\mathcal{M}_{pf}$. Hence the requirement of large values of Q^2 adds an additional suppression. Consequently the two amplitudes $\mathcal{M}_{pi}$ and $\mathcal{M}_{pf}$ as defined above can be neglected and the dominant mechanism for hadronic initial or final state radiation under these conditions is DVCS.

One of the first complete field-theoretical calculations for Bremsstrahlung was done by Mo and Tsai in 1969 [MT69]. They also derived the cross-section for Bremsstrahlung with excitation of resonances or even an inelastic breakup of the nucleon. Since then some research has been done to check if their approach was correct. Especially the contribution of multiple photon emission was predicted to be sizable by some authors [Cha80]. In 1983 EMC showed that the predicted excess of photons could not be found [Muon84]. Quite interestingly the measurement at values of $0.5 < y < 0.9$ did not show any contributions from DVCS either, although it is not clear how sensitive the experiment would have been to that. Later measurements apparently confirmed the approach taken by Mo and Tsai [E$^+$01].

As the Bethe-Heitler process is an important contamination to measurements of the polarisation dependent structure functions of the nucleon, until recently considerable theoretical work has been spent (e.g. [AIS$^+$97]) to provide these calculations also for polarised beam and target particles. In principle the same formulae can also be used for nuclear targets, where the nuclear masses and formfactors have to be inserted. The more complicated case of a spin-1 target has been explicitly calculated in [KM03].

Higher order radiative corrections still pose an uncertainty in the calculations. In general it can be expected that numerous low energy photons ($E_\gamma \ll 1$ GeV) will be radiated in addition to the high energy photon. Evidence for multiple photon emission has been reported in reference [TVFS00]. Furthermore loop corrections will directly modify the cross-section for single photon emission.

The implications for observables like asymmetries are unclear. However it has been discussed that higher order processes with additional virtual photon exchanges can also lead to a beam charge asymmetry of the BH cross-section (cf. [MT69]).

2.10. Interference with Bremsstrahlung

As has been shown in the previous section, DVCS is only a special case of initial or final state radiation by the nucleon. As a consequence the invariant amplitude for Bremsstrahlung including DVCS has to be calculated by

$$\mathcal{M} = \mathcal{M}_{ei} + \mathcal{M}_{ef} + \mathcal{M}_{DVCS,i} + \mathcal{M}_{DVCS,f}. \tag{2.108}$$

The cross-section is then given by

$$d\sigma = \frac{|\mathcal{T}|^2}{4\sqrt{(k^\mu P_\mu)^2 - m_e^2 M^2}} \frac{1}{(2\pi)^5} \delta^4(k + P - k' - P' - v) \frac{d^3k'}{2E'} \frac{d^3P'}{2E'_P} \frac{d^3v}{2E_\gamma}, \tag{2.109}$$

where $\mathcal{T}$ denotes the matrix element $\mathcal{M}$ summed over the final spin states and suitably balanced for the incoming spin-states. For a fixed-target experiment the cross section is [BMK02]

$$\frac{d\sigma}{dx_B\, dQ^2\, dt\, d\phi} = \frac{\alpha^3 x_B y}{16\pi^2 Q^2 \sqrt{1+\epsilon^2}} \cdot \frac{2\pi y}{Q^2} \cdot \left|\frac{\mathcal{T}}{e^3}\right|^2, \tag{2.110}$$

where $\epsilon = 2x_B \frac{M}{\sqrt{Q^2}}$ and

$$|\mathcal{T}|^2 = |\mathcal{T}_{BH}|^2 + |\mathcal{T}_{DVCS}|^2 + \mathcal{I}. \tag{2.111}$$

This decomposition directly implies that the interference term $\mathcal{I}$ is constrained by the Cauchy-Schwarz inequality:

$$\mathcal{I}^2 \leq 4|\mathcal{T}_{BH}|^2|\mathcal{T}_{DVCS}|^2 \tag{2.112}$$

Consequently in a logarithmic plot the logarithm of the cross-section of the interference term may not be much larger than then mean value $\frac{1}{2}(\log\sigma_{DVCS} + \log\sigma_{BH})$. Many existing models do not fulfil this requirement outside the region of their applicability.

The three contributions can be split into harmonic functions in ϕ according to:

$$\begin{aligned}
|\mathcal{T}_{BH}|^2 &= \frac{e^6}{x_B^2 y^2(1+\epsilon^2)^2 t P_1(\phi)P_2(\phi)} \times \\
&\quad \{c_0^{BH} + \sum_{n=1}^{2} c_n^{BH}\cos(n\phi) + s_1\sin(\phi)\}, &(2.113)\\
|\mathcal{T}_{DVCS}|^2 &= \frac{e^6}{y^2Q^2}\{c_0^{DVCS} + \sum_{n=1}^{2} c_n^{DVCS}\cos(n\phi) + \sum_{n=1}^{2} s_n^{DVCS}\sin(n\phi)\}, &(2.114)\\
\mathcal{I} &= \frac{\pm e^6}{x_B y^3 t P_1(\phi)P_2(\phi)}\{c_0^I + \sum_{n=1}^{3} c_n^I\cos(n\phi) + \sum_{n=1}^{3} s_n^I\sin(n\phi)\}, &(2.115)
\end{aligned}$$

where the negative sign of the interference term corresponds to positive beam charge and the positive sign to negative beam charge. Although this decomposition is the same as given in reference [BMK02], the signs of the coefficients are different due to the different definition of the angle ϕ. As $\phi_{\mathrm{BMK}} = \pi - \phi$, odd cosine coefficients as well as even sine coefficients have a flipped sign with respect to this reference.

A further decomposition is possible that depends on the target polarisation. Picture 2.13 illustrates the situation in the target rest-frame. Two angles enter in addition: The polar angle θ_s between the target polarisation vector $\vec{S}$ and the virtual photon and the azimuthal angle ϕ_s that gives the direction of the polarisation vector with respect to the photon production plane.

The following decomposition into target polarisation dependent moments is then possible for the nucleon:

$$c_n = c_{n,up} + \Lambda\{c_{n,LP}\cos(\theta_s) + c_{n,TP}(\phi_s)\sin(\theta_s)\}, \tag{2.116}$$

where Λ denotes the value of the target polarisation along the polarisation vector. In this notation the target polarisation Λ from reference [BMK02] has been extracted from the coefficients in order to be consistent with reference [KM03]. For polarised targets a difficulty arises from this convention in the experiment: The target polarisation is always longitudinal or transverse with respect to the lepton beam and not with respect to the virtual photon. Hence depolarisation effects have to be included which lead to a mixture of the longitudinal (LP) and transverse (TP) moments. However, for HERMES kinematics the longitudinal term dominates to a good approximation. For this effect the term "depolarisation" will be used, as the effective longitudinal polarisation of the nucleon is smaller than the experimentally prepared polarisation along the beam axis. This should not be confused with the depolarisation expressed by the factor D that occurs in the interpretation of DIS.

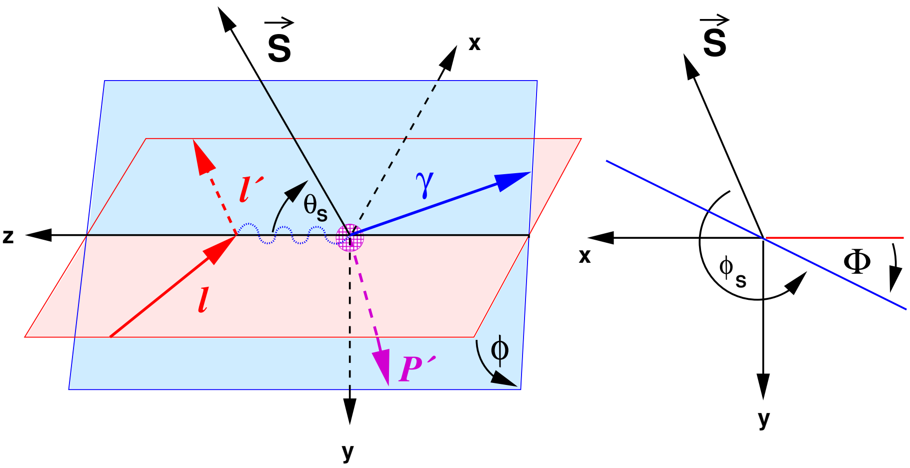

Figure 2.13.: Definition of coordinates: The angle θ_s is the angle between the virtual photon and the spin vector of the target (left). In the projection along the z-axis ϕ_s is the angle between the spin-vector and the scattered nucleon (right).

In principle the angle ϕ_s, that is used in the above decomposition of moments, is a separate degree of freedom such that the cross-section for a transversely polarised target is also differential in ϕ_s. It will be shown later that for a target with longitudinal target polarisation ϕ_s is related to ϕ, such that the given four-fold differential cross-section is correctly defined although it depends on ϕ_s.

So far nothing specific has been said about the type of the nucleon/nucleus. Hence the analogous expressions can be used for the deuteron with the exception of additional spin-dependent moments. For a spin-1 target it reads:

$$\begin{aligned} c_n &= \frac{3}{2}\Lambda^2 c_{n,up} + \Lambda\{c_{n,LP}\cos(\theta_s) + c_{n,TP}(\phi_s)\sin(\theta_s)\} + (1-\frac{3}{2}\Lambda^2) \\ &\quad \times\{c_{n,LTP}(\phi_s)\sin(2\theta_s) + c_{n,LLP}\cos^2(\theta_s) + c_{n,TTP}(\phi_s)\sin^2(\theta_s)\}, \end{aligned} \tag{2.117}$$

where the moments with index LLP, LTP and TTP are needed for the additional degrees of freedom.

In this case Λ is the quantum number for the z-component of the target spin measured with respect to the polarisation vector. This is not simply the vector-polarisation of the target; instead a target state with given vector- and tensor-polarisation can be written as a sum over the three values of Λ.

For an unpolarised target one recovers the value $c_n = c_{n,up}$. A purely tensor-polarised target in which $\Lambda = 0$ results in

$$c_n = \{c_{n,LTP}(\phi_s)\sin(2\theta_s) + c_{n,LLP}\cos^2(\theta_s) + c_{n,TTP}(\phi_s)\sin^2(\theta_s)\}.$$

For $\Lambda \neq 0$ all coefficients contribute.

The summation of different moments according to the target polarisation is done for the BH term, the DVCS term and the interference-term separately. As the BH term does not depend on the GPDs, its contribution in the case of the proton is quite straight-forward. As long as the target is unpolarised the cross-section is an even function in ϕ and hence only cosine-terms are non-zero. Only in the case of transverse target-polarisation a non-zero sine-moment is found. No single-spin-asymmetries exist and only double-spin asymmetries are possible as in the case of elastic scattering.

For deuterium the BH term gets more complicated as soon as the target is polarised; the quadrupole-moment of the deuteron leads to differences between the vector-polarisation balanced state $\Lambda = \pm 1$ and the pure state $\Lambda = 0$. Again the same is true for elastic scattering on the deuteron.

In most cases it is not very practical to decompose the BH cross-section into moments as the full BH contribution is known without introducing the rules for the counting of twist. Hence often the exact BH cross-section is used in analytical models.

At HERMES kinematics the contribution of the pure DVCS cross-section is usually assumed to be rather small compared with the BH part. This entails that the potentially second largest contribution originates from the interference term. In the theoretical description of the process interference amplitudes can be introduced to express the observed cross-section moments in terms of the Compton formfactors.

For an unpolarised hydrogen target the leading twist interference amplitude $\mathcal{C}^I_{up}$ can be written as

$$\mathcal{C}^I_{up} = F_1\mathcal{H} + \xi(F_1 + F_2)\tilde{\mathcal{H}} - \frac{t}{4M^2}F_2\tilde{\mathcal{E}}. \tag{2.118}$$

The additional interference amplitude for the case of longitudinal target polarisation is:

$$\mathcal{C}^I_{LP} = \xi(F_1 + F_2)(\mathcal{H} + \frac{x_B}{2}\mathcal{E}) + F_1\tilde{\mathcal{H}} - \xi(\frac{x_B}{2}F_1 + \frac{t}{4M^2}F_2)\tilde{\mathcal{E}}. \tag{2.119}$$

Using these definitions the leading twist moments for an unpolarised target or a target with longitudinal polarisation can be written as:

$$\begin{aligned}
c^I_{1,up} &= 8K(2 - 2y + y^2)\Re\mathfrak{e}\mathcal{C}^I_{up}, && (2.120)\\
s^I_{1,up} &= 8K\lambda y(2 - y)\Im\mathfrak{m}\mathcal{C}^I_{up}, && (2.121)\\
c^I_{1,LP} &= 8K\Lambda\lambda y(2 - y)\Re\mathfrak{e}\mathcal{C}^I_{LP}, && (2.122)\\
s^I_{1,LP} &= 8K\Lambda(2 - 2y + y^2)\Im\mathfrak{m}\mathcal{C}^I_{LP}, && (2.123)
\end{aligned}$$

where λ denotes the instantaneous beam polarisation and K is a kinematicsl factor as defined in reference [BMK02]. At leading twist also a constant moment $c^I_{0,up}$ is found, but it is kinematically suppressed and has a complicated dependence on the Compton formfactors. The second moments depend on twist-3 GPDs but Gluon transversity only shows up in the moments $c^I_{3,up}$ and $s^I_{3,LP}$. All other moments are higher twist and will not be considered in this thesis. A similar formalism can be used to express the moments of the deuteron cross-section in terms of the corresponding Compton formfactors.

In the approximation of a loosely bound np-system, the vector-polarisation of the deuteron results also in a polarisation of the bound nucleons. For the states $\Lambda = \pm 1$ the spins of the proton and the neutron are aligned and have the same polarisation $\Lambda = \pm 1$. This implies that measurements on the deuteron, in which it breaks up, provide the possibility for studying a polarised neutron target. The state with $\Lambda = 0$ results in a vanishing polarisation of the nucleons. In this approximation the initial deuteron state with $\Lambda = 0$ should behave like an unpolarised target.

One important fact has to be stressed: The coefficients c_n^I or s_n^I are not the Fourier coefficients of the cross section. Instead there is a strong ϕ-dependence due to the lepton-propagators which appears as P_1 and P_2 in the prefactor. The BH term as well as the interference term depend linearly on $\frac{1}{P_1 P_2}$ due to some cancellations that occur for the BH term. If the DVCS term can be neglected this leads to the practical result that each experimental event can be weighted by $P_1 P_2$ and the remaining ϕ-dependence is then really given by the coefficients c_n and s_n.

2.11. Definition of Good Observables

Although theory predicts the differential cross-sections, which contain all required information, usually experimental rates are so low in the case of hard exclusive reactions that it is not even approximately possible to measure the cross-section in small bins in x_B, Q^2, t and ϕ. In addition the measurement of cross-sections with sufficient precision requires a very good understanding of detector efficiencies and acceptance. Hence many efforts have been spent to define integrated and stable observables such that also the present experimental data can be used to its maximum benefit.

From the experimental point of view it is helpful to define asymmetries between datasets with different charges of the beam or different polarisations of the involved particles, in which acceptance and background effects cancel approximately.

One asymmetry that has turned our to be very important is the beam spin asymmetry A_{LU} (BSA) on an unpolarised target:

$$A_{LU}(\phi) = \frac{N^+(\phi) - N^-(\phi)}{N^+(\phi) + N^-(\phi)}, \tag{2.124}$$

where $N^+(\phi)$ and $N^-(\phi)$ denote the luminosity weighted numbers of single photon events for positive and negative beam helicity, respectively. Using the expressions given above and fixing the asymmetry to one point in x_B, Q^2 and t it is clear that the propagators will cancel completely if the DVCS term proportional to $|\mathcal{T}_{DVCS}|^2$ and all background contributions are neglected in the denominator. The remaining result is

$$A_{LU}(\phi) \approx (1+\epsilon^2)^{-2} \frac{x_B}{y} \frac{\sum_n \pm s_{n,up}^I \sin(n\phi)}{\sum_n (c_{n,up}^{BH} \pm c_{n,up}^I) \cos(n\phi)}. \tag{2.125}$$

The sign of the asymmetry depends on the beam charge as indicated by the $\pm$. Since ϵ is a small number, while s_1^I is the leading twist moment in the numerator and c_0^{BH} the leading moment in the denominator, often the approximation is used that

$$A_{LU}(\phi) \approx \pm \frac{x_B}{y} \frac{s_{1,up}^I}{c_{0,up}^{BH}} \sin(\phi). \tag{2.126}$$

In this approximation the following problems remain:

- c_0^{BH} depends on the exact kinematics and also s_1^I has a kinematical dependence. This means that the value of A_{LU} is not constant and that an integration over a kinematical region results in a more or less well-defined mean-value.

- The assumption that the DVCS contribution in the denominator is small needs not be true for all kinematics. At HERMES kinematics Monte Carlo calculations show that the DVCS cross-section for deuterium can amount to about 30% of the BH cross-section (in agreement with reference [KN02a]).
- The term c_1^{BH} in the denominator can couple to the leading asymmetry moment and thus produce higher moments.

Often the statement is made that $d\sigma^+ - d\sigma^- \propto \sin(\phi)$. This is misleading or even wrong, since the propagators introduce additional cosine moments into the cross-section. Predictions for A_{LU} on the proton according to Müller et al. are shown in figure 2.14 and agree well with present HERMES data. This asymmetry gives access to the imaginary part of the Compton amplitude $\mathcal{C}_{up}$ and is therefore related to the values of the GPDs at $x = \xi$.

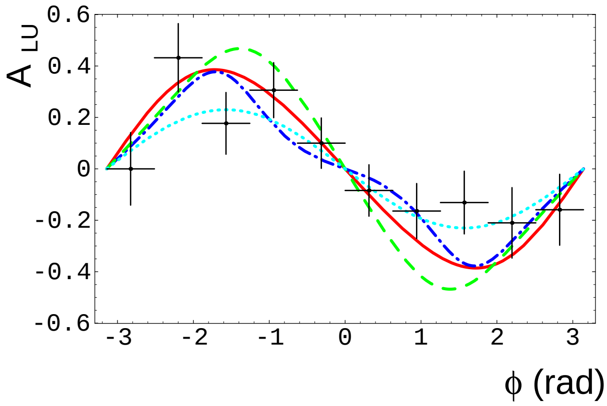

Figure 2.14.: Different model predictions for A_{LU} on the proton in comparison to published HERMES results. Taken from reference [BMK02].

The same asymmetry can also arise in the coherent process on nuclei. Due to the dominance of the Compton-formfactor $\mathcal{H}$ for nuclei with spin 0 and spin $\frac{1}{2}$, or the formfactor $\mathcal{H}_1$ for targets with spin 1 some simple relations can be given for the expected values of the asymmetry A_{LU}. For positrons scattering off a proton target this is:

$$A_{LU}^p(\phi) \approx -\sqrt{\frac{-t(1-y)}{Q^2}}\pi x_B \left[e_u^2 u_{val}\left(\frac{x_B}{2}\right) + e_d^2 d_{val}\left(\frac{x_B}{2}\right)\right]\sin\phi, \tag{2.127}$$

where the quark densities u_{val} and d_{val} of the u and d valence quarks are evaluated at $\frac{x_B}{2}$. For the deuteron it is:

$$A_{LU}^d(\phi) \approx -\sqrt{\frac{-t(1-y)}{Q^2}}\pi x_B \frac{e_u^2 + e_d^2}{2}\left[u_{val}\left(\frac{x_B}{2}\right) + d_{val}\left(\frac{x_B}{2}\right)\right]\sin\phi. \tag{2.128}$$

Similar formulae are obtained for heavier targets. These predictions are valid for $-t_0 \ll -t \ll M^2$ which is difficult to fulfil for nuclear targets due to the steep slope of the nuclear formfactor. Hence t is always rather close to t_0 at HERMES.

There are strict constraints on the observed ϕ-dependence of the interference term due to the invariance under the parity operator in strong and electromagnetic interactions: For example $A_{LU}(-\phi) = -A_{LU}(\phi)$. This is the reason for the fact that even functions cannot be observed in the beam-spin asymmetry. It is interesting to note that the the same constraint exists also for the target spin asymmetry.

A second important observable is the beam charge asymmetry (BCA). As can be seen in the decomposition of the interference term $\mathcal{I}$, all moments flip their sign with a change of the beam charge. This occurs as the BH amplitudes $\mathcal{M}_{ei}$ and $\mathcal{M}_{ef}$ depend on the square of the beam charge, while the DVCS process depends linearly on the beam charge. Thus the beam charge cubed determines the sign of the interference term. Obviously the beam-charge-asymmetry A_{CU} defined in the following way picks out the cosine coefficients of the cross-section:

$$A_{CU}(\phi) = \frac{N^+(\phi) - N^-(\phi)}{N^+(\phi) + N^-(\phi)} \tag{2.129}$$

for event number N^+ and N^- for positive or negative beam charge respectively and an unpolarised lepton beam as well as an unpolarised target.

This can be interpreted as

$$A_{CU}(\phi) \approx -(1+\epsilon^2)^{-2} \frac{x_B}{y} \frac{\sum_n c^I_{n,up} \cos(n\phi)}{\sum_n c^{BH}_{n,up} \cos(n\phi)}. \tag{2.130}$$

Due to the sign-change the interference term vanishes this time in the denominator. Again a further simplification is possible:

$$A_{CU}(\phi) \approx -\frac{x_B}{y} \frac{c^I_{1,up}}{c^{BH}_{0,up}} \cos(\phi). \tag{2.131}$$

The beam-charge asymmetry requires unpolarised lepton-beams. Another possibility is to use polarised electron and positron beams but with the same beam polarisation λ. It is obvious that in such a case the s_1-coefficient of the interference term cancels in the denominator, but that it will contribute to the numerator:

$$A_{C,\lambda}(\phi) \approx -\frac{x_B}{y} \frac{c^I_{0,up} + c^I_{1,up} \cos\phi + \lambda s^I_{1,up} \sin\phi}{c^{BH}_{0,up}}, \tag{2.132}$$

such that all leading twist coefficients for an unpolarised target can be measured at the same time. Moreover, in contrast to the BSA, the interference term cancels completely in the denominator. On the other hand the combination of different beam-charges adds a systematic experimental error such that the usual BSA is safer in terms of systematics. Even unbalanced beam polarisations can be used, which will be discussed in chapter 6.

The beam charge asymmetry accesses the real part of the Compton amplitude C_{up} and thus is related to integrals of the type $P\int_{-1}^{+1} H(x,\xi,t)(\frac{1}{x-\xi} + \frac{1}{x+\xi})\,dx$. Obviously it is not possible to get directly from this quantity to the quantity $\int_{-1}^{+1} H(x,\xi,t)\,dx$ that shows up in Ji's sumrule. Hence the BCA as well as the BSA mainly serve to constrain the possible GPD-models.

Predictions for the BCA by Müller et al. together with preliminary HERMES data on the proton are shown in figure 2.15. None of the different models can be completely excluded with

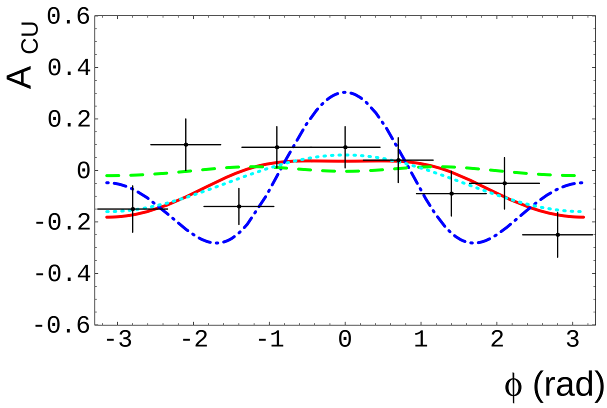

Figure 2.15.: Different model predictions for A_{CU} on the proton in comparison to preliminary HERMES results. Taken from reference [BM02].

the present statistical accuracy of the data. In reference [BMK02] a prediction for the ratio of the leading asymmetry moments c_1^{BCA} and s_1^{BSA} in the case of the proton is made:

$$\frac{c_1^{BCA}}{s_1^{BSA}} \approx \frac{2-2y+y^2}{(2-y)y} \cdot \frac{e_u^2 R^{u_v} u_{val}(\xi) + e_d^2 R^{d_v} d_{val}(\xi)}{e_u^2 u_{val}(\xi) + e_d^2 d_{val}(\xi)}. \tag{2.133}$$

The values for R^{u_v} and R^{d_v} are model dependent and are given by the ratio $R^q = \frac{\Re\mathrm{e}\mathcal{H}^q}{\Im\mathrm{m}\mathcal{H}^q}$ of the corresponding valence quark distributions. Although the exact values depend on the kinematics, R^{q_v} should be negative. At $x_B = 0.13$ and $Q^2 = 2.7$ GeV^2 the value according to this model is $c_1^{BCA}/s_1^{BSA} \sim -0.8$.

For nuclear targets it can be expected that binding effects will modify the BCA with respect to the case of the nucleon. The predicted effects can be model-dependent; e.g. in the case of deuterium the GPD H_3 being induced by the sea-quarks is at the moment unconstrained [KM03]. Other authors explicitly predict a possible increase of the BCA for nuclear spin 0 targets [FS04, GS03].

Especially for spin $\frac{1}{2}$ and spin 1 targets, another interesting asymmetry can be constructed using an unpolarised beam and a (vector-) polarised target. This target spin asymmetry (TSA) A_{UL} is defined as

$$A_{UL}(\phi) = \frac{N^+(\phi) - N^-(\phi)}{N^+(\phi) + N^-(\phi)}, \tag{2.134}$$

where N^+ and N^- denote the event numbers for target polarisation anti-parallel to the incoming lepton beam and target polarisation parallel with respect to the lepton beam. As well as the following tensor asymmetry, this asymmetry suffers from depolarisation effects and strictly speaking polarisation is required with respect to the virtual photon. Moreover for a deuterium target a contamination of the $\Lambda = 0$ spin state will usually be present. Depending on this contribution, small dilution effects can result from the tensor-moments. Hence in the case of deuterium the interpretation of this asymmetry gets more complicated.

For the proton the asymmetry A_{UL} results in:

$$A_{UL}(\phi) \approx (1+\epsilon^2)^{-2} \frac{x_B}{y} \frac{\sum_n \pm s^I_{n,LP} \sin(n\phi)}{\sum_n (c^{BH}_{n,up} \pm c^I_{n,up}) \cos(n\phi)} \tag{2.135}$$

or approximately

$$A_{UL}(\phi) \approx \pm \frac{x_B}{y} \frac{s^I_{1,LP}}{c^{BH}_{0,up}} \sin(\phi). \tag{2.136}$$

The ratio with respect to the BSA can be written as

$$\frac{A_{UL}(\phi)}{A_{LU}(\phi)} \approx \frac{2-2y+y^2}{(2-y)y} \left[\frac{e_u^2 \Delta u_{val} + e_d^2 \Delta d_{val}}{e_u^2 u_{val} + e_d^2 d_{val}} + \frac{x_B}{2} \frac{F_2}{F_1} \right]. \tag{2.137}$$

The ratio is expected to be positive and small. In the case of the deuteron the formula gets more complicated and involves the 3 formfactors of the deuteron:

$$\frac{A_{UL}(\phi)}{A_{LU}(\phi)} \approx \frac{2-2y+y^2}{(2-y)y} \frac{G_1 - \tau G_3}{G_1 - \frac{2}{3}\tau G_3} \left[\frac{\Delta u_v + \Delta d_v}{u_v + d_v} + \frac{x_B}{2A} \frac{G_2}{G1 - \tau G_3} \right]. \tag{2.138}$$

In this case it is not quite clear what to expect, since the result is very sensitive to additional contributions from $\mathcal{H}_3$ and $\mathcal{H}_5$. Several model predictions for the asymmetry A_{UL} in coherent BH/DVCS on the deuteron are shown in figure 2.16. The shown models only differ in their respective treatment of valence and sea quarks.

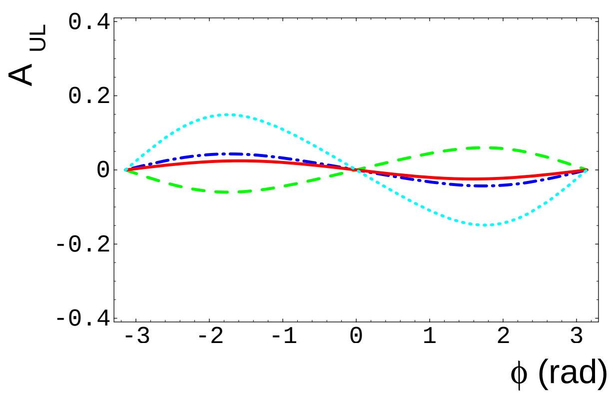

Figure 2.16.: Target spin asymmetry A_{UL} on the deuteron for $x_B = 0.1$, $Q^2 = 2.5$ GeV^2 and $t = -0.2$ GeV^2. Various model predictions are shown according to reference [KM03].

All mentioned asymmetries can be obtained for spin $\frac{1}{2}$-targets as well as for spin 1 targets. There are four more asymmetries that can only be defined for a spin 1 target and can be measured at HERMES.

The first asymmetry is obtained for a tensor polarised target, in which only the spin-states $\Lambda = \pm 1$ are present. It is called $A_{L\pm}$ and is obtained from data sets $N^+(\phi)$ and $N^+(\phi)$ with positive and negative beam helicity, respectively:

$$A_{L\pm}(\phi) = \frac{N^+(\phi) - N^-(\phi)}{N^+(\phi) + N^-(\phi)}. \tag{2.139}$$

In contrast to the usual beam spin asymmetry tensor effects are included such that the final relation is approximately:

$$A_{L\pm}(\phi) \sim \pm \frac{x_A}{y} \frac{s^I_{1,up} - \frac{1}{3} s^I_{1,LLP}}{c^{BH}_{0,up} - \frac{1}{3} c^{BH}_{0,LLP}} \sin(\phi). \tag{2.140}$$

Similarly the beam charge asymmetry $A_{C\pm}$ can be defined, which depends on the tensor coefficient $c^I_{1,LLP}$.

The third asymmetry involving tensor polarisation is the tensor asymmetry A_{zz} itself:

$$A_{zz}(\phi) = \frac{N^+(\phi) - N^-(\phi) - 2N^0(\phi)}{N^+(\phi) + N^-(\phi) + N^0(\phi)}. \tag{2.141}$$

It can be calculated for a defined beam charge and helicity. The result is rather complicated and involves a constant term due to the tensor asymmetry of the BH process:

$$A_{zz}(\phi) \approx \frac{(c^{BH}_{0,up} - c^{BH}_{0,LLP}) \pm \frac{x_A}{y}((c^I_{0,up} - c^I_{0,LLP}) + (c^I_{1,up} - c^I_{1,LLP}) \cos\phi)}{c^{BH}_{0,up}}, \tag{2.142}$$

or more explicitly

$$A_{zz} = \frac{-4\tau G_3(G_1 - \tau G_3)}{2G_1^2 + (G_1 - 2\tau G_3)^2} \pm \frac{x_A \sqrt{\frac{-t}{Q^2}(1-y)}}{y} 3G_1 \left[f_1 \cos\phi + f_2 \lambda \frac{y(2-y)}{2 - 2y + y^2} \sin\phi \right]. \tag{2.143}$$

f_1 and f_2 denote the real and imaginary parts of a combination of Compton formfactors. Apparently the BH asymmetry as well as the interference term asymmetry vanish for small values of $|t|$. Hence both effects can be difficult to observe at the typical HERMES kinematics.

It is possible to evaluate the constant BH term of the asymmetry A_{zz} by inserting the corresponding formfactors. The prediction for the constant term in equation 2.143 are shown in figure 2.17. Although the constant term due to the BH tensor-asymmetry can be large for higher values of $|t|$, it is because of dilution below 10% for $-t < 0.05$ GeV^2. Since this is the region of interest for HERMES it will be difficult to see the effect of this term.

Various model predictions for the asymmetry A_{zz} at HERMES energies are shown in figure 2.18. The thick-dotted, horizontal line shows the strong constant BH asymmetry in agreement with figure 2.17.

In order to remove the constant term two more complicated asymmetries have been suggested that isolate the functions f_1 and f_2. The first suggestion was to calculate the asymmetry A_{Czz} that is based on four different datasets with 2 charges and 2 polarisation states but vanishing beam polarisation:

$$\begin{aligned} A_{Czz(\phi)} &= \frac{(N^+(\phi) + N^-(\phi) - 2N^0(\phi))_{e^+} - (N^+(\phi) + N^-(\phi) - 2N^0(\phi))_{e^-}}{(N^+(\phi) + N^-(\phi) + N^0(\phi))_{e^+} + (N^+(\phi) + N^-(\phi) + N^0(\phi))_{e^-}} \\ &\approx \frac{x_A}{y} \frac{c^I_{1,up} - c^I_{1,LLP}}{c^{BH}_{0,up}} \cos\phi. \end{aligned} \tag{2.144}$$

This asymmetry is related to the function f_1. In principle it can be extracted at HERMES , but with the existing datasets it is preferable to study the effect of the coefficient $c^I_{1,LLP}$ in the

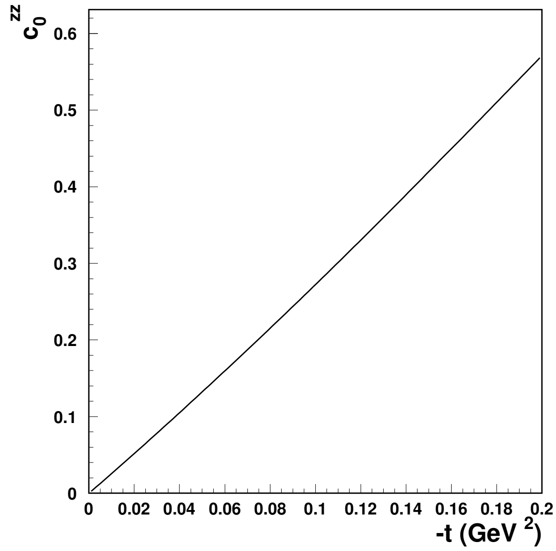

Figure 2.17.: Constant tensor-asymmetry of the Bethe-Heitler process, calculated using equation 2.143.

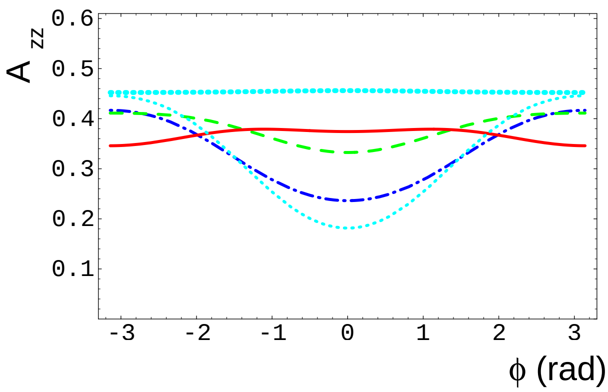

Figure 2.18.: Tensor asymmetry A_{zz} on the deuteron for $x_B = 0.1$, $Q^2 = 2.5$ GeV^2 and $t = -0.2$ GeV^2. Various model predictions are shown according to reference [KM03].

tensor asymmetry A_{zz}. The other asymmetry based on 4 different data sets is obtained for 2 beam helicities and 2 target polarisation states but the same beam charge:

$$\begin{aligned} A_{Lzz}(\phi) &= \frac{(N^+(\phi) + N^-(\phi) - 2N^0(\phi))_{\lambda=1} - (N^+(\phi) + N^-(\phi) - 2N^0(\phi))_{\lambda=-1}}{(N^+(\phi) + N^-(\phi) + N^0(\phi))_{\lambda=1} + (N^+(\phi) + N^-(\phi) + N^0(\phi))_{\lambda=-1}} \\ &\approx \pm \frac{x_A}{y} \frac{s^I_{1,up} - s^I_{1,LLP}}{c^{BH}_{0,up}} \sin\phi. \end{aligned} \tag{2.145}$$

It is related to the function f_2. Model predictions for the asymmetry A_{Lzz} at HERMES energies are shown in figure 2.19.

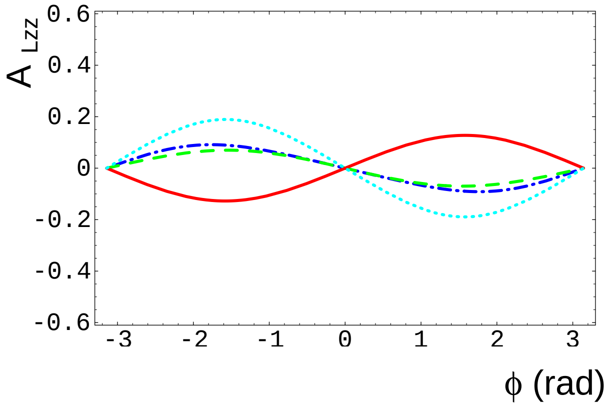

Figure 2.19.: Spin-Tensor asymmetry A_{Lzz} on the deuteron for $x_B = 0.1$, $Q^2 = 2.5$ GeV^2 and $t = -0.2\,\mathrm{GeV}^2$. Various model predictions are shown according to reference [KM03].

3. Deeply Virtual Compton Scattering at the HERMES-Experiment

3.1. Overview of the Present Apparatus

The HERMES-Experiment has been explained in detail in [HERMES98] and various other publications. It is a multi-purpose spectrometer for polarised lepton-hadron scattering that is based on a fixed-target setup. The lepton beam is provided by the lepton ring of the HERA accelerator at DESY/Hamburg. Positrons or electrons can be injected, accelerated to an energy of 27.57 GeV and stored. A schematical drawing of the HERA-facility is shown in figure 3.1

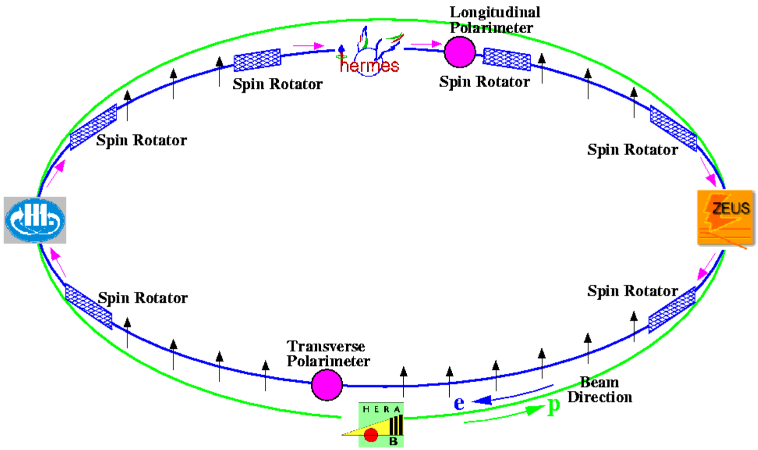

Figure 3.1.: HERA consists of an electron/positron storage ring and a proton storage ring. H1 and ZEUS observe the collisions of the stored particles, while HERMES uses only the lepton beam and a fixed atomic gas target. The spin rotators for ZEUS and H1 have been added in 2001.

At the moment there are two other HERA experiments, H1 and ZEUS, in which protons at an energy of 920 GeV collide with the leptons. This allows to cover a large kinematical range in Q^2 and x_B which is required for the study of scaling violations in deep inelastic scattering. In the case of DVCS both experiments can also contribute, but in a very different kinematical regime, i.e. at very small values of x_B and y, where the DVCS-amplitude dominates over the Bethe-Heitler-amplitude. More details can be found in [ZEUS03, H101].

Storage rings offer an interesting possibility to study physics with a polarised electron/positron-beam: Due to an asymmetry in the emission of synchrotron-radiation in the field of the dipole magnets (Sokolov-Ternov-Effect [BDS$^+$75]) the HERA lepton beam is self-polarising, as long as the beam optics is tuned accordingly. The maximum achievable polarisation can be degraded by beam-beam interaction at the collider experiments as well as by an imperfect arrangement of the magnets. Under normal conditions the polarisation buildup can be described by an exponential of the form

$$P_B = P_0(1 - e^{-\frac{t}{t_0}}), \tag{3.1}$$

where P_0 is in the order of 60% and the time-constant t_0 is typically less than 1 hour. In front of the HERMES-experiment and behind it, special magnet arrangements called spin-rotators convert the transverse polarisation of the lepton beam into a longitudinal polarisation at HERMES .

Especially with unstable beam-conditions the polarisation can suddenly change and hence it is important to monitor it continuously. Two instruments are used for that: Both are Compton-Backscattering-Polarimeters which are based on the collision of circularly polarised laser light with the lepton beam.

The velocity of the leptons leads to a strong Lorentz-Boost of the back-scattered photon. Therefore a small calorimeter, capable of absorbing photons of several GeV energy, is required to detect the final state photons. Characteristic asymmetries in the cross-section allow for the calculation of the beam polarisation. While the "TPOL" is located close to the HERA west-hall and studies the reaction of circularly polarised photons and transversely polarised leptons, the "LPOL" is located in the neighbourhood of HERMES and observes the reaction of photons with longitudinally polarised leptons.

Since both polarimeters measure the same polarisation a systematic cross-check is possible. In general the fractional error on the measured beam-polarisation is 1.6% for the LPOL [B$^+$02] and 3.4% for the TPOL [HERMES99] . For data-analysis the best working polarimeter provides the polarisation value.

The HERMES-experiment itself was designed for the study of inclusive and semi-inclusive reactions and uses a polarised/unpolarised internal gas-target that is schematically shown in figure 3.2. An atomic beam source (ABS) [N$^+$03] provides polarised hydrogen or deuterium gas by means of Stern-Gerlach-Separation. The gas is injected into a storage cell and the adiabatic change of the magnetic field allows to move the quantisation axis into a longitudinal or transverse direction inside the cell. Two alternative target magnets are used for this purpose. During the periods of data-taking that were used for this thesis, the longitudinal magnet with a nominal field of $B = 0.35$ T was installed. Since there is no entrance or exit window of the target cell, a very efficient pumping system is needed to remove the gas that leaves the beam-pipe through holes at both ends of the cell.

In order to monitor the target polarisation an arrangement of sextupole magnets similar to the ABS receives a small amount of target gas that is extracted from the centre of the cell. This Breit-Rabi-Polarimeter (BRP) measures the polarisation value and thus allows for a check of the correct operation of the atomic beam source. The overall polarisation is determined in the following way:

$$P = \alpha_0(\alpha_r + (1 - \alpha_r)\beta)P_a, \tag{3.2}$$

where α_0 is the initial fraction of atoms from dissociated molecules. It is obtained from the number of molecules n_m and the number of atoms n_a by $\alpha_0 = n_a/(n_a + 2n_m)$. α_r is the fraction of atoms that do not recombine and P_a is the polarisation of the atoms. βP_a is the nuclear polarisation of atoms that have recombined to a molecule. This quantity is not very well known;

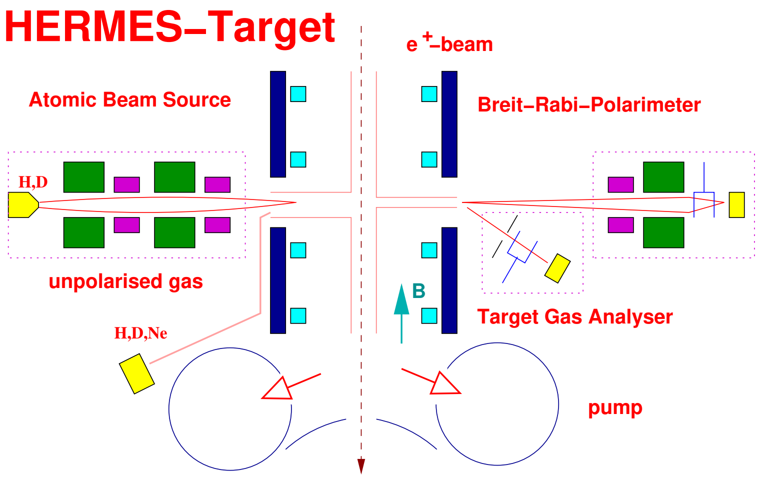

Figure 3.2.: The HERMES target provides polarised and unpolarised gas. In the case of polarised gas the degree of dissociation and the atomic polarisation are continuously monitored.

for hydrogen it is at least limited by $0.2 \leq \beta \leq 1$ [Kol98] but no such limit exists for deuterium. The value of P_a is continuously measured by the BRP, while the value of α_r is obtained from the target-gas analyser (TGA). The results of the TGA indicated that there was almost no recombination inside the target cell in 2000 [The02]. As the polarisation for 1998 and 1999 was determined in a different way [Bec03], the parameter β has no impact on this analysis.

Although in practice eigenstates of atomic polarisation are injected, they are very close to the eigenstates of nuclear polarisation because of the strong magnetic field. This can be seen from the hyperfine structure scheme shown in figure 3.3. In a very weak magnetic field electrons and protons couple to an effective particle with Landé-factor g and total angular momentum F. In this case the states with $M_F = 0$ have an average nuclear polarisation of $\langle m_I \rangle = 0$. In the limit of a very strong field - as encountered in the HERMES target - 4 eigenstates with quantum numbers $m_I = \pm\frac{1}{2}$ and $m_S = \pm\frac{1}{2}$ are obtained. In spite of the strong field the injected nuclear polarisation is always less than 100% (typically in the order of 90%) due to an imperfect separation of hyperfine states.

In the case of deuterium, the situation gets more complicated. In order to describe the population of the three levels with different quantum numbers m_I two quantities are defined: The vector polarisation P is given by

$$P = \frac{n^+ - n^-}{n^+ + n^- + n^0}, \tag{3.3}$$

while the tensor polarisation T is given by

$$T = \frac{n^+ + n^- - 2n^0}{n^+ + n^- + n^0}, \tag{3.4}$$

where n^+, n^- and n^0 denote the expectation values for the occupation numbers of the levels $m_I = +1$, $m_I = -1$ and $m_I = 0$, respectively. It is obvious that $-1 < P < 1$ and $-2 < T < 1$. The results of a detailed analysis [The02] for the year 2000 dataset is shown in table

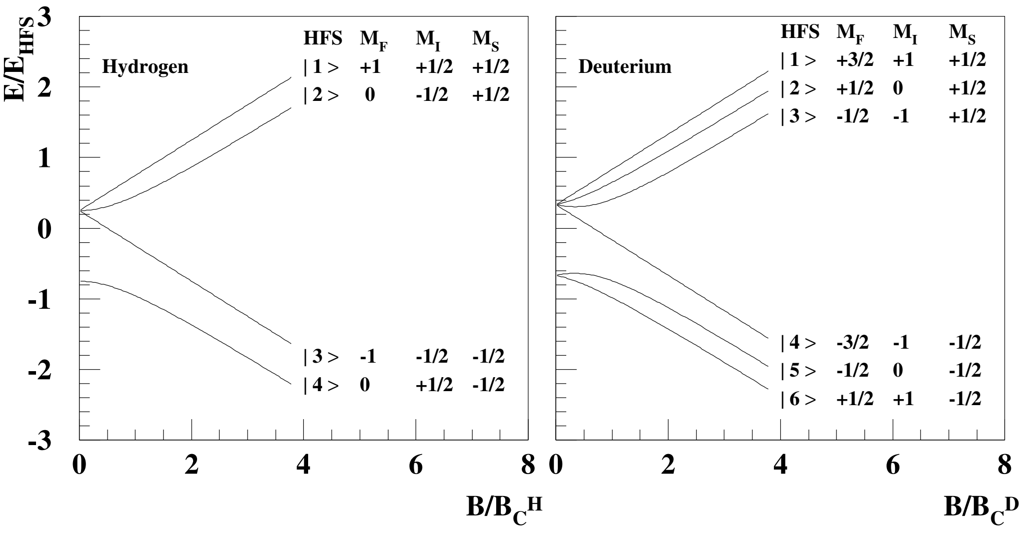

Figure 3.3.: The energy splitting of the Hyperfine-Levels for hydrogen and deuterium as a function of the magnetic field. The quantum numbers F and m_F are used at weak fields, while m_s and m_I are good quantum numbers for strong fields. For deuterium one obtains: $E_{HFS} = 1.35 \cdot 10^{-6}$ eV and $B_C = 11.7$ mT.

Table 3.1.: The values are quoted for the polarisation of the vector polarised deuterium dataset from the year 2000 [The02]

Target State	Injected States	P	ΔP	T	ΔT
+	$\|1>+\|6>$	+0.851	± 0.031	+0.800	± 0.025
-	$\|3>+\|4>$	-0.840	± 0.028	+0.853	± 0.027
0	$\|2>+\|5>$	-0.011	± 0.005	-1.655	± 0.049

3.1. According to reference [Bec03] the vector polarisation for 1998 was $\pm 0.856 \pm 0.064$ and the vector polarisation for 1999 was $\pm 0.832 \pm 0.058$.

Apart from polarised gas provided by the ABS unpolarised molecular gas can be injected using the unpolarised gas feed system (UGFS). So far hydrogen, deuterium, helium, nitrogen, neon, krypton and xenon have been used. The target density that is provided by the ABS is limited to about $2 \cdot 10^{14}$ nucleons/cm^2 due to technical limitations of the Stern-Gerlach-setup. For the UGFS no such limit exists. However the allowed target density is limited by the lifetime of the lepton-beam. Under usual running conditions the beam lifetime is > 10 h. The total lifetime τ can be written as

$$\frac{1}{\tau} = \frac{1}{\tau_{HERMES}} + \frac{1}{\tau_{HERA}} \tag{3.5}$$

The contribution τ_{HERMES} must be greater than 45 hours under normal running conditions. This limits the target density that can be achieved with the UGFS to about $10\times$ the polarised density. Due to a special agreement, HERMES is allowed to increase the target density as soon as the lepton beam current falls below ~ 15 mA (the typical beam current after injection was ~ 35 mA in 2000). During these end-of-fill running periods, the background rates are typically rather low, and high quality data can be collected at comparatively high luminosities. Under these conditions the target density can reach about 100 $\times$ the polarised density. The main part of the unpolarised deuterium data from 2000 was taken under such conditions.

An ultimate limit on the density provided by the UGFS arises from the deadtime of the HERMES Data Acquisition (DAQ) (max. trigger rate ~ 500 Hz), from an increasing background of Møller-electrons in the HERMES front-region and beam instabilities at very low lifetimes ($\tau \leq 1$ h). For an electron beam the lifetime is usually worse, as a better vacuum inside the ring is required. Until now only one year of electron data (1998) was taken.

The reaction products of the interaction of beam leptons with target atoms are observed by the HERMES-spectrometer. This is shown in figure 3.4. Before particles leave the target-chamber through a thin stainless steel exit window, they hit a silicon detector (Lambda Wheels, LW) that has recently (2003) been installed inside the target vacuum. Together with the following Drift-Vertex-Chamber (DVC) this detector allows tracking outside the standard HERMES-acceptance. For the reconstruction of the front partial tracks inside the standard acceptance present tracking productions mainly rely on the front drift chambers (FCs) that are installed in front of the spectrometer magnet.

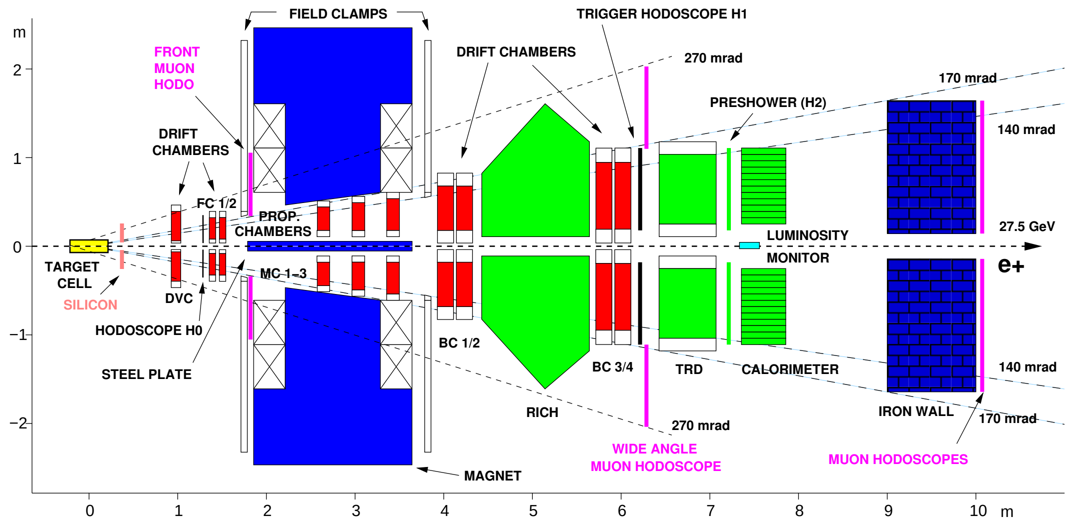

Figure 3.4.: The HERMES-spectrometer: Tracking chambers (DVCS, FC, Mc, BC) are shown in red, particle identification detectors (RICH, TRD, H2, calorimeter) in green and passive materials in dark blue. All muon hodoscopes are plotted in magenta.

A large spectrometer magnet with an integrated field strength of $B \times l \approx 1.4$ Tm deflects charged particles after they have passed the front detectors. Inside the magnet three multi-wire proportional-chambers have been installed that have a moderate spatial resolution but are not very sensitive to the strong magnetic field.

Behind the magnet a number of drift-chambers (BC 1-4) are installed that detect the backward partial tracks of charged particles. Finally the tracks hit the preshower detector and the electromagnetic calorimeter (CALO). The calorimeter provides an energy-measurement for electrons and photons and allows to identify hadrons which have a lower energy-deposition at the same particle momentum due to the different shower evolution.

In addition the backward part of HERMES contains 2 other detectors that are only needed for particle identification (PID): The ring-imaging Čerenkov-counter (RICH) and the transition radiation detector (TRD). A more detailed description of these detectors will be given in section 3.3.

Finally three hodoscopes are installed that have a rather low granularity. The hodoscopes H0, H1 and H2 (=Preshower) are used together with the calorimeter to form the standard DIS-trigger at HERMES. In addition a number of muon hodoscopes enlarge the HERMES acceptance for decays of charmed particles that can decay into muons.

The luminosity monitor (LUMI) measures the achieved luminosity by detecting symmetric Møller or Bhabha scattering on the electrons of the target gas.

3.2. The Tracking system

The HERMES tracking system consists of three drift-chambers in the front-region, three multi-wire-proportional chambers (MCs) inside the spectrometer magnet and four drift-chambers in the backward region. For the present tracking productions of the years 1998 to 2000 the Drift-Vertex chamber (DVC) has not been used due to unsolved questions about its alignment. Also the MCs are not actively used for this analysis, as they are only added if low momentum tracks fail to hit the backward chambers. Due to the high lepton momenta in the case of DVCS this should not happen. However, short tracks found by the MCs act as a veto.

All tracking chambers have wires along three different directions. This allows to resolve tracking ambiguities if several tracks hit the chamber at the same time. The typical resolution of all drift chambers is in the order of 200 $\ldots$ 300 μm (cf. [HERMES98]). The single plane efficiency of the chambers is continuously monitored. For 2000 it was usually above 95%. As an example one of the backward chambers is shown in figure 3.5.

The area covered by the tracking chambers defines the acceptance for charged tracks. As an additional requirement the tracks have to pass the opening of the spectrometer magnet and they have to hit the calorimeter in order to obtain a trigger signal and particle identification. Due to the rather long target cell of 40 cm this translates into a rather complicated acceptance of the whole spectrometer. In a first approximation the acceptance of HERMES is given in terms of the angles θ_x and θ_y defined by the momentum components p_x, p_y and p_z of a charged track:

$$\theta_x = \arctan(p_x/p_z), \tag{3.6}$$

$$\theta_y = \arctan(p_y/p_z). \tag{3.7}$$

The acceptance is then approximately given by $|\theta_x| < 170$ mrad and 40 mrad$< |\theta_y| <$140 mrad.

Alignment of all tracking detectors is achieved by using a laser alignment system. In addition alignment runs are taken in which the spectrometer magnet is switched off. This allows to align front and back chambers with respect to each other.

There are several indications that this alignment procedure has a limited precision: It was found that detectors that have not been moved between 2 years seem to change their position in space [Kis03]. Moreover tilts or offsets of the whole detector system cannot be found using internal alignment, but their effects are seen in the reconstructed beam-position and external offsets e.g. with respect to the calorimeter.

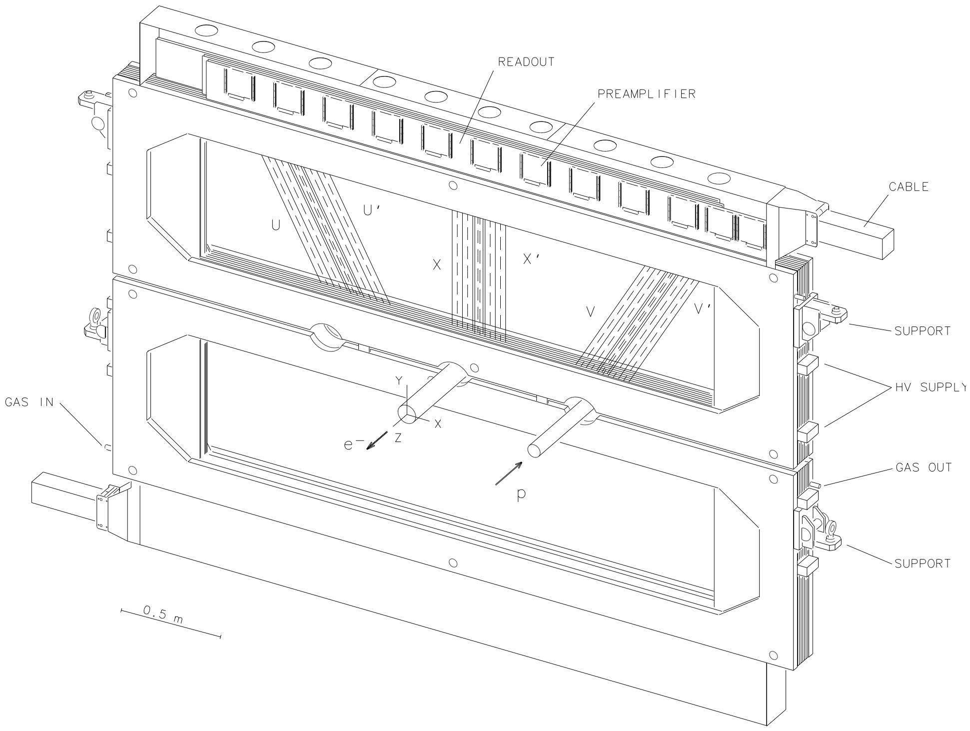

Figure 3.5.: Backward drift chamber at HERMES.

Not only the detectors determine the resulting performance of the tracking system, also a highly efficient reconstruction code is needed. The HERMES Reconstruction Code (*hrc*) is based on a tree-search algorithm [Wan96] that allows for a very quick determination of particle tracks from a given set of detector hits: Possible hit patterns are created by tracking ideal particles through an ideal detector. A comparison of the measured hit-pattern and the database allows track-finding. Afterwards the tracks are reconstructed under the assumption that the front-track and the back-track have to form one continuous curve (force-bridging). *hrc* also assigns corresponding hits in the calorimeter to each track. The momentum of the particle is calculated from the deflection in the magnetic field of the spectrometer magnet.

The momentum and angular resolution for DVCS events was obtained from Monte Carlo and is plotted in figure 3.6. It is significantly worse than the resolution that was achieved before 1998 [HERMES98].

3.3. The PID-Detectors

For the case of BH/DVCS the main interest in terms of PID is a clear separation of leptons and hadrons. Several PID-detector types are realized in the HERMES experiment.

The first PID detector to be traversed by particles is a ring-imaging Čerenkov-counter. Čeren-kov-counters exploit the fact that particles inside a dielectric medium emit Čerenkov-radiation as soon as they are moving faster than the in-medium speed of light c_m. The photons

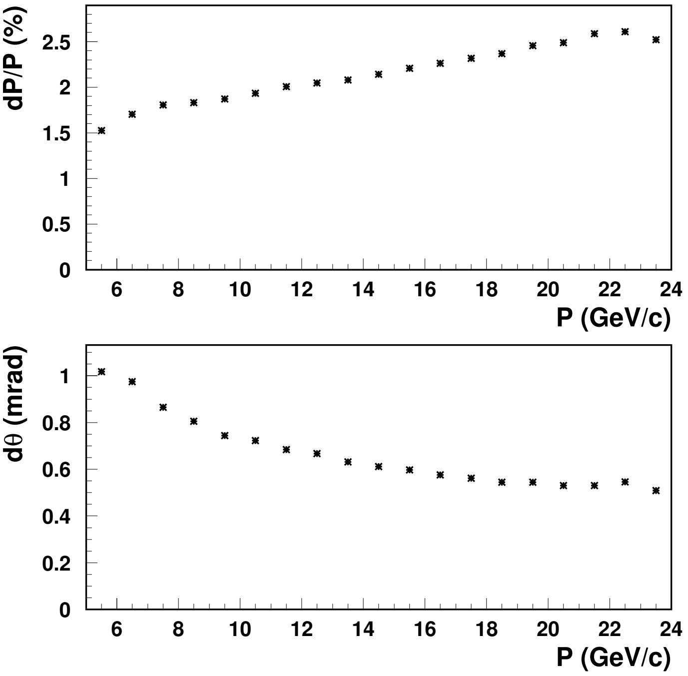

Figure 3.6.: The resolution of the HERMES-spectrometer for leptons from exclusive BH/DVCS events: The momentum resolution (top) is obtained from a Gaussian fit in order to suppress the long tails due to Bremsstrahlung emitted in the spectrometer. The angular resolution (bottom) in the angle θ with respect to the beam is obtained as RMS-value.

are emitted under a characteristic opening angle θ_C with respect to the direction of motion of the particle. θ_C is related to the velocity v of the particle by the relation:

$$\cos\theta_C = \frac{c_m}{v}. \tag{3.8}$$

The number of emitted photons per unit wavelength and unit pathlength is given by

$$\frac{dN}{d\lambda\, ds} = 2\pi\alpha\left(1 - \left(\frac{c_m}{v}\right)^2\right)\frac{1}{\lambda^2} \tag{3.9}$$

and approaches its maximum if v is close to the vacuum speed of light. This implies that scattered electrons or positrons at any momentum will always yield a higher light output and wider opening angle than hadrons at the same momentum.

In the case of a ring-imaging Čerenkov-counter a special mirror system is used to produce an image of the opening angle on a plane that is covered by photomultiplier tubes. It is clear that the identification of the rings is not a trivial task, as only a few photons per track are collected and rings of several tracks can overlap. Hence PID-efficiencies of a RICH depend on track multiplicities.

For HERMES a special version of a RICH was build that uses two different radiators: Aerogel with a refractive index of $n = 1.03$ and C_4F_{10}-gas with a refractive index of $n = 1.0014$.

The opening angles of the 2 Čerenkov-cones together allow particle identification over a large momentum range as is shown in figure 3.7. As can be seen from the plot, the lepton/hadron separation is only significant for particle momenta below 3 GeV due to the uncertainty in the reconstructed angle θ_C. The data sample for DVCS is typically centred at medium values of y. This is the reason why the RICH, that has been installed since the 1998 running period, is not very important for DVCS. However, the additional material added by the RICH can lead to incompatibilities of datasets between the RICH-era and previous years, as it strongly degrades the momentum resolution of the tracking system (cf. previous section).

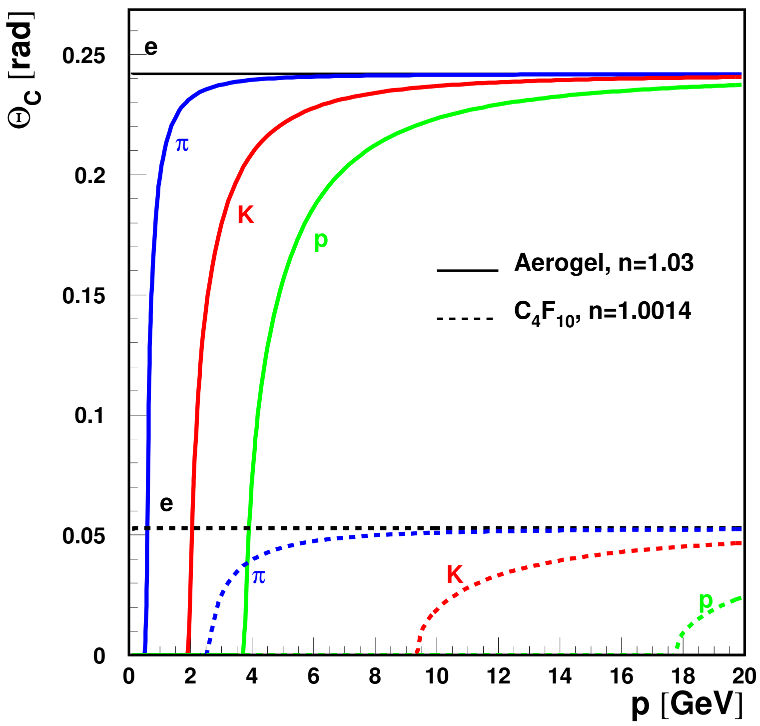

Figure 3.7.: Opening angle of the Čerenkov-cone as a function of particle type and momentum. Only below $p = 3$ GeV/c a separation between electrons/positrons and pions is achieved.

At higher particle momenta - which are typical for DVCS - the Transition Radiation Detector (TRD) is much more important than the RICH. Transition radiation is emitted by an ultra-relativistic particle that crosses the boundary between 2 dielectric media. For a single transition between a dielectric medium with plasma-frequency ω_{pf} and vacuum the mean radiated energy is given by

$$W_{TR} = \frac{2}{3}\alpha\gamma\omega_{pf}, \tag{3.10}$$

where γ is the relativistic constant given by $\gamma = 1/\sqrt{1-(\frac{v}{c})^2}$. The spectrum exhibits a cut-off such that the frequency ω of emitted photons is mostly below $\gamma\omega_{pf}$. Since the radiated energy as well as the cut-off are proportional to the relativistic factor γ, particles with the same momentum behave very differently if their rest masses are sufficiently different.

In practice, the detector has to provide many medium/vacuum transitions, since the number N of radiated photons per transition is small. The mean number of photons above a threshold of $\omega > 0.15\gamma\omega_{pf}$ is approximately 0.5α. Consequently materials like foil stacks, fibres or foams are commonly used. At the same time there is a minimum thickness of the dielectric for efficient radiation; this is described by the length z_f of the formation zone for transition radiation. For polyethylene at 10 keV and $10^3 < \gamma < 10^4$ a typical value of $z_f = 10$ μm is found. The formation zone in air is about 100 times longer. The named materials are well suited for these requirements and at HERMES loosely packed polyethylene fibres with a typical diameter of about 20 μm are used. In the HERMES TRD only transition radiation from particles with $\gamma > 920$ can be observed, which means that almost all electrons/positrons are above this threshold and almost all hadrons are below this threshold.

The emerging photons with X-ray energies are then detected by multiwire proportional chambers. Also hadrons will deposit some energy in the chambers due to ionisation loss. However, because of the smaller signal they are well separated from leptons. The TRD can provide an even better particle identification by combining the signals of all 6 subsequent TRD modules into a truncated mean value. This is shown in figure 3.8. A basic and efficient PID-cut can be

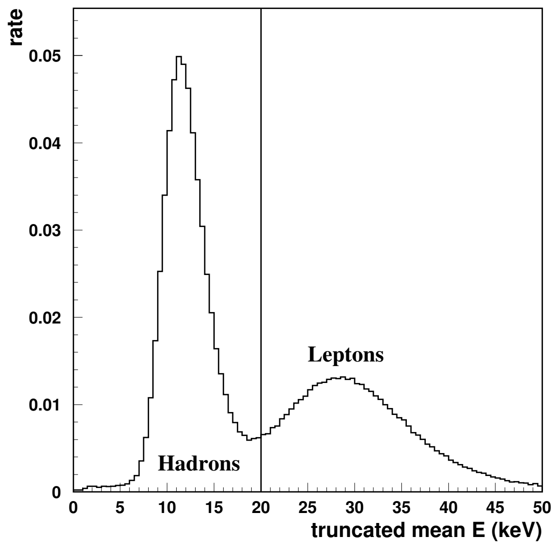

Figure 3.8.: Lepton PID using the truncated mean value of the raw TRD signals. The data corresponds to 25 runs of the 00c1-production.

applied by requiring that the truncated mean should be above or below 20 keV. This method will be used in this thesis if raw reconstructed event files are considered for systematic studies. For the main data productions a more refined PID is achieved [Wen03, Kai97] that leads to the logarithmic quantity

$$PID_5 = \log_{10}\left(\frac{\mathcal{L}_D^e}{\mathcal{L}_D^h}\right), \tag{3.11}$$

where $\mathcal{L}_D^e$ is the probability that a lepton gives the measured signal and $\mathcal{L}_D^h$ is the probability that a hadron gives the measured signal. These probability distributions are normalised to one. They are sometimes called parent distributions and can be obtained from test-beam experiments. At HERMES they can be extracted from measured data, since the different PID-detectors can be assumed to be statistically independent.

Another PID-detector is the preshower hodoscope H2. It consists of a layer of lead (1.1 cm) which corresponds to about 2 radiation lengths and an array of vertical scintillator panels behind it. The panels are 9.3 cm wide and 91 cm long which leads to a rather limited spatial resolution. The preshower detector exploits the fact that electromagnetic showers originating from an electron or positron start usually much earlier than hadronic showers. This means that the energy deposition of a lepton in the preshower is statistically higher due to the larger number of tracks, while hadrons usually only leave the signal of one minimum ionising particle. The preshower response of electrons and hadrons for deuterium data from the year 2000 is shown in figure 3.9.

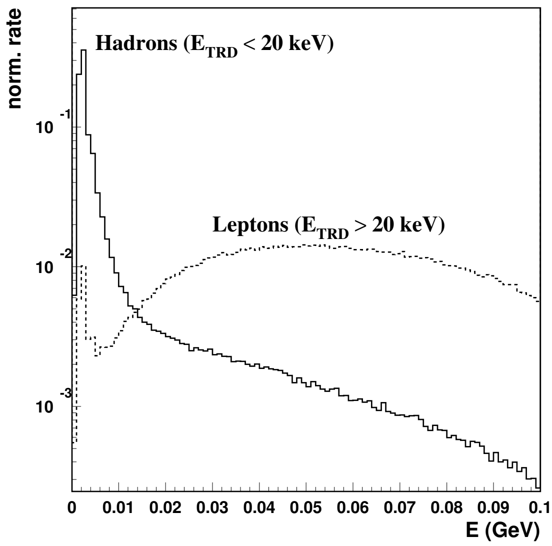

Figure 3.9.: Lepton PID using the preshower signal. A cut on the truncated mean value of the TRD is imposed such that hadrons and leptons are approximately separated. Both distributions are independently normalised to an area of one. The data corresponds to 25 runs of the 00c1-production.

It can be seen that the energy deposition of hadrons is typically smaller than 0.01 GeV, while the energy deposition for electrons is usually larger. The preshower response is momentum dependent as shown in figure 3.10. This means that in contrast to the TRD a hard cut on the preshower response will not only select leptons, but also prefer high lepton momenta.

The preshower can also be used in the case of photon-detection. With a statistical probability that is somewhat lower than for leptons, also high energy photons will start an electromagnetic shower in the preshower. The implications of such a preshower hit will be discussed in section 3.5.

The final PID-detector is not really a PID detector on its own: The electromagnetic calorime-

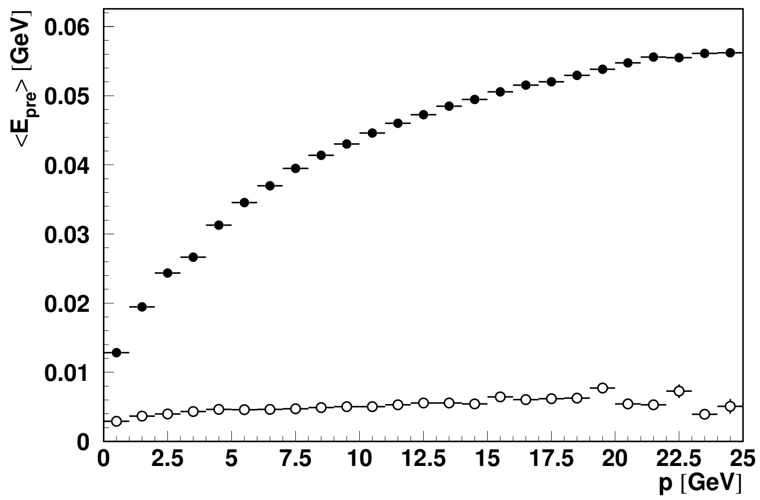

Figure 3.10.: Preshower signal depending on the particle momentum. Taken from [Kai97]. Solid circles denote leptons and open circles denote hadrons.

ter of HERMES measures the energy deposition of particles in a wall of 840 lead-glass-blocks; this energy deposition can be compared with the momentum of the particle that is determined from the tracking detectors in combination with the spectrometer magnet. The calorimeter is shown in figure 3.11.

The calorimeter blocks are made of the lead glass type F101 by Lytcarino, which is a pure Čerenkov-Radiator. The blocks cover an area of 9 cm × 9 cm and are 50 cm long. The radiation length of F101 is 2.78 cm and the Moliere radius is 3.28 cm. This leads to the result that even for the highest lepton energies at HERMES most of the shower is contained inside the calorimeter; the typical cluster size is 3 × 3 blocks for an electromagnetic/hadronic shower. Hadronic showers are not contained inside the depth of the calorimeter, which leads to the effect that a depth of only 30 cm would provide even better possibilities for particle identification. On the other hand the detection efficiency of such a system would be slightly lower.

The calorimeter is continuously monitored using the response to laser pulses (gain monitoring system / GMS). This procedure allows to study changes in the baseline as well as in the gain of the photomultiplier tubes. The energy of an incident lepton is obtained by a clustering algorithm which identifies hit arrays of up to 9 blocks and a subsequent cubic calibration curve that relates the signal in the cluster to the energy of an assumed lepton track. (This function is almost of the type $E_{cluster} = const. \times signal$ and only has marked deviations from this behaviour at very low lepton energies.) As energy and momentum of an electron/positron are identical at the observed energies, the calorimeter can be calibrated by using the tracking system and requiring a ratio of $E'/p' = 1$. In order to deal with instabilities, a year is typically divided into several periods that have a slightly different block-by-block calibration.

The ratio E'/p' can also be used as a starting point for a logarithmic PID as in the case of the TRD. The logarithmic PIDs of the calorimeter and the preshower detector are combined to the quantity PID_2. As the uncorrelated probabilities leading to PID_2 and PID_5 can be multiplied to provide combined probabilities, the quantities PID_2 and PID_5 have to be added to obtain a

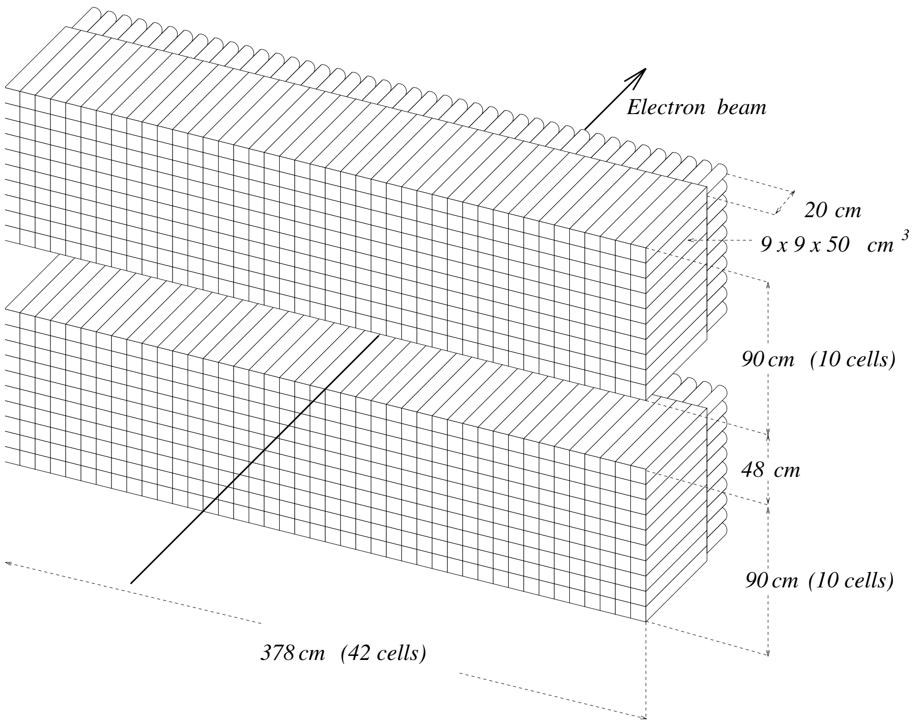

Figure 3.11.: Arrangement of calorimeter blocks for the HERMES-calorimeter.

combined PID. Finally due to the fact that the initial fluxes of leptons and hadrons are different the flux factor ϕ can be added:

$$\phi = \frac{N_e}{N_h}. \tag{3.12}$$

This flux-factor has to be subtracted in order to obtain the flux-corrected overall PID-value:

$$PID_{total} = PID_2 + PID_5 - \log \phi. \tag{3.13}$$

The interpretation of PID_{total} is that particles with $PID_{total} > 0$ have a higher probability of being a lepton than being a hadron, while for $PID_{total} < 0$ the opposite is true. At HERMES the flux-factor is usually in the order of $\phi \approx 1$, while $|PID_2 + PID_5|$ is usually much larger than 1 for leptons as well as hadrons. Hence the correction due to the flux-factor can also be neglected to a good approximation.

Moreover, in the case of DVCS the statistics does not allow to determine the lepton or hadron flux in small kinematical bins with all analysis cuts imposed. On the other hand a flux factor determined from an inclusive dataset would be too sensitive to different background situations in different years. This could introduce a false asymmetry in the case of the beam charge asymmetry, even if the detector response is the same.

The distribution of $PID_2 + PID_5$ for deuterium data of the years 2000 and 1998 is shown in figure 3.12. Two sets of events are used that will be defined in the following sections. While the single photon events still have a remaining contribution from hadrons, the exclusive event

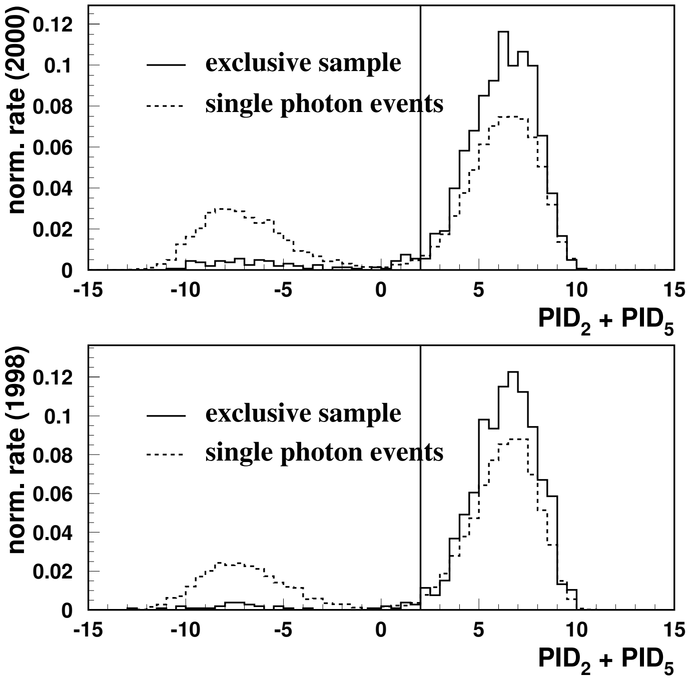

Figure 3.12.: The quantity PID_2+PID_5 is shown for leptons from single photon events (dashed) as well as from the exclusive events (solid). Unpolarised data from 2000 (top) and 1998 (bottom) is displayed.

kinematics removes almost all of it. Obviously the cut of $PID_2 + PID_5 < 2$ that will later be used does not cut strongly into the distributions. This means that the flux-factor correction that could move the optimum PID-cut by $\sim \pm 1$ has no effect. It is also clear that differences in the PID between the two years cannot lead to false asymmetries as long as the determined PID-value is not completely wrong.

3.4. Data Quality for DVCS

For any analysis at HERMES it must be ensured that the condition of the lepton-beam, the HERMES-target and all relevant sub-detectors allows the acquisition of useful data. Consequently apart from the fast readout of single event data, the slow control branch of the HERMES data-acquisition collects information about the detector status over longer time periods. When ever available - usually in intervals of seconds to minutes - this information is checked for potential problems and written to tape. Later it is merged with the tracked event data in a so-called μDST production.

Some information about the detector quality is already present in the μDSTs, but in general a more up-to-date data-quality can be taken from the 'bad-burst-lists' that are created by the data quality group. In this case the detector status per burst is encoded into a bit-pattern with

Table 3.2.: The listed bad bits were checked for data with an unpolarised target (bad bits && 0x503E13DC = 0).

bit	meaning	remark
2	select reasonable dead time	-
3	select reasonable burst length	$0 < L \leq 11$ s
4	select reasonable beam current	5 mA$< I_{beam} \leq 50$ mA
6	not first burst in a run	-
7	good μDST records	-
8	PID available	-
9	logbook: analysable	-
11	logbook: unpolarised data	-
12	logbook: DQ-info available	-
15	unpolarised target gas	valve settings
17	no dead blocks in CALO	-
18	no dead blocks in H2 or LUMI	-
19	TRD working	-
20	no high-voltage trips	-
21	no strange CALO or RICH	exclude some runs
28	beam polarisation available	$t < 5$ min since measurement
30	select reasonable dead time	fractional live-time $0.5 < f < 1.0$

32 bits. As several bits are related to the target status, different bit-patterns have to be checked for polarised or unpolarised periods of data-taking. The required bit-patterns for both cases are shown in tables 3.2 and 3.3. Although the bad bits are given for the top and the bottom half of HERMES separately, both halves are required to pass the cut at the same time.

Since the RICH detector is not very efficient at the typical high lepton energies in DVCS, no cuts are applied on the status of this detector. (Consequently the value PID_3, which includes the RICH, cannot be used for lepton identification.)

Some additional cuts were applied on burst level: For the datasets with unpolarised target gas the LUMI-rate r is limited to a range of $5.0 < r < 10000$. For the polarised dataset the analogous cut is encoded into bit 5. Only for the vector-polarised dataset a cut of $0.5 < |P| < 1.5$ is applied on the vector-polarisation of the target. This removes a few bursts with low or illegal target polarisation and makes sure that the mean polarisation for the target spin asymmetry can be taken from reference [Bec03]. For the tensor polarised data it is instead required that either $-2.5 < T < 1.5$ or $0.5 < T < 1.5$.

Independent of the target polarisation state the beam polarisation is limited to a realistic value of $|P_B| < 80$ %. Only for measurements that explicitly depend on the beam-polarisation, a lower cut on it is needed. It is placed at $|P_B| > 30$ %. To simplify the analysis the same dataset is also used for all other asymmetries. For the electron data of 1998 this cut is omitted as this data is not used to calculate a beam spin asymmetry. Additional checks are done on the consistency of the data structures in each file of the data production.

Table 3.3.: The listed bad bits (encoded in a hexadecimal number) were checked for data with a vector polarised target (bad bits && 0x5DBF97FD $= 0$). For the tensor polarised data taken at the end of 2000 the cut "bad bits && 0x59BF97FC $= 0$" is used, i.e. bits 26 and 0 are omitted for obvious reasons.

bit	meaning	remark
0	longitudinal target pol.	-
2	select reasonable dead time	-
3	select reasonable burst length	$0 < L \leq 11$ s
4	select reasonable beam current	5 mA$< I_{beam} \leq 50$ mA
5	select reasonable luminosity	-
6	not first burst in a run	-
7	good μDST records	-
8	PID available	-
9	logbook: analysable	-
10	logbook: polarised data	-
12	logbook: DQ-info available	-
15	polarised target gas	valve settings
16	target working	-
17	no dead blocks in CALO	-
18	no dead blocks in H2 or LUMI	-
19	TRD working	-
20	no high-voltage trips	-
21	no strange CALO or RICH	exclude some runs
26	no tensor polarisation	-
28	beam polarisation available	$t < 5$ min since measurement
30	select reasonable dead time	fractional live-time $0.5 < f < 1.0$

3.5. Cuts on Lepton and Photon Kinematics

It is clear that a number of requirements have to be fulfilled at event level that are either dictated by the HERMES-acceptance or by the physics of interest. The study of DVCS at HERMES relies on the detection of one lepton track with the charge of the lepton beam and a high energy photon that causes an untracked cluster in the calorimeter. To be more precise also additional short tracks that do not hit the calorimeter indicate the wrong event type; these tracks can be reconstructed with the help of the magnet chambers and are detected above momenta of about $P = 0.5$ GeV/c.

For additional photons the detection threshold in the calorimeter is even lower, but due to the background situation at HERMES, data-productions only include photon clusters above $E = 0.8$ GeV. One exception is made for photons which point along the front partial track of a long track; the energy of these photons is stored for values as low as $E = 0.21$ GeV. If the track belongs to an electron or positron, it is very likely that the cluster was caused by Bremsstrahlung emitted inside the spectrometer. It was checked that only a negligible effect is seen, if such clusters with an energy of more than $E = 0.8$ GeV are included as a veto.

It is also required that the event has been recorded due to the standard DIS trigger (trigger 21) which is formed from the trigger hodoscopes and the calorimeter. More details on this trigger will be given in section 3.7. In this way it is avoided that other triggers that are also sensitive to lepton tracks (like trigger 18) but are sometimes heavily prescaled have an impact on the dataset. In general the inclusion of these other triggers would only marginally increase the available event statistics.

After the triggering lepton is identified by $PID_2 + PID_5 > 2$, cuts due to detector geometry are applied. The track may not hit the calorimeter at the edges, as the shower will not be contained inside the calorimeter. Under these conditions the trigger threshold as well as the PID would have unpredictable effects. For the reconstructed x- and y-position of the lepton cluster this means

$$|x_{cluster}| < 175 \text{ cm}, \tag{3.14}$$

$$30 \text{ cm} < |\mathrm{y_{cluster}}| < 108 \text{ cm}. \tag{3.15}$$

The momentum threshold for the lepton is chosen as follows: Although the highest included trigger-threshold in the dataset is at a lepton cluster energy of 3.5 GeV, it has been found in [Ell03] that a restrictive cut of $\nu < 22$ GeV should be used to improve the comparability of data from 1998 and 2000. This can be related to a slightly different response of the trigger system, which is not surprising, as the correct calorimeter calibration can only be done after the data has been taken. In addition for 1998 the problem was seen that one of the target spring fingers at the end of the cell was bent into the beam halo. This led to an excess of low energy leptons in the HERMES acceptance. It is difficult to judge which of the two effects has a bigger impact on the momentum distribution of inclusive leptons that was studied in [Ell03]. While spring finger events can be expected to fail the exclusivity cuts for DVCS, the trigger threshold would have a real impact also for exclusive events.

In order to reduce all external background, cuts on the reconstructed vertex are imposed. The true vertex distribution is given by the density profile of the gas inside the target cell and the beam position and width. Along the z-direction the gas density profile is almost triangular with its maximum density at $z = 0$ cm and almost vanishing density at $z = -20$ cm and

$z = 20$ cm. Tracks that do not point to this region can originate from lepton scattering on solid material inside the target chamber or secondary vertices. A prominent source of background is the collimator C2 which stops 4 cm in front of the cell at $z = -24$ cm. In order to remove such background a cut of -18 cm$< v_z < 18$ cm is applied. v_z is calculated as the z-position of the point of closest approach between the front track and the nominal beam axis. The distance between the track and the beam at this point is called transverse vertex v_t.

As will be shown later, cuts on v_t should always cut far outside the reconstructed beam-profile. Otherwise the mean value of the reconstructed momentum will be systematically wrong. The true beam dimensions are about $\sigma_x \approx 0.25$ mm and $\sigma_y \approx 0.07$ mm at the position of the HERMES-target. Because of the tracking resolution of HERMES the true distribution of v_t is much broader such that a cut at $v_t < 0.75$ cm should be used. At larger transverse separations, the tracks are probably not directly originating from the beam and hence the event has to be discarded.

From the physics point of view not all leptons are of interest: The study of DVCS requires leptons with deeply virtual scattering kinematics. Hence cuts on the inclusive kinematical variables are needed:

- $Q^2 > 1$ GeV^2: hard virtual photon,
- $W^2 > 4$ GeV^2: outside resonance region.

In order to reduce the background, the following more restrictive cuts are applied according to the results in reference [Ell03]:

- 1 GeV$^2 < Q^2 < 10$ GeV^2,
- $W^2 > 9$ GeV^2,
- 0.03$< x_B <$0.35.

For the photon cluster there are also cuts that are related to the experiment and cuts that are related to the physics process under study. From the experimental point of view, the cluster must not be too close to the edge of the calorimeter as the reconstructed energy will again be wrong; however the photon must also pass the opening of the spectrometer magnet, and since the photon is not deflected by the magnetic field, this translates directly into a very restrictive cut on $x_{cluster}$. Moreover, as the measured energy is used to calculate the photon kinematics also more restrictive cuts on $y_{cluster}$ are introduced:

$$|x_{cluster}| < 125 \text{ cm}, \tag{3.16}$$
$$33 \text{ cm} < |\mathrm{y_{cluster}}| < 105 \text{ cm}. \tag{3.17}$$

In addition a cut on the associated signal in the preshower detector of $E_{pre} > 1$ MeV is introduced. This has three reasons: First of all some limited PID is possible with this cut: Neutrons and a very small fraction of not reconstructed charged hadron tracks will be rejected. Secondly, background from the proton beam is reduced: Since such showers enter the calorimeter from the back, they do not necessarily hit the preshower as well. Finally the preshower signal is required in order to obtain an improved energy resolution of the calorimeter for photons.

As was discussed in [Ely02] the probability that a photon starts an electromagnetic shower in the preshower detector is slightly lower than the same probability for a lepton of the same energy. Consequently the reconstructed photon-energy in the CALO will be slightly higher for the photon. One possibility to deal with this different shower evolution is to multiply the measured photon energy by a correction factor of 0.97 and to assume that the average shower centre occurs 9.5 cm later than in the case of the lepton. Although this procedure may work well for the reconstruction of the π^0 from its decay-photons, a different procedure is advisable in the case of DVCS. As the main concern is exclusivity of the data sample it is better to reject events which do not have a signal in the preshower detector and thus to improve the energy resolution for the remaining sample.

If the preshower has fired, the following shower evolution for initial photons and leptons is very similar and no correction factor for the energy is needed. Energy and momentum resolution of the calorimeter will be discussed in more detail in chapter 5.

There is also a cut that is motivated by the background situation in the experiment: At low cluster energies there is a high probability for the detection of decay photons from π^0 and η-decay. In addition uncorrelated background will decrease with increasing cluster energy. As DVCS at HERMES is mainly found at medium energies of about 15 GeV, a cut on the cluster energy was applied at 3 GeV.

3.6. Exclusivity Cuts

Finally, a number of requirements are necessary in order to achieve an exclusive data-sample. A very effective cut is possible due to the fact that the BH and DVCS amplitudes peak along the direction of an assumed virtual photon. This allows to place a cut on the angle θ_{γ,γ^*} between the real and the virtual photon in the laboratory system. For the first DVCS-analysis at HERMES a cut of $\theta_{\gamma,\gamma^*} < 70$ mrad was used. If the virtual photon points towards the centre of one calorimeter half, the maximum value of θ_{γ,γ^*}, for which all values of ϕ can be detected, is about 50 mrad; hence strong acceptance effects can be expected with this cut. Also due to the strong background at large values of θ_{γ,γ^*} the upper cut was later lowered to 45 mrad in reference [Ell03].

Due to smearing effects that will be discussed in the following chapter, also a lower cut on θ_{γ,γ^*} is needed. It is placed at 5 mrad and will be discussed in section 5.5.

In addition a cut has to be placed on the variable t: An upper limit is needed due to background conditions; moreover the factorisation theorem for DVCS requires that $|t| \ll Q^2$.

The straightforward calculation of t from the lepton and photon kinematics leads to

$$t = (\mathbf{q} - \mathbf{v})^2 = -Q^2 - 2E_\gamma(\nu - \sqrt{\nu^2 + Q^2}\cos\theta_{\gamma,\gamma^*}). \tag{3.18}$$

An inspection of this result shows that the energy of the photon enters as a factor only in the second term. Since t is small in comparison with $Q^2 >$, the magnitude of the second term must be similar to Q^2. This is the reason, why the energy resolution of the calorimeter, which is in the order of a few per cent, leads to a large uncertainty in t.

In order to eliminate this uncertainty without detecting the hadronic final state, a price has to be paid: If the process was elastic, energy and momentum conservation can be used to remove E_γ from the calculation of t. In a closed expression this 'constrained t' denoted as t_c

can be written in the following way:

$$t_c = \frac{-Q^2 - 2\nu(\nu - \sqrt{\nu^2 + Q^2}\cos\theta_{\gamma,\gamma^*})}{1 + \frac{1}{M}(\nu - \sqrt{\nu^2 + Q^2}\cos\theta_{\gamma,\gamma^*})}, \tag{3.19}$$

where the proton mass is assumed for the mass M of the recoiling target particle. For a free target proton at rest the constrained t_c is mathematically identical to the true t. For background processes on the other hand there is no obvious relation between t and t_c. If the hit target particle is not detected, differences are also obtained for the coherent process and the incoherent process depending on the assumed target mass. Moreover, for the incoherent process problems enter due to the Fermi-motion of the nucleon; in the following discussions this point will be neglected, and only the quasi-free case will be considered.

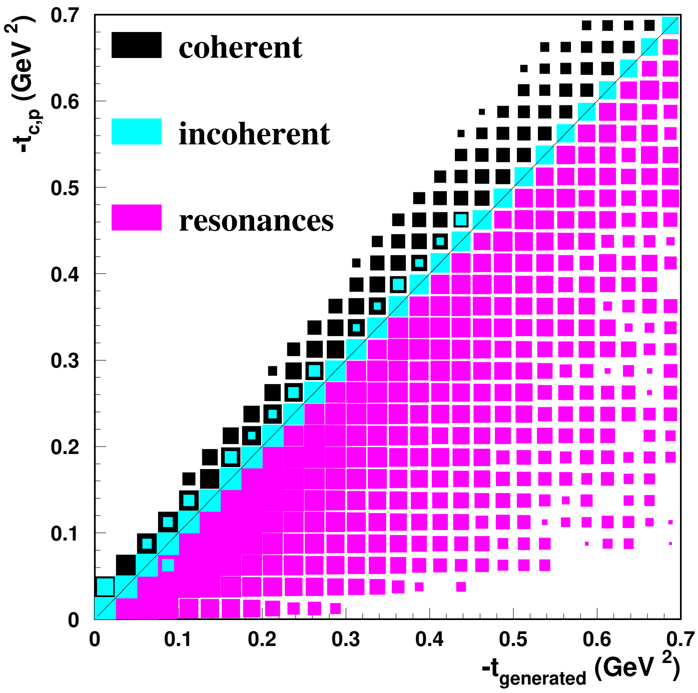

Figure 3.13.: Monte Carlo prediction (Deuterium target) for constrained t ($t_{c,p}$) vs. generated t. An ideal HERMES-acceptance is included but smearing is switched off. The coherent, elastic process, the incoherent, elastic process and the incoherent process with resonance excitation are shown separately.

Figure 3.13 shows a Monte Carlo simulation for a Deuterium target with an ideal HERMES acceptance and no smearing or detection inefficiency. The constrained t assuming the proton mass, $t_{c,p}$, is plotted vs. the generated t. For the incoherent process the two quantities are equal. Also for the coherent process they are similar, at least at small values of t, where it is actually observed. For the resonance region this correlation is completely lost. However the resonances are not the main point of interest and for a separation of the different processes t_c is still useful as will be discussed in section 6.9.

Table 3.4.: The listed requirements were used to select "single photon events".

cut	meaning
trigger=trigger21	only use standard DIS trigger
$\lvert x_{cluster,e}\rvert < 175$ cm	lepton hit position on calorimeter
30 cm $< \lvert \mathrm{y_{cluster,e}}\rvert < 108$ cm	lepton hit position on calorimeter
$\nu < 22$ GeV	energy transfer from lepton
-18 cm$< v_z < 18$ cm	longitudinal lepton vertex position
$v_t < 0.75$ cm	transverse lepton vertex position
$PID_2 + PID_5 > 2$	particle identification as lepton
1 GeV$^2 < Q^2 < 10$ GeV^2	4-momentum transfer
$W^2 > 9$ GeV^2	invariant final state mass
$\lvert x_{cluster}\rvert < 125$ cm	photon hit position on calorimeter
33 cm $< \lvert \mathrm{y_{cluster}}\rvert < 105$ cm	photon hit position on calorimeter
$E_\gamma > 3$ GeV	cluster energy
$E_{pre} > 0.001$ GeV	preshower energy for cluster
5 mrad$< \theta_{\gamma,\gamma^*}$ <45 mrad	angle between real & virtual photon
$\lvert t_c\rvert < 0.7$ GeV^2	4-momentum transfer to target (elastic case!)

For the data analysis a cut of $|t_c| < 0.7$ was applied according to the results in reference [Ell03]. In the following, all events that pass the cuts until now will be referred to as "single photon events". The cuts are summarised in table 3.4.

Although the cuts on θ_{γ,γ^*} and t lead to an increase of the fraction of exclusive events inside the data sample, even with a perfect spectrometer they will not totally exclude non-exclusive events. This can only be achieved by applying a cut on the missing mass which is defined in the following way:

$$M_x^2 = (\mathbf{k} + \mathbf{P} - \mathbf{k}' - \mathbf{v})^2. \tag{3.20}$$

with the 4-vectors defined in section 2.1. As the obtained values for M_x^2 can also be negative with the given resolution of HERMES , there is no reason to consider M_x. However it has been used in previous publications and can be defined as the square root of $|M_x^2|$, while the sign is taken from M_x^2. Clearly the same problems as for t enters here with nuclear targets: The vector $\mathbf{P}$ depends on the mass of the interacting particle. In the following the mass of an on-shell proton will be inserted, but in reality also the coherent reaction on the Deuteron can occur. In practice a similar behaviour is found, which means that a cut on M_x under the assumption of the proton mass also keeps the other exclusive reaction type, but discards background.

This is shown in figure 3.14. The reason for this can be seen if M_x^2 is written in the following way:

$$M_x^2 = m_p^2 + 2m_p(\nu - E_\gamma) + t. \tag{3.21}$$

t does in this case not depend on the proton mass as it is obtained according to equation 3.18. Since t and $\nu - E_\gamma$ are small for the coherent as well as for the incoherent process, the missing mass distribution for both of them peaks at $M_x^2 = m_p^2$, if m_p is assumed to be the mass of the

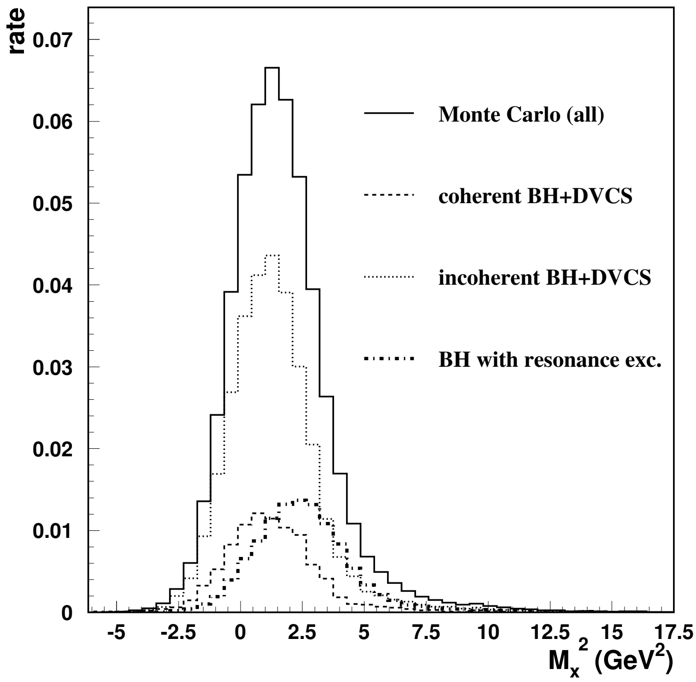

Figure 3.14.: Monte Carlo prediction for the event distribution in M_x^2 obtained for BH/DVCS on a deuterium target. Coherent as well as incoherent exclusive events accumulate at the proton mass. The peak for resonance excitation is slightly displaced.

hit target-hadron. With the kinematical resolution of HERMES the coherent process is indistinguishable from the incoherent process as seen in the figure. The resonances are on the other hand moved to higher missing masses.

In order to select exclusive events, all cuts for single-photon events are applied and in addition it is required that -2.25 GeV^2 $< M_x^2 < 2.89$ GeV^2. The remaining event sample will be referred to as "exclusive sample".

The kinematical correlations within this dataset are shown for polarised and unpolarised deuterium-data from 2000 in figure 3.15. There is a strong correlation between x_B and Q^2 due to the HERMES-acceptance (cf. section 3.8). As both variables can also be related to y, it will be non-trivial to discriminate between an x_B, y or Q^2 dependence of asymmetries.

3.7. Luminosity and Normalisation

The **observed** event rate R in an experiment is related to the cross-section under study by

$$R = d\sigma\mathcal{L}\mathcal{E}, \tag{3.22}$$

where $\mathcal{L}$ denotes the luminosity and $\mathcal{E}$ denotes the efficiency. The following effects contribute to the detection efficiency at HERMES :

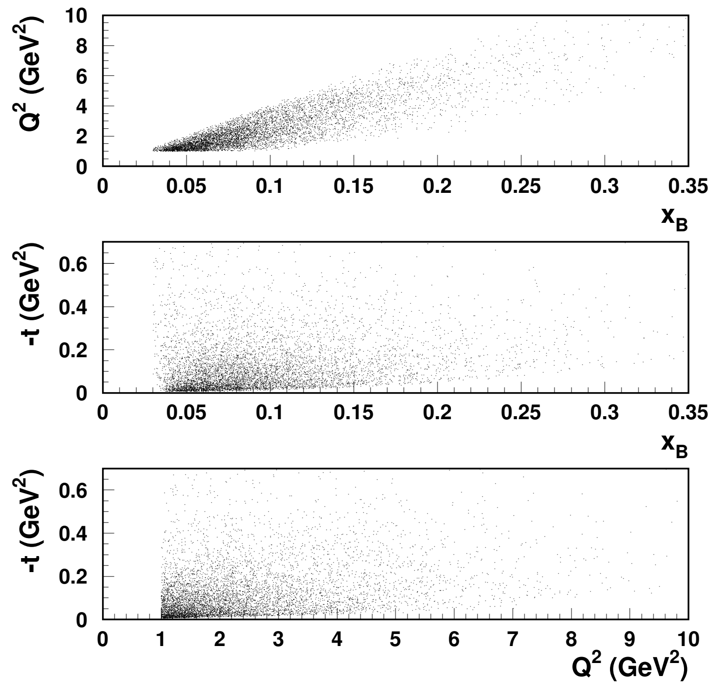

Figure 3.15.: Selected exclusive events plotted as 2d distributions in the variables x_B, Q^2 and t.

1. Detector dead-time (mostly due to the read-out cycle): It is continuously monitored by the DAQ.
2. Trigger efficiencies: They are in general high; remaining uncertainties will be discussed below.
3. Detection efficiencies: The efficiencies of all tracking detectors are usually only studied for whole detector planes and calculated in the offline production.
4. Track finding efficiency: It originates from the interplay of detection efficiencies, misalignment, multiple scattering of particles and the track reconstruction algorithm and is assumed to be very high.

Even if all effects are taken into account, the measurement of an absolute cross-section is not trivial. On the other hand it is easy to normalise different datasets to the same luminosity, by using the proportionality to the rate of accepted deep inelastic scattering events $\dot{N}_{DIS} \propto \mathcal{L}$. As long as the experimental setup is not changed, the relation

$$\frac{N_{DIS,1}}{N_{DIS,2}} = \frac{\int_1 dt\,\mathcal{L}}{\int_2 dt\,\mathcal{L}} \tag{3.23}$$

between the respective event numbers $N_{DIS,1/2}$ and the integrated luminosities of the two samples is strictly valid. In principle this method is applicable in the case of beam-spin and beam-charge asymmetries. For target-spin asymmetries the DIS-cross-section contains double-spin asymmetries such that the proportionality constant between N_{DIS} and $\mathcal{L}$ depends on the beam and target polarisation.

As soon as datasets for different years are compared, changes in the apparatus as well as accumulating radiation damage can lead to different detection efficiencies or to a different detector acceptance. Thus problems with DIS-normalisation can occur, if the HERMES data that was taken before the installation of the RICH detector in 1997 is merged with the dataset from 1998 to 2000.

Some uncertainty for the dataset from 1998 to 2000 is due to the change from an electron to a positron beam. Since the polarity of the spectrometer magnet was not reversed, this means e.g. that low momentum leptons for 1998 are deflected into the right-hand side of the HERMES calorimeter, while they were deflected to the left-hand side for 1999 and 2000. In addition leptons with the same initial momentum vectors pass the HERMES spectrometer on very different trajectories.

The known main differences in DIS-counting between 1998 and 1999/2000 (cf. [dN02, dN01]) are on the other hand due to experimental problems and not to the beam charge:

- the bent target spring-finger in 1998,
- differences in the trigger response.

A detailed treatment of the efficiency of the trigger 21 that is also required for DVCS events is given in [dN02]. It turned out that the H0-hodoscope, which is required to fire in order to obtain the standard DIS-Trigger No. 21, has a varying efficiency over the years. Trigger 21 is formed from an above-threshold signal in the hodoscopes H0, H1 and H2 and a cluster with an energy deposition of more than 1.4 GeV in the case of polarised target gas or more than 3.5 GeV in the case of unpolarised target gas. H0 consists of 2 unsegmented scintillator planes at a position of $z = 145$ cm. The dimensions are 60 cm$\times 20$ cm$\times 0.32$ cm and each plane is connected to four photo-multiplier tubes.

In 1998 a low gain of one or more PMs caused an efficiency drop in the lower right corner of the H0 (viewed along the lepton beam direction), while in 2000 some radiation damage was found close to the beam-pipe in the upper half. The inefficiencies of H0 can be studied by using the Trigger 18, which only contains the H1, the H2 and the calorimeter (in 2000 a trigger signal from the MCs was included in trigger 18 but not in trigger 21; however, this has no effect on the following discussions). Assuming that all trigger detectors have uncorrelated trigger efficiencies, which is certainly valid for leptons at such energies, events with trigger 18 can be used in the following way: If trigger 18 has fired and a lepton track is found that points to the H0-hodoscope, the probability $P(21 \wedge 18)$ that trigger 21 has fired in addition provides the trigger efficiency of the H0:

$$P(H0) = \frac{P(21 \wedge 18)}{P(18)} = \frac{P(H0 \wedge 18 \wedge 18)}{P(18)} = \frac{P(H0) \cdot P(18)}{P(18)}. \tag{3.24}$$

In the case of DIS-counting the position dependence of $P(H0)$ can be ignored and only the integrated probability over the whole area of the H0 is used.

The event-by-event efficiency of the H0 depends also on the hit multiplicity:

- For events with additional tracks, the H0-efficiency is strongly increased. Since hadrons have at least the same energy deposition in the H0 as high momentum leptons, the prob-

Table 3.5.: For DIS-counting at least one long lepton track fulfilling the shown requirements was needed per event.

requirement	meaning
$\lvert x_{cluster,e}\rvert < 175$ cm	lepton hit position on calorimeter
30 cm $< \lvert \mathrm{y_{cluster,e}} \rvert$	lepton hit position on calorimeter
$\nu < 22$ GeV	energy transfer from lepton
-18 cm$< v_z < 18$ cm	longitudinal lepton vertex position
$v_t < 0.75$ cm	transverse lepton vertex position
$PID_2 + PID_5 > 1$	particle identification as lepton
$Q^2 > 1$ GeV^2	4-momentum transfer
$W^2 > 4$ GeV^2	invariant final state mass

ability to fire H0 in the presence of an additional hadron is

$$P(H0)_{total} = 1 - (1 - P(H0)_{lepton})(1 - P(H0)_{hadron}). \tag{3.25}$$

If the detection probabilities for both particles are 90%, the combined efficiency amounts to 99%. The additional particles can also have very low momenta such that they are not reconstructed by the tracking system.

- H0 can also be triggered by uncorrelated particles. Even for an empty target the rates of the two H0-halves are in the order of 0.5 MHz due to beam-related background. For end-of-fill running the random H0-rate can be in the order of several MHz due to low energy Møller/Bhabha electrons from the target. Hence the H0-efficiency depends on the target density.

For the purpose of DIS-counting it is certainly advisable, to calculate the trigger-efficiency exactly for the same dataset and with exactly the same cuts as for DIS-counting. The only difference is that DIS-counting requires trigger 21 (the same trigger as the DVCS-analysis), while the efficiency calculation uses the sometimes heavily prescaled trigger 18. As the prescale-factor for trigger 18 was not constant, target-density effects will not cancel completely, but for this analysis their impact is small. This will become clear when the effects of the correction are discussed in section 6.3. Also an additional momentum-dependent correction as suggested in [dN02] will not be applied.

For the DIS counting and the DIS-trigger efficiency calculation, the event cuts shown in table 3.5 were used apart from the burst cuts defined before. The requirements for y, Q^2 and W^2 are the standard ones for DIS; the requirement for ν as well as the vertex cuts are motivated by the target spring-finger. Again the requirement for ν also eliminates differences in the trigger-threshold of the calorimeter. The efficiency corrected DIS-event number is in the end obtained from $N_{corr} = N_{DIS}/P(H0)$.

The DIS-normalisation is not sensitive to dead-time corrections or global tracking inefficiencies, as the DIS events as well as the DVCS events will be affected in the same way. This allows to obtain precise asymmetries, although the absolute cross-section cannot be measured in this way.

At HERMES a second method can be used to measure the luminosity directly: The luminosity monitor - a small calorimeter close to beam-pipe - observes symmetric Bhabha/Møller scattering on the electrons of the target gas. In the symmetric case two leptons with similar energies are obtained under back-to-back kinematics with respect to the beam. The luminosity monitor provides a measured coincidence rate R_{LUMI} that is related to the integrated luminosity L by a luminosity constant $\mathcal{C}$:

$$L = \mathcal{C}A/Z \int dt\, R_{LUMI}(t), \tag{3.26}$$

where A denotes the number of nucleons per nucleus and Z denotes the number of protons per nucleus. For the years 1999/2000 a detailed study [Els02] provided a value of $\mathcal{C} = 417$ mbarn^{-1}. The value for these years is very reliable, while uncertainties remain for 1998 due to a shifted and/or unstable beam-position. In addition $\mathcal{C}$ for 1998 is reduced by a factor of about 0.6 to take into account the different cross-sections for Møller scattering and Bhabha scattering (together with pair annihilation).

As the luminosity monitor is a separate system with very high live-time, the measured luminosity has to be decreased by the the relative spectrometer live-time in order to obtain the observed luminosity. Global tracking efficiencies are not taken into account. Especially for the year 2000 this normalisation has obvious advantages, as an absolute cross-section measurement is possible for DVCS. In particular a quantitative comparison of data and Monte Carlo is possible.

Depending on the asymmetry, both normalisation methods can have advantages and disadvantages. In the case of the BCA only the DIS-normalisation can be used, due to the limited accuracy of $\mathcal{C}$ for 1998. For the case of the BSA the LUMI-normalisation and the DIS-normalisation are equivalent, but the DIS-normalisation will be used. In the case of the target spin asymmetry it is preferable to split the dataset into four different parts with different spin orientations of the beam and target particles. In this case the (fitted) LUMI-rate should be used to obtain the correct normalisation for all four datasets. In the case of tensor polarisation dependent asymmetries, both methods for normalisation are again equivalent, as the tensor asymmetry of DIS is known to have only a small effect on the total DIS-statistics. Here the LUMI-normalisation has been chosen.

3.8. Trigger Efficiencies for DVCS

Also in the case of DVCS the trigger efficiencies of the H0-hodoscope have to be considered. Two main differences occur with respect to the calculation for the DIS-events:

- For DVCS only one charged track passes H0.
- The trigger efficiency has to be known depending on the hit-position on H0.

Here a 2-dimensional efficiency distribution has to be created for single-lepton events. The number of untracked clusters is irrelevant in this context; the only possible dissimilarity between such single track events and DVCS-events with tracks of the same kinematics is due to additional tracks that have not been reconstructed. Consequently the trigger efficiency can be slightly overestimated if additional clusters are due to not reconstructed tracks. In the calculation of the efficiency the same cuts have been applied as for DIS-counting.

The hit position on the H0-hodoscope is obtained under the assumption that the lepton originated from the beam, which is ensured by the cut on the transverse vertex. The hit position on the H0 is calculated by

$$x = (145\ \mathrm{cm} - \mathrm{v_z}) \tan\theta_\mathrm{e} \cos\phi_\mathrm{e}, \tag{3.27}$$

$$y = (145\ \mathrm{cm} - \mathrm{v_z}) \tan\theta_\mathrm{e} \sin\phi_\mathrm{e}, \tag{3.28}$$

where θ_e and ϕ_e denote the polar and the azimuthal angle of the lepton.

Some compromise has to be made for the binning: At the centre of the H0 the event rates are rather high, while they are much lower at the edges. Close to the edges only a few events per bin are usually obtained. The bin size was adjusted such that also the bins on the edges contain at least one event (final bin size $4\ \mathrm{cm}\times 4\ \mathrm{cm}$). Most of the DVCS-candidates have lepton tracks close to the centre such that the statistical uncertainty of the correction is low. The distribution of events firing triggers 18 and 21 for the unpolarised deuterium dataset of 1998 and 2000 is shown in figure 3.16.

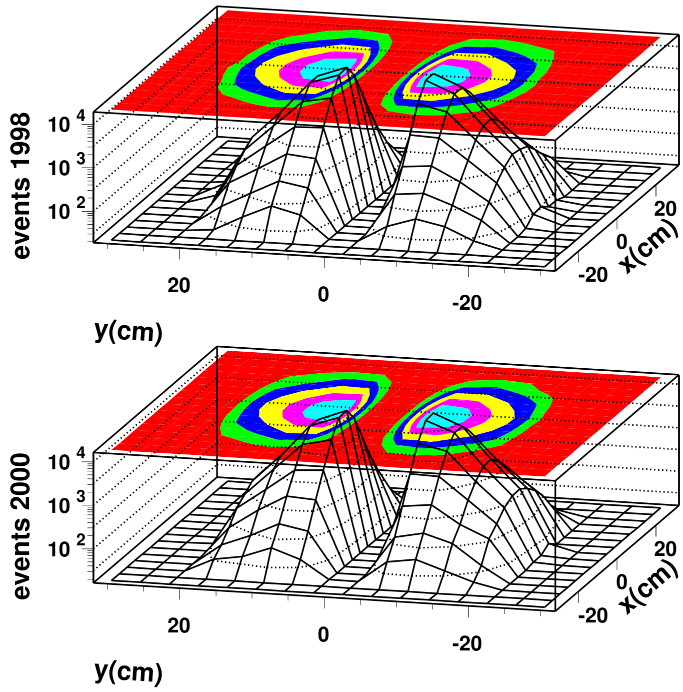

Figure 3.16.: Trigger 18&21 events at position of H0: The number of events that have triggered trigger 18 and trigger 21 and contain exactly one good track (identified as a lepton), that points to the H0-hodoscope, is shown as function of the hit position on the hodoscope. Unpolarised deuterium data from 1998 and 2000.

The trigger efficiencies for the unpolarised deuterium dataset from the years 1998 and 2000 is shown in figure 3.17.

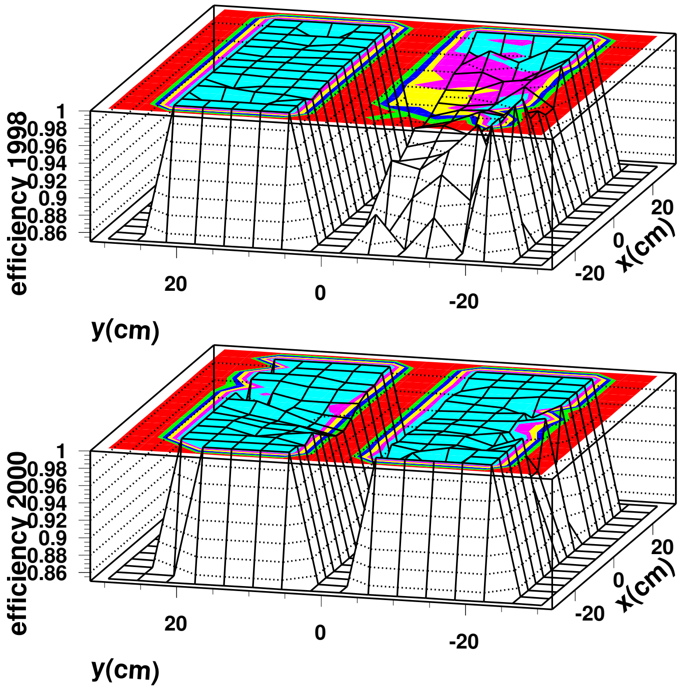

Figure 3.17.: Single track trigger efficiency of the H0 hodoscope depending on the hit position. Unpolarised deuterium data from 1998 and 2000 is shown.

3.9. Constraints on DVCS Kinematics

The discussed requirements for the DVCS-kinematics together with the HERMES-acceptance lead to a very complicated multi-dimensional acceptance. This means that effectively the acceptance in x_B and Q^2 is much smaller than the region that is obtained for inclusive or semi-inclusive measurements.

In order to get a better understanding of the expected effects a four-dimensional acceptance map was generated that depends on the 4 kinematical quantities x_B, Q^2, t and ϕ. Only elastic single photon production on a proton was considered in this case. A 2-dimensional numerical integration was done with respect to the longitudinal lepton vertex v_z and the angle ϕ_e around the lepton beam. The HERMES-acceptance for the photon and the lepton were approximated by a box-acceptances at the position of the calorimeter. In the case of the lepton the deflection in the magnetic field of the spectrometer magnet was obtained from the same look-up table that is used by *hrc*. All other kinematical cuts were not used for this study.

The main interest was to identify the region in x_B, Q^2 and t for which full coverage in ϕ is obtained. This is necessary since the GPD-models depend on all of these variables and consequently nothing is known about the asymmetries in gaps of the acceptance. For four fixed values of Q^2 and $x_B = 0.1006$ the acceptance $\mathcal{A}$ in terms of t and ϕ is shown in figure 3.18. These plots are obtained at four grid points of the acceptance map, but the acceptance at any point in kinematics can be obtained from multidimensional, linear interpolation.

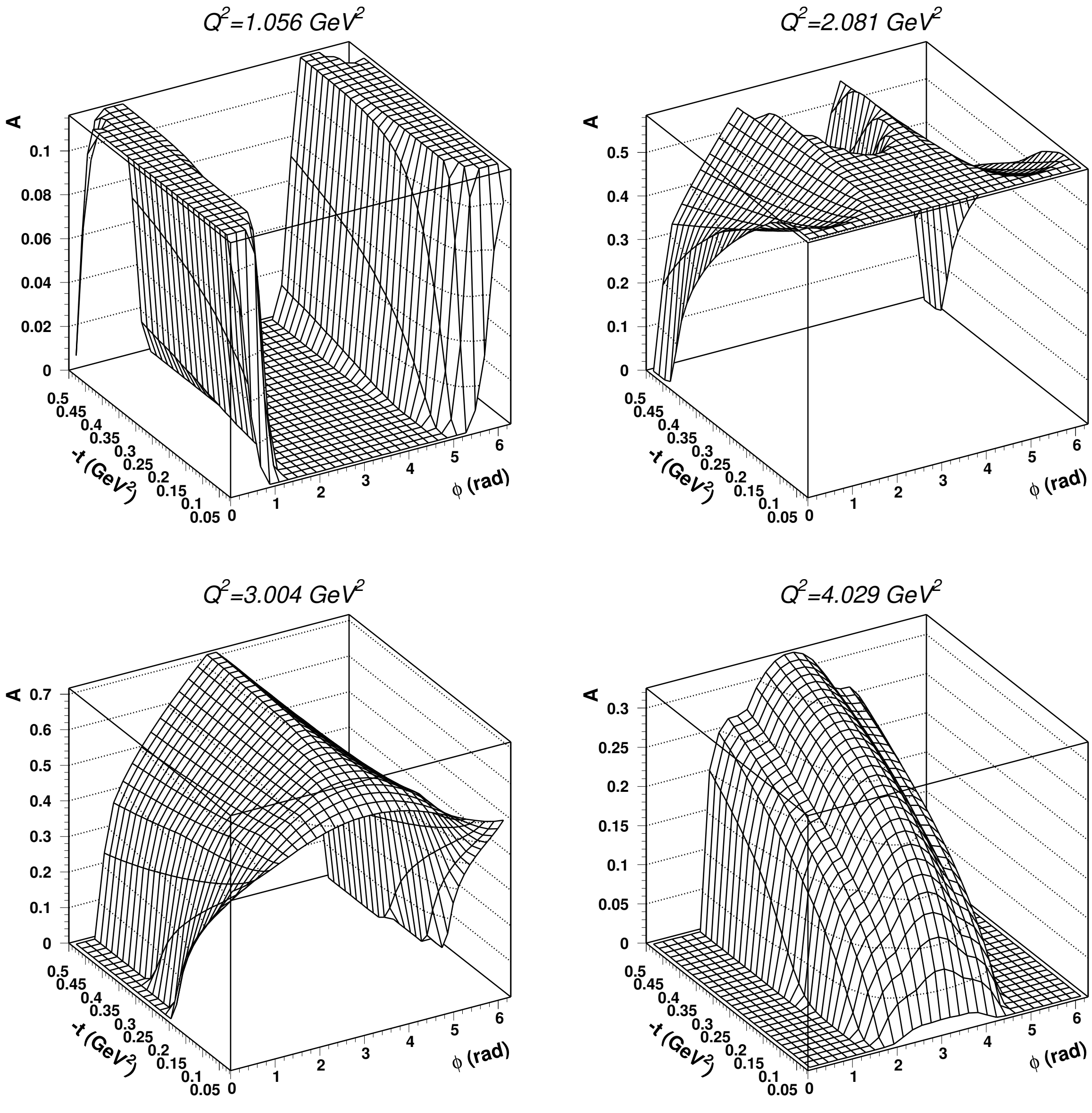

Figure 3.18.: 2d slices of the 4d acceptance map. The acceptance is plotted as a function of ϕ and t at a fixed value of $x_B = 0.1006$ and the indicated value of Q^2. Only the geometrical acceptance and the momentum threshold are included in the calculation of the acceptance map.

For low values of Q^2 the virtual photon points towards the outer edge of the calorimeter; consequently the acceptance is poor for $\phi \approx \pi$, as the real photon is emitted under large angles θ with respect to the beam. The larger $|t|$, the larger is θ if $0.5\pi < \phi < 1.5\pi$. For intermediate values of Q^2 the virtual photon points toward the centre of the calorimeter. At low values of $|t|$ no gaps are seen in the acceptance; only for larger values of $|t|$ the acceptance decreases for all values of ϕ. For larger values of Q^2 the virtual photon points toward the inner edge of the calorimeter. In this case angles of $\phi \approx 0$ are related to photons that are too close to the beam.

In addition to the photon also the scattered lepton enters into the overall acceptance, which makes its behaviour non-trivial.

As all gaps in four dimensions lead to uncertainties in the cross-section, there is no point in calculating an average 2d-acceptance depending on x_B and Q^2. Instead a meaningful 2-dimensional plot can be obtained by plotting the minimum value of the acceptance function for all values of ϕ and $|t| < |t_{max}|$ as a function of x_B and Q^2. This is shown in figure 3.19 for $|t| < 0.2$ GeV^2. A narrow band in x_B and Q^2 is obtained; for larger values of $|t|$ this band is even smaller, while for smaller values of $|t|$ it is wider but the t-cut would remove most of the data.

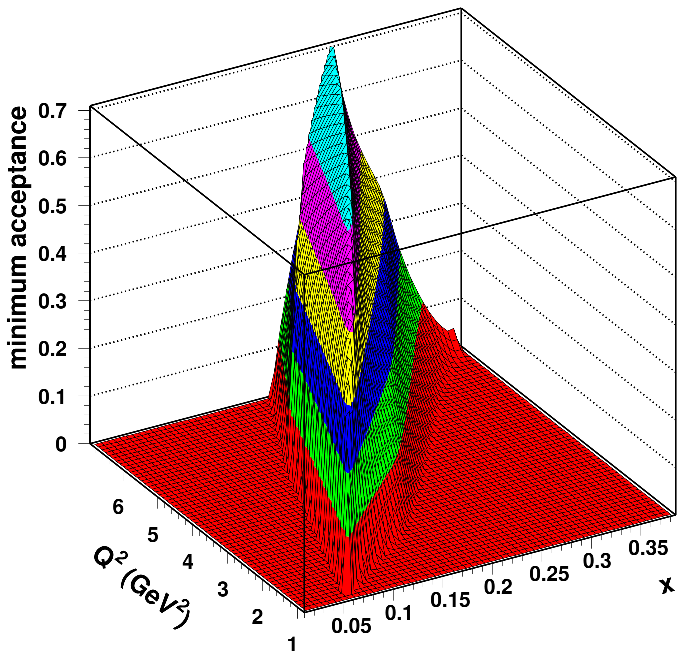

Figure 3.19.: Minimum acceptance for $-t < 0.2$ GeV^2 and all values of ϕ as a function of x_B and Q^2. The region of full kinematical coverage is much smaller than typical kinematical region for semi-inclusive measurements at HERMES .

The kinematical region for which the minimum acceptance never falls below 10% can be parametrised by the following requirements, all of which have to be fulfilled simultaneously:

$$-t[\mathrm{GeV}^2] < 0.2, \tag{3.29}$$
$$Q^2[\mathrm{GeV}^2] > 15x_B + 0.2, \tag{3.30}$$
$$Q^2[\mathrm{GeV}^2] > 25x_B - 1.6, \tag{3.31}$$
$$Q^2[\mathrm{GeV}^2] < 50x_B - 2.0, \tag{3.32}$$
$$Q^2[\mathrm{GeV}^2] < 35x_B, \tag{3.33}$$
$$Q^2[\mathrm{GeV}^2] < 9, \tag{3.34}$$
$$x_B < 0.35. \tag{3.35}$$

If these restrictions are used for deuterium or hydrogen data, only about 30% of the total statistics survive. The upper cut of $Q^2 > 9$ GeV^2 could also be extended towards higher values, but the statistics in this region is very limited. The cut of $x_B < 0.35$ is due to the fact that $-t_0$ is larger than 0.2 GeV^2 for high values of x_B and the rate of truely exclusive events above $x_B = 0.35$ is small. The selected region is shown in 3.20.

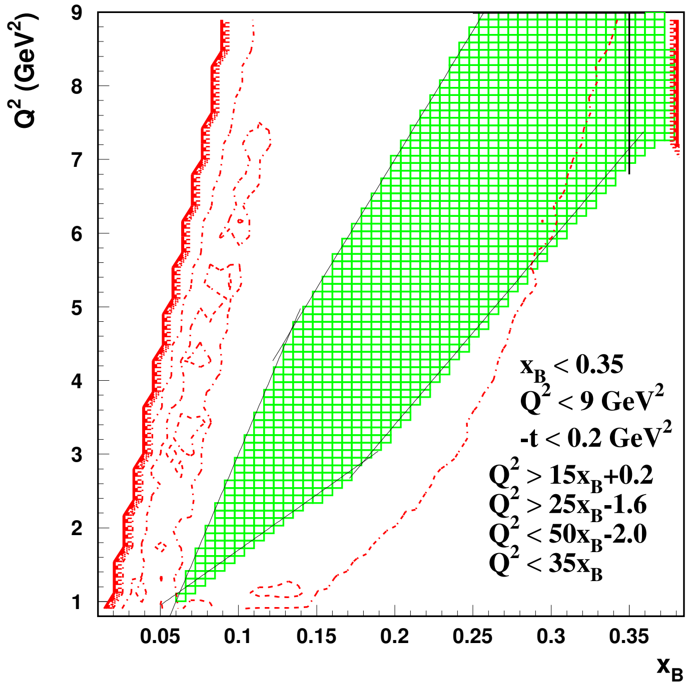

Figure 3.20.: Complete acceptance in x_B and Q^2: In the chequered region the acceptance is always larger than 10% for $-t < 0.2$ GeV^2. The straight lines show the parametrisation of this region given in the plot. The contours indicate smearing effects as discussed in the text.

The boxes show the region of $\mathcal{A} > 0.1$ according to the numerical integration. The lines represent the given parametrisation of the boundaries of this region. The thick lines on the left and the right indicate the unavoidable cutoff due to the kinematics. The dashed contours indicate the size of expected smearing effects: For each point in x_B, Q^2, t and ϕ event kinematics were smeared using the HERMES smearing generator; the acceptance for these smeared events was then compared with the ideal acceptance at the original kinematics. In the plot the maximum deviation for $-t < 0.2$ GeV^2 and all values of ϕ is shown as a function of x_B and Q^2. The deviation is usually below 2% with the maximum values towards low values of x_B and outside the selected region. In practice this knowledge does not solve the inverse problem, namely the question about the uncertainty of the acceptance value for each event (which enters the acceptance correction described in appendix C.3). It only indicates that smearing effects lead to a small deviation from the ideal acceptance function such that the simple geometrical acceptance model is well motivated.

From this discussion it is clear that a major fraction of the data originates from parts of the acceptance, for which certain regions in ϕ cannot be detected. This leads to the complication that events at each value of ϕ originate from very different and acceptance dependent regions in x_B, Q^2 and t. Consequently the interpretation of the measured asymmetries is not trivial as long as the available statistics does not allow a three-dimensional binning in x_B, Q^2 and t.

4. *gmc_dvcs* - An Event Generator for DVCS at HERMES

4.1. A specific GPD Model for DVCS

Although the asymmetries defined in chapter 2 are directly related to the GPDs, a quantitative understanding of observed experimental results requires a correct modelling of all involved cross-sections. This refers to the signal of interest as well as to all background processes.

Hence a Monte Carlo event generator has been written that uses the GMC-framework within the HERMES programming environment. The generator was called *gmc_dvcs* and contains several theoretical ingredients that will be discussed in this section.

The most important ingredients were the suggestions for GPD models from references [VGG99], [Rad99] and [GPV01]. For the special case of DVCS on the nucleon at HERMES, five different models have been discussed in reference [KN02b] and a routine for the calculation of the cross-section has been provided by the authors. Since the GPD $\tilde{E}$ does not enter in DVCS with an unpolarised target, only H, $\tilde{H}$ and E were considered. The five GPD-models were chosen to be:

1. The 3 GPDs H, $\tilde{H}$ and E are not skewed and factorise in an x-dependent part and a t-dependent part according to equations 2.43 to 2.48.

2. The GPDs are "skewed" using the double distribution formalism according to equations 2.52 to 2.54. The parameter b is set to $b = 1$. As in all other considered models the t-dependence factorises.

3. The same as the previous model but with $b = 3$.

4. In addition to the double distribution formalism of models 2 & 3 the D-term is added according to the predictions of the chiral quark-soliton model. b is set to $b = 1$.

5. The same as the previous model but with $b = 3$.

This corresponds to models A ... E from reference [KN02b] in the same order.

The unconstrained contribution of the sea-quarks was treated in the same way as the contribution of the valence quarks for the GPDs H and E and completely ignored for the GPD $\tilde{H}$. There is no reason, why this should be expected [BFM00], but the approach is taken due to the lack of better knowledge. The twist-3 sector is ignored. However, the moments s_2^I and c_2^I that are traditionally attributed to higher twist, have also small contributions from leading twist, which are included.

In order to provide a very fast algorithm suitable for Monte Carlo generation the routine uses separate look-up tables for the values of the GPDs at $x = \xi$ and the integrals of the type $\mathcal{P} \int \frac{H}{x \pm \xi} dx$. The time needed to evaluate the integral for each single event would be prohibitive.

A qualitative understanding of the predictions can be obtained by discussing the in-plane cross-section. In this plot only the case is considered in which the lepton scattering plane and the photon production plane are identical. This corresponds to $\phi = 0$ or $\phi = \pi$ where in the case of $\phi = 0$ the emitted photon is closest to the scattered lepton. In the rest frame of the target particle the in-plane angle θ_{ip} can be defined using the angle θ_{γ,γ^*} between the 3-vector $\vec{q}$ and the 3-vector of the real photon $\vec{v}$:

$$\theta_{ip} = \begin{cases} \theta_{\gamma,\gamma^*} & \text{for } \phi = 0 \\ -\theta_{\gamma,\gamma^*} & \text{for } \phi = \pi \end{cases} . \tag{4.1}$$

For fixed values of x_B and Q^2 the angle θ_{γ,γ^*} increases monotonically with increasing $|t|$ and the same is true for θ_{ip}. The five-fold differential cross-section $\frac{d\sigma}{dE'\, d\Omega_e\, d\Omega_\gamma}$ can then be plotted as a function of θ_{ip}. The in-plane cross-section is very instructive, as all maxima of the cross-section are in this plane. They occurr along the direction of the vector $\vec{q}$ (at $\theta_{ip} = 0$) along the direction of the beam (first maximum at positive values of θ_{ip}) and along the direction of the scattered lepton (second maximum at positive values of θ_{ip}). Outside the plane all three maxima are to a first approximation radially symmetric with respect to $\vec{q}$, $\vec{k}$ and $\vec{k}'$ due to their dependence on $\frac{1}{t^2}$ and the lepton propagators, respectively.

The in-plane cross-section for positrons and model 1 at $Q^2 = 1$ GeV^2 and $x_B = 0.1$ is shown in figure 4.1. It is split into the 3 contributions from the BH-term, the DVCS-term and the interference term. Due to the logarithmic scale, the negative region of the interference-term at $\theta_{ip} < 0$ does not appear in the plot.

The BH contribution as well as the sum of all contributions (total) exhibits sharp peaks of initial and final state radiation at positive values of θ_{ip}. The BH peak along the direction of the vector $\vec{q}$ ($\theta_{ip} = 0$) is in comparison much lower. For the DVCS-process only a peak at $\theta_{ip} = 0$ is seen, as in this case this direction coincides with the direction of the virtual photon.

Although the BH-amplitude is valid for all values of θ_{ip} - with varying additional contributions of higher order processes - the DVCS amplitude in the discussed approximation is only known for $|t| \ll 1$ GeV^2. Hence an upper limit of $-t < 0.8$ GeV^2 is applied, which corresponds to the cutoff at $\theta_{ip} = 10°$ in the plot. Beyond this value the amplitudes of the DVCS-term and the interference term get inconsistent. Due to the acceptance of the HERMES-calorimeter this is not relevant as the regions of inconsistency are anyway not observed.

The in-plane cross-section is not sensitive to the beam polarisation, since the helicity dependent $\sin(n\phi)$-moments do not contribute for $\phi = 0$ or $\phi = \pi$. E.g. the $\sin(\phi)$-moment leads to a modulation such that the cross-section for real photons above the lepton-scattering plane is enhanced while it is reduced below the plane or vice versa. On the other hand the BCA has an obvious effect on the in-plane cross-section as a flip of the beam charge flips the sign of the interference term.

It is interesting to note that the relative size of the BH-amplitude with respect to the DVCS-amplitude depends strongly on kinematics. On average the BH-amplitude dominates the statistics at HERMES but especially at $\theta_{ip} < 0$ the DVCS amplitude can be larger. The general assumption that the DVCS-term can always be neglected is therefore not true. The DVCS

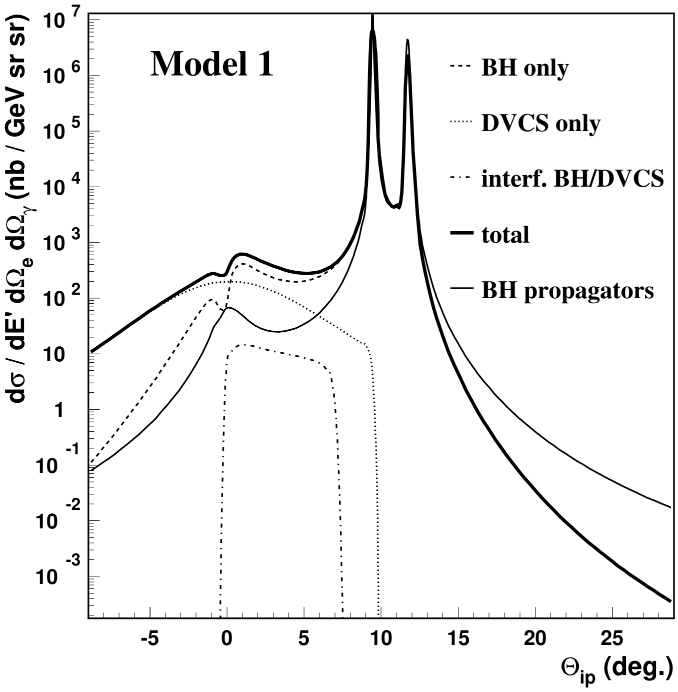

Figure 4.1.: In-plane cross-section for the proton at $Q^2 = 1\,\mathrm{GeV}^2$ and $x_B = 0.1$ according to model 1. The three contributions from the BH, the DVCS and the interference term are shown separately. Also the propagator cross-section (i.e. $c_{0,up}^{BH} = 1$, all other coefficients set to zero) is shown. Apparently it is a rather good approximation to the complete BH cross-section.

contribution at $\phi \approx \pi$ can certainly have an impact on extracted asymmetry-moments that are believed to originate only from the interference term.

In figure 4.2 the other 4 models are shown for positrons with the same event kinematics. The variations of the predicted BCA are seen as differences of the interference term cross-sections, which are mainly due the first cosine moment. Consequently the interference term cross-section is large, when the D-term is included as in models 4 and 5. Depending on the model the DVCS cross-section varies only by a factor of 2 at this kinematics as can be seen from the plots.

The in-plane cross-section for scattering on the neutron can be obtained from the same models. In the region, where the electric formfactor dominates (i.e. low values of $|t|$) the neutron BH-term is strongly suppressed with respect to the proton BH-term. At larger values of $|t|$ the magnetic form-factor leads to an increase of the neutron cross-section relative to the proton cross-section. On the other hand the pure DVCS-cross-section of the neutron is only slightly reduced with respect to the proton, since

$$\sigma \propto |\mathcal{H}|^2 \propto (\sum_q n_q e_q^2)^2 \tag{4.2}$$

if the differences in the valence quark distributions of u-quarks and d-quarks are neglected. n_q

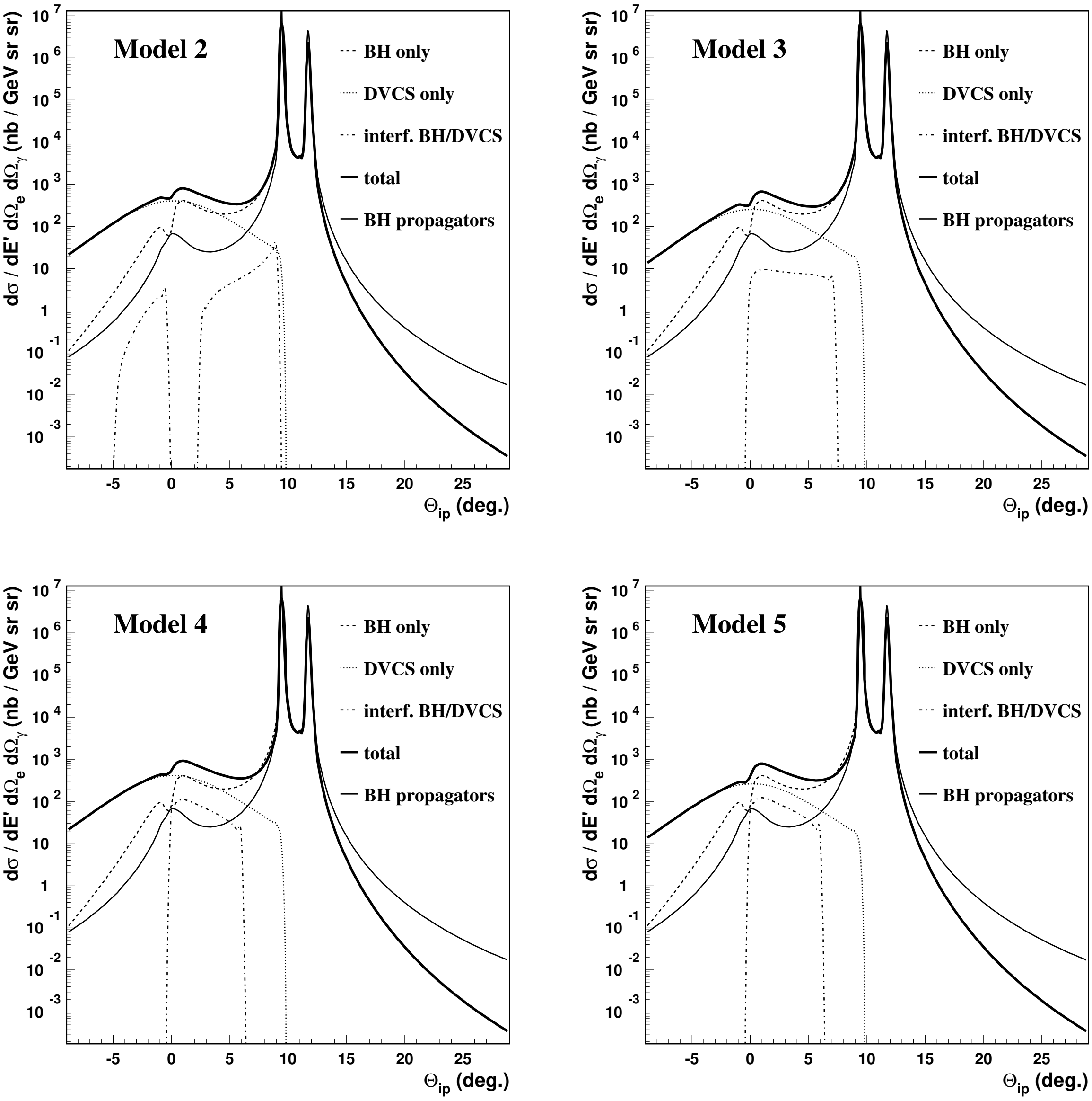

Figure 4.2.: In-plane cross-section for $Q^2 = 1$ GeV^2 and $x_B = 0.1$ according to models 2 to 5 (from top to bottom). The same quantities as in figure 4.1 are shown.

denotes the number of valence quarks of the respective flavour. One in-plane cross-section for the neutron is shown in figure 4.3.

For the proton the beam spin asymmetry was calculated using model E from reference [KN02b] that corresponds to the 5th model from above. Figures 4.4 and 4.5 show the defined beam spin asymmetry A_{LU} for a positron sample and an electron sample as a function of the angle ϕ for a fixed kinematical point, namely $Q^2 = 2$ GeV^2, $x_B = 0.2$ and $-t = 0.15$ GeV^2 (bottom plot). The central plot shows the shape of the averaged cross-section depending on ϕ with arbitrary normalisation. It is obvious that the cross-section is dominated by the BH-term

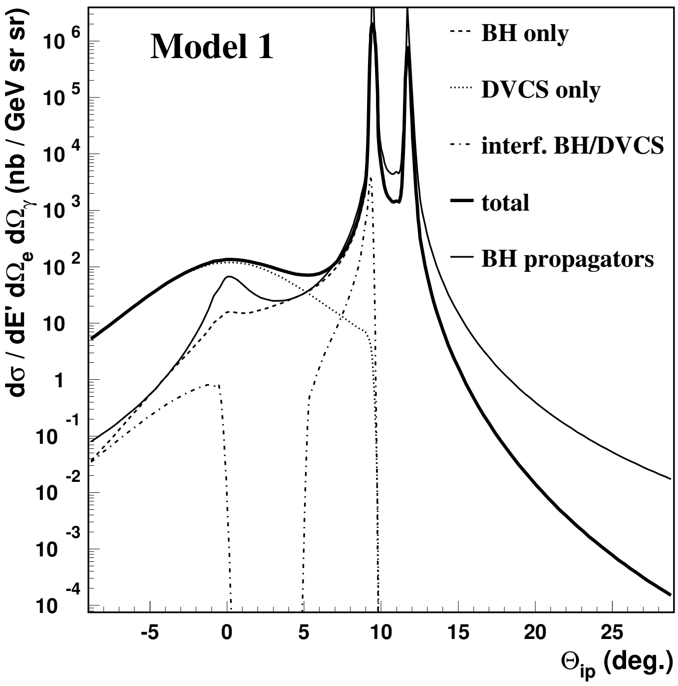

Figure 4.3.: In-plane cross-section for the neutron at $Q^2 = 1$ GeV^2 and $x_B = 0.1$ according to model 1. The three contributions from the BH, the DVCS and the interference term are shown separately. Also the propagator cross-section (i.e. $c^{BH}_{0,up} = 1$, all other coefficients are set zero) is shown.

that peaks at $\phi = 0$ due to the lepton propagators. The top plot shows the induced cross-section asymmetry, $N^+(\phi) - N^-(\phi)$ without dividing by the sum. In this plot the leading contributions from $\cos\phi$ or $\sin\phi$ are deformed by the propagator terms.

The beam charge does not only invert the sign of A_{LU}; the term $c^I_{1,up}$ which is related to the BCA also changes the ϕ-dependence. If the first moment of the BCA has a positive sign as predicted by this model, $N^+(\phi) + N^-(\phi)$ will be flatter for electrons than for positrons. This introduces higher moments that depend on the beam charge into the measured BSA.

Figure 4.6 shows the BSA for positrons scattering off a proton target at $x = 0.1$, $Q^2 = 2.0$ GeV^2 and $t = -0.15$ GeV^2. Figure 4.7 shows the same asymmetry for a neutron target, which leads to the opposite sign of the sine-moment. Although the asymmetry on the neutron is different, the absolute cross-section of the neutron is smaller than for the proton due to the fact that the formfactor F_1 is close to zero. Consequently a mixture of quasi-free protons and neutrons as in the case of deuterium will be dominated by the proton cross-section as well as by the proton asymmetry.

Figures 4.8 and 4.9 show the BCA for the same kinematical point and a proton or neutron target, respectively. Again the asymmetry on the neutron is only a small contribution to an averaged asymmetry.

For the target spin asymmetry the GPD $\tilde{E}$ would be needed, which is not implemented in

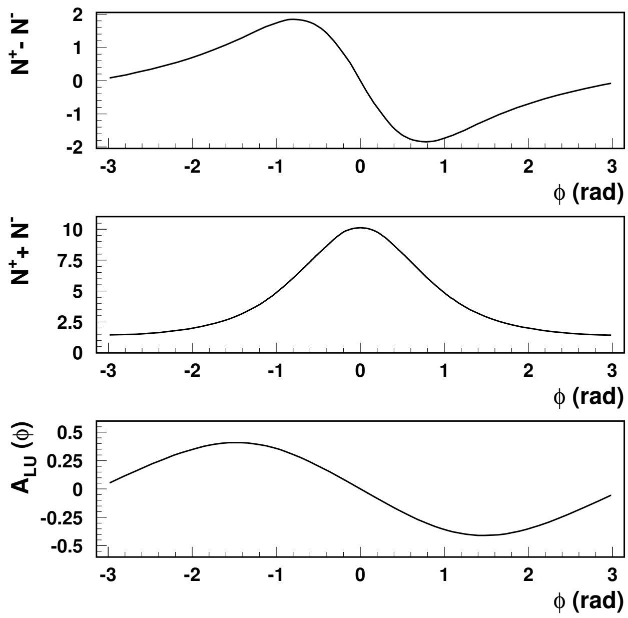

Figure 4.4.: Model predictions for A_{LU} on the proton with positron beam. Cross-section difference (top), averaged cross-section (center) and asymmetry (bottom).

the described models. Hence no predictions will be shown here.

4.2. Coherent DVCS on the Deuteron

The cross-section for the coherent BH-process on the deuteron is obtained from the formula by Mo and Tsai [MT69]. Since the target polarisation of a deuterium target is not taken into account in this Monte Carlo generator, only 2 formfactors of the deuteron are needed to describe this process. The formfactors W_1 and W_2 were taken from reference [E6175] and are identical to the formfactors G_1 and G_2 of reference [MT69].

For this process it is practical to use the variable x_A and to set the target mass to M_A; there is then no difference between the formulas for the proton or the deuteron. On the other hand for a Monte Carlo generator the generation limits on x_A should be readjusted: The Detector acceptance depends on the lepton track as well as on the direction of the real photon. As the direction of the real photon for given values of x_B, Q^2 and t is only weakly influenced by the target mass (cf. discussion of t_c in section 3.6) the acceptance stays almost constant in terms of these variables. Hence for heavier targets the same range in x_B should be generated as for the proton.

In principle the required range in t can also be adjusted, as the cross-section of this process is typically only important for $|t| < 0.1$ GeV^2, while the incoherent process on the constituents of the deuteron dominates above this value. The in-plane cross-section for the deuteron is shown at the end of this chapter.

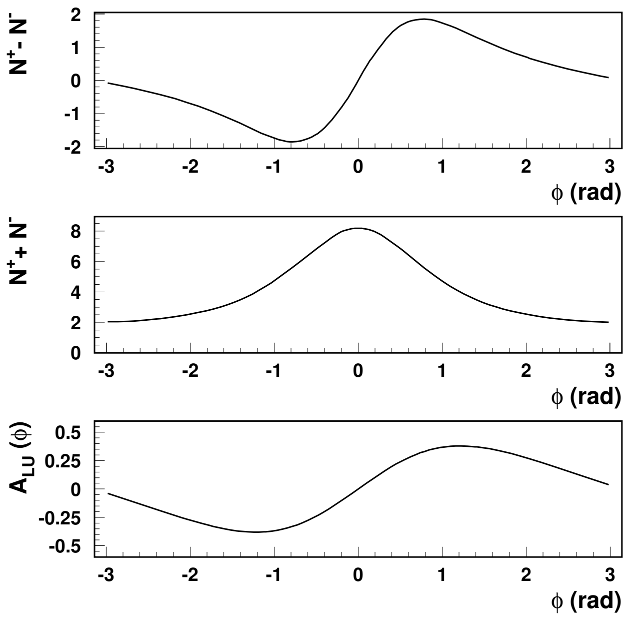

Figure 4.5.: Model predictions for A_{LU} on the proton with electron beam. Cross-section difference (top), averaged cross-section (center) and asymmetry (bottom).

There are predictions for coherent DVCS on the deuteron by Müller and Kirchner [KM02], which are only valid for $|t| \gg |t_0|$. Although this requirement is not strictly fulfilled at HERMES , the predicted A_{LU} from equation 2.128 was employed as a modulation factor of the coherent BH-cross-section:

$$\sigma_{coherent}(x, Q^2, t, \phi) = \sigma_{BH}(x, Q^2, t, \phi) \cdot (1 \pm \lambda A_{LU}) \tag{4.3}$$

For the Monte Carlo generator the parametrisation "MRS Set (A) (L230-MSb) and low Q^2 Structure Functions" of the parton distribution library was used [PB93]. Since the other model uncertainties are already sizable, the exact choice of the parton distribution set should only have a minor impact. Using this parametrisation a BSA of $A_{LU} \approx -0.13 \sin\phi$ can be expected at $x = 0.1$, $Q^2 = 2.0$ GeV^2 and $t = -0.05$ GeV^2. In this case the problem persists that this formula should only be evaluated at $|t| \gg |t_0|$. On the other hand there is almost no coherent scattering left for $|t| \gg |t_0|$ due to the rapid fall-off of the electrical formfactor of the deuteron. Hence this approximation is certainly limited in its accuracy and an exact calculation of the BH and DVCS-amplitudes would be preferable.

The beam charge asymmetry is in general predicted to be small at low values of $|t|$ and hence its effect was neglected for the deuteron. As the quantitative contribution of the coherent scattering on the deuteron is small in comparison with the incoherent processes, no further efforts were made to improve this model.

An important feature of deuterium is that apart from the nuclear ground state with a binding energy of 2.2 MeV there are no coherent nuclear excitations. Hence it is not necessary to

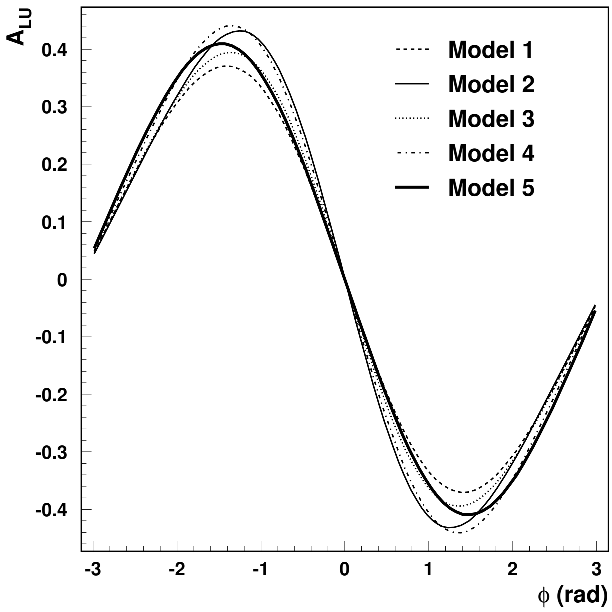

Figure 4.6.: Model predictions for A_{LU} on the proton with a positron beam. Models as in reference [KN02b].

consider nuclear transition GPDs.

4.3. Suppression of the Incoherent Channel at Low $|t|$

DVCS on the deuteron can happen in 2 ways; either the process is coherent and the deuteron is preserved in the final state or the deuteron breaks up in a quasi-elastic reaction. Although the coherent process is already complicated, a lot of theoretical uncertainties enter for the quasi-elastic process.

It is known that at large momentum transfers - e.g. in the electro-dissociation of deuterium - the incoherent impulse approximation allows a very good description of the experimental data [B$^+$81]. In this picture the lepton interacts only with one nucleon inside the deuteron. The properties of the hit nucleon are only slightly modified due to binding effects like Fermi-motion, nuclear shadowing, etc.. The remaining nucleon is considered as a spectator and is usually left with its original Fermi-momentum. The same picture can be invoked for deep inelastic scattering on the deuteron.

This situation is changed for the case of BH/DVCS. Although in DVCS the momentum transfer to the quark is given by Q^2, the total momentum transfer to the nucleon is only given by t. Hence already kinematical arguments based on the observed Fermi-motion of the nucleons suggest a reduction of the cross-section for low values of t. Even worse, in the case of BH one basically considers elastic scattering of a lepton and a nucleon with very low 4-momentum transfer $|t|$. In analogy to electro-disintegration [FA79] a number of complications will occur

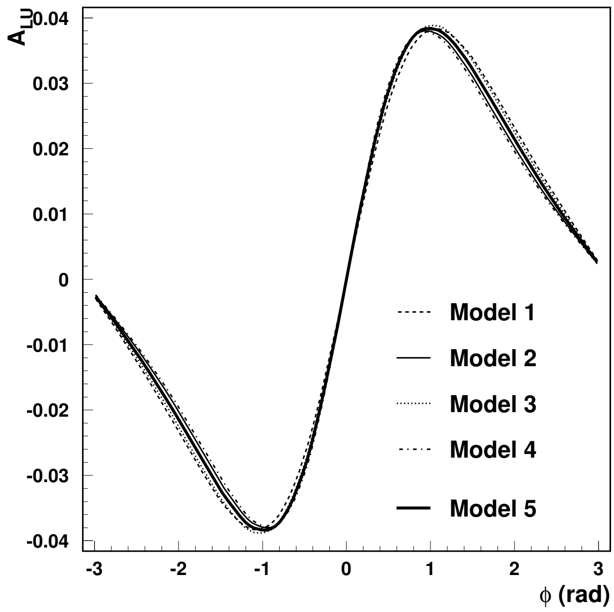

Figure 4.7.: Model predictions for A_{LU} on the neutron with a positron beam. Models as in reference [KN02b].

as soon as the spectator nucleon is not at rest: Meson exchange currents will show up and modifications of the cross-section of more than 30% are possible. In principle these results could also be employed for the calculation of the BH-process. However at the moment nothing is known about the DVCS-process and consequently this approach has not been considered in more detail.

Even the simple picture of the impulse approximation requires some more consideration. The process of quasi-elastic scattering on the deuteron is shown in figure 4.10. The nucleon N and the spectator nucleon N_s are moving inside the deuteron D. While the nucleon N is hit by a virtual photon and gets accelerated, the spectator nucleon is unaffected by the loss of its partner. Without shadowing corrections the cross-section can be obtained by calculating

$$\sigma = \int d^3 p_s \, |\phi(\vec{p}_s)|^2 (\sigma_p(\vec{p}_s) + \sigma_n(\vec{p}_s)) c_f(\vec{p}_s), \tag{4.4}$$

where $|\phi(\vec{p}_s)|^2$ is the probability to find a nucleon with momentum $\vec{p}_s$ in the deuteron and $c_f(\vec{p}_s)$ is a correction factor because of the dependence of the particle flux on $\vec{p}_s$ (see equation 4.7).

In a non-relativistic 2-nucleon model of the deuteron the proton and the neutron are simply moving in a central potential (e.g. [HJ62, Rei68, Kra76]). The momentum distribution of the 2 particles is then given by the modulus $|f(\vec{p}_s)|^2$ of the 3d Fourier transform of the ground-state wave-function. The spectator nucleon simply leaves the reaction as an on-shell particle with this momentum. In reference [AW73] this idea is discussed and the problem appears that also comparatively high momenta of at least 500 MeV/c are found. Hence a relativistic modification

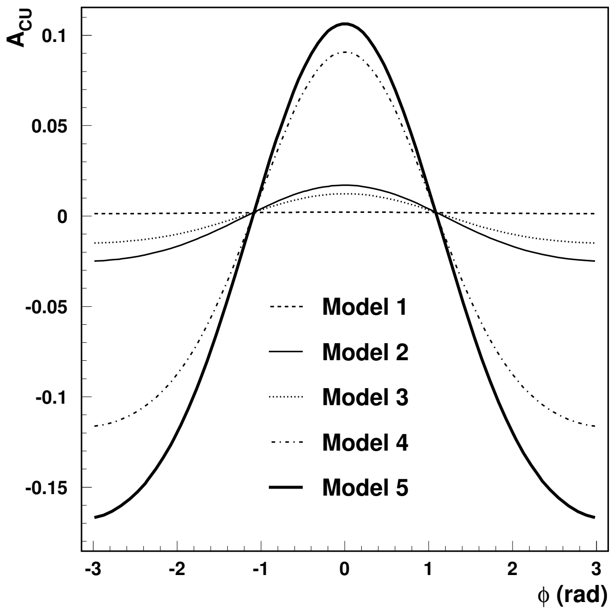

Figure 4.8.: Model predictions for A_{CU} on the proton. Models as in reference [KN02b].

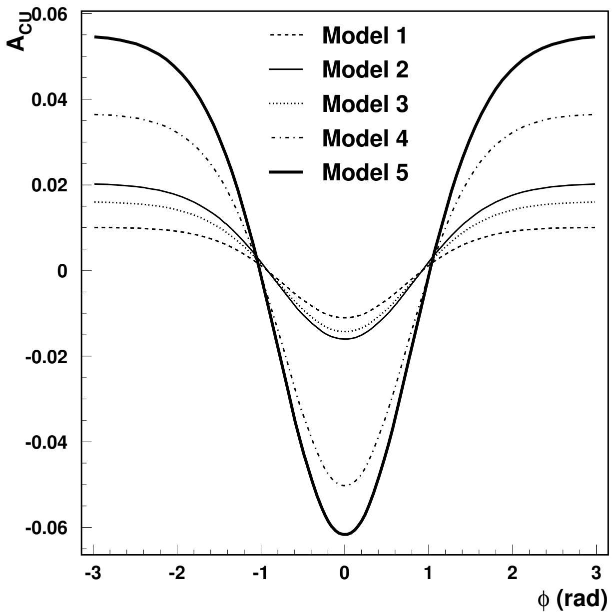

Figure 4.9.: Model predictions for A_{CU} on the neutron. Models as in reference [KN02b].

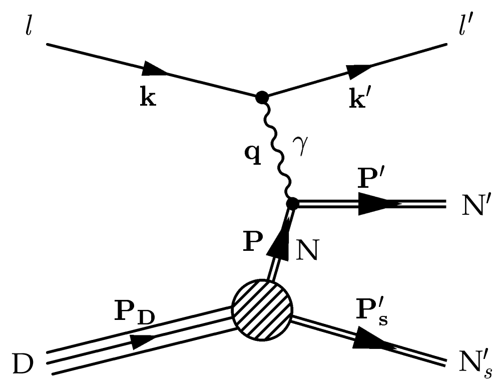

Figure 4.10.: Spectator Mechanism: One Nucleon N inside a deuteron D is hit by a virtual photon with 4-momentum **q**. While the spectator nucleon continues as a free particle into its initial direction of motion, the hit nucleon is put on-shell by the virtual photon.

of the kind

$$|\phi(\vec{p}_s)|^2 = N\frac{M}{E_s}|f(\vec{p}_s)|^2 \tag{4.5}$$

is suggested, where N is the correct normalisation factor. A theoretical uncertainty arises as it is not clear, if present parametrisations refer to $|\phi(\vec{p}_s)|^2$ or $|f(\vec{p}_s)|^2$. Hence in a first approach the spectator momentum in the Monte Carlo Generator is taken from the non-relativistic parametrisation of reference [Kra76], with the kinematical limit of $P_s < 500$ MeV/c and no further correction. It agrees with the more recent parametrisation in reference [B+81].

It is interesting to note that already for such spectator momenta the hit nucleon can be far off its mass-shell. The mass can be calculated by:

$$M_N = \sqrt{(M'_N + M_{N_s} - B - E_{N_s})^2 - p'^2_{N_s}}, \tag{4.6}$$

where p'_{N_s} denotes the 3-momentum of the spectator nucleon and B is the binding energy. A spectator momentum of 500 MeV/c corresponds to a mass of only 640 MeV of the hit nucleon. Under these conditions it is not quite clear which form-factors should be used for this nucleon, but the authors of reference [AW73] suggest that the form-factors G_1 and G_2 according to the definitions in reference [MT69] should be unchanged with respect to the free nucleon.

An analytical evaluation of the problem directly results in 2 features:

1. The CMS-momenta of the virtual photon and the struck nucleon depend on the direction of motion of the nucleon. Consequently the effective beam-energy is increased or decreased.

2. The flux factor in the nucleon rest frame is different from the flux factor obtained for a nucleon at rest in the target cell.

Although this intuitive approach is only a first step, such calculations yield a good description of quasi-elastic scattering on the deuteron [AW73].

In a Monte Carlo simulation a different approach is possible that avoids the explicit evaluation of the integral over the spectator momentum: After a momentum vector $\vec{p}'_{N_s}$ has been sampled from the known distribution $|\phi(\vec{p}_s)|^2$, the reference frame can be boosted and rotated to the frame in which a lepton moving along the z-axis towards the positive z-direction collides with the off-shell-nucleon at rest.

In this frame the differential cross-section $\frac{d\sigma}{dx_B\, dQ^2\, dt\, d\phi}$ is calculated for random points in kinematics. Although the BH-cross-section for the off-shell nucleon can be obtained using the formfactors, the behaviour of the DVCS-cross-section is not discussed in literature. Hence it was assumed that the cross-section is the same as for an on-shell nucleon at rest that collides with the lepton-beam of changed energy.

Thus for a fixed vector of $\vec{p}_s$ a Monte Carlo integration of the cross-section can be done within some kinematical limits. The cross-section will not change when the kinematics is transformed to the original reference frame. In this transformation the invariant variables Q^2 and t are unchanged, while x_B, ϕ and ϕ_e are changed (x_B is not really changed, but the identity $x_B = Q^2/(2M\nu)$ is not valid if the target is moving).

Although the obtained cross-section is correct in the laboratory frame, the flux factor has to be corrected for the fact that the proton is moving in this frame and that there is no head-on collision. With respect to an assumed target particle at rest a correction factor of

$$c_f = \frac{\sqrt{|\vec{v}_k - \vec{v}_s|^2 - |\vec{v}_k \times \vec{v}_s|^2}}{v_k} \tag{4.7}$$

has to be applied, where $\vec{v}_k$ denotes the velocity of the lepton and $\vec{v}_s$ denotes the velocity of the spectator nucleon. The modification of the cross-section due to the different effects is not quite clear at first sight.

It turns out that the procedure leads to a suppression of the cross-section at low values of $|t|$ that has mostly a kinematical reason: In the discussion of the value of $|t_0|$ it has been pointed out that for different masses M and M' the limit t_0 is still zero at $Q^2 = 0$ GeV^2. However, if M' is larger than M, t_0 drops much faster with Q^2 than for the elastic case, where $M' = M$. Hence the required increase in the mass of the hit-nucleon leads to higher values of $|t_0|$ and hence the reaction is kinematically forbidden for low values of $|t|$.

This model has the attractive feature that a spectator nucleon with approximately correct kinematics is generated in addition to the recoil nucleon. Furthermore energy and momentum conservation are satisfied. On the other hand it is based on a rather naive approach and some arguments are quite arbitrary. Hence, although a correction for binding effects using this method improves the agreement with the observed t-distribution for BH/DVCS at HERMES, the suppression is apparently underestimated as will be shown later.

A similar kinematical suppression is achieved in the model by de Forest and Walecka [DFW66], which is strictly speaking only valid for heavy nuclei. Assuming that the nucleons inside the nucleus populate a Fermi-sphere up to the Fermi-momentum p_F, scattering on a nucleon is only possible if it is ejected from the sphere. It is clear that for low momentum transfers only a very small part of the nucleons close to the surface can participate. Hence the number of nucleons and thus the quasi-elastic cross-section is decreased at low values of $|t|$. Neglecting the nuclear binding energy and making several approximations, this can be described by a suppression factor applied to the cross-section:

$$d\sigma = \left(\sum_n d\sigma_n + \sum_p d\sigma_p\right) \cdot \left(-\frac{-3t}{4p_F} - \frac{1}{16}\left(\frac{-t}{p_F}\right)^3\right). \tag{4.8}$$

Obviously the problem remains that neither energy- nor momentum-conservation are satisfied. In principle the remaining nucleus stays at rest with some negative kinetic energy. While these approximations maybe valid for nuclei like Neon or Krypton, they fail for the deuteron. The vaguely defined Fermi momentum in the deuteron is 70 MeV/c and about 55% of the observed spectator protons have momenta below this value (cf. the parametrisation in [Kra76]). Again the kinematical factor underestimates the suppression at low values of t.

A different approach to the problem was e.g. suggested in reference [Ber72]. Instead of explicitly considering Fermi-motion described by the deuteron wave-function, the required knowledge about binding effects is taken from the elastic formfactor of the deuteron. Within the impulse approximation and the closure approximation it can be shown that the following relation is observed in elastic and quasi-elastic scattering of leptons on the deuteron [Ber72]:

$$\frac{d\sigma_{total}}{d\Omega} \approx \frac{d\sigma_{p,free}}{d\Omega} + \frac{d\sigma_{n,free}}{d\Omega}. \tag{4.9}$$

This relation is valid under the assumption that the electric form-factor of the neutron can be neglected. On the other hand

$$\frac{d\sigma_{total}}{d\Omega} = \frac{d\sigma_{p,bound}}{d\Omega} + \frac{d\sigma_{n,bound}}{d\Omega} + \frac{d\sigma_D}{d\Omega}, \tag{4.10}$$

which allows to calculate the sum of the bound nucleon cross-sections from the free nucleon cross-sections, since the coherent cross-section $d\sigma_D$ is known.

Especially at low momentum transfers Q^2 the dominant contributions to the total deuterium cross-section $d\sigma_{total}$ are due to the electric formfactors of the proton and the deuteron. Consequently a similar effect is achieved by adding a suppression factor that only modifies the electric form-factor of the proton. This has been pointed out in reference [E6175]:

$$G^2_{E,p,bound} = (1 - F^2(Q^2))G^2_{E,p,free}, \tag{4.11}$$

$$G^2_{M,p,bound} = G^2_{M,p,free}, \tag{4.12}$$

$$G^2_{E,n,bound} = 0, \tag{4.13}$$

$$G^2_{M,n,bound} = G^2_{M,n,free}, \tag{4.14}$$

where the formfactor $F^2(Q^2)$ of the deuteron is taken from the same reference. These modified formfactors can then also be used for the Bethe-Heitler cross-section. On the other hand the effect on the DVCS cross-section is unclear. Since no better knowledge exists the following 2 cases can be considered:

- The DVCS amplitude is not suppressed. Since the BH-amplitude is real and simply decreased in strength, the complex phase between the 2 amplitudes remains the same. Hence all asymmetries would increase in the region in t where binding effects are important as long as $\sigma_{BH} > \sigma_{DVCS}$.

- The DVCS amplitude is suppressed such that the asymmetry is conserved. This can be done by calculating a suppression factor s from the free BH-cross-section and the bound BH-cross-section as

$$s = \frac{\sigma_{BH,bound}}{\sigma_{BH,free}}. \tag{4.15}$$

  This suppression is then applied to the DVCS-cross-section as well as to the interference term. Thus the BH and DVCS amplitudes are consistently suppressed. Since the BH-cross section on the neutron is not modified, this leads to the peculiar prediction that the neutron contribution is stronger than the proton contribution at very low values of $|t|$.

In the event-generator the second procedure was used. The combination of all mentioned contributions allows for a good description of the $|t|$ distribution that is measured for exclusive single-photon-events at HERMES. This is shown in figure 4.11 that contains the model according to reference [E6175] as well as the model according to reference [AW73] and the sum of the free particle cross-sections of proton, neutron and deuteron. The sum of the free cross-sections apparently overestimates the observed rates by more than 50% for low values of $|t|$, while the model from reference [E6175] seems to give the best description in this region. If all models would underestimate the cross-section at low $|t|$ the situation would be less clear, since the difference could be due to the coherent DVCS contribution.

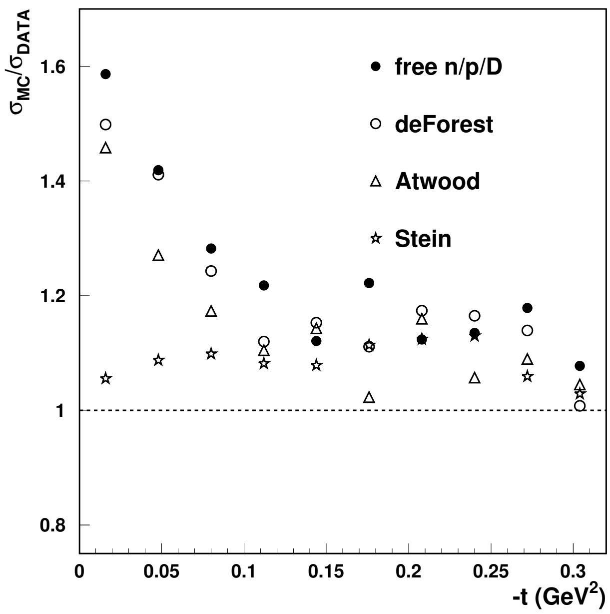

Figure 4.11.: Comparison of different Monte Carlo models with experimental data at low values of t vs. t. Monte Carlo and data are normalised to each other using the luminosity monitor. The predicted rate is devided by the observed rate and the ratio is plotted. Apparently the model "Stein" according to [E6175] gives the best agreement.

All in all the Monte Carlo allows for a good description of the data. However, the arbitrariness of the assumptions shows that the obtained asymmetries may be wrong, even if the GPD-models are correct.

4.4. Bremsstrahlung with Resonance Excitation

In addition to the truly exclusive processes discussed before, the experimental result also receives contributions from non-exclusive background processes. The most important background that is at least approximately known is caused by the Bethe-Heitler process with excitation of the hit nucleon into a resonant state. The cross-section for this process can be calculated with the formula of reference [MT69], provided that the transition form-factors of the nucleon are known.

In reference [MT69] the case of Δ(1232)-excitation is explicitly treated using the measurements of the transition formfactor from reference [DT68]. In this picture a fixed mass (1232 MeV) is assigned to the Δ-resonance. This is not relevant if the Δ-excitation is considered as just another radiative correction, for which the true final state of the Δ stays unobserved. As the HERMES recoil detector will be able to detect the decay products of the Δ, the model had to be modified. This was achieved by generating the final state mass of the Δ as a truncated Breit-Wigner-curve with correct width.

The problem that arises in this treatment is that the value of t_{min} varies with the generated mass. Moreover the whole kinematics is changed such that the final mass distribution can be distorted or wrong in its absolute size. It was checked that distortion effects are small; the following more refined treatment also indicates that the cross-section from this simplified model is correct.

An improved approach is possible, if the whole resonance region is treated as continuum. In this case measurements are usually expressed in terms of the cross-sections for longitudinally and transversely polarised photons σ_L and σ_T, respectively. The relation to the structure functions W_1 and W_2 are given by:

$$W_1 = \frac{K}{4\pi^2\alpha}\sigma_T, \tag{4.16}$$

$$W_2 = \frac{K}{4\pi^2\alpha}\frac{q^2}{q^2+\nu^2}(\sigma_T+\sigma_L). \tag{4.17}$$

One can introduce the following definitions for the energy K needed to produce the mass W in photoproduction, the virtual photon-flux Γ_T and the polarisation parameter ϵ:

$$K = \frac{W^2-M^2}{2M}, \tag{4.18}$$

$$\Gamma_T = \frac{\alpha}{2\pi}\frac{K}{q^2}\frac{E'}{E}\frac{1}{1-\epsilon}, \tag{4.19}$$

$$\epsilon = \left[1+2\tan^2\left(\frac{\theta}{2}\right)\left(1+\frac{\nu^2}{q^2}\right)\right]^{-1}. \tag{4.20}$$

The variable R is defined as

$$R = \frac{\sigma_L}{\sigma_T}. \tag{4.21}$$

For $Q^2 \rightarrow 0$ the cross-section σ_L approaches zero, hence R tends to zero in the same limit. In existing measurements of the cross-section in the resonance region, usually the quantity $\sigma_{\gamma^*,p} = \sigma_T + \epsilon\sigma_L$ is measured (cf. [E6175, B+76]) that can be obtained from experiments without performing a Rosenbluth-separation according to:

$$\frac{d\sigma}{d\Omega\, dE'} = \Gamma_T(\sigma_T + \epsilon\sigma_L) \tag{4.22}$$

measured as a function of ϵ.

Various parametrisations exist for $\sigma_{\gamma^*,p}$: Three different datasets at different values of ϵ have been used in [B+76] to produce parametrisations depending on Q^2 for small bins in W. The one with the smallest statistical errors is based on measurements at SLAC and is valid for $\epsilon > 0.9$. A comparison with the other datasets shows that systematical differences exist between the measurements such that it is impossible to extract R from the parametrisations (σ_L would be negative in some regions).

Apart from this procedure, the SLAC-data can also be directly interpolated: In reference [E6175] the value of $\sigma_{\gamma^*,p}$ is parametrised for a fixed-target experiment at different beam-energies, for which the angle θ is constant at $4°$. Four resonances and a continuous background are needed to describe the data for each beam-energy. The parametrisations are given as a function of W at 6 fixed beam energies. Hence Q^2 determines the required beam-energy and the cross-section can be obtained by performing a linear interpolation between 2 measured energies. A value of $R = 0.23\ GeV^{-2} \cdot Q^2$ was used by the authors in the calculation of the fit parameters, hence the same value has to be used to get back to the original value of $\sigma_{\gamma^*,p}$. The results of this interpolation agree very well with the first parametrisation by Brasse et al. [B+76] that is based on the same experimental data. This is shown in figure 4.12 for a fixed value of $Q^2 = 0.5$ GeV^2.

In both references R is needed in order to obtain σ_L and σ_T separately. This separation is necessary, as the kinematics of BH will cover some range in ϵ. R is difficult to extract and at the moment independent measurements with low accuracy exist. Measurements [B+72, A+72a, B+78b] indicate that R is typically small, i.e. only 10% to 20%. In the Monte Carlo it can therefore be set to zero.

The average value of R in the DIS-region is much better known. Relying on duality e.g. the parametrisation by Whitlow [Whi90] can be used to calculate R. As this parametrisation rises strongly at low values of Q^2, it is set to the value at $Q^2 = 0.35$ GeV^2 for smaller values of Q^2. As a starting point also the fixed value of $R = 0.18$ at SLAC/HERMES-kinematics can be used [R+75]. In the near future the quantity R will be studied by the CLAS-experiment. It can be expected that although R is small, it can change quickly in the resonance region; this was e.g. observed for the Δ-resonance [B+72].

A comparison can be made with the transition-formfactor-approach mentioned before. The inplane cross-section obtained from the first Brasse-parametrisation for $W < 1.4$ GeV using $R = 0$ was compared with the results of the form-factor based calculation. The ratio of the results vs. θ_{ip} is shown in figure 4.13 and shows a reasonable agreement. The discrepancy is less than 20% for the kinematical range of interest.

Finally also MAID2000 [DHKT99] can be used to calculate σ_L and σ_T for the single meson-production channels. This model is in good agreement with present experimental data for low energy electron-proton scattering. As the two cross-sections are already separated, no additional assumptions about R have to be made.

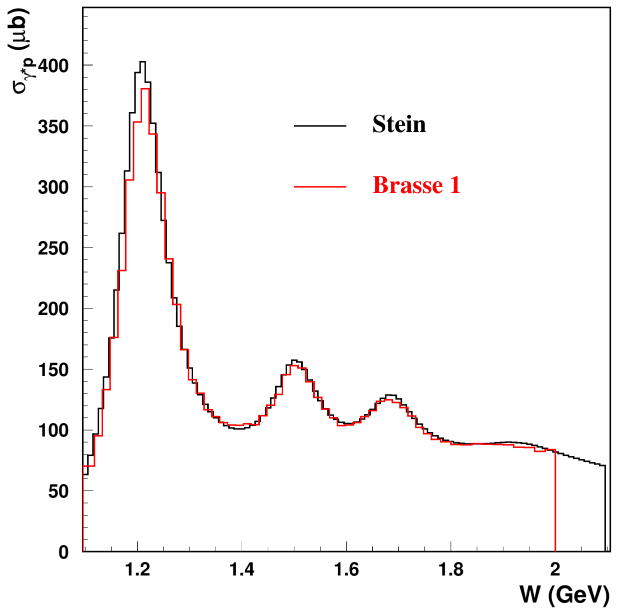

Figure 4.12.: 2 different parametrisations of the same SLAC-data: The photoproduction cross-section $\sigma_{\gamma^*,p}$ vs. W at a value of $Q^2 = 0.5$ GeV^2 is calculated according to parametrisations in [E6175] (Stein) and [B$^+$76] (Brasse).

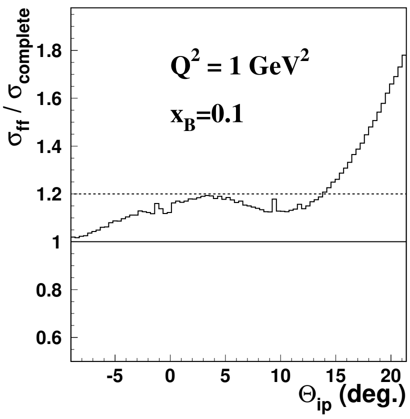

Figure 4.13.: Comparison of different parametrisations for the Δ-resonace: The in-plane cross-section for BH with Δ-excitation of the proton at $Q^2 = 1$ GeV^2 and $x_B = 0.1$ was obtained from a transition-formfactor parametrisation [DT68] and a continuous parametrisation of $\sigma(W)$. The ratio is shown vs. the in-plane angle θ_{ip}.

Alternatively it was studied if the generator can use the cross-section that is measured in the scattering of real photons on hydrogen. This corresponds to the limit of $Q^2 \to 0$ that will be representative for the lowest values of Q^2 in BH. Inclusive data exists from the tagged photon-beam at Daresbury [A+72b], while σ_T for various final states was measured by the ABBHHM-collaboration [ABBHHM68, ABBHHM66]. However, as the existing inclusive parametrisations from lepton-scattering are much more precise, the results were in the end not included into the event generator.

In the case of the neutron experimental results are less abundant. Measurements on the deuteron indicate that in the resonance region the proton and the neutron cross-section have the same order of magnitude [E6175]. This is also obtained from the MAID-model. Usually problems with the extraction procedure remain due to the binding-effects in the deuteron. The average deuteron cross-section was not used for *gmc_dvcs*, as the final state is then unknown. If the Recoil Detector will ever be operated with deuterium gas the veto capabilities for non-exclusive events will depend on it.

4.5. Resonance Fragmentation

Although in most cases the final state of the resonances will be outside the geometrical acceptance as well as the accessible momentum range at HERMES, future detectors like the Recoil detector will try to detect the final state. Hence at least an approximate model is required for the fragmentation of the nucleon resonances.

A very simple approach was taken to satisfy these requirements: The separation of the inclusive cross-section into single sub-processes was based on MAID. This allowed for the description of the reactions as shown in table 4.1. The cross-section for the process $\gamma^* P \to p\pi^0$ is shown in figure 4.14.

As each resonance has a different behaviour in σ_L and σ_T, in principle a Monte Carlo generator would have to generate both contributions separately such that the decay mode is correct. In the approximation that the contribution from σ_T is much larger at low values of Q^2 this can be avoided by selecting the decay-mode only from the relative size of σ_T. In practice the total σ_T was taken from the inclusive cross-sections and the decay-mode was calculated from the relative contribution of each channel to this inclusive cross-section.

As the sum of the cross-sections from MAID does not agree with the independent parametrisation for the inclusive cross-section, the following procedure was used to select the final state:

- Below the $\Delta(1232)$ resonance only single-meson-production was allowed.
- Above this value the remaining inclusive cross-section was attributed to multiple meson production.

In the case of single meson production MAID also gives predictions for the angular dependence of the decays. It was not attempted to transfer this angular dependence to the higher order BH-process; instead an isotropic decay was assumed. It is clear that this is a very rough assumption, but since the detection probability for decay products in HERMES is low, its present impact is small. Also for the design of future detector extensions, the isotropic distribution is sufficient, as angular modulations have a comparatively small effect on the detection efficiency. On the other hand, the momenta of the decay particles are much more important in terms of efficiency.

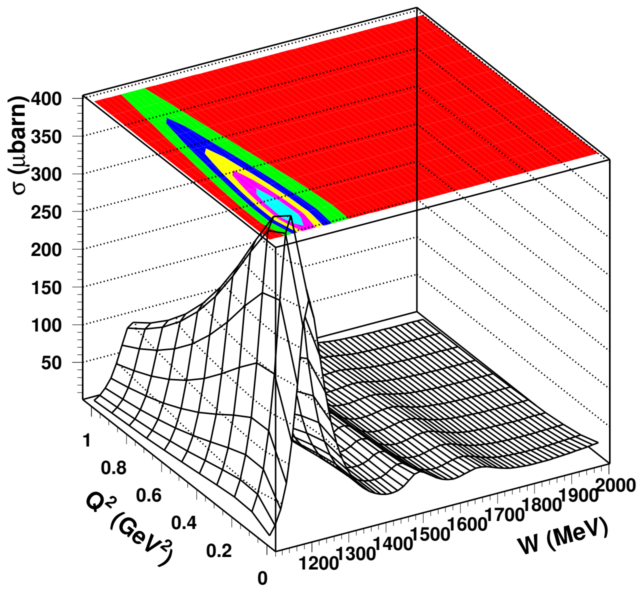

Figure 4.14.: The cross-section σ_T for the process $\gamma^* p \to p\pi^0$ according to the MAID model [DHKT99].

Table 4.1.: Processes for which cross-sections σ_L and σ_T are predicted by MAID.

No.	Target	hadronic final state
1	p	p π^0
2	p	n π^+
3	p	Λ K^+
4	p	Σ^0 K^+
5	p	Σ^+ K^0
6	p	p η
1	n	n π^0
2	n	p π^-
3	n	Λ K^0
4	n	Σ^- K^+
5	n	Σ^0 K^0
6	n	n η

Again in the low $|t|$-region a comparison with photoproduction data is possible. For these datasets the angular decay distribution was not analysed, but on the other hand also decays into several charged particles were studied. A compilation of data from ABBHHM and Daresbury is shown in figure 4.15. For large values of W there are apparently decays involving neutral particles such that the single contributions do not add up to the inclusive dataset. At

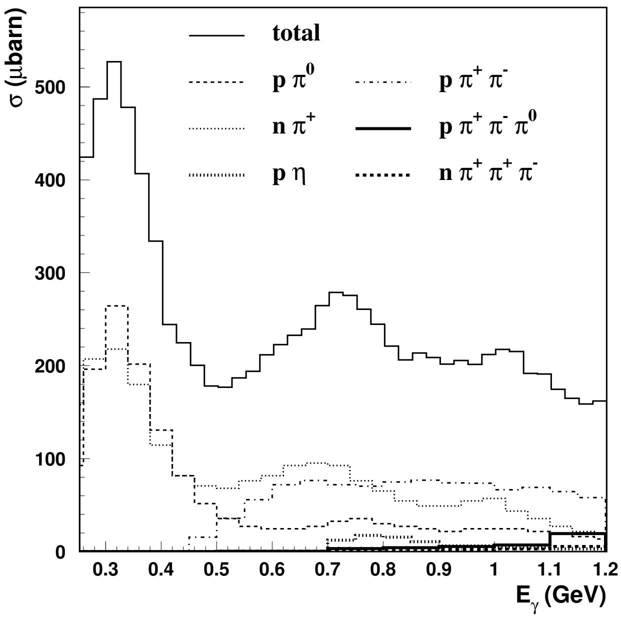

Figure 4.15.: The real photoproduction cross-section from reference [A+72b] vs. the photon energy. The cross-sections of the subprocesses are taken from references [ABBHHM68, ABBHHM66].

the same time it is found that for $E_\gamma < 1.2$ GeV (i.e. $W < 1.8$ GeV) the most important multi-particle state is due to the decay into a $\Delta(1232)$ and an additional pion [ABBHHM68]. This has two consequences:

- The 3-particle state is dominated by 2 subsequent 2 particle decays instead of a pure phase-space decay. In the generator the Δ-mass is obtained from a truncated Lorentz-curve, for which the Δ-mass is also rejected, if $m_\Delta + m_\pi > W$. In order to conserve the inclusive cross-section a new Δ-mass is chosen for the same lepton kinematics until the event is kinematically possible. The same treatment is used for $W > 1.8$ GeV, but in any case very few of these events pass the present or future exclusivity cuts.
- As argued in [A+72b] the decay into a $\Delta(1232)$ and a pion results in 2 particles with known isospin. Since the decay into $\Delta^{++}\pi^-$ is known from [ABBHHM68], isospin-relations allow to estimate the contributions of the decay modes that involve neutral particles. For the proton the predicted ratio $\Delta^{++}\pi^- : \Delta^+\pi^0 : \Delta^0\pi^+$ is $3 : 2 : 1$. The following decay of the Δ can again be taken from isospin relations: $(\Delta^0 \to p\pi^-) : (\Delta^0 \to n\pi^0) = 1 : 2$ and $(\Delta^+ \to p\pi^0) : (\Delta^+ \to n\pi^+) = 2 : 1$.

Again an isotropic decay is calculated for the two 2-pion decays. In general the generated number of 2-particle decays will be sensitive to systematic differences between the inclusive measurement and the single-meson cross-sections.

The case of the neutron can be treated in a similar way. MAID allows predictions for all important single-meson-production processes, while the inclusive neutron cross-section can be approximated by the one on the proton. As the inclusive proton cross-section from [B+76] is systematically higher than the cross-section that would be expected for the free neutron, the cross-section for $\Delta + \pi$ production will be overestimated. If on the other hand only the processes from MAID are used for the inclusive cross-section, the $\Delta + \pi$ production will be underestimated (namely left out altogether). Hence reality is expected to be between the two limits. For $\Delta+\pi$ production similar decay ratios as for the proton can be calculated from isospin relations.

The proposed method results in a lower cross-section for BH with resonance excitation than calculated by the standard HERMES Monte Carlo. A comparison is shown in figure 4.16. The HERMES Monte Carlo typically overestimates the cross-section, especially below the Δ-resonance. Thus it could not be used for simulations of the future recoil detector (cf. chapter 8).

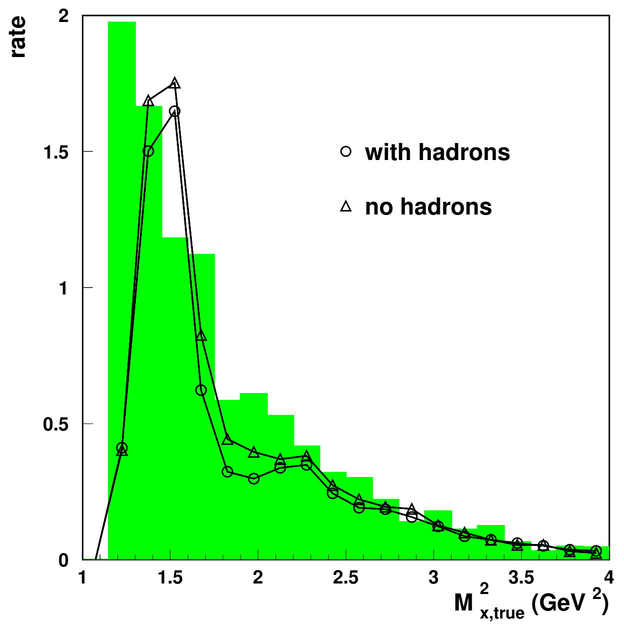

Figure 4.16.: Improvement of Monte Carlo: The predicted rate for BH events (deuterium) with resonance excitation, that pass all analysis cuts, is shown as a function of the true missing mass squared. The HERMES Monte Carlo uses a smooth extrapolation to low values of Q^2 and W^2 (histogram) which is mostly above the first resonance parametrisation by Brasse at al. (triangles). In addition the decay products of the resonances (which are not included in the HERMES Monte Carlo) veto some of the events (circles).

4.6. Estimates for the DVCS-contribution to Resonance Excitation

Although Deeply Virtual Compton Scattering can also occur with target excitation or fragmentation, only very little is known about this semi-exclusive process, which is usually denoted as associated DVCS (ADVCS). Since ADVCS with Δ-excitation is theoretically the cleanest reaction as well as the dominant background for elastic DVCS, attempts have been made [FPS98, GMV03] to obtain a quantitative descriptions of this background.

To be more precise, there are actually two main contributions that occur up to an invariant final state mass of $M_x = 1.35$ GeV (cf. reference [GMV03]): A non-resonant background that is obtained from a soft pion expansion and the resonant state of the $\Delta(1232)$ with its known transition form-factors.

The mathematical approach is different for the 2 contributions: The soft pion expansion allows a direct relation of the required transition GPDs to the conventional GPDs of the nucleon. At the same time the soft pion theorem can also be used for pion electroproduction, i.e. the associated BH. In this case the axial form-factors $g_A(Q^2)$ and $h_A(Q^2)$ of the nucleon have to be known. Knowledge about the latter one is limited, but its effect can be shown to be small. In the chiral limit ($m_\pi \to 0$) the soft pion expansion is expected to give reliable results up to the center of the Δ-resonance.

The resonant contribution on the other hand is model dependent, as there is no knowledge about the transition GPDs for the Δ. Only the large N_c limit can be used to relate these GPDs to the GPDs of the nucleon as stated in equations 2.65 to 2.67. The Bethe-Heitler process for the Δ depends on the formfactors $G^*_M(Q^2)$, $G^*_E(Q^2)$ and $G^*_C(Q^2)$ that are defined in reference [JS73].

Obviously this treatment of the BH-process with resonant excitation should be equivalent to the BH-process using the inclusive electroproduction cross-sections σ_L and σ_T as described in the previous paragraph. As a test in reference [GMV03] a comparison is made for the predicted σ_T at $Q^2 = 0$ and the measured σ_T from photoproduction experiments. For $M_x > 1.25$ GeV increasing deviations are found that amount to more than 30% at $M_x = 1.3$ GeV. This clearly limits the applicability for to the situation at HERMES, where final state masses up to $M_x = 2.0$ GeV mix with the exclusive dataset.

However, the results give some indication of the effects of ADVCS. It can be quantified by introducing a modification factor $R_{BSA}(W_{max})$ that relates the observed asymmetry A^{exp}_{LU} up to the final state mass W_{max} to the asymmetry of the elastic process A_{LU} by $A_{LU} = R_{BSA} \cdot A^{exp}_{LU}$. For typical HERMES kinematics and a proton target this is shown in figure 4.17. The expected correction is in the order of +10% and thus the resonances act as a small dilution.

It is interesting to note that the asymmetry $A_{LU}(W)$ for the 2 decay channels $ep \to e\gamma p\pi^0$ and $ep \to e\gamma n\pi^+$ behaves quite differently. While the asymmetry for the neutral pion production rises towards the elastic asymmetry for small values of W, the charged pion production is predicted to have a small and constant asymmetry (< 0.1).

In contrast to the BSA the BCA is predicted to have a quite different behaviour. The prediction is especially sensitive to the size of the D-term which enters at the same time in the exclusive process and the semi-exclusive process. If the D-term is large, the correction factor $R_{BCA}(W_{max})$ is expected to be small as can be seen in figure 4.18. If the D-term vanishes, the effect on the remaining small and negative elastic BCA can be quite dramatic; i.e. a change by more than 80% is possible as the BCA of the Δ-resonance is in this model always positive. The

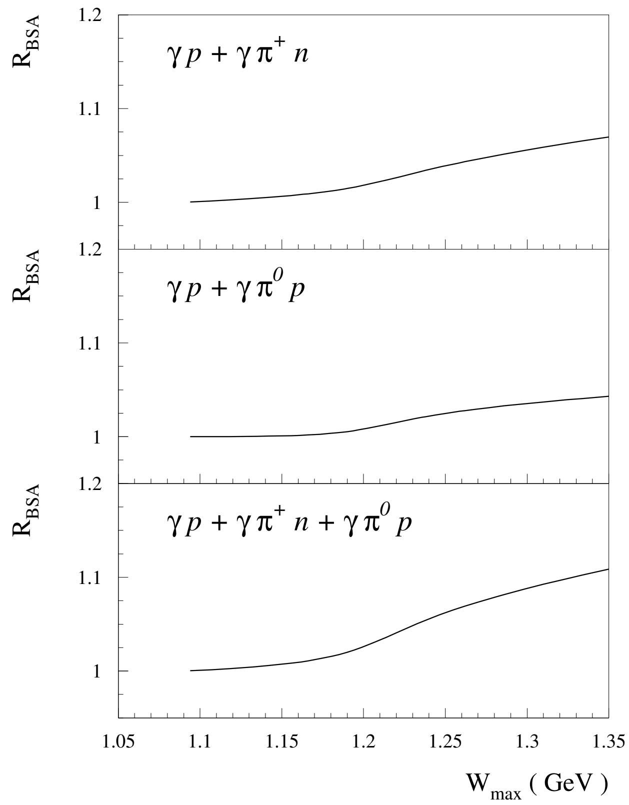

Figure 4.17.: The correction factor $R_{BSA}(W_{max})$ as taken from reference [GMV03]. The kinematics is given by E_{beam} = 27 GeV, Q^2 = 2.5 GeV^2, $x_B = 0.15$ and $t = -0.25$ GeV^2.

asymmetry $A_{CU}(W)$ is predicted to have a complicated dependence on W.

Although these calculations are very instructive, some knowledge is still missing before a correction factor like R_{BSA} can be applied to HERMES-data: First of all the contamination depends very much on the observed kinematics, especially on t. Consequently a complete Monte Carlo simulation would be required to get a reliable value of the correction factor. Secondly an extension towards higher masses would be needed as they still contribute about half as much as the $\Delta(1232)$ to the present event sample at HERMES. In the case that resonance excitation will be studied using the recoil detector, the possible decay-branches of these higher resonances have to be included. Consequently no attempt was made to include DVCS with resonance excitation into the Monte Carlo, as the existing estimates are only partly applicable.

4.7. *gmc_dvcs* and Other Generators

gmc_dvcs should not be seen as a stand-alone generator. Although it can account for about 90% of the observed events within the exclusive event cuts, three other important contributions are missing and have to be taken from different event generators:

1. Semi-inclusive π^0-production can be simulated using the standard HERMES-generator

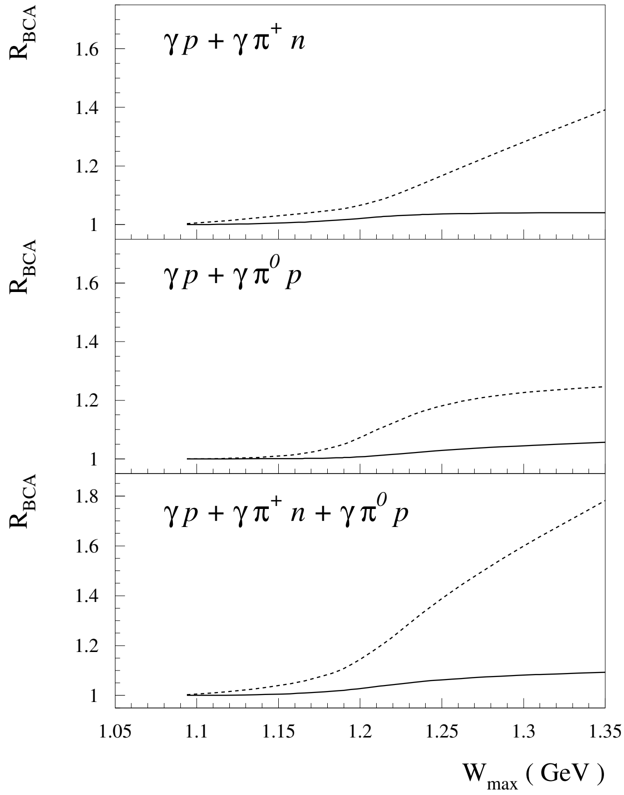

Figure 4.18.: The correction factor $R_{BCA}(W_{max})$ as taken from reference [GMV03]. The kinematics is given by $E_{beam} = 27$ GeV, $Q^2 = 2.5$ GeV^2, $x_B = 0.15$ and $t = -0.25$ GeV^2. For the solid curve a D-term contribution has been added to the model of the dashed curve.

gmc_disng or the new generator *gmc_pythia*.

2. Diffractive meson production with subsequent decay of e.g. an ω-meson can only be simulated using *gmc_pythia*.

3. Exclusive π^0-production can be simulated using *gmc_pion* based on the model from reference [VGG99].

In all cases the decay-photon of a π^0 is misidentified as an exclusive photon. As *gmc_pythia* [SLM01] is very slow and radiative corrections for the neutron are still missing in it, it was decided to use only the generators *gmc_disng* and *gmc_pion*.

For *gmc_pion* it is known that it can approximately reproduce the observed exclusive π^+-cross-section at HERMES . This is shown in figure 4.19. The model "VGG: LO+power corrections" that overestimates the observed cross-section was used in a Monte Carlo simulation to estimate the cross-section of the process $ep \to ep\pi^0$. It was assumed that the cross-section for the neutron is $\sigma_n = (0.5 \pm 0.5)\sigma_p$. Although exclusive pion-production contributes in the exclusive missing mass region, the cross-section is very small, as will be shown below.

The generator *gmc_disng* is tuned to reproduce the charged particle fluxes at HERMES . However, it cannot very well simulate the missing mass distribution of single photon events in

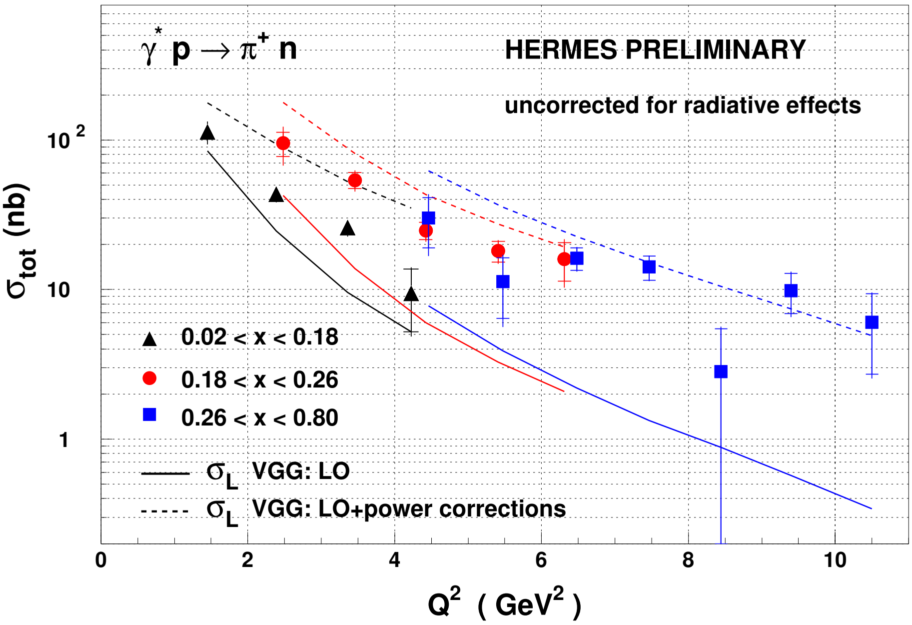

Figure 4.19.: The total photoproduction cross-section σ_{TOT} for exclusive π^+ production as a function of x_B and Q^2. Two different model calculations are shown in the plot.

the case of BH/DVCS. Part of this problem can be attributed to the missing diffractive meson production processes. In order to cure this problem an effective reweighting procedure has been suggested in [Ell03]. Under the assumption that the distribution is mainly wrong due to the generated meson multiplicities the distribution in W^2 can be seen as the source of the problem.

This distribution can be adjusted to the observed W^2 distribution for large missing masses (i.e. $M_x^2 > 6\,\text{GeV}^2$) by using a second order polynomial fit of the $N_{predicted}(W^2)/N_{generated}(W^2)$. After applying the correction factor as a function of W^2 to all values of M_x^2 a reasonable extrapolation for low missing masses is obtained. The effect is shown in figure 4.20 for Monte Carlo and positron data from 1999/2000. Although this reweighted Monte Carlo can reproduce the typical kinematic distributions for $M_x^2 > 6$ GeV^2, it it still an extrapolation at low missing masses, where diffractive processes become more important. Moreover a different reweighting factor is needed in order to describe the missing mass distribution of exclusive two-photon production, such that the interpretation of an increased π^0-flux is questionable.

4.8. Combined Monte Carlo Predictions

A qualitative understanding of the Monte Carlo predictions for the deuteron can be obtained by considering the in-plane cross-section that has been introduced in section 4.1. In figure 4.21 the cross-section is shown for the free proton, the free neutron, the deuteron and resonance excitation on the proton with $M_x \leq 1.4$ GeV. The free proton and neutron cross-sections were calculated using GPD model 5.

First of all the coherent deuteron is only important at low values of $|t|$, which is purely

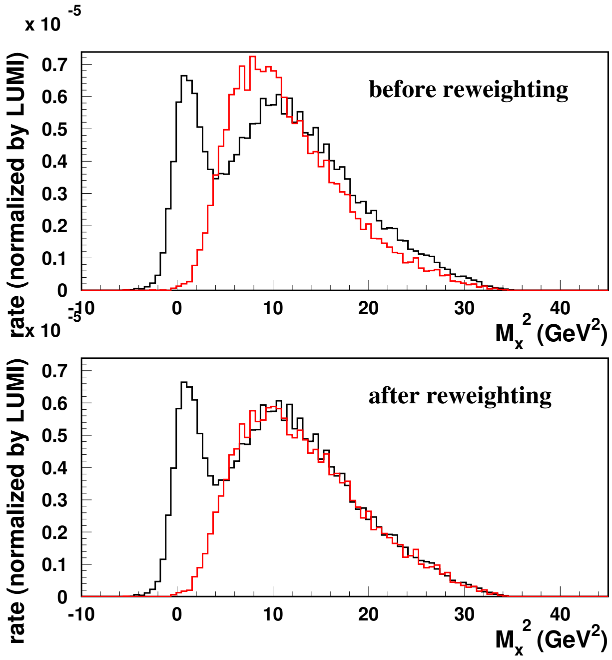

Figure 4.20.: Reweighting of semi-inclusive MC: The semi-inclusive MC (red) is reweighted in order to reproduce the W^2-distribution of the data (black) for $M_x^2 > 6$ GeV^2. Before the correction (top) the Monte Carlo overshoots at low missing masses; after the correction this problem has disappeared.

related to the formfactor of the deuteron. As long as the hadronic final state is not observed, there is no way to discriminate between the coherent and the incoherent process, since the kinematics is very similar.

Secondly the neutron contribution is much smaller than the proton contribution. However, the asymmetries on the proton and on the neutron are very different and for the neutron DVCS has a much bigger contribution. Hence it is not advisable to neglect the neutron contribution in general.

Finally the resonances add an important contribution; again it is small, but it has a different dependence on ϕ, as can be seen by comparing positive values for θ_{ip} and negative values for θ_{ip} at the same $|\theta_{ip}|$. At $\phi \approx 0$ a clear enhancement of the cross-section is seen, which is due to the lepton propagator of the initial state radiation. On the other hand the QED-Compton-peak at $|\theta_{ip}| \to 0$ is strongly suppressed, as $|t_0|$ is larger for $M > M_p$. The resonances on the neutron are expected to yield approximately the same cross-section in addition. The exact composition of the detected event sample will later be discussed in the context of background.

Including all mentioned contributions the Monte Carlo can well describe the experimental data. This is shown in figure 4.22. The Monte Carlo is normalised to the measured luminosity such that a quantitative comparison is possible. Given the precision of the detector digitisation in the Monte Carlo, deviations of up to 10% could be expected. Apart from a slight displacement of the exclusive peak - which is very sensitive to the calibration of the calorimeter - the obtained agreement is very good.

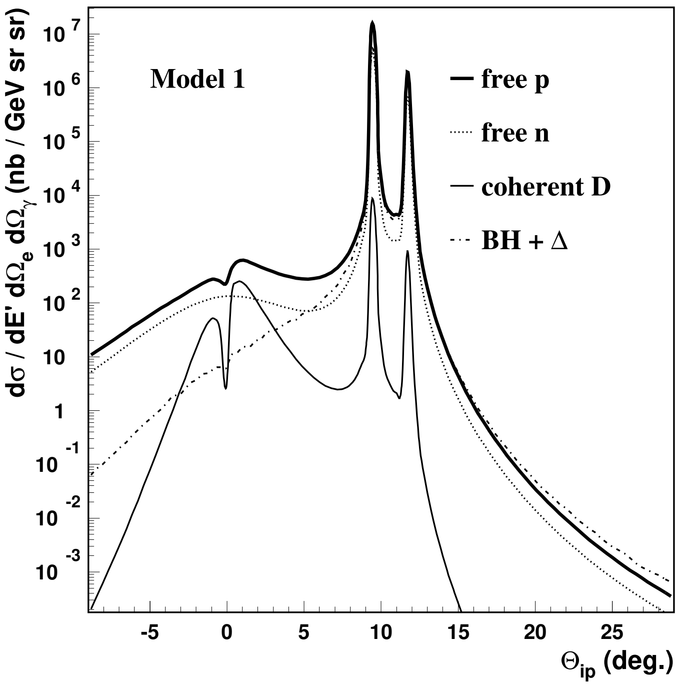

Figure 4.21.: In-plane cross-section of the deuteron at $Q^2 = 1$ GeV^2 and $x_B = 0.1$ according to model 1. The cross-section for a free proton, a free neutron and coherent scattering on the deuteron are shown. In addition incoherent BH with resonance excitation for $W < 1.4$ GeV is plotted.

Also the kinematical distributions are well described by the Monte Carlo. Due to details of the calorimeter response in this case only a shape comparison is shown (figure 4.23). Otherwise the normalisation of the result would be very sensitive to the missing mass cut. Apart from the ϕ-distribution, excellent agreement is found, which indicates that all important processes have been included in the simulation. The event distribution in ϕ is very sensitive to the calorimeter calibration or recalibration (cf. following chapter). It has been checked that e.g. a cluster position dependent recalibration of the photon energy yields a slightly better agreement with the simulation. This is shown in figures 4.24 and 4.25, where the same quantities are plotted as in figures 4.22 and 4.23, but the position dependent recalibration of the data from all years is applied. Nevertheless the simulation is in any case sufficiently precise to interpret the very inhomogeneous data set in terms of single processes, which will be needed in chapter 7.

As a conclusion the observation and interpretation of DVCS/BH on the deuteron at HERMES is more complicated than in the case of the proton. The coherent process is rather rare and and also the elastic neutron cross-section is small. At large values of $|t|$ the neutron resonances contribute in addition to the proton resonances. Also the semi-inclusive background is slightly stronger than on the proton.

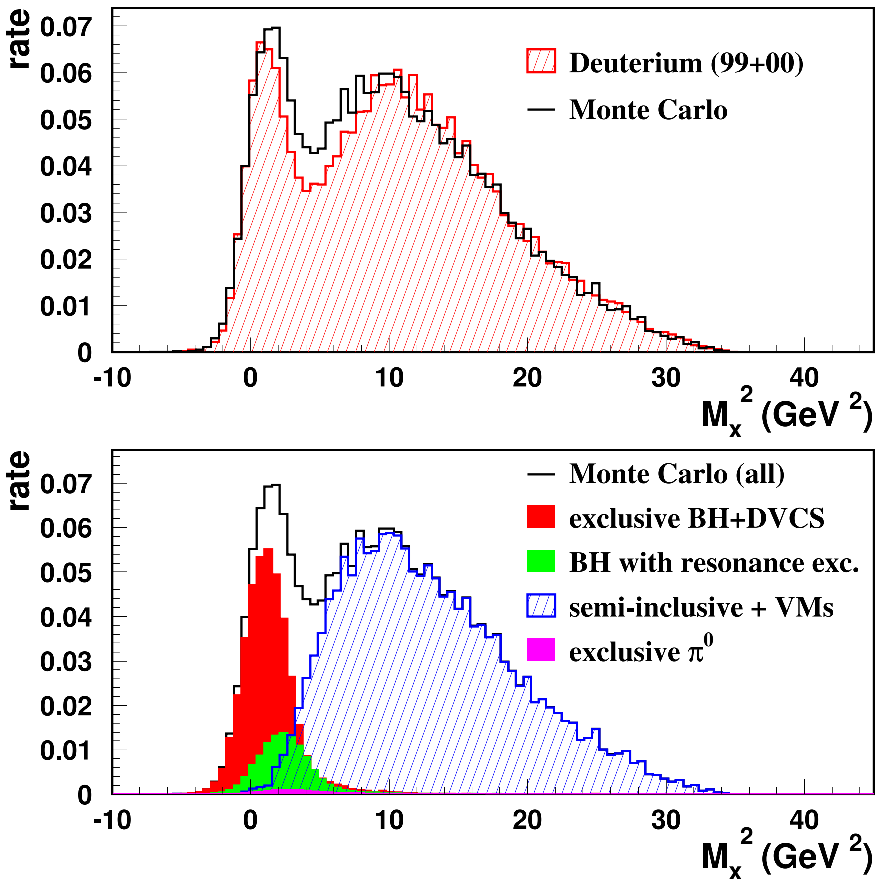

Figure 4.22.: Quantitative comparison of missing mass distributions for data and MC: All important processes are simulated in the MC and the resulting missing mass distribution is compared with the measured one (polarised and unpolarised deuterium data for 1999/2000) (top). In the bottom plot the single contributions as obtained by the MC simulation are shown separately.

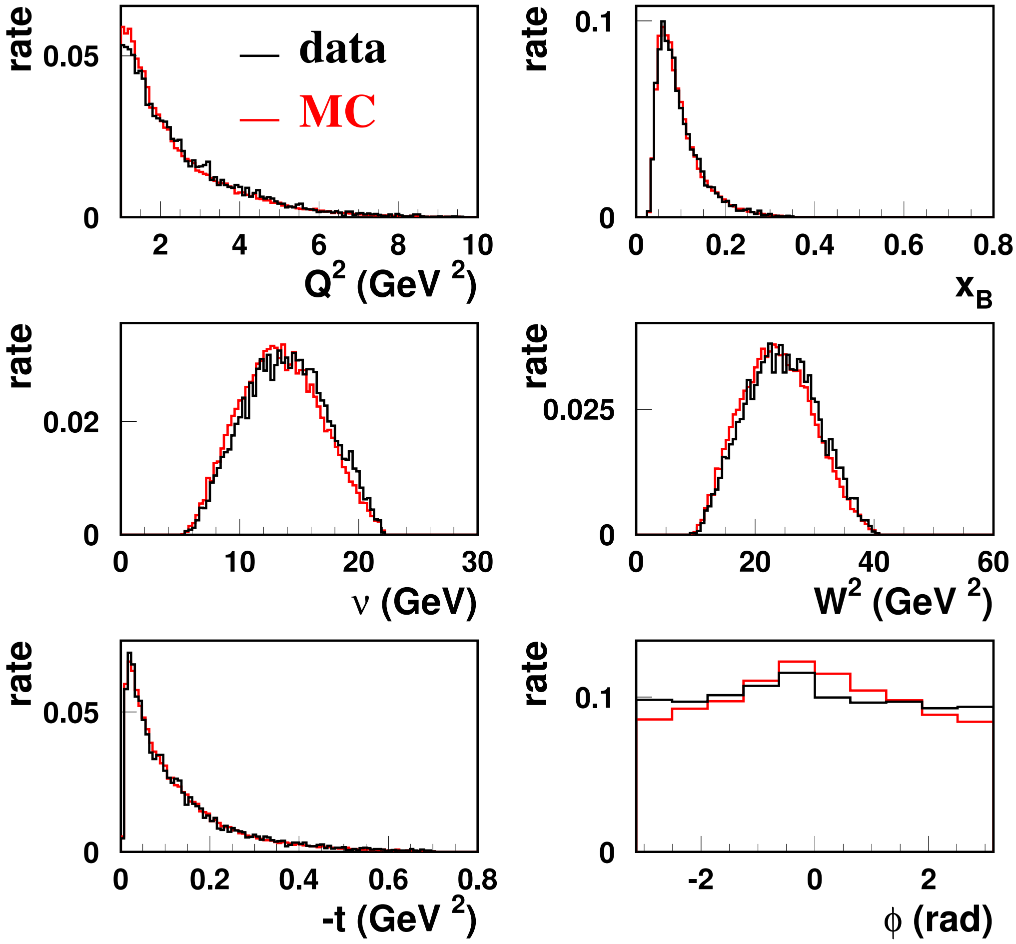

Figure 4.23.: Kinematical distributions of the exclusive event sample in x_B, Q^2, W^2, ν, $-t$ and ϕ from Monte Carlo (red/grey) and data (black). Normalised to the same area.

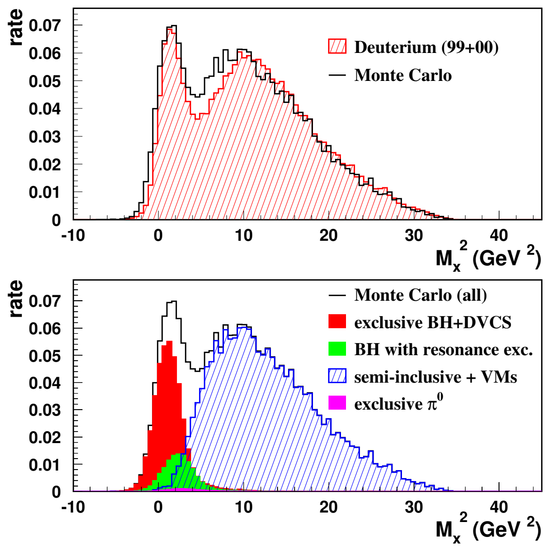

Figure 4.24.: Quantitative comparison of missing mass distributions using a different recalibration: All important processes are simulated in the MC and the resulting missing mass distribution is compared with the measured one (polarised and unpolarised deuterium data for 1999/2000) (top). In the bottom plot the single contributions as obtained by the MC simulation are shown separately. The position dependent recalibration for the calorimeter is used.

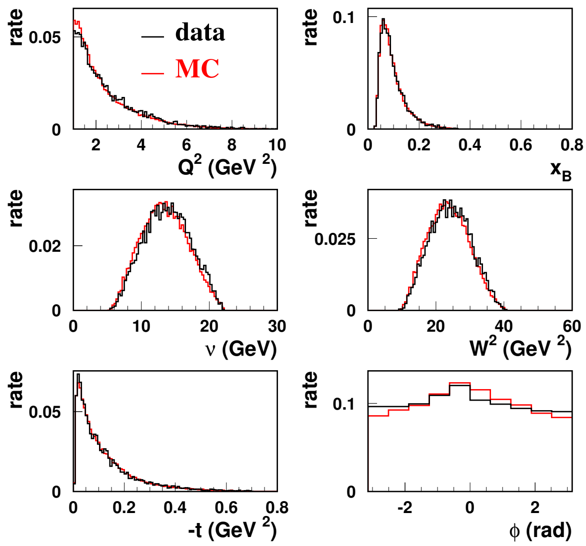

Figure 4.25.: Kinematical distributions of the exclusive event sample in x_B, Q^2, W^2, ν, $-t$ and ϕ from Monte Carlo (red/grey) and data (black). Normalised to the same area. The position dependent recalibration for the calorimeter is used.

5. Systematic Studies of the Detector Response

5.1. Introduction

Before an extraction of asymmetries in exclusive photon-production is possible, a number of cross-checks on the quality and consistency of the datasets have to be made. For the case of the proton, many experimental effects have already been studied in great detail [Ely02, Ell03, HERMES01a]. Since DVCS in interference with BH is an extremely rare process, it is usually not possible to split the statistics into small bins. This means that experimental artefacts are more difficult to spot.

In terms of detector response the most critical asymmetry is the beam-charge asymmetry, since data from different years and different beam charges have to be combined. Consequently most of the consistency checks compare the positron data with the electron data.

5.2. Lepton Momentum Resolution

One main concern was that differences in the reconstructed momentum of charged particles could exist between the two periods, which could e.g. be due to misalignment in combination with the charge flip. This would immediately lead to an apparent beam charge asymmetry.

To estimate the size of such effects it was studied, if there is a dependence of the exclusive missing mass on tracking parameters like the transverse vertex v_t of the scattered lepton. The result for single photon events with additional cuts on the transverse vertex of 2 mm$< v_t <$ 7.5 mm and 0 mm$< v_t <$ 1 mm is shown in figure 5.1 (distributions normalised to same area). As can be seen there is a dramatic effect of the cut: For large transverse distances the two missing mass distributions are displaced by about 1 GeV^2. Neither is there a good agreement at low values of v_t.

The shift can be attributed to the determination of the lepton momentum p' as can be proven by studying the dependence of $(p' - E')/p'$ for leptons on the transverse vertex. This dependence for different tracking methods and 25 runs from 2000 is plotted in figure 5.2. In addition 24 runs from 1998 are also shown. The top plot shows $(p' - E')/p'$ for DIS-leptons (i.e. e^- in 1998, e^+ in 2000), while the bottom plot shows $(p' - E')/p'$ for charge symmetric leptons (i.e. e^+ in 1998, e^- in 2000).

Obviously the effect is not related to the tracking method, although it appears to be less severe if the DVCs are included. Moreover, the same charge leads to the same effect for both years. Consequently this is not related to a change in alignment between the two years.

In order to explain the effect the knowledge is required that the reconstructed beam position that is seen by the upper and lower half of the HERMES spectrometer is not identical to the true

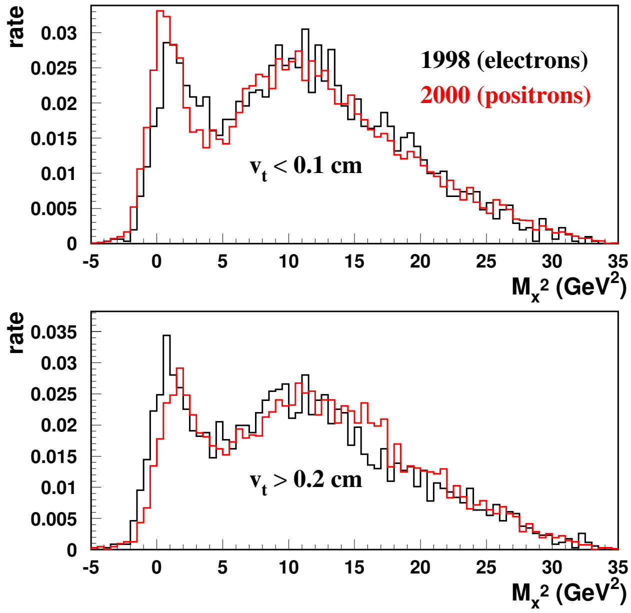

Figure 5.1.: Missing mass distribution for electron data (1998) and positron data (2000) if cuts on the transverse vertex v_t are applied. The distributions are normalised to the same area.

beam position. Otherwise, the transverse vertex distribution would peak at $v_t = 0$. This can be studied in more detail by looking separately at the 4 quadrants of HERMES , which can be defined by requiring positive or negative values of the lepton momentum components p'_x and p'_y. The transverse vertex distribution for leptons in the four quadrants and two different tracking methods is shown in figure 5.3. While the standard method is based on hits reconstructed in the FCs and the BCs, the alternative method is based on the FCs and the DVCs. Both methods agree in the result that the beam is displaced with respect to its nominal position.

The true beam position can be approximately obtained by plotting the transverse vertex for leptons vs. the azimuthal angle ϕ_e of the scattered lepton in a polar diagram (figure 5.4). This peculiar representation has to be interpreted in the correct way: In principle the maximum event density is expected to have the shape of a symmetric '8' if the beam is displaced by a larger distance than the vertex resolution of the spectrometer allows to resolve. Due to the vanishing HERMES acceptance for $\phi_e = 0$ and $\phi_e = \pi$, this curve is not complete as can be seen. The maximum values for v_t (i.e. the top and the bottom points of the '8') are obtained if the tracks are in the 2d-projection perpendicular to the line which contains the true beam and the reconstructed beam. (Values of v_t close to zero are obtained, if the tracks point along this line.) The maximum value for v_t indicates the distance between the true beam position and the nominal beam position. The plot shows that the true beam position at the beginning of 1998 was displaced by about 2 mm. Either was the true beam position at $x < 0$ and $y > 0$, or it was at $x > 0$ and $y < 0$.

Monte Carlo simulations were done to study the observed effects for such a displaced beam. The aim is to understand the impact on the reconstructed momentum and to verify

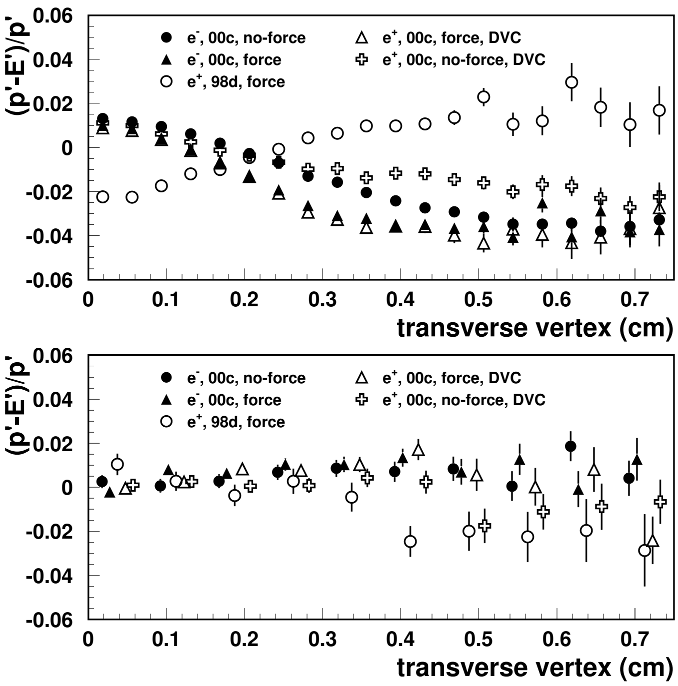

Figure 5.2.: $(p' - E')/p'$ vs. v_t for several different tracking productions. The top plot contains DIS-leptons, the bottom plot charge symmetric leptons for 1998 and 2000. The PID is obtained from a cut of $E > 20$ keV on the truncated mean value of the TRD.

that the vertex distribution can be reproduced. The relevant results for a beam position of $x = -1.5$ mm ($x = -2.0$ mm) and $y = 1.0$ mm ($y = 1.5$ mm) are shown in figure 5.5. In this plot the ratio $(p' - E')/p'$ vs. v_t for electrons (top), v_t vs. ϕ_e (bottom left) and the v_t distribution (bottom right) are shown. Obviously the ideal Monte Carlo geometry can reproduce the v_t-dependence of the reconstructed momentum as soon as a displaced vertex is assumed; the reconstructed momentum does not depend on v_t for a beam at its nominal position. Good agreement between data and MC is found for the top spectrometer half ($\phi_e > 0$) if a displacement of $x = -2.0$ mm$/y = 1.5$ mm is assumed. The worse agreement for the bottom half is due to a relative mis-alignment of both halves that corresponds to about 1 mm in y of the reconstructed vertex. The slope of $(p' - E')/p'$ vs. v_t is found to be inverted if the beam position stays approximately the same but the beam charge is changed.

In order to explain the source of the effect, first a perfectly aligned experiment should be considered: If the front track is reconstructed by the FCs under a wrong angle θ_x, this will lead to an offset in the reconstructed signed vertex v_x, which is defined as the x-position of the track at $y = 0$. At the same time the bending of the track in the magnetic field of the spectrometer magnet is either overestimated or underestimated depending on the beam-charge. Due to the difference between the nominal and the real beam position, v_t is correlated with v_x such that a cut on v_t leads to changes in the **average** reconstructed momentum. It is important that the lepton momentum for each event is not changed due to the different beam-position. This has

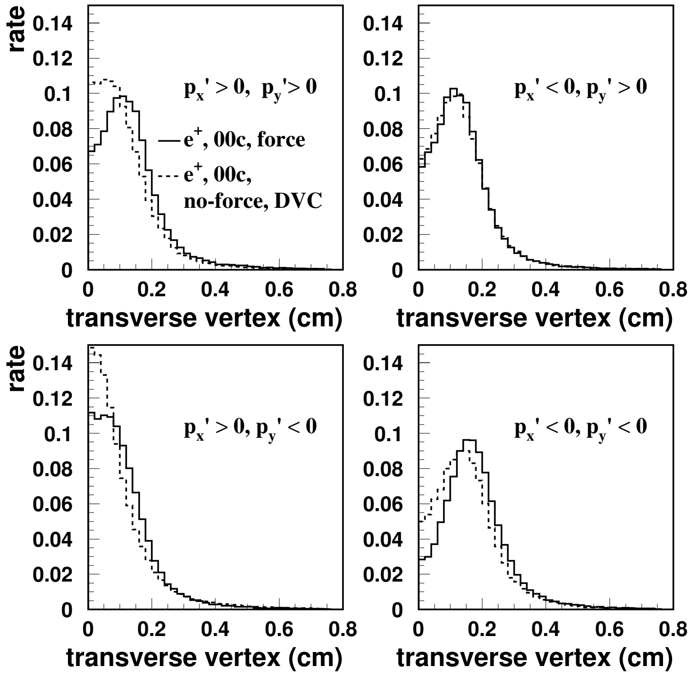

Figure 5.3.: Transverse vertex distribution of lepton tracks for 25 runs of the year 2000. The standard tracking method (force) was compared with an alternative tracking method (no-force, DVC).

been explicitly checked by recalculating the momentum for each event.

If the true beam-position is known, the remaining vertex coordinated v_x has approximately a linear correlation with $(p' - E')/p'$ as is expected from the underlying mechanism. It is clear that in this case either a v_x and momentum dependent correction can be applied to p' or that a restrictive cut on v_x can isolate events for which p' is better known. On the other hand, the time-dependent beam position has to be known with high accuracy, before such an attempt can be made. Ideas for this exist [Kis03], but detailed studies are still necessary.

For the time being, the best way to handle these correlations between p' and v_t is to apply a cut on v_t which only cuts away the far tails in the v_t-distribution. The Monte Carlo predicts that in this case no problems can be expected. Hence a cut at $v_t = 7.5$ mm seems to be safe. As a conclusion no indication for a wrong momentum determination has been found, although the present tracking method leaves room for an improvement of the resolution.

5.3. Calorimeter: Position Resolution

One contribution to smearing effects that will be discussed in section 5.5 is due to the position resolution of the calorimeter. This is limited due to statistical fluctuations in the evolution of electromagnetic showers. In addition also the position reconstruction algorithm can artificially

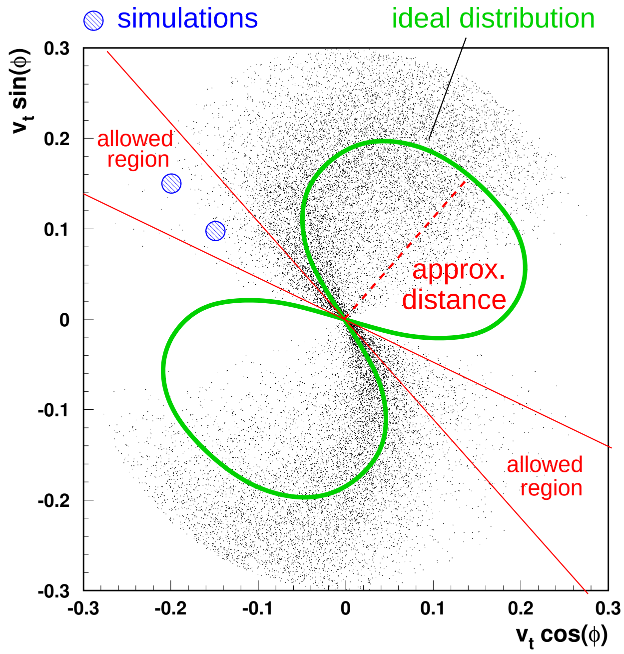

Figure 5.4.: Event distribution in $v_t \sin(\phi_e)$ vs. $v_t \cos(\phi_e)$ for single photon events from the first 1500 runs of 1998. Here ϕ denotes the azimuthal angle of the scattered lepton around the beam. The allowed region for the beam position in x and y is marked. The approximate distance between the nominal and the real beam position is indicated and the ideal curve for a complete HERMES acceptance is shown ('8'). The markers indicate the beam positions that were used for Monte Carlo studies.

degrade the resolution and especially lead to a systematic position dependent bias. In order to avoid this effect, the position reconstruction algorithm must be adjusted to the observed shower profile as has been discussed e.g. in [Sur98]. The logarithmic weighting technique from this reference is now also used at HERMES. It works in the following way:

- If the HERMES-Reconstruction-Code (*hrc*) detects a maximum of the energy deposition in one calorimeter block, this block will be combined with the neighbouring 8 blocks to form a cluster. The energy deposition Q_i in each block is measured in units of ADC-channels.

- The position of the cluster in x is obtained from [Ely02]

$$x = \frac{\sum w_i, x_i}{\sum w_i}, \tag{5.1}$$

where

$$w_i = \begin{cases} W_0 + \ln\left(\frac{Q_i}{Q}\right) & \text{for} \frac{Q_i}{Q} > e^{-W_0} \\ 0 & \text{else} \end{cases} \tag{5.2}$$

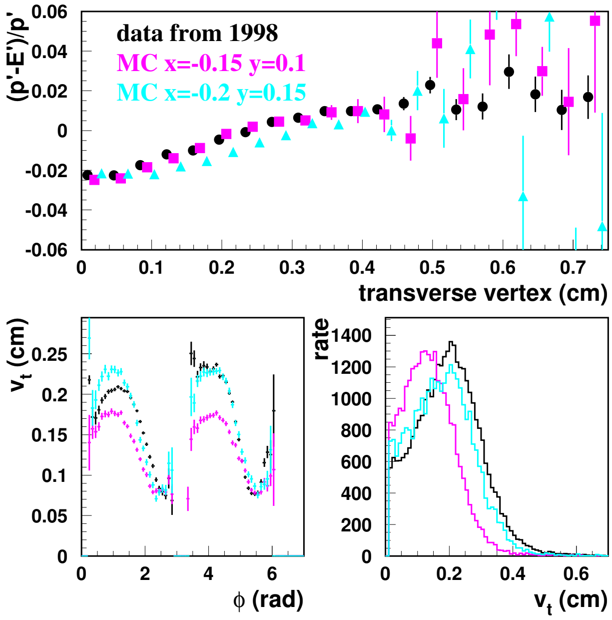

Figure 5.5.: Comparison of data and Monte Carlo for a shifted beam position: The three plots show that the ratio $(p' - E')/p'$ vs. the transverse vertex v_t as well as v_t vs. ϕ_e for data from 1998 can be explained by the Monte Carlo if a displaced beam at $x = -0.2$ cm and $y = 0.15$ cm is assumed.

and

$$Q = \sum_i Q_i. \tag{5.3}$$

- The energy E of the cluster in units of GeV is obtained from a calibration curve as $E = E(Q)$.

The constant W_0 can be tuned to obtain a flat event distribution in x and y. The naive expectation would be that clustering effects are eliminated in this way. For the short-range effects, which depend on the hit position relative to the block boundaries, this is certainly true. However, this does not guarantee that the obtained hit position always marks the photon track at the same depth in z.

The z-position of the cluster is actually not accessible from first principles, as it it does not correspond to the centre of gravity of the energy deposition. Instead it depends on the clustering algorithm and properties of the calorimeter blocks like the absorption length of visible light. In the reconstruction algorithm it is always possible to choose a different z-position and apply a correction to the x- and y-position such that the new 3d space point lies again on the photon trajectory. Also combinations of corrections in x, y and z are possible. In the following studies it was decided to choose an optimum hit-plane in z and to allow constant offsets in x and y as a higher order correction. The results can be shown to be equivalent to fixing an arbitrary z-position and to apply a first-order polynomial correction on x and y as suggested in [Ell03].

One interesting aspect is that the reconstruction algorithm implicitly assumes a symmetric lateral shower profile. For the typical impact angles at HERMES of up to ~ 200 mrad this is not fulfilled and the effects described above can certainly be expected. There is no compelling reason why the optimum z-position should be the same for the x and the y-coordinate as the real photon trajectory need not pass through the reconstructed x- and y- position at the same point in z. Consequently the procedure as described above will only give an approximate solution to retrieving the original photon trajectory in the best possible way.

In order to fix the free parameters of the reconstruction method, an analysis of Monte Carlo data and real events is needed. As the shower evolution depends critically on the lepton/photon energy, all studies must be made at the typical photon-energies for DVCS-candidates of (13.8 ± 3.5) GeV. The following procedure can be used to study the problem:

1. The generated photon direction and the reconstructed photon direction are compared using Monte Carlo data.
2. Monte Carlo is also used for the leptons but this time the reconstructed lepton cluster is compared with the hit position of the backward lepton track.
3. If the Monte Carlo simulation predicts that the obtained results agree due to a similar shower evolution for photons and leptons, real lepton tracks can be used to obtain the best reconstruction parameters for real photon clusters. (Thus an exact agreement of data and Monte Carlo is not required.)

For the Monte Carlo study exclusive single photon production on the proton was generated according to the exclusive BH cross-section. For the real data 25 runs from 00c production and 24 runs of the 98d0 production were used.

In the Monte Carlo simulation the optimum z-position for the photon reconstruction is found between 734 cm and 737 cm. The y-position is better reconstructed for $z = 734$ cm, while the x-position prefers $z = 737$ cm. This is shown in figure 5.6. For the same z-position, the hit-position of leptons in the Monte Carlo was compared with the reconstructed hit position of the backward lepton track. This is show in figure 5.7. An approximate agreement is found for the two cases such that the shower evolution seems to be similar and moreover accessible using the backward lepton tracks.

Now it is possible to apply this knowledge to lepton tracks in the real data. It can be seen that the optimum calorimeter position is now between 729 cm and 732 cm. Again the lower value is preferred by the y-position and the upper value is preferred by the x-position. This is shown in figure 5.8.

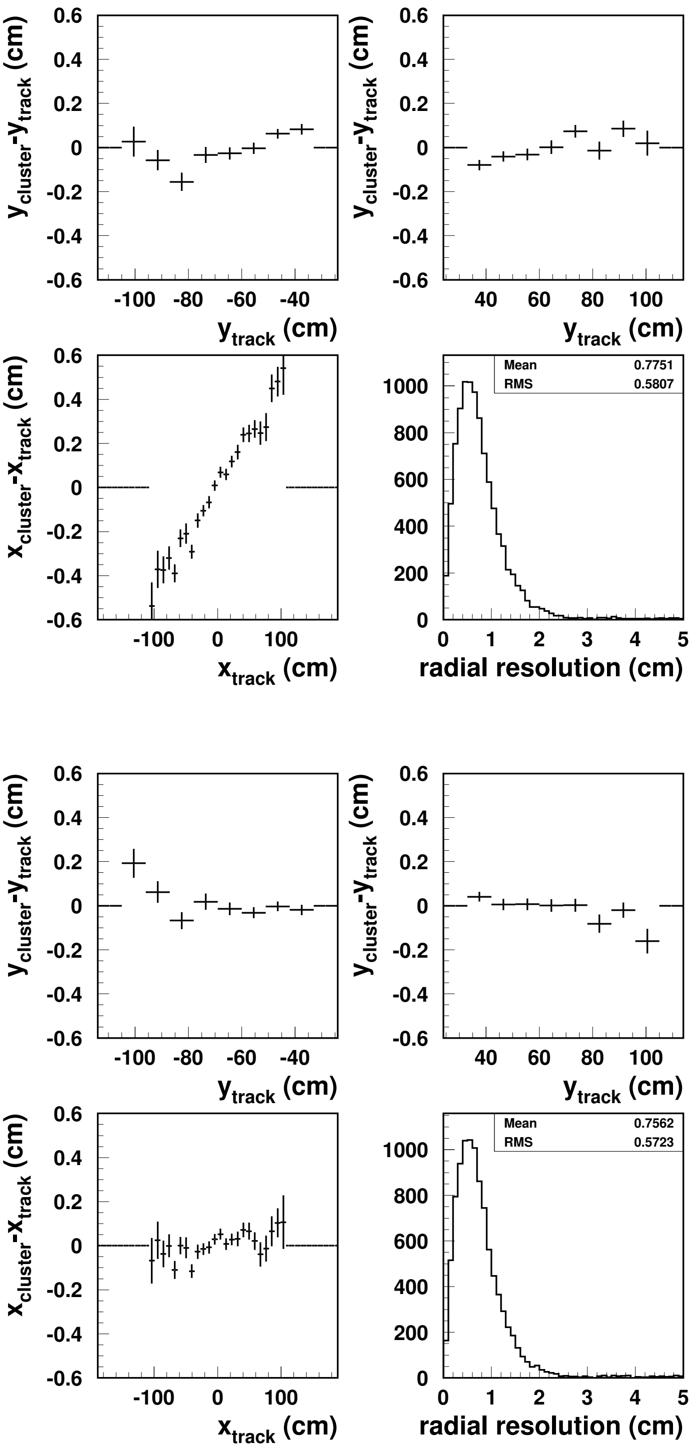

Figure 5.6.: Monte Carlo study of photons: The top plot is for the assumption of $z_{calo} = 734$ cm, the bottom plot is for $z_{calo} = 737$ cm. The hit position of the original photon track is compared with the reconstructed cluster position; for the two top plots a constant offset has been subtracted that has been obtained from a Gaussian fit to the 1d projection.

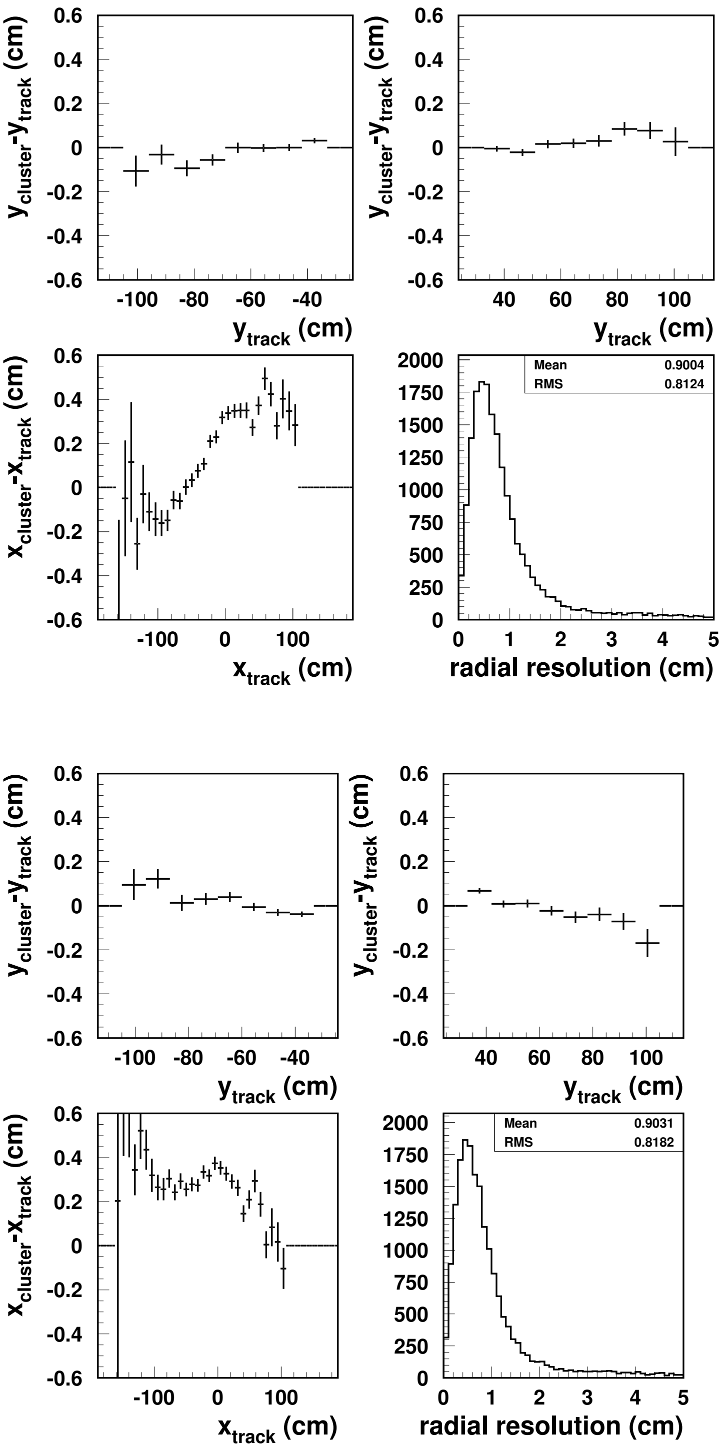

Figure 5.7.: Monte Carlo study of leptons: The top plot is for the assumption of $z_{calo} = 734$ cm, the bottom plot is for $z_{calo} = 737$ cm. The hit position of the backward charged track is compared with the reconstructed cluster position; for the two top plots a constant offset has been subtracted that has been obtained from a Gaussian fit to the 1d projection.

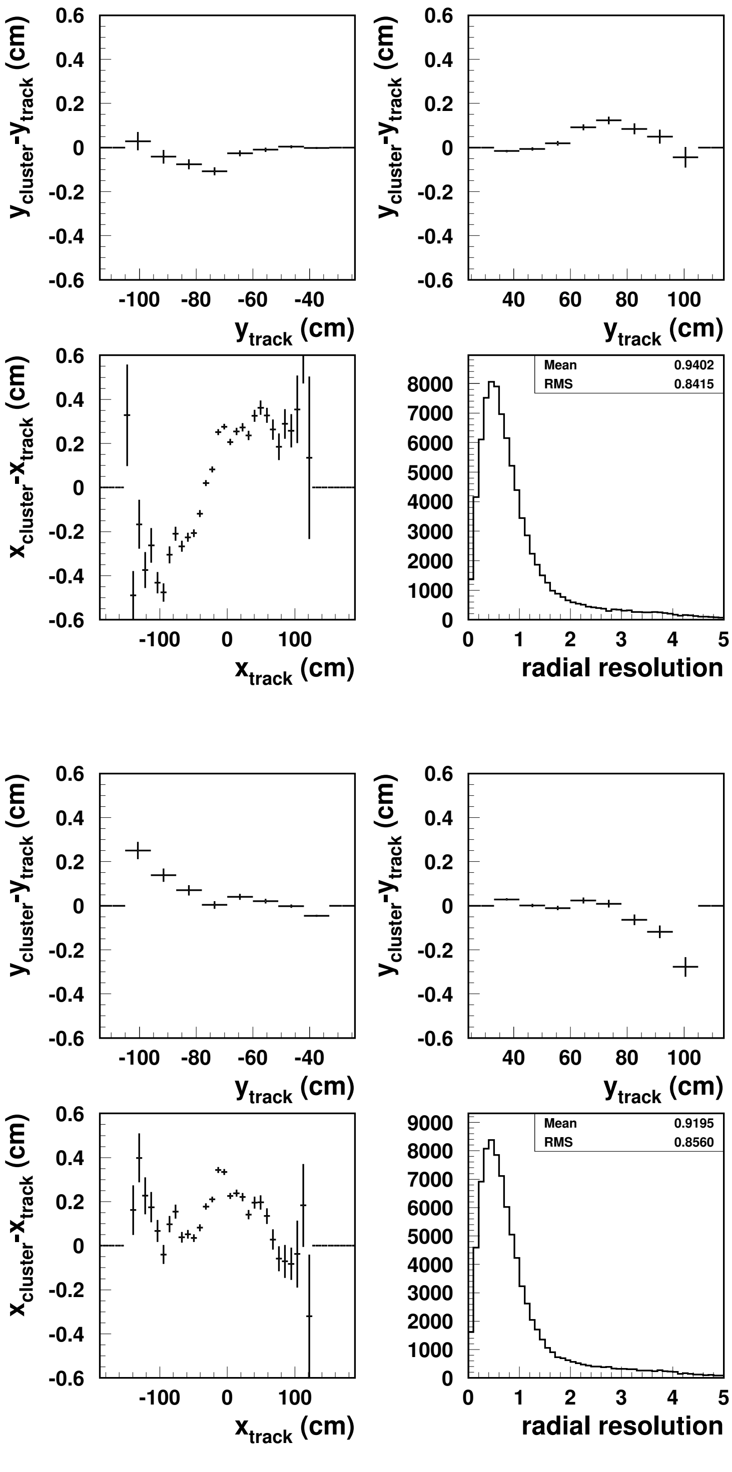

Figure 5.8.: Leptons from Data (2000): The top plot is for the assumption of $z_{calo} = 729$ cm, the bottom plot is for $z_{calo} = 732$ cm. The hit position of the backward charged track is compared with the reconstructed cluster position; for the two top plots a constant offset has been subtracted that has been obtained from a Gaussian fit to the 1d projection.

Table 5.1.: Shift in the y-position of the calorimeter. The true hit position is obtained from $y_{true,top} = y + dy$.

	dy (top)	dy (bottom)
00c1	-0.51 cm	+0.03 cm
98d0	-0.51 cm	+0.08 cm

For all distributions in y an offset has been subtracted for the top and the bottom part of the calorimeter independently. This offset was determined from a Gaussian fit to the one-dimensional histogram of $y_{cluster} - y_{track}$. The obtained offsets are compatible with the values from reference [Ell03]: For the top part it was found to be about 0.5 mm, for the bottom part it was found to be about 0 mm. The exact offset for 1998 and 2000 are shown in table 5.1. They are consistent and consequently no artificial asymmetries are expected due to the position reconstruction in the calorimeter.The full transformation to the correct cluster position is:

$$x_{true} = x, \tag{5.4}$$
$$y_{true,top} = y - 0.5 \text{ cm}, \tag{5.5}$$
$$y_{true,bottom} = y, \tag{5.6}$$
$$z_{true} = 729 \text{ cm} \tag{5.7}$$

for leptons. For the Monte Carlo in the present version the following transformation is required in order to obtain equivalent results:

$$x_{true} = x, \tag{5.8}$$
$$y_{true,top} = y - 0.2 \text{ cm}, \tag{5.9}$$
$$y_{true,bottom} = y + 0.2 \text{ cm}, \tag{5.10}$$
$$z_{true} = 734 \text{ cm}. \tag{5.11}$$

The correction in the Monte Carlo purely originates from the shower profile. In reality, the whole calorimeter appears to be shifted by -0.2 mm in addition. If this is a true shift or an effect due to misalignment of the tracking system is not known at the moment.

It was argued by the HERMES calorimeter group that the shower evolution for photons starts later than for leptons. This additional shift of approximately one radiation length leads to the following transformation:

$$x_{true} = x, \tag{5.12}$$
$$y_{true,top} = y - 0.5 \text{ cm}, \tag{5.13}$$
$$y_{true,bottom} = y, \tag{5.14}$$
$$z_{true} = 732 \text{ cm}. \tag{5.15}$$

However, this additional shift is not reproduced by the Monte Carlo as can be seen in figures 5.6 and 5.7. According to the simulation the reason is that a shift of 0.5 radiation lengths is only seen if the cut on the preshower signal is omitted. Nevertheless in agreement with the calorimeter group this transformation will be used for the analysis of real data, while for the

Monte Carlo the correction from equations 5.8 ... 5.11 will achieve the same angular resolution. In order to obtain the same acceptance in data and Monte Carlo this transformation is partly converted into a linear correction on the cluster position:

$$x_{true} = x, \tag{5.16}$$
$$y_{true,top} = 0.9937(y - 0.2 \text{ cm}), \tag{5.17}$$
$$y_{true,bottom} = 0.9937(y + 0.2 \text{ cm}), \tag{5.18}$$
$$z_{true} = 732 \text{ cm}. \tag{5.19}$$

Thus cuts that are applied on x_{true} and y_{true} have the same effect on the real data as on simulated events.

The impact of the correction to the cluster position is in general small. The maximum change of the angle θ_γ of the reconstructed photon with respect to the beam is only about 1 mrad. In addition there is no danger of false asymmetries, as the alignment was apparently unchanged between 1998 and 2000.

5.4. Calorimeter: Calibration

A good and equivalent calibration of the calorimeter for the years 1998 and 2000 is vital for the extraction of the BCA. The reason is that a position dependent mis-calibration of the calorimeter will systematically change the reconstructed missing mass. As the cut on the missing mass is applied in a densely populated region, small shifts in the missing mass can lead to visible changes in the number of accepted events. This affects the overall normalisation (i.e. the extracted constant moment of the BCA) and can also introduce false angular dependences.

The calorimeter calibration is much less critical for most of the other physics processes that are studied at HERMES and hence until now the employed calibration procedure was sufficient. The reason is that the calorimeter is usually only used for the trigger and the PID; in both cases a mis-calibration in the order of one percent may be acceptable, while this will already lead to visible effects in DVCS asymmetries.

Recently it has been noticed that for this high required accuracy the data production from the year 2000 still had problems with the way in which the calibration constant was obtained for each block of the calorimeter. A new data production may solve some of the observed problems. In the meantime the mis-calibration of the calorimeter has to be studied and possible effects have to be estimated. For this purpose two different approaches were taken:

1. fitting of the M_x distributions
2. study of the ratio E'/p' depending on p' for lepton tracks

The first method uses the single-photon events from 1998 and 1999/2000 and adjusts the relative normalisation as well as a constant factor a multiplied to the photon cluster energy from 2000 in order to minimise χ^2. A fit for the unpolarised data is shown in figure 5.9. The obtained 2d-map of χ^2 indicates that the calorimeter calibration is not at its optimum value. In the 1d projection under the assumption of a correct normalisation, a fit with a second order polynomial results in $a = 1.012$. All fit results are summarised in table 5.2. The same fit can be done for the reconstructed π^0-mass by using 2-photon events. However the result differs,

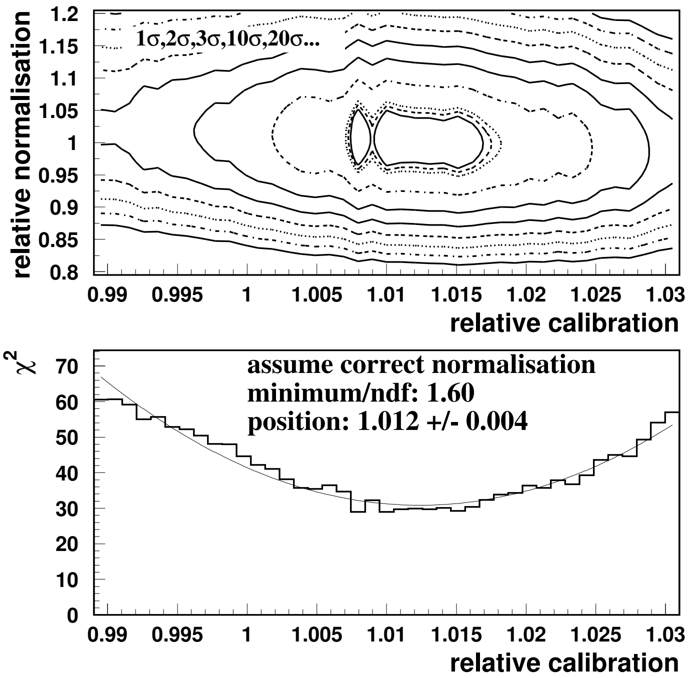

Figure 5.9.: Recalibration of calorimeter: The normalised missing mass distributions for 1998 and 1999/2000 were compared in the exclusive region (-2 GeV^2 $< M_x <$ 10 GeV^2, 20 bins). χ^2 of the difference was calculated and plotted as a function of the normalisation and the calibration factor for 2000 (top). In the bottom plot the minimum is determined as a function of the calibration factor.

Table 5.2.: Recalibration factors for the year 2000 obtained from a fit of the missing mass distributions

dataset	recalibration	χ^2/ndf
unpolarised	(1.012 ± 0.004)	1.60
polarised	(1.024 ± 0.004)	1.06

depending on the exact cuts. This indicates that E'/p' may have a momentum dependence or a dependence on the hit position.

The second method simply considers the E'/p'-ratio depending on the momentum for leptons of single-photon events. The result averaged over the whole calorimeter is shown in figure 5.10. As can be seen, the ratio E'/p' is not flat in p. Instead the energy measured by the calorimeter falls below the momentum for low momenta as well as for high momenta. It is not clear if this is a real effect; again the p-dependence can also be due to a local miscalibration of the calorimeter or overlapping clusters. The effect does not depend on the method, since also a Gaussian fit to the distribution gives the same result for low momenta. For medium lepton momenta the difference between E'/p' and one is usually smaller than 1%, but $(E'/p')_{1998}/(E'/p')_{2000}$ is systematically larger than one. Again the polarised dataset shows a larger mis-calibration, but the obtained values at medium energies are somewhat lower than the result from the fitting of missing mass distributions.

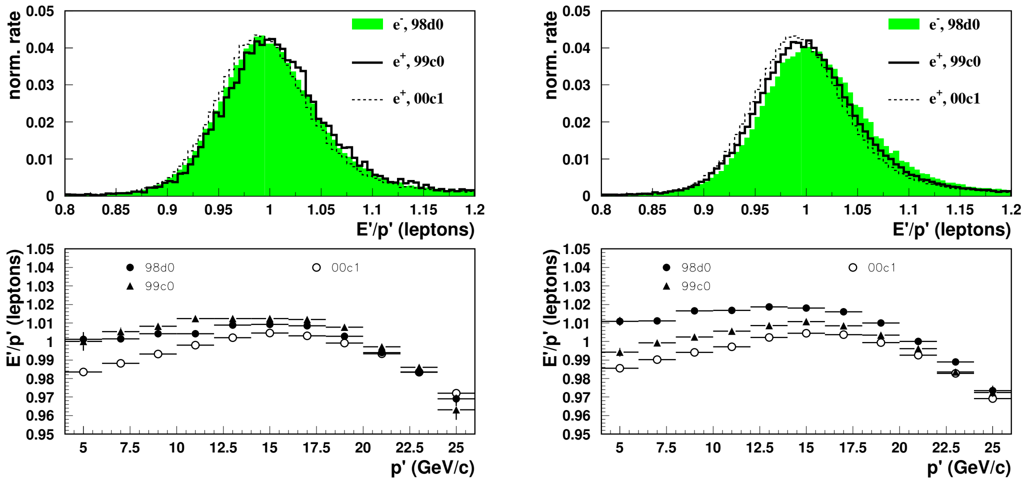

Figure 5.10.: E'/p' for leptons and different years: The left plot is based on unpolarised data, the right plot on polarised data. The ratio E'/p' for leptons from single photon events (not all kinematical cuts applied) is shown in the top plot. Small displacements between different years are seen. In the bottom plot the momentum dependence of E'/p' is shown (leptons with front-track clusters rejected).

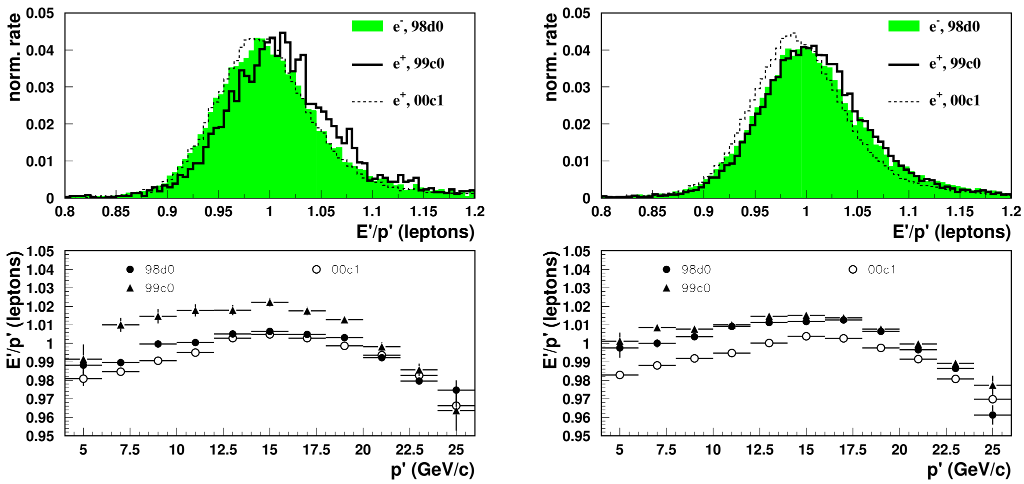

Figure 5.11.: E'/p' for leptons and different years (4th quadrant): The same quantities as in figure 5.10 are shown, but this time only leptons hitting the fourth quadrant ($p'_x < 0$, $p'_y < 0$) are used. The agreement of 1998 and 2000 is here very good, while 1999 is obviously different.

In reality the problem of calibration is more complicated: Already each of the 4 spectrometer quadrants has a different average calibration. For example the same quantities as in figure 5.10 are shown for the fourth quadrant in figure 5.11. For the unpolarised data the relative calibration of 1998 and 2000 agrees well in this quadrant, while 1999 is displaced by about 1% with respect the to the whole dataset. For the polarised dataset the calibration in 1998 is at low momenta 1% lower than for the whole dataset data, while the calibration from 2000 appears to be the same as for all data. This indicates local problems with the calibration. In order to study this in more detail, DIS events were used to calculate the mean value of E'/p' depending on the hit position on the calorimeter. The results for 1998 and 2000 are shown in 5.12. It can be seen that for low values of $|y|$ and large values of $|x|$, the average E'/p' is about 1.03, while it is smaller than 1 for $x \approx 0$. It has been verified that also if a Gaussian fit is used instead of the mean value these results are obtained. In fact the whole peak in E'/p' is shifted by an amount that is in the order of the nominal energy resolution of the calorimeter. However although the effect has been confirmed [Has03], the reason for it is unclear. Another interesting feature is that the ratio of the two histograms in figure 5.12 results in a centrosymmetric deviation, which is much harder to explain than a left-right asymmetry that could be due to the particle charge.

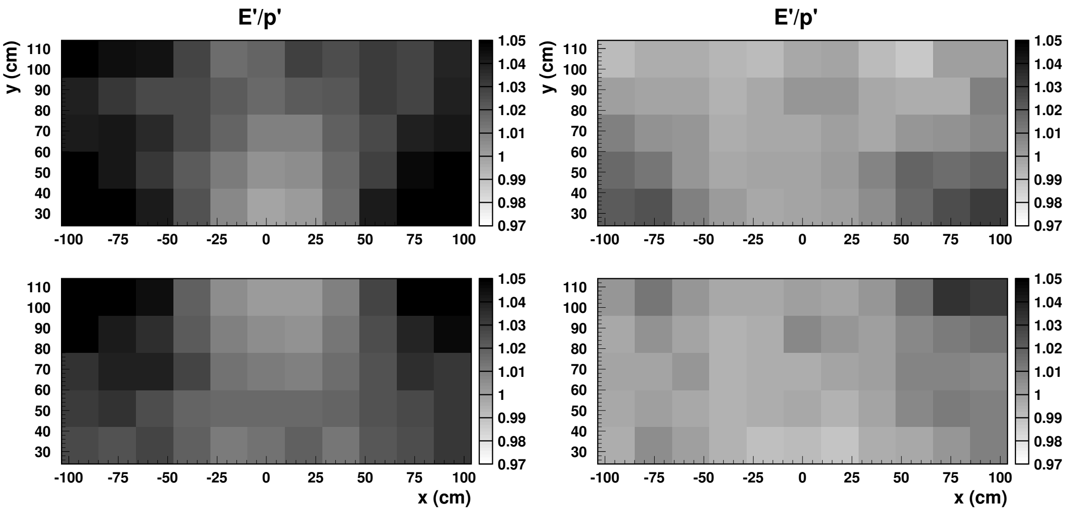

Figure 5.12.: E'/p' depending on the hit position at the calorimeter for 1998 (left) and 2000 (right). DIS-events from the μDST productions were used to create the plot. The mean value of E'/p' is shown in each bin.

In order to remove at least the most obvious difference in calibration between 1998 and 2000, the constant calibration factors from table 5.2 were applied to the dataset from 2000. Remaining effects of the local mis-calibration will be discussed together with all other systematic errors.

5.5. Detector Smearing

Although smearing effects cannot generate false asymmetries, they can strongly dilute or deform the asymmetry such that asymmetry moments are mixed. In previous discussions of this topic [Ely02, Ell03] the main interest was in the smearing of the photon direction, since the original clustering algorithm at HERMES was the main problem. The new clustering algorithm has eliminated this problem and now the resolution is actually limited by the momentum resolution for the scattered lepton.

Smearing effects are mainly of interest as they change the relative direction of the real photon with respect to the virtual photon. Therefore they change the value of the azimuthal angle ϕ as well as the polar angle θ_{γ,γ^*} and t_c. It is clear that the effects in ϕ will diverge for small values of θ_{γ,γ^*} or $|t_c|$.

The smearing of the photon vector is more or less isotropic. This can be studied by using the Monte Carlo and comparing the generated photon direction with the reconstructed photon direction. If one plots the differences $d\theta_x$ and $d\theta_y$ (where θ_x and θ_y are defined by equations 3.6 and 3.7) in the generated and reconstructed angles, the obtained distribution is radially symmetric. Depending on the clustering algorithm this is not necessarily true.

One can also argue that if an inclined track hits the calorimeter, the position resolution can be different along the projection of the direction of motion to the CALO surface or perpendicular to it. Again the effect is very small and in order to demonstrate it a suitable projection to two dimensions is needed. This was achieved by rotating the positive x^*-axis along the beam (compare figure 5.13), until the generated photon points towards it. θ_x^* and θ_y^* for the reconstructed and the generated photon are defined in analogy to θ_x and θ_y. The vertical distance $d\theta_y^*$ between the reconstructed and the generated photon can be plotted vs. the horizontal distance $d\theta_x^*$. This is shown in plot 5.14 (bottom, right). The obtained values for the resolutions from Gaussian fits are shown in table 5.3.

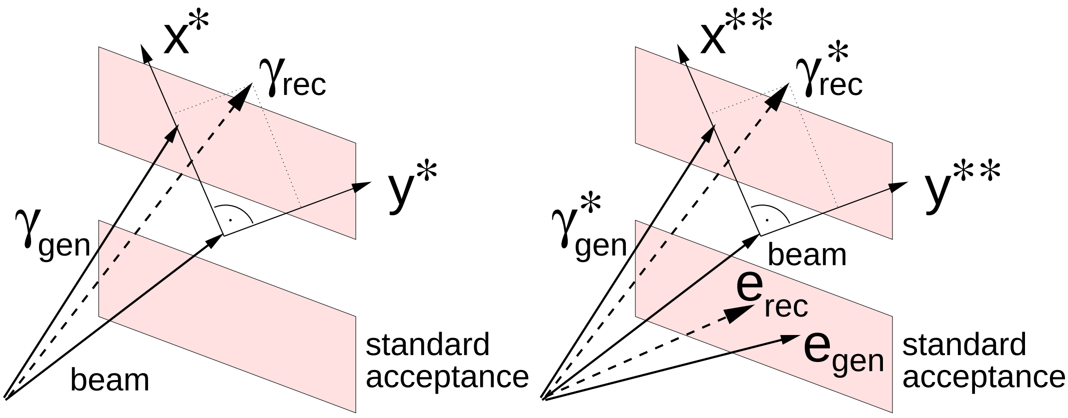

Figure 5.13.: Definition of the rotated coordinate systems x^*/y^* and x^{**}/y^{**}. The corresponding angle θ_x^* is e.g. obtained from $\theta_x^* = \arctan(p_x^*/p_z)$ where p_x^* denotes the momentum component of the reconstructed photon along x^*.

For the lepton the situation is very different. The angular resolution for the lepton is very good and translates into a good angular resolution for the virtual photon. However, the momentum resolution has an additional large impact. It can be shown that to a good approximation the resolution in the polar angle θ of the virtual photon with respect to the beam is given by:

$$d\theta_{\gamma^*} = \frac{EE'}{(E-E')^2}\theta_e(dp'/p'). \tag{5.20}$$

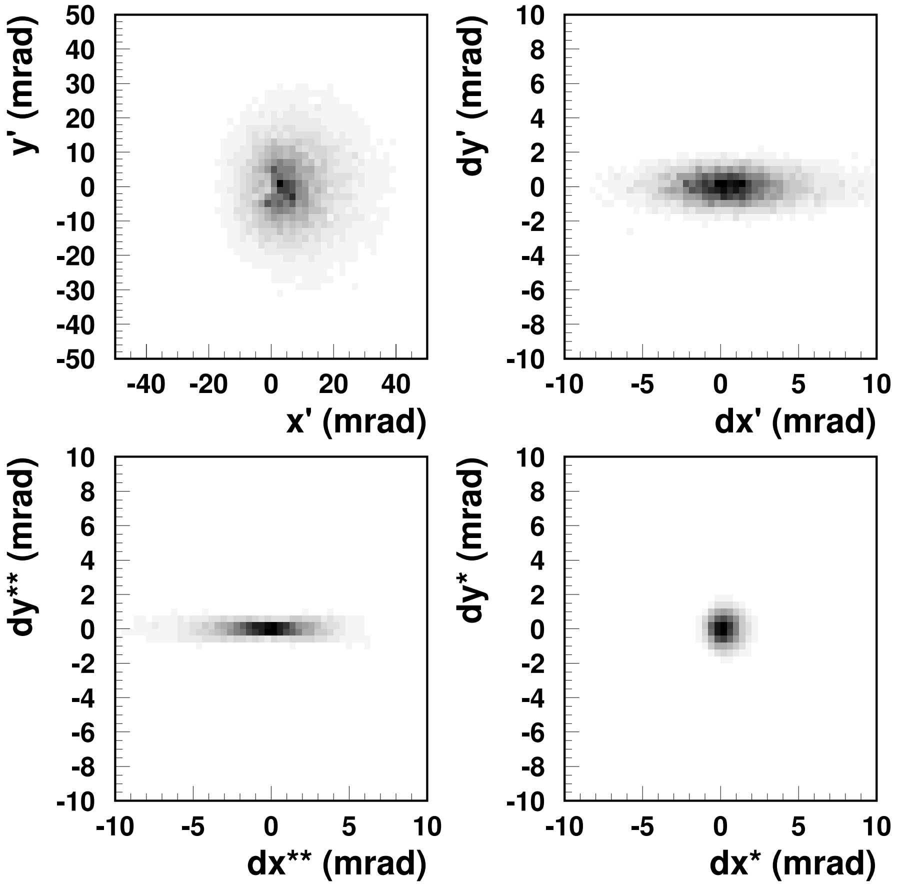

Figure 5.14.: Monte Carlo study of smearing effects. Top left: Event distribution in θ'_y vs. θ'_x. Top right: Resolution in θ'_y vs. resolution in θ'_x. Bottom left: Resolution $d\theta^{**}_y$ vs. $d\theta^{**}_x$ due to the lepton. Bottom right: Resolution $d\theta^{*}_y$ vs. $d\theta^{*}_x$ due to the photon.

Table 5.3.: From the Monte Carlo exclusive BH/DVCS events have been selected and the resolutions are shown. The total resolution is the same as expected from error-propagation.

particle/resolution	polar ($d\theta^*_x$, $d\theta^{**}_x$, $d\theta'_x$)	perpendicular ($d\theta^*_y$, $d\theta^{**}_y$, $d\theta'_y$)
photon	0.75 mrad	0.69 mrad
lepton	3.1 mrad	0.44 mrad
total	3.2 mrad	0.82 mrad

The typical energy of DVCS/BH-leptons inside the cuts is about 13.5 GeV. The typical angle θ_e of the scattered lepton is about 80 mrad and dP/P is about 2%. This results in an uncertainty of $\sim$ 3 mrad, but the distribution can even be expected to be non-Gaussian due to the strong dependence on E'.

Also this effect has been studied in a MC simulation. This time the positive x^{**}-axis is rotated until the generated virtual photon points towards it. The event distribution depending on $d\theta_x^{**}$ and $d\theta_y^{**}$ is again shown in plot 5.14 (bottom, left). The smearing is unidirectional, mainly along the x^{**}-axis, and the obtained values are in good agreement with the expectations (table 5.3).

Finally the combined effect can be shown in a more simple visualisation of the problem: The coordinates ϕ and θ_{γ,γ^*} can be transformed to quasi-Cartesian coordinates by:

$$\theta'_x = \theta_{\gamma,\gamma^*}\cos\phi, \tag{5.21}$$

$$\theta'_y = \theta_{\gamma,\gamma^*}\sin\phi. \tag{5.22}$$

The resolutions $d\theta'_x$ and $d\theta'_y$ have been obtained from Monte Carlo and the result is again shown in figure 5.14 (top, right). To a good approximation it represents a folding of the 2 previous probability distributions, such the the obtained resolutions can be calculated from the previous ones. Obviously the photon resolution dominates along θ'_y, while the lepton resolution dominates strongly along θ'_x. Given the resolution of about 3 mrad in θ'_x, the lower cut for θ_{γ,γ^*} was set to 5 mrad.

This can also be motivated by an additional Monte Carlo study. The exclusive coherent and incoherent BH events inside the exclusive cuts were reweighted by a constant asymmetry according to

$$d\sigma = d\sigma_{BH}(1 \pm 0.5\cos\phi), \tag{5.23}$$

where the sign of the amplitude depends on the beam charge. The asymmetry is extracted using a 5-parameter fit of the kind

$$A(\phi) = c_0 + c_1\cos(\phi) + c_2\cos(2\phi) + c_3\cos(3\phi) + s_1\sin(\phi) \tag{5.24}$$

to describe the asymmetry

$$A(\phi) = \frac{N^+(\phi) - N^-(\phi)}{N^+(\phi) + N^-(\phi)} \tag{5.25}$$

in ten bins in ϕ. The reconstructed asymmetry depending on θ_{γ,γ^*} is shown in figure 5.15. Obviously smearing effects are very large below 5 mrad, which supports this value as lower cut value. But also for very large values of θ_{γ,γ^*} smearing effects never disappear. The situation is different in the case of the BSA which is shown in the same plot.

Apparently the one-directional smearing has a much bigger impact on cosine moments than on sine moments. This is intuitively clear, since in the case of cosine moments, the maximum of the asymmetry can overlap with the minimum of the asymmetry due to the unidirectional smearing along dx'.

Since the first cosine moment can be expected from theory to give the dominant contribution to the beam charge asymmetry, the impact of higher moments to the first moment will be small. In addition the coupling of higher moments and smearing results only in a small first moment. This can be verified by explicitly generating higher moments and extracting the resulting first moment. For example for figure 5.16 a constant asymmetry moment $c_2^{BCA} = 0.5$ has been generated and the extracted cosine coefficients c_0^{BCA} to c_3^{BCA} have been plotted as a

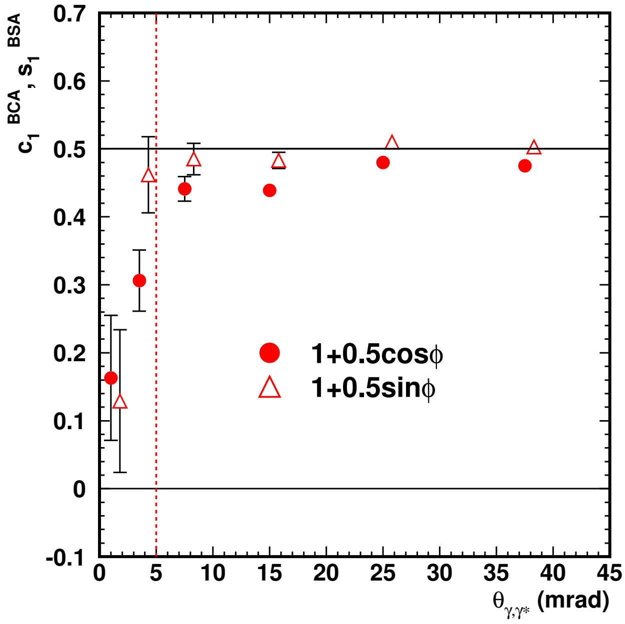

Figure 5.15.: Recovery of generated moments: A constant cosine/sine moment was applied as BCA/BSA to the elastic coherent and incoherent BH-cross-section on the deuteron. The reconstructed asymmetry moment c_1/s_1 is shown as a function of θ_{γ,γ^*}.

function of θ_{γ,γ^*}. As can be seen the resulting moment c_1^{BCA} is below 10% of the generated moment c_2^{BCA}.

Although it may not be obvious in these studies, the introduction of a much larger asymmetry amplitude than in reality has no impact on the relative change of the amplitude. As smearing is a linear operation, the large amplitude only reduces the statistical error of the Monte Carlo, while the ratio of the generated and the reconstructed amplitude is independent of the size of the generated amplitude.

As a conclusion smearing effects will be seen and require a lower cut on θ_{γ,γ^*} of 5 mrad. They will still allow to extract the leading asymmetry moments, but their impact on sub-leading moments is more complicated. Smearing effects will be one important contribution to the systematic error.

5.6. Tracking Efficiencies

In contrast to smearing effects which only mix existing asymmetry moments, tracking efficiencies can have the same effect as trigger efficiencies and lead to false asymmetry moments.

In order to get an estimate on the size of the effect, the flux of DIS leptons can be studied: A closer look at the DIS-lepton-distributions for 1998 and 2000 demonstrates that the shapes in x_B, Q^2, etc. are not identical. Even if high lepton momenta are selected in order to eliminate trigger threshold effects, the disagreement is still found.

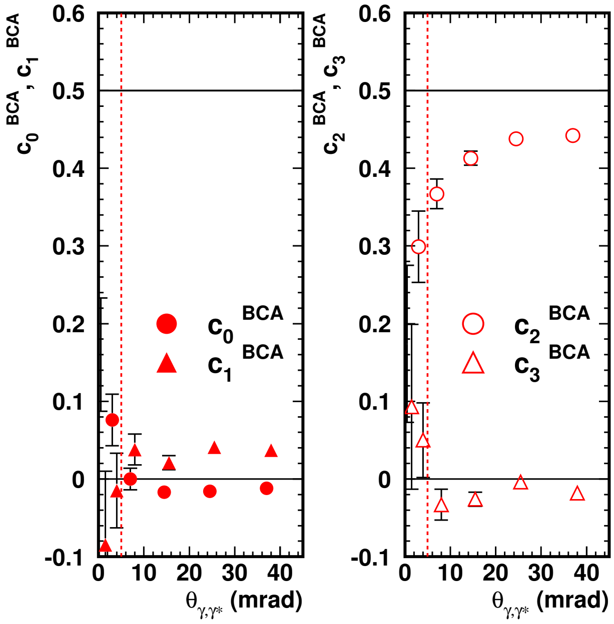

Figure 5.16.: Recovery of generated moments: A constant $\cos(2\phi)$ moment of 0.5 was applied as BCA to the elastic coherent and incoherent BH-cross-section on the deuteron. The reconstructed asymmetry moments are shown as a function of θ_{γ,γ^*}.

The remaining effect can be due to background, mis-alignment or combined tracking/trigger efficiencies. Under the assumption that the tracking/trigger efficiencies are the main contribution they can be extracted by a comparison of lepton fluxes from different years.

For this test, the same cuts were applied on the lepton kinematics as for BH/DVCS-leptons. The ratio of the lepton fluxes from 1998 and 2000 depending on θ_x and θ_y is shown in figure 5.17. It can be seen that the ratio in the bottom half is reduced by about 12% with respect to the top half. This is about twice the expected effect from the different trigger efficiencies of the H0-hodoscope.

The binning of the lepton fluxes in θ_x and θ_y moreover allows for a "flux-normalisation" of the BH/DVCS events. The detection efficiency $\mathcal{E}_{BH/DVCS}$ for a BH/DVCS event is given by the product of the detection efficiencies of the lepton $\mathcal{E}_e$ and the photon $\mathcal{E}_\gamma$, if the event kinematics is kept fixed. The observed number of events $dN^{\pm}_{BH/DVCS}$ for positive (negative) beam charge is then

$$dN^{\pm}_{BH/DVCS} = L\mathcal{E}_e\mathcal{E}_\gamma d\sigma^{\pm}_{BH/DVCS}. \tag{5.26}$$

$\mathcal{E}_\gamma$ will usually be high (≈ 1), since dead blocks in the calorimeter are noticed at once. However, for the beam charge independent lepton flux it is found that

$$dN^{\pm}_{DIS} = L\mathcal{E}_e d\sigma_{DIS}. \tag{5.27}$$

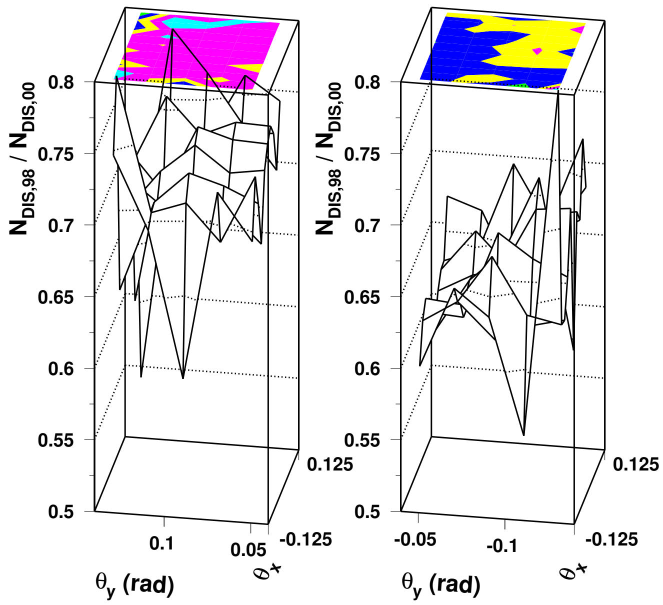

Figure 5.17.: Ratio of the lepton-fluxes for 1998 and 2000 in bins of θ_x and θ_y; left: top spectrometer half, right: bottom spectrometer half.

Hence

$$\frac{d\sigma^{+}_{BH/DVCS}}{d\sigma^{-}_{BH/DVCS}} = \frac{dN^{-}_{DIS}}{dN^{+}_{DIS}} \times \frac{dN^{+}_{BH/DVCS}}{dN^{-}_{BH/DVCS}}. \tag{5.28}$$

In practice the event weight $L\epsilon$ in all extraction formulas (cf. chapter B) is replaced by 1 for the reference year 2000 and by $\frac{dN^{+}_{DIS}}{dN^{-}_{DIS}}$ for the year 1998. The dataset from 1999 with its limited statistics is omitted in this study. Although the efficiency correction is somewhat larger than the pure trigger efficiency correction, the result for the BCA with unpolarised deuterium is found to be the same as with trigger efficiency correction and DIS normalisation. Hence the flux-normalisation will not be considered for the final results.

5.7. Internal Differences of Datasets

Especially in the case of the BCA the consistency of the datasets has to be ensured. The most critical distributions in this case are the missing mass and the t distribution.

In figure 5.18 the missing mass distribution is shown for the unpolarised datasets (top plot) and the polarised datasets (bottom plot). In each plot the electron data from 1998 is compared with the positron data from 1999/2000. No trigger efficiency correction was applied. Since the applied recalibration of the calorimeter for the year 2000 was optimised for this comparison with electron data, good agreement is found. Thus it is clear that the distributions of the elec-

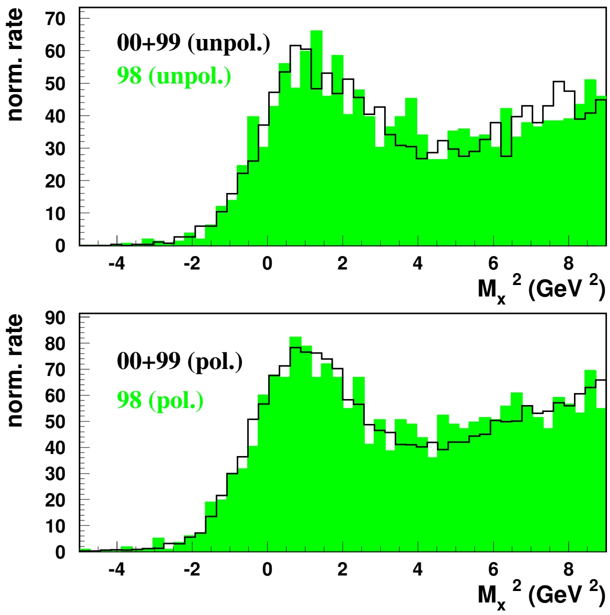

Figure 5.18.: Missing mass distribution (comparison): After recalibration of the calorimeter a nice agreement of the missing mass distributions for an electron and a positron beam is found. Unpolarised data (top) and polarised data (bottom) is shown separately.

tron and positron data agree for unpolarised and polarised target gas independently. However, also the agreement between the unpolarised and the polarised dataset is apparently good.

Figure 5.19 shows the corresponding distributions in t. Again the agreement is good. Notably there is no indication for a sharp peak at low values of t for the year 1998. This would indicate coherent BH/DVCS events on the target spring finger. Many other cross-checks have also been performed and no differences due to apparative effects have been found.

5.8. Systematic Differences of Data / Monte Carlo

It has already been mentioned that particle transport and detector digitisation in the Monte Carlo is not in all respects perfect. While there are no reasons to doubt the performance for particle tracking, it is known that the response of the PID-detectors in the Monte Carlo deviates from reality. Due to this problem, the PID in the MC is not used and instead obtained from the generated particle type. This is a good approximation due to the good PID performance of HERMES .

Some other comments are in order: As has been shown in section 5.3, the reconstructed position in the calorimeter is systematically different and the z-position of the shower-centre is shifted by about 5 cm with respect to reality. Apart from this effect the spatial resolution of the spectrometer is rather well reproduced as can be seen in figure 5.7 and 5.8.

The energy-resolution of the calorimeter in the Monte Carlo is also not perfectly simulated.

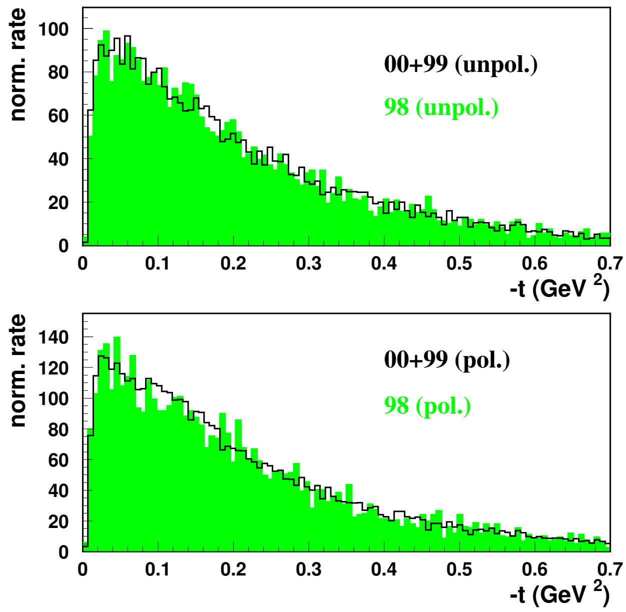

Figure 5.19.: t distribution (comparison): Good agreement of t distributions for an electron and a positron beam is found (constrained t). Unpolarised data (top) and polarised data (bottom) is shown separately.

In order to pin down the problem, first the behaviour for leptons is studied. For these it is possible to compare the cluster energy with the particle momentum from tracking. According to [A$^+$98] the energy resolution for positrons/electrons is given by:

$$\Delta E/E = \frac{0.051}{\sqrt{E}} + 0.02 + \frac{0.1}{E}. \tag{5.29}$$

This resolution has been verified using real lepton tracks from data as shown in figure 5.20. The difference between the experimental curve for the leptons and the parametrisation in equation 5.29 is due to the momentum resolution for the leptons of about 2%. A comparison with a Monte Carlo simulation for leptons exhibits a difference: While at low energies, the resolution is better reproduced, the resolution at high energies differs relatively by more than 20% (same figure). Since the shower centre for photons that have triggered the preshower detector and electrons is at the same z-position, one can also assume that the obtained energy-resolution for photons has the same problem. This is also confirmed in the Monte Carlo (same figure), as the expected energy resolution for leptons and photons is essentially the same.

The disagreement in the calorimeter response between Monte Carlo and data has the consequence that the width of the exclusive peak is usually overestimated by the Monte Carlo as can also be seen by a close inspection of the published comparison [HERMES01a].

However, the disagreement also has another reason, as the mean value of the reconstructed photon cluster energy in the Monte Carlo is systematically higher than the generated energy. This leads to an energy-dependent displacement of the exclusive missing mass peak towards

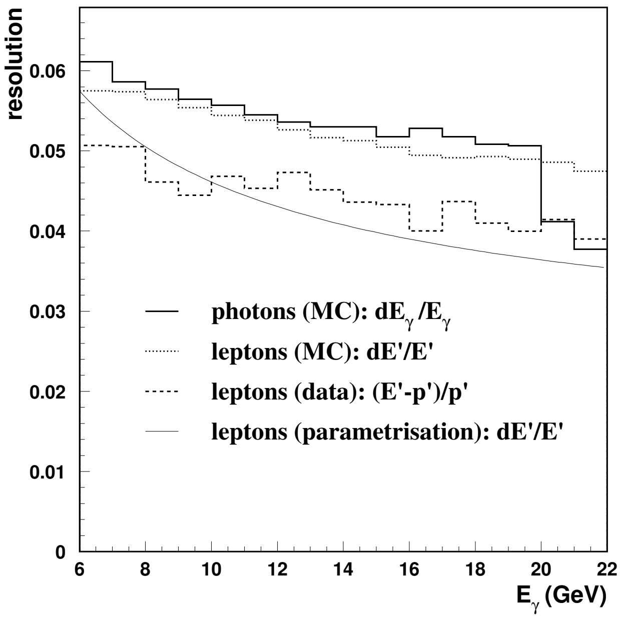

Figure 5.20.: Energy resolution in Monte Carlo: The dashed line is the width of $(E' - p')/p'$ for leptons from real data. The thin solid line is the official parametrisation for dE'/E' . The thick solid line is the photon energy resolution dE_γ/E_γ obtained from the Monte Carlo, the dotted line is the energy resolution dE'/E' for leptons in the Monte Carlo.

negative missing masses. Consequently a linear correction is applied:

$$E_{true}/E_{reconstructed} = 1 + 0.015 - 0.0025 E_{reconstructed}. \tag{5.30}$$

The situation is more complicated, because the Monte Carlo predicts a difference between the energy depositions of a photon or a lepton, especially at high energies. Hence, although the correction provides a correct calibration for photons, the calibration of the leptons is predicted to be wrong; e.g. the recalibrated energy is by two per cent too low at an energy of 20 GeV.

The problem is that also in the data the lepton cluster energy is apparently underestimated at high momenta by approximately the same amount (cf. figure 5.10). Thus the recalibrated Monte Carlo seems to reproduce the data (especially if the data is not recalibrated), although the original difference between the real and the simulated calorimeter is not clear. This indicates the principle problem that neither the momentum dependent calibration of the calorimeter in the experiment nor the calibration in the simulation is reliable and any recalibration can be applied to one dataset or the other.

In order to reduce the photon energy resolution in the Monte Carlo to the nominal value for leptons, it was also attempted to recalculate the cluster energy from the original photon energy using the known resolution of the calorimeter. The correction was only applied to the MC-data produced with *gmc_dvcs* as the semi-inclusive background is anyway normalised to the data. In addition for exclusive events it is usually very easy to identify the cluster that belongs to the high-energy photon; consequently the cluster energy was modified if

$$\theta_{\gamma,reconstructed;\gamma,real} < 30\,\mathrm{mrad}, \tag{5.31}$$
$$0.5 < E_{\gamma,reconstructed}/E_{\gamma,real} < 1.5. \tag{5.32}$$

In this case the reconstructed energy was obtained from the generated photon energy by smearing it with a Gaussian of the known width according to equation 5.29. Correlations of the cluster energy with the signal in the preshower were neglected; in principle a shower that starts very early could give a higher deposition in the preshower but a lower deposition in the calorimeter. It was found that the obtained missing mass resolution is better than observed in reality (even the position dependent recalibration of the calorimeter in the real data does not completely eliminate this discrepancy). An additional constant term of up to 0.01 added in equation 5.29 is needed to explain the data. This may hint at a remaining momentum dependent mis-calibration of the data or other more subtle effects. Hence this recalculation of the cluster energy will not be used in this thesis. However, already the recalibration of the Monte Carlo can solve the biggest discrepancy with respect to the data.

Finally for the preshower it is found that the MC-digitisation seems to reproduce all features. On the other hand a quantitative statement is difficult as the signal distribution in the preshower changes depending on the missing mass. Thus the imperfect calorimeter response prevents the preshower response from being studied in more detail.

6. Deeply Virtual Compton Scattering Deuterium: Extraction Methods

6.1. Choice of the Extraction Method

It has been discussed in section 2.11 that suitable combinations of datasets with different beam charge as well as different beam/target polarisation can be used to extract characteristic asymmetries of the BH/DVCS cross-section. These asymmetries can be related to different combinations of Compton Formfactors.

While it is comparatively easy to confirm or to disprove the existence of an asymmetry within the statistical errors, a clear determination of its size is much more difficult. This has a number of reasons:

Firstly, the asymmetries are not of the simple kind that is usually encountered at HERMES. For example in the case of semi-inclusive asymmetries in pion production the polarisation dependent cross-section factorises approximately like

$$\sigma(x_B, Q^2, t, \phi) = \sigma_{unpol}(x_B, Q^2, t)(1 \pm PA\sin(\phi)), \tag{6.1}$$

where P denotes either the beam or the target polarisation and A is the amplitude of the asymmetry. Instead the beam spin dependence of the cross-section in BH/DVCS approximately factorises like

$$\begin{aligned} \sigma(x_B, Q^2, t, \phi) \quad = \quad & \sigma_{prop}(x_B, Q^2, t, \phi)(c_0^{BH} + c_1^{BH}\cos\phi \pm P_B(s_1^I \sin(\phi) + s_2^I \sin(2\phi))) + \\ & \sigma_{DVCS,unpol}(x_B, Q^2, t, \phi), \end{aligned} \tag{6.2}$$

where the moment s_1^I is the quantity of interest and σ_{prop} is defined in appendix B. This shows that first of all there is an unknown contribution $\sigma_{DVCS,unpol}(x_B, Q^2, t, \phi)$ which is not small at HERMES kinematics and affects at least the normalisation of the extracted asymmetry. Secondly the unpolarised cross-section itself has a prominent ϕ-dependence due to σ_{prop} and c_1^{BH}. And thirdly also the polarisation dependent term has an additional ϕ-dependence that is due to the factor σ_{prop}. The predicted values of the interference term moments $s_{1,up}^I$ and $s_{2,up}^I$ according to the 5 models in the Monte Carlo is shown in figure 6.1 for the average kinematics of the same four bins in t that are later used in the analysis of the deuterium data. The predicted coefficient s_2^I at leading twist is much smaller than s_1^I (note the different scale!). Models 2 and 4 as well as models 3 and 5 give identical results as the only difference is the D-term that does not contribute to the sine-moments. However, the predicted BSA is different for these models (compare figure 4.6) due to $\sigma_{DVCS,unpol}(x_B, Q^2, t, \phi)$ that contributes on the 10%-level to the proton cross-section. This is a consequence of the definition of the BSA according to equation

2.124:

$$A_{LU}(\phi) = \frac{1}{\langle P_B \rangle} \frac{N^+(\phi) - N^-(\phi)}{N^+(\phi) + N^-(\phi)}, \tag{6.3}$$

where $\langle P_B \rangle$ is the average beam polarisation defined as $\langle P_B \rangle = \frac{1}{2}(\langle P_B \rangle^+ - \langle P_B \rangle^-)$ in terms of the average beam polarisations $\langle P_B \rangle^+$ and $\langle P_B \rangle^-$ of the two datasets. The asymmetry moments c_m^{FM} and s_m^{FM} are extracted by a fit of the form

$$A(\phi) = c_0^{FM} + \sum_{m=1}^{M} (c_m^{FM} \cos(m\phi) + s_m^{FM} \sin(m\phi)) \tag{6.4}$$

to the asymmetry in I bins in ϕ. Another important feature is that this definition of the BSA does not allow to extract the correct ratio of first moment to second moment due to the higher BH-moments that contribute in the denominator. The extracted ratio can be wrong by a factor of 10 or more in the case of the BSA. Thus also higher twist effects would not be clearly separated from leading twist effects.

While a different extraction method may be able to preserve the ratio of higher moments to the leading moment, it is very difficult to measure the absolute size of the moments due to the contribution of $\sigma_{DVCS,unpol}(x_B, Q^2, t, \phi)$. The problem of the extraction method will be discussed in great detail in appendix B.

It turns out that the so-called fit-method (FM) as defined above, performs still much better in terms of a separation of leading/higher twist than the so-called moment-method (MM) that has also been used at HERMES for DVCS-analysis. Moreover, while the ϕ-binning effects of the FM can be shown to be under control, the MM is much more sensitive to acceptance effects as will be discussed in appendix C. Until now the only suggested method to compensate for this ("matrix method"), can be shown to give rather undefined results as it is impossible to specify, what the result should be (asymmetry at bin-centre, asymmetry in some kinematical range, etc.).

In contrast to this the very flexible Monte Carlo fitting method (MCF) is in principle able to extract the coefficients s_1^I, s_2^I, etc. of the interference term directly if enough statistics of data with different beam charge and beam polarisation exists. However a very good Monte Carlo simulation of the BH-cross-section and all possible background contributions is required. The procedure is outlined in appendix B. At the moment such a complete extraction is not possible; hence a more simple version of the MCF ("propagator fit") has been tested that gives compatible results to the FM but is expected to preserve the ratio of higher moments to the leading moment better. The MCF is the method that is the least sensitive to smearing effects as the Monte Carlo simulation includes these effects. Due to the better transparency of the FM and also because of the consistency with previous releases, the HERMES DVCS group has decided not to use the MCF at the moment. Hence the FM will also be used in this thesis for the extraction of the asymmetries.

Another principle problem that is connected to the assumed factorisation of the cross-section is the rather low statistics of the present data which forces large kinematical bins. It will be shown in appendix B that practically all methods suffer from the dependence of the asymmetry on x_B, Q^2 and t, such that the leading asymmetry moment at the average kinematics of a bin can in extreme cases be different by 20% or more (BCA) from the leading asymmetry moment

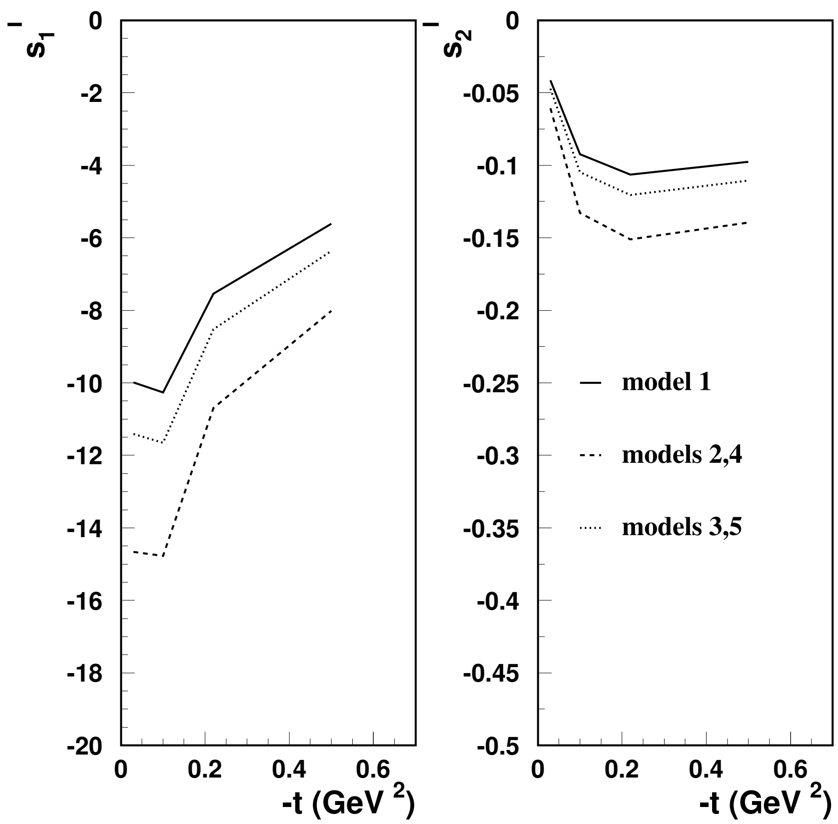

Figure 6.1.: Moments $s^I_{1,up}$ and $s^I_{2,up}$ according to equation 2.115 derived from models 1 . . . 5 for a proton target.

integrated over the observed statistics in this bin. Moreover the effect is acceptance dependent. It is impossible to apply an acceptance correction or bin-centring correction, as the HERMES acceptance has one important effect: It removes the singularities of the BH-cross-section from the observed data-sample. It would be meaningless to extrapolate the HERMES-results to some larger region in x_B, Q^2 and t as this would almost certainly include the singularities. Moreover such an extrapolation is impossible, as the information in the observed region does not fix the GPDs and thus the asymmetry outside of this interval is unknown. This indicates that with the present statistics is is not possible to quote the value of an asymmetry at one kinematical point without this acceptance related error of 10% (BSA) or 20% (BCA) for the leading moment. While the sub-leading moment of the BSA, seems to be well reproduced for the BSA it can be overestimated by a factor of 2 for in the BCA.

Apart from the mentioned problems that are also expected for a hydrogen target, in the case of deuterium two additional problems enter: The dataset is a mixture of coherent BH/DVCS, incoherent BH/DVCS and BH/DVCS with resonance excitation. Thus even if only one process results in a non-zero asymmetry, this asymmetry would be strongly diluted and the dilution factor could only be taken from some Monte Carlo model. This shows that the asymmetries on the deuteron are only well interpretable in terms of the GPDs if the final states of the target can be discriminated. As an additional complication nuclear binding effects can disturb the incoherent process at low momentum transfers t. In this case a very good understanding of the binding effects is necessary, which does not exist at the moment.

Hence an extraction of GPDs from the present deuterium dataset seems to be impossible. Even in the case of hydrogen sufficient statistics in combination with a complicated extraction method (e.g. MCF) will be needed to obtain a precision measurement with a good separation of higher and leading twist.

6.2. Statistical Aspects, Binning and Consistency Check

It has been mentioned before that the binning in ϕ that is required for the fit-method has some impact on the extracted results. This problem is independent of smearing or acceptance effects and is only due to the way in which the one-dimensional distribution in ϕ is analysed.

Even with almost infinite statistics, binning leads to problems: The number of events N inside the bin corresponds to the integral over $dN/d\phi$, however, it is compared with a cross-section model for $dN/d\phi$ at the bin-centre (times the bin-size). The difference depends on the exact shape of $dN/d\phi$ and it is difficult to make general statements if the distribution is unknown. Problems will especially occur if the typical scale for fluctuations is much smaller than the bin-width.

In the case of DVCS the situation is less critical, as the lowest asymmetry moments are dominant and also the cross-section $d\sigma/d\phi$ itself multiplied by the box-like HERMES acceptance $\mathcal{A}$ is not expected to exhibit strong higher moments. In order to estimate the size of binning effects, a reasonable approximation is that the asymmetry consists of the leading Fourier moments only. In addition the statistical error in all bins is assumed to be the same, which is a reasonable approximation as long as the asymmetry $A(\phi)$ in each bin is not too large. This is due to the fact that the error bar is expected to behave like $dA = const. \times \sqrt{1 - A^2}$.

Since error bars of fixed size are used, the ratio of the extracted asymmetry moment and the generated asymmetry moment does not depend on the amplitude of the generated moment. Hence in order to obtain the fractional deviation it is possible to choose an amplitude of $A = 1$ instead of dividing by the original amplitude later.

The function $dN/d\phi$ is then integrated inside each bin in ϕ and a least square fit can be applied to it. In the fit the generated harmonic as well as a constant term were included. The ratio of the reconstructed asymmetry moment to the generated asymmetry moment for only one generated moment (s_1 or s_3) is shown in figure 6.2. A spike in the extracted asymmetry is seen if s_3 is extracted with only 3 bins; this should certainly no be attempted in reality. Apart from that a very fast convergence is seen. The relative error in the amplitude with 10 bins is 1.6% (of the amplitude) for s_1 and s_3. The same error is also obtained for a moment s_{15} and 10 bins but it is clear that this will not work if any other harmonics have a non-zero-value.

Another question is, how much a leading moment will change in the presence of a higher sub-leading moment that is not included in the fit, or in the case where it is included in the fit. This is shown in figure 6.3. A moment with an amplitude of $s_3 = 0.5$ is added in both cases. Expect for the fourth bin there is no difference between the two plots. Hence for a realistic number of bins the first moment is apparently not sensitive to the presence of a higher

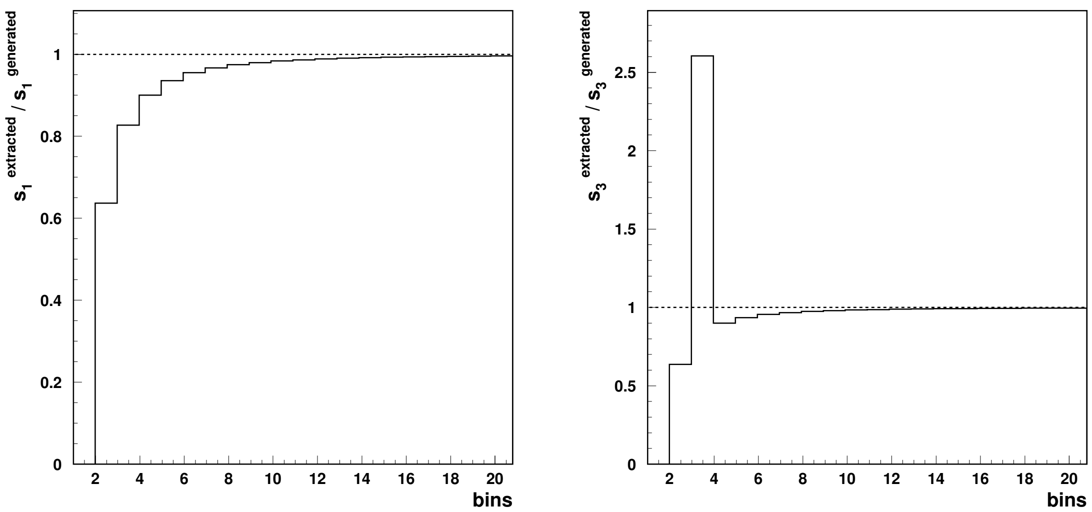

Figure 6.2.: Ratio of the extracted to the generated amplitude s_1 of a true first (left) sine-moment and ratio of the extracted to the generated amplitude s_3 of a true third (right) sine-moment. Apart from the original moment the fit contained only the constant term.

moment. The obtained error is again 1.6% for s_1 and s_3.

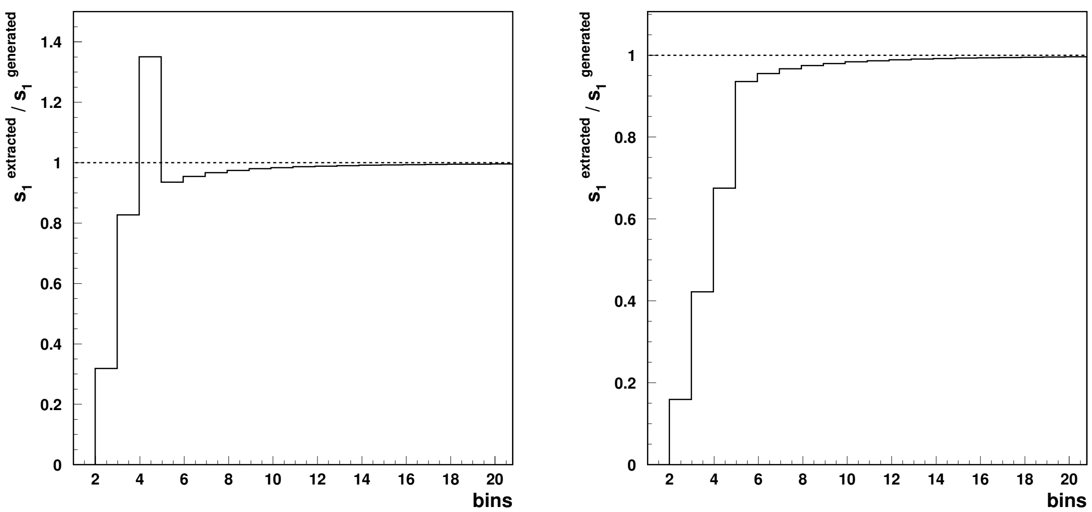

Figure 6.3.: Ratio of the extracted to the generated amplitude of the first sine-moment, if the additionally generated third sine-moment is included in the fit (left) or not (right).

In the next step, a one-dimensional Monte Carlo generator was used. 1000 events of each charge were generated; this is a representative number for the DVCS-analysis without kinematical binning. Asymmetry moments were introduced by the hit-and-miss method. It was made sure that the probability for accepting events was small (in the order of 1%) such that the limit of a Poisson-distribution was reached.

As a first step a sine-moment was generated and extracted again by a fit. Since in this case the error bars scale with the asymmetry, a realistic value of the asymmetry of $s_1 = 0.1$ was chosen. This was repeated 100 times and the mean value as well as the standard deviation were calculated. In figure 6.4 the standard deviation is compared with the mean value of the estimated error (left) and the mean value of the extracted s_1 is compared with the generated value (right). Apparently also in this case a quick convergence towards the original value of 0.1 is found. Due to statistical fluctuations, the obtained Gaussian error on the asymmetry is 0.1 standard-deviations. Hence the statistical error of the mean value is 0.003 and the dependence on the binning cannot be seen in comparison to the generated asymmetry. Instead, as the same dataset is used for all different binnings, the comparison of the 20-bin fit and the 10-bin fit can be used and yields an apparent reduction of the amplitude by about 2%. The obtained behaviour is similar to the analytical model shown before. The error estimate and the true standard deviation in figure 6.4 agree. The systematic difference between the generated and reconstructed asymmetry that is due to binning effects is not reflected in this quantity.

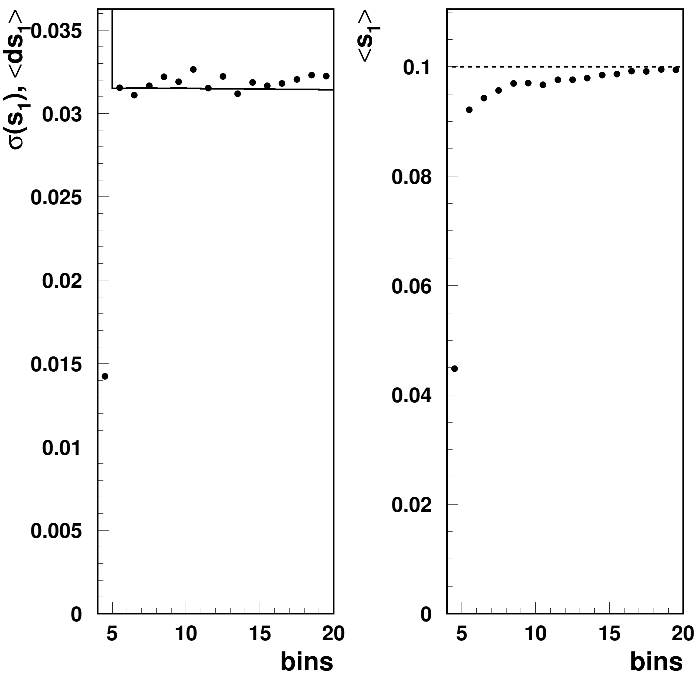

Figure 6.4.: Left: Error estimate (histogram) in comparison with the true standard deviation (dots) depending on the number of bins. Right: Extracted mean value (dots) and generated value of 0.1 (dashed line).

The same procedure can be repeated under the condition that the same expectation value for the number of generated events instead of the same number of generated events is used for

Events per subsample	fixed No. of events	expectation value
1000	$0.097 \pm 0.033(0.031)$	$0.097 \pm 0.033(0.031)$
500	$0.100 \pm 0.043(0.044)$	$0.099 \pm 0.045(0.044)$
100	$0.117 \pm 0.101(0.099)$	$0.117 \pm 0.100(0.098)$
50	$0.104 \pm 0.160(0.137)$	$0.100 \pm 0.170(0.135)$

Table 6.1.: Results of a fit in 10 bins in ϕ for different subsets (rows) and different event-numbers (columns). A cross-section of $\sigma = \sigma_0(1 \pm 0.1 \sin\phi)$ was generated. The entries show the mean-value of the extracted coefficient s_1 together with its standard-deviation. The average error estimate is shown in brackets. The fit function contained the coefficients c_0, s_1, s_2 and s_3.

the 100 subsets. However the result is unchanged. This calculation was repeated for 500, 100 and 50 events of each charge. The obtained values for 10 bins are listed in table 6.1. The error bars are partly correlated as the same set of generated events is used and only later split into subsamples of the required size.

Apparently there is not much difference between the results for a fixed number of events and the result with statistical fluctuations of the number of events. With decreasing event number both methods still give the same result and also the mean value is correct. However, the estimated error can be smaller than the true standard deviation as soon as the average value of events per bin is close to 5 (i.e. 50 events per dataset).

This means that the obtained error for low statistics may slightly underestimate the true error bar. In addition a systematic offset between the generated and the obtained value is possible that is again not reflected in the standard deviation of the subsamples.

In order to check this under realistic conditions, the following procedure was used:

- The distributions $A(\phi) = \frac{N^+(\phi) - N^-(\phi)}{N^+(\phi) + N^-(\phi)}$ and $S(\phi) = N^+(\phi) + N^-(\phi)$ were calculated for the asymmetry in ten bins in ϕ. Trigger efficiency corrections were neglected, as they are known to be small and they would disturb the following procedure.
- A 7-parameter fit of the form

$$f(\phi) = c_0 + c_1 \cos(\phi) + c_2 \cos(2\phi) + c_3 \cos(3\phi) + s_1 \sin(\phi) + s_2 \sin(2\phi) + s_3 \sin(3\phi) \quad (6.5)$$

  was applied to A as well as to S.
- Using the fitted functions for A and S, events were generated by the hit-and-miss method with a cross-section:

$$\sigma = S(\phi)(1 \pm A(\phi)) \quad (6.6)$$

- 100 subsets of events were considered, as only additional systematic errors of more than 10% of the statistical error were considered as being serious. The same fit function that is later used in the analysis is applied for the subsets and the mean value of an extracted parameter as well as its standard deviation is obtained.

A difference between the extracted mean-value and the generated mean value would be proven, if the result was statistically significant with the taken approach. The same would be true for a too large error bar.

t in GeV^2	$N(+)$	$N(-)$	originally measured s_1	reobtained s_1
$0.00 < -t < 0.06$	187	467	-0.401 ± 0.115	$-0.411 \pm 0.114(0.115)$
$0.06 < -t < 0.14$	145	393	-0.082 ± 0.128	$-0.086 \pm 0.115(0.131)$
$0.14 < -t < 0.30$	92	277	-0.064 ± 0.156	$-0.037 \pm 0.194(0.154)$
$0.30 < -t < 0.70$	45	122	-0.403 ± 0.217	$-0.448 \pm 0.263(0.218)$
all	469	1259	-0.229 ± 0.071	$-0.225 \pm 0.073(0.072)$

Table 6.2.: The table shows the originally measured asymmetry moment s_1 of the A_{LU} in 4 bins in t. It is compared with the reobtained moment s_1 after a statistical simulation with 100 subsamples. The given value is the mean value and the standard deviation for the 100 subsamples. The value in brackets gives the average error estimate.

The results of this check for the BSA on unpolarised deuterium in four bins in t are shown in table 6.2. In contrast to the fourth bin, the reobtained error in the third bin is actually overestimated; both datapoints were checked with a larger number of sub-samples and the systematic error of the error estimate was found to increase from about 10% in the third bin to about 25% in the last bin. Hence the results get increasingly unstable towards larger values of $|t|$. Moreover the intermediate 7 parameter fit gives a rather different result, e.g. -0.317 ± 0.236 instead of -0.403 ± 0.217 in the fourth bin.

Based on this knowledge the last two bins will be combined in the analysis if the number of events of either dataset falls below 100. This occurs only for the asymmetries A_{LU} and A_{Lzz}. However, apart from that it was not found to be necessary to assign an additional contribution to the systematic error .

6.3. Stability of Results

In order to study the stability of the obtained results a number of systematic checks were done. In contrast to chapter 5 the impact on the extracted asymmetry is directly studied.

First the number of fit parameters was determined that should be used in the extraction of the asymmetry. From the results of the previous section it can be expected that the different Fourier moments have only a small interaction with each other. This was confirmed by using two different fit-functions for the BCA. The five parameter fit was defined by

$$A(\phi) = c_0 + c_1 \cos(\phi) + c_2 \cos(2\phi) + c_3 \cos(3\phi) + s_1 \sin(\phi), \tag{6.7}$$

where c_1 is expected to be the leading contribution. c_0 can originate from the constant term of the asymmetry, but is also sensitive to bin-centring, smearing or calibration effects. The same is true for the higher twist moments c_2 and c_3. Due to the results of section B all these sub-leading coefficients can be extracted but will be hard to interpret. The moment s_1 is introduced to absorb the effects of a remaining BSA, since the datasets do not have a vanishing beam polarisation. Alternatively the 3 parameter fit of the form

$$A(\phi) = c_0 + c_1 \cos(\phi) + s_1 \sin(\phi) \tag{6.8}$$

was applied. The results of the different fits are shown in figure 6.5. The coefficients c_1 and c_0 are similar for the two fit functions and seem to be different from zero; however even for the highest $|t|$-bins the statistical significance of this deviation is less than 2σ. Inside the error bars the higher coefficients (c_2, c_3) seem to be compatible with zero. Apparently the additional coefficients of the five parameter fit have no impact on the other coefficients. Moreover the quality of the fits gets worse as the number of degrees of freedom increases, while χ^2 is not improved. Consequently it was decided to use the 3 parameter fit for the final results. In the case of the BSA and the TSA the 3 parameter fit

$$A(\phi) = c_0 + s_1 \sin(\phi) + s_2 \sin(2\phi) \tag{6.9}$$

will be used. In this case the parameter c_0 is kept, as it must be zero due to the invariance under parity. A non-zero value will immediately indicate an experimental problem. The coefficient s_2 was found to improve χ^2/ndf in some bins. This is not surprising, since especially for the BSA the large first moment can also induce an observed second moment.

Another point of concern was the impact of the trigger efficiency correction on the extracted BCA. In principle there is no reason to expect that the obtained effect vanishes: The hit position of the lepton track on the H0-hodoscope is correlated with the region in ϕ that gets populated by exclusive single photon events. Hence a reduced trigger efficiency by about 10% in 1998 can also change the asymmetry in single ϕ-bins by this amount. In reality the statistical error is by far too big to be sensitive to such effects. As long as the trigger efficiency correction (or more precisely the H0-correction) is consistently applied to the exclusive single photon events and the DIS events that are used for normalisation, no impact of the correction is seen. This is shown in figure 6.6 for the BCA on unpolarised deuterium. Consequently it was decided to keep the correction but to add no separate contribution to the systematic error that would be due to the expected accuracy of the trigger efficiency correction. Only for the tensor asymmetries that are based on the tensor polarised data from the end of the 2000 running period the trigger-efficiency correction is omitted, because the dataset is too small to determine it accurately.

Finally, in order to verify the reproducibility of the results a thorough cross-check of three independent analysis codes was made. As can be seen in figure 6.7 the results agree exactly.

6.4. Treatment of Target Polarisation: TSA

In the following discussions Λ will denote the magnetic quantum number of a target hadron with respect to the quantisation axis that is defined by the angles ϕ_s and θ_s shown in figure 2.13. The quantity P on the other hand will denote the (vector) polarisation of the target hadron in the HERMES reference system. Similarly λ will be used to for the constant polarisation of an ideal lepton beam, while $\langle P_B \rangle$ is the time averaged measured polarisation of the HERA lepton beam.

In the case of the Target-Spin-Asymmetry target dilution and depolarisation effects have to be taken into account. Target dilution is due to the presence of the $\Lambda = 0$ state and can be obtained from the moment decomposition 2.117 under the assumption that $\theta_s = 0$. The moments are then:

$$c_n = \frac{3}{2}\Lambda^2 c_{n,up} + \Lambda c_{n,LP} + (1 - \frac{3}{2}\Lambda^2) c_{n,LLP} \tag{6.10}$$

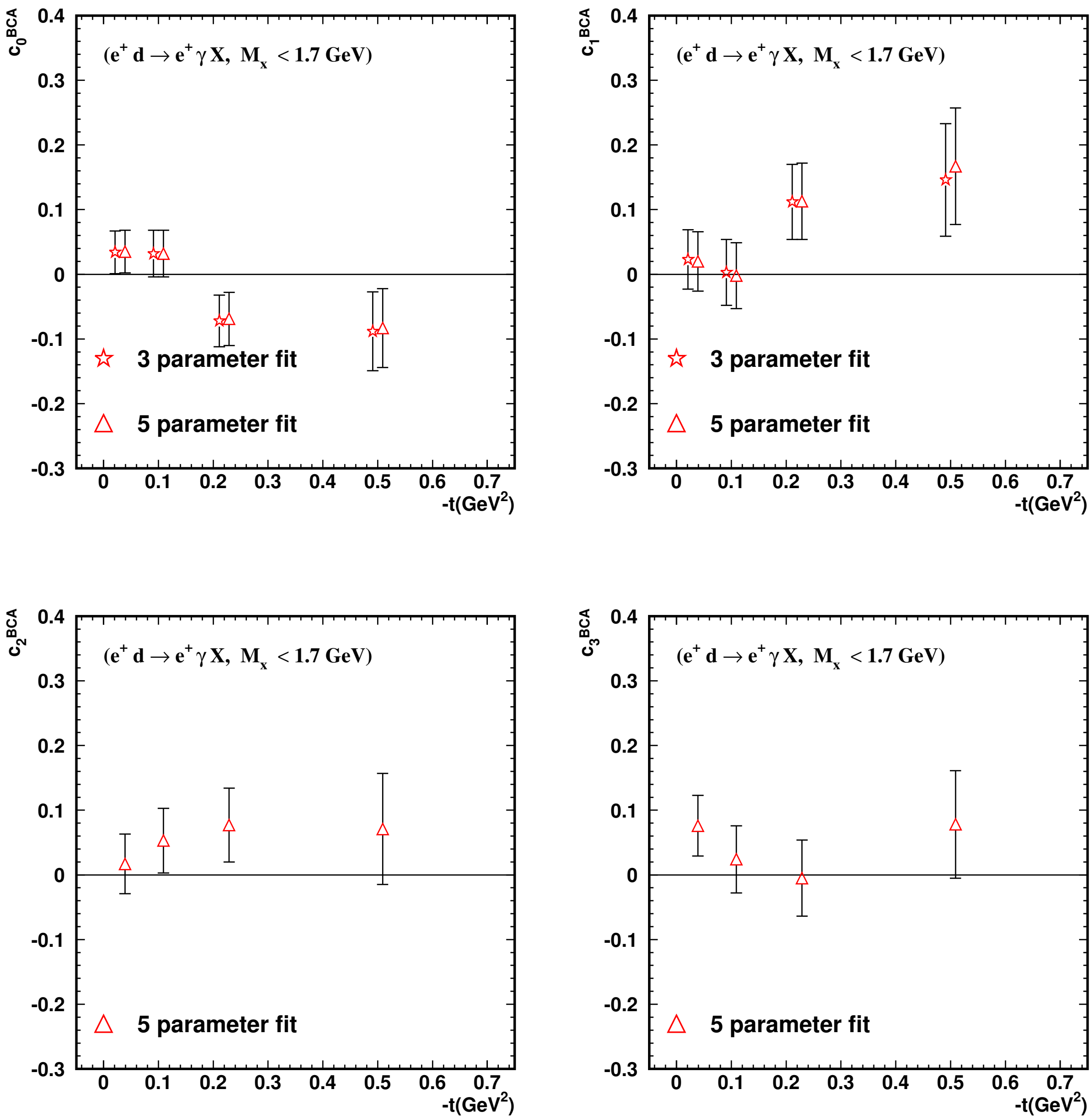

Figure 6.5.: Impact of the number of fit parameters on the leading coefficients c_0 (top left) and c_1 (top right). The coefficients c_2 (bottom left) and c_3 (bottom right) are only determined in the 5 parameter fit.

For 2 ideal states with $\Lambda = +1$ and $\Lambda = -1$ this results in

$$c_n^+ = \frac{3}{2}c_{n,up} + c_{n,LP} - \frac{1}{2}c_{n,LLP}, \tag{6.11}$$

$$c_n^- = \frac{3}{2}c_{n,up} - c_{n,LP} - \frac{1}{2}c_{n,LLP}. \tag{6.12}$$

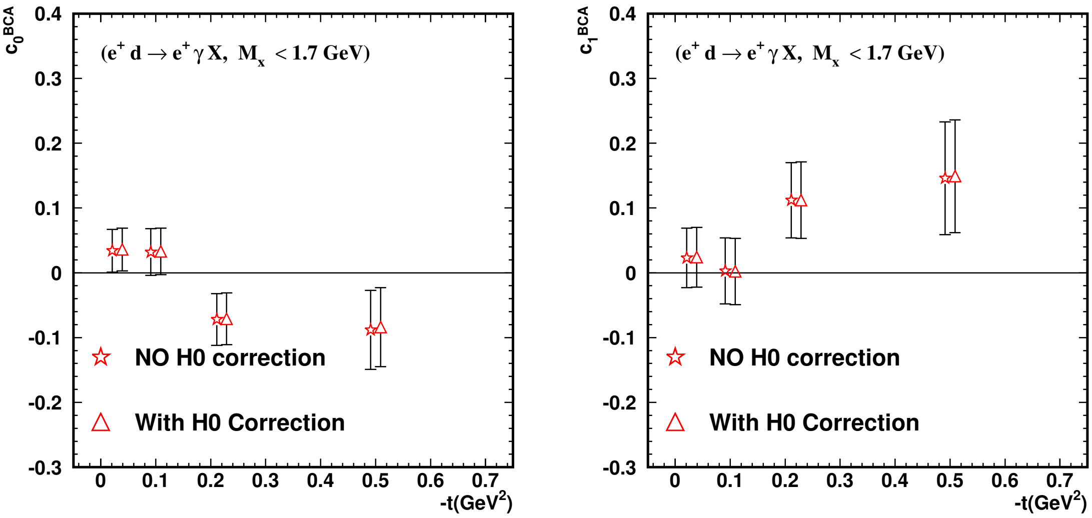

Figure 6.6.: Impact of the H0-correction on the extracted coefficients c_0 (left) and c_1 (right) of the beam charge asymmetry on unpolarised deuterium.

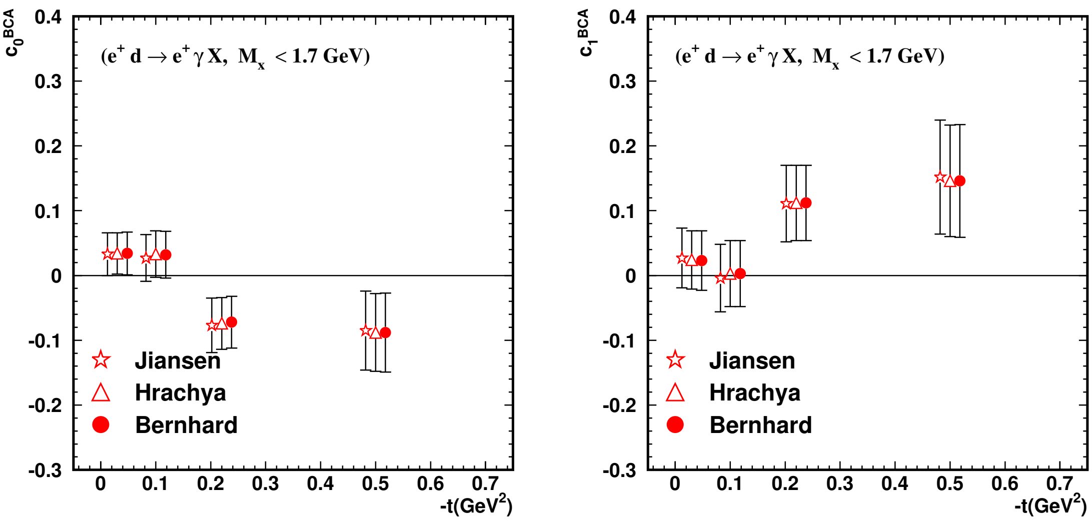

Figure 6.7.: Comparison of three independent analysis codes. The results for the coefficients c_0 (left) and c_1 (right) of the beam charge asymmetry on unpolarised deuterium are compared.

In the approximation that only the leading terms are needed, the asymmetry becomes

$$A_{UL} \approx -\frac{x_A}{y} \frac{s^I_{1,LP}}{\frac{3}{2}c^{BH}_{0,up} - \frac{1}{2}c^{BH}_{0,LLP}} \sin\phi \tag{6.13}$$

for a positron beam. In reality mixed polarisation states are used. In terms of the vector polarisation P and the tensor polarisation T, the relative fractions of the target states are:

$$n^+ = \frac{1}{6}(2 + T + 3P), \quad (6.14)$$

$$n^- = \frac{1}{6}(2 + T - 3P), \quad (6.15)$$

$$n^0 = \frac{1}{3}(1 - T). \quad (6.16)$$

(6.17)

If one assumes that the real (+)-state has the polarisation (P, T) and the real (-)-state has the polarisation $(-P, T)$, the expected moments are

$$c^+_{n,real} = (1 + \frac{1}{2}T)c_{n,up} + Pc_{n,LP} - \frac{1}{2}Tc_{n,LLP}, \quad (6.18)$$

$$c^-_{n,real} = (1 + \frac{1}{2}T)c_{n,up} - Pc_{n,LP} - \frac{1}{2}Tc_{n,LLP}. \quad (6.19)$$

After dividing by the average vector polarisation defined as $\langle P\rangle = \frac{1}{2}(P^+ - P^-)$ in terms of the polarisations P^+ and P^- of the two datasets the result is

$$A_{UL,real}(\phi) = \frac{1}{P}\frac{N^+(\phi) - N^-(\phi)}{N^+(\phi) + N^-(\phi)} \approx -\frac{x_A}{y}\frac{s^I_{1,LP}}{(1 + \frac{1}{2}T)c^{BH}_{0,up} - \frac{1}{2}Tc^{BH}_{0,LLP}}\sin\phi. \quad (6.20)$$

In contrast to the ideal result the tensor polarisation T has an impact on the normalisation. For the dataset from 2000 it was measured as $T_+ = 0.800 \pm 0.025$ and $T_- = 0.853 \pm 0.027$ [The02] for the two vector-polarised states. For 1999 no recent analysis exists, but since the dataset is much smaller than the one from 2000 and no dramatic changes were seen in the vector-polarisation, it is assumed that the same tensor polarisation can also be used for 1999. A tensor polarisation of $T = \frac{1}{2}(T_+ + T_-) = 0.827$ with error $dT = \sqrt{(\frac{1}{2}(T_+ - T_-))^2 + (\frac{1}{2}(dT_+ + dT_-))^2} = 0.037$ will be used in the following analysis.

The effect of the tensor polarisation on the obtained asymmetry $A_{UL,real}$ can be estimated from the known value of the constant BH term in the tensor asymmetry A_{zz}:

$$A^{BH}_{zz} = \frac{-4\tau G_3(G_1 - \tau G_3)}{2G_1^2 + (G_1 - 2\tau G_3)^2} = \frac{c^{BH}_{0,up} - c^{BH}_{0,LLP}}{c^{BH}_{0,up}}, \quad (6.21)$$

which is known to be less then 0.1 for the typical values of t that are observable at HERMES (cf. figure 2.17). As $0.9c^{BH}_{0,up} < c^{BH}_{0,LLP} < c^{BH}_{0,up}$, one can show that even a tensor polarisation of 0.9 leads only to an uncertainty in the normalisation of less than 0.5%. Hence it will be neglected in the assignment of systematic errors.

For the incoherent process the complication of the tensor polarisation drops out: Here the TSA is expected to be that of a free nucleon, at least in the limit of large momentum transfers t: In the approximation of a weakly bound system it can be assumed that only the initial polarisation of the hit nucleon influences the cross-section. While the tensor state is unpolarised in terms of the nucleon polarisations, both nucleon spins have to be aligned in order to give the vector polarised states. This implies that the nucleon polarisation of each nucleon is given by

$$P = \frac{n^+ - n^-}{n^+ + n^0 + n^-} \quad (6.22)$$

Table 6.3.: The effective target polarisation for the combined dataset of 1999 and 2000 is obtained from the single values by linear weighting. The weight is obtained from the luminosity measured by the luminosity monitor. The errors were propagated linearly to account for possible correlations.

year	$\langle P \rangle$	relative fraction
1999	0.832 ± 0.058	0.157
2000	0.846 ± 0.030	0.843
all	0.844 ± 0.034	

with the above defined probabilities for the occupation of the 3 deuterium states. In this case the result is

$$A_{UL,real}(\phi) \approx -\frac{x_A}{y}\frac{s^I_{1,LP}}{c^{BH}_{0,up}}\sin\phi. \tag{6.23}$$

It has to be noted that in both cases - coherent and incoherent scattering - the observed TSA will be proportional to the average vector polarisation $\langle P \rangle$ of the deuterium, such that

$$A_{UL}(\phi) = \frac{1}{\langle P \rangle}\frac{N^+(\phi) - N^-(\phi)}{N^+(\phi) + N^-(\phi)} \tag{6.24}$$

gives in both cases the correct results. The spectator picture suggests that the same is true in the case of resonance excitation.

On the whole this justifies that the same formula for the TSA is used for different physics-processes. However, it is much less clear, how to interpret the TSA of such a mixed dataset. The average target polarisation P that enters into this formula is obtained from the known target polarisations of 1999/2000 using linear weighting. The results are given in table 6.3. As the error is dominated by the error of the polarisation measurements and not by the differences between years or datasets, a more refined treatment seems to be unnecessary.

6.5. Double Spin Asymmetry and TSA

In practice equation 6.24 is not directly applicable for the situation at HERMES , as a vanishing beam polarisation is required for both target polarisations separately. If the beam polarisation for the two target polarisations was different from zero and had two different values P_B^+ and P_B^-, a remaining beam spin asymmetry could contaminate the TSA. Fortunately this is not possible at HERMES due to the frequent flipping of the target polarisation. Hence only the case is relevant where $P_B^+ = P_B^- \neq 0$. In this case double-spin asymmetry moments will enter that depend linearly on $\lambda \times \Lambda$. As these are only cosine moments, the impact on the measured sine-moments can be expected to be small. However, it is the cleaner procedure to balance the beam polarisation of the datasets to $\langle P_B \rangle = P_B^+ = P_B^- = 0$, where $\langle P_B \rangle$ is averaged over both target states. The balancing can be achieved by weighting of the datasets and consequently the following extraction will be used for the TSA:

$$A_{UL}(\phi) = \frac{1}{\langle P \rangle}\frac{(a_1 N^{+\Rightarrow} + a_2 N^{+\Leftarrow}) - (a_3 N^{-\Rightarrow} + a_4 N^{-\Leftarrow})}{(a_1 N^{+\Rightarrow} + a_2 N^{+\Leftarrow}) + (a_3 N^{-\Rightarrow} + a_4 N^{-\Leftarrow})}, \tag{6.25}$$

Table 6.4.: The fit-results for the TSA are compared for a three-parameter fit and different methods for beam polarisation balancing.

method	c_0	s_1	s_2
equation 6.25	0.030 ± 0.015	-0.027 ± 0.022	-0.024 ± 0.022
only L-weighted	0.030 ± 0.016	-0.027 ± 0.022	-0.024 ± 0.022
run-cuts	0.038 ± 0.016	-0.024 ± 0.023	-0.027 ± 0.023

where the normalisation constants are chosen to be

$$a_1 = \frac{1}{L^{+\Rightarrow}} \frac{-P_B^{\Leftarrow}}{P_B^{\Rightarrow} - P_B^{\Leftarrow}}, \tag{6.26}$$

$$a_2 = \frac{1}{L^{+\Leftarrow}} \frac{+P_B^{\Rightarrow}}{P_B^{\Rightarrow} - P_B^{\Leftarrow}}, \tag{6.27}$$

$$a_3 = \frac{1}{L^{-\Rightarrow}} \frac{-P_B^{\Leftarrow}}{P_B^{\Rightarrow} - P_B^{\Leftarrow}}, \tag{6.28}$$

$$a_4 = \frac{1}{L^{-\Leftarrow}} \frac{+P_B^{\Rightarrow}}{P_B^{\Rightarrow} - P_B^{\Leftarrow}}. \tag{6.29}$$

The $+(-)$-sign denotes the target polarisation being antiparallel (parallel) to the lepton beam momentum, which coincides with the conventional theoretical definition (e.g. in [KM03]) but is opposite to the definition in the HERMES coordinate system [Bec03]. The luminosities of each dataset are denoted as $L^{+/-\Rightarrow/\Leftarrow}$ where the signs denote the target polarisation state and the arrows denote the beam polarisation state. This approach has to be compared with two alternative methods: In reference [L$^+$02] the weights a_i only contain the different luminosities, but not the beam-polarisation. As the average beam polarisations are $P_B^{\Rightarrow} = 0.527$ and $P_B^{\Leftarrow} = -0.541$, this approximation is very good. In addition the polarisation balancing to a value of $|P_B^{\Rightarrow}| = |P_B^{\Leftarrow}| = 0.541$ can be achieved by cutting away a number of runs. The result for the coefficients c_0, s_1 and s_2 using the three-parameter fit are shown in table 6.4. While the value for c_0 is for all methods positive and about two σ away from zero, s_1 and s_2 are in all three cases negative and about one sigma away from zero. Apparently this result is very insensitive to the chosen method and no systematic error will be assigned due to the balancing of the beam polarisation. The coefficient c_0 seems to be too large as it is expected to be zero from theory. Therefore it has e.g. been checked that also DIS-normalisation - which is less safe in terms of double-spin asymmetries - gives a result of $c_0 = 0.038 \pm 0.016$ using the run-cuts. This is compatible with the corresponding result in table 6.4 and indicates that the value of c_0 does not originate from problems with the luminosity measurement.

The reason for this insensitivity to the balancing of P_B is that the double spin asymmetry is very small. It is possible to study the double spin asymmetry directly by calculating the TSA for datasets with large beam polarisation. In this case only weighting by luminosity is required. For the case of a nucleon the asymmetry can then be interpreted as

$$A_{UL}(\phi) \approx \frac{\lambda(c_{0,LP}^{BH} \mp \frac{x_B}{y} c_{0,I}^{BH}) \mp \frac{x_B}{y} s_{1,LP}^{I} \sin(\phi)}{c_0^{BH}}, \tag{6.30}$$

Table 6.5.: The fit-results for the TSA are obtained from 3 different dataset with the indicated beam polarisation. In addition the results of a pure BH-simulation are shown. Only statistical errors are shown.

dataset	description	P_B	$\langle P \rangle$	c_0'	c_1'
1	98,e^-	-0.512	0.832	0.122 ± 0.072	-0.224 ± 0.102
2	99/00,e^+	-0.541	0.842	-0.070 ± 0.046	0.128 ± 0.065
3	99/00,e^+	0.527	0.843	0.042 ± 0.035	0.040 ± 0.050
4	MC,e^+	1	1	0.060 ± 0.019	0.037 ± 0.027

in analogy to equation 2.136 without beam polarisation. The three-parameter fit is used to extract the parameters c_0, c_1 and s_1 from data. The coefficient of the constant term that is extracted in the fit is divided by the measured signed beam polarisation P_B in order to obtain approximately:

$$c_0' = \frac{c_{0,LP}^{BH} \mp \frac{x_B}{y} c_{0,LP}^{I}}{c_{0,up}^{BH}}, \tag{6.31}$$

where $\pm$ denotes the beam charge. The same is done for the first cosine moment to determine c_1'. Predictions for the elastic coherent and incoherent BH asymmetry moments c_0' and c_1' can be obtained from Monte Carlo (*gmc_disng*). In analogy to elastic ep scattering the cross-section is larger if the lepton spin and the nucleon spin are antiparallel. Together with the moments extracted from data the moments from this prediction are shown in table 6.5. The data is split into 3 samples with different beam charges and polarisations. As long as the interference term contributions $c_{0,LP}^{I}$ and $c_{1,LP}^{I}$ are small, the results for c_0' and c_1' of all datasets should agree with each other and with the values from the Monte Carlo. While the dataset from 1999/2000 with positive beam helicity agrees in reality nicely with the BH-prediction provided by the Monte Carlo, the other two periods are only in marginal agreement with this prediction. It is not possible to explain the difference between the two datasets from 1999/2000 by the DVCS contribution $c_{0,LP}^{DVCS}$, as also for this process all possible moments that contribute to the double-spin asymmetry are proportional to $P \times P_B$. A difference between 1998 and 1999/2000 could only be explained by a strong, charge dependent interference term. Clearly it is not possible to verify or explain the double spin asymmetry in a consistent way, such that the main information of these measurements is that all cosine moments are small and do not disturb the measurement of the sine-moments in the beam polarisation balanced TSA.

6.6. Depolarisation Effects and TSA

So far one important effect that enters for all asymmetries with polarised targets has been neglected: It was assumed that the longitudinal polarisation of the target nucleus is along the direction of the incident virtual photon. In reality the longitudinal polarisation is obtained with respect to the incoming electron. This means that the polarisation vector is rotated away from the direction of the virtual photon by up to $\theta_{\gamma^*} = 250$ mrad. In this case all terms in the decomposition of the moments (2.116,2.117) can contribute, and all of the additional terms contain harmonic functions of the angle ϕ_s between photon production plane and target polarisation vector.

However, the longitudinal target at HERMES requires that $\vec{S}||\vec{k}$ and this automatically fixes $\phi_s = \pi - \phi$ or $\phi_s = 2\pi - \phi$. Written in terms of the leading harmonic functions this means

$$\sin(\phi_s) = \pm\sin(\phi), \tag{6.32}$$

$$\cos(\phi_s) = \mp\cos(\phi), \tag{6.33}$$

where the + (-) sign denotes positive (negative) target polarisation P. Consequently the coefficients $c^I_{n,TP}$ ($s^I_{n,TP}$) themselves depend on ϕ and the angular dependence of the cross-section gets contributions from these coefficients times their associated functions $\cos(n\phi)$ ($\sin(n\phi)$). Only if these additional contributions that enter at order $\sin\theta_s$ are neglected, a ϕ-independent depolarisation would be observed:

$$c_n^+ = \frac{3}{2}c_{n,up} + c_{n,LP}\cos\theta - \frac{1}{2}c_{n,LLP}\cos^2\theta, \tag{6.34}$$

$$c_n^- = \frac{3}{2}c_{n,up} - c_{n,LP}\cos\theta - \frac{1}{2}c_{n,LLP}\cos^2\theta. \tag{6.35}$$

In order to take this pure depolarisation effect into account, a relative systematic error of 3% will be assigned to the TSA, but no explicit correction will be applied. Although it is impossible to correct for the additional transverse components, at leading twist the first moment receives no transverse contribution. This is found for the coherent as well as for the incoherent process. The only leading transverse components that appear for an unpolarised beam are in both cases:

$$c^I_{1,TP} \propto \sin\phi_s \Im m\mathcal{C}^I_{TP-}, \tag{6.36}$$

$$s^I_{1,TP} \propto \cos\phi_s \Im m\mathcal{C}^I_{TP+}. \tag{6.37}$$

Both terms flip their sign if the sign of the target polarisation P is flipped, i.e. $\phi_s \to \phi_s + \pi$. Both terms also lead to an apparent $\sin 2\phi$-moment, as $\cos\phi\sin\phi = \frac{1}{2}\sin(2\phi)$. This shows that while the first sine moment of the target spin asymmetry is only reduced by the factor $\cos\theta_s$, the second moment receives in addition a contribution proportional to $\sin\theta_s$ from the transversely polarised target component. Some estimate on the size of these contributions is possible, when the HERMES-data taken with the transversely polarised hydrogen target will be analysed (cf. estimates in [ENVY04]).

In contrast to the depolarisation effects on the BH/DVCS interference term, the normalisation to the BH-process is not affected if a nucleon is considered as target hadron. The average of the event rates with positive and negative target polarisation will be the same as the event rate for an unpolarised target. For deuterium the situation is different as $c^{BH}_{n,LLP}$ in equation 6.20 has to be multiplied by $\cos^2(\theta_s)$. Using the estimate that $c^{BH}_{0,LLP} \approx c^{BH}_{0,up}$ this would lead to an additional reduction of the extracted s_1 moment by about 3% (relative). Due to the dominance of the incoherent process in the lowest bin in t, the real uncertainty is about 1%. Hence this is not considered as a contribution to the systematic error in the following analysis.

In summary depolarisation effects are unavoidable but presumably small, especially for the leading sine-moment. Hence they are not considered as a serious problem.

6.7. Treatment of Target Polarisation: Tensor Asymmetries

The different tensor asymmetries (cf. chapter 2) give access to the moments of the interference term with index LLP. As most of the HERMES data is taken with large values of the vector polarisation P and a tensor polarisation of $T \approx 1$, a good statitical significance is obtained for the asymmetries $A_{L\pm}$ and $A_{C\pm}$.

In the approximation that the BH-amplitude dominates the BSA $A_{L\pm}$ (positron beam) is calculated as:

$$A_{L\pm}(\phi) = \frac{1}{\langle P_B \rangle} \frac{N_{\pm}^{+}(\phi) - N_{\pm}^{-}(\phi)}{N_{\pm}^{+}(\phi) + N_{\pm}^{-}(\phi)} \approx -\frac{x_A}{y} \frac{s_{1,up}^{I} - \frac{1}{3} s_{1,LLP}^{I}}{c_{0,up}^{BH} - \frac{1}{3} c_{0,LLP}^{BH}} \sin\phi, \tag{6.38}$$

where the notation is again taken from references [KM03] and [BMK02].

In reality the true value of the tensor polarisation enters such that the correct result is

$$A_{L\pm,true} \approx -\frac{x_A}{y} \frac{s_{1,up}^{I} - \frac{T}{2+T} s_{1,LLP}^{I}}{c_{0,up}^{BH} - \frac{T}{2+T} c_{0,LLP}^{BH}} \sin\phi, \tag{6.39}$$

where the value of the tensor-polarisation for the HERMES data is $T = 0.827 \pm 0.025$.

A more direct way to study tensor-components is the asymmetry A_{zz}, which is defined as

$$A_{zz}(\phi) = \frac{N^{+}(\phi) + N^{-}(\phi) - 2N^{0}(\phi)}{N^{+}(\phi) + N^{-}(\phi) + N^{0}(\phi)}, \tag{6.40}$$

where N^{+}, N^{-} and N^{0} denote the normalised number of DVCS-events for the respective target state. To a good approximation this asymmetry can only be non-zero for the coherent process, as the single nucleons for the states $N^{+} + N^{-}$ and N^{0}, respectively, are unpolarised in the spectator picture. As long as an unpolarised beam of one charge is used, the cosine coefficients (index LLP) can be picked out as can be seen in equation 2.142:

$$A_{zz}(\phi) \approx \frac{(c_{0,up}^{BH} - c_{0,LLP}^{BH}) - \frac{x_A}{y}((c_{0,up}^{I} - c_{0,LLP}^{I}) + (c_{1,up}^{I} - c_{1,LLP}^{I}) \cos\phi)}{c_{0,up}^{BH}}. \tag{6.41}$$

As was discussed in the case of the target-spin asymmetry, the constant tensor asymmetry of the Bethe-Heitler process is known to be less than 10% (if the dilution with the incoherent process is taken into account). In the presence of a beam polarisation, also sine coefficients appear in the numerator as well as in the denominator:

$$\begin{aligned} A_{zz}(\phi) \quad \approx \quad & \frac{1}{c_{0,up}^{BH} - \frac{x_A}{y} \lambda s_{1,up}^{I} \sin\phi} \times (c_{0,up}^{BH} - c_{0,LLP}^{BH}) - \frac{x_A}{y}((c_{0,up}^{I} - c_{0,LLP}^{I}) + \\ & (c_{1,up}^{I} - c_{1,LLP}^{I}) \cos\phi + \lambda(s_{1,up}^{I} - s_{1,LLP}^{I}) \sin\phi). \end{aligned} \tag{6.42}$$

From the BSA it is known that $\frac{x_A}{y} \lambda s_{1,up}^{I} \leq 0.2 c_{0,up}^{BH}$. As this contribution to the denominator is small, its impact can be estimated from a Taylor expansion ($\frac{1}{1+x} \approx 1 - x + x^2$). Each non-zero asymmetry moment in the numerator couples to the sine-moment from the denominator and hence already the constant BH-asymmetry of $\leq$ 10% will lead to an observed sine moment of $\leq$ 2% instead of a constant moment.

This shows that for a precision measurement of the coefficient $s_{1,LLP}$ a different approach should be taken. Instead of the pure tensor asymmetry, the asymmetry A_{Lzz} can be defined, which uses two datasets with beam polarisations $\lambda = 1$ ($\Rightarrow$) and $\lambda = -1$ ($\Leftarrow$):

$$A_{Lzz}(\phi) = \frac{(N^+ + N^- - 2N^0)^{\Rightarrow} - (N^+ + N^- - 2N^0)^{\Leftarrow}}{(N^+ + N^- + N^0)^{\Rightarrow} + (N^+ + N^- + N^0)^{\Leftarrow}}. \tag{6.43}$$

It has the advantage that the BH-tensor asymmetry in the numerator as well as the $s^I_{1,up}$-moment in the denominator are cancelled. The result is then:

$$A_{Lzz}(\phi) \approx -\frac{x_A}{y} \frac{(s^I_{1,up} - s^I_{1,LLP}) \sin\phi}{c^{BH}_{0,up}}. \tag{6.44}$$

In this case the moment $s^I_{1,LLP}$ is accessible in a much cleaner way, although the difference with respect to an extraction from A_{zz} will be invisible with the present error bars.

In order to make consistent use of the same datasets as before, the tensor asymmetries A_{zz} and A_{Lzz} can be obtained from a combination of unpolarised and vector-polarised deuterium data according to

$$A_{zz}(\phi) = 2\frac{d\sigma^{\pm} - d\sigma^{up}}{d\sigma^{up}}, \tag{6.45}$$

where $N^{\pm}$ is the number of DVCS-events from a vector-polarisation balanced data sample and N^{up} is the number of events from an unpolarised DVCS data-sample. The functional form of this asymmetry differs from all other asymmetries due to the different denominator.

Again one can introduce the luminosity and efficiency corrected event-numbers $k_i^{\pm}$ and k_i^{up} in analogy to the definitions in appendix B. The corresponding error is denoted by $dk_i^{\pm}$ and dk_i^{up}, respectively. Including the tensor polarisation T of the target, the asymmetry in the i-th bin can be written as:

$$A_{zz,i} = \frac{2}{T}\frac{k_i^{\pm} - k_i^{up}}{k_i^{up}} \tag{6.46}$$

with an error of

$$dA_{zz,i} = 2\sqrt{\left(\frac{1}{k_i^{up}} dk_i^{\pm}\right)^2 + \left(\frac{k_i^{\pm}}{(k_i^{up})^2} dk_i^{up}\right)^2}. \tag{6.47}$$

The asymmetry A_{Lzz} is determined in a similar way. As all extractable sine-moments are proportional to the beam polarisation, it is necessary to divide by the average beam polarisation P_B:

$$A_{Lzz,i} = \frac{2}{T\langle P_B\rangle} \frac{(k_i^{\pm\Rightarrow} - k_i^{up\Rightarrow}) - (k_i^{\pm\Leftarrow} - k_i^{up\Leftarrow})}{k_i^{up\Rightarrow} + k_i^{up\Leftarrow}}, \tag{6.48}$$

where the error is due to the errors of each of the four independent datasets.

In principle the extraction of A_{Lzz} requires that all datasets are balanced to the same beam polarisation. Otherwise the remaining BSA can mimic a tensor asymmetry. However, the present statistics does not allow to balance the beam polarisation for all datasets. Hence the strategy was to balance the beam polarisation for the vector polarisation balanced and the unpolarised target for each beam polarisation state separately. The obtained values were $P_B^+ = 0.506$ and $P_B^- = -0.577$, respectively. In this way the unpolarised BSA cancels in the numerator as the results of both brackets (i.e. $k_i^{\pm\Rightarrow} - k_i^{up\Rightarrow}$ and $k_i^{\pm\Leftarrow} - k_i^{up\Leftarrow}$) will be zero if there is no tensor asymmetry. The remaining effect on the normalisation that originates from the denominator is small.

There is also another possibility to extract the asymmetries A_{zz} and A_{Lzz}: At the end of the running period of 2000 the target was operated in a different mode such that a rapid change of a tensor polarisation $T_1 \sim 1$ and a tensor polarisation $T_2 \sim -2$ was achieved. The exact values were $T_1 = 0.827 \pm 0.037$ as before and $T_2 = -1.655 \pm 0.049$. Thus the average tensor polarisation can in this case be defined as

$$\langle T \rangle = \frac{T_1 - T_2}{3}. \tag{6.49}$$

If the luminosity weighted BH/DVCS events with polarisation T_1 in the ϕ-bin i are denoted as $k_i^{\pm}$ and the events with polarisation T_2 are denoted as k_i^0 the asymmetries A_{zz} and A_{Lzz} can be calculated as

$$A_{zz,i} = \frac{2}{\langle T \rangle} \frac{k_i^{\pm} - k_i^0}{2k_i^{\pm} + k_i^0} \tag{6.50}$$

and

$$A_{Lzz,i} = \frac{2}{\langle T \rangle \langle P_B \rangle} \frac{(k_i^{\pm\Rightarrow} - k_i^{0\Rightarrow}) - (k_i^{\pm\Leftarrow} - k_i^{0\Leftarrow})}{2k_i^{\pm\Rightarrow} + k_i^{0\Rightarrow} + 2k_i^{\pm\Leftarrow} + k_i^{0\Leftarrow}}. \tag{6.51}$$

This expression requires that $T_2 \approx -2T_1$ such that the tensor polarisation cancels in the BH-cross-section that is used for normalisation. The beam polarisation for this dataset is by chance already balanced inside the error bars ($P_B^+ = 0.529, P_B^- = -0.546$).

Due to the rather limited statistics, it is difficult to measure the tensor asymmetries. Moreover, due to the strong dilution with incoherent data, also for the lowest values in $|t|$ the coherent asymmetry is expected to be small.

In the lowest t-bin also another complication arises: until now it has been assumed that the incoherent cross-section cannot have a tensor asymmetry. However, this is only approximately true. It has been pointed out in [F$^+$96] that a tensor asymmetry in photodisintegration is possible and that it is sensitive to the deuterium wave-function. This asymmetry will be studied at the BLAST experiment [BLAST98]. Consequently, especially in the lowest t-bin where binding effects dominate, also the incoherent process can have a tensor asymmetry at least due to the BH-process.

6.8. Systematic Errors

Systematic errors are obtained after all hardware corrections are applied to the data, but before a background correction is done. Several sources of systematic errors have been studied. They are summarised in table 6.6.

The main impact of the calorimeter calibration is expected in the case of the BCA, because data of different years with different calibration algorithms is compared. As has been shown in

Table 6.6.: The table shows all systematic errors that are considered to be important together with the asymmetries that are affected.

source of error	effect	asymmetries
calorimeter calibration	false moments	$A_{c\pm}$, A_{zz}, A_{Lzz}
smearing	leading moment ↓, other moments ?	all asymmetries
unbalanced beam polarisation	moment mixing	$A_{c\pm}$, A_{LU}
error on beam polarisation	normalisation	A_{LU}, $A_{L\pm}$
error on target polarisation	normalisation	A_{UL}, A_{zz}, A_{Lzz}
depolarisation effects	normalisation	A_{UL}, A_{zz}, A_{Lzz}

section 5.4 an effective recalibration is needed to obtain compatible missing mass distributions for 1998 and 1999/2000. Using the three-parameter fit, the BCA on an unpolarised deuterium target has the moments $c_0 = -0.030 \pm 0.020$, $c_1 = 0.069 \pm 0.028$, $s_1 = 0.014 \pm 0.028$ before recalibration and $c_0 = -0.006 \pm 0.020$, $c_1 = 0.054 \pm 0.028$, $s_1 = 0.020 \pm 0.028$ after recalibration. Obviously c_0 is very sensitive to the recalibration. Two other methods have been applied to estimate the systematic error because of the calorimeter.

The first scenario is to take the position dependent calibration factor that was used to obtain figure 5.12 and was extracted from the data. This should at least give some idea about changes that are expected if an alternative calibration procedure was used for the calorimeter. The obtained result is $c_0 = -0.027 \pm 0.020$, $c_1 = 0.063 \pm 0.028$, $s_1 = 0.014 \pm 0.028$.

The t dependent BCA derived from these three methods is compared in figure 6.8. Obviously the moment c_0 is more unstable than c_1. The position dependent recalibration seems to agree better with the results that are obtained without a recalibration factor for the year 2000. Since both recalibration methods lead to equivalent missing mass distributions for electron and positron data, the observed differences in the extracted moments are a well motivated estimate for the remaining error due to the calorimeter calibration.

In the second scenario a worst case estimate is made: As can be seen in figure 5.12 the local miscalibration for each year is in the order of ± 5 %, while the maximum local difference between 1998 and 2000 after the application of a constant recalibration factor is in the order of ± 1%. Consequently this was assumed to be the maximum amplitude for an arbitrary modulation. The worst case will approximately occur, if the calibration of the calorimeter is changed in the following way:

$$E_{calo,modified} = E_{calo}(1 + A_1 \cos\phi), \tag{6.52}$$

where A_1 is some arbitrary amplitude. This recalibration will shift the missing mass distribution and systematically change the accepted event statistics depending on ϕ. As there is no constant proportionality between the accepted event rate and the calorimeter calibration, also other moments like a constant term can be introduced in this way.

The recalibration was directly applied to all taken positron data with an unpolarised target, after the measured energy for 2000 had been corrected by the usual constant factor of 1.012. The effect on the t-dependence of c_0 and c_1 for the BCA with an unpolarised deuterium target is shown in figure 6.9. A strong systematic shift of the constant term by about 0.02 is found if

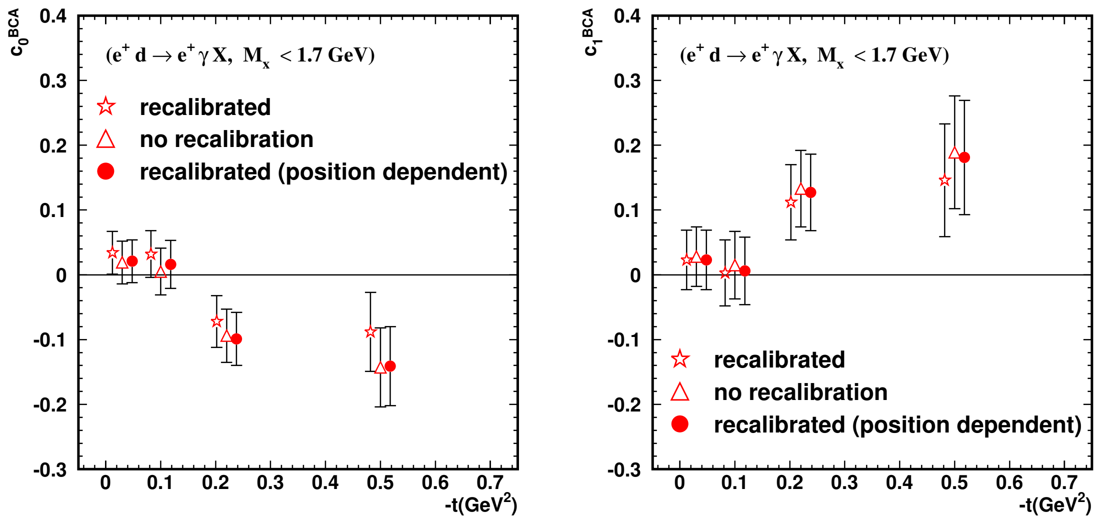

Figure 6.8.: Comparison of the coefficients c_0 and c_1 for the BCA on unpolarised deuterium for three different calibration methods: no recalibration, a constant calibration factor for 2000 as determined in section 5.4 or a position dependent recalibration for all years as discussed in the same section.

the recalibration is applied. The shift for the first cosine moment is only in the order of 0.01 in all bins in t.

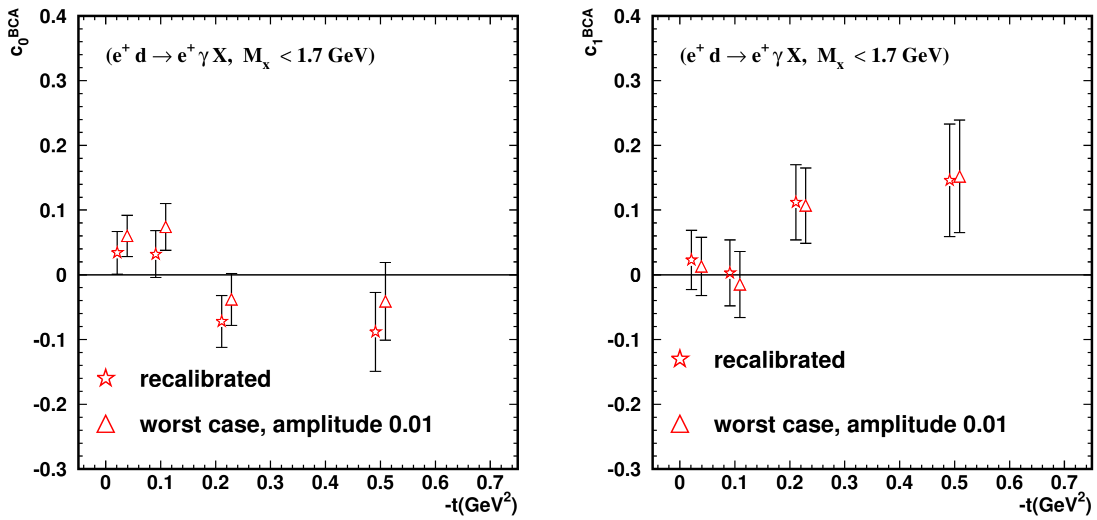

Figure 6.9.: Comparison of the coefficients c_0 and c_1 for the BCA with recalibration (triangles) or without recalibration (stars). In both case unpolarised deuterium data is shown for which the usual recalibration factor of 1.012 is applied to 2000 data.

Although this is approximately the worst case scenario it is not realistic because of 2 reasons: First the mis-calibration of the calorimeter is assumed to be different if the photon hits the same position, but the lepton has a different direction. Secondly, this mis-calibration shows up as an obvious displacement of the missing mass peak for the two years. In addition all these studies will probably overestimate the real error, as the inclusion or exclusion of single events also leads to statistical effects that are not part of the systematic error. Nevertheless all three methods lead to an upper limit on the absolute uncertainty of about 2% in the moment c_0 and about 1% in the moments c_1 and s_1. This error does not scale with the size of an existing asymmetry: Even if there is no asymmetry at all, a shift in the missing mass distribution together with the cut on the missing mass will produce a false asymmetry of this size. The determined errors will be assigned for A_{CU} as well as $A_{C\pm}$.

In the case of the tensor asymmetries a different calorimeter calibration of the polarised data and the unpolarised data taken at higher target density could also introduce a false asymmetry. Using different methods of recalibration as discussed at the beginning of this chapter an error of ± 0.02 was determined for the moment c_1 of the asymmetry A_{zz}. An error of ± 0.03 will be used for the asymmetry moment s_1 of the asymmetry A_{Lzz}. No error will be assigned to the BSA, which mainly relies separately on the datasets with and without target polarisation from 2000, such that differences can be expected to be much smaller. For the alternative method in which datasets with large positive and negative tensor polarisation there is also no error due to the calorimeter calibration.

A second source of systematic errors is detector smearing. As has been found in section 5.5, even with a lower cut of 5 mrad on θ_{γ,γ^*} smearing effects are still present. The remaining smearing for an asymmetry generated according to equation 5.23 has been obtained in a Monte Carlo simulation in 4 bins in t. The generated constant moment s_1 was 0.5; as has been explained in section 5.5 the fractional change of the asymmetry does not depend on its amplitude in this method. It can be seen in figure 6.10 that remaining smearing effects reduce the asymmetry moment c_1 by up to 15% (i.e. 0.425 in the plot) in the lowest $|t|$ bin. This value includes binning effects as discussed in section 6.2.

The assumption of a constant asymmetry that has been made for these studies has a non-trivial problem: It is predicted in publications that the asymmetry is larger for small values of y which corresponds to low momenta of the scattered lepton. Hence the smearing would mostly occur in a region, where the asymmetry is large, such that the smearing effects would be underestimated by this study. This has been checked by extracting the raw asymmetry in bins of y for polarised and unpolarised deuterium data. From figure 6.11 no experimental evidence exists that the BCA would be primarily located at low values of y, which is consistent with the Monte Carlo results for the BSA and the BCA. On the whole this indicates that smearing effects in the order of 15% will be realistic at least for low values of $|t|$. A comparison of smeared and smearing-free Monte Carlo results using realistic GPD models indicates in addition that smearing effects for all bins in t - including a non-constant asymmetry - will not be larger. Hence a relative uncertainty of 15% has been assigned to the leading cosine-moment in the case of the BCA. For sub-leading moments like the constant term or the $\cos(2\phi)$ moment the situation is much more difficult, as they are contaminated by a contribution from the leading moment that is independent of the size of the particular sub-leading moment. This is another reason, why these moments are difficult to interpret and will not be considered in the following.

In the case of the beam-spin asymmetry the smearing effects are weaker as can be seen in figure 6.12. The generated moment s_1 is inside the error bars compatible with its generated

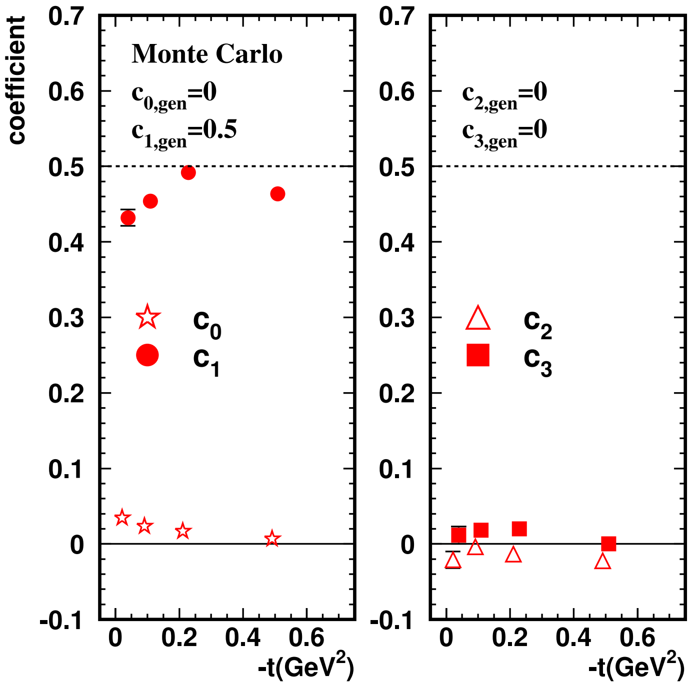

Figure 6.10.: Smearing effects (BCA) binned in t: The five-parameter fit has been used to extract the first 4 cosine moments of the BCA from Monte Carlo data that was generated with a first moment of 0.5. The results are plotted vs. t.

value. As a very conservative estimate a relative error of only 5% of the asymmetry amplitude was assigned to s_1 in the case of the BSA and the TSA. This includes already the contribution from binning effects in ϕ. As the BSA calculated from data does not exhibit a strong dependence on y the simulation from figure 6.12 can be assumed to be representative. In addition a comparison between a smeared and a smearing-free Monte Carlo confirms an upper limit of 5%.

In the case of the BCA it was discussed if a remaining beam polarisation P_B for the two beam-charges can have an effect. The beam polarisations for the two data-samples are shown in table 6.7. As only one beam-polarisation was used in 1998, it is impossible to balance the beam polarisation to zero for the extraction of the BCA. In order to minimise the error bars it was instead decided to included all available data irrespective of the beam polarisation.

As can be seen from equation 2.132 the situation of the beam-charge asymmetry for the unpolarised deuterium target is uncritical, as the BSA will cancel exactly in the denominator. This is also true for large kinematical bins. The BSA in the numerator is taken into account by the fit coefficient s_1 which is expected to have the same value as s_1 from the BSA multiplied by P_B. Inside the error bars this is found to be fulfilled.

In the case of the BCA on the polarised deuterium it can be argued that a Taylor-expansion can be performed to study the expected effects. It is found that in leading order the cosine moment is modified in its amplitude by a term that depends on the coefficient s_1^{BSA} from the

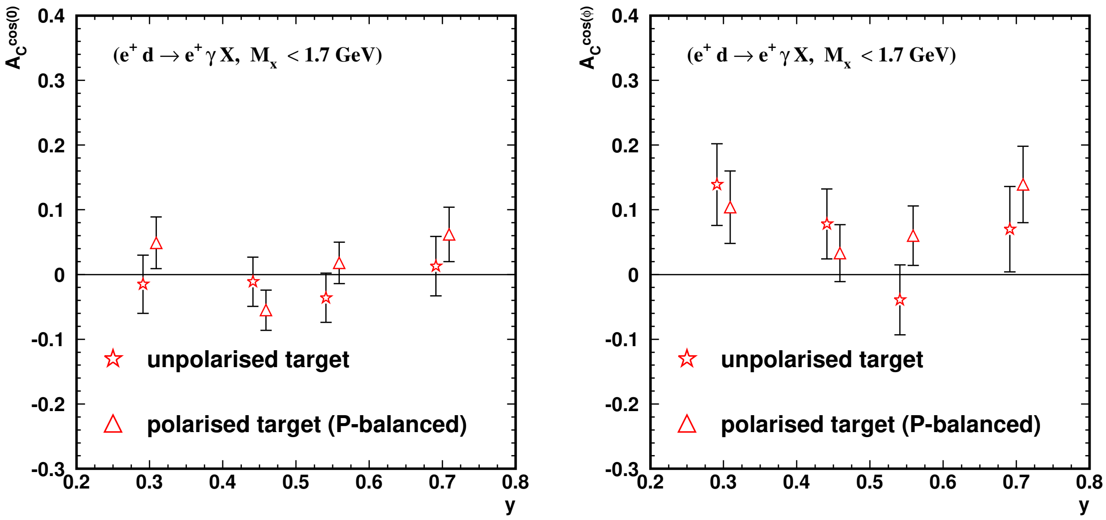

Figure 6.11.: Comparison of the coefficients c_0 and c_1 for the BCA on polarised and unpolarised deuterium in 4 bins in y. No clear dependence on y is observed.

Table 6.7.: Beam polarisations of the four datasets that are used to calculate a beam charge asymmetry. For the polarised datasets the polarisations are very different.

target/beam-helicity	+	-
polarised	+14%	-51%
unpolarised	-30%	-31%

beam spin asymmetry (positron data) according to:

$$c_1^{observed} = (1 + \frac{1}{8}(P_B^+ - P_B^-)^2 (s_1^{BSA})^2) c_1^{BCA}. \tag{6.53}$$

For the BCA on the polarised deuterium target this implies a relative error in the order of 0.5%. Also a Monte Carlo simulation based on a realistic BSA shows no impact inside the statistical errors of the simulation. Hence it was decided to neglect this contribution.

The same situation is encountered in the case of the BSA itself. If the two beam polarisations are not equal and opposite in sign, the remaining change of the s_1 moment can be expected to be

$$s_1^{observed} = (1 + \frac{1}{8}(P_B^+ + P_B^-)^2 (s_1^{BSA})^2) s_1^{BSA}. \tag{6.54}$$

As the two polarisations are very similar, this error is so small that it will not be considered in more detail.

For the BSA one error on its normalisation will arise from the measurement of the beam polarisation. According to the errors quoted by the polarimeter group (cf. section 3.1) the

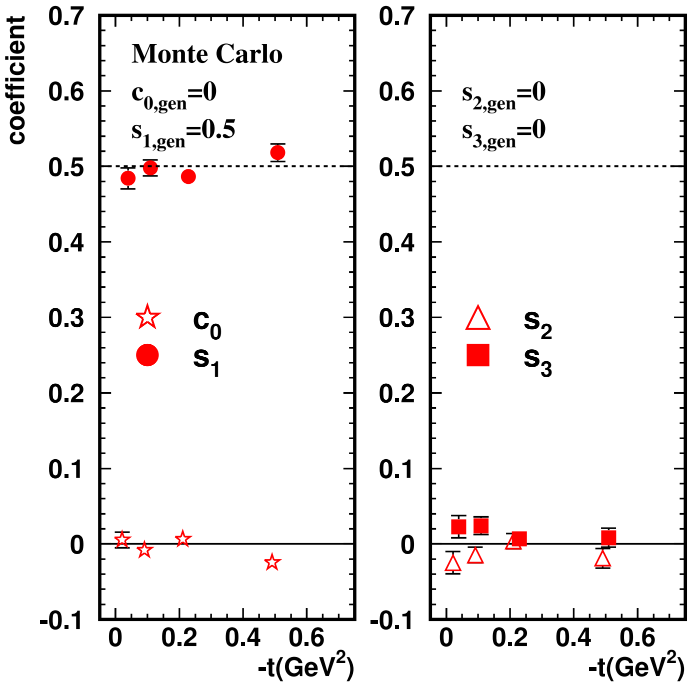

Figure 6.12.: Smearing effects (BSA) binned in t: A five-parameter fit has been used to extract the first 3 sine moments and the first two cosine moments of the BSA from Monte Carlo data that was generated with a first sine moment of 0.5. The results are plotted vs. t.

polarisation can systematically be wrong by about 2% (relative error), if the LPOL is assumed to dominate the dataset. Hence a relative error of 2% of the asymmetry is assigned due to the polarisation measurement.

The main error for the target spin asymmetry is due to the error of the measured value of the target polarisation. A fractional error of 4.0% is assigned (cf. section 6.4). This hardly matters, as the target spin asymmetry is anyway found to be small. For the tensor asymmetries, the error on the tensor polarisation has to be taken into account. It leads to a fractional error of 4.5% for the method with tensor polarisations $T \sim 1$ and $T \sim 0$ and 2.5% for tensor polarisations $T \sim 1$ and $T \sim -2$. The s_1-moment is in addition expected to scale with the beam polarisation, hence a fractional error of 2% enters for A_{Lzz} in order to take this into account.

Both the TSA and the tensor asymmetries are affected by depolarisation effects. As has been pointed out, the leading effect for the TSA is a wrong normalisation of the asymmetry. In section 6.4 a fractional error of 3% has been assigned. In the case of the tensor asymmetries the longitudinal contribution scales with $\cos^2(\theta_{\gamma^*})$, such a fractional error of 6% has to be assigned. In both cases the error is uni-directional, but this does not matter as the obtained systematic error is anyway much smaller than the statistical error.

The applied systematic errors are listed in table 6.8. Moments that are not listed are either forbidden (e.g. c_0 for the BSA), very uncertain (e.g. c_2 for the BCA) or not interesting (c_0 for A_{zz}, where the trivial BH-contribution is dominating). The obtained corrected results are

Table 6.8.: The extracted asymmetries together with the assigned systematic errors are listed. The top table gives the single contributions and the bottom table the final values. The errors in brackets are assigned if the tensor-asymmetries are calculated from unpolarised and vector polarisation balanced data.

Asymmetry	coefficient	errors
BSA	s_1	smearing 5%, beam polarisation 2%
BCA	c_1	smearing 15%, CALO-calibration ± 0.01
TSA	s_1	smearing 5%, depol. 3%, target pol. 4%
A_{zz}	c_1	smearing 15%, depol. 6%, target pol. 2.5% (4.5%), CALO-calibration 0 (± 0.02)
A_{Lzz}	s_1	smearing 5%, depol. 6%, target pol. 2.5% (4.5%), beam pol. 2%, CALO-calibration 0 (± 0.03)

Asymmetry	coefficient	fractional error	constant error
BSA	s_1	5.4%	-
BCA	c_1	15.0%	0.01
TSA	s_1	7.1%	-
A_{zz}	c_1	16.3% (16.8%)	(0.02)
A_{Lzz}	s_1	8.4% (9.2%)	(0.03)

understood to be valid inside the HERMES acceptance within the given cuts. All complications mentioned in appendices B and C enter in addition. Hence there can be a 20-30% difference if the results of this analysis are compared with the theory predictions at bin-centre. In addition the model dependent DVCS-cross-section has a substantial contribution and theory has to take this into account.

Finally the results are not corrected for radiative effects. Although these can be expected to be suppressed by one order of $\alpha_{e.m.}$ they are not necessarily small in all kinematical regions. It has been pointed out in reference [V$^+$00] that for DVCS at JLAB energy ($E_b = 6$ GeV) virtual radiative corrections lead to a reduction of the BH/DVCS process by about 23% due to their impact on the BH-cross-section. The contribution of real photon emission is on the other hand expected to be small. As most of the real photon emission will occur along the incident and the outgoing lepton, there is also no possibility to study this higher order process at HERMES experimentally. The total predicted effect on the BSA at JLAB-energy is in the order of 5% (fractional error). With the present statistical errors this uncertainty is still acceptable, but future high precision experiments will suffer from it. Hence existing calculations from reference [V$^+$00] or [BK03] have to be implemented consistently into the Monte Carlo and the expected error on all asymmetries has to be estimated for the individual detector.

6.9. Determination of Background Fraction

It has been discussed that the dataset that is used for the DVCS-analysis on the deuterium target originates from very different processes. Theoretically the coherent process may be the most interesting one as it is already discussed in several publications.

However the experimental situation is very difficult; as long as the recoiling target particle is not detected, a missing mass analysis from the photon and lepton kinematics is the only possibility to ensure exclusivity for all kinematics. Consequently a resolution of better than 2.2 MeV - corresponding to the binding energy of the deuteron - would be required to separate the deuteron from a dissociated proton/neutron-pair. This is clearly not feasible with the high beam-energy at HERMES . The only other possibility to isolate the coherent process, is to exploit the different t-dependence of the coherent and the incoherent process. However, as the enhancement of the coherent process is proportional to the charge of the nucleus squared, there is no enhancement at all for the deuteron. Consequently, as the cross-section of the coherent process is quite low even for low values of $|t|$, the analysis cannot focus on this process alone.

It can also be argued that the much more abundant incoherent process should be studied as it clearly dominates at intermediate values of t. In this case one would concentrate on the information that can be extracted about the neutron. The neutron is especially interesting [B$^+$03], as it gives access to the GPD E. However, as long as the final state cannot be identified, the proton cross-section will dominate by far. In addition resonance excitation in BH on the neutron is comparatively strong and thus it will be difficult to isolate elastic BH/DVCS on the neutron by a comparison with proton data. Thus also the incoherent process has a limited relevance and can only be used to confirm the proton data inside the statistical error bars.

Finally, for large values of $|t|$ it is impossible to subtract the background from BH/DVCS with resonance excitation, as it is responsible for at least 30% of the observed statistics and has unknown asymmetries. Thus also this process cannot and should not be excluded from the dataset.

Since at least the beam spin and the beam charge asymmetry are caused by contributions from all mentioned processes, it was decided to consider all of them as signal. The relative contributions can only be obtained from the Monte Carlo but have rather large systematic errors, since the DVCS-cross-section for the coherent process as well as for the incoherent process with resonance excitation has been omitted and is in any case model dependent. As has been pointed out in section 4.5 an upper and a lower limit for the BH contribution to resonance excitation can be derived by different treatments of the neutron cross-section in the resonance region. Both models are compatible with the observed data. The predicted composition of the selected dataset - omitting background contributions - is shown in figure 6.13. As the contributions from all different processes have very similar distributions in the inclusive scattering variables (x_B, Q^2, etc.), t is the only common variable that allows for an approximate separation of the different processes. With the present statistics, a kinematical binning only in t was chosen for this reason.

In addition to these inter-related processes, there is also a true background from very different processes that have been discussed in chapter 4. The general problem is that not only exclusive π^0- or η-production, which are by nature almost indistinguishable from BH/DVCS under certain meson decay kinematics, but also semi-inclusive processes can leak into the exclusive bin: Due to the statistical fluctuations in the measured energy deposition in the calorimeter, the energy of the single photon cluster can be overestimated such that the missing mass gets close to the exclusive range. The missing mass resolution from the Monte Carlo is only about $\Delta M_x^2 \approx 1.5$ GeV^2, which is clearly not enough to obtain a good separation.

In order to study this in more detail, all positron data from 1999 and 2000 was combined and the missing mass distribution was analysed (cf. figure 5.18). Obviously it is not possible to apply a side-band-subtraction for the background in the exclusive region. Three different methods have been used to estimate the background within the cuts for DVCS events:

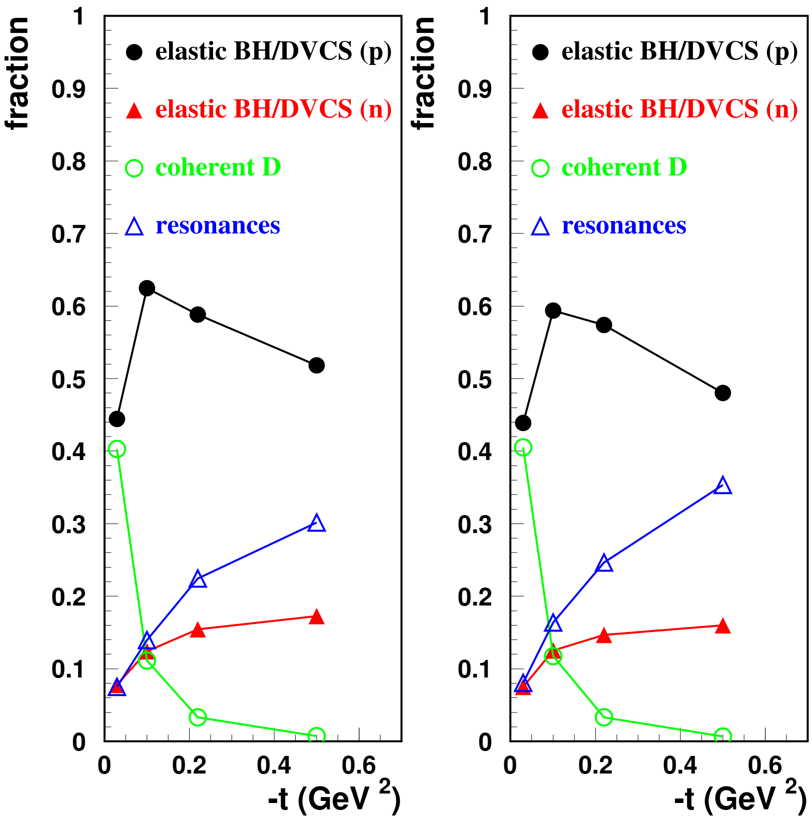

Figure 6.13.: Contributions of different processes vs. t: The relative contributions of all BH/DVCS-type processes in the exclusive sample are shown for the standard MC-model (left) and the model based on the neutron resonance cross-section obtained from MAID2000 (right). The bins in t are chosen to yield approximately the same statistics in each bin.

1. Fit of a second order polynomial+Gaussian to the data, where the missing mass range of $-5\text{ GeV}^2 < M_x^2 < 10\text{ GeV}^2$ has been selected. All standard cuts are applied to the data. Usually the fitted background contribution is positive in the exclusive interval. This fit will provide a pessimistic estimate for the background, as a long tail of the background towards low missing masses is fitted.

2. Fit of a positive first order polynomial+Gaussian to the data; all cuts are the same as in the previous method. The fit is constrained such that the background contribution has to be positive.

3. Comparison of Monte Carlo and data: The predicted cross-section for decay-photons in the exclusive bin is divided by the experimentally observed cross-section.

The results of all three methods are shown in figure 6.14. The results of the first two methods are very similar and the estimated accumulated contamination at $M_x^2 = 2.89\text{ GeV}^2$ is 22.3%

or 24.7%, respectively. From the width of the Gaussian peak, the respective missing mass resolution is estimated to be 1.3 GeV^2 and 1.4 GeV^2.

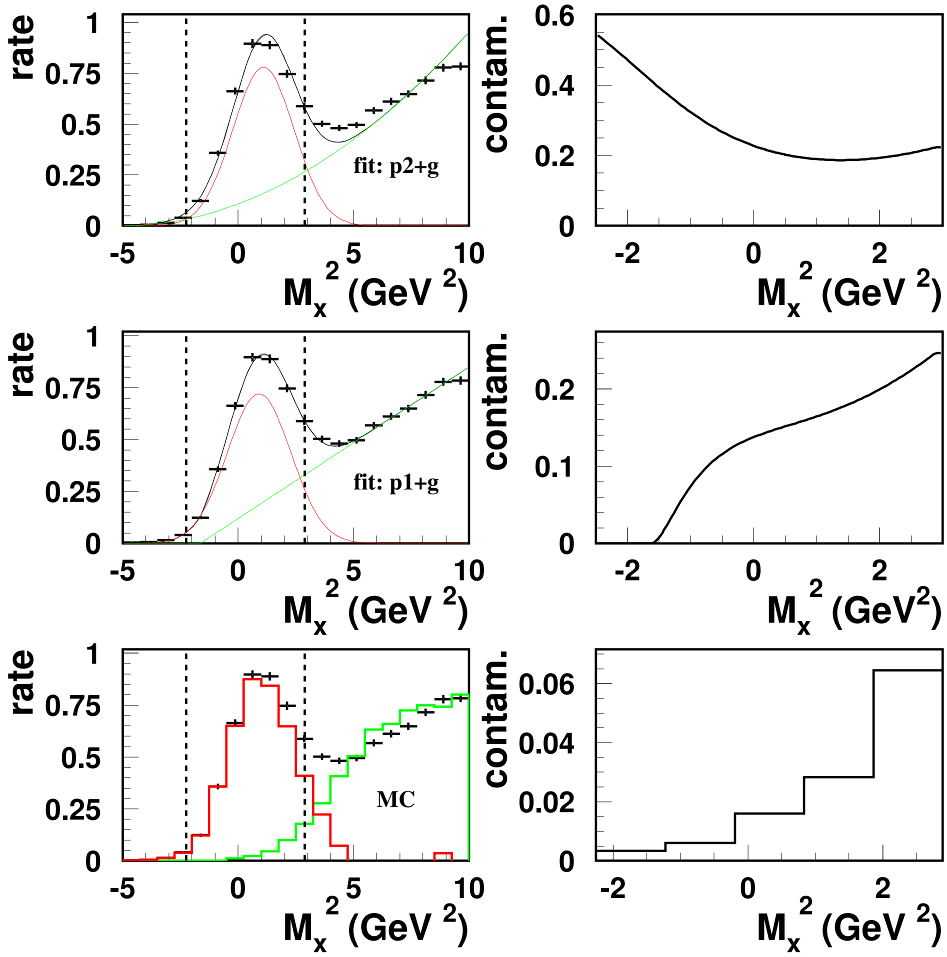

Figure 6.14.: Different methods to determine the background: The missing mass distribution of all positron data was fitted by a Gaussian plus a second order polynomial (top,left) to obtain the accumulated contamination in dependence on the upper cut on M_x^2 (top,right). The same was done using a Gaussian plus a first order polynomial that was constrained to be positive (middle). For the bottom plots the contamination predicted by the Monte Carlo was compared with the measured event distribution (bottom, left). The contamination depending on the upper cut on M_x^2 is also shown (bottom,right).

The third method is based on Monte Carlo. For the semi-inclusive background the decay photon cross-section obtained from *gmc_disng* is reweighted according to the procedure described in section 4.7. Thus it reproduces the data in all kinematic variables for missing masses above 6 GeV^2. Then the obtained missing-mass distribution in the exclusive region is compared with the measured missing mass distribution. Data and Monte Carlo are integrated from $M_x^2 = -2.25\ \mathrm{GeV}^2$ to an upper limit on M_x^2. The accumulated contamination depending on this upper limit is also shown shown in figure 6.14 (bottom,right) and amounts to 6.4% below $M_x^2 = 2.89\ \mathrm{GeV}^2$. The same procedure is applied for exclusive pion production simulated by *gmc_pion*. The estimated background due to exclusive π^0-production in the exclusive DVCS/BH-region is 1.1%. The assigned errors are much larger than the statistical errors in order to be insensitive to the exact background model. A relative error of $1/2$ is assigned for the semi-inclusive contribution such that even without reweighting of the Monte Carlo the result is still inside the error bars. A relative error of $1/3$ is assigned to the exclusive contribution as the neutron cross-section was estimated to be $\sigma_n = (0.5 \pm 0.5)\sigma_p$. Thus the final result for the background contribution to the observed data is $(7.5 \pm 3.2)\%$. The background contamination per bin in t is shown in figure 6.15.

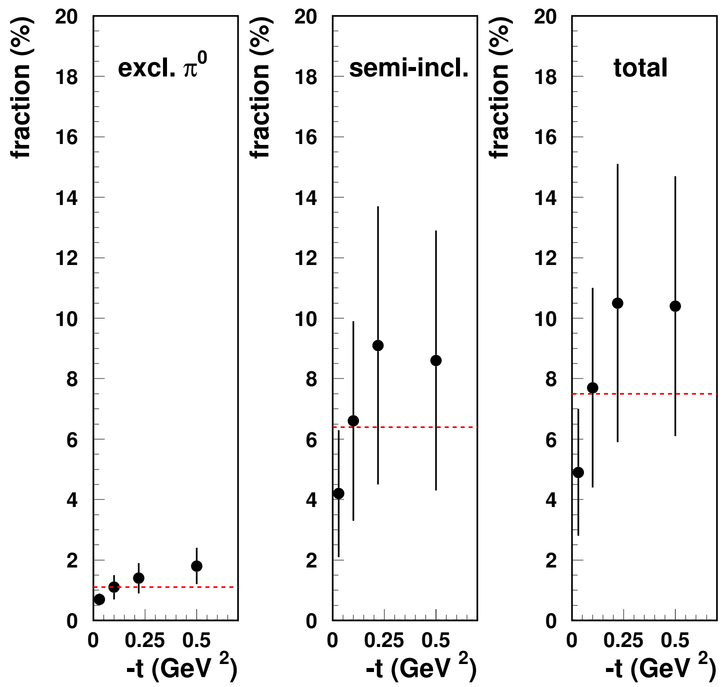

Figure 6.15.: Fraction of the data due to background vs. t for three different processes: exclusive π^0-production (left), semi-inclusive π^0-production (middle), and combined (right). The horizontal lines indicate the background fractions for the whole range in t.

It is found that the fits to the data predict a much higher background; the result is larger by a factor of two to three compared with the Monte Carlo result. One reason is that the exclusive peak is not a true Gaussian; instead there is a tail towards higher missing masses due to apparative effects. This disturbs the fit. Another reason is that there is no real reason for a linear extrapolation with this very extreme kinematics. For example fits tend to predict sizable background down to $-2\ \mathrm{GeV}^2$. The Monte Carlo on the other hand shows that the background drops much faster and that it effectively stops at $0\ \mathrm{GeV}^2$. This is also in agreement with the Monte Carlo simulation of the missing mass distribution that is shown in section 4.8. An additional inconsistency shows up, if the cut on the cluster energy is lowered from 3 GeV to 1 GeV: While it is known that this cut has practically no effect on the exclusive BH/DVCS-events and that it must reduce the background, the fits now predict a background contamination of 22.0% and 1.5% respectively. This open disagreement shows that fits do not allow to make a usable prediction for the background contamination.

6.10. Determination of Background Asymmetry

Before a background-correction can be applied, the asymmetry of the background has to be estimated in some way. In the case of the BCA this is not necessary, as the various background processes cannot have a BCA. For all other asymmetries this is not true and hence a better understanding of the background events is necessary.

According to the Monte Carlo simulation the main sources for the contamination are decay-photons (as has been claimed before). For 98% of the semi-inclusive events populating the exclusive interval in missing mass, a hard decay photon with sufficient energy is produced by the event generator. In 72% of the cases a π^0 meson with sufficient energy was present; in all of these cases at least one additional meson is formed that together with the remaining nucleon has a low invariant mass below 2 GeV.

An obvious question is, under which circumstances semi-inclusive π^0-decay photons can be misidentified as exclusive photons. Two different cases are encountered, which are shown in figure 6.16 and figure 6.17. In both figures the first plot shows the energy of the leading generated photon subtracted from the energy of the leading generated π^0. As a cluster energy of more than 3 GeV and a low missing mass is required, the leading photon should indeed originate from the leading pion and the difference is the energy of the second photon.

In the first case the energy of this photon is quite low, typically below 2 GeV (indicated as filled histogram in figure 6.16). At the same time also the energy of the π^0 is rather low (top right). The angular distribution of the second photon in θ_x and θ_y is shown in the third plot (bottom left). The photon is either outside the geometrical acceptance of HERMES or it is below the detection threshold. Some of the photons are stopped in the septum plate at low values of $|\theta_y|$. There is a good correlation between the energy of the leading photon and the energy of the cluster (bottom right). However, the cluster energy is consistently overestimated such that the events pass the cut on the missing mass. For these events the decay is very asymmetric: the leading photon receives most of the energy and is close to the direction of flight of the pion, while the second low energy photon is emitted under large angles. This process constitutes about three quarters of the semi-inclusive π^0-contamination.

For the second less abundant category of background events, the energy of the second photon is rather high and typically above 2 GeV (top left plot of figure 6.17). Also the energy of the decaying pion is quite high (top right). Due to the Lorentz boost the two photons are rather close to each other in this case; the plot of $\Delta\theta_y$ vs. $\Delta\theta_x$ shows that the distance in either variable is less than 20-25 mrad. As the calorimeter blocks have apparent dimensions of 12 mrad $\times$12 mrad, this can be interpreted as the maximum distance such that the two photons cannot be separated. The reconstructed energy of the cluster is a little bit larger than the energy of the pion as the cut on the missing mass has to be passed. In this second case the decay of the π^0 is highly symmetric such that the energy of the two photons is similar and the minimum opening angle is achieved.

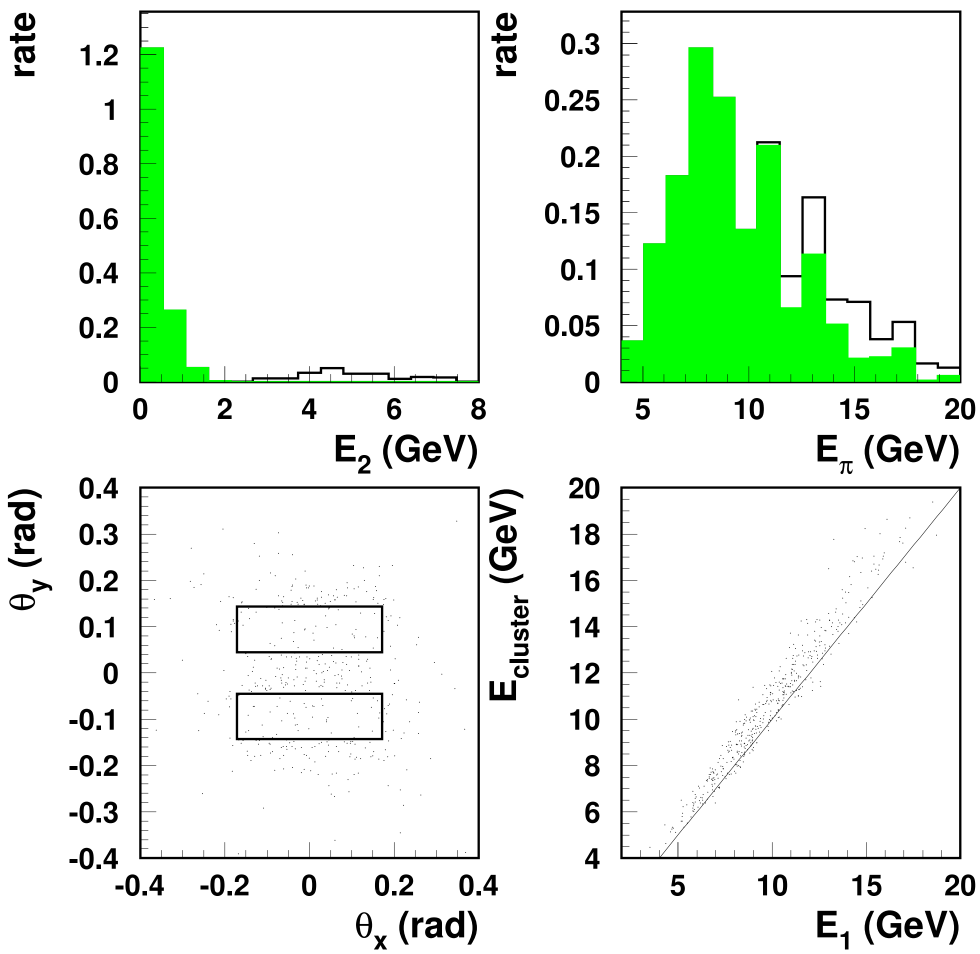

Figure 6.16.: Semi-inclusive π^0 with very asymmetric decay: For all π^0-events in the Monte Carlo that pass the exclusive DVCS-cuts, the generated energy of the leading photon was subtracted from the energy of the leading pion. The event rate was plotted vs. this energy E_2 of the second photon (top left) and events with low E_2 were selected. The same events are shown as the solid histogram in the plot of event rate vs. pion momentum (top right). For these events the angles θ_x and θ_y of the second photons are compared with the geometrical HERMES-acceptance (bottom left) and the energy of the reconstructed cluster is plotted vs. the energy E_1 of the leading photon (bottom right).

In figure 6.18 the opening angle (symmetric decay) for π^0s is shown depending on the pion momentum. At momenta below 10 GeV/c the second cluster will always be separated from the first one.

For both types of π^0-events the registered cluster position is very close to the original direction of flight of the pion. In the first case this happens as the leading photon takes over most of the pion momentum. In the second case the overlapping clusters will lead to an effective

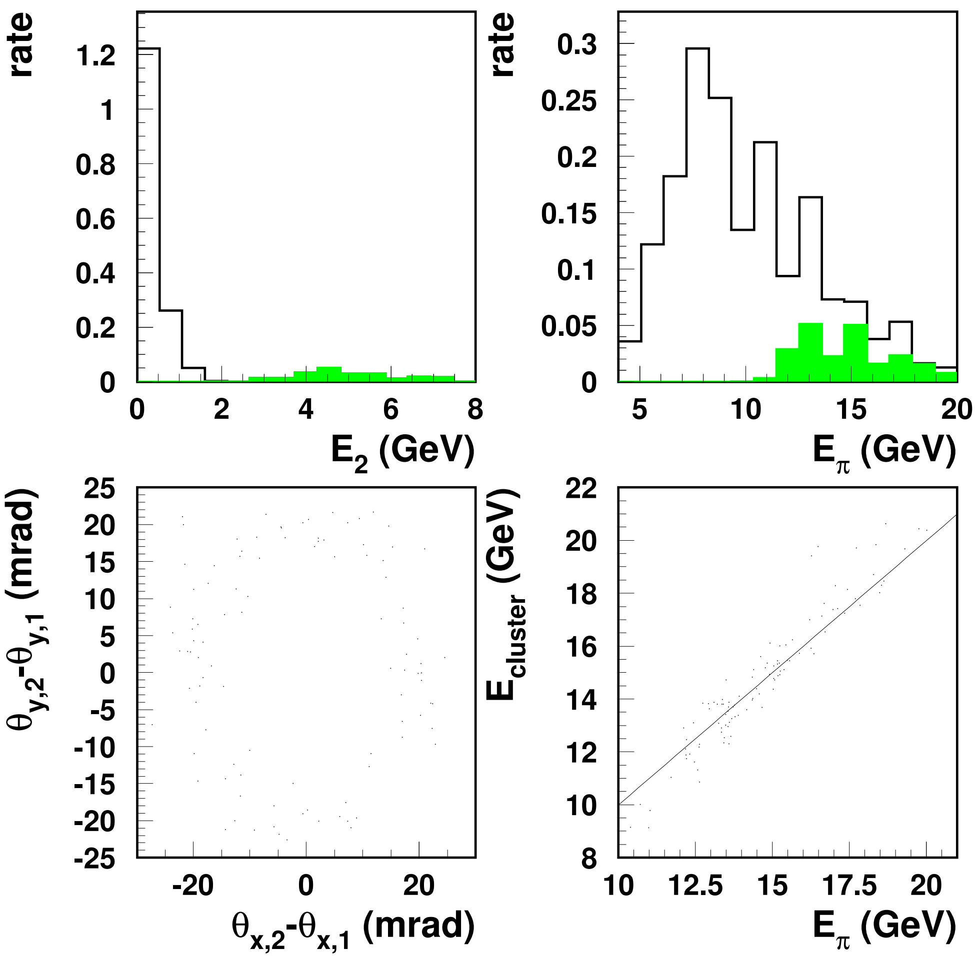

Figure 6.17.: Semi-inclusive π^0 with overlapping clusters: For all π^0-events in the Monte Carlo that pass the exclusive DVCS-cuts, the generated energy of the leading photon was subtracted from the energy of the leading pion. The event rate was plotted vs. this energy E_2 of the second photon (top left) and events with high E_2 were selected. The same events are shown as the solid histogram in the plot of event rate vs. pion momentum (top right). For these events the distance $d\theta_x$ and $d\theta_y$ between the two photons is plotted vs. each other (bottom left) and the observed cluster energy is shown vs. the energy of the pion (bottom right).

cluster centre that is very close to the original π^0-trajectory. Consequently one can assume that any asymmetry in ϕ present in the pion distribution is more or less preserved in the apparent single photon sample that acts as a background in the case of DVCS. The same two event types are also encountered for exclusively produced π^0s, where the contribution of the second type is enhanced ($\sim 42\%$) due to the larger average pion momenta.

In order to obtain an estimate for the value of the azimuthal meson asymmetry, exclusive and semi-exclusive π^0 events were selected with the same event cuts and data quality as the

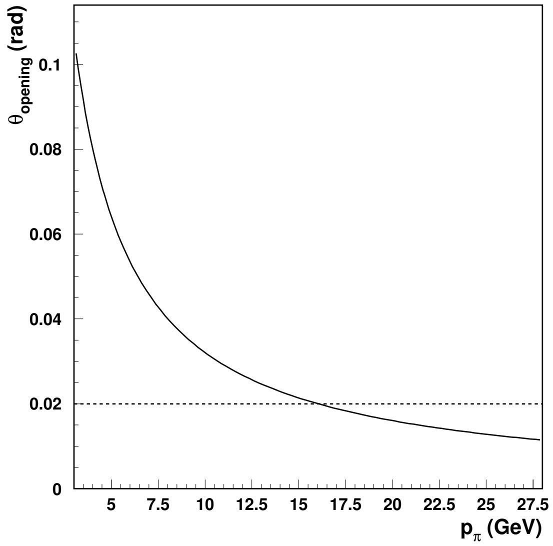

Figure 6.18.: Minimum opening angle between the two decay photons of a π^0-meson as a function of the pion momentum.

DVCS-events. The only difference was that two clusters with a summed energy of more than 3 GeV were required instead of one cluster and that the second cluster as well as the first cluster must have a preshower signal larger than 0.001 GeV. The purpose was to select exactly those events that decay more symmetrically than required for the first case or less symmetrically than required for the second case in the Monte Carlo. The reconstructed π^0 mass was required to be in the following interval:

$$100 \text{ MeV} < \text{m}_\pi < 180 \text{ MeV}. \tag{6.55}$$

Using this cut, it is made sure that the same π^0-asymmetry as in the case of the DVCS contamination is studied. The background asymmetry was computed for the whole dataset of each asymmetry, without binning in t in order to keep enough statistics. The results for the asymmetries under study are summarised in table 6.9. In addition to the extracted asymmetries, similar quantities from present semi-inclusive HERMES-analyses are included. The variable z is defined as $z = E_\pi/\nu$ and in the limit of $z \to 1$ the semi-inclusive results should agree with the results of this study.

The background asymmetries behave as expected: In order to create a beam charge asymmetry in semi-inclusive π^0-production, higher order radiative corrections are needed. Since the π^0 in contrast to the photon cannot be emitted by the lepton, loop diagrams with at least two exchanged virtual photons must interfere with the leading order diagram (see comment in [MT69]). It is consequently not expected that such an asymmetry is observable at HERMES and an asymmetry of zero ($A_\pi = 0 \pm 0$) will be assumed.

The beam-spin asymmetry in semi-inclusive π^0 production at HERMES has recently been found to be very small [HERMES04a]. The agreement of this study with the results of the semi-inclusive analysis is good inside the error bars. Hence the pion asymmetry is assumed to be

Table 6.9.: The measured asymmetries are obtained from exclusive 2-photon production in the exclusive missing mass region. A cut on the 2 photon-invariant mass is applied in order to select π^0 decay photons. The same three-parameter fits were used as in the data analysis and the moments c_0, s_1 and c_0/s_2 (depending on the asymmetry) were extracted. Results from present HERMES analysis are added, where the exclusivity of the π^0 production is ensured by selecting large values of z instead of applying cuts on the missing mass. Both approaches have to yield compatible results.

method	c_0	c_1	s_1	s_2
A_{LU}	0.162 ± 0.121	-	-0.025 ± 0.162	-0.044 ± 0.161
$A_{L\pm}$	0.106 ± 0.063	-	-0.008 ± 0.085	-0.020 ± 0.088
A_{LU} in [HERMES04a]:				
• $z = 0.84$	-	-	-0.001 ± 0.029	-
• $z = 0.96$	-	-	-0.001 ± 0.042	-
A_{CU}	0.004 ± 0.050	0.004 ± 0.070	-0.099 ± 0.070	-
$A_{C\pm}$	0.012 ± 0.043	-0.029 ± 0.063	0.000 ± 0.058	-
A_{UL}	0.003 ± 0.039	-	0.055 ± 0.053	-0.009 ± 0.055
A_{UL} in [HERMES03a]:				
• $z = 0.86$	-	-	0.056 ± 0.025	-
• $z = 0.97$	-	-	0.097 ± 0.039	-
A_{zz} ($P_B = 0.00$)	-0.253 ± 0.215	0.005 ± 0.318	0.446 ± 0.284	-
A_{zz} ($P_B = -0.29$)	-0.102 ± 0.194	-0.339 ± 0.270	0.618 ± 0.245	-
A_{zz} ($T \sim -2, 1$)	0.092 ± 0.124	-0.329 ± 0.172	0.101 ± 0.172	-
A_{Lzz}	-0.244 ± 0.407	-	0.273 ± 0.542	-0.264 ± 0.548
A_{Lzz} ($T \sim -2, 1$)	-0.058 ± 0.231	-	0.153 ± 0.321	0.094 ± 0.337

$s_{1,\pi} = -0.001 \pm 0.042$.

The target spin asymmetry in semi-inclusive pion productions is known to be non-zero at HERMES-kinematics [HERMES03a]. Consequently this DVCS-asymmetry may receive the largest correction. Again the results of the two different analyses agree inside the error bars. Furthermore also in the present study a value of $s_1 = 0.083 \pm 0.033$ is obtained if the cut on t is removed and an upper limit of $\theta_{\pi^0,\gamma^*} < 100$ mrad is imposed instead of 45 mrad. Hence an asymmetry of $s_{1,\pi} = 0.097 \pm 0.039$ will be assumed.

Not very much is known about tensor-effects. Assuming that coherent π^0 production is only a small contribution, they can be expected to be weak. This is compatible with the data. Since the error bars are already very large, the background asymmetry for the moment c_1 of the asymmetry A_{zz} has been set to zero ($A_\pi = 0 \pm 0$). The same is done for the moment s_1 of the asymmetry A_{Lzz} ($A_\pi = 0 \pm 0$).

As soon as the pion asymmetry is known, a correction is only possible if the asymmetry transfer factor f is known. The asymmetry of the decay photon is related to the azimuthal meson asymmetry by

$$A_{bkg} = f \times A_\pi. \tag{6.56}$$

In the special case of BH/DVCS this asymmetry transfer is very close to one: Within the statistical errors no deviation from this value has been obtained in the Monte Carlo. Hence in all following discussions a value of $f = 0.95 \pm 0.05$ will be assumed.

6.11. Background Correction

Only the exclusive and semi-inclusive meson decay background is explicitly corrected for. The following formula is used:

$$A_{corr.} = \frac{1}{1-\eta} A_{meas.} - \frac{\eta}{1-\eta} A_{bkg}, \tag{6.57}$$

where η denotes the fraction of the dataset due to background: $\eta = \frac{N_{bkg}}{N_{tot}}$. This formula is directly applicable for the BSA, the BCA and the TSA. For the tensor asymmetries it is also applicable but strictly speaking η is now defined as $\eta = \frac{N_{bkg,unpol}}{N_{tot,unpol}}$. As it has anyway been assumed that the background contamination is the same in all datasets, this detail is not important.

The background correction is applied after the systematic error has been calculated for the asymmetry. The error calculation yields

$$\begin{aligned}
dA_{A_{meas.}} &= \frac{1}{1-\eta} dA_{meas}, \\
dA_{A_{bkg}} &= \frac{\eta}{1-\eta} dA_{bkg}, \\
dA_\eta &= \frac{1}{(1-\eta)^2}(A_{meas} - (2-\eta)A_{bkg})d\eta, \\
dA_{corr.} &= \sqrt{dA^2_{A_{meas}} + dA^2_{A_{bkg}} + dA^2_\eta}
\end{aligned} \tag{6.58}$$

and the systematic error is propagated by

$$dA_{syst.,corr.} = \frac{1}{1-\eta} dA_{syst.}. \tag{6.59}$$

It is trivial to show that the above equation is true for asymmetries of count rates in individual bins. However, here it will be used to correct asymmetry moments. Hence it has been numerically verified that the result agrees with the direct, bin-wise correction that results in

$$\begin{aligned} N^+_{corr.} &= N^+ - 0.5\eta(1 + A_{bkg})(N^+ + N^-)\sin(\phi), \\ N^-_{corr.} &= N^- - 0.5\eta(1 - A_{bkg})(N^+ + N^-)\sin(\phi). \end{aligned} \tag{6.60}$$

After this bin-wise correction to a simulated dataset the asymmetry can be fitted using the usual procedure. It turns out that with ten bins the results are absolutely equivalent as long as no error on η and A_{bkg} is assumed. If these error are included, the error bars in all bins get correlated and without taking this into account the bin-wise correction would fail. Based on this result, the background correction suggested above will be used. It also keeps a nice symmetry in the treatment of the background and the signal.

So far one aspect has been neglected: The unpolarised background cross-section can be very different from the one of the signal such that η is not the same in all bins. The main effect is that the angular dependence of the background in the denominator "mixes" the asymmetry moments of the numerator. Hence e.g. a non-zero first moment of the asymmetry can be turned into additional other non-zero moments by a background without asymmetry that depends strongly on ϕ. In the simulation these effects have been found to be small. It is also possible to estimate the size of the observed effects: In a rather simplified model the background can be assumed to have a non-zero first cosine moment in the cross-section, but no dependence on charge or polarisation. The measured asymmetry can then be written as

$$A_{meas.} = \frac{N^+_{BH/DVCS} - N^-_{BH/DVCS}}{(N^+_{BH/DVCS} + N^-_{BH/DVCS})(1 + \frac{\eta}{1-\eta} + b\cos\phi)}, \tag{6.61}$$

where $\eta/(1-\eta)$ is the background-to-signal ratio and b is related to the angular dependence of the background cross-section. b has to be smaller than $\eta/(1-\eta)$ in order to conserve positivity of the background cross-section. Hence under normal conditions $1 \gg \eta/(1-\eta) > b$. Using a Taylor-expansion and an asymmetry of the signal of $A_{DVCS}(\phi) = c_1 \cos\phi$, this leads to

$$A_{meas.}(\phi) = c_1((1 - \frac{\eta}{1-\eta})\cos\phi - \frac{b}{2} - \frac{b}{2}\cos(2\phi)). \tag{6.62}$$

While the first term is the pure dilution that can be corrected for by the approach above, additional moments are generated, namely $c_0 = -c_1\frac{b}{2}$ and $c_2 = -c_1\frac{b}{2}$. Both are proportional to the true asymmetry moment c_1 but smaller than $c_1\eta/(2(1-\eta))$. A similar result is obtained in the case of a sine-shape asymmetry. As the typical asymmetries are below $c_1 = 0.3$, the maximum induced second moment with $\eta/(1-\eta) < 0.1$ is $c_{2,measured} = 0.015$. With the present precision of DVCS-measurements, this error can be neglected and the higher moments will anyway not be discussed.

7. Deeply Virtual Compton Scattering on Deuterium: Results

7.1. Introductory Comments

Due to the extraction procedure suggested in the previous section it is impossible to give the background fraction or the systematic error as a function of ϕ. Instead, both informations are only available for the leading asymmetry moment if it is considered as a function of the four-momentum transfer t. In this case the datapoints will be corrected for the background contribution and the systematic error will be shown as an error band.

If the leading moment is shown as a function of M_x, this can only be seen as a supportive plot, as the result is only determined by the missing mass resolution of HERMES. Hence also for this plot no background fraction or systematic error will be given. The systematic error can be expected to be larger as the effect of the calorimeter calibration will be worse for a fine binning in M_x.

In the case of the BSA unpolarised deuterium data from 1996/1997 is used for comparison. As these are only included for a consistency check, they are not corrected for background or supplied with a systematic error. This would require a more detailed study of the consistency of this dataset. In a second comparison the results for the BSA on hydrogen as supplied in reference [Kop04] are shown. These preliminary results are at present also without background correction or a systematic error.

7.2. Beam Spin Asymmetry A_{LU}

The beam spin asymmetry and the beam charge asymmetry are the most basic asymmetries in DVCS: They can be measured for all nuclear targets and are directly related to the imaginary and the real part of the amplitude $\mathcal{C}$ in which the GPD H/H_1 plays the leading role. Furthermore they are independent of depolarisation effects and the beam spin can only have two orientations in contrast to the spin of a nuclear target.

The beam spin asymmetry A_{LU} requires an unpolarised target and only one beam charge. In order to use a very homogeneous dataset, only positron data from 1999 and 2000 have been combined and the pre-RICH era has only be considered for a cross-check.

The uncorrected result for A_{LU} is plotted in figure 7.1 for the whole dataset from 1999/2000 and in ten bins in ϕ. The three-parameter fit results in the values shown in the figure. A clear left/right-asymmetry is visible; this is related to the moment s_1 that is negative and has a deviation of 3σ from zero. The second sine moment seems to be positive with a significance of 2σ and c_0 is compatible with zero. From theory it is expected that the coefficient c_0 is exactly zero due to invariance under parity. The coefficient s_1 is predicted to be the leading one which is obviously confirmed. The coefficient s_2 improves the quality of the fit slightly from $\chi^2/ndf = 1.82$ to $\chi^2/ndf = 1.12$. As discussed in section 2.10 a large value for s_2 can be a sign for higher twist effects, but even with a better statistical significance this could not be concluded. If s_2 is non-zero, it is due to moment mixing (smearing, bin-centring, etc.) difficult to interpret in the presence of the stronger moment s_1. The background corrected result for s_1 is

$$s_1 = -0.246 \pm 0.078(stat.) \pm 0.013(syst.).$$

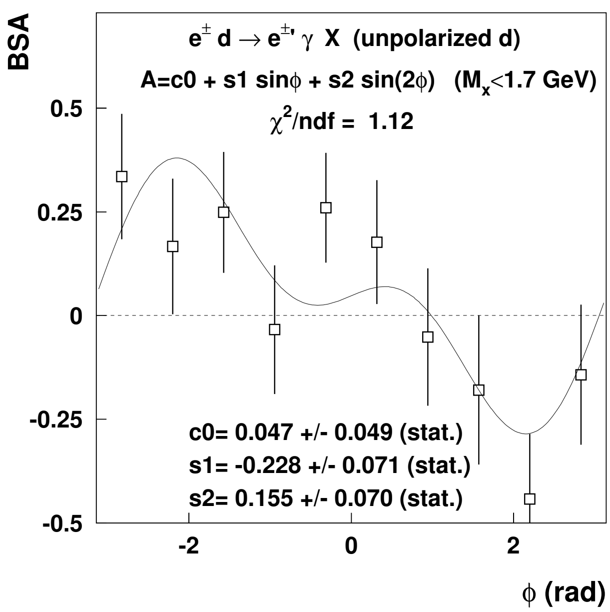

Figure 7.1.: Beam spin asymmetry on unpolarised deuterium (1999/2000) in ten bins in ϕ (without background correction). The three parameter fit and its coefficients are also shown.

The coefficient s_1 is shown in 3 bins in t in figure 7.2. In addition a preliminary analysis of deuterium data from 1996/97 is plotted. For this comparison both results are shown without background correction or systematic error band. A very good agreement is obtained although smearing effects are expected to result in a smaller background contamination for 1996/97. The background-corrected result for the asymmetry A_{UL} from 1999/2000 is shown together with its systematic error bars in figure 7.3.

The binning in t has been chosen, since although the resolution in t for the incoherent process is affected by Fermi-motion of the nucleons, it is the best variable to discriminate between different processes. Moreover the number of events is too small to perform a multi-dimensional binning and additional one-dimensional dependencies on x_B or Q^2 contain no additional information: Due to the HERMES-acceptance, small values of $|t|$ also correspond to small values of x_B and Q^2. With increasing $|t|$ also the mean values of these variables increase. The average kinematics for each bin in t is shown in table 7.1.

The large asymmetry in the lowest t-bin may have an implication as such an enhancement

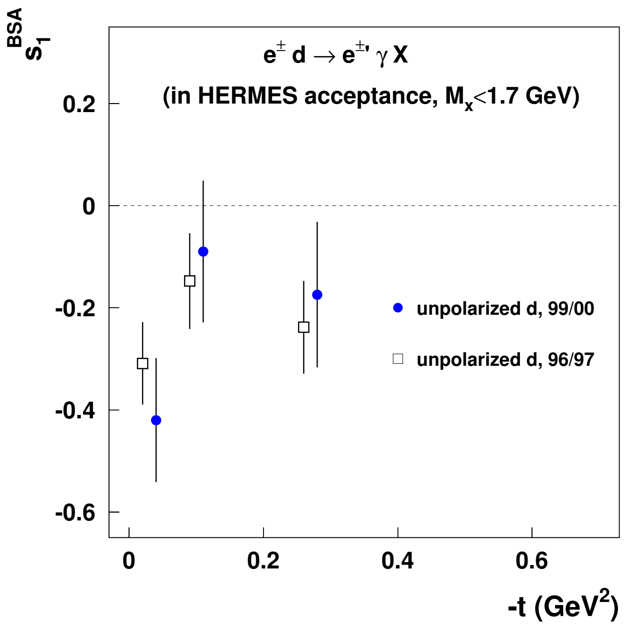

Figure 7.2.: The coefficient s_1 of the three-parameter fit applied to A_{LU} in 3 bins in t. No background-correction is applied and no systematic error is shown.

Table 7.1.: Average kinematics of the four bins in t.

t	$\langle x_B \rangle$	$\langle Q^2 \rangle$	$\langle -t \rangle$
$0.00 < -t < 0.06$	0.08	1.9	0.03
$0.06 < -t < 0.14$	0.10	2.5	0.10
$0.14 < -t < 0.30$	0.11	2.9	0.20
$0.30 < -t < 0.70$	0.12	3.6	0.42

has not been seen for the proton data [Ell03]. A comparison of the first cosine moments vs. $|t|$ for unpolarised proton data and unpolarised deuterium data is shown in figure 7.4. Both data samples are analysed in the same way, but at the moment no background correction or systematic error is available for the proton results [Kop04]. Hence both results are shown without background correction or systematic error, although these will be similar for hydrogen and deuterium data. In comparison the size of the asymmetry on the deuteron is compatible with the proton asymmetry at medium values of $|t|$ but much larger at small values of $|t|$.

On the other hand, inside the error-bars the asymmetry does not differ significantly from a flat behaviour. If the signal in the first bin is only due to the coherent process, the coherent asymmetry corrected for dilution would be close to 0.8. This is much more than theoretical predictions suggest (cf. section 2.11). On the other hand the impact of binding effects on the additional incoherent contribution is unclear.

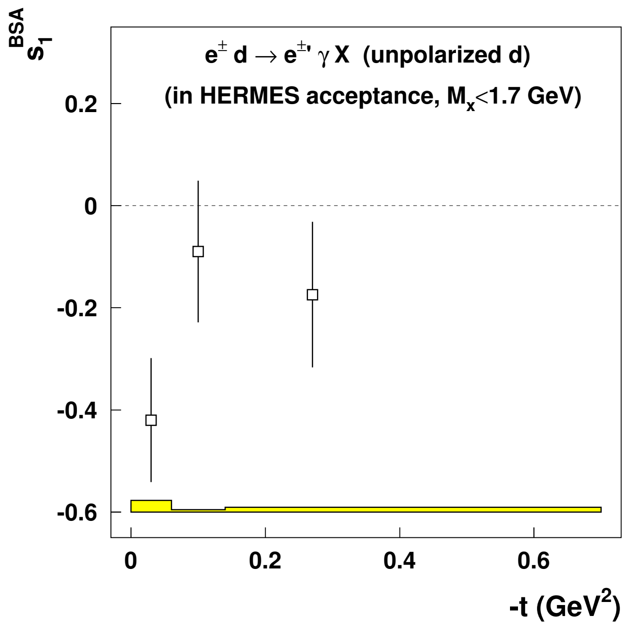

Figure 7.3.: The coefficient s_1 of the three-parameter fit applied to A_{LU} in 3 bins in t. The result is corrected for background.

In order to study the agreement of the data with expectations based on GPD-models, the t-dependence of the BSA can be compared with Monte Carlo simulations. Due to the relative fractions of the contributing processes, the predicted asymmetry is mainly sensitive to the asymmetry of the incoherent, elastic process. Even in the lowest bin in $-t$ its contribution to the event rate amounts to approximately 50%. As a complete Monte Carlo is used for the comparison, no additional uncertainty due to acceptance effects is encountered. Hence the model has to match the data inside the statistical errors, without additional bin centring errors. The systematic error is shown without the contribution from smearing, as smearing is already included in the Monte Carlo. The measured results together with the 5 models suggested in [KN02b] are shown in figure 7.5. The other ingredients of this complete model are discussed in chapter 4. In general the differences between the five models are much smaller than the statistical error bars of the data. Hence these models are indistinguishable in the case of the A_{LU}.

Although the agreement of the data with all models in the lowest bin in t is not very good, especially this bin is sensitive to other assumptions apart from the selected GPD model. While no dramatic effects are expected, the simulated BSA of the coherent process should in principle be taken from the correct formula for $t \approx t_0$ instead of equation 2.128. In addition the model for binding effects in the incoherent process is very arbitrary and can have some impact in this bin.

Also an agreement between data and simulation for large values of t is not necessarily expected, since there the contribution as well as the asymmetry of BH/DVCS with resonance excitation is unknown. Hence only in the central bin the GPD-models have to reproduce the observed asymmetry, which apparently they do.

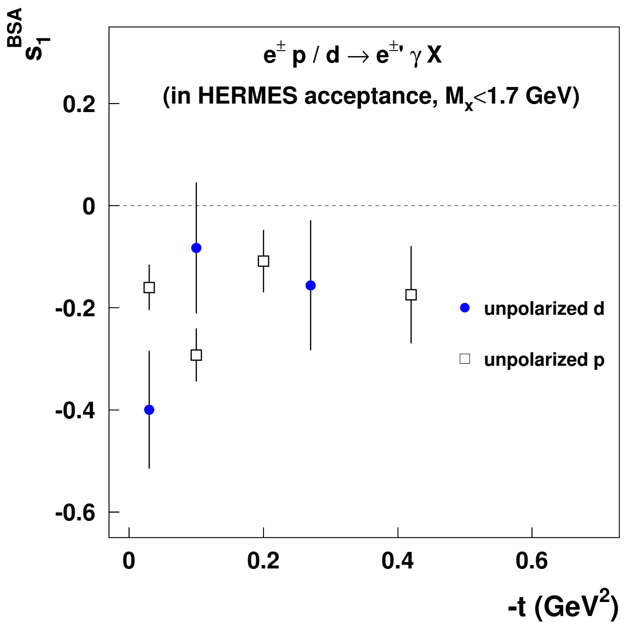

Figure 7.4.: First cosine moment of the BSA versus $-t$ for unpolarised deuterium and unpolarised hydrogen [Kop04]. No background-correction is applied and no systematic error is shown.

In figure 7.6 the asymmetry is plotted vs. missing mass for the data periods of 1996/1997 and 1999/2000. The upper cut on $|t|$ and the upper cut on θ_{γ,γ^*} have been removed in order to reduce the error bars in the non-exclusive region. For both periods of data-taking no asymmetry is seen outside the exclusive interval; if there is an asymmetry in the last M_x bin, it is only observed for leptons and photons of very low energies that are typical of this bin. Thus they are far away from the kinematic domain of BH/DVCS. Due to the larger smearing effects in 1999/2000 as compared with 1996/1997 the BH/DVCS asymmetry extends also into the fourth bin (1.4 GeV$< M_x < 2.4$ GeV).

7.3. Beam Spin Asymmetry $A_{L\pm}$

As has been discussed before, the BSA can also be calculated for a vector-polarisation balanced dataset with large positive tensor polarisation. In contrast to the conventional BSA, this result is also sensitive to the tensor moments $c^{BH}_{0,LLP}$ and $s^{I}_{1,LLP}$ (cf. section 2.11). It is known that $c^{BH}_{0,LLP} \approx c^{BH}_{0,up}$ for the coherent process in the region where it is actually observed at HERMES. Furthermore the tensor asymmetry in the incoherent process can also be assumed to be small, such that a difference between $A_{L\pm}$ and A_{LU} is mostly related to the moment $s^{I}_{n,LLP}$ of the interference term.

The result for the asymmetry $A_{L\pm}$ in ten bins in ϕ is shown in figure 7.7. No background correction has been applied for this figure. Clearly a very nice $\sin(\phi)$ curve is obtained, where the value of χ^2/ndf is rather good. The $\sin(2\phi)$ moment is zero or slightly negative inside the

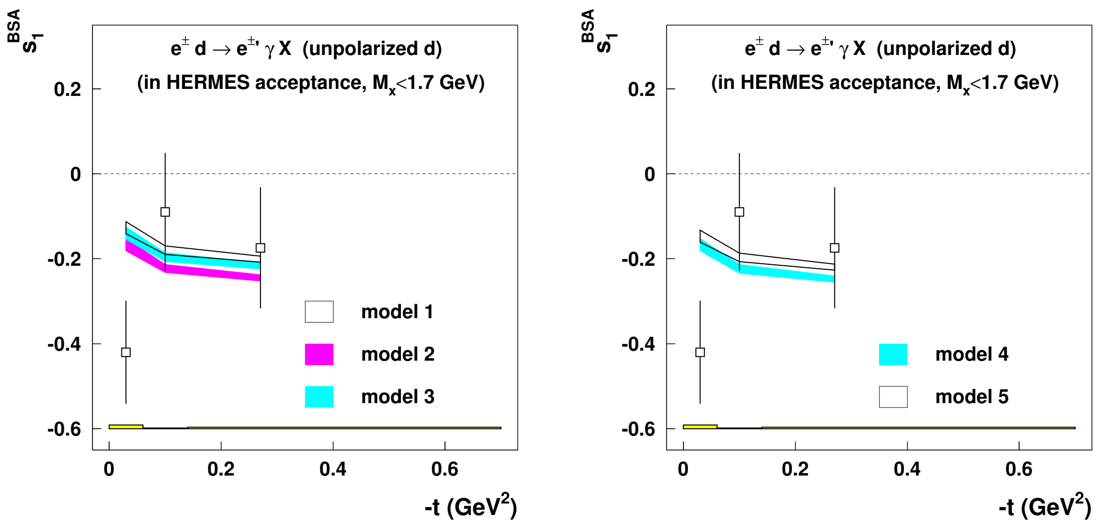

Figure 7.5.: The coefficient s_1 of the three-parameter fit applied to A_{LU} in 3 bins in t. The result is corrected for background; the systematic error does not include smearing effects. This is compared with the results of a complete Monte Carlo simulation and the 5 different models from chapter 4.

error bars, which is in contrast to the positive coefficient s_2 found for A_{LU}. The constant term is about 1.5σ away from zero.

Apparently there is no conclusive evidence for the existence of a moment s_2 since A_{LU} as well as $A_{L\pm}$ are statistically dominated by the same incoherent process. The moment c_0 is forbidden by the invariance of the process under the parity operator; the obtained deviation is not big enough to indicate an experimental problem. The background corrected result for s_1 is

$$\boxed{s_1 = -0.138 \pm 0.038(stat.) \pm 0.007(syst.).}$$

Due to the much larger dataset the error bars are much smaller than in the case of the A_{LU} and it is possible to consider four bins in t. The background corrected t-dependence of the asymmetry moment s_1 of $A_{L\pm}$ is shown in figure 7.8. A direct comparison of A_{LU} and $A_{L\pm}$ is shown in figure 7.9. Here for consistency reasons the binning with 3 bins has been adopted for both asymmetries.

The dependence of the moment s_1 of $A_{L\pm}$ on the variable t is rather flat. At least for the first 3 bins it is negative with a significance of about 2σ. In the lowest t-bin a discrepancy is seen with respect to the A_{LU}. The effect is on the verge of being significant, especially since the data from 1996/97 supports the large asymmetry of the unpolarised data. A difference between the two asymmetries would be related to binding effects in the coherent process and thus the GPDs H_3 and H_5 of the deuteron. In the kinematical approximation from reference [KM03] the ratio

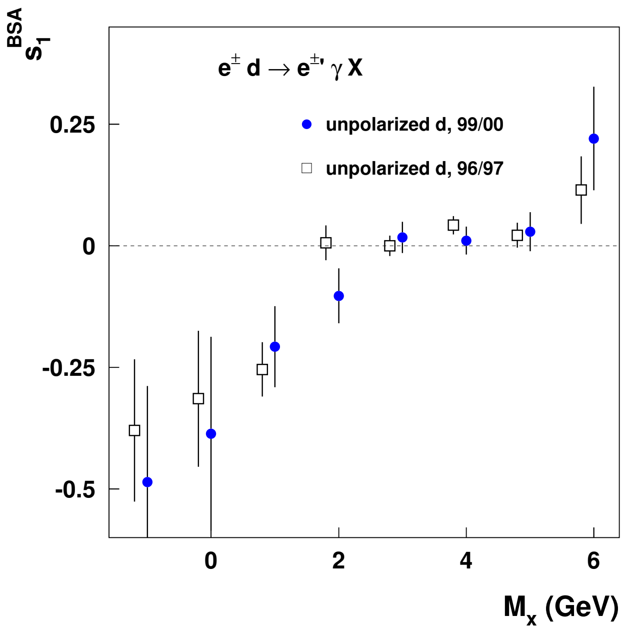

Figure 7.6.: The coefficient s_1 of the three-parameter fit applied to A_{LU} in 8 bins in M_x. The upper cut on $|t|$ and θ_{γ,γ^*} have been removed in order to increase the statistics in the semi-inclusive region in M_x.

of A_{LU} and $A_{L\pm}$ for a pure coherent deuterium sample can be written as

$$\frac{s_1^{A_{LU}}}{s_1^{A_{L\pm}}} = \frac{2G_1^2 + 2(G_1 - 2\tau G_3)^2}{2G_1^2 + (G_1 - 2\tau G_3)^2} \times \frac{\Im m(2G_1\mathcal{H}_1 + (G_1 - 2\tau G_3)(\mathcal{H}_1 - 2\tau\mathcal{H}_3) + \frac{2}{3}\tau G_3\mathcal{H}_5)}{\Im m(2G_1(\mathcal{H}_1 - \frac{1}{3}\mathcal{H}_5) + 2(G_1 - 2\tau G_3)(\mathcal{H}_1 - 2\tau\mathcal{H}_3 - \frac{1}{3}\mathcal{H}_5))}, \tag{7.1}$$

where $\mathcal{H}_3$ and $\mathcal{H}_5$ are the Compton formfactors related to H_3 and H_5, respectively, and all other occurring quantities are defined in chapter 2.

As there is apparently no difference between A_{LU} and $A_{L\pm}$ in the region where the incoherent process dominates, it is in principle possible to combine the data for $|t| > 0.06$ GeV^2. However, in this case the sample with the polarised target will dominate strongly and therefore no statistical benefit is expected. Hence a comparison of the model prediction for an unpolarised target and the datapoints for the polarised target only is shown in figure 7.10. Apparently all models are in quantitative agreement with the observed asymmetry.

The first sine moment of the asymmetry $A_{L\pm}$ vs. missing mass is shown in figure 7.11. It seems to behave differently from the first moment of A_{LU} vs. missing mass. While the asymmetry for the polarised target tends towards zero for low missing masses, the asymmetry for the unpolarised target drops continuously towards -0.5. For all bins in the exclusive region s_1 of the A_{LU} is below s_1 of $A_{L\pm}$ and hardly compatible inside the error bars. For both asymmetries s_1 seems to be positive in the highest missing mass bin. The reason for this behaviour is

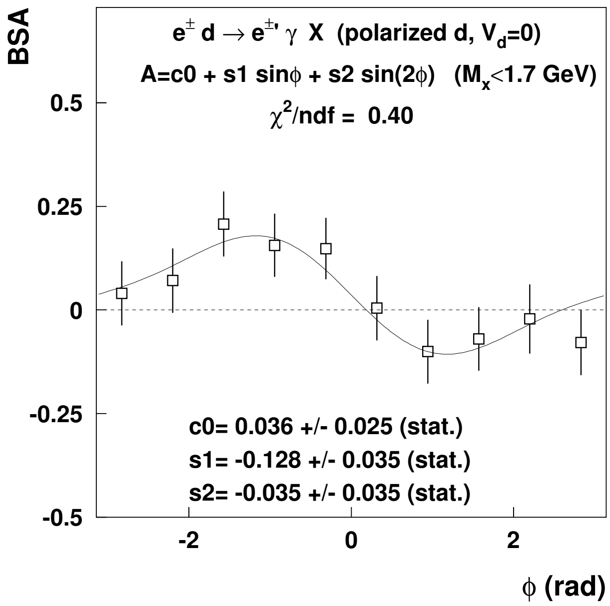

Figure 7.7.: Beam spin asymmetry on vector-polarisation balanced deuterium (1999/2000) in ten bins in ϕ. The three parameter fit and its coefficients are also shown.

unclear. Even a remaining different calibration of the calorimeter cannot necessarily explain the discrepancy. On the other hand for both asymmetries it is found that in the region were most of the semi-inclusive statistics is located (2.4 GeV$< M_x < 5.4$ GeV) the remaining background asymmetry is very small.

One remarkable feature of the interference of BH and DVCS is that the sign of the BSA depends on the beam charge. This is the reason, why the asymmetry observed at CLAS [CLAS01] has the opposite sign of the asymmetry observed at HERMES. As the electron statistics at HERMES is limited and only one beam-polarisation was used in 1998, it is not possible to construct an asymmetry $A_{LU}(\phi)$ for electron data. However, in order to verify qualitatively the sign flip, also the cross-section moments defined in equation B.10 can be calculated for each charge and polarisation separately. Apart from the trigger efficiency correction, no further correction was applied. Only for this test the beam polarisation for 1998 was required to be $|P_B| > 0.3$. The results for unpolarised and polarised deuterium are shown in table 7.2. They clearly confirm the expected sign-flip depending on beam charge and polarisation.

7.4. Beam Charge Asymmetry A_{CU}

For the beam charge asymmetry unpolarised deuterium data from 1998 (electrons), 1999 and 2000 (positrons) was used. The BCA can especially suffer from trigger inefficiencies as well as misalignment or track-finding efficiencies, as data of different years with different lepton charges are combined.

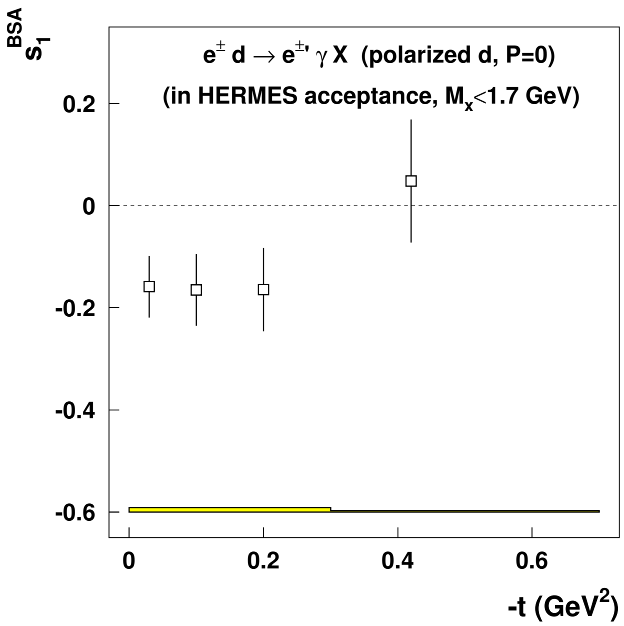

Figure 7.8.: The coefficient s_1 of the three-parameter fit applied to $A_{L\pm}$ in 4 bins in t.

Table 7.2.: The first sine moment of the observed ϕ distribution divided by $|P_B|$ is shown in the table depending on beam polarisation and beam charge. In addition the moment is shown separately for unpolarised (unpol.) and vector-polarisation balanced (pol.) target gas.

dataset	P_B	sine moment (eq. B.10)
98,e^-,pol.	-0.51	-0.113 ± 0.086
98,e^-,unpol.	-0.37	-0.132 ± 0.121
99/00,e^+,pol.	-0.54	0.068 ± 0.055
99/00,e^+,unpol.	-0.59	0.094 ± 0.068
99/00,e^+,pol.	0.53	-0.193 ± 0.042
99/00,e^+,unpol.	0.51	-0.356 ± 0.123

The beam charge asymmetry in 10 bins in ϕ is shown in figure 7.12. While the coefficient c_0 is compatible with zero, the coefficient c_1 is found to be positive with about 2σ significance. s_1 is zero inside the error bars. The obtained value for χ^2/ndf does not necessarily support the chosen fit function; errors in the analysis are on the other hand excluded as has been demonstrated by the cross-check in the previous chapter. For s_1 the expected value is $s_1 \approx \langle P_B \rangle \times s_1(A_{LU}) \approx 0.07 \pm 0.02$ which is fulfilled inside the error bars. However, this comparison suffers from the fact that the error bars of the two measurements are statistically correlated. The background corrected result for c_1 is

$$\boxed{c_1 = 0.058 \pm 0.030(stat.) \pm 0.014(syst.).}$$

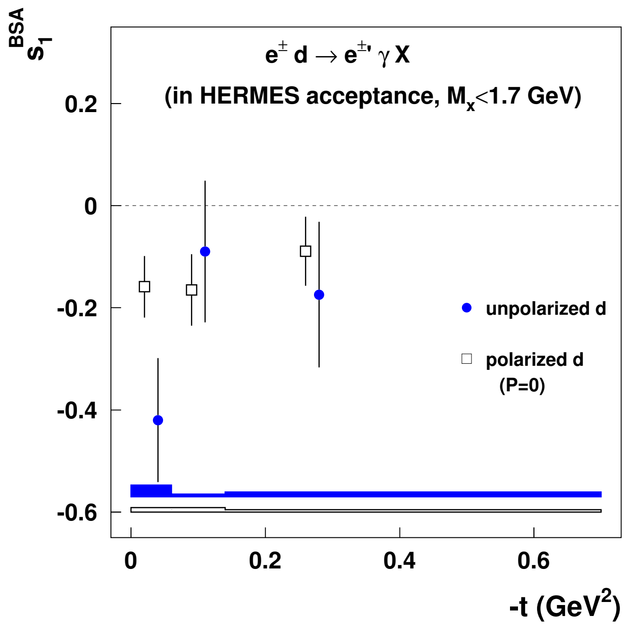

Figure 7.9.: The coefficient s_1 of the three-parameter fit applied to A_{LU} or $A_{L\pm}$, respectively, in 3 bins in t.

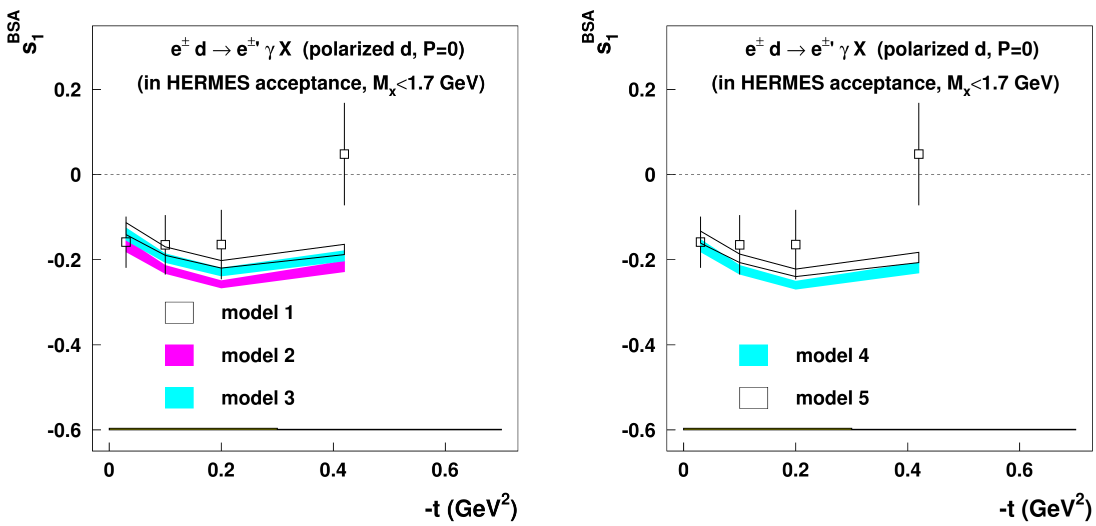

Figure 7.10.: The coefficient s_1 of the three-parameter fit applied to $A_{L\pm}$ in 4 bins in t. The result is corrected for background; the systematic error does not include smearing effects. This is compared with the results of a complete Monte Carlo simulation and the 5 different models from chapter 4.

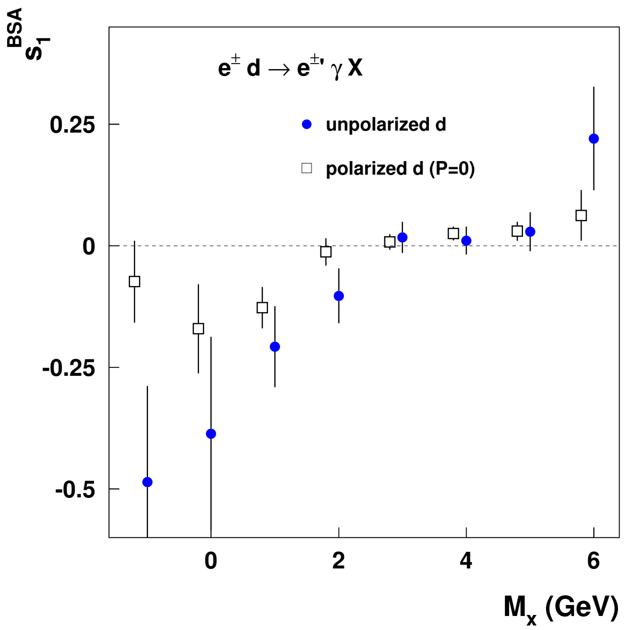

Figure 7.11.: The coefficient s_1 of the three-parameter fit applied to A_{LU} and $A_{L\pm}$, respectively, in 8 bins in M_x. The upper cut on $|t|$ and θ_{γ,γ^*} have been removed in order to increase the statistics in the semi-inclusive region in M_x.

The first cosine moment of the asymmetry binned in t is shown in figure 7.13. It can be seen that it is positive and seems to rise with increasing $|t|$. This rather large positive value is compatible with GPD-models including the D-term: As the D-term is an odd-function that is only non-zero inside the ERBL-region, its size is experimentally unconstrained and can have an almost unknown effect on all cosine moments of the interference term. However, the statistical significance of the measurement of c_1 is limited. Due to the low statistics as well as the expected systematic uncertainties, it was also not attempted to specify the kinematical dependence or the systematic error of the constant term or the higher moments.

A comparison of the measured t-dependence of the first cosine moment of the BCA with its predicted value from Monte Carlo is shown in figure 7.14. Models 4 and 5 that include the D-term according to the parametrisation from reference [GPV01] as well as the other models typically stay below the observed results in amplitude. This is more clearly seen, if the tensor polarised dataset is included (cf. following section).

The first cosine moment of the beam charge asymmetry vs. missing mass is shown in figure 7.15. A clear enhancement is seen in the exclusive region. Also here the asymmetry is still seen in the fourth bin (1.4 GeV$< M_x <$ 2.4 GeV) as in the case of A_{LU}. This is not excluded by the fractions of the contributing processes (cf. figure 4.22) and may indicate a non-zero asymmetry of BH/DVCS with resonance excitation.

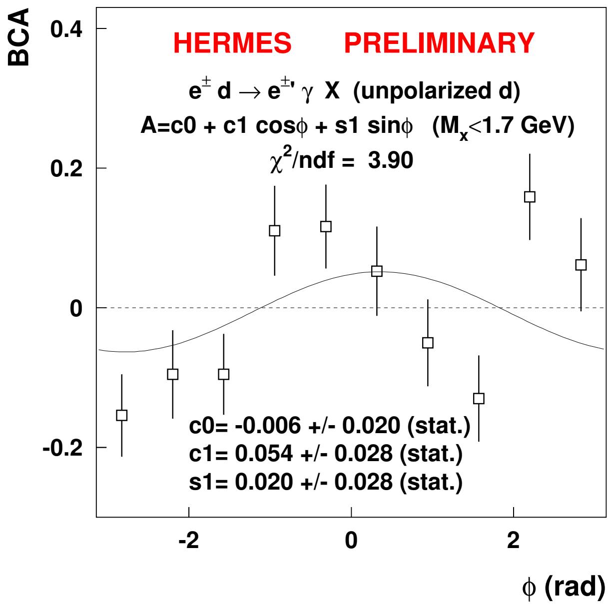

Figure 7.12.: Beam charge asymmetry on unpolarised deuterium (1998, 1999/2000) in ten bins in ϕ. The three parameter fit and its coefficients are also shown.

7.5. Beam Charge Asymmetry $A_{C\pm}$

Also the BCA can be extracted from a vector polarisation balanced dataset. The result for this asymmetry $A_{C\pm}$ in ten bins in ϕ is shown in figure 7.16. The moment c_1 is positive and 2.8σ away from zero, while the moment c_0 as well as the moment s_1 is compatible with zero inside the error bars. The low value of c_0 as well as the good quality of the fit ($\chi^2/ndf = 0.29$) indicates that the moment c_1 is indeed the leading asymmetry moment, which is also expected from theory. The value of s_1 is expected to be approximately $s_1 \approx \langle P_B \rangle \times s_1(A_{L\pm}) \approx 0.02 \pm 0.01$ which is obviously fulfilled inside the error bars.

The background corrected result for c_1 is

$$\boxed{c_1 = 0.072 \pm 0.026(stat.) \pm 0.015(syst.).}$$

The first cosine moment of the asymmetry $A_{C\pm}$ is plotted vs. t in figure 7.17. In addition the first moment of the asymmetry A_{CU} is shown in the same figure. The results are obviously very similar. In both cases the BCA drops quickly to zero for low values of $|t|$. For this reason it is reasonable to combine the unpolarised and the polarised dataset. As they contain similar numbers of events, the statistical error is strongly reduced. The asymmetries are combined in each bin in ϕ such that the statistical error is minimised (cf. [Lyo86]). In this way possible asymmetries between polarised and unpolarised count rates (not asymmetries) are removed, which would not happen if the datasets were merged directly. The obtained result is shown in figure 7.18. It is compared with 5 different model predictions.

Obviously all models underestimate the asymmetry at high values of $|t|$; at least in the third

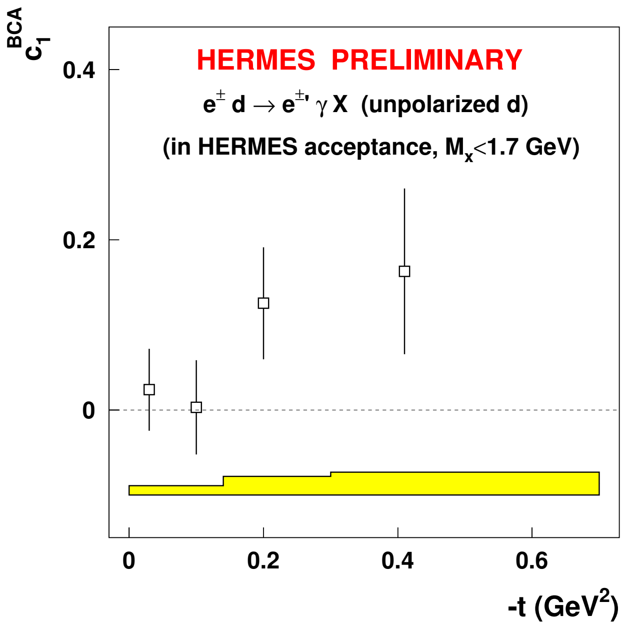

Figure 7.13.: The coefficient c_1 of the three-parameter fit applied to A_{CU} in 4 bins in t. The result is corrected for background.

bin, the datapoint is more than 2σ above the prediction according to model 5. All other models, especially those which do not include the D-term (1 . . . 3) are even lower and thus more than 3σ away from this datapoint. However, since this statistically significant asymmetry is only seen for these large values of t, there is a strong impact of the resonances. As these contribute 50% or more to the last t-bin and about 25% to the previous one, they alone can already be responsible for the observed discrepancy.

Apart from the last t-bin, where proton and neutron resonances may act differently, there is also good agreement between the free proton and the deuteron. This is shown in figure 7.19. The analysis and all cuts are equivalent for the two targets.

7.6. Target Spin Asymmetry

In contrast to the BSA or the BCA the target spin asymmetry (TSA) has the advantage that due to the rapid target spin flip at HERMES it will be difficult to obtain false asymmetries from slow changes, e.g. in calibration. A non-zero target spin asymmetry can be expected for the proton as well as for the deuteron [KM03, BMK02], but different GPD-models tend to give very different predictions. In the case of the proton the TSA is especially sensitive to the GPD $\tilde{H}$.

The TSA in 10 bins in ϕ is shown in figure 7.20. There seems to be a positive constant term with 2σ significance, while the first and the second sine moment are negative and about one σ away from zero. As all cosine moments are forbidden by invariance of the cross-section under the parity operator, the constant term is expected to be zero. This is still compatible with the

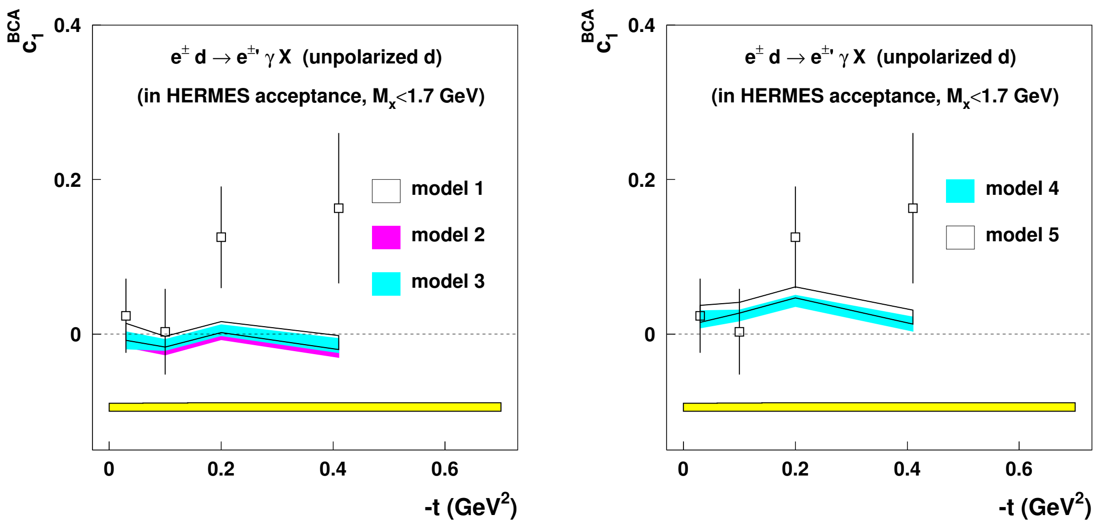

Figure 7.14.: The coefficient c_1 of the three-parameter fit applied to A_{CU} in 4 bins in t. The result is corrected for background; the systematic error does not include smearing effects. This is compared with the results of a complete Monte Carlo simulation and the 5 different models from chapter 4.

experimental result. The background corrected result for s_1 is

$$\boxed{s_1 = -0.037 \pm 0.025(stat.) \pm 0.002(syst.).}$$

It is expected to be the leading asymmetry moment, but is found to be zero or only slightly negative. $|s_1|$ is increased after the correction due to the positive asymmetry of the background. In contrast to a previous analysis [L$^+$02] there is no indication for a significant $\sin(2\phi)$ moment.

In order to separate the contributions from the different processes, the first sine moment of the TSA is plotted vs. t in figure 7.21. Inside the error bars it is compatible with zero and a large positive value as well as a large negative value can be excluded inside the observed range in t. As there is no consistent simulation of the TSA in the Monte Carlo, it is difficult to state, whether this automatically rejects some of the models in references [KM03, BMK02] as these models also predict a strong dependence e.g. on x_B.

It has not been attempted to extract a double spin asymmetry A_{LL} as defined in reference [BMK02]. In principle the asymmetry coefficient $c^I_{1,LP}$ will also show up in the TSA if the beam-polarisation is not balanced. However, as was shown in table 6.5, inside the error bars not even the leading c_0-moment is found that can be expected from the BH-process.

7.7. Tensor Asymmetries

Apart from the target spin asymmetry, a spin 1 target also allows a non-zero tensor asymmetry A_{zz}. First the asymmetry will be discussed that is derived from unpolarised and vector-

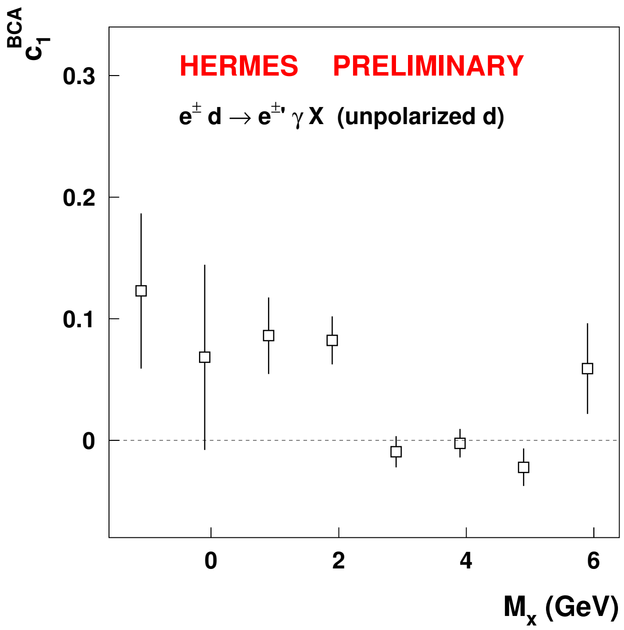

Figure 7.15.: The coefficient c_1 of the three-parameter fit applied to A_{CU} in 8 bins in M_x. The upper cut on $|t|$ and θ_{γ,γ^*} have been removed in order to increase the statistics in the semi-inclusive region in M_x.

polarisation balanced data. It has been studied for two different average beam polarisations of the data samples: 0% and -29%. The reason for this is the following: In order to remove all $\sin(\phi)$-moments of the tensor asymmetry, the beam polarisation should be zero. However, a beam-polarisation of -29% allows for better error-bars, since the smaller unpolarised dataset has this mean polarisation. If, and how much moment mixing occurs due to the remaining $\sin(\phi)$-moments in the denominator is not certain; however the effects on the extracted c_1-moment should be similarly small as the effects of the unbalanced beam-polarisation on the BCA.

The tensor asymmetry for the two average beam polarisations is shown in figure 7.22. The moments c_0 and c_1 are inside their statistical error bars compatible with zero. Especially for the sample with -29% beam polarisation the fit quality is not very good. It can be improved to a value of $\chi^2/ndf = 2.19$ if a s_2 moment is included into the fit in addition. This is shown in figure 7.23. Its interpretation is, however, very questionable.

The tensor asymmetry can also be obtained from the tensor polarised dataset that was taken at the end of the year 2000. As this is based on a completely different data-sample, an independent cross-check is obtained. The results are shown in figure 7.24. The size of the statistical error bars is in this case considerably smaller, but due to the much more limited statistics, a kinematical binning into several bins is not possible. Instead, only the fit for the lowest bin in t is also shown in figure 7.24.

In both plots the asymmetry moments s_1 and c_1 are compatible with zero. The asymmetry moment c_0 is in both cases positive with a significance of about 2σ. This can be interpreted as

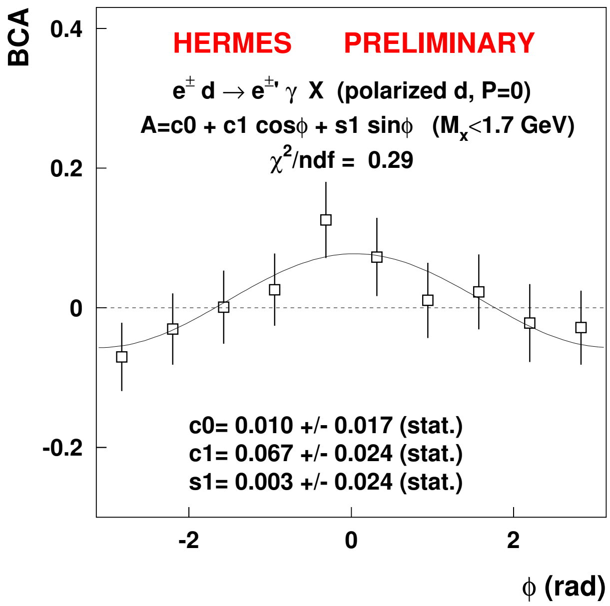

Figure 7.16.: The beam charge asymmetry on polarised deuterium (1998, 1999/2000) in ten bins in ϕ. The three parameter fit and its coefficients are also shown.

the effect of the tensor asymmetry of the coherent BH-process.

The asymmetry moment c_1 from this dataset is

$$\boxed{c_1 = 0.051 \pm 0.075(stat.) \pm 0.008(syst.)}$$

for the whole dataset and

$$\boxed{c_1 = -0.093 \pm 0.118(stat.) \pm 0.015(syst.)}$$

in the lowest bin in t, where the coherent process contributes.

Inside the error bars the values of s_1 and c_1 for the different datasets agree. The indication for a non-zero constant moment that is found for the tensor-polarised data is not seen from the combination of vector-polarisation balanced and unpolarised data. However, this can be related to a slightly different calorimeter calibration for the combined two data samples.

For the polarised/unpolarised dataset from 1999/2000 kinematical binning is statistically possible, although the error bars are large. The tensor asymmetry from these data as a function of t is shown in figure 7.25. The left hand plot shows the first cosine moment, while the second plot shows the second sine moment. While the cosine moment is always zero inside the error bars, there seems to be an indication for a polarisation dependent $\sin(2\phi)$ moment. Apparently this moment is found in the whole t-range (cf. figure 7.23) which indicates that it is most probably an experimental artefact or an unlikely statistical fluctuation. The only other explanation would be a non-vanishing large tensor effect also for the incoherent process, where in addition the higher twist moment s_2 has to be approximately -0.9 (after dividing the extracted fit parameter by the beam polarisation).

In order to access the beam polarisation dependent tensor-moment s_1 the asymmetry A_{Lzz}

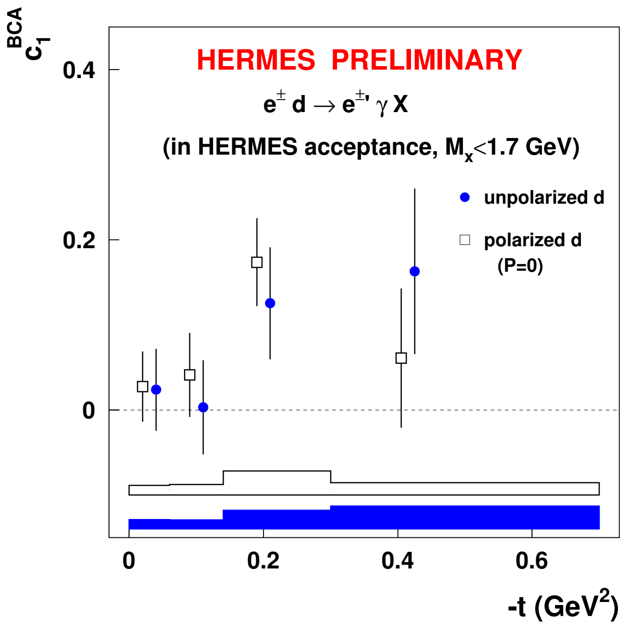

Figure 7.17.: The coefficient c_1 of the three-parameter fit applied to A_{CU} or $A_{C\pm}$, respectively, in 4 bins in t. The result is corrected for background.

was calculated from unpolarised and vector-polarisation balanced deuterium data. It is shown in 10 bins in ϕ in figure 7.26. Clearly the error bars are large, but again a large s_2 coefficient is found (2σ deviation from zero) while the coefficient s_1 is zero inside the error bars. The large s_2-moment reflects the large value of the same moment that was found in the case of A_{zz}. As the datasets have a very strong overlap, this agreement is expected but no additional proof for the existence of an apparent moment s_2.

The assumption that the extracted moment s_2 is not due to the BH/DVCS cross-section is supported by the tensor-polarised dataset from 2000. The asymmetry shown in figure 7.27 (left plot) has smaller error bars and shows no indication of a $\sin(2\phi)$ moment. All extracted moments are compatible with zero inside the error bars. The second plot in figure 7.27 (right) shows the asymmetry for low values of $|t|$ ($-t < 0.06$ GeV^2). Also here all moments are inside of 1.5σ compatible with zero.

The asymmetry moment s_1 from this dataset is

$$\boxed{s_1 = -0.117 \pm 0.136(stat.) \pm 0.010(syst.)}$$

for the whole dataset and

$$\boxed{s_1 = -0.255 \pm 0.213(stat.) \pm 0.021(syst.)}$$

in the lowest bin in t, where the coherent process contributes.

Finally for the vector polarisation balanced / unpolarised dataset it is again possible to extract the $|t|$-dependence of the coefficient s_1 of the asymmetry A_{Lzz}. This is shown in figure 7.28. No clear deviation from zero is seen, but the error bars are admittedly rather large.

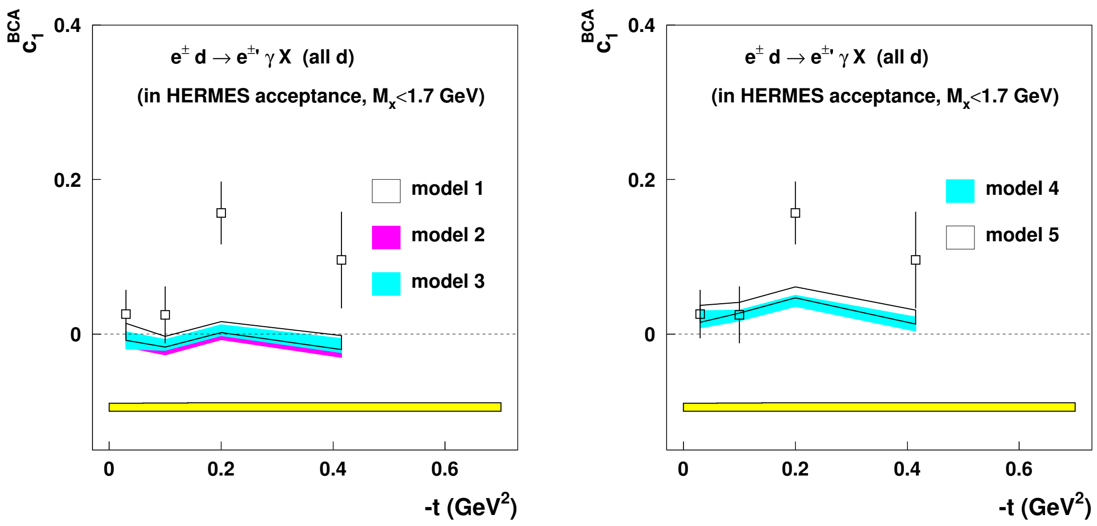

Figure 7.18.: The coefficient c_1 of the three-parameter fit applied to the combined BCA in 4 bins in t. The result is corrected for background; the systematic error does not include smearing effects. This is compared with the results of a complete Monte Carlo simulation and the 5 different models from chapter 4.

7.8. Summary and Conclusion

In this analysis all possible asymmetries of the BH/DVCS interference term have been extracted that can be accessed with a longitudinally polarised deuterium target and a polarised electron/positron beam. HERMES is the first experiment to perform these measurements; as it was designed for the study of completely different physics processes, the statistical accuracy of these results is limited and it was mainly attempted to obtain the leading asymmetry moments that correspond to leading twist.

In terms of the leading asymmetry moments, clear evidence for a beam spin asymmetry due to the interference of BH and DVCS has been found. Its behaviour is compatible with existing model calculations. The same is true for the beam charge asymmetry which is affected by larger uncertainties, since different years with different beam charges have to be combined.

There is at present no indication for a strong target spin asymmetry in the HERMES data. However, as the asymmetry is predicted to be quite sensitive to the specific kinematics [KM03], this does not exclude a sizable asymmetry for other experiments.

Tensor asymmetries can be extracted from the existing datasets, but have much larger errors than the other asymmetries. Depending on the event sample an unphysical moment s_2 is observed with 3σ significance which hints at incompatibilities between the polarised and unpolarised dataset. It is unclear if the difference between A_{LU} and $A_{L\pm}$ in the lowest bin in $|t|$ is a statistical fluctuation or related to the same effect. If such a difference exists, it is related to the tensor moment $s^I_{1,LLP}$ and thus also the moment s_1 of the asymmetry A_{Lzz} would be expected to be non-zero. This is not confirmed if A_{Lzz} is extracted from unpolarised and vector-polarisation balanced deuterium data, which is effectively a sub-sample of the same

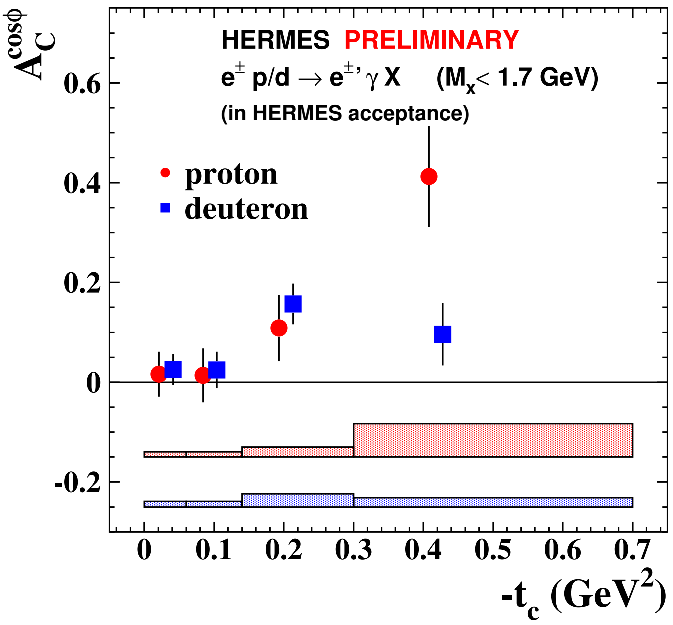

Figure 7.19.: The coefficient c_1 of the three-parameter fit applied to the BCA on hydrogen and deuterium, respectively, in 4 bins in t. The deuterium dataset is merged from unpolarised and vector-polarisation balanced target states. The result is corrected for background.

dataset.

A different analysis based on tensor-polarised data ($T \approx 1$ / $T \approx -2$) yields smaller statistical error bars, since error propagation favours this method. On the other hand due to the low number of events only the lowest $|t|$-bin has enough statistics to allow for a correct extraction of the asymmetry moments and their errors. For the whole t-range as well as for the lowest bin in t, the result for s_1 and s_2 of the asymmetry A_{Lzz} are compatible with zero inside the error bars. This suggests that a true discrepancy between A_{LU} and $A_{L\pm}$ is unlikely. In general much more event statistics would be necessary to study the tensor asymmetries in detail.

At the moment it is not expected that more target-polarised deuterium data will be taken at HERMESsuch that this problem cannot be solved. The remaining experimental problem of the calorimeter calibration on the other hand will be corrected for in the new offline production of the data taken in the year 2000. If this correction does not improve the situation, it is suggested to reconsider the proposed position dependent recalibration of the calorimeter (cf. section 5.4). This method eliminates the discrepancy between the missing mass distributions for positron and electron data, removes the obvious mis-calibration of the calorimeter for low values of $|\theta_x|$ and large values of $|\theta_y|$ and leads to a better agreement of data and Monte Carlo simulation.

A more ambitious analysis of the available data for DVCS would face the following problems: Although it has been checked that the higher asymmetry moments obtained in the fits are inside the error bars not larger than the leading asymmetry moments, an explicit extraction of higher twist effects is very difficult. Firstly, at present the statistical error bars of the leading coefficients are so large that a statistically meaningful ratio of leading moment to sub-leading mo-

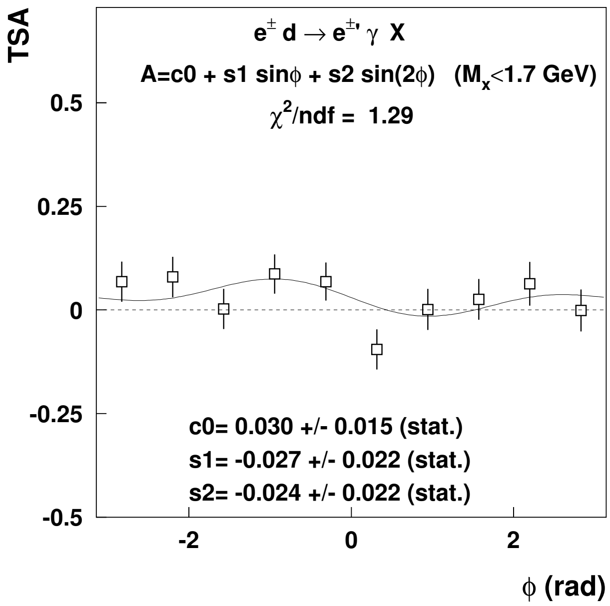

Figure 7.20.: The target spin asymmetry on vector polarised deuterium (1999/2000) is plotted in ten bins in ϕ. The three parameter fit and its coefficients are also shown.

ment cannot be obtained. Secondly, kinematical smearing affects the higher moments stronger than the leading ones. And finally acceptance dependent bin-centring effects as well as the higher BH-moments lead to moment mixing, such that extracted higher moments can be by a factor of 10 or more larger than the original ratio $c^I_{2,up}/c^I_{1,up}$ or $s^I_{2,up}/s^I_{1,up}$.

Finally, although the leading moments of the BSA and the BCA have non-zero values, the interpretation of these asymmetries is difficult: With the present apparatus the datasets consist of events that are due to 5 different processes, even after a background correction is applied:

- coherent BH/DVCS on the deuteron,
- incoherent BH/DVCS on the proton,
- incoherent BH/DVCS on the neutron,
- incoherent BH/DVCS on the proton with excitation of a nuclear resonance,
- incoherent BH/DVCS on the neutron with excitation of a nuclear resonance.

Hence it is impossible to disentangle the different contributions to the asymmetries and even if one process has no asymmetry at all, this cannot be noticed. Consequently the obtained results can be used to constrain GPD models, but a consistent theoretical understanding of all encountered physics processes is required.

It is clear that the detection of the recoiling target particles would allow for the separation of the different processes, but they are usually far outside the standard HERMES acceptance. In

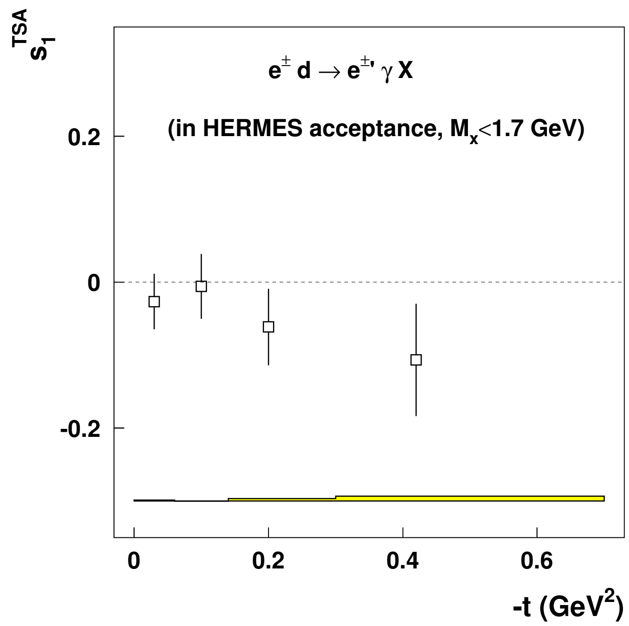

Figure 7.21.: The coefficient s_1 of the three-parameter fit applied to the TSA on deuterium is shown in 4 bins in t. The result is corrected for background.

order to solve this problem that is also encountered in the case of the hydrogen analysis, the installation of a recoil detector is currently prepared. Its design and planned operation will be discussed in the remaining chapters.

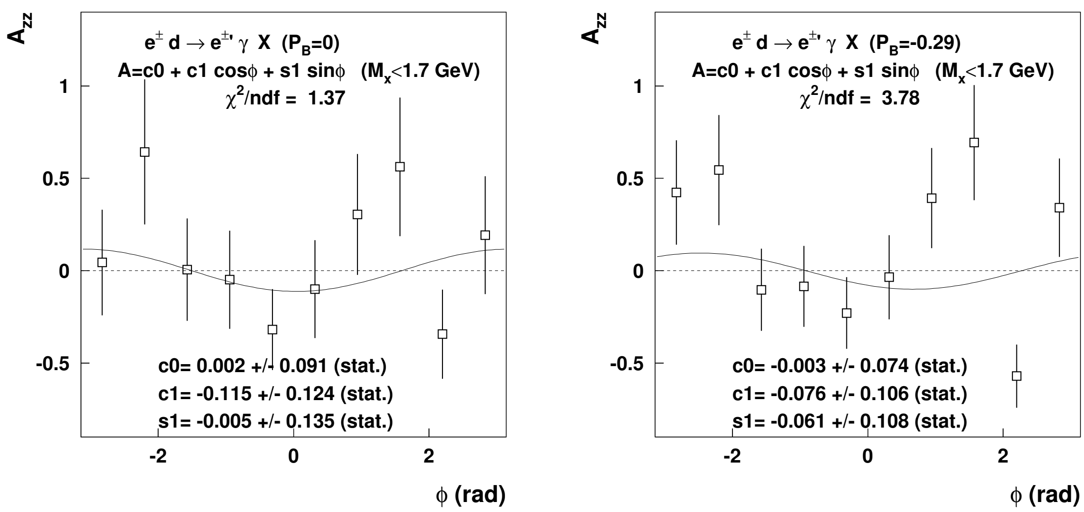

Figure 7.22.: The tensor asymmetry A_{zz} obtained from unpolarised and vector polarised deuterium (1999/2000) in ten bins in ϕ. The three parameter fit and its coefficients are also shown. The left-hand plot is for a balanced beam polarisation of $P_B = 0$, while the right-hand plot is for a balanced beam polarisation of $P_B = -0.29$.

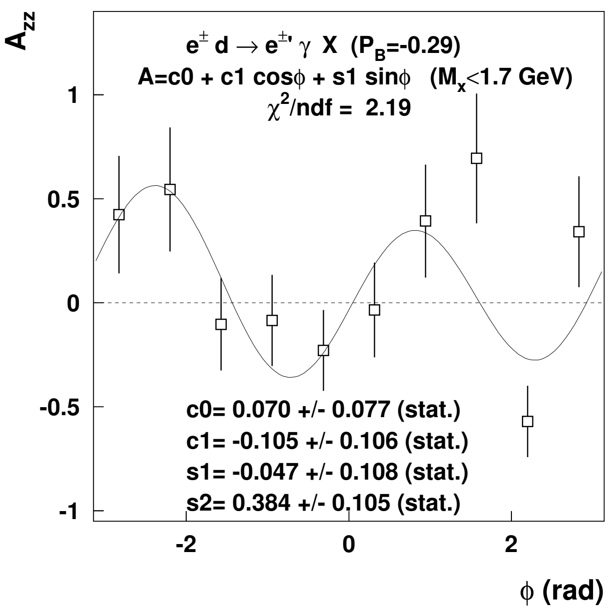

Figure 7.23.: The tensor asymmetry A_{zz} obtained from unpolarised and vector polarised deuterium (1999/2000) in ten bins in ϕ. A four parameter fit containing the moments c_0, c_1, s_1 and s_2 and its coefficients are also shown. The beam-polarisation is balanced to $P_B = -0.29$.

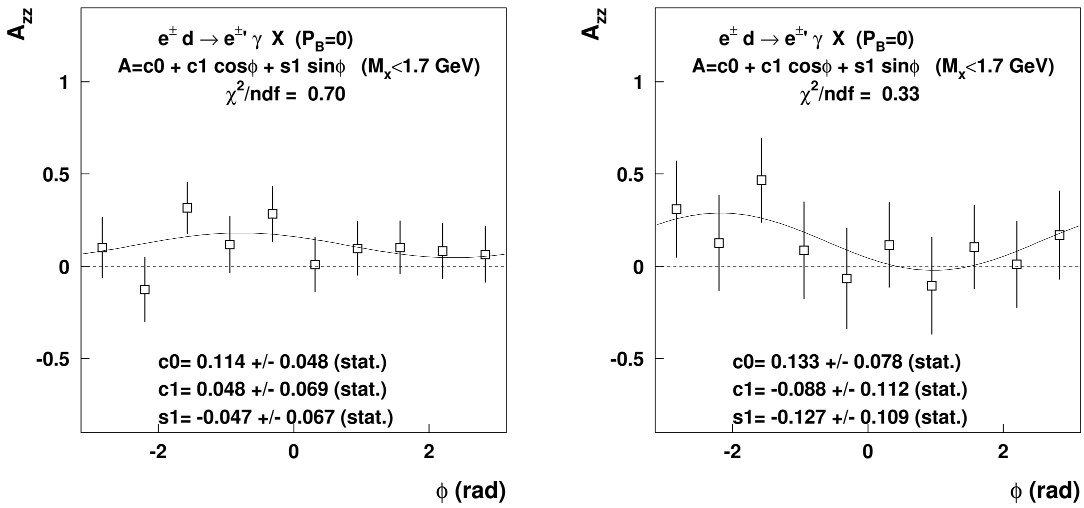

Figure 7.24.: The tensor asymmetry A_{zz} obtained from tensor polarised deuterium (2000) in ten bins in ϕ. The three parameter fit and its coefficients are also shown. The asymmetry for the whole dataset (left plot) and only for $-t < 0.06\ \mathrm{GeV}^2$ (right plot) are shown.

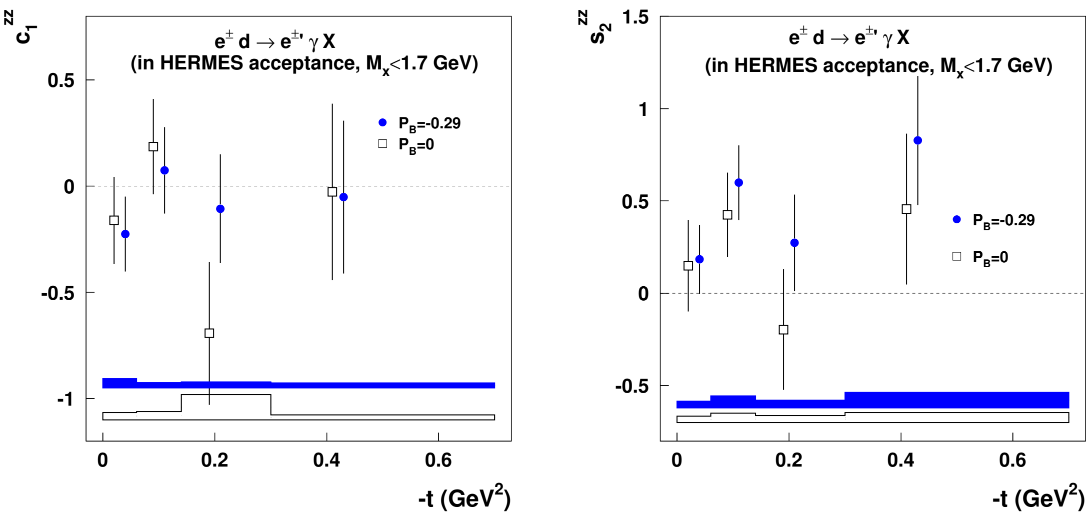

Figure 7.25.: The coefficient c_1 of the three-parameter fit applied to A_{zz} on deuterium in 4 bins in t (left). The coefficient s_2 (right) for an additional term $s_2 \sin(2\phi)$ that is included into the fit is also shown (systematic errors are assumed to be the same as for s_1 of the asymmetry A_{Lzz}). The results are corrected for background.

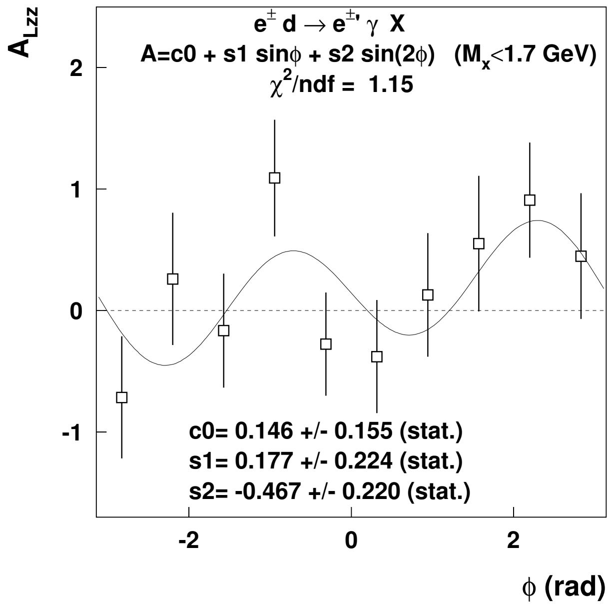

Figure 7.26.: The tensor asymmetry A_{Lzz} obtained from unpolarised and vector polarised deuterium (1999/2000) in ten bins in ϕ. The three parameter fit and its coefficients are also shown.

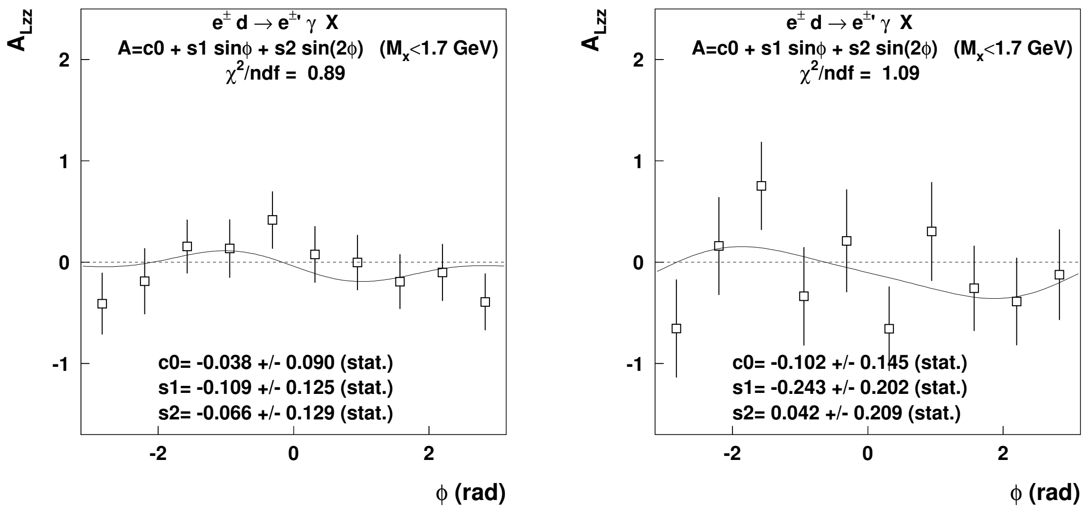

Figure 7.27.: The tensor asymmetry A_{Lzz} obtained from tensor polarised deuterium (1999/2000) in ten bins in ϕ. The three parameter fit and its coefficients are also shown. The asymmetry is shown for the whole range in t (left) and only for the first bin in t (right).

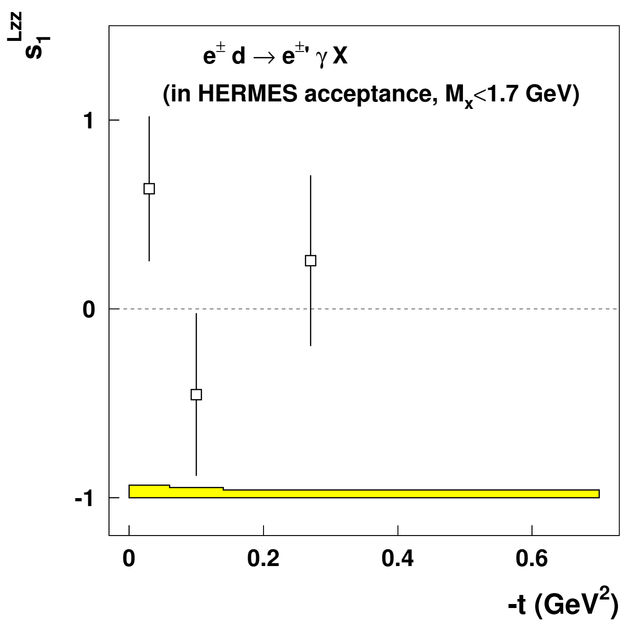

Figure 7.28.: The coefficient s_1 of the three-parameter fit applied to A_{Lzz} on deuterium in 3 bins in t. The result is corrected for background.

8. Design of the HERMES Recoil Detector

8.1. Required Improvements

The discussions of the previous chapters show that a main experimental problem in the study of hard exclusive reactions is the requirement to select one specific exclusive process. The present missing mass resolution of $\Delta M_x^2 \approx 1.5$ GeV^2 (from the simulation) is not sufficient to accomplish this. Other exclusive processes like π^0-production, or also semi-inclusive processes with special decay kinematics can mimic the reaction of interest.

A procedure similar to a sideband-subtraction is not possible, since exclusive BH/DVCS-events are located at the lower edge of the missing mass distribution. The extrapolation of DIS-type contributions to the exclusive region requires a good understanding of detector smearing as well as of fragmentation processes under very special decay kinematics. If an interpretation in terms of GPDs is aimed for, it is also necessary to remove BH/DVCS with resonance excitation from the data-sample.

In order to reduce such background from the very beginning it is better to choose a hydrogen target than a deuterium target. Thus also the complication of nuclear binding effects is avoided. The rejection of the remaining background requires a new detector - the HERMES Recoil Detector - as improvements on the existing apparatus are essentially not possible. This has the following reasons:

1. The main contribution to the missing mass resolution is due to the energy resolution of the calorimeter. The nominal resolution of several calorimeters [Par00] is plotted in figure 8.1. While the resolution of the HERMES calorimeter is worse than for other lead glass calorimeters, its performance is similar e.g. to sandwich calorimeters. For HERMES an important contribution to the energy resolution at low and medium energies is due to the preshower detector. The width of the exclusive peak in the missing mass distribution could be reduced by removing the preshower (a minimum value of 1.0 GeV^2 could be achieved). However, this is not possible, as the preshower is an essential detector for particle identification, i.e. it is especially needed for all non-exclusive physics programs. In addition the improved resolution would still not be sufficient to separate exclusive BH/DVCS from resonance contributions.

2. Another contribution to the missing mass resolution arises from the momentum resolution for the lepton track. In this case it is known that the insertion of the RICH detector together with the removal of the high resolution VCs degraded the momentum resolution from about 1% to about 2% (cf. figure 3.6 and reference [HERMES98]). The RICH detector is needed for all other physics programs such that it cannot be removed. The vertex chambers (VCs) were foreseen in the original design of the HERMES spectrometer, but due to technical problems they were only operated in 1996. These chambers allowed

to obtain a tracking resolution in the front-region that was dominated by multiple scattering. However, also if a detector similar to the VCs would be installed and the RICH removed, the missing mass resolution would only be improved to 1.3 GeV^2.

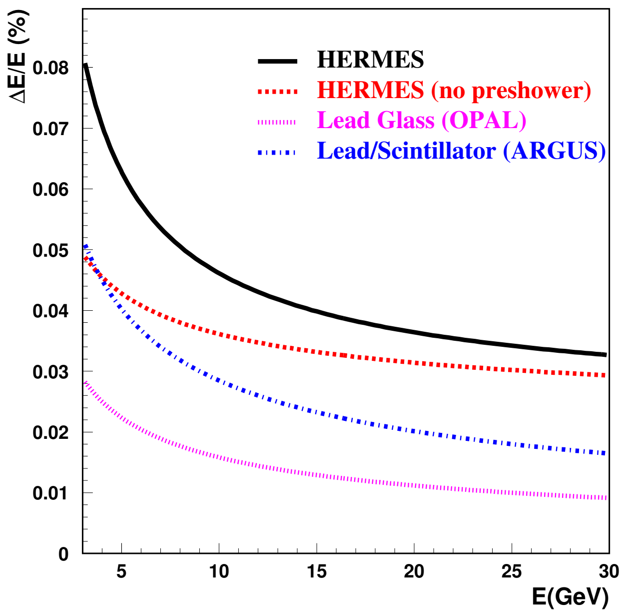

Figure 8.1.: Energy resolution of 3 different calorimeters [Par00]: HERMES , OPAL and ARGUS. In addition the resolution of the HERMES-calorimeter is shown, if the preshower is removed.

This indicates that essentially a new spectrometer, especially designed for exclusive reactions, would be needed in order to improve exclusivity by means of a missing mass analysis [Ryc02, Group01].

On the other hand an additional detector with limited dimensions can be added to detect the hadronic final state of the exclusive reactions. Such a detector need not provide a trigger signal or a very advanced particle identification and can therefore be constructed with only a few detector layers of limited complexity.

In this case a compromise has to be made between statistics and the number of accessible observables: On the one hand high target density is needed to collect enough BH/DVCS-events within the assigned running period of 2 years (2005-2007). This automatically rules out a polarised internal gas target. The removal of the present polarised gas feed system also frees a lot of space around the target region, such that the recoil detector can cover a larger acceptance. On the other hand, the change to unpolarised hydrogen gas limits the physics program to the measurement of the BCA and the BSA only. The measurement of a target spin asymmetry is excluded. Consequently the recoil detector in combination with the HERMES spectrometer can only be seen as a pioneering experiment, while a complete extraction of the GPDs requires a lot more work.

The contribution of HERMES to a possible extraction of the GPDs can be summarised as follows: In principle 8 independent quantities, namely the real and imaginary parts of the 4 Compton Form Factors (CFFs) of the proton can be measured in DVCS. The measurement of the BSA and the BCA constrains only one linear combination of the CFFs (real and imaginary part). The analysis is non-trivial, as the pure DVCS cross-section σ_{DVCS} cannot be neglected but contributes on the 10%-level to the observed rates [KN02a]. And even if all CFFs were known, the GPDs cannot be extracted at a single point, but are only accessible due to their evolution in Q^2 (cf. [Fre99]). A flavour separation into u and d quarks requires in addition complementary data from at least one exclusive meson production process.

On the whole this indicates that measurements with the recoil detector do not allow for a direct determination of the GPDs but rather provide observables that can be compared with theoretical models of the GPDs which can in turn be compared with lattice calculations. Consequently it was decided to dedicate the 2 years of operation to studies with unpolarised hydrogen only. Projections for this program have been made in [KN02b].

The main goal of the recoil detector is the observation of the recoil proton that is emitted in hard exclusive photon/meson production. However, even if a proton is observed, it is not totally obvious that this detection of an additional particle also improves exclusivity. In fact, a missing mass analysis including the recoil proton track will not be successful in separating zero missing mass from the missing mass of a pion. Figure 8.2 illustrates the reason for this by showing a typical DVCS-event: The longitudinal components of the particle momenta along the beam are of very different size. Since the relative momentum-resolution $\Delta P/P$ for leptons and photons is roughly independent of the momentum and in the order of 2% and 4%, respectively, it is clear that the small longitudinal momentum of the recoil proton is practically unknown and additional pions could be produced. On the other hand the transverse momentum components of all 3 particles are of similar size such that a comparison can be meaningful. A recognition of a different final state is made feasible by the fact that additional slow pions from target fragmentation processes can have transverse momenta in the order of 100 MeV/c or more.

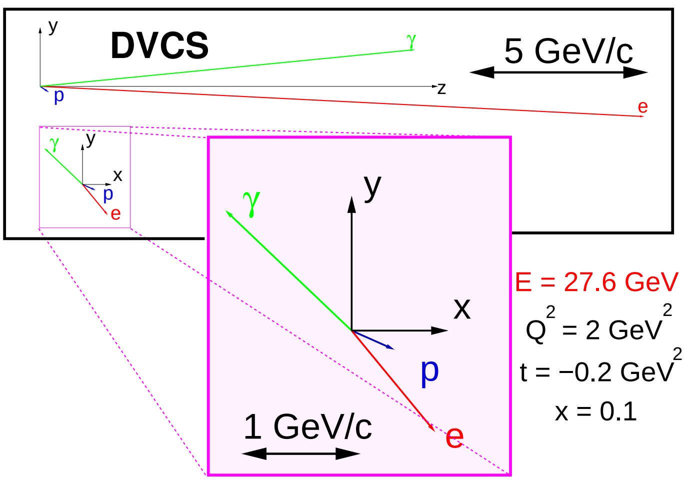

Figure 8.2.: Typical event kinematics for DVCS at HERMES in two different projections: Along the x-axis (top) and along the z-axis (bottom).

One limitation of this comparison is that it fails for certain kinematics: If an additional pion is emitted close to the beam direction, it cannot be deduced from a recoil-detection-technique. This shows that the recoil detector is only able to remove background processes with some probability. Even a perfect recoil detector could not improve this situation. Due to the suggested application of the detector its resolution only has to be as good as required by the resolution of the spectrometer. As has been shown in [Kra00] this can be translated into a required resolution of $\delta\phi_p < 0.1$ rad for the angle of the proton around the direction of the lepton beam, while the resolution for the transverse momentum component should be smaller than 10%. If the detector resolution is better, this will only have a marginal impact on the background rejection.

Obviously the acceptance of the recoil detector should be as large as possible. This means that the detector has to detect recoil protons from the lowest to the highest expected momenta and also the coverage in solid angle should be large. Again, as the recoil detector acts as a supplement to the spectrometer, the required acceptance of the recoil detector is defined by the acceptance of the spectrometer and the cuts on kinematics that are imposed.

Apart from this positive detection of recoil protons, it may also be possible to operate the recoil detector as a veto counter: In all kinds of exclusive processes additional charged pions can cause low momentum tracks in the full range in θ_p with an enhancement into the forward direction. Due to the relatively low pion mass, such tracks can have the energy deposition of a minimum ionising particle, although the momentum is only in the order of a few 100 MeV/c. If possible these tracks have to be detected. This fixes the minimum detector threshold for the energy deposition.

In order to discriminate between a recoil proton and a π^+ of the same momentum a limited PID is required. For DVCS the more dangerous species are the π^0s: As they are not charged, a proton instead of a neutron will emerge from the hydrogen target. If the cut on the proton kinematics is not successful, it may be interesting to look for the decay photons of the π^0. This requires some detector with high conversion probability for the photons as well as high detection efficiency for the beginning shower. It is not necessary to contain the shower inside the detector; on the other hand, the spatial resolution for the position of the shower should be sufficient.

The criteria for the recoil detector can be summarised in the following way:

- Recoil protons:
  - large acceptance (defined by physics cuts and spectrometer acceptance),
  - angular resolution and momentum resolution defined by spectrometer,
  - high detection efficiency,
  - no trigger output required.
- Charged pions:
  - very large acceptance (as hermetic as possible),
  - moderate angular and momentum resolution,
  - very high detection efficiency,
  - no trigger output required.

- π^0-decay photons:
  - very large acceptance (as hermetic as possible),
  - moderate angular resolution, no momentum determination,
  - very high detection efficiency,
  - no trigger output required.

8.2. Conceptual Design

In order to meet these requirements it is first of all necessary to study the required acceptance for DVCS protons. *gmc_dvcs* has been used to obtain the distribution of recoil protons from a hydrogen target. The analysis cuts for the events to be detected have to be adapted to the new situation:

All cuts that are related to the inclusive scattering kinematics of the lepton will essentially be the same as in chapter 7. The cut of 3 GeV on the cluster energy does not cut into the exclusive statistics and can still be used. The cut on the preshower energy drastically improves the energy resolution of the calorimeter and should be kept.

Other cuts can probably be released: The lower cut of $\theta_{\gamma,\gamma^*} > 5$ mrad on the angle between the real and virtual photon will not be needed, as the opening angle between the virtual photon and the recoil proton is sufficiently large that the angle ϕ can still be reconstructed with high precision. The upper cut on θ_{γ,γ^*} and the upper cut on $|t|$ that are used at the moment are necessary to suppress the background. Since the exclusivity is determined using the recoil detector, it may be possible to open these cuts and e.g. go back to the cut of $\theta_{\gamma,\gamma^*} < 70$ mrad that was used for the first HERMES publication. As this leads to a very inhomogeneous acceptance, for all following simulations the cut on t has been skipped, while the upper cut on θ_{γ,γ^*} has been kept. The cut on the square of the missing mass can be raised to 5 GeV^2 or more.

Only protons from events that pass the cuts have to be detected by the recoil detector. In figure 8.3 the distribution of these recoil protons is shown in dependence on the angle θ_p relative to the beam and the recoil proton momentum p_p. As p_p is directly related to t (in the non-relativistic limit $p_p = \sqrt{-t}$), increasing p_p also means increasing $-t$. This implies that the lowest proton momenta correspond to the lowest values of $|t|$. In order get close to the limit of $t = 0$ for which Ji's sumrule is defined (cf. section 2.3), these protons are of special interest.

Consequently the aim must be to have a detector component that is able to spot protons close to the primary vertex. This is necessary in order to minimise the amount of inactive material in front of the device. The technical realisation of this problem has been studied at HERMES for quite some time [HER97, vB+98] in a different context. It turns out that semiconductor-sensors are well suited for this purpose as they can be installed inside the HERMES target chamber without affecting the target vacuum ($\sim 10^{-8}$ mbar) or being affected by the vacuum. In this case the detector is only separated from the primary vertex by the target cell made of aluminium. The present cell has a wall-thickness of 75 μm, but in future the cell-wall can be much thinner ($\leq 50\mu$m). It was discussed to replace the target cell with a different internal gas target type, e.g. a cluster target or a jet target, but the spatial dimensions of these devices turned out to be incompatible with the requirement of covering a large acceptance with sensors.

The expected occupancy of the semiconductor-detector is still rather low such that silicon strip counters can be used. Since this is already a quite conventional detector type, research

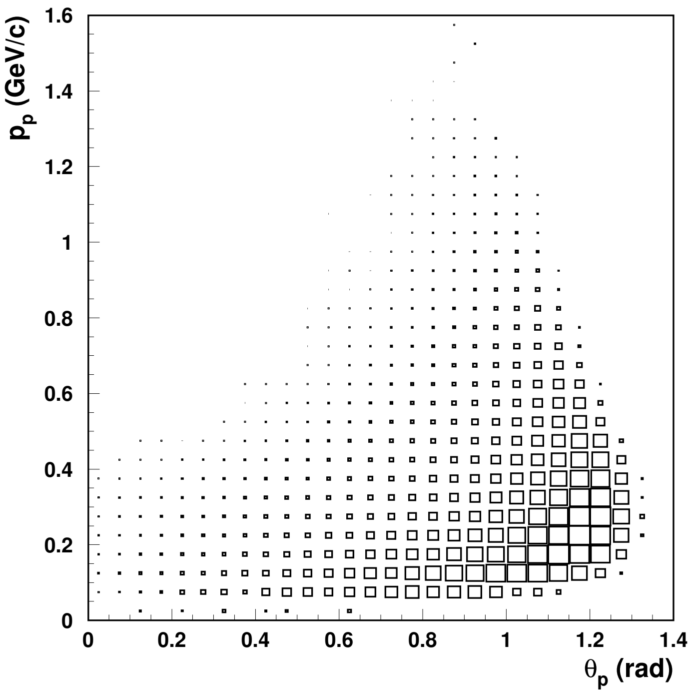

Figure 8.3.: Distribution of recoil protons within the applied cuts as function of the angle θ_p and the momentum (p_p).

efforts on the sensor layout could be minimised. Considerable knowledge about this detector type exists at HERMES and also readout chips that are tuned to the HERA bunch-frequency are available.

In order to obtain a momentum measurement and particle identification for such low momentum particles, two silicon detectors can be combined to form a silicon telescope. If the particle is stopped, its energy can directly be measured, while the PID can be obtained from dE/E. If the particle penetrates both layers, no particle identification is possible but the particle momentum can still be calculated from the energy deposition in both layers under the assumption that it was a proton.

This technique is only applicable for proton momenta below 500-700 MeV/c as for higher momenta the fluctuations in energy loss together with the very flat Bethe-Bloch-curve do not allow for a momentum measurement. On the other hand higher momenta can be of interest, since the BSA as well as the BCA are predicted to be large for large values of $|t|$. Consequently, these protons of higher momenta have to be detected and identified by a second, outer detector component.

In this momentum range protons from background processes are more frequent. For scattering off a hydrogen target the most probable final states in BH with resonance excitation are $n\pi^+$ and $p\pi^0$. The predicted distribution of p and π^+ is shown in figure 8.4. It can be shown that the decay proton can only be emitted into the forward hemisphere, while the decay pions also populate the backward hemisphere. Due to the velocity of the resonant state the decay proton direction in the laboratory frame is very close to the direction of the momentum-transfer Δ.

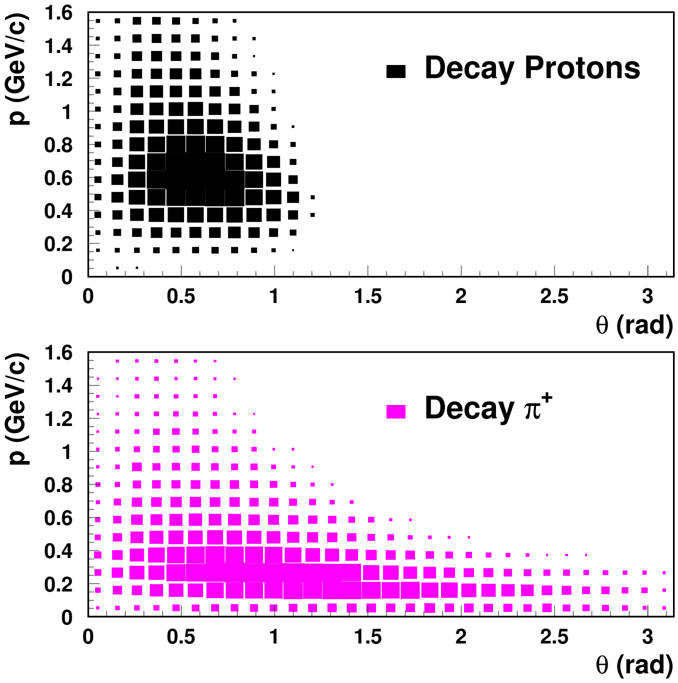

Figure 8.4.: Distribution of decay protons and pions within the applied cuts as function of the angle θ with respect to the beam and the momentum (p).

Several detector types can be considered to spot these particles as well as exclusive recoil protons: In theory it is still possible to absorb protons of such momenta in a very thick block of material. However, already for momenta of 250 MeV/c Germanium crystals of 10 cm length are needed (cf. [FB00]). The costs for the coverage of a large region in solid angle are prohibitive due to the length of the HERMES target cell. At higher momenta additional problems are expected, as the proton can be converted into a neutron inside the detector volume. Also reactions of the type

$$pp \to \Delta p \tag{8.1}$$

can take place at momenta of about 870 MeV/c.

A more realistic method would be the use of time-of-flight techniques. In this case a vacuum vessel of fairly large dimensions would be needed (cf. [COSY-TOF98]). This is in conflict with the available space and especially the turbo-pumps at the down-stream end of the target chamber.

Consequently the best possible detector type was found to be a solenoidal magnet combined with layers of tracking detectors. Such a magnet is anyway required to protect the inner silicon detectors from intense Møller background. A rather strong field is needed to obtain sufficient track bending over a distance of about 20 cm.

Several different detector types were considered for the tracking detector, while a maximum of active area together with a minimum of support structure was aimed for:

- Silicon detectors: A lot more silicon than for the inner detector would be needed to construct a tracking detector. A finer strip pitch as well as a different geometry would be required. In addition a dedicated production of readout chips would have been necessary. Due to the available time-scale - the detector was originally scheduled to be installed in the summer of 2004 - this option would have been difficult.

- Straw Tubes: The spatial resolution as well as the possibility to operate them in strong magnetic fields makes this detector type very attractive. They were proposed at a rather late stage of the detector design and could therefore not be included.

- Fibre Tracker: Scintillating fibres can be arranged in self-supporting barrels; readout electronics as well as fibre materials are available off-the-shelf. Due the expected rather low multiplicities, long fibres of about 30 cm can be used. The energy deposition in the fibres is proportional to the measured ADC-signals.

The decision was taken in favour of the fibre-tracker which appeared to be the most promising detector to be ready in time. It will allow for a measurement of the momentum as well as the energy deposition such that also a limited PID will be possible.

The tasks of the fibre tracker will be to identify recoil protons and to reject events with charged pions. This means that minimum ionising particles have to be detected, which is also important if the recoil detector is used for other physics processes apart from DVCS.

Finally photons have to be tagged in some outer detector. Since photon signals have to be separated from neighbouring charged tracks, a good position resolution is required. Moreover the expected decay photons cover a large range in momentum. As the evolving electromagnetic shower will either start (and stop) very early or very late, several sensitive detector layers are needed. The predicted distribution of decay-photons is shown in figure 8.5.

For technical reasons the photon detector will have a similar length as the fibre tracker, which also ensures that charged tracks can be separated from photons. In order to detect photons under $\theta \approx \pi$ relative to the beam a scintillator end cap was considered. However, it would have a very large cross-section for beam-related background such that this option was discarded. The final detector will consist of three barrels of tungsten and scintillator bars in three different orientations.

In order to achieve an almost hermetic acceptance for veto purposes, the existing silicon detector - the Lambda wheels - have been integrated into the design of the recoil detector. For tracks originating at the target the acceptance of the silicon detector and the Lambda wheels join seamlessly.

The final design of the recoil detector is shown in figure 8.6. The beam enters the detector from the left hand side. After a hard exclusive reaction has occurred, the recoil protons leave the thin-walled target cell and first hit the silicon detectors. These are mounted in roof-shaped structures inside the beam vacuum. Subsequently the protons traverse the target chamber (1.3 mm of aluminium) and hit the fibre detector. Particles of sufficient momentum will finally be seen in the photon detector. The drawing also shows the surrounding superconducting magnet which supplies a rather inhomogeneous field of 1T ($\pm 20\%$) inside the tracking volume and has extended stray fields. Furthermore an additional collimator (C3) is shown which is installed into the front part of the target chamber.

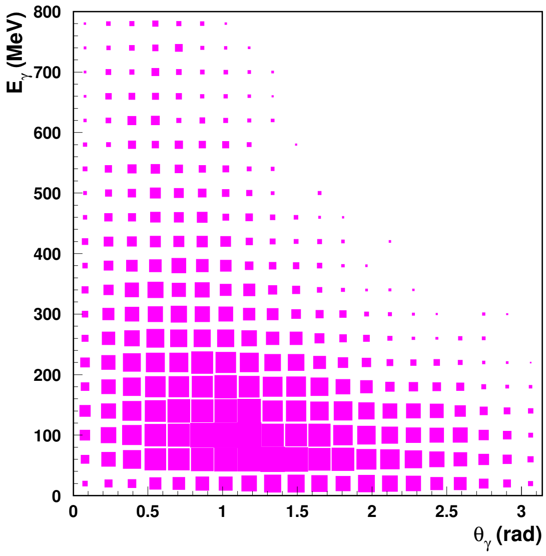

Figure 8.5.: Distribution of π^0 decay photons within the applied cuts as function of the angle θ with respect to the beam and the photon energy.

8.3. The Silicon Detector

The silicon detector is based on the sensor design TTT that had already been developed for the TIGRE experiment [O'N03] and was available from the company MICRON SEMICONDUCTOR LTD., Sussex,UK. It is a large (6 inch technology) double-sided silicon strip PIN-detector with an area of 99×99 mm and 128 AC-coupled strips per side. One corner of the p-side (i.e. the junction side of the sensor) is shown in figure 8.7. The standard technical parameters of the device are given in table A.1. Modifications of the standard design will be discussed in appendix A.1. Two sensors are used per module, as can be seen in figure 8.8.

The 128 read-out pads of the sensors are connected to thin flexfoils (50 μm Kapton) which transmit the signals to an array of charge-sharing capacitors at the beginning of the electronics hybrid. Each detector channel is connected to two different readout chips; one connection is direct, the other one includes a capacitor of $C = 10$ pF. The first chip allows for a high gain readout, while the second chip registers only a fraction of the input charge and allows for a low-gain readout of the same detector strip. The ratio of the two signals is about 0.27 as long as both channels are not saturated. In this way the dynamic range of the detector is considerably enlarged [K$^+$02].

In order to buffer, amplify and serialise the detector signals, the HELIX3.0 chip is used. Its functionality is explained in reference [FB99] and more information about its operation can be obtained from [Vel02].

Basically the chip amplifies the incoming charge pulse and differentiates it in order to obtain a short (< 100 ns) pulse that is proportional to the input charge. This signal is stored in one of 128 pipeline cells; the pipeline is switched with the HERA bunch frequency (96 ns). If an external trigger is applied the chip stops and goes back a number of cells (this is called "latency")

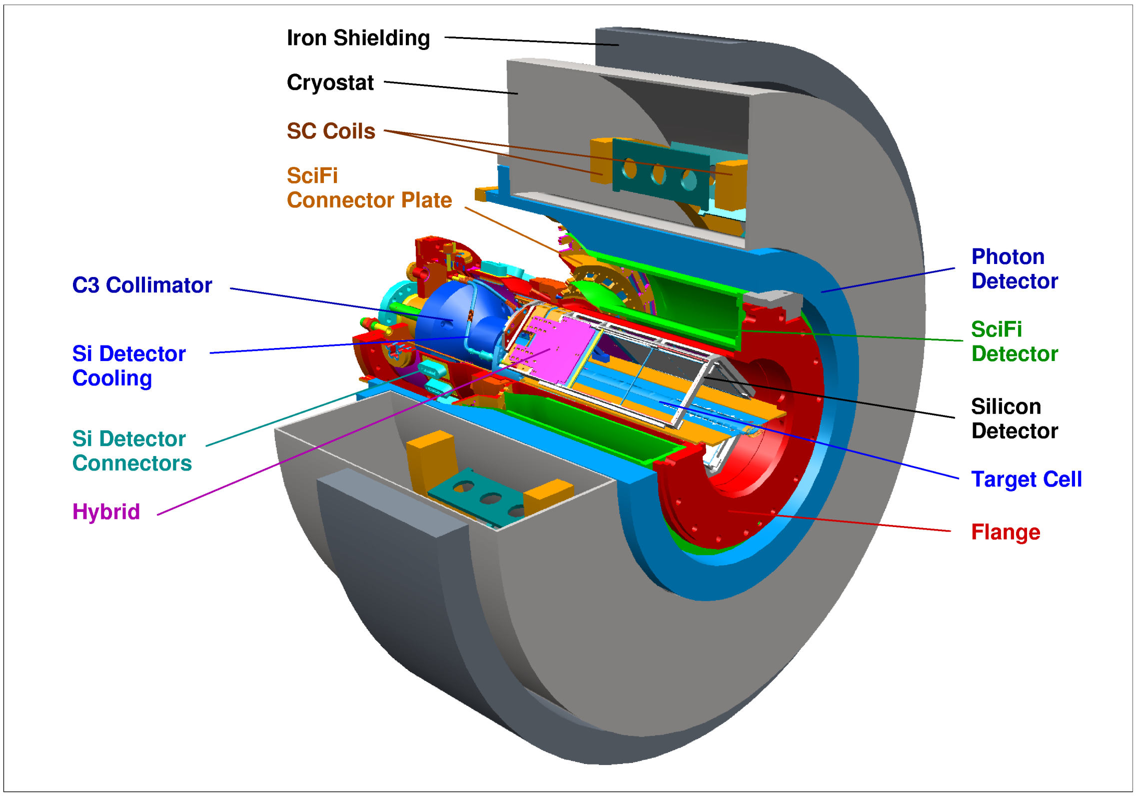

Figure 8.6.: The HERMES Recoil Detector in its final state: Particles emerge from the target cell, traverse the central silicon detector and leave the vacuum trough a thin aluminium wall. Afterwards they pass two layers of fibres and the photon detector.

to find the charge that was stored for the time of the triggered event.

All 128 channels of one HELIX chip are than multiplexed and amplified in order to transmit the information with only one analogue output line. In addition the 4 HELIX chips of each detector side are connected into one daisy chain and will be read out one after the other. When the readout with a frequency of 10 MHz is finished, the scanning mode is enabled again.

The chips were purchased as whole wafers from NIKHEF, Amsterdam. They were carefully tested for functionality of all registers. In addition the function and homogeneity of all pipeline cells was tested [IIM04], and the chips were sorted according to these criteria. This was necessary in order to obtain the required energy resolution of the system.

In addition to the HELIX chips the hybrids also contain electronic dosimeters (radfets) for radiation monitoring and temperature sensors. Furthermore output line drivers are present that are used to obtain differential signals from the HELIX output. One Kapton-layer of the hybrid is extended, such that a 25 pin D Sub plug can be attached to the vacuum connector in the service chamber. This is an elegant way to ensure that the system is vacuum compatible.

Due to the large power consumption of the HELIX chips (about 2 W per hybrid), an efficient water/alcohol cooling is necessary. The cooling liquid circulates the two roof-shaped aluminium blocks, into each of which 4 modules are mounted (cf. figure 8.6). Outside the vacuum a commercial cooling system is installed that is connected to the roofs through flanges in

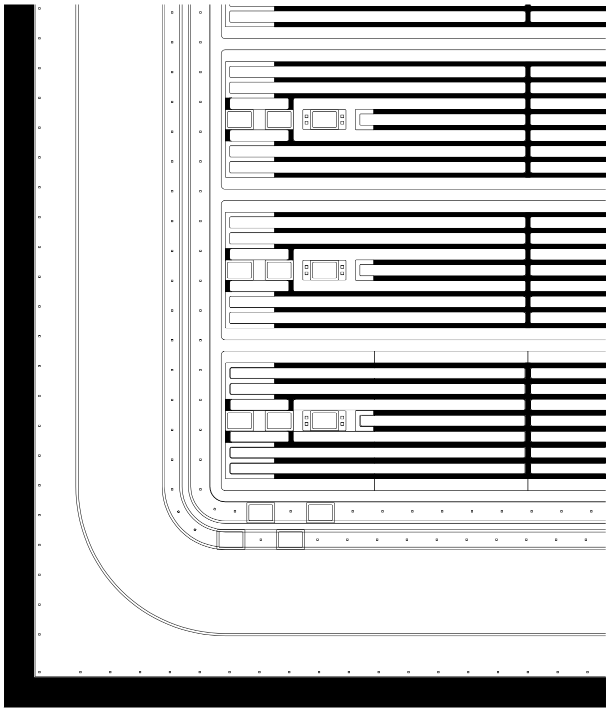

Figure 8.7.: One corner of the p-side of the TIGRE detector. The solid horizontal strips are part of the metallisation layer; they act as coupling capacitors. All rectangular fields represent bond-pads. The surrounding ring structure of one metallised bias ring and one metallised guard ring is visible.

the service chamber.

Additional electronics is needed outside the vacuum to operate the detector: An analogue-digital-converter (HADC), a sequencer for addressing the HELIX chips (HLCU), an auxiliary module (ACC) and high- as well as low- voltage power supplies. All modules are interfaced to the HERMES data acquisition, such that they can be controlled remotely.

The technical performance of the silicon detector is in one respect even better than initially requested [HERMES01b]: The high-gain signal can be used to detect MIPs with a signal to noise ratio of about 7. This means that the silicon provides space-points that can be combined with the spacepoints of the fibre tracker in order to determine the particle momentum for much higher momenta than originally planned.

8.4. The Fibre Detector

The fibre detector consists of scintillating fibres of the type Kuraray SCSF 78 M (S-type) with a diameter of 1 mm and an attenuation length of > 3.5 m (cf. [HER02]). The active volume is 28 cm long and stops at the downstream end at the flange that is located in front of the lambda wheels. In order to improve the light yield, the fibres are mirrored at this end.

Two fibre barrels with an inner diameter of 109 mm and 183 mm, respectively, were constructed. Each barrel consists of two layers: The fibres of the inner layer is aligned with the

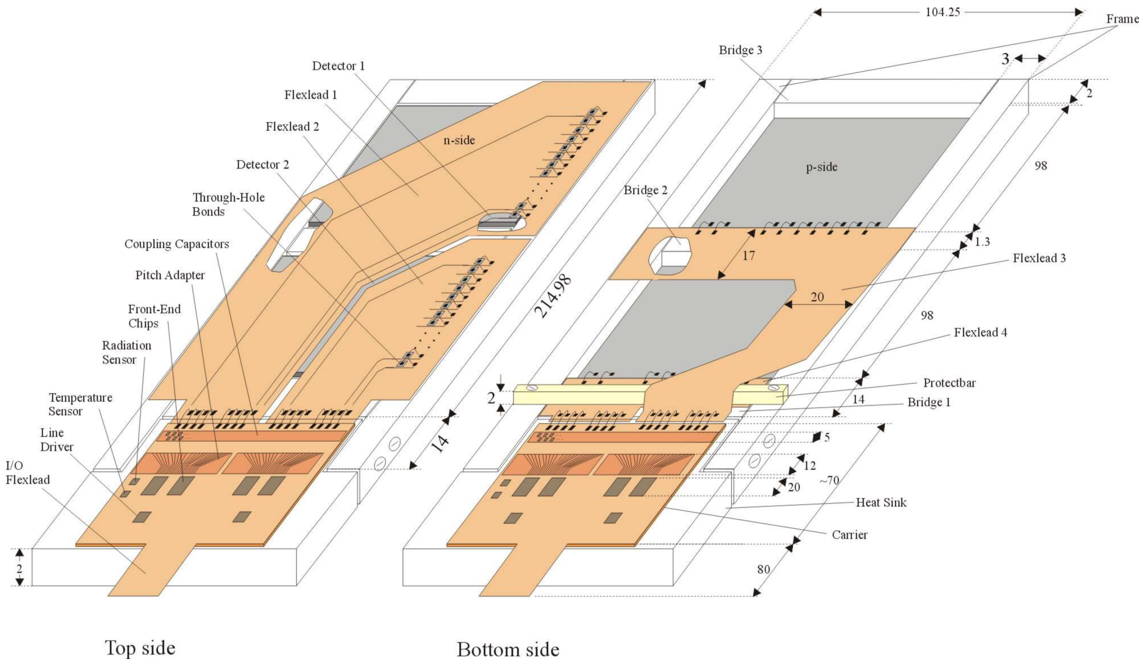

Figure 8.8.: One silicon module (top/bottom side): For the inner detector layer the top side shows towards the beam, for the outer detector layer the bottom side shows towards the beam. The two TIGRE detectors with the 4 connecting flexfoils are shown In addition the most important electronic components are indicated.

beam, while the fibres of the outer layer (stereolayer) are inclined by 10°. Each layer in turn consists of two sublayers that are shifted by half a fibre such that the 2nd sublayer is put into the grooves formed by the first sublayer.

The first barrel consists of 658 fibres per sublayer in the first layer and 660 fibres per sublayer in the second layer; the second barrel consists of 1102 fibres per sublayer in the first layer and 1090 fibres per sublayer in the second layer. The sublayers were assembled in modules such that single modules with defects could have been discarded. One test module for the fibre detector is shown in figure 8.9. An alignment of the final barrels is presently done in the DESY-22 testbeam.

Figure 8.9.: The end of one fibre test module. Two sublayers of fibres with a diameter of 1 mm form one layer.

Since the space around the target chamber is quite limited and also because of the strong magnetic stray fields of the solenoid, light-guides of 4 m length are used to direct the scintillation light towards the shielded photomultiplier arrays on both sides of the recoil detector. In order to minimise the costs, 64-channel PMTs are used (Hamamatsu Multianode PMT assembly H7546B). At the same time the compact design of these PMTs is needed because of the limited available space in the HERMES target region. The readout-electronics is based on the HADES RICH readout [K+99].

In contrast to the silicon readout which is based on a pipeline front-end chip, the readout of the fibre tracker uses the GASSIPLEX chip which is a hold-and-sample chip. Due to this fact the readout of the fibres integrates over 6 adjacent HERA bunches, which would increase the random background by the same factor. In order to avoid this, a fast timing signal can be extracted from the 12th dynode of the PMT, which is an analogue 'or' over all channels of one PMT [Har04b]. This means that random background can be vetoed if the typical occupancy is moderate.

8.5. The Photon Counter

The photon counter consists of 3 layers of scintillator bars with tungsten as a converter. The scintillators are 1.0 cm thick, while the tungsten layers have thicknesses of 1.8, 1.0 and 1.0 radiation lengths, respectively. One radiation length of tungsten corresponds to 3.5 mm. A cut through the detector is shown in figure 8.10.

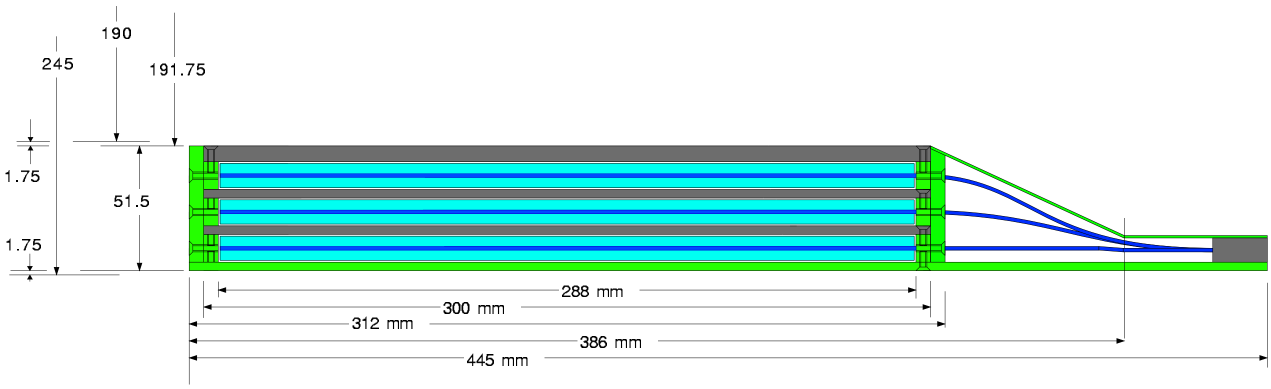

Figure 8.10.: Cut through the photon counter barrel: Three layers of scintillator bars are installed in three different direction. Tungsten layers of different thicknesses act as converters.

The first layer consists of 60 trapezoidal blocks that are aligned with respect to the beam. The 2nd and 3rd layer consist of 44 bars each; they are twisted by $\pm 45°$ with respect to the beam such that hit reconstruction gives unambiguous results for the hit position of a charged particle track. For photons the ability to reconstruct hits depends on the number of layers that are penetrated by the shower.

The scintillation light of each bar is collected by two lightguides that are glued into grooves on its sides. The light guides transfer the light to 64 channel PMTs of the type Hamamatsu H7546. The signal is read out by an ADC and simultaneously a fast trigger signal is provided that can be used as a trigger for cosmics runs. Due to the low number of detector channels it is possible to resort to commercial modules for these tasks. The ADC signal can be used to separate single particle tracks from electromagnetic showers, and also PID is possible if the energy deposition is compared with the momentum measured by the fibre tracker.

The detection efficiency of the photon counter is mainly limited by the allowed geometry of the device: From figure 8.5 it is known that some part of the photons is emitted under low angles. Photons below $\theta = 220$ mrad will hit the HERMES acceptance while photons up to $\theta = 400$ mrad hit no detector at all. Since the minimum threshold for the HERMES calorimeter is at present 0.8 GeV, all these photons are lost. However, such a lost photon is usually correlated with another decay photon that is emitted under much larger angles. Consequently the thickness of the converters has been optimised such that for photon detection a value close to the geometrical limit is obtained: The chance to detect at least one photon is 77-80% [Bor02], while the chance to detect both photons is much lower (18-20%).

It will depend on the background conditions if a single photon cluster can be used as a veto or not.

9. Expected Performance of the Recoil Detector

9.1. The Recoil Detector Monte Carlo

In order to obtain best-knowledge predictions for the detector performance during the design phase, the following considerations were made:

- At HERMES a complete simulation framework exists that allows to simulate a physics event, to track the generated particles inside the detector volume and to reconstruct the tracks from the digitised detector information. As the code structure is rather restrictive, quick changes in the detector geometry are not possible.
- To a good approximation, the recoil detector has no impact on particles that are emitted into the standard HERMES acceptance.
- The target chamber for the year 2000 was similar to the future target chamber in the respect that a thin-walled target cell was present and that the chamber did not cut into the standard acceptance. All other detector components were the same as for the future recoil detector run.

Consequently it was decided to simulate DVCS events in the HERMES Monte Carlo framework, using the geometry of the year 2000. Only the target gas distribution was changed to range from $z = 5$ to $z = 20$ cm with a peak at 12.5 cm. All necessary informations about the reconstructed photon and lepton were extracted from the HERMES-Monte Carlo and the results together with the kinematics of all non-detected particles were put into a stand-alone Monte Carlo code. This production chain is shown in figure 9.1.

First *gmc_dvcs* is used to generate exclusive and semi-exclusive single photon events on the proton. Then the Hermes Monte Carlo (*hmc*) simulates the emerging particle tracks in the HERMES spectrometer. *hmc* is based on the Monte Carlo library GEANT 3.21 [B$^+$94], and uses - as most of the other HERMES software - ADAMO [PTG94] to store and manipulate the data. The energy loss in each detector is digitised according to its properties and stored as hit information.

Afterwards the HERMES Reconstruction Code (*hrc*) reconstructs particle tracks as well as clusters in the calorimeter. It is the same code that is used for the reconstruction of real data. Its output files in general contain more information than needed for a typical analysis. Consequently the program *writeDST* condenses its output and stores all information about generated and reconstructed particle tracks in separate ADAMO tables.

At this point the standard HERMES software is interfaced to the recoil detector development tools: The program *pextra* analyses the reconstructed events and applies all necessary analysis

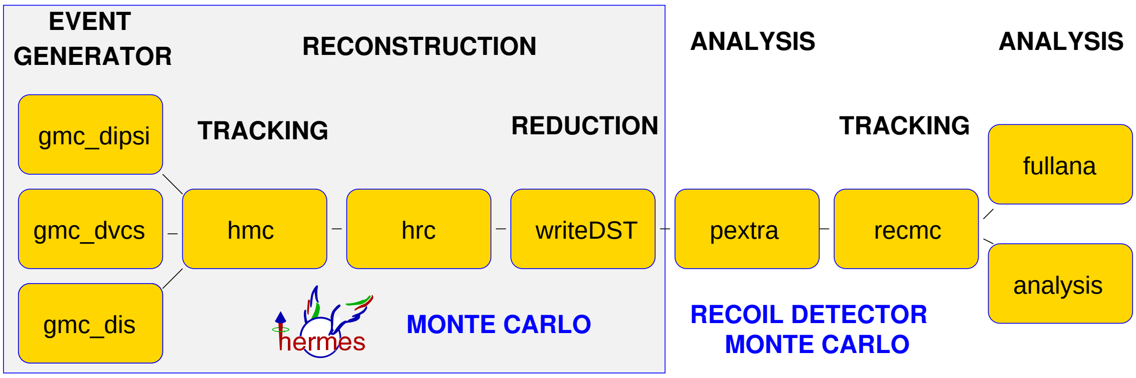

Figure 9.1.: Production chain for development Monte Carlo: Several programs belonging to the standard HERMES software (left) are used to simulate BH/DVCS events with the experimental setup of the year 2000. Afterwards all necessary information is extracted (*pextra*) and low momentum tracks are retracked in an independent front-end simulation (*recmc*). The digitised hit information is interpreted by the front-end tracking code (*fullana*).

cuts. For the selected good events the reconstructed tracks as well as all generated tracks are stored as compact HBOOK ntuples [BL87].

These are read in by the simulation tool *recmc*, which is also based on GEANT 3.21. It only contains the geometry of the future HERMES front region and retracks the particles that were not seen by HERMES. The geometry in *recmc* is in some aspects not the final one, as the development of this program was almost stopped, when a part of it migrated into *hmc* [She04]. However the program still allows a more accurate simulation than *hmc* in terms of digitisation and reconstruction. Consequently *recmc* can still be used to predict the final detector performance. The status of the geometry is summarised in table 9.1.

Especially the photon counter is quite outdated in its geometry. However, no effort was spent to change this, as the photon counter has only a small contribution to the background rejection probability. Moreover, the special geometry of the twisted bars for the 2nd and 3rd layer cannot be simulated by GEANT and it is also still not fully defined, how the photon counter will be used in the reconstruction of clusters or tracks. Hence, although the outdated geometry will lead to a smaller detection efficiency for photons, it will yield a conservative estimate and not have a big impact on the total detector performance of the recoil detector.

For most of the other features the implemented geometry is either an older version and approximately correct - as in the case of the magnet - or it is a reasonable approximation - as in the case of the straight fibre geometry.

As an example, figure 9.2 shows the recoil detector in the simulation together with a typical BH-event with resonance excitation. The lepton and photon that are detected in the HERMES spectrometer are omitted, but the decay products of the nucleon resonance are shown. Solid (red) lines denote charged particle tracks, dotted (blue) lines represent photons and dash-dotted (black) lines are neutrons. The diameter of the hit markers is proportional to the energy deposition in the corresponding detector-layer. Two decay photons leave the target cell towards the lower left corner and are detected by showers in the photon counter. In addition a proton escapes into the forward direction and hits the Lambda Wheels (two hits marked in

Table 9.1.: Status of Monte Carlo geometry and digitisation. All features that predominantly determine the detector performance are included.

Detector	feature	comment
Silicon	position, geometry and materials	correct
	recent Kapton foil design (cf. [Kra03])	correct
	detector split into 128×128 active cubes	better than *hmc*
	detector noise 20 keV per channel	not split into high/low gain
Fibres	position, geometry and materials	correct
	digitisation of fibre response	most recent
	each fibre treated as single volume	better than *hmc*
	straight fibres with stereoangle $\pm 5°$	good approximation
Photon. C.	position, geometry	roughly correct
	two layers of straight scintillators	outdated
	granularity: 2×72 scintillator bars	approximately ok
Magnet	position, geometry and materials	approximately correct
	magnetic field map	approximately correct
C3-coll.	position, geometry	roughly correct

upper right corner). There are no neutrons.

Figure 9.3 shows the detailed geometry simulation of the silicon detector including all Kapton foils above and below the active detector volume.

In order to serve as a universal simulation tool *recmc* has two important features:

- The events can either be read from an input file, or one of the internal background generators can be called. These internal generators can simulate collimator scattering, Møller or Bhabha scattering, pair annihilation and elastic ep-scattering. Of course also particles with specific kinematics can be generated for testing purposes.

- The output can either consist of the true hit positions and energy depositions or a fully digitised list of hit detector channels.

The undigitised output requires a lot less simulated detector volumes; it is thus faster and can directly be interpreted. The program *analysis* merges the information from *recmc* with the output of the HERMES Monte Carlo and allows a quick study of experimental parameters (i.e. energy resolution, strip width, etc.).

The more advanced program *fullana* reads the hit detector channels and performs a complete reconstruction of the event. The reconstruction code will be discussed in more detail in the following section and can serve as a first step towards the final recoil detector tracking code. The output of *fullana* is almost equivalent to the output of *analysis* such that the fast and the precise digitisation can be compared in more detail. In both cases the final output consists of HBOOK ntuples that can be analysed using PAW [BCVZ89].

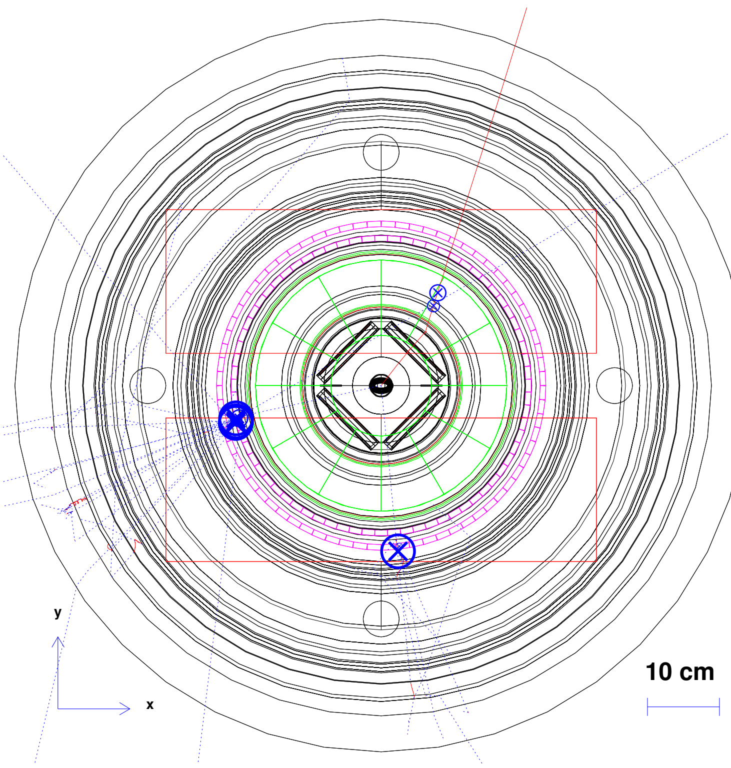

Figure 9.2.: Simulation of a typical BH event with resonance excitation: The recoil detector is viewed along the direction of the beam. All coloured parts correspond to active detector volumes, where hits are marked by crosses. Two decay photons are detected by showers in the photon-counter. In addition a decay proton hits the Lambda Wheels.

9.2. A Preliminary Reconstruction Code

In contrast to the HERMES main spectrometer there is almost no redundancy in detector planes for the recoil detector. This means that often a hit pattern does not have a unique interpretation in terms of particle tracks. Consequently the problem of track finding can be expected to be more severe than the problem of track fitting and noise or background hits are difficult to sort out. A similar situation has already been encountered in the case of the Lambda Wheels, where the overlap with the DVC acceptance is used to reduce the number of possible hit combinations.

In general the final reconstruction code must pay attention to the special physics reactions under study:

- Depending on the particle momentum a varying number of detector hits can be expected. Especially for protons of low momenta only the silicon detectors will supply hit information. However, as has been shown in [Fie00] this information is enough, as the protons also yield a higher energy deposition than most of the background processes.

- Due to the low particle momenta, the approximation of an ideal detector with no interacting materials - as made in the case of *hrc* - is obviously wrong. Multiple scattering is severe and limits the required strip or fibre pitch.

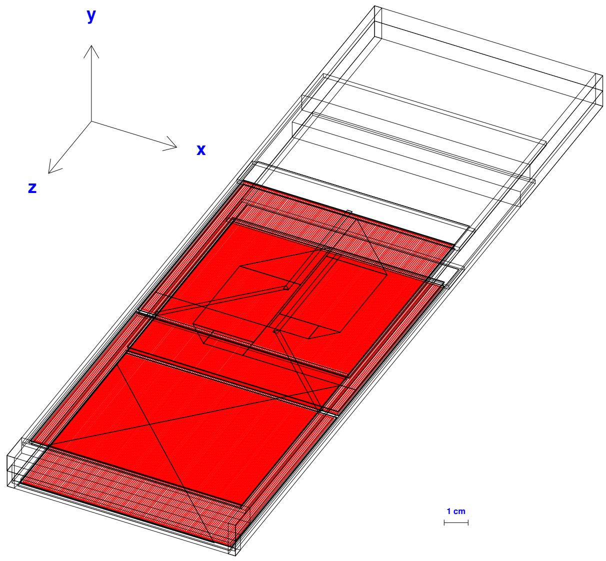

Figure 9.3.: Geometry of the silicon modules in the simulation: It includes the division into 128 strips as well as all Kapton foils inside the detector acceptance.

- The magnetic field is quite inhomogeneous. As there was no space to include field clamps at the end of the iron yoke, the field varies by $\pm 20\%$ inside the tracking volume. Consequently the particle tracks are only approximately given by the helix curve that is expected for an ideal solenoid.
- Particle identification at HERMES is based on the PID-quantities as defined in chapter 3. It is suggestive to introduce similar quantities that depend on the ratio of energy deposition E and particle momentum p. However, as the same value for p enters into the ratio E/p for all detector layers, all these PID-quantities are correlated. This means that an offline extraction of the parent distributions as in the case of HERMES is not possible. Instead the parent distributions have to be extracted from testbeam experiments or purely from Monte Carlo.
- The code has to be fast: Even in the case of high multiplicities all tracks that could originate from the target cell have to be spotted. Especially in the case of the fibres, the number of permutations to be tried increases exponentially with the number of hits.
- Some events may require the identification of a second decay vertex. If e.g. a K^+ is seen in HERMES, the tracking code should try to find the decay vertex of a Λ-Hyperon. Such a tracking task is even more sensitive to the background situation, as combinations of hits have to be tested without the requirement that the tracks have to point to the beam.

It is clear that all these issues require more consideration and that the development of the final tracking code will be a complex task. However, in order to estimate the achievable tracking performance a rather basic tracking code has been developed: silicon and fibre tracklets are reconstructed independently of each other; if they agree within some boundaries they are merged to form one track, otherwise each tracklet becomes a track. In the approximation of straight tracks the corresponding clusters in the photon counter are eliminated. Untracked clusters as well as additional tracks veto a potential DVCS event. The structure of the code is shown in figure 9.4.

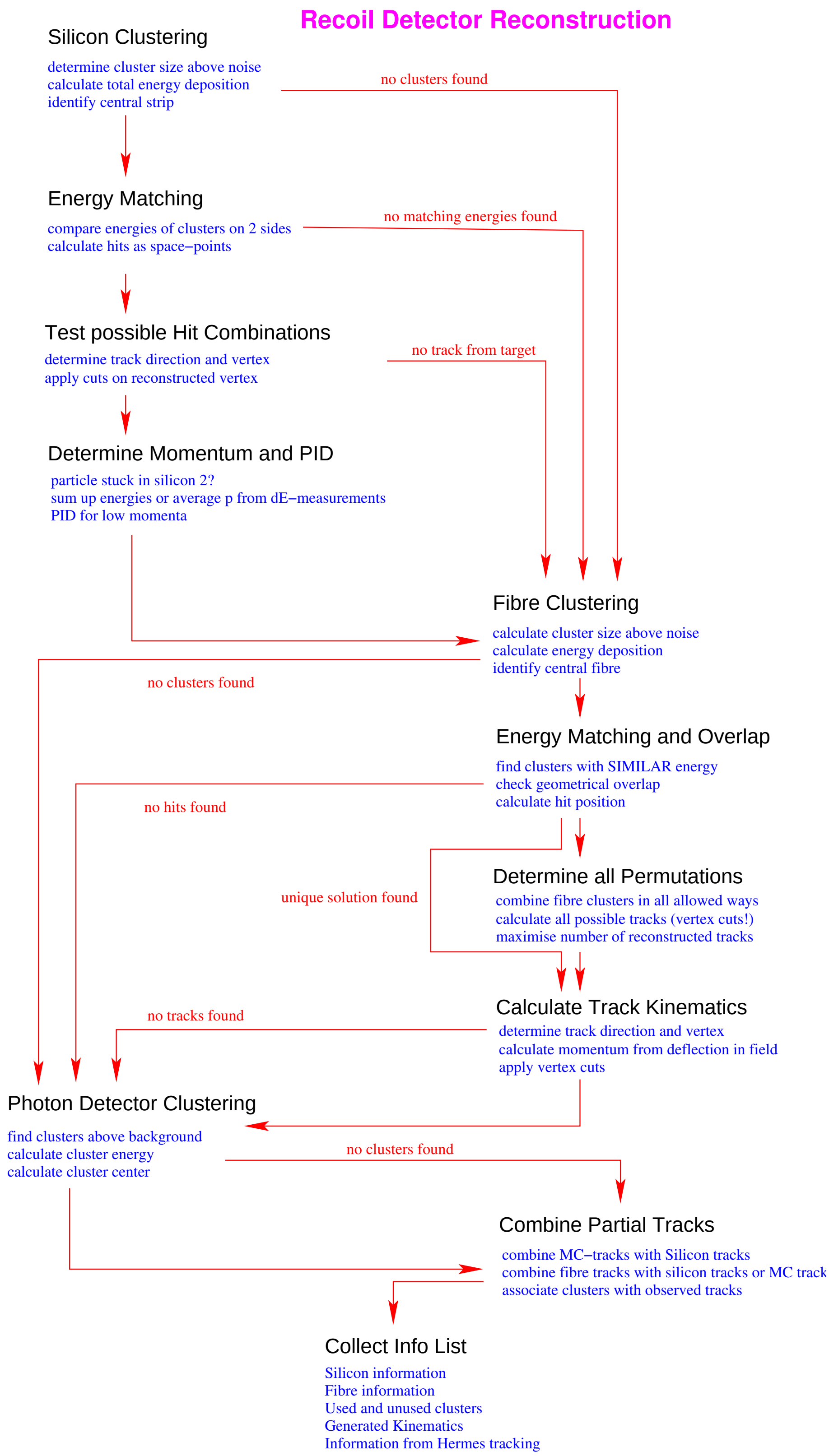

Figure 9.4.: Preliminary reconstruction code for the Monte Carlo and its structure.

Although the final clustering algorithm still has to be agreed on, the program uses the following procedure for all detectors: If a channel containing a signal above a threshold T2 is found, the signal of the previous channel is added to the cluster if its signal is above a threshold T1. Otherwise the cluster extends as long as the channels are above T2. Again one more channel is included if it is above T1. Finally the signal of the whole cluster must be above a threshold T3. The energy of all channels is added up to obtain the cluster energy, while the hit position is determined using the centre of gravity method.

E.g. in the case of the silicon detectors, T1 corresponds to 50 keV or about 3σ of the pedestal noise. This is the foreseen hardware cut that will be done by the ADC to sparsify the channels. T2 is already 200 keV or 10σ of the pedestal noise. Since only hits with an energy deposition of more than 500 keV allow a momentum determination with some accuracy, T3 is set to this value. This procedure removes MIPs from the silicon data and will not be the final one. In general T3 should at least be larger by a factor of 2 than T2: For geometrical reasons, protons can only traverse 2 strips, hence the minimum single strip charge is about 50% lower than the cluster charge. If T2 and T3 are chosen to be identical, the detector efficiency for low energy depositions will systematically depend on the hit position.

For silicon hits above 500 keV it will definitely be possible to match the energy deposition of front and back side such that a true 3d hit position is found. According to reference [Fie00], the multiplicity for such energy depositions can be expected to be sufficiently low. A silicon tracklet is formed from two such hits in the two layers of the silicon detector.

In the case of the fibres the situation is more complicated, since ambiguous patterns of hit fibres can be obtained if several minimum ionising particles hit the detector at the same time. The following strategy has been devised to obtain the 3d hit positions and to disentangle the tracks: Due to random noise or Cherenkov light in the lightguides, single clusters can light up that have no analogue in the adjacent stereo layer. In this case the channel has no overlap with another hit channel in the stereolayer and is consequently discarded. As a second step an overlap matrix of all clusters in one layer is created; rows and columns correspond to cluster positions in the two sublayers, respectively, and non-zero entries are used to mark possible combinations of the clusters.

The obtained pattern can have unique solutions for the 3d hit positions, even if many matrix element are non-zero. This can be seen in the following way: If only one entry in a row or a column has a non-zero value, the corresponding crossing defines exactly one hit and the row and the column of it can be deleted from the matrix. Now it is possible that again one row or column contains exactly one entry. In some cases the matrix will be completely empty in the last step and the problem has been solved. Apart from problems due to random clusters or detector inefficiencies this method works reliably.

If the matrix cannot be reduced in this way, some filled area in it will remain. In this case the tracking code switches to the permutation mode, which can be very time-consuming. This code checks all possible combinations of clusters in the first layer and combines them with all possible combinations of clusters in the second layer in order to obtain all possible tracks. If the number of track candidates exceeds some reasonable number (e.g. 10^6) the code gives up immediately; otherwise it would get stuck for events that are not interesting, as they are probably due to non-exclusive background. The number of 10^6 corresponds to at least 6 tracks originating from the target within $\Delta\phi \approx 10^\circ$ in the azimuthal angle ϕ around the beam.

For each random combination of clusters it is first checked that the combination is consistent with the hit pattern. The reason is that filled areas in the matrix can still contain a few empty entries. These veto certain cluster combinations; in this process the assumption is used that each cluster in a sublayer may only be used for one hit. Afterwards all possible straight tracks are calculated from the determined 3d hit pattern. It is checked that the track points to the target cell and that the azimuthal distance between the hit in the first layer and the second layer is below $\Delta\phi = 0.3$ rad. This value is a compromise that will still allow the detection of low momentum pions. The deflection of protons in the magnetic field is usually much less, as protons of the corresponding low momenta are absorbed in the inner detector layers or the target chamber. The number of possible tracks is calculated for each combination of clusters and the combination allowing for the highest number of tracks is selected. If there are several such combinations, the first one is taken, but of course this need not be the correct choice. Finally all possible tracks selected in this way are stored.

The treatment of the photon-counter is at the moment rather simple: Clusters are formed and the hit energy together with the hit position in the angle ϕ around the beam are stored.

After these track finding routines the interpretation of the pattern can start. First, all silicon tracks become final tracks, as they are the most reliable candidates. Then the corresponding fibre track is looked for and included into the same track, if the track direction matches within some limits. Otherwise a new final track is created. As a last step, all clusters in the photon counter that can be associated with tracks are stored together with these tracks. Remaining clusters are stored as untracked clusters.

Now the calculation of momenta and PID can be performed: For tracks detected in the silicon, the angle of incidence α has to be calculated. Then the corrected energy deposition in both layers is obtained from

$$E_{corr} = E\cos(0.79\alpha) \tag{9.1}$$

according to reference [Fie00]. This empirically found quantity allows to estimate, if a proton got stuck in the second silicon layer or not. If $E_{corr,1} > 3.0$ MeV the particle was most likely absorbed. If $E_{corr,1} < 2.4$ MeV it certainly penetrated the second layer. As has been discussed in [Kra00], pions will always end up in this category, as they are typically located at $E_{corr,1} <$ 2.4 MeV and $E_{corr,1} < 2.0$ MeV. The simulation predicts that DVCS recoil protons of up to $P = 180$ MeV/c can be identified in this way. Assuming that the particle is a proton, its momentum is calculated in three different ways depending on $E_{corr,1}$:

1. $E_{corr,1} > 3.0$ MeV: The proton got stuck in the second layer and the kinetic energy is equal to the total measured energy $E_1 + E_2$ minus the energy deposition in the intermediate materials. Due to the design of the Kapton foils this correction is position dependent. As has been discussed in [Kra03] it can be taken care of by adding a constant offset to the calculated momentum. The values are 8, 9, 15 and 20 MeV/c for $0\ldots 3$ Kapton foils to be traversed. Obviously, even with no Kapton foil the target cell (simulated as 75 μm of aluminium) has an effect.

2. 2.4 MeV$< E_{corr,1} < 3.0$ MeV: It is not clear if the proton got stuck and only the energy deposition of the first layer can be used to determine the momentum. It is calculated from a lookup-table as $p_p = p_1(\alpha, E_1)$. The lookup-table is shown in figure 9.5. As long as the energy resolution due to noise in the electronics is much better than the fluctuations in energy loss, the momentum resolution will be visibly worse than in the first case. The momentum is already high enough that the number of traversed Kapton foils is no longer important.

3. $E_{corr,1} < 2.4$ MeV: The proton passed the second layer and another lookup-table $p_2(\alpha, E_2)$ can be used to obtain the particle momentum from its energy deposition in this layer. Since the particle momentum is sufficiently large, the fluctuations in energy loss of the first and second layer are approximately uncorrelated. Thus the arithmetic mean value $p_p = 0.5(p_1(\alpha, E_1) + p_2(\alpha, E_2))$ will strongly improve the momentum resolution.

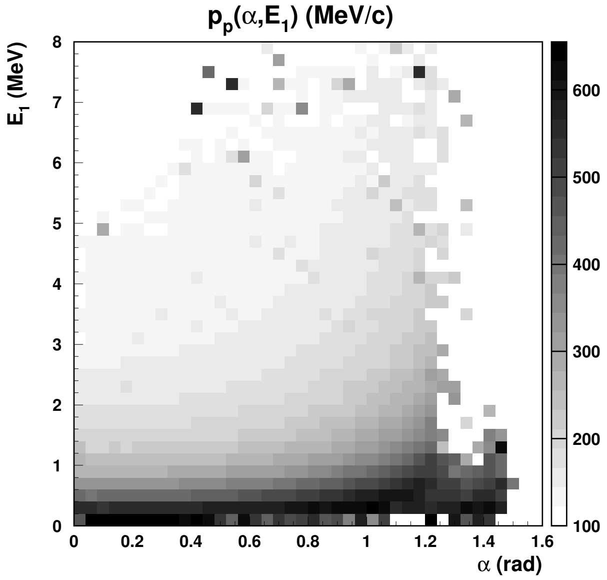

Figure 9.5.: Average proton momentum as function of the angle of incidence α and the energy deposition in the first silicon layer.

The lookup tables are obtained from Monte Carlo. To a good approximation it is sufficient to simulate an isotropic distribution of protons without a magnetic field in order to obtain it. This means that the lookup-table can also be taken from measurements in a testbeam at different energies, if the agreement of reality and Monte Carlo is insufficient. However, this procedure does not yield the optimum results: At momenta below 500 MeV/c the energy loss of the protons is well described by a Gaussian distribution and no Landau tail is seen. This is the reason why in principle the method works well. On the other hand the dependence of $p_p(E_1)$ gets very flat for higher momenta and exhibits a Landau tail; thus the momentum distribution for a fixed energy deposition has a long tail towards large values that depends on the cutoff in the simulation or the range of momenta available in the testbeam. The effect of this tail is that $\langle P \rangle$ obtained from such a lookup-table can be systematically too high for the case of DVCS, as the cross-section for higher momenta is low. Thus the optimum value in the lookup table is flux-dependent and the simple mean value $\langle P \rangle$ as used in this thesis may not be the best solution.

One feature of the silicon detector is that its resolution in the angle ϕ_p around the beam is method-dependent. If the beam position is known with sufficient accuracy (i.e. ≤ 1 mm), ϕ_p is ideally determined from the hit position in the first layer only, assuming that the particle track was a straight line. Potentially the larger lever arm - 5.8 cm instead of 1.5 cm - combined with the rather small beam size - typical values in the HERMES interaction region are $\sigma_x \approx 0.25$ mm and $\sigma_y \approx 0.07$ mm [Dür98] - leads to a better result than the calculation of ϕ_p from the two silicon hits. The feasibility depends on an exact knowledge of the beam position; therefore this method was not used for the simulation.

However, one important correction to the track direction is in any case needed: Due to the strong magnetic field the value of ϕ_p determined in either way is not the original value of ϕ_p. Monte Carlo results show, that a good correction - including material effects - can be obtained from the following parametrisation:

$$d\phi = \frac{a_1}{a_2 + p_t} + a_3, \tag{9.2}$$

where p_t denotes the transverse momentum of the proton and the parameters $a_1 \ldots a_3$ have approximately the following values: $a_1 = -18.6$ MeV/c, $a_1 = -12.2$ MeV/c and $a_3 = -0.556 \times 10^{-2}$.

In the case of the fibre tracker the particle momentum is obtained from the deflection in the magnetic field. Due to its inhomogeneity, the particle track is not exactly given by a helix. In addition multiple scattering is severe as some of the particles will just about reach the last fibre layer. For the reconstruction code this has not been studied in detail and the tracks have been assumed to form perfect circles in the projection along the beam. The momentum was determined from the curvature together with a constant magnetic field of 1 T. As the fibre tracker consists of only 2 layers, the beam position has to be used in order to reconstruct the arc. In this case the knowledge of the beam position is mandatory; depending on the noise in the silicon detectors the final solution may be to take one hit from there, but this would reduce the detector acceptance. For the simulation only the beam profile in x and y, but no uncertainty in the beam position has been included. It will be discussed in section 9.5 how the beam position in principle can be determined.

PID with the fibre tracker is based on two ideas: Pions of negative charge can directly be identified by the wrong sign of the deflection angle. As these events can only be confused with exclusive events if at least one additional pion (π^+) and a neutron are produced, such events are rather rare for the present exclusivity cuts. The more difficult PID is based on the fact that protons at a fixed momentum deposit more energy in the fibres than pions of the same momentum. Consequently e.g. the requirement that

$$E_1 + E_2 > \frac{a_1}{P} + \frac{a_2}{P^2} \tag{9.3}$$

can be used to select protons for momenta below 650 MeV/c. E_1 and E_2 are the energy depositions in the respective layers, P is the particle momentum and a_1 and a_2 are parameters that depend on the exact operation of the PMs and have to be adjusted for the final setup.

9.3. Expected Detector Performance

The expected detector performance can be split into two different categories: The first one characterises the performance of the recoil detector in terms of acceptance, detection efficiency and resolution. The second category describes the improvements in the analysis of BH/DVCS-events that are possible by combining the recoil detector data with the data obtained from the main spectrometer. As all simulation results are fully digitised and reconstructed, it is clear that the obtained values are realistic and close to the ones that are finally obtained in the experiment. In the end a different reconstruction code can certainly lead to slightly different or improved results.

The acceptance for exclusive recoil protons obtained with the recoil detector is shown in figure 9.6. The first plots (top, left) shows the acceptance in θ_p which is defined as the polar angle with respect to the beam. In agreement with figure 8.3 the acceptance is largest in the region where most of the recoil protons are expected. The geometrical acceptance in θ_p of the silicon detector and the fibre detector without a magnetic field is shown in figure 9.7. While the geometrical acceptance of the fibre detector reaches 100%, the maximum geometrical acceptance of the silicon detector is limited by the second silicon layer. Thus the maximum value can only be 76% due to the gaps in ϕ_p. If the silicon detector can successfully register MIP hits, it will almost reach this geometrical limit, although no momentum determination will be possible without additional hits in the fibres.

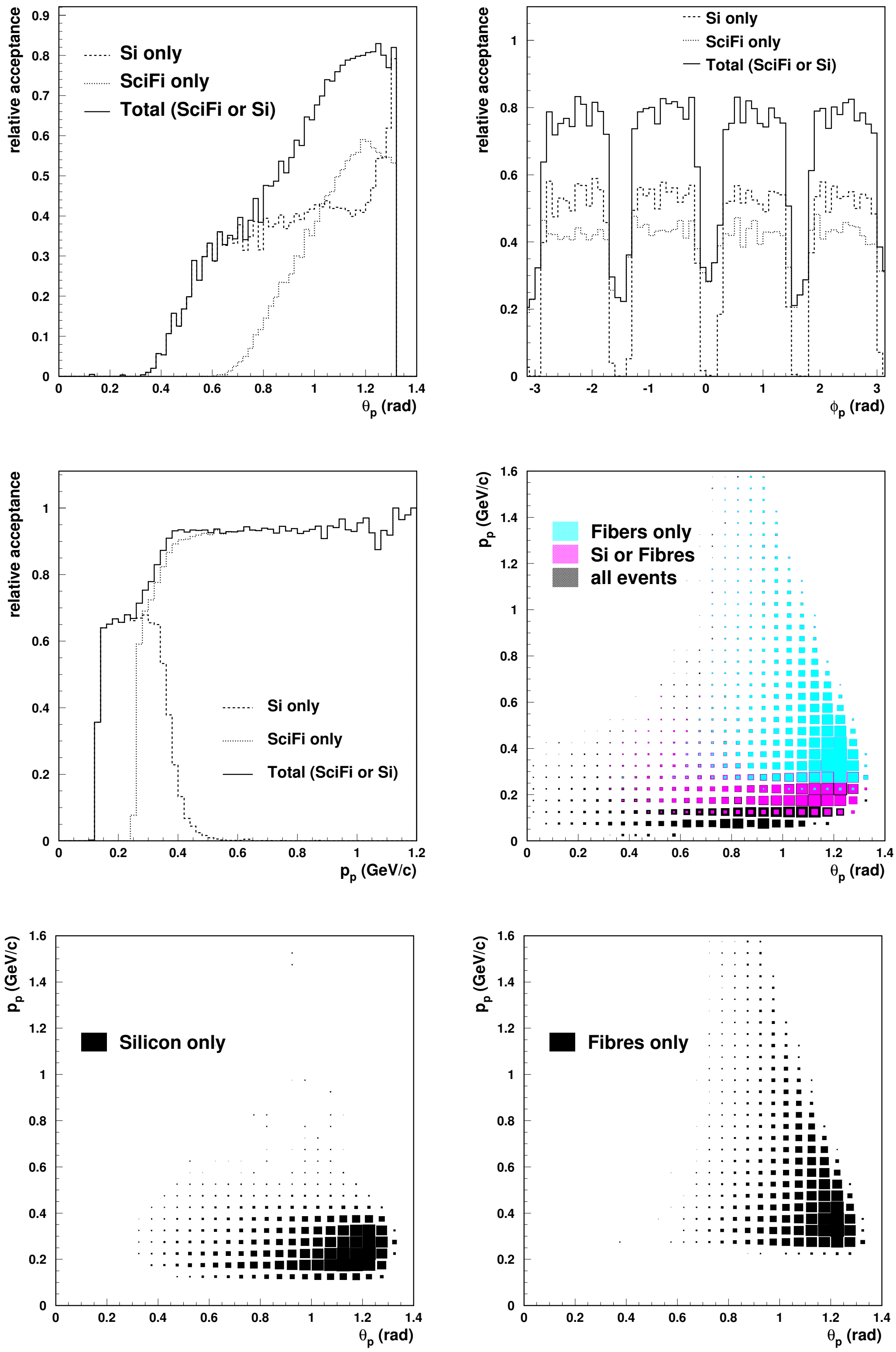

Figure 9.6.: Detector acceptance in θ_p with respect to the beam, ϕ_p around the beam and in the momentum p_p. The fourth plot (centre, right) shows the event distribution in θ_p and p_p in comparison with the detected events. The acceptance is calculated for exclusive BH/DVCS events that pass the discussed analysis cuts. The two bottom plots show only the rates that are detected in the silicon (left) and the fibres (right) as a function of θ_p and p_p.

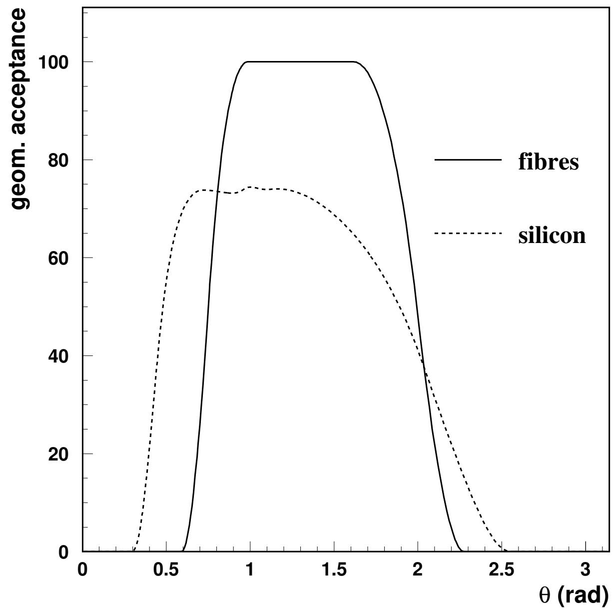

Figure 9.7.: Geometrical acceptance in θ of the silicon and the fibre detector.

In the one-dimensional plot of the acceptance versus ϕ_p derived from the Monte Carlo simulation (top, right in figure 9.6) the gaps are clearly seen. However the plot is a bit mis-leading as the maximum value for the acceptance of the silicon detector is low due to higher proton momenta that are not detected with the set energy threshold. Also the fibre detector has a lower efficiency in the gaps in ϕ due to the holding structure of the silicon modules. Here the maximum value of the acceptance is due to the low proton momenta that are not seen.

In the case of low background it is possible that even single silicon hits are sufficient to confirm a recoil proton if the signal is large enough. In this case, the much better acceptance of the first silicon layer could be used with a geometrical acceptance in ϕ_p of up to 88%.

The plot of acceptance versus particle momentum (centre, left in figure 9.6) demonstrates nicely, that the silicon detector and the fibre tracker are complementary: While the silicon detector covers the lowest proton momenta of about ≤ 130 MeV/c to medium values of 400 MeV/c, the fibre detector is needed for momenta above this value. This can also be seen in the remaining three plots, that show the generated events and the events that are detected by the silicon detector or the fibre detector as a function of θ_p and p_p.

It was discussed to use thinner silicon for the first detector layer, but apart from much higher costs the benefit from 200 μm sensors would have been marginal. This is partly due to the target cell and the Kapton foils. The low momentum cut-off for an isotropic distribution of protons is shown in figure 9.8; the lowest momenta are seen for perpendicular incidence of the particles. Since the region of highest target density coincides with the centre of the first TIGRE sensor, the central region of this detector was left open in the flex-foil design such that only the top Kapton foil has to be traversed. This region may be interesting for the detection of spectator protons from the breakup of the deuteron (cf. [Fie00, HER97]).

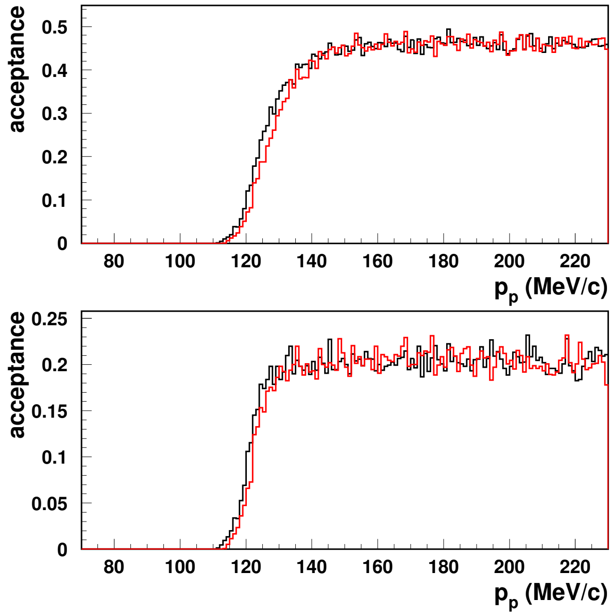

Figure 9.8.: Low momentum cutoff for two different Kapton foil designs (red/black). Differences are small but the one with the better performance (black) has been chosen. While the top plot shows the momentum cutoff for the whole detector assuming an isotropic distribution of protons, the lower plot shows the cutoff for the region of the upstream sensor, where no Kapton foils are between the two silicon layers.

In terms of detector resolution the initial requirements are fulfilled. The geometrical resolution in ϕ, θ and z_{vertex} is shown in figure 9.9. Obviously the resolution in ϕ is much better than initially required value of 0.1 rad. The resolution in θ and z_{vertex} is less important for the DVCS-analysis; however, it is possible that z_{vertex} can be used in order to refit the event kinematics and obtain a better momentum resolution for the lepton track in the HERMES spectrometer.

The momentum resolution of the silicon detector is shown in figure 9.10 (top). In comparison the projection from reference [HER02] is included. At low momenta a marked difference is seen, since the simulation of the Kapton foils together with an improved reconstruction was only done for reference [Kra03]. The momentum resolution of the fibre tracker in comparison with projections from reference [HER02] are shown in the same figure (bottom). The momentum resolution is slightly worse due to additional material in the silicon support structures and the larger fibre diameter of 1 mm for both layers.

In the second category of characteristic quantities the improved measurement of t and ϕ for exclusive single photon events is important. Since reference [HER02] the calculation of t from the lepton and photon information has been changed to the constrained t as was discussed in section 3.6. Consequently the t-resolution of the spectrometer has been improved. The resolution in t for the silicon detector, the fibre tracker and the main spectrometer is shown in figure 9.11. For the spectrometer the resolution is calculated from t_c while for the other two detectors t is obtained from the proton momentum according to $t = -2m_p(E_p - m_p)$. At low

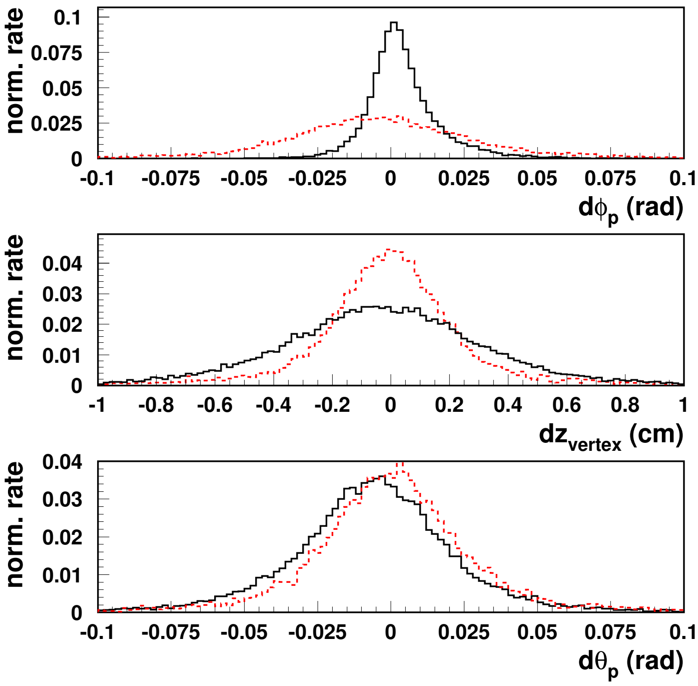

Figure 9.9.: Expected resolution of the silicon detector (dashed) and the fibre detector (solid) for the angle ϕ_p around the beam (top), the reconstructed z-coordinate of the vertex (middle) and the angle θ_p with respect to the beam (bottom).

momenta the silicon detector has a much better resolution than the spectrometer and covers values of up to $-t = 0.2$ GeV^2. The fibre tracker on the other hand starts at $-t = 0.1$ GeV^2 but does not improve the t-resolution. Since this measurement is totally independent from the measurement provided by the spectrometer, the combination of both results may still have a reduced error.

The resolution in the azimuthal angle ϕ as defined in chapter 2 is shown in figure 9.12. Since the spread of $\delta\phi = \phi_{reconstructed} - \phi_{generated}$ is strongly non-Gaussian, the resolution $d\phi$ is calculated as the truncated RMS value of $\delta\phi$ inside $|\delta\phi| < 1$ rad. Otherwise the RMS fluctuates strongly due to events in the tails of the distribution. For all values of t the ϕ-resolution provided by the recoil detector is much better than the resolution of the main spectrometer. This is due to the much larger opening-angle of the proton track with respect the virtual photon in comparison with the opening-angle of the real photon with respect to the virtual photon. Although smearing effects are in this way strongly reduced, the lower momentum cut-off in the silicon still eliminates events at low values of θ_{γ,γ^*} such that statistics is lost.

Finally the interplay of the recoil detector with the main spectrometer allows the application of new exclusivity cuts. As has been discussed before in section 8 the transverse momentum balance can be exploited. In references [HERMES01b, HER02] this was done by applying cuts on 2 separate quantities as shown in figure 9.13:

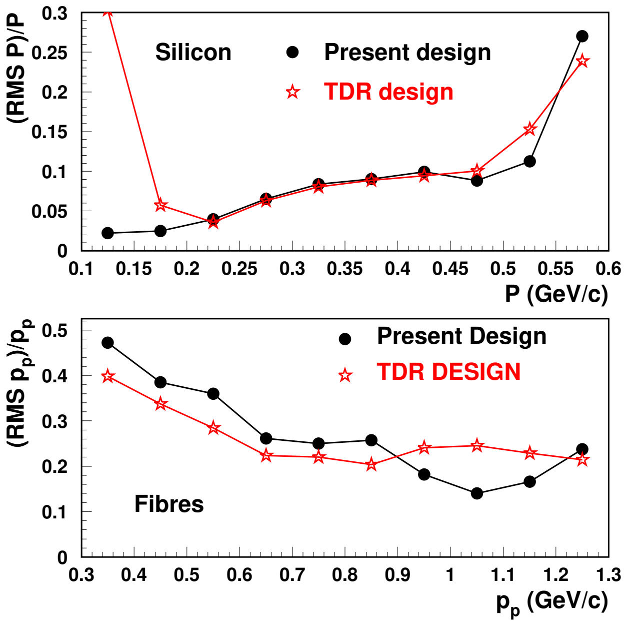

Figure 9.10.: Momentum resolution as function of the momentum for BH/DVCS recoil protons. The top plot is for the silicon detector and the bottom plot is for the fibre detector.

Table 9.2.: Suggested hard cuts on the quantities ω and R as defined in figure 9.13.

	Fibres	Silicon
R	$0.5 < R < 1.5$	$0.5 < R < 1.5$
ω	$\omega < 0.25$	$\omega < 0.5$

- The angle ω between the missing transverse momentum vector and the transverse momentum vector of the proton must be below some upper limit.
- The ratio R of the missing transverse momentum and the transverse momentum of the proton must be about 1.

The suggested hard cuts are summarised in table 9.2. In the end it may be better to use t-dependent cuts, since the background at low values of t is very small, while the transverse momentum vector provided by the spectrometer is almost unknown. It may also be preferable to use instead some kind of improved coplanarity cut in order to eliminate the calorimeter calibration as an uncertainty. As long as no data from the recoil detector exists, it is hard to make a solid statement about the best possible exclusivity cut.

The effect of the cut is shown in figures 9.14 and 9.15. All distributions are normalised to unity. The solid lines represent detected exclusive recoil protons, while the dashed line in figure 9.14 and the dotted line in figure 9.15 show detected protons from BH with resonance excita-

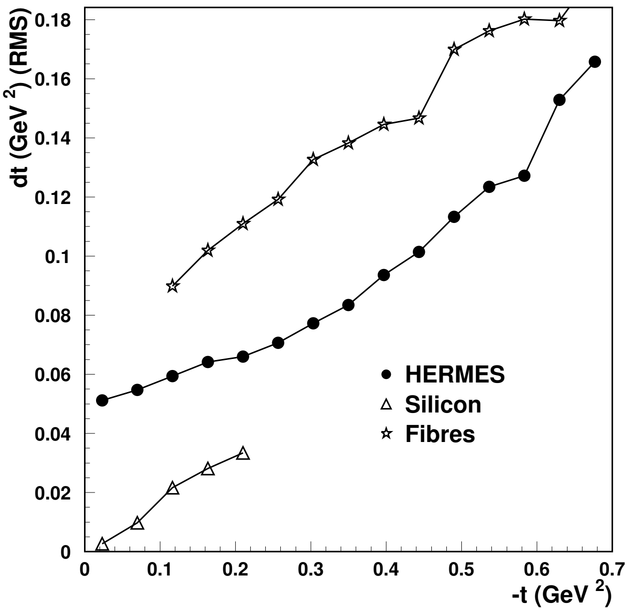

Figure 9.11.: The resolution in t is shown for the HERMES main spectrometer (t_c), the silicon detector and the fibre tracker.

tion and subsequent decay of this state. The dashed line corresponds to the whole resonance region with $M < 2.0$ GeV, while the dotted line represents the Δ-resonance ($M < 1.4$ GeV). Apparently the cuts are a bit more effective in removing the higher resonances, while the Δ-resonance is the more critical state due to its low invariant mass. For these plots no cut on the missing mass has been applied, but the effect on these distributions would be small.

Within this approach the number of events passing the exclusivity cuts has been determined with the present Monte Carlo model, where the cut on the missing mass has been set to $M_x^2 < 5\,\mathrm{GeV}^2$. For the technical design report no cut on M_x was necessary, as the semi-inclusive contributions were not considered. A comparison of the different cut efficiencies is shown in table 9.3. Obviously the resonant states have already a rather low probability of emitting a decay proton into the detector acceptance such that the number of detected events is small. In addition the coplanarity cut removes many of them and if the particle identification of the fibre tracker is working reliably, an additional reduction can be achieved. Finally if the background conditions allow the rejection of single cluster events and events with more than one reconstructed track, only a very small fraction of the resonant background passes the cuts. The probability to detect exclusive π^0 events that have been mis-identified as DVCS-candidates is very high, as the t-distribution for exclusive π^0 production is less peaked at low values of $|t|$. Thus a larger fraction of these than of BH/DVCS events passes the detection threshold of the silicon counter. Also the probability to accept such an event as BH/DVCS event is very high. However the fraction of these events is low and the recoil detector will also allow to improve the knowledge about exclusive π^0-production such that it can be subtracted with more confidence. The given percentages for the inclusive events and the exclusive π^0 events have been calculated

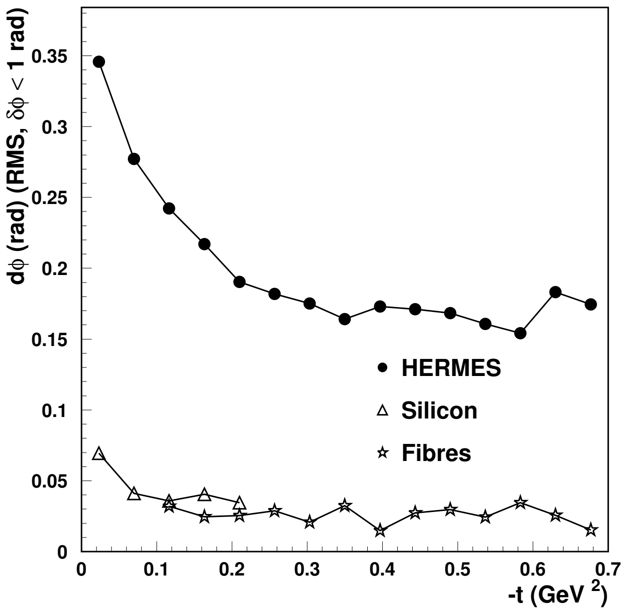

Figure 9.12.: Resolution in the azimuthal angle ϕ around the direction of the virtual photon versus $-t$ for the three different detectors.

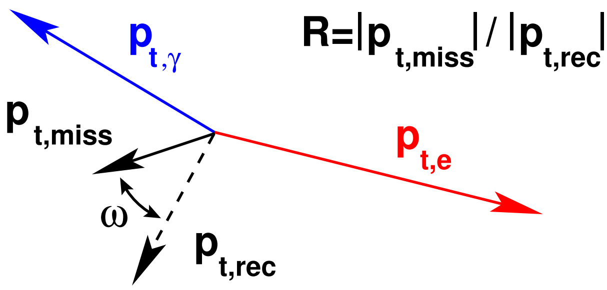

Figure 9.13.: Definition of ω and R: The missing transverse momentum vector $\vec{p}_{t,miss}$ is reconstructed from the observed transverse momentum vectors of the photon $\vec{p}_{t,\gamma}$ and the lepton $\vec{p}_{t,e}$. $\vec{p}_{t,rec}$ is the transverse momentum vector of a proton that is detected in the recoil detector. The angle ω and the ratio R are defined in the drawing.

for the whole datasets, irrespective of the particular process that led to the mis-identification of an event as exclusive DVCS-candidate (cf. section 6.10).

It is interesting to note that the cut efficiency of 51% for exclusive DVCS events means only a reduction of the event number by about 45% with respect to the present event cuts. This is due to the increased upper cut of $M_x^2 < 5$ GeV^2 on the missing mass. Some fraction of the rejected event sample is moreover due to leptons that cannot be used anyway, as they have radiated a photon before being deflected in the magnetic field of the spectrometer magnet.

The original fractions of the different processes inside the present analysis cuts is shown in

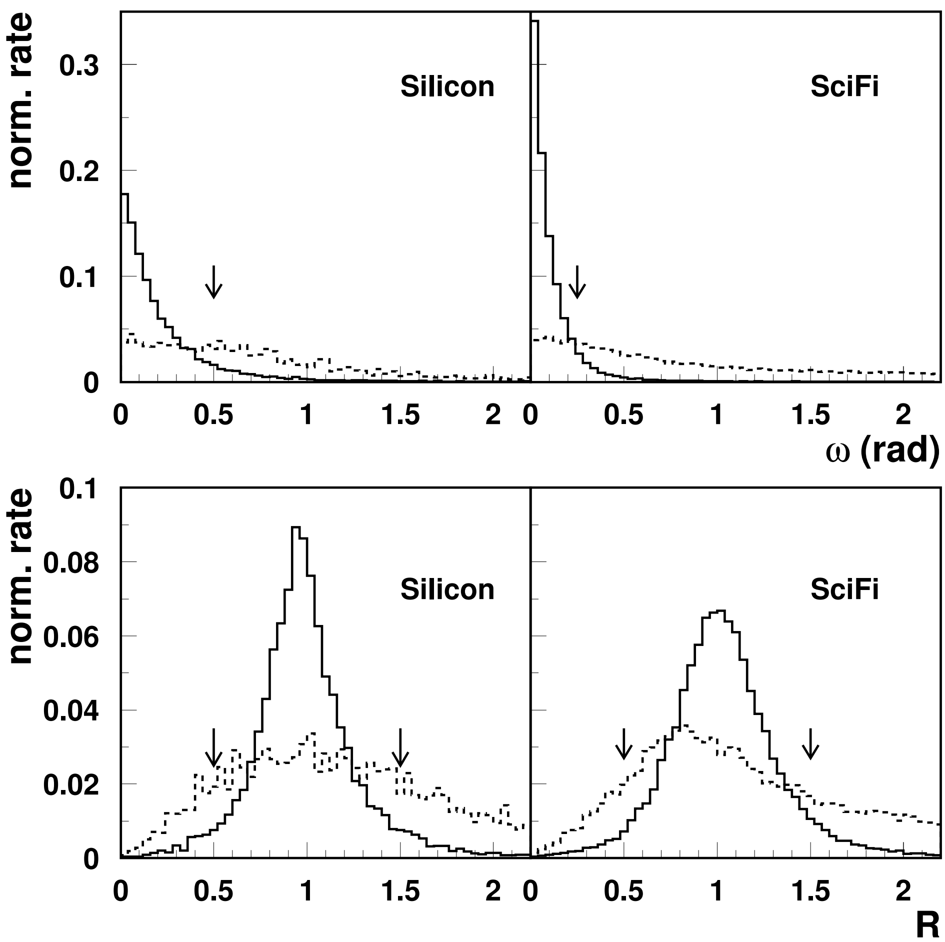

Figure 9.14.: Effect of the coplanarity cut for exclusive events (solid) and BH/DVCS events with resonance excitation (dashed). The top plots show the cut on ω, while the bottom plots shown the cut on R. The proposed cut limits are indicated by arrows.

table 9.4. The remaining fractions after the installation of the recoil-detector are shown in the same table. Figure 9.16 shows the missing mass distribution of hydrogen with all single photon event cuts applied. The distribution for hydrogen data from the year 2000 is well reproduced by the Monte Carlo (top plot). The single contributions in the Monte Carlo are shown in the bottom plot. Obviously the contamination with BH/DVCS with resonance excitation is smaller than for deuterium.

Finally the impact of the recoil detector on the missing mass analysis has to be studied. The recoil detector will not directly improve the missing mass resolution, but it will improve exclusivity. This is shown in figure 9.17. The top plot shows the missing mass distribution of all processes with the future target cell if the present analysis cuts are used; the bottom plot

Table 9.3.: Effect of exclusivity cuts: Percentage of detected events in the recoil detector, events which contain one positively identified recoil proton and events which are furthermore vetoed by additional tracks or clusters in the recoil detector. Since the technical design report (TDR, [HER02]) updates and improvements have been made on the event generator as well as on the detector geometry.

Process	detected	passing p_t-cut and PID	passing total cut
TDR			
BH/DVCS	68%	53%	52%
BH,Δ	47%	13%	8%
Present model			
BH/DVCS	65%	52%	51%
BH,Δ	50%	8%	4%
BH,$M > 1.4$ GeV	44%	2%	1%
inclusive	42 %	3 %	2 %
excl. π^0	80 %	57 %	55 %

Table 9.4.: Comparison of the composition of the datasamples: The fractional contributions of all processes are shown for the present analysis cut and without a recoil detector(left) and the future situation (right) when all exclusivity cuts are applied and the recoil detector is installed. Under these conditions only a extended cut of $M_x^2 < 5$ GeV^2 on the missing mass will be necessary.

Process	present situation	with recoil detector
BH/DVCS	83%	97%
BH,Δ	7%	$< 1\%$
BH,$M > 1.4$ GeV	3%	$< 1\%$
inclusive	6%	$< 1\%$
excl. π^0	1%	1%

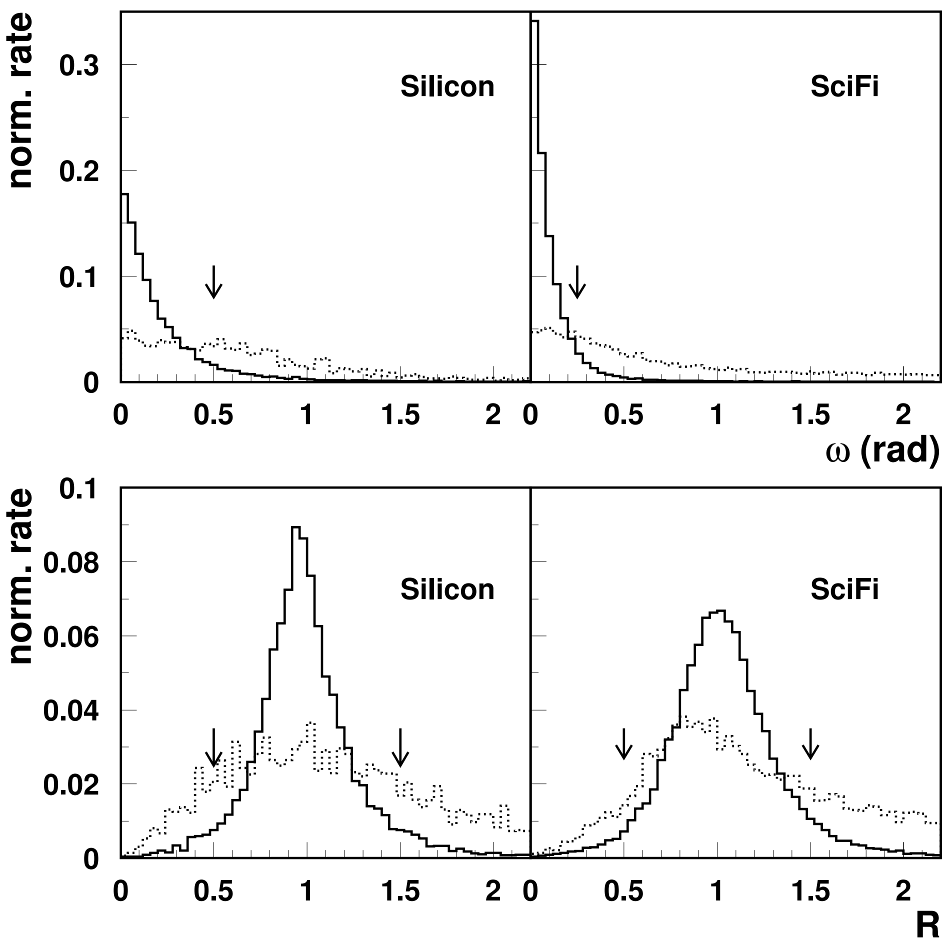

Figure 9.15.: Effect of the coplanarity cut for exclusive events (solid) and BH/DVCS events with Δ-excitation (dotted). The top plots show the cut on ω, while the bottom plots shown the cut on R. The proposed cut limits are indicated by arrows.

shows the same distributions when all exclusivity cuts are applied. Essentially all background contributions are removed even for large missing masses. Only the relative rate of exclusive π^0 events below the BH/DVCS peak is approximately unchanged.

One uncertainty in the present analysis originates from the missing-mass cut and its strong dependence on the calorimeter calibration. If the cut on the missing mass is placed at $\sqrt{5}$ GeV, it only removes some outliers but is no longer sensitive to the calorimeter calibration, as there are very few outliers with large spacing in M_x. But also the transverse momentum cut depends on the calorimeter calibration. It can be shown that in case of problems the recoil detector may also be operated without this originally forseen cut, since already the detection of a proton alone selects the exclusive or semi-exclusive region. Thus if only PID and a single cluster veto

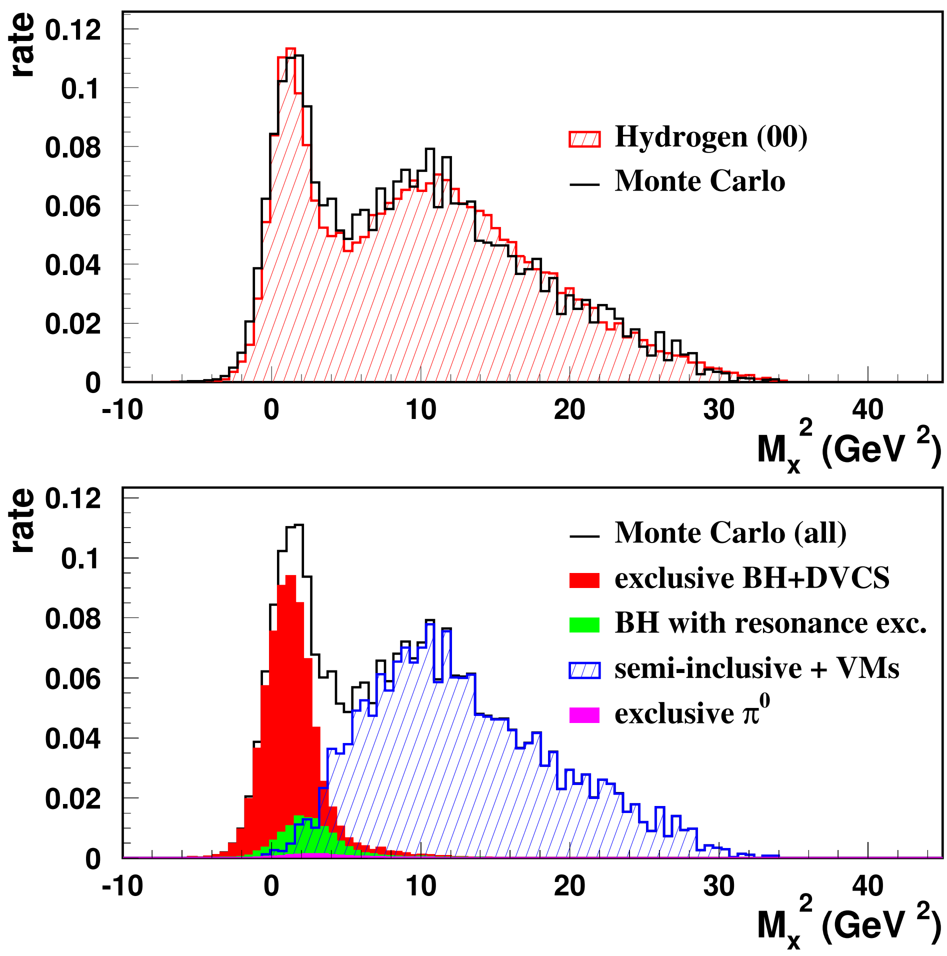

Figure 9.16.: Quantitative Comparison of data and MC: All important processes are simulated in the MC and the resulting missing mass distribution is compared with the measured one (unpolarised high density hydrogen data for 2000) (top). In the bottom plot the single contributions are shown separately.

are used, the exclusive contribution can already be increased to 94%.

It is interesting to note that a much better recoil detector would not improve the situation. The reason is that the resolution in ω and R is mainly determined by the spectrometer. This can be seen in figure 9.18 which shows the resolution of the spectrometer for the transverse missing momentum in terms of its azimuthal angle ϕ around the beam and its magnitude. Missing momenta above 500 MeV are shown as solid line, missing momenta below this value are shown as dashed line. In comparison with figures 9.9 and 9.10 it is clear that the angle ω is in any case dominated by the spectrometer, while the ratio R is only dominated by the spectrometer for the low momentum protons that are typically found in the silicon detector.

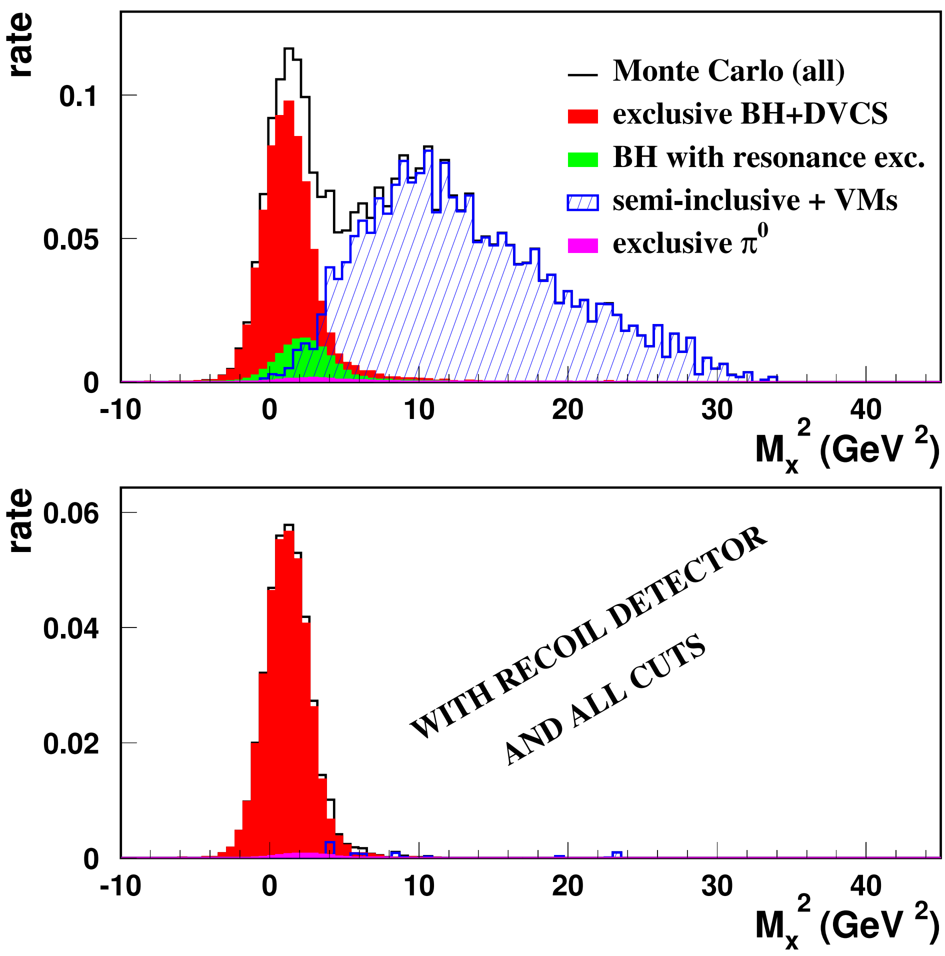

Figure 9.17.: Effect of the exclusivity cuts on the missing mass distribution: The missing mass distribution for hydrogen using the future target density profile is compared with the one when the recoil detector is used in addition (simulation, same normalisation as in figure 9.16).

An improvement of this would have required more space or a different detector technology.

Another important fact is that the tracks calculated for the main spectrometer by *hrc* have to be corrected for the deflection in the magnetic field of the solenoid. For the shown Monte Carlo studies the magnetic field in *hmc* has been set to zero in the target region. It was shown in a separate Monte Carlo study that the track direction of charged tracks at the position of the H0-hodoscope (i.e. in front of the first presently used drift chambers) is mainly rotated in ϕ with respect to the original momentum vector. It can be shown that a correction of the kind

$$d\phi = \frac{eBL}{P\cos(\theta)}, \qquad BL = 0.175\ \mathrm{Tm} \tag{9.4}$$

reduces this offset such that inside the resolution given by multiple scattering in the target re-

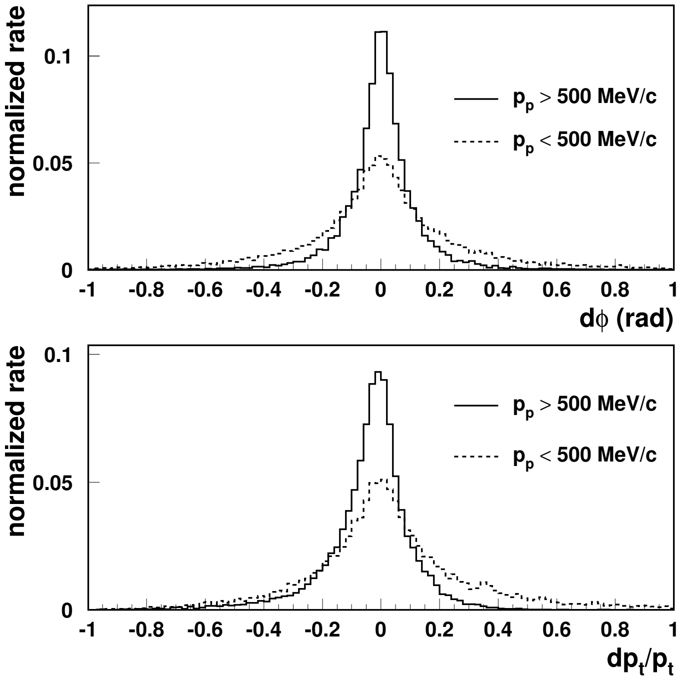

Figure 9.18.: Resolution of the main spectrometer for the transverse momentum of recoil protons. The distribution in the angle ϕ around the beam (top) and the relative deviation of the transverse momentum $(p_{t,reconstructed} - p_{t,generated})/p_{t,generated}$ (bottom) is shown.

gion the effect of the target magnet practically vanishes. The above equation is exactly valid for a homogeneous, magnetic field B confined inside a length L that acts on particles of momentum P and charge e. The inclusion of the reconstructed vertex only marginally improves the correction inside this approach.

9.4. Background Estimates

Uncorrelated background processes have two different effects on the Recoil Detector. If they occur too often they will cause radiation damage of the device; even if they are less frequent they can have an impact by adding false tracks to triggered events. Due to the bunched structure of the HERA beam this requires rates in the order of 1 particle per bunch or 10 MHz in order to be dangerous. The different background processes can be classified according to their dependence on beam currents (I_e, I_p) and target density (ρ). The processes are listed in table 9.5.

Although the frequency of hadronic showers in the HERMES spectrometer should scale with the proton current, it is much more dependent on instabilities of the proton beam. At the moment it can be large enough that some of the standard HERMES triggers, that do not use the calorimeter, have to be prescaled [HER04]. Usually trigger 21 which includes the hodoscope

Table 9.5.: Classification of background processes. Their impact as well as the corresponding counter measures are listed.

process	effect	solution
processes $\propto I_p$:		
hadronic showers	false tracks	rare in HERMES front region
processes $\propto I_e$:		
synchrotron radiation	hits in lightguides	apparently not critical
	detector hits	energy ≤ 50 keV
		$\Rightarrow$ not seen by detectors
collimator scattering	false tracks	C3-collimator + magnetic field,
		additional lead bricks (?)
processes $\propto I_e \times \rho$:		
Møller scattering (e^-e^-)	false tracks	detector geometry + magnetic field
Bhabha scattering (e^+e^-)	false tracks	detector geometry + magnetic field
Pair annihilation (e^+e^-)	detector hits	low rates
Compton Scattering (γe^-)	false hits	low rates (?)
Elastic scattering (ep)	false tracks	limited target density

H0 is not affected by such problems. Consequently it is assumed that the corresponding low momentum tracks do not reach the HERMES front region.

Synchrotron radiation affects the recoil detector in two ways: Firstly it can cause random photons in the lightguides of the fibre tracker and the photon counter. Present test measurements indicate that the chance for this is low [Har04a]. Secondly the photons can hit the detectors, which is avoided by proper shielding: At the moment the HERMES collimator system consisting of the collimators C1 and C2 is installed in order to protect the thin-walled target cell. The collimator C1 is located at -2 m in the HERMES reference system and absorbs most of the primary radiation inside the beam pipe. It is realized in the form of 2 movable collimators and a wall of lead bricks between them. The collimator C2 which is located at -45 cm is only hit by photons which have undergone scattering on C1 and prevents these photons from hitting the target cell. It is known that at the moment neither the cell nor the sensitive cell-coating are damaged.

As the new target cell occupies the same space as the downstream part of the old target cell, it will be protected as well. Synchrotron-radiation that is scattered on the target cell and hits the silicon detectors, will be rare and direct hits of the detectors are avoided by the lead bricks. In addition the minimum detection threshold in all detectors is above 50 keV and the number of synchrotron-photons drops almost exponentially with their energy [Dür98].

Scattering of beam electrons on the collimators is on the other hand a more severe problem and considerable work has been spent to understand this source of background [T+03, VES02, Kro01]. Apart from extreme situations in which the beam orbit gets unstable and is consequently dumped [vB+03], electromagnetic showers are mostly due to electrons which are only a bit outside of the nominal envelope-ellipse of the beam. Although the beam profile close to the centre of the beam is rather well-known, the flux of these particles that are more than 15 σ away from the nominal beam-orbit is difficult to measure or calculate.

During injection these particles will directly hit the collimator C2 since C1 is open in order to allow for a different beam optics. Under these conditions all detectors can receive sizable radiation damage. Around a beam energy of 18 GeV the collimator C1 is closed and all electromagnetic showers will start there.

The only way to make any prediction for detector rates is based on the idea that a shower simulation has to be made in the Monte Carlo. The resulting rates in all present detectors will then allow for an extrapolation to the future recoil detector. This simulation has been started using the program *recmc*. The most important parts along the beam-pipe in front of HERMES have been included and some random start distribution of hits on the collimators has been used.

The number of particles created in a shower is enormous, as one beam lepton can produce about 25000 electron positron pairs with enough momentum to be detected in the silicon detector. Consequently an exact simulation of the shower evolution is difficult, if not impossible. Especially since many objects in the HERMES area are not included, the simulation can only act as a first estimate.

In order to perform a rough normalisation, the hit rate in the H0-hodoscope can be used. The typical rate in the H0-hodoscope during empty target runs or ABS density is about 0.5 MHz in both detector halves. The hit threshold must be below the typical MIP-signal of 0.5 MeV and was assumed to be 0.4 MeV. In order to allow for a comparison with the present high-density runs, the C3 collimator was removed in the geometry and the magnetic field was switched off. The expected rate of events with an energy deposition of $E > 50$ keV in the silicon detectors is 1.7 $\times$ the rate of the top or bottom part of the hodoscope. Thus the total rate for such collimator events would be about 1 MHz for the silicon detector. After inserting the collimator C3 and switching on the target field, the rate in the silicon detector is reduced by a factor of 2.0. For the fibre detector rates before and after insertion of the collimator C3 are about two times higher. The final collimator design [T$^+$03] is very close to the design worked out in [Kro02], which is used in this thesis. The results in [T$^+$03] are based on hit rates in the DVCs and the conclusion is very similar.

More detailed research has been done by inserting a background test detector [VES02] into the target-chamber that is presently used together with a transverse target magnet. Even if information from the Lambda Wheels is added, it is very difficult to extrapolate the results to the acceptance of the recoil detector. Thus collimator background is still a point of concern that may limit the ability to detected MIP-tracks for veto purposes in the recoil detector.

Most of the background processes that take place inside the target gas are theoretically much easier to handle: In the case of an electron beam the beam particles will scatter off the bound electrons inside the target gas (Møller scattering). A similar process is possible in the case of a positron beam (Bhabha scattering). In both cases the cross-section diverges for low momentum transfers between the two particles; the hit electron from the target gas emerges at rather large angles approaching $\frac{\pi}{2}$. Assuming the foreseen target density of 10^{16} cm^{-2} hydrogen atoms, without the magnetic field the hit rate ($dE > 50$ keV) in the silicon detector would be about 20 hits per bunch. Since the t-channel amplitude dominates under this kinematics the projected rate for Møller and Bhabha scattering is the same. As soon as the target field is switched on, the rate reduces to 0.001 hits per bunch. As has been explained in [HERMES01b], geometrically no direct hit of the detector is possible any longer and this rate is entirely due to electrons that have been strongly scattered in the wall of the target cell.

In principle also pair annihilation is possible for a positron beam. However, the cross-section of this process does not diverge for low momentum transfers and consequently the expected rates are very low (10^{-4} hits per bunch in the fibre detector).

Another badly known contribution is due to synchrotron-radiation that undergoes Compton-Scattering in the target gas and hits the silicon-detector. Estimates for this process have been made in [HER97], but are not very precise. However, the present successful operation of the Lambda-Wheels at the same target density indicates that the effect will not be critical.

Finally another process exhibits a divergence of its cross-section for low momentum transfers (i.e. $Q^2 \ll 1$ GeV^2), namely elastic ep-scattering. This process is dangerous as the scattered protons - in contrast to the Møller electrons - are hardly deflected by the magnetic field. In addition the expected energy deposition is large, and the random rate per bunch is high enough to coincide with exclusive events. There is no possibility to suppress this contribution by a special detector design; it may be possible to subtract the events due to their fixed correlation between momentum and opening angle. At a target density of 10^{16} cm^{-2} the hit rate in the silicon detector amounts to 0.01 hits per bunch.

9.5. Alignment, Calibration and Efficiencies

In order to ensure optimum performance of the recoil detector system, special care must be taken with respect to alignment, calibration and efficiencies. The alignment procedure is envisaged to be done in a number of steps:

1. Due to the rather wide strip pitch of the silicon detector, the machining tolerances of the target chamber and the holding structure will be sufficient for the relative alignment of the silicon modules. The only uncertainty arises from the exact position of the sensors in the plane of the module frame. This can be measured by optical methods during the installation of the detectors.

2. Both barrels of the fibre tracker will be aligned in the DESY22 testbeam [SS04]. During cosmic runs prior to the installation of the recoil detector in HERMES the fibre detector can be aligned with the silicon detector.

3. The whole recoil detector must be aligned with respect to the HERA-beam. This can only be done, when the detector is in operation. One possibility is the usage of spectator protons from deuterium breakup; at moderate target densities the silicon detector will be able to reconstruct their origin if the magnetic field is off. If proton momenta above 200 MeV/c are selected from a sample of 2×10^5 DIS events on deuterium , the beam position can be fixed with a resolution of at least 1 mm.

4. The recoil detector must be aligned with respect to the HERMES spectrometer. As mentioned in [HER02] this can be achieved by considering elastic ep-scattering at a lower beam energy of 12 GeV. From a technical point of view this beam energy is feasible as has been proven in the running period of 2000.

Only if the alignment is done with sufficient accuracy, the missing transverse momentum from the main spectrometer can be combined with the proton momentum measured by the recoil detector. This is not entirely trivial, as the internal alignment of HERMES is still being optimised (cf. chapter 5).

The functionality of the fibre tracker critically depends on the beam-position, if the track is not detected in the silicon counters. Therefore an online monitoring of the beam position with an accuracy of less than 0.5 mm is desirable. After the initial alignment of detector and beam, this is possible by using the beam position monitors of HERA. A resolution of the required value can be achieved with these devices [Els01].

Also detector calibration is an important issue: For the fibre tracker the energy calibration will determine the local detection efficiency as well as the ability to use the detector for PID. While the PM-tubes have been calibrated in a LED test stand [HT04], the calibration of the complete setup can be done during the alignment testbeam. In the final experiment it is presently discussed to install a gain monitoring system [Hoe04] that can also be used for the photon detector.

For the silicon detector the calibration is even more important, as it determines its ability to measure the particle momentum. The ultimate aim is to know the energy deposition of a hit in the silicon detector if a signal above threshold is measured in several detector channels. First one can consider the simple case in which a proton hits the surface at the centre of one strip under an angle of 90°. In this case it is clear that the measured signal in this strip will be proportional to the deposited energy in the silicon. Consequently a "single-strip calibration" can be done to study this linear dependence. Assuming that the detector behaviour is not too sensitive to the specific environment, such a calibration is possible at any test-beam with sufficient momentum range.

At the moment test experiments at DESY [G$^+$04] as well as at the Erlangen Tandem accelerator [Vog03, Pic03] are done. While the DESY22 testbeam allows for the measurement of MIP-signals with an electron beam of a few GeV, the Tandem accelerator provides protons with momenta between 75 MeV/c and 137 MeV/c, which have a similar energy deposition as low momentum recoil protons.

While the calibration of the MIP-signal will mainly be important for the study of detection efficiencies, the calibration of the low gain signal is crucial for the momentum measurement. Under the condition that the fluctuations in energy loss - and not the quality of the electronics - dominate the energy resolution , the calibration of the low-gain channel should be done with an accuracy of about 1 %. This is mostly required for protons that get stuck in the second silicon layer: The simulation shows that protons at a momentum of 125 MeV/c ($E_{kin} = 8.29$ MeV) under perpendicular incidence deposit 6.85 MeV in both silicon layers if they traverse exactly one Kapton foil-layer. The expected width of the distribution is 0.068 MeV. For protons of 140 MeV/c, which penetrate both silicon layers under perpendicular incidence, only the energy deposition in the first layer matters. It is 2.83 MeV with a width of 0.098 MeV which corresponds to a required accuracy of the calibration of 3.5 %.

If the calibration is less precise the effect will have an impact on the achieved momentum resolution. Apart from momenta below the punch-through point of about 140 MeV/c, an accuracy of 5 % may still be sufficient (the present lookup-table for the particle momentum has a bin-width of 0.2 MeV). In principle this is no problem: Present testbeam experiments indicate a signal to noise ratio of about 40 at low proton momenta, which demonstrates that a sufficient resolution of the electronics is achieved. Under these conditions a calibration is possible with a moderate number of hits per strip (< 100).

However in practice a number of problems remain:

1. Interchange of electronics components: The present electronics setup of Hybrid, ACC and

HADC entails that each component affects the detector gain in a non-multiplicative way.

2. Stability: Temperature as well as low voltage settings are not necessarily reproducible between the testbeam and the final experiment. Also cable lengths may be different. If parameters of the HELIX chip or high voltage settings have to be changed for some reason, the detector gain for the new settings is unknown.

3. Radiation Damage: Although the HELIX chips are radiation tolerant (< 250 krad) and the TIGRE sensor itself is still expected to work after several Mrad, the detector gain may drop with time.

As a conclusion, the initial calibration of the detector should be as good as possible, but a means for online calibration is definitely needed. This will be discussed in the following section.

In addition to these technical problems also a more principle problem exists: The so-called single-strip calibration is not suitable as soon as tracks pass through two neighbouring strips, e.g. if they arrive under some flat angle. In this case clusters of hit strips are observed. However also for the ideal tracks considered before, cross-talk leads to the formation of a cluster. The difficulty is now to device a clustering algorithm that includes as many strips as necessary to measure the energy of the particle, no matter if the cluster is caused by true charge-sharing on the detector or cross-talk. The typical cluster-size due to charge-sharing will be below 3 due to the very broad strips. The cluster size due to cross-talk on the detector and the HELIX-chip can be as large as 5 for low momentum protons. In this way, the single-strip-calibration is insufficient and has to be replaced by a calibration of the cluster (depending on the clustering algorithm) or some more elaborate scheme.

Finally detector calibration is impeded by the fact that the TIGRE sensors are not exactly 300 μm thick and that not all of this is active detector material. The delivered batch of 25 good TIGRE sensors has a varying thickness of 295 $\ldots$ 316 μm. These values were measured by the manufacturer and have been confirmed using a micrometer screw on the supplied test-structures. The different detector thickness matters, if the particles of the test beam punch through the detector (DESY22, Erlangen Tandem). It does not matter if the particles get stuck in the detector (Erlangen Tandem). Thus the combination of both results allows to disentangle the electronics gain from the original energy deposition. The 7 % variation in the detector thickness may lead to the necessity of separate momentum lookup-tables for each detector.

In addition according to the manufacturer up to 4 μm on each surface consist of inactive material (cf. appendix A.1). The inactive surface layer has already been observed in [Wie98] for a similar silicon strip counter using the Erlangen Tandem beam. If the thickness of this layer is known, its main effect can be absorbed in the applied momentum offset for the case, in which the recoil proton gets stuck in the second layer. It will have to be seen, if $12\ \mu$m of $Si/SiO_2/Al$ have a sizable effect compared with the Kapton foils. At higher momenta the passive surface layers can be neglected in the momentum reconstruction.

Detector efficiency is a different point that seems to be uncritical for low momentum protons in the silicon detector. It is known that the efficiency of the silicon detectors is very uniform; also hits between neighbouring strips show almost ideal charge sharing [Vog03], which will also be discussed in section 9.7. A number of dead strips exist but they are known from the beginning. If additional dead strips develop during the operation of the detector, they can be identified by considering a few non-sparsified pedestal runs, since dead strips do not take part in the usual common-mode-fluctuations of the Detector channels.

9.6. Elastic Protons and the Silicon Detector

As has been discussed above, the rate of elastically scattered protons in the recoil detector is high. This can also be seen as an advantage, since they allow to monitor the functionality of the silicon detector. While the scattered lepton will only in very few cases hit the HERMES standard acceptance, the luminosity monitor is able to spot the leptons at very low values of Q^2. Its nominal acceptance is 4.6 mrad to 8.5 mrad (cf. [Els01]) which corresponds to $Q^2 = 0.016 \ldots 0.055$ GeV^2 for elastic electron proton scattering.

As these electrons hit the luminosity monitor with almost the original beam energy, they are already now used to calibrate the calorimeter blocks of this detector. In order to do this, a standard HERMES trigger exists (at the moment trigger 9) that causes a readout of all detectors if the hit energy in the luminosity monitor exceeds 25 GeV. The trigger rate of trigger 9 compared to the DIS trigger 21 is at the moment about 5 % during high density running. It will have to be studied if this rate is sufficient. In principle the predicted rates can also be obtained from Monte Carlo, but this requires detailed understanding of the beam-pipe-geometry and the acceptance of the luminosity monitor.

The protons belonging to these triggered events have momenta of $P = 125 \ldots 235$ MeV/c. This momentum range is ideal to obtain double hits with sizable energy deposition in the silicon detector; for example in the second layer hits between 1 and 6 MeV are observed. The distribution of the protons in θ and p is shown in figure 9.19. As the resolution of the silicon detector in the angle θ is for these momenta worse than 0.03 rad, it is clear from the plot that the momentum derived from this correlation has an error of more than 50 MeV/c. This is not sufficient for an energy calibration of the silicon detector. However, due to the clean signature, the elastic protons can e.g. be used to select the correct timing for the silicon detector. The timing of the fibre tracker can then be adjusted with respect to the silicon detector.

In addition the elastic protons allow gain monitoring of the silicon detector: The characteristic energy deposition of the break-through point in the second silicon layer can be used to check the overall detector calibration. The expected energy deposition of protons in the second layer is shown in figure 9.20. Only an angle of $\phi = \pi/4$ around the beam is considered and no electronic noise is assumed. A sharp edge is seen at about 6 MeV energy deposition, and a calibration accuracy of ± 0.2 MeV or 3% seems to be realistic. As soon as the breakthrough point is found, the energy deposition in the first layer can be calculated for protons that are close to this point in the second layer. For the special case of figure 9.20 an energy deposition of 3.0 MeV is expected in the first layer and a calibration accuracy of ± 0.1 MeV or again 3% seems to be feasible. In practice this method has two drawbacks as it relies on the Monte Carlo (because of the relation between first and second layer) as well as on a good knowledge of the breakthrough-point for each detector. Moreover it is not certain, if enough statistics can be accumulated; e.g. for figure 9.20 50000 elastic protons have been generated for $\phi = \pi/4$. Apparently a more detailed study using a full simulation of the acceptance of the luminosity monitor is necessary, but a strip by strip calibration using elastic protons may be difficult.

9.7. Low Momentum Test Beam

Several testbeam experiments have been carried out to study the feasibility of the recoil detector project. Two of them - the Erlangen testbeam and the GSI testbeam - have taken place under

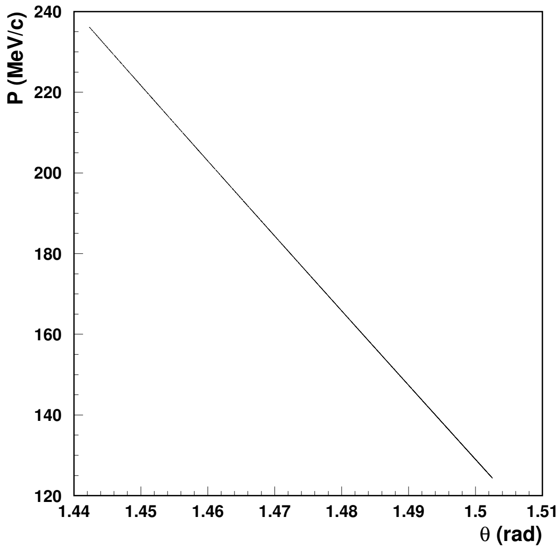

Figure 9.19.: Momentum of elastically scattered protons versus the scattering angle θ of the protons relative to the beam.

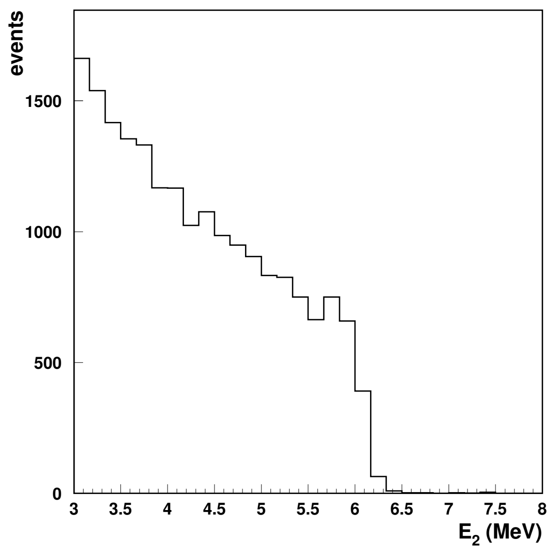

Figure 9.20.: Energy deposition of elastically scattered protons in the second silicon layer. A fixed angle of $\phi = \pi/4$ (angle around the beam) is assumed, such that the breakthrough point is not washed out. The scattered lepton is inside the nominal acceptance of the luminosity monitor. No electronics noise is simulated.

participation of the Erlangen group and the results will be summarised here.

The first testbeam at the Erlangen tandem accelerator (August 2002) demonstrated, that the proposed silicon detector system can fulfil all requirements and that a detector calibration at this facility is possible. Details about it can be found in [Vog03] and [Pic03].

The Erlangen Tandem accelerator is a continuous beam machine of the Van der Graaf type. It can be used to accelerate protons or medium sized nuclei to energies of 3 to 10 MeV per charge. The intrinsic energy resolution is very good ($< 0.1\%$) [Wie98] and the beam current can be reduced to achieve useful rates of 10 Hz to 1000 Hz. The detector can be placed into a vacuum chamber such that the conditions of operation are very close to the setup at HERA.

For the first experiment an off-the-shelf TIGRE detector was combined with a readout-system that is also used in the H1-experiment [E$^+$97]. This system is based on the APC128 [HP93] readout chip. One of these hybrids was mounted on a holding frame as shown in figure 9.21. In contrast to the figure only the central strips of the TIGRE detector were attached to the hybrid as the originally foreseen pitch-adapter could not be bonded. The hybrid was supported by a massive block of aluminium in order to keep a stable temperature of the readout chip.

Protons of 6.22, 7.00 and 8.00 MeV kinetic energy were used and a surface barrier diode behind the detector served as a trigger detector. As the diode was calibrated using an α-source, the energy deposition in the silicon detector could be directly measured at the same time. Thus the calibration was almost independent of energy loss calculations.

The common mode of the detector was calculated from several non-hit strips that were always outside the proton beam. Pedestals were not measured online but taken in a separate pedestal run. After common mode subtraction and pedestals subtraction the event data was scanned for proton hits. A typical event is shown in figure 9.22. In most of the cases only one strip is hit. This can be seen by looking at the two central strips hit by the beam and plotting one energy deposition vs. the other one. A triangle as shown in figure 9.23 is obtained. Due to cross-talk 5 blobs are seen: Hits in the two strips, cross-talk hits from the outer neighbours and no hit at all. Linear charge sharing between the strips 6 and 7 is observed as a straight line connecting the two corresponding blobs.

The energy deposition for hits in strip 6 at the three different energies is shown in figure 9.24. A calibration constant of 54 keV/channel was determined using the energy deposition in the trigger diode. At a beam energy of E_{kin} = 7.00 MeV ($P = 115 MeV/c$) the peak had a width of 0.22 MeV, while the baseline noise was 0.13 MeV. The predicted energy loss fluctuation by GEANT was 0.075 MeV which indicates that the noise of the electronics dominated. The exact dependence of the electronics noise was not measured, but may contain - among others - a contribution $\propto \sqrt{E}$ (cf. [Wie98]). It is clear that this energy resolution would not have permitted the detection of minimum ionising particles with a most probable energy deposition of only sim80 keV in 300 μm of silicon. In principle a double readout of pipeline cells using different amplification factors may be possible to detect them in addition; however, such a solution was no longer studied after the decision had been taken to use the HELIX3.0 chip instead of the APC.

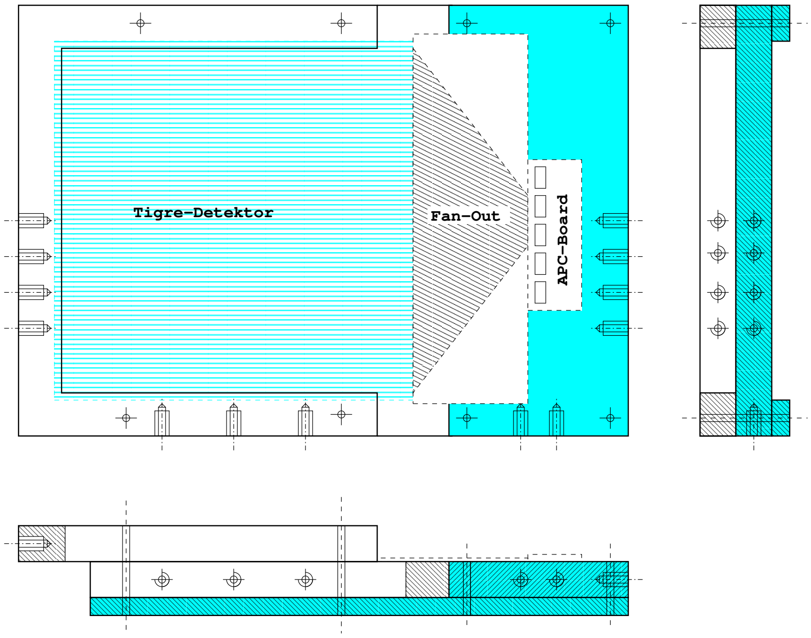

Figure 9.21.: The APC test detector: The TIGRE detector was mounted in a plexiglass frame, the hybrid was supported by a massive aluminium block in order to stabilise its temperature. The shown fan-out between sensor and hybrid was in reality replaced by a much smaller one due to technical problems.

9.8. High Momentum Test Beam

A more up-to-date study of the final readout system was possible during the GSI testbeam (December 2003). At the GSI accelerator a secondary hadron beam of momenta between 300 MeV/c and 900 MeV/c was supplied for a test setup in cave A. The beam consisted of pions, protons and deuterons. The test setup is schematically shown in figure 9.25. Since the beam momentum was given at the exit window of the beam-pipe, the silicon detector was installed as the first device in order to obtain the best possible measurement of deposited energy vs. momentum. Behind it a multi-wire proportional chamber (MWPC) was mounted for reasons of beam diagnosis. One fibre-module and one photon detector module were installed behind the MWPC. 3 different scintillation counters were used as trigger detectors and for time of flight separation of the 3 particle types.

The first silicon detector of the final kind was equipped with the electronics as explained

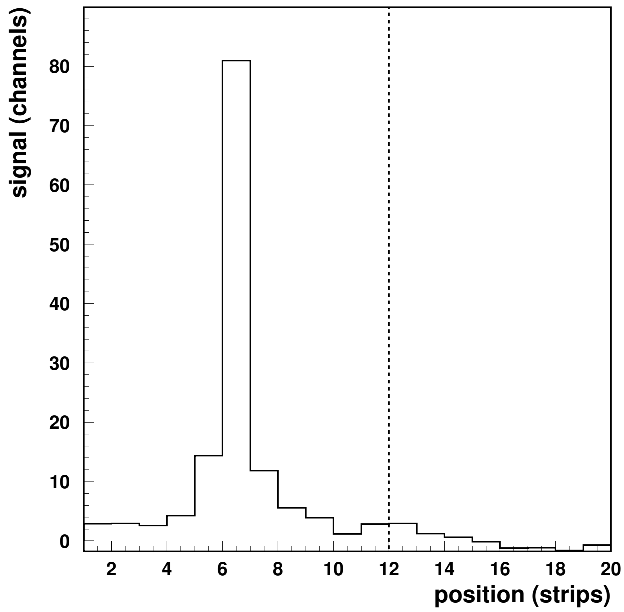

Figure 9.22.: Typical proton hit in the test detector: Strip 6 is hit, while the neighbouring channels respond due to electronic cross-talk on the sensor. The cross-talk on the read-out chip is in contrast very low. Pedestal and common mode correction are applied; the common mode has been obtained from the last 8 channels which cannot be hit for geometrical reasons.

in section 8.3, but due to a broken Kapton foil only the p-side of the detector was working. Two TIGREs of a preproduction were used for the prototype. Several bad capacitors lead to a number of bad detector strips, and the nominal value of the bias resistors was 2 MΩ instead of the final value of 7.5 MΩ. The silicon module was mounted on a rotatable table with a precise scale, where the rotation axis was along the vertical direction. In order to allow for future clustering studies, the detector was mounted in the horizontal and in the vertical position and for both cases a number of different angles were scanned. As the strips of the p-side are aligned with the long side of the module, the typical cluster size for the horizontal orientation was one, while it was larger for the vertical orientation.

Figure 9.26 shows the time of flight (TOF) spectrum obtained from the first and the last trigger scintillator at a beam momentum of 600 MeV/c. The three particle types are clearly separated. Figure 9.27 shows the beam profile for the same momentum; the hit region ranges from strip 46 to strip 75. The region from strip 56 to strip 71 is used for the following analysis and hits in the remaining strips inside the beam profile are used as a veto. Noisy strips are omitted in the plot and correspond to dead detector channels, which do not take part in the common mode fluctuations. It is interesting, that the cross-talk on the HELIX-chip in combination with common mode noise also makes the neighbouring strips very noisy. This means that for strong common mode noise one unbonded strip corresponds to a loss of 3 strips. For all beam momenta at GSI only the high gain channel provided good information. The energy spectrum of the proton hits in the high gain channel at a momentum of 600 MeV/c is shown in

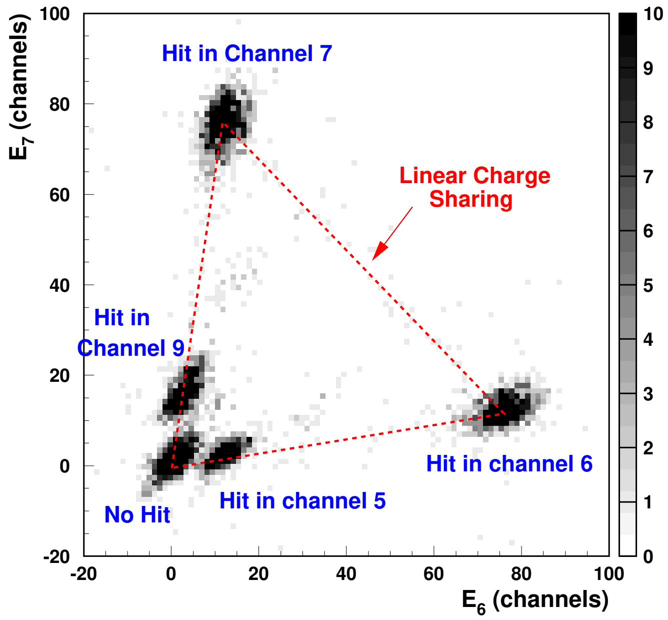

Figure 9.23.: Signal in channel 6 vs. signal in channel 7 for a 7 MeV continuous proton testbeam. Pedestal and common mode correction are applied.

figure 9.28. As the proton can hit dead strips, the strip with the maximum energy deposition can in very few cases be due to noise or cross-talk; this causes the tail on the left, while the signal peak is well described by a Landau curve.

Figure 9.29 shows the deposited energy by the protons as a function of beam momentum and the rotation angle α in the horizontal orientation (upper plot). Only the central strip of each cluster was used to determine the hit energy; for momenta of 300 MeV/c two Gaussians were fitted while for higher momenta the sum of a Gaussian and a Landau peak was fitted. The bottom plot shows the same results with the same fits from Monte Carlo, where the scale for the hit energy is in MeV. The 600 MeV/c and 900 MeV/c samples consistently result in a calibration constant of 280 channels per MeV. All 300 MeV/c samples result in a calibration constant of 316 channels per MeV. This suggests that the true beam momentum is lower than 300 MeV/c such that the true energy deposition is a bit higher. In addition the momentum distribution of the beam can be broadened if the lower momentum is due to multiple scattering.

The solid curves in figure 9.29 correspond to fits of the kind

$$E = E_0 \cos^{-1} \alpha, \tag{9.5}$$

with E_0 as the only fit parameter. As can be seen the fit is good and indicates that the energy loss in this momentum range is mainly proportional to the traversed distance in the silicon. This is no longer valid for momenta below 150 MeV/c.

In contrast to measurements at the Erlangen test beam, Landau tails of the energy loss are clearly visible (cf. figure 9.28). Hence only for the lowest momentum a Gaussian fit is possible such that the energy resolution can be directly calculated. The obtained width of the

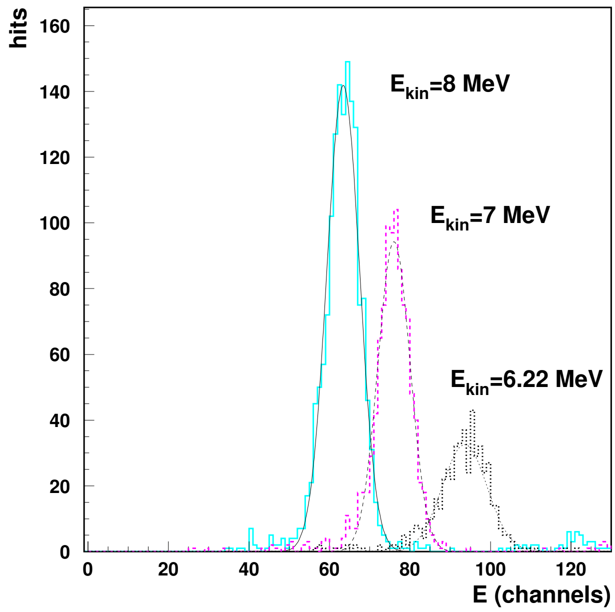

Figure 9.24.: Signal in channel 6 for 3 different proton beam energies. Pedestal and common mode correction are applied.

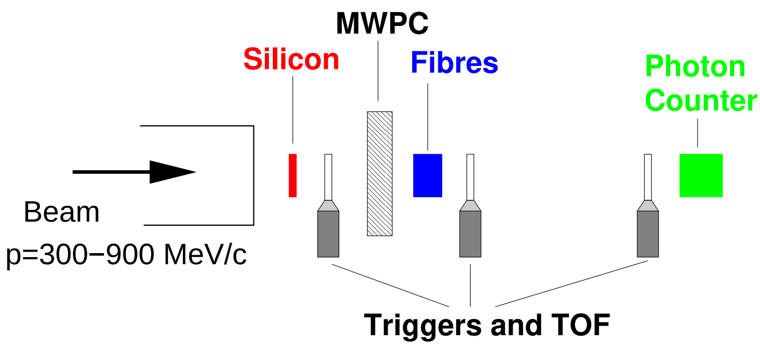

Figure 9.25.: Experimental setup for the GSI testbeam: A mixed hadron beam (protons, pions, deuterons) of momenta between 300 MeV/c and 900 MeV/c was provided by the accelerator. Test modules of all components of the recoil detector were installed. Scintillation counters were used for the trigger and for the particle identification.

peak is about 0.15 MeV in contrast to the value of 0.08 MeV that would be due to energy loss fluctuations. The electronics noise can thus be estimated as 0.12 MeV at an energy deposition of about 0.7 MeV. However, this is only an upper limit on the noise, since the initial momentum distribution of the beam may also broaden the curve.

For lower energy depositions the estimated noise is much smaller. For the highest proton momenta under an angle of $\alpha = 0$ the distribution is compatible with a noise of only 0.03 MeV

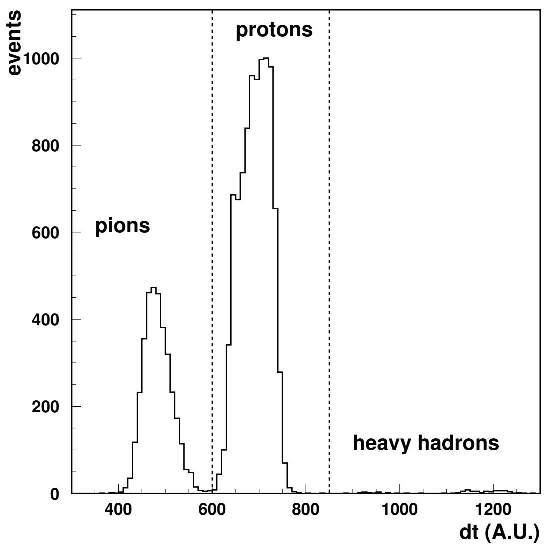

Figure 9.26.: Time difference between the hits in the first and the last trigger scintillator in arbitrary units. A good separation of pions and protons is obtained.

at an energy deposition of 0.15 MeV. This is shown in figure 9.30. A value of 0.04 MeV at 0.35 MeV energy deposition is found for 600 MeV/c protons under $45°$. This indicates that the initial design goal of $dE < 0.05$ MeV can be reached for the lowest energy depositions. For higher energy depositions a parametrisation of the noise has to be obtained from a more detailed analysis of all presently taken testbeam data. It is difficult to predict the exact noise behaviour theoretically as the fluctuation in the number of generated charges (cf. [Lut99])

$$dE = \sqrt{0.115 \times 3.63\ eV \times E} \tag{9.6}$$

is a very small contribution and most of the signal dependent noise is due to more complicated mechanisms. On the whole no problems with the energy resolution are expected and the predictions of the design simulation are still realistic. A separate detailed discussion of the GSI testbeam results is in preparation.

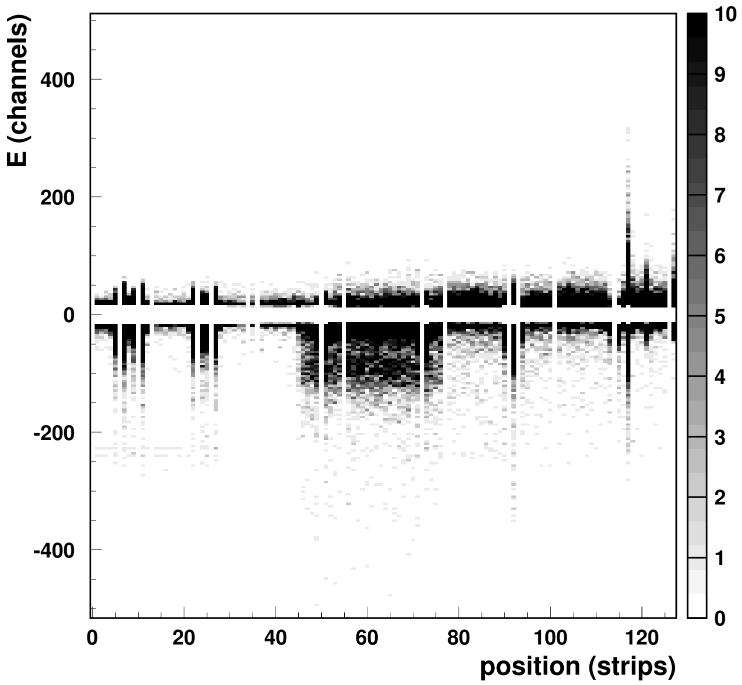

Figure 9.27.: Signals in all strips for all triggered events at a beam energy of 600 MeV/c. Unbonded strips are left out. The beam profile is seen with negative hit values in the middle. The width corresponds to the size of the trigger scintillator.

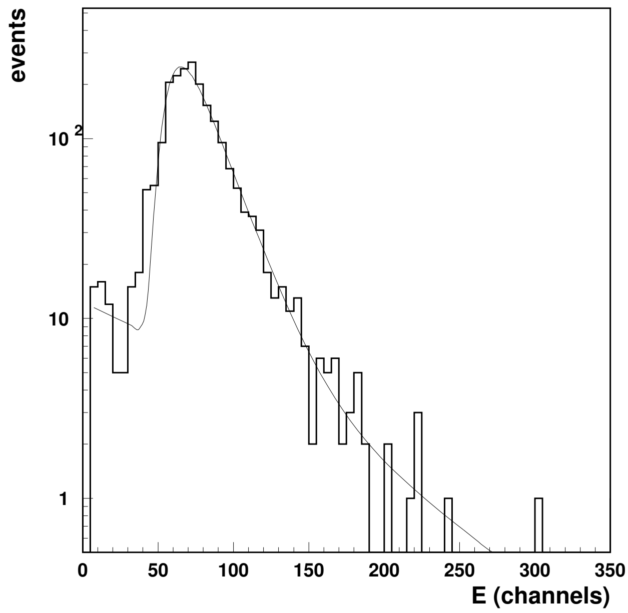

Figure 9.28.: Energy spectrum for protons at an angle of $\alpha = 0$ and a momentum of $P = 600\ MeV/c$. A Gaussian (pedestal tail on the left) plus a Landau curve is used as fit function. A reasonable agreement is found; in principle the Landau should also be convoluted with a Gaussian but the effect on the peak position is small.

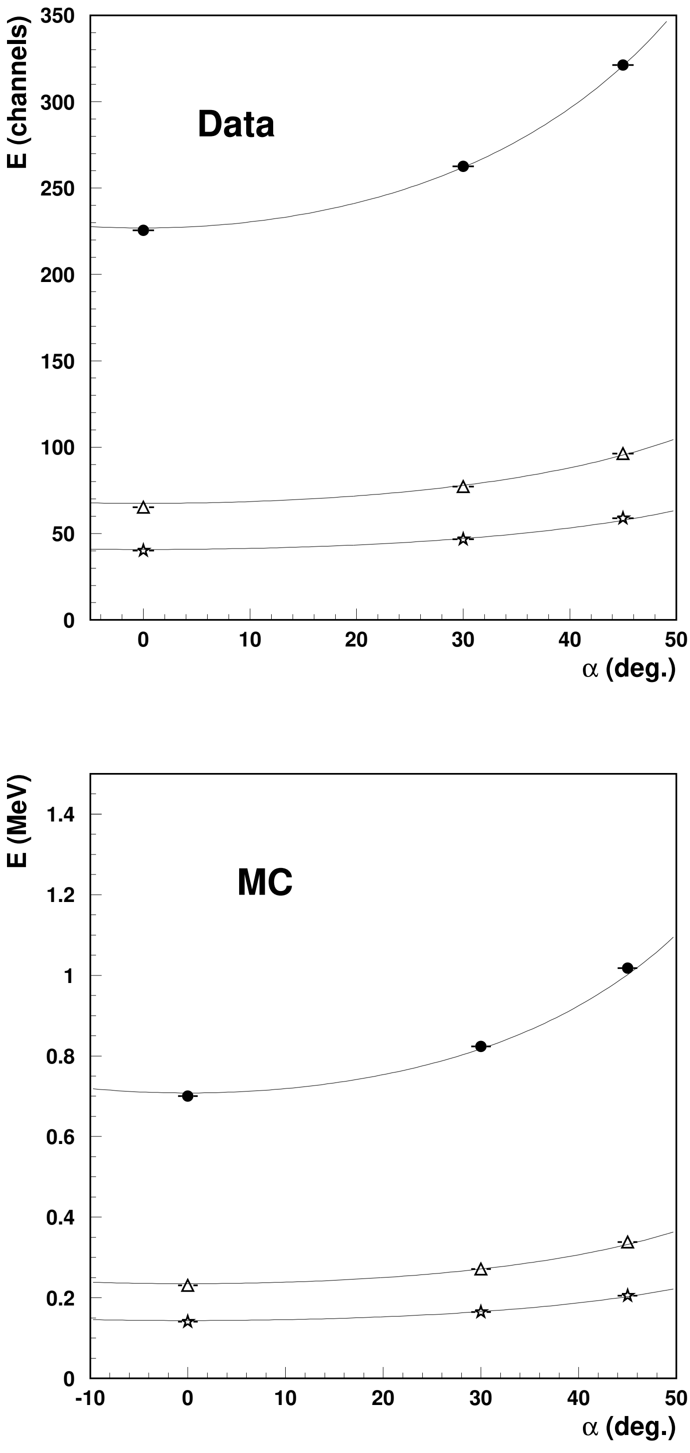

Figure 9.29.: Most probable energy deposition obtained from the discussed fits as a function of the angle of incidence α. The first set of data points (top curve) corresponds to $P = 300\ MeV/c$, the second set (middle) to $P = 600\ MeV/c$, the third set (bottom curve) to $P = 900\ MeV/c$. The fit curves are of the form $E = E_0 \cos^{-1}\alpha$. The top plot is obtained from data, the bottom plot from Monte Carlo.

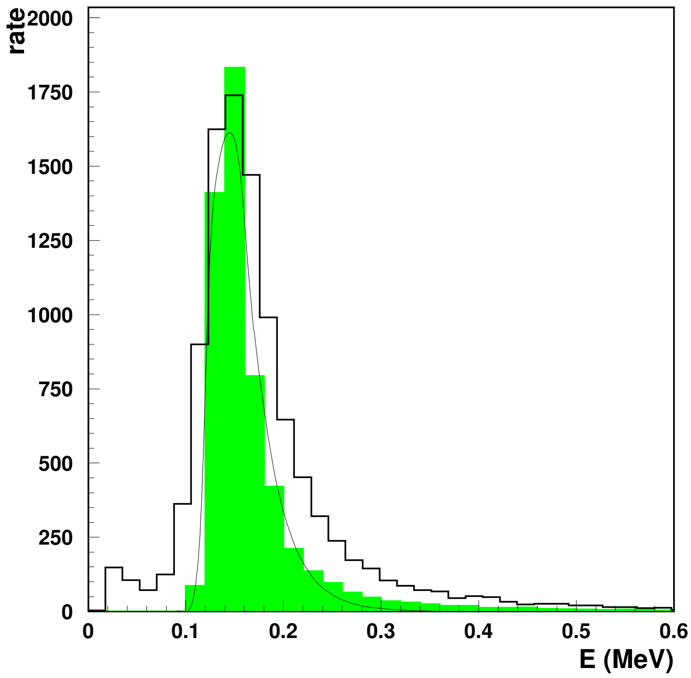

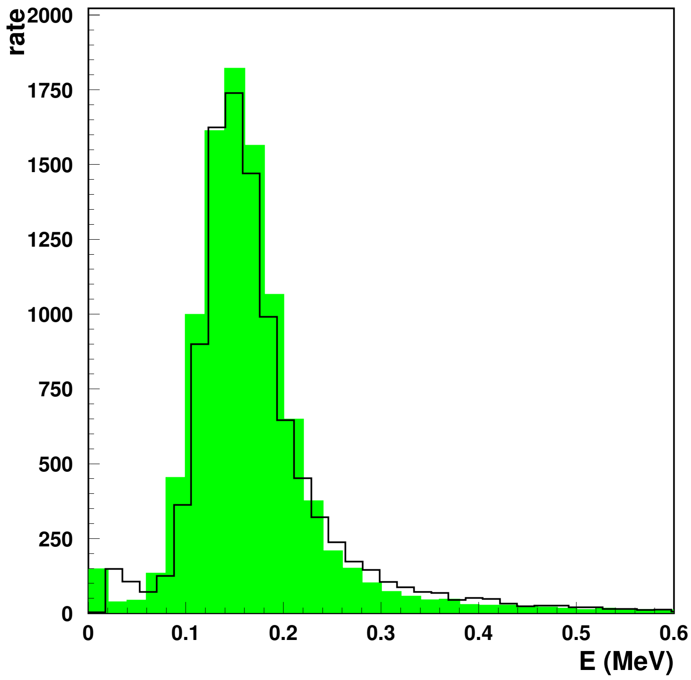

Figure 9.30.: Measured energy spectrum for protons under $\alpha = 0$ at $P = 900\,\mathrm{MeV/c}$ (black curve in both plots) in comparison with the ideal prediction from the simulation (solid histogram, top) and a simulation which includes Gaussian noise with a width of 0.03 MeV (solid histogram, bottom). The normalisation of the simulated hit rate is arbitrary. A very good agreement of the shapes of the energy spectra is found.

A. Quality Check for Silicon Sensors

A.1. Test of TIGRE surface structures

The standard design of the TIGRE detector has the parameters shown in table A.1. Soon it became clear that two important modifications were necessary for the application at HERMES :

- increased oxide thickness for the coupling capacitors,
- reduced resistance for the bias resistors.

Both modifications were necessary as the TIGRE was not designed to be operated under high background conditions. Instead it was build for rather low hit rates and high energy resolution.

In the environment of a storage ring occasional peaks in the radiation can lead to large amounts of free charges inside the detector depletion zone. Without the bias resistors, a high current through the detector would be seen at the same time. Due to the presence of the resistors, the voltage drop across the detector can be strongly reduced; in this case the voltage drop occurs across the bias resistors of both sides. Since the readout chips are still at the nominal potential of the detector side, the voltage drop is also seen across the corresponding coupling capacitors.

The original capacitors were designed to stand voltages in the order of less than 1 V. As more than 20 V can be expected if the two detector sides are effectively shortened, the capacitors

Table A.1.: The design parameters of the standard TIGRE detector.

Parameter	Value
sensor size	99 mm $\times$ 99 mm
active area	97.3 mm $\times$ 97.3 mm
silicon thickness	300 μm
strip pitch	758 μm
strip separation	56 μm
coupling capacitance	1 nF
total strip capacitance	52 pF (p), 70 pF (n)
polysilicon bias resistor	50 MΩ
depletion voltage	50 V (Max.)
metallisation	0.8 μm
maximum voltage	2 $\times$ depletion voltage

would break through and large currents could enter the HELIX input lines. In order to avoid this, the capacitors had to be reinforced. Even with this modification the problem is not fully solved as a huge current pulse enters the input channels of the HELIX chip. In this way one or more HELIX chips will be destroyed but permanent damage to the sensor is avoided.

A very reliable method would have been to add a layer of silicon nitride on top of the oxide layer. Since the manufacturer did not have the apparatus to produce this, it was instead attempted to add a second layer of oxide with different parameters for the CVD-process but the same lithographic mask. After a test production with 2 detectors, the results were satisfactory. It was found that also a thicker metallisation was needed in order to fill the wire-holes through the oxide layer. The final layering scheme at the surface is shown in figure A.1. This modification also decreased the loss due to capacitor shorts: Instead of up to 3 shorts per detector side usually no short at all occurred for the detectors of the main production.

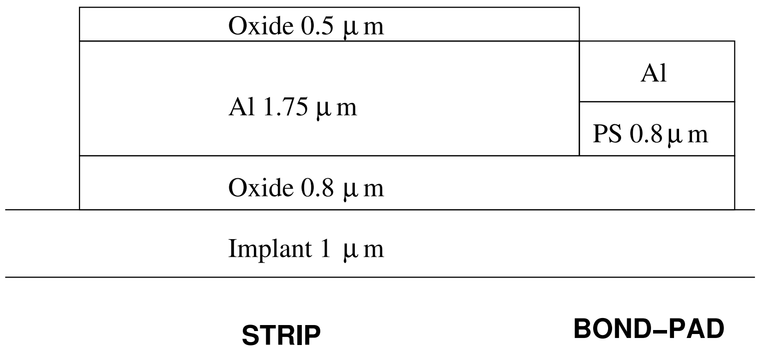

Figure A.1.: The passive material on top of the active silicon volume: PS denotes the polysilicon as support of the bond-pad. The implant depth after diffusion is about 1 μm. Depending on the hit position the passive material can amount to about 4 μm.

Another important modification concerned the bias resistors: The design value was 50 MΩ, but it was experimentally found that the spread around this resistance was wide. Especially very high values were also seen. With a typical strip capacitance of about 50 pF (neglecting the capacitance of the readout-chip) such a resistance leads to a time constant of 2.5 ms. The new design value of 7.5 MΩ reduces this time to 0.38 ms. This implies that single strip hit rates of less than 1 kHz will not lead to a catastrophic build-up of charge. The additional noise due to the lowering of the capacitance can be estimated to be only 1.4 % of the total noise [Pei92].

Each TIGRE detector of the final production was provided with a separate data sheet that provided measurements by the manufacturer:

- coupling capacitance for all 256 capacitors,
- IV-curve of the device,
- depletion voltage (presumably obtained from the detector capacitance),
- typical values of bias resistors.

In order to cross-check and extend these measurements a number of quantities was measured using a probe-station of the type Süss SOM4 that was equipped with a HP 4156A Precision Semiconductor Parameter Analyser. The p-side structures can directly be measured without mounting the detector. Some of the n-side structures are on the other hand only accessible if the bias voltage is applied. This was achieved by using a special mounting frame (figure A.2) that allowed a non-permanent mounting of the double sided detectors. p- and n-side bias rings were bonded at the Chair of Applied Physics, University of Erlangen.

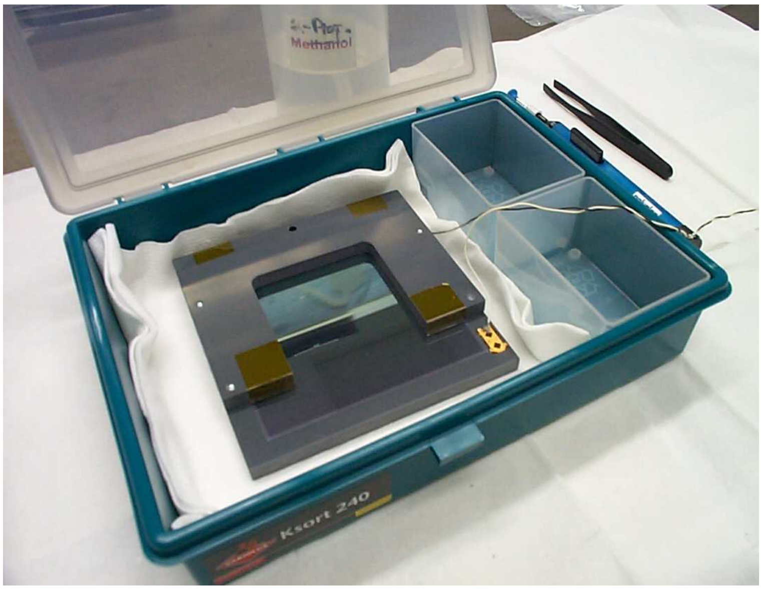

Figure A.2.: A holding frame with a mounted TIGRE sensor in its storage box.

The following features were checked for each detector:

- 3 different bias resistors on each side (including the single strip currents on the n-side),
- 3 inter-strip resistances on each side,
- the resistance of 3 coupling capacitors on each side ,
- the depletion voltage as defined by the point of inter-strip separation on the n-side,
- the IV-curve.

The following defects were found:

- The single strip currents of the first strip on the n-side was sometimes unstable at a time-scale of a few seconds.
- In very few cases the inter-strip separation on the p-side was bad (last strips on p-side).
- The depletion voltage of some detectors showed large local variations. Depletion voltages above 70 V were measured (the nominal value was 50 V $\pm$ 10 V).
- One detector had bad contacts on one side.

In total 2 detectors were rejected because of high depletion voltage and one detector was rejected because of the bad contacts. A typical I/V-curve is shown in figure A.3.

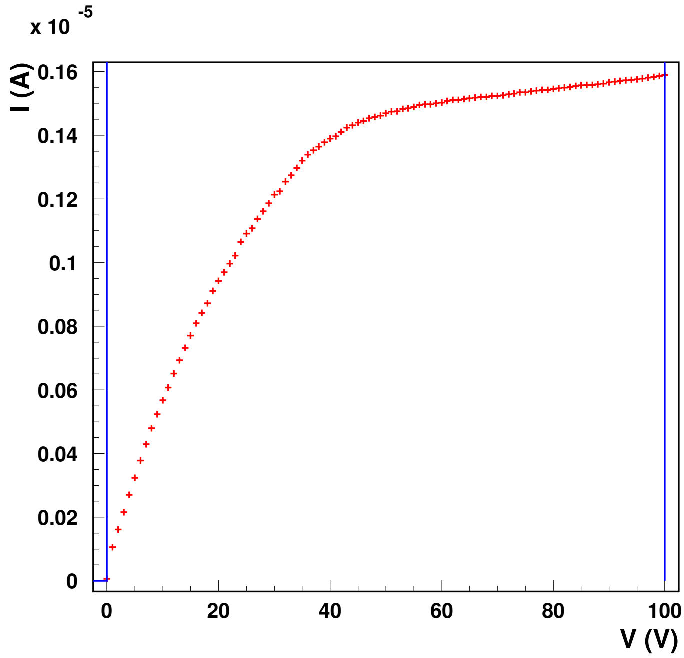

Figure A.3.: IV-curve for sensor 2185-02.

A.2. Test of TIGRE stability

As the detectors had not been tested for longterm stability by the manufacturer, this test was also done in Erlangen. It is known that in order to measure the stability of a silicon strip detector, the surrounding ambient and materials have to be chosen with care. The original holding frames were made out of Teflon that was glued to aluminium plates. Household glue (UHU) was used to attach the bondable Kapton pads. Sheets of the paper that were part of the original packaging of the detectors were used to fix the detectors inside the frames without applying too much pressure. Each detector frame was put into a plastic box and stored under cleanroom conditions at about 60 % relative humidity. The detectors were operated at a bias voltage of 100 V that was supplied by a A515 / SY527 power supply made by CAEN, Italy.

During the first test it was observed that several detectors got unstable after an operation of only a few days. Local strip currents were as high as 3 μA in contrast to the usual value of about 10 nA. Especially on the p-side isolated regions of bad strips were found. Several sources of the problem were considered:

- air too humid,
- mechanical surface damage,
- contamination by ions from the frame materials.

Especially the frame materials were a point of concern: While the manufacturer suggested to use only the paper and not the Teflon, various experiments use Teflon for such tests but no paper.

Rather soon it turned out that similar mounting frames consisting of PVC and Kapton tape guaranteed stable detector operation over several weeks. Later a combustion of the paper under well-defined conditions showed that it contained large amounts of soluble ions. Using frames of paper/PVC and Kapton/Teflon it was finally established that the paper was responsible for all problems.

The origin of the problem can be explained by an the accumulation of charges on the detector surface: Due to the rather wide strip separation of the TIGRE detector (56 μm), the electrical field is not confined inside the device. Instead it extends into the touching materials. If movable ions exist there, they will drift towards the detector surface and act as an additional surface charge in the covering oxide layer. This leads to an increased field-strength and finally to an avalanche break-through at the surface as was discussed in [R$^+$96].

Using typical values of the diffusion constant D [WMF96], it can be shown that the contaminating ions must still be very close to the detector surface ($\leq$ a few nm) as the drift distance x in an electric field E is given by

$$x = \frac{eDt}{kT} E, \tag{A.1}$$

where e is the electron charge, k the Boltzmann constant and T the temperature. The ion charge is assumed to be one in units of the electron charge.

Due to this fact it was found that a surface cleaning using de-ionised water could successfully remove all problems. All detectors were returned to the manufacturer for this cleaning procedure.

The final stability test for each detector was done using the PVC/Kapton frames. All detectors were found to be stable for at least three weeks under cleanroom conditions. A typical measurement is shown in figure A.4. The day/night fluctuations in temperature are clearly seen.

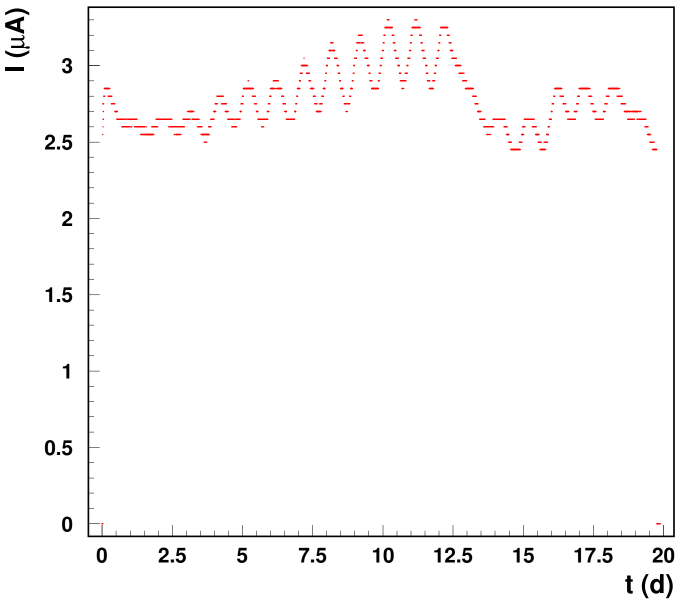

Figure A.4.: Longterm stability of the detector 2185-02 at 100 V after the surface had been cleaned. Within 3 weeks of operation no problem was seen. The structures in the curve are due to day-night temperature fluctuations.

B. Different Extraction Methods

There are different possibilities to calculate the asymmetries of interest. Three different methods will be discussed which all have advantages as well as disadvantages. The methods are:

1. Fit Method (FM),
2. Moment Method (MM),
3. Monte Carlo Fitting (MCF).

Mathematically the extracted quantities are not equivalent, although the numerical values can be similar under certain conditions. In the following the discussion will focus on the Beam Charge Asymmetry (BCA), but similar equations hold for the spin dependent asymmetries.

B.1. Fit Method

The fit method extracts the asymmetries that have been suggested in many theory papers and are discussed in chapter 2. In the analytical limit the result for the c_1-coefficient of the fit-method can be written as

$$c_1^{FM} = \frac{1}{\pi} \int_{-\pi}^{\pi} \frac{\frac{d\sigma^+}{d\phi} - \frac{d\sigma^-}{d\phi}}{\frac{d\sigma^+}{d\phi} + \frac{d\sigma^-}{d\phi}} \cos\phi \, d\phi. \tag{B.1}$$

In practice the events numbers for positive and negative beam charge are taken in I bins in ϕ, labelled by the index i. The luminosity and trigger efficiency corrected events numbers $k_i^{\pm}$ for two different beam charges $+/-$ are obtained from:

$$k_i^{\pm} = \frac{1}{L^{\pm}} \sum_{n=1}^{N^{\pm}} \frac{1}{\epsilon_n}, \tag{B.2}$$

where $L^{\pm}$ is the integrated luminosity of the datasets, the index n counts the events in the particular bin i and ϵ_n is the trigger efficiency for the event n. The second index i is omitted for the quantities $N^{\pm}$ and ϵ_n in order to improve the readability. The error on the quantity k_i for each beam charge is obtained from

$$dk_i = \sqrt{\frac{1}{L^2} \sum_{n=1}^{N} \frac{1}{\epsilon_n^2}}, \tag{B.3}$$

where the charge index has also been omitted.

It is useful to think of the statistical error in terms of the effective number of events N_{eff} ([Lyo86]). This is defined as

$$N_{eff} = \frac{k_i^2}{dk_i^2} \tag{B.4}$$

and is the number of hypothetical events with $\epsilon_n = 1$ that would give the same ratio of the event number relative to its error. Obviously N_{eff} is always smaller than N, which demonstrates that a non-constant value for ϵ_n will always lead to larger relative errors.

The asymmetry A_i in the ϕ-bin i is then calculated from $k_i^\pm$ for the two different beam charges according to

$$A_i = \frac{k_i^+ - k_i^-}{k_i^+ + k_i^-} \tag{B.5}$$

and the error on this quantity is

$$dA_i = \sqrt{\left(\frac{2k_i^+}{(k_i^+ + k_i^-)^2}\right)^2 (dk_i^-)^2 + \left(\frac{2k_i^-}{(k_i^+ + k_i^-)^2}\right)^2 (dk_i^+)^2}. \tag{B.6}$$

If the asymmetry depends linearly on the beam/target-polarisation, A_i as well as dA_i have to be divided by the mean value of the polarisation

$$\langle P \rangle = \frac{1}{2}(\langle P^+ \rangle + \langle P^- \rangle). \tag{B.7}$$

A truncated Fourier-series can be fitted to the obtained histogram of A_i, where $A(\phi)$ is identified with the value A_i at the bin centre of the bin i:

$$A(\phi) = c_0^{FM} + \sum_{m=1}^{M} (c_m^{FM} \cos(m\phi) + s_m^{FM} \sin(m\phi)). \tag{B.8}$$

Since Gaussian error treatment breaks down as soon as the event numbers $N_i^\pm$ are very small, typically $N_i^\pm > 5$ must be required, such that the error bar is approximately given by $\sqrt{N_i^\pm}$. The same requirement translates to $N_{eff,i}^\pm > 5$ in the general case of weighted events numbers $k_i^\pm$. On the other hand the number of bins I must still be large enough, such that higher Fourier coefficients can still be picked out. If the highest Fourier coefficient is of order M, the requirement $I \gg 2M$ should be satisfied. There is no obvious solution to obtain a bin-free fit, as the asymmetry in contrast to a pure event distribution depends on the combination of events from different datasets with similar values of ϕ.

It is clear that in this procedure two arbitrary choices have to be made:

- The number of bins can be chosen inside the discussed limits.
- The fitted Fourier coefficients can be selected at random. For example in the beam charge asymmetry higher sine-coefficients can be assumed to be zero, but they can also be included into the fit in order to get an estimate of remaining experimental errors.

More detailed studies on the numerical effects are presented in section 6.2.

It is important to note that the fit will always converge with a unique result: This can also be determined analytically as the fit function is a sum of linearly independent functions with corresponding coefficients (cf. reference [Lyo86]).

B.2. Moment Method

In order to avoid the mentioned complications, a different approach has been suggested by introducing the moment method. This method is used at HERMES e.g. in the polarisation analysis of the Λ-decay. In the analytical limit it simplifies e.g. to

$$c_1^{MM} = \frac{2\int_{-\pi}^{\pi}(\frac{d\sigma^+}{d\phi} - \frac{d\sigma^-}{d\phi})\cos\phi\, d\phi}{\int_{-\pi}^{\pi}(\frac{d\sigma^+}{d\phi} + \frac{d\sigma^-}{d\phi})\, d\phi} \tag{B.9}$$

for the first cosine moment of the asymmetry. This definition of the BCA is e.g. suggested in [FS04] but probably due to the extraction method that was used in previous HERMES publications. It can be seen that this is different from the quantity which is obtained from the fit-method.

In practice the asymmetry can be obtained without the need for either binning or fitting. Including the trigger efficiency correction, the result is:

$$c_1^{MM} = \frac{2}{K^+ + K^-}\left(\sum_{n=1}^{N^+}\frac{\cos\phi_n}{L^+\epsilon_n} - \sum_{n=1}^{N^-}\frac{\cos\phi_n}{L^-\epsilon_n}\right), \tag{B.10}$$

where $K^\pm$ is given by the sum over all events of the respective beam charge:

$$K^\pm = \sum_{n=1}^{N^\pm}\frac{1}{L^\pm\epsilon_n}. \tag{B.11}$$

This can be interpreted as the expectation value for the observable $Q_n = 2q\cos(\phi_n)$, where q is the beam charge in units of e:

$$c_1^{MM} = \frac{\sum_n Q_n \cdot \frac{1}{L^q\epsilon_n}}{\sum_n \frac{1}{L^q\epsilon_n}}. \tag{B.12}$$

It would be confusing to state that each event is "weighted by the observable" Q, since the observable is treated differently than the trigger efficiency and luminosity weight $\frac{1}{L^q\epsilon_n}$. Again the result can be divided by the mean value for the polarisation (equation B.7) if a polarisation dependent asymmetry is extracted. The error on c_1^{MM} is

$$dc_1^{MM} = \sqrt{\frac{\sum_n (Q_n - c_1^{MM})^2 \cdot \frac{1}{L^q\epsilon_n})}{(N_{eff}-1)\sum_n \frac{1}{L^q\epsilon_n}}}. \tag{B.13}$$

Even for very low event numbers ($N \approx 10$) this error estimate seems to be correct.

However, the method has other problems:

- Even if the cross-section as well as the acceptance function were one-dimensional, the result would strongly depend on the acceptance. In the case of a one-dimensional problem, the asymmetry extracted by the fit method is on the other hand independent of the acceptance function. This means that an acceptance correction is mandatory for the moment method.

- In the case of DVCS the BH-propagators do not cancel such that the leading twist coefficient can also generate "higher moments" in the moment method. Neglecting moment mixing the result for the first cosine moment is

$$c_1^{MM} \approx -\frac{x_B}{y} \frac{2 \int \frac{1}{P_1 P_2} (c_0^I + c_1^I \cos(\phi)) \cos\phi \, d\phi}{c_0^{BH} \int \frac{1}{P_1 P_2} d\phi}. \tag{B.14}$$

  As the lepton propagators, or more precisely P_1 and P_2 depend strongly on kinematics, the results can be unpredictable.

- Although an arbitrary number of cross-section moments can be calculated according to the equations above, there is no quantity like χ^2 that shows, how many moments are really needed to describe the data. Furthermore it is clear that the higher moments are meaningless as soon as the order of the moment is larger than the event number, but there is no argument at which order the problem starts.

B.3. Factorisation for Fit Method and Moment Method

By accident the results from the fit-method and the moment method show an apparent agreement at HERMES. The reason for this is that the BH-propagators cause a peak in the photon production cross-section for $\phi \approx 0$ (cf. figure 4.4), while the HERMES-acceptance is low in this region for most of the observed phase space. Consequently the event distributions in ϕ are almost flat. As soon as the distribution is exactly flat, the mathematical expressions leading to the fit method or the moment method are identical.

Consequently the moment method has often been considered as a cross-check of the fit method, although the raw extracted moments at HERMES are expected to differ considerably from the acceptance-free theoretical prediction.

Both methods, the moment method and the fit method have one essential problem as soon as the asymmetry is considered in its dependence on x_B, Q^2 and t: Both methods assume that the cross-section factorises. The fit-method assumes a factorisation of the following form:

$$\frac{d\sigma}{dx_B \, dQ^2 \, dt \, d\phi} = g(x_B, Q^2, t, \phi) \cdot [1 \pm (c_0 + c_1 \cos(\phi))] \tag{B.15}$$

in the case of the beam charge asymmetry. g contains the complete kinematical dependence, while c_0 and c_1 are assumed to be constant. In the case of DVCS this factorisation is approximately valid. It is only violated by higher moments of the BH-cross-section and the DVCS-cross-section, both of which are presumably small.

The moment method on the other hand assumes a factorisation of the following form:

$$\frac{d\sigma}{dx_B \, dQ^2 \, dt \, d\phi} = g(x_B, Q^2, t) \cdot [1 + c_1^c \cos(\phi) \pm (c_0 + c_1 \cos(\phi))], \tag{B.16}$$

where the additional coefficients $c_1^c, c_2^c, \ldots$ do neither depend on kinematics nor on the beam charge but are constant. In this case the higher moments of the BH- and the DVCS-cross-section together with the prominent ϕ-dependence of the lepton-propagators can approximately be included in the coefficients c_1^c, $c_2^c \ldots$, but the strong kinematical dependence of the propagators on x_B, Q^2 and t is ignored. In addition also the moments c_0, c_1, etc. contain a contribution from the propagators (cf. equation B.14).

This shows that neither the fit method nor the moment method can exactly recover the original coefficients c_0^I and c_1^I even if an ideal dataset of infinite statistics would exist.

B.4. Monte Carlo Fitting

Consequently a different method has been proposed that uses different assumptions and can at least serve as a cross-check: The Monte Carlo fitting method is based on the idea that free parameters in the Monte Carlo should be adjusted until agreement with experimental distributions is obtained. The solution for the free parameters describes then the true asymmetry (cf. section 11.1.2 of [Tyt01]).

The Monte Carlo fitting method has the advantage that a priori it does not assume a special factorisation of the cross-section. Instead any cross-section model and any asymmetry model depending on kinematics can be used such that the method becomes very flexible. It can deal with acceptance effects, smearing effects and background at the same time, since the background can simply be added for the cross-section model. However, it may be rather complicated to propagate systematic errors on the background.

In principle it is possible to disentangle all cross-section contributions in the following way: First one would start with a charge and polarisation balanced dataset in which the interference term cancels. A fit of the known BH-cross-section together with an unknown DVCS cross-section to the normalised experimental data would fix the DVCS cross-section. Then a charge balanced dataset with non-zero beam polarisation can be used to isolate the BSA of DVCS, whose first sine moment is due to higher twist. After that the dataset can be split into the two charges, and a fit of $\sigma_{BH} + \sigma_{DVCS} + \sigma_I$ to the data of either charge would determine the interference term.

In reality this is not possible for several reasons: First of all the absolute cross-section normalisation of data and Monte Carlo is at the moment limited in its accuracy. It is certainly not sufficient to determine the contribution from σ_{DVCS} precisely, the more so since badly known background processes enter. Secondly also DVCS with resonance excitation can cause a charge-dependent interference term such that the measured charge asymmetry is not directly related to the GPDs of the nucleon. Thirdly the detector simulation in the HERMES Monte Carlo has at present known defects for the case of DVCS (cf. section 5.8). It is not absolutely certain that these defects can be neglected for a fit. Finally, no matter which parameters are fitted, they will have a variation in x_B, Q^2 and t. Hence large statistics with fine binning would be needed in order to avoid bin-centring effects.

Consequently a complete fit of the discussed kind was not attempted. Instead simplified cross-section models had to be used that try to absorb all different contributions:

1. The most basic fit that will certainly give a good description of the data is:

$$\sigma^{\pm} = \sigma_{BH,p(free)} \cdot \left(1 + \sum_m c_m^{(1)\pm} \cos m\phi + \sum_m s_m^{(1)\pm} \sin m\phi \right) \tag{B.17}$$

   for positive/negative beam charge, where the superscript (1) denotes the fit-type. The BH-process on the proton is a good approximation, since it can be expected that similarly to the case of elastic scattering, the total (coherent and incoherent) BH-cross-section is mostly given by the sum of the contributions from a free proton and a free neutron. As the charged proton dominates, $\sigma_{BH,p(free)}$ is the most relevant part of the total cross-section.

For the BSA the fitted coefficients $s_m^{\pm}$ are expected be equal and close to the BSA from the fit method. For the BCA the result is changed by the constant moment of the interference term such that c_m^+ and c_m^- will be slightly different. On the other hand this fit function does not fully exploit the possibilities of the MCF.

2. The propagator fit assumes a cross-section of the form:

$$\sigma^{\pm} = \sigma_{prop} \cdot (1 + \sum_m c_m^{(2)\pm} \cos m\phi + \sum_m s_m^{(2)\pm} \sin m\phi) \tag{B.18}$$

for positive/negative beam charge, where σ_{prop} is given by:

$$\begin{aligned} \frac{d\sigma_{prop}}{dx_B\, dQ^2\, dt\, d\phi} &= \frac{\alpha^3 x_B y}{16\pi^2 Q^2 \sqrt{1+\epsilon^2}} \times \\ & \frac{2\pi y}{Q^2} \frac{1}{x_B^2 y^2 (1+\epsilon^2)^2 t P_1(\phi) P_2(\phi)}. \end{aligned} \tag{B.19}$$

σ_{prop} is approximately the same for all DVCS/BH-like processes. If the coefficients $c_1^{(2)+}$ and $c_1^{(2)-}$ have been determined for both beam charges separately, a relation to the moment c_1^I can be found by calculating

$$c_1^{MCF} = \frac{c_1^{(2)+} - c_1^{(2)-}}{2}. \tag{B.20}$$

The analytical limit of this expression for a small bin in kinematics is

$$c_1^{MCF} = \frac{1}{2}\left(\frac{2\int_{-\pi}^{\pi} (d\sigma^+/d\sigma_{prop}) \cos\phi\, d\phi}{\int_{-\pi}^{\pi} (d\sigma^+/d\sigma_{prop})\, d\phi} - \frac{2\int_{-\pi}^{\pi} (d\sigma^-/d\sigma_{prop}) \cos\phi\, d\phi}{\int_{-\pi}^{\pi} (d\sigma^-/d\sigma_{prop})\, d\phi} \right). \tag{B.21}$$

This is approximately equal to

$$c_1^{MCF} \approx -\frac{x_B}{y} \frac{c_1^I}{c_0^{BH}}, \tag{B.22}$$

if c_0^I as well as σ_{DVCS} and the background are neglected. The prefactor x_B/y is caused by the definitions in chapter 2, while the effective coefficient c_1^I in the case of the deuteron is a mixture of the coherent and the incoherent process. For intermediate values of t it is mostly given by incoherent scattering on the proton and the neutron:

$$c_1^I \approx \frac{1}{2}(c_1^{I,p} + c_1^{I,n}), \tag{B.23}$$

$$c_0^{BH} \approx \frac{1}{2}(c_0^{BH,p} + c_0^{BH,n}). \tag{B.24}$$

3. The best knowledge fit assumes a cross-section of the kind:

$$\begin{aligned}\sigma^{\pm} &= \sigma_{BH,D} + \sigma_{BH,p} + \sigma_{BH,n} + \sigma_{BH,res} + 2\sigma_{prop}\frac{x_B}{y} \cdot \\ &\quad (1+\epsilon^2)^2 \left(\sum_n c_n^{(3)\pm} \cos n\phi + \sum_n s_n^{(3)\pm} \sin n\phi \right), \end{aligned} \tag{B.25}$$

where $\sigma_{BH,D}$ is the BH-cross-section on the deuteron, $\sigma_{BH,p/n}$ is the cross-section on the bound proton/neutron and $\sigma_{BH,res}$ denotes the BH-cross-section with resonance excitation of the proton or the neutron. As long as $c_0^I = 0$ and the DVCS contribution σ_{DVCS} as well as the background cross-section are either known or negligible, this fit will directly extract the moments of interest, i.e.

$$c_1^{(3)+} = -c_1^I, \tag{B.26}$$
$$c_1^{(3)-} = c_1^I, \tag{B.27}$$

where

$$c_1^I = \frac{1}{2}(c_1^{p,I} + c_1^{n,I}). \tag{B.28}$$

In reality it is possible that $c_1^{(3)+} \neq -c_1^{(3)-}$. One can try to obtain a partial cancellation by taking

$$c_1^I \approx \frac{1}{2}(c_1^{(3)-} - c_1^{(3)+}), \tag{B.29}$$

but the systematic error due to this assumption is not clear.

After one of these fit functions has been chosen, suitable observables for the comparison of data and MC have to be defined. The Monte Carlo fitting method discussed here uses cross-section moments as defined in equation B.12 for both beam charges separately. The first four sine moments s_m^{MM} ($1 \leq m \leq 4$) and the first four cosine moments c_m^{MM} ($1 \leq m \leq 4$) are considered.

For each charge the fit-parameters are varied - i.e. the Monte Carlo is reweighted - in order to minimise

$$\chi^2 = \sum_m \left(\frac{(c_m^{MM,MC} - c_m^{MM,data})^2}{\delta c_m^{(MM,MC)2} + \delta c_m^{(MM,data)2}} + \frac{(s_m^{MM,MC} - s_m^{MM,data})^2}{\delta s_m^{(MM,MC)2} + \delta s_m^{(MM,data)2}} \right) \tag{B.30}$$

by changing the values of $c_m^{MMK,MC}$ and $s_m^{MMK,MC}$. Since the moments correspond to a decomposition into orthogonal functions, the correlation coefficients are small and are neglected in this definition of χ^2. However, correlations are in principle possible. This can be seen in the extreme case, where a flat distribution of events is generated inside an interval $\phi \in [-a, a]$, with $a \ll \pi$. For a as large as $a = 0.5$ a simulation results in a correlation coefficient that is still in the order of 1 for the moments c_1^{MM} and c_2^{MM}.

Table B.1.: Comparison of the fit method, the moment method and the MC-fitting method in the form of the propagator fit.

	Acceptance Correction	allowed smearing	binning effects	luminosity needed	extractable coefficients	interpretation of result
FM	included (partly)	$\phi \to \phi' = \phi$ allowed	arbitrary ϕ-bins	yes	~ 4	$\propto \frac{s_n^I}{c_0^{BH}}$
MM	matrix meth.	$\phi \to \phi' = \phi$ allowed	-	yes (standard), no (see below)	all	X-section moments
MCF	included	all: $\phi' \neq \phi$, (intra-bin)	-	no	~ 4	$\propto \frac{s_n^I}{c_0^{BH}}$

B.5. Comparison of Methods

The comparison of the fit method, the moment method and the propagator fit method is given in table B.1. The point "Acceptance Correction" will be discussed in the following section.

For all methods smearing effects pose a problem, apart from the unlikely case that events are always reconstructed with the original value of ϕ and some smeared kinematics in x_B, Q^2 and t, that is inside the same kinematical bin ($\phi \to \phi' = \phi$). While it is impossible to correct for smearing effects in the fit method or the moment method (cf. following section), the MC-fitting method can at least correct for smearing in ϕ as long as inter-bin-migration is rare. A simultaneous fit of several kinematical bins could in principle solve this problem.

One disadvantage of the fit method is that it is sensitive to binning effects in ϕ. On the other hand it is shown in section 6.2 that these effects are under control.

While the fit-method and the moment method need an external measurement of luminosity, modified versions of the moment method can take the normalisation directly from the dataset, e.g.:

$$c_1^{MM\prime} = \frac{2}{K^+} \sum_{n=1}^{N^+} \frac{\cos \phi_n}{L^+ \epsilon_n} - \frac{2}{K^-} \sum_{n=1}^{N^-} \frac{\cos \phi_n}{L^- \epsilon_n}. \tag{B.31}$$

However the analytical limit of this expression is different and more complicated. In the case of the MCF no external normalisation is needed.

The moment method allows to extract an arbitrary number of moments, while the fit method as well as the MC-fitting method have a limited number of parameters, but a confidence level that can be derived from χ^2. The fit method as well as the propagator fit try to extract results that are more closely related to the GPDs, while the moment method tries to extract cross-section moments.

The result of using the three different extraction methods on Monte Carlo data at a fixed kinematical point is shown in figure B.1. The simulation is based on GPD model 5 (cf. section 4.1) and contains only elastic coherent and incoherent BH/DVCS. No detector acceptance has been included and only the analytical limits of the three methods are shown. The first and the second moment extracted from the three methods are plotted for four fixed points in kinematics. These points correspond to the average experimental kinematics of the same 4 bins in t that will later be used for data analysis. In addition the result of the MCF is included, under the assumption that the coefficient c_0^I according to equation 2.115 is zero. This result is labelled "ideal", since it preserves the ratio of leading twist to higher twist, while the normalisation is changed due to the coherent contributions and the pure DVCS-cross-section. This is unavoidable if the DVCS-cross-section is not explicitly subtracted before the analysis of asymmetries. The ideal result in terms of the proton/neutron averaged incoherent asymmetry moments can be written as

$$c_1^{ideal} \approx -\frac{x_B}{y}\frac{c^I_{1,up,incoh.}(t)}{c^{BH}_{0,up,incoh}(t) + \int \frac{1}{\sigma'_{prop}(t)}\frac{d\sigma_{DVCS,incoh.}(t)}{dP_e\, d\Omega_e\, d\Omega_\gamma}d\phi + \int \frac{1}{\sigma'_{prop}(t)}\frac{d\sigma_{coh.}(t_d)}{dP_e\, d\Omega_e\, d\Omega_\gamma}d\phi}, \tag{B.32}$$

where it has been assumed that the BCA of the coherent process is negligible and nuclear suppression effect at low $|t|$ are included in the proton/neutron averaged moments. All differential cross-sections are taken as $d\sigma/(dP_e\, d\Omega_e\, d\Omega_\gamma)$ and the weight σ_{prop} has been modified by the corresponding Jacobian in order to obtain σ'_{prop}. The reason is that the differential dt must be eliminated, since the range in θ_{γ,γ^*} that is defined by a range in $t_{c,p}$ corresponds to a different range in t for the coherent process on the deuteron. Hence, also t for the calculation of the coherent process has to be recalculated as t_d from the opening angle θ_{γ,γ^*}.

These curves are compared to the approximation of equation 2.131 (approximation). Apparently the moment method is strongly disturbed by the propagators such that extensive mixing between the first and the second moment is seen: The leading moment is reduced and the sub-leading moment increased. Also the fit-method leads to a second moment that is considerably too large. The MCF is slightly sensitive to the moment c_0^I such that the ratio leading to higher twist is a bit too small. Still the result of the MCF is close to the ideal result; it is similar to the FM for the leading moment but better reproduces the true size of the sub-leading moment. All methods do not agree with the approximation of equation 2.131 due to the DVCS-cross-section.

With the present statistical accuracy of the data it is difficult to verify the expected differences between the extraction methods. Moreover detector acceptance has an impact on the moment method and makes its output more similar to the fit method. The results for the beam-charge asymmetry on an unpolarised deuterium target without acceptance or background correction are derived from all 3 methods and shown in figure B.2. The numerical results of all methods are very similar and the expected differences (figure B.1) are smaller than the statistical errors.

For the final analysis the fit method is used because of the discussed advantages and its much more transparent calculus. Also the background correction is rather uncomplicated in the fit method. For future applications this decision can be reconsidered; otherwise even if enough statistics exists to identify higher twist effects, the FM may not allow to extract them cleanly. Under these conditions the MCF is preferable.

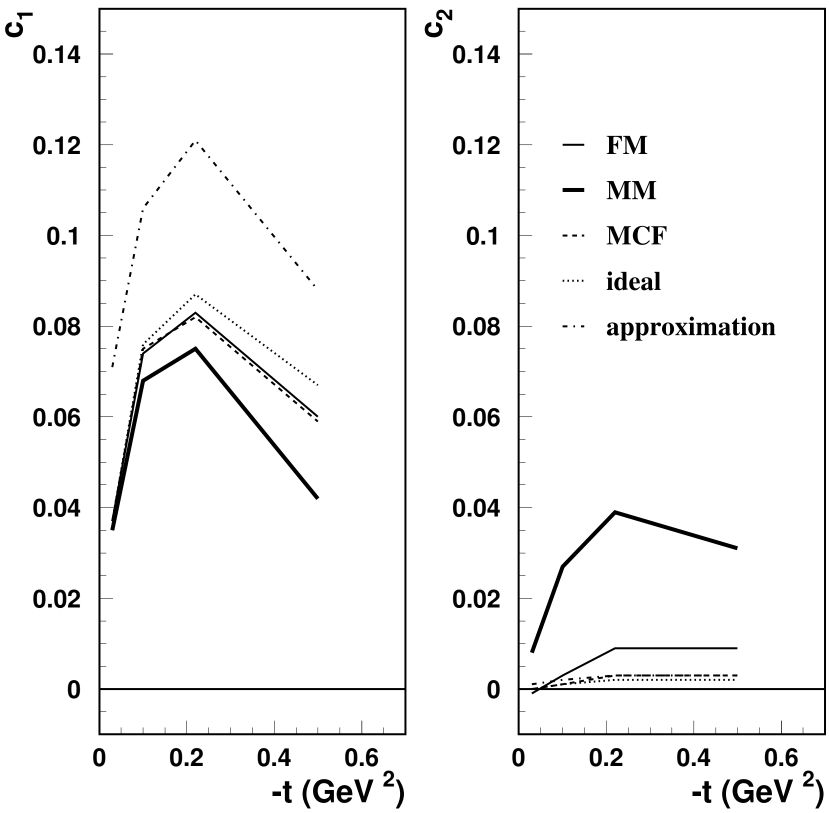

Figure B.1.: Analytical limits of 3 different extraction methods applied to the Monte model based on GPD model 5. The 4 points in t are evaluated at the average kinematics of data binned in the same intervals in t. In addition to FM, MM and MCF the "ideal" result is shown that is obtained by using the MCF and artificially setting c_0^I to zero. The curve "approximation" indicates the frequently made approximation of equation 2.131.

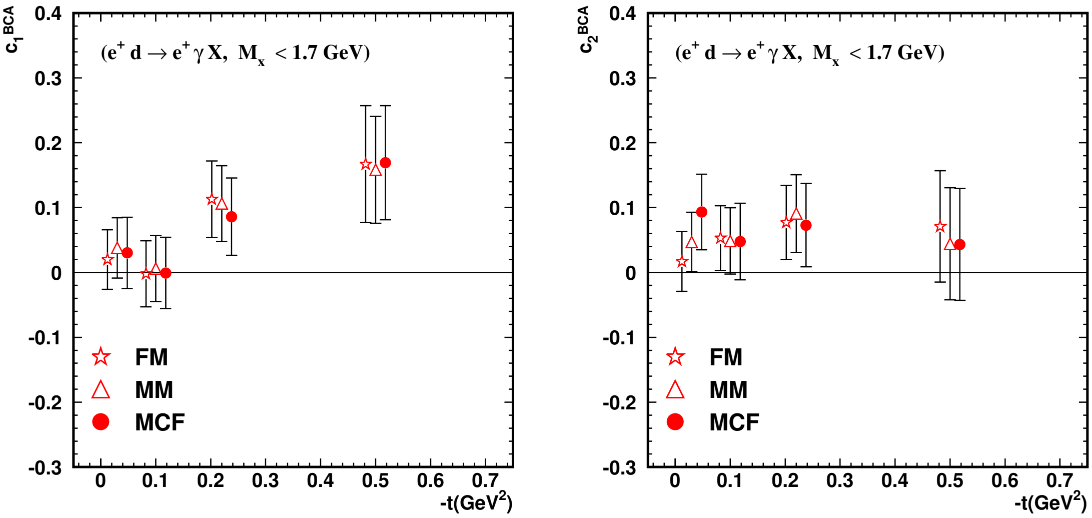

Figure B.2.: Comparison of the three extraction methods FM (fit function from equation 5.24), MM and MCF (propagator fit) for the extracted moments c_1 (left) and c_2 (right) of the beam charge asymmetry on unpolarised deuterium.

C. Treatment of Acceptance Effects

C.1. Bin-Centring Effects

As has been mentioned in the previous section, the fit-method is due to its definition rather insensitive to acceptance effects. However, acceptance has an impact on possible bin-centring errors. These "bin-centring" effects as discussed below, can only occur if an asymmetry depends on several kinematical variables but is only binned in one (i.e. ϕ) or two (i.e. ϕ, t) of them due to limited statistics.

The effect can be discussed in a hypothetical 2-dimensional model, which depends on the angle ϕ, but only on one additional coordinate θ: The functions

$$\frac{d\sigma^+}{d\phi\, d\theta} = 1 + \frac{\theta}{\pi}\cos\phi, \tag{C.1}$$

$$\frac{d\sigma^-}{d\phi\, d\theta} = 1 - \frac{\theta}{\pi}\cos\phi \tag{C.2}$$

can be used to calculate a local asymmetry $A(\phi,\theta) = \frac{d\sigma^+ - d\sigma^-}{d\sigma^+ + d\sigma^+}$. The acceptance is given by $\pi > \theta > |\phi|$. After integration over θ the obtained asymmetry is then

$$A(\phi) = (\pi + |\phi|)\frac{\cos\phi}{2\pi}, \tag{C.3}$$

which obviously contains higher cos-moments. Moreover the average kinematics is at $\phi = 0$ and $\theta = \frac{2\pi}{3}$ and the distribution is only approximately described by the local asymmetry

$$A(\phi, \frac{2\pi}{3}) = \frac{2}{3}\cos\phi, \tag{C.4}$$

as can be seen in figure C.1.

Obviously the integrated result contains other moments then the initial $\cos\phi$. Notably also a rather strong constant term of $c_0 = -1/\pi^2$ is induced, where c_0 is defined by the following decomposition of the asymmetry:

$$A(\phi) = c_0 + \sum_m c_m \cos(m\phi) + \sum_m s_m \sin(m\phi). \tag{C.5}$$

This shows that although the results obtained by the fit-method can certainly be compared with theoretical predictions that have explicitly been integrated over the HERMES-acceptance, a comparison with the local asymmetry at the "centre of gravity" of the bin is not allowed. Also at any other point, the integrated asymmetry and the local asymmetry do not agree. Moreover, different experiments that measure at exactly the same mean value of θ but have a different acceptance function, will also obtain a different asymmetry.

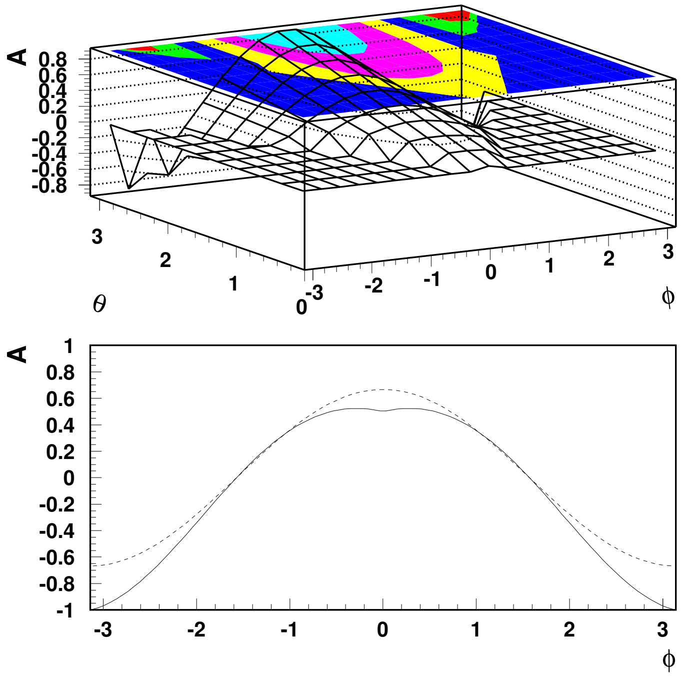

Figure C.1.: Bin-centring effects in a simple model: The top plot shows the original local asymmetry A, where outside the acceptance A is set to zero. The bottom plot shows the integrated asymmetry (solid) and the asymmetry at the mean value of θ (dashed).

It is clear from this that an important acceptance problem can result from the usual practice of comparinf with values at bin-centre. Consequently it is important to estimate the bin-centring error that is obtained with the HERMES acceptance. In order to avoid a mixing with smearing effects, non-smeared Monte Carlo events have been generated inside an ideal HERMES-acceptance. Only the elastic coherent and incoherent process, but no background contributions have been included. The results for the fit-method with 12 bins in ϕ and 3 different GPD models are shown in figure C.2. The datapoints are the extracted asymmetry moments in each bin in t, while the lines indicate the acceptance free asymmetry moments (fit-method) at the average kinematics of the bins. The top plots show the comparison for the BSA and the bottom plots the comparison for the BCA.

In the case of the beam spin asymmetry (top plot) the coefficient s_2 is well reproduced, while the coefficient s_1 is systematically underestimated by up to 10% for all bins in t. In the case of the beam charge asymmetry (bottom plot) c_1 is underestimated, while c_2 is overestimated. The bin-centring error on the beam charge asymmetry seems to be larger than the error on the beam spin asymmetry. As in the simple example discussed above, this can happen if the variation of a coefficient c_1 inside a bin couples to the acceptance function. Although the absolute error is in the order of 1%, the relative error for c_1 is about 20%, for c_2 it is even 100%. It is unclear how to extrapolate this error to the experiment, if the measured asymmetry is very different from the Monte Carlo asymmetry (as for the BCA). As the error depends on the value of each GPD in its

3 dimensional parameter space, it is difficult to derive a solid statement about the bin-centring error or even a bin-centring correction from this knowledge. It is unclear, how much the result changes for other possible parametrisations of the GPDs.

In addition it is important to note that the moment c_2 in figure C.2 is not related to a true moment c_2^I, but almost entirely due to the effects shown in figure B.1. The same is true for the moment s_2. Consequently no attempts have been made to measure or interpret higher asymmetry moments, since they are at least not accessible with the present statistics in hand and in addition more strongly affected by smearing (cf. chapter 3).

The bin-centring error due to the coupling of non-constant asymmetry moments to the acceptance will show up for the fit-method as well as for the moment method. It could be eliminated in the MC fitting-method, if the variation of the asymmetry was known apart from one unknown parameter. In the toy model discussed above the fit function

$$\sigma = c_0 + c_1 \frac{\theta}{\pi} \cos\phi + c_2 \frac{\theta}{\pi} \cos 2\phi \tag{C.6}$$

would actually lead to the correct result for the coefficient c_1, while the coefficients c_0 and c_2 would strictly be zero inside their error bars. In practice, this knowledge is at present not available.

C.2. "Acceptance Correction" for the Moment Method

Although it cannot solve the problem of bin-centring errors, an acceptance correction is unavoidable for the moment method. This is because even if a cross-section factorises as in equation B.16, it will not be extracted in the correct way, if an acceptance function is taken into account.

So far the so-called matrix method has been used for this purpose. It is based on the idea that for a one-dimensional cross-section $\sigma(\phi)$ the obtained event-distribution $N(\phi) = \sigma(\phi)\mathcal{A}(\phi)$ can be written as a Fourier series that depends on the Fourier moments of the cross-section (c_m/s_m) and the Fourier moments of the acceptance function $\mathcal{A}(\phi)$ (c'_m/s'_m):

$$\begin{aligned} c''_0 + \sum_m (c''_m \cos(m\phi) + s''_m \sin(m\phi)) &= (c'_0 + \sum_m (c'_m \cos(m\phi) + s'_m \sin(m\phi))) \times \\ &\quad (c_0 + \sum_m (c_m \cos(m\phi) + s_m \sin(m\phi))). \end{aligned} \tag{C.7}$$

The matrix relation is then:

$$\begin{pmatrix} c''_0 \\ c''_1 \\ c''_2 \\ s''_1 \\ s''_2 \end{pmatrix} = \begin{pmatrix} c'_0 & \frac{1}{2}c'_1 & \frac{1}{2}c'_2 & \frac{1}{2}s'_1 & \frac{1}{2}s'_2 \\ c'_1 & c'_0 + \frac{1}{2}c'_2 & \frac{1}{2}(c'_1 + c'_3) & \frac{1}{2}s'_2 & \frac{1}{2}(s'_1 + s'_3) \\ c'_2 & \frac{1}{2}(c'_1 + c'_3) & c'_0 + \frac{1}{2}c'_4 & \frac{1}{2}(s'_3 - s'_1) & \frac{1}{2}s'_4 \\ s'_1 & \frac{1}{2}s'_2 & \frac{1}{2}(s'_3 - s'_1) & c'_0 - \frac{1}{2}c'_2 & \frac{1}{2}(c'_1 - c'_3) \\ s'_2 & \frac{1}{2}(s'_1 + s'_3) & \frac{1}{2}s'_4 & \frac{1}{2}(c'_1 - c'_3) & c'_0 - \frac{1}{2}c'_4 \end{pmatrix} \times \begin{pmatrix} c_0 \\ c_1 \\ c_2 \\ s_1 \\ s_2 \end{pmatrix}. \tag{C.8}$$

Since the absolute normalisation is not of interest, one can simply set $c_0 = c'_0 = 1$. The coefficient c''_0 is then

$$c''_0 = 1 + \frac{1}{2}(c_1 c'_1 + c_2 c'_2 + s_1 s'_1 + s_2 s'_2) \tag{C.9}$$

and the observed moments are (the moments are always normalised to the observed number of events $(N^+ + N^-) \propto c_0''$):

$$\begin{pmatrix} c_1''/c_0'' \\ c_2''/c_0'' \\ s_1''/c_0'' \\ s_2''/c_0'' \end{pmatrix} = \frac{1}{c_0''}\mathcal{B} \times \begin{pmatrix} c_1 \\ c_2 \\ s_1 \\ s_2 \end{pmatrix} + \frac{1}{c_0''}\begin{pmatrix} c_1' \\ c_2' \\ s_1' \\ s_2' \end{pmatrix}, \tag{C.10}$$

where the matrix elements of the 4×4-matrix $\mathcal{B}$ can be taken from equation C.8. Since the original matrix elements have to be derived from the observed ones, a matrix inversion with a subsequent iterative algorithm determines the true matrix elements as outlined in [Ely02].

As this method provides cross-section moments and not asymmetry moments, another step must be taken: If the asymmetry was e.g. defined as

$$c_1^{MM\prime} = \frac{1}{N^+}\sum_{n=1}^{N^+}\cos(\phi_n^+) - \frac{1}{N^-}\sum_{n=1}^{N^-}\cos(\phi_n^-) = \frac{1}{2}\left(\frac{c_1^+}{c_0^+} - \frac{c_1^-}{c_0^-}\right) \tag{C.11}$$

with acceptance free events numbers N^+ and N^-, no problem would arise as both terms could be corrected independently. In reality the beam-charge asymmetry c_1^{MM} is defined as

$$c_1^{MM} = \frac{2}{N^+ + N^-}\left(\sum_{n=1}^{N^+}\cos(\phi_n^+) - \sum_{n=1}^{N^-}\cos(\phi_n^-)\right) = \frac{c_1^+ - c_1^-}{c_0^+ + c_0^-}, \tag{C.12}$$

which demonstrates that equation C.10 is not applicable. Instead, the luminosity weighted moments c_m'' and s_m'' have to be calculated according to

$$\begin{aligned} c_0''^{\pm} &= \frac{1}{L^\pm}N, \\ c_1''^{\pm} &= \frac{2}{L^\pm}\sum_n \cos(\phi_n), \\ c_2''^{\pm} &= \frac{2}{L^\pm}\sum_n \cos(2\phi_n), \\ s_1''^{\pm} &= \frac{2}{L^\pm}\sum_n \sin(\phi_n), \\ s_2''^{\pm} &= \frac{2}{L^\pm}\sum_n \sin(2\phi_n) \end{aligned} \tag{C.13}$$

and the original moments have to be calculated by a simple matrix inversion of equation C.8. The coefficient c_0' can still be identified with 1 as long as the same acceptance correction is applied to the two different data samples. The inclusion of the trigger-efficiency correction is straight-forward and has been omitted for reasons of better readability.

Even if the matrix-method for acceptance correction is correctly applied, it has other more subtle difficulties in the case of DVCS:

The moment method assumes that the cross-section factorises as shown in equation B.16. Under this condition the multidimensional problem in x_B, Q^2, t and ϕ can be reduced to a one-dimensional problem and the acceptance function $\mathcal{A}$ together with the function g can be used to obtain an effective acceptance $\mathcal{A}'$:

$$\mathcal{A}'(\phi) = \int\int\int dx_B\, dQ^2\, dt\, \mathcal{A}(x_B, Q^2, t, \phi) g(x_B, Q^2, t). \tag{C.14}$$

In reality, the cross-section does not factorise in this way, as the BH-propagators lead to quickly changing cross-section moments depending on x_B, Q^2 and t. Hence no matter which effective acceptance $\mathcal{A}'$ is assumed, systematic errors of unknown size can be expected.

Previously $\mathcal{A}'(\phi)$ was obtained from a Monte Carlo simulation with a modified cross-section model that had to be flat in ϕ (the function g may not depend on ϕ). It is clear that a change to this model will directly change the result of the acceptance correction. If one assumes that

$$g(x_B, Q^2, t) = \frac{d\sigma_{BH}(x_B, Q^2, t, \phi_0)}{dx_B\, dQ^2\, dt\, d\phi}, \tag{C.15}$$

the result for $\mathcal{A}'(\phi)$ will depend on the value of ϕ_0, which would not happen if factorisation was perfect. For $|\phi| \gg 0$ factorisation will appear to work, but for $\phi \approx 0$ the proximity to the peak of the initial state BH-radiation causes large deviations. E.g. the calculated coefficient c_1' changes by more than a factor of 2 if the results for $\phi_0 = \pi$ is compared with the result for $\phi_0 < 0.05\pi$. As asymmetry moments depend on the whole range in ϕ it is clear that the breakdown of factorisation for $\phi \approx 0$ affects the whole procedure.

Finally until now no real error propagation was made. This point is not trivial, as not only an error has to be assigned to each matrix and vector element above, but also the error must be propagated through a matrix inversion or even an iterative process.

All in all this means that the matrix method has the following features:

- It is well suited for problems, where the discussed factorisation is approximately valid, but this is questionable in the case of DVCS.
- It relies heavily on the Monte Carlo; in contrast to the propagator fit method a good, factorising cross-section model is required.
- Error propagation is non-trivial.
- It is unclear, how to interpret the acceptance corrected results, since it is known that the assumed factorisation does not work.
- The method does not correct for smearing effects, although Monte Carlo is used that contains information about smearing.

The last point may not be obvious. The matrix method assumes that the observed event distributions are obtained from the product of the acceptance function and the cross-section. Consequently in the extraction of $\mathcal{A}'$, an enhanced number of events at some value of ϕ is interpreted as an enhanced acceptance. However, the enhancement can also be due to events that have been smeared systematically into this region. A known class of such events is due to leptons that emit Bremsstrahlung inside the HERMES-spectrometer, such that the lepton momentum is underestimated. Thus the apparent direction of the virtual photon is changed and the events move towards $\phi = \pi$.

These complications with the moment method were another reason, why the fit-method has been used for this thesis.

One comment should be made: Although the results of the matrix method are in principle questionable, its numerical effects are so small (cf. [Ell03]) that previous HERMES results are inside their statistical errors unaffected. Therefore at the moment no difference is seen between the moment method and the fit method; also the acceptance corrected moment method yields a similar result inside the statistical errors.

C.3. Acceptance Correction by Event Weighting

As has been discussed in section 3.9 there is also a possibility to apply a direct and model independent acceptance correction to the fit method as well as to the moment method. This is done by inserting the value of the acceptance function $\mathcal{A}(x_B, Q^2, t, \phi)$ into the event weight; the trigger-efficiency ϵ_n for the event n has to be multiplied with its known acceptance $\mathcal{A}_n$ in all formulas. In addition the kinematical region parameterised in the same section has to be selected.

It is instructive to consider the distributions in ϕ inside the selected region before and after the acceptance correction. This is shown in figure C.3. In addition the ϕ-distribution using all data is plotted. While the ϕ-distribution for the whole dataset is very flat, the ϕ-distribution for the selected region with $\mathcal{A} > 0.1$ peaks strongly at $\phi = 0$. The additional change due to the acceptance weight is small. This enhancement can be interpreted as the effect of the Bethe-Heitler propagators (cf. figures 4.4 and 4.4) that is not visible in the ϕ-distribution of the whole dataset due to the HERMES acceptance. In addition a slight left/right-asymmetry is observed that can be explained with a remaining beam spin asymmetry due to the unbalanced beam polarisation.

This acceptance correction method has the advantage that bin-centring effects cannot occur: The value of the asymmetry is provided for the whole kinematical region shown in figure 3.20 and not identified with the value at bin-centre. On the other hand smearing effects are still present. Due to the severe restrictions in kinematics, this method was not used for the analysis of asymmetries.

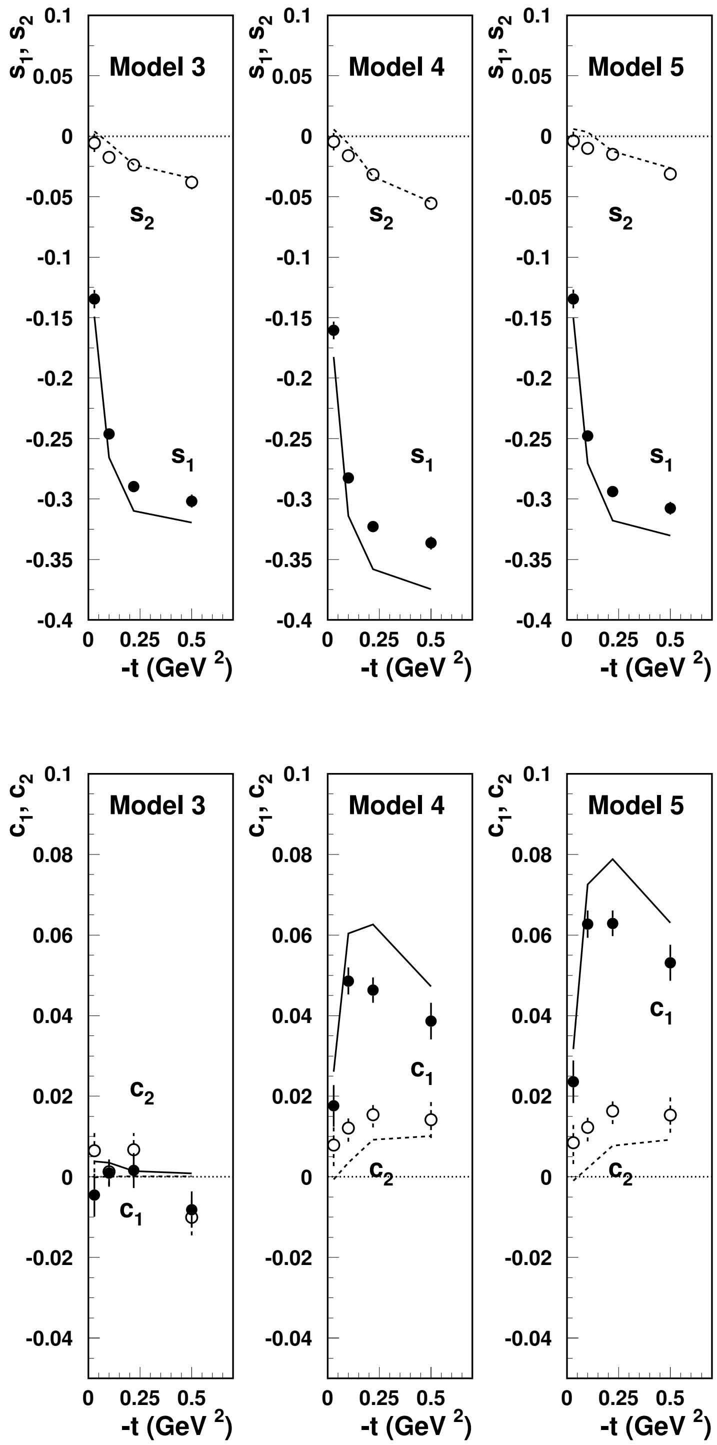

Figure C.2.: Top: Integrated asymmetry (datapoints) and asymmetry at the mean value of kinematics (solid line) for the beam spin asymmetry in four bins in t. The coefficient s_1 is shown as closed circles/solid line, the coefficient s_2 is shown as open circles/dashed line. Bottom: Coefficients c_1 (full circles/solid lines) and c_2 (open circles/ dashed lines) for the beam charge asymmetry.

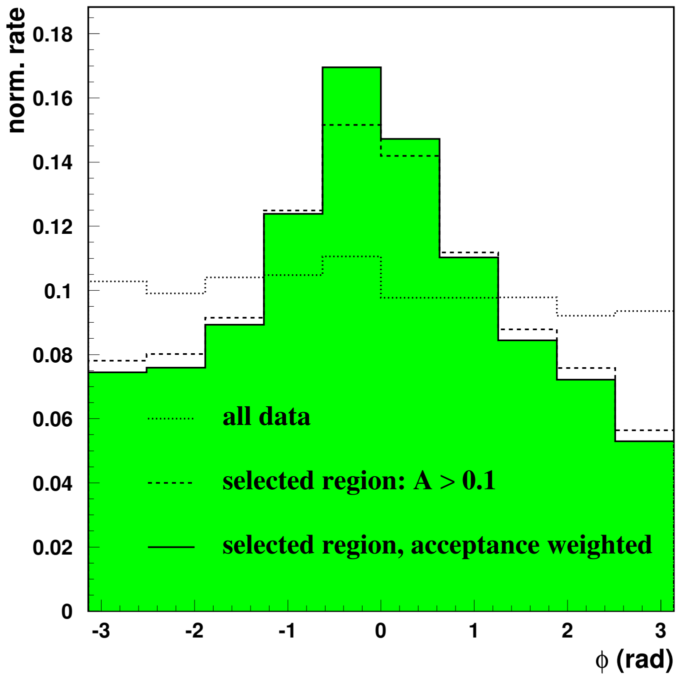

Figure C.3.: Events distribution in ϕ for the exclusive sample of all deuterium data from 1998, 1999 and 2000 (dotted). In addition it is shown for the kinematical region indicated in figure 3.20 (dashed) and in the same region weighted for acceptance (solid). The strong angular dependence is due to the BH-propagators (cf. figure 4.4).

D. How to use *gmc_dvcs*

D.1. *gmc_dvcs* as Phase Space Generator

gmc_dvcs is a standard HERMES event generator. This means that it is controlled via the KUIP interface and that its output is stored in the ADAMO data format. *gmc_dvcs* uses the following external input files:

- gpd.dat: Parametrisation of the Compton Form Factors of the nucleon according to reference [KN02b].

- maid2000.rz: Histogram files of the single meson productions cross-sections σ_L and σ_T according to the MAID2000 online calculator [DHKT99]. All cross-sections are stored as HBOOK-histograms with 1.1 GeV< M < 2.0 GeV and Q^2 < 1 GeV^2.

- BHelec.out, BHposi.out, DVCS1elec.out, DVCS1posi.out: four-dimensional lookup tables of the DVCS cross-section provided by J. Volmer using the code of reference [VGG99].

No card-file (card.ffr) is needed. The available set options are shown in table D.1.

In the most simple case the generator can be used as a pure phase space generator for exclusive meson/photon production. In order to select this functionality the proton should be selected as target particle; beam and target polarisation as well as the beam charge will be ignored. Any of the five mesons $(\gamma, \pi^0, \pi^+, \rho, K^+)$ can be produced (*mode*), where in case 5 the associated strange Baryon will be a Λ^0. Only the values of $Spectrum = 0, 1$ are allowed, where "flat" means that the distribution is generated as being flat in x_B, Q^2 and t, while "t-slope" means that x_B and Q^2 are flat but t is generated as $\exp(bt)$, where b is the set parameter *slope*. Due to the t-dependence of the GPDs the slope of the DVCS-cross-section and exclusive meson production is very similar - at least in factorising GPD models. The typical experimental slope at HERMES energies is in the order of 6 GeV^{-2} [Tyt01]. The kinematical dependence of the BH-cross-section is much more complicated and cannot be approximated by a simple slope in t.

The field $DMode$ steers the fragmentation of the target hadron; only $DMode = 0, 1, 2$ are allowed in the phase space generator. 0 denotes no target fragmentation, i.e. the elastic process. 1 denotes an excited nucleon state that is sampled from a Breit-Wigner-curve with the parameters of the Δ(1232)-resonance. Its decay fraction into the channel $\Delta^+ \to p\pi^0$ is given by isospin symmetry [MS94] as $2/3$, while the other channel $\Delta^+ \to n\pi^+$ has a probability of $1/3$. The exact value can be modified using the field *dprop*. $DMode = 2$ can only be selected for ρ^0-production. In this case the mass of the resonant nucleon state is given by the mass distribution from reference [E66597]. Again the decay ratio can be controlled using the field *dprop*; in this case its true value is unknown.

Table D.1.: Options of the generator *gmc_dvcs*.

field	default	comment
Set TarA	1	: target atomic number
Set TarZ	1	: target charge
Set BeamParType	POSI	: beam particle type
Set PBValue	1.	: beam polariz value
Set PTValue	0.	: targ polariz value
Set Mode	1	: eventtype 1...5 (gamma,rho,pi+,pi0,K+)
Set DMode	4	: delta=1; rhoDD=2; res=3; mix=4;
Set Spectrum	3	: flat=0; t-slope=1; BH=2,3(opt); DVCS=4; full=5;
Set GPDtype	5	: GPDs (DVCS): -2,-1 (Vdh), 1...5 (V.K.)
Set Rtype	0	: R=0.(0),0.18(1),Brasse(2),DIS(3),0.5(4),MAID(5)
Set XType	1	: resonances: 1-3(Brasse),4(Stein),5(Maid)
Set DeutEMode	3	: elastic bh: 0(no);1(no assym);2(-0.25),3(Kirchner);
Set DeutSMode	1	: qel. bh: 0(no);1(Stein);2(Atwood);3(free);4(deForest);
Set TMIN	-8.	: minimum t
Set TMAX	0.	: maximum t
Set dprop	0.666	: Delta decay propabilities
Set cutmeson	0.250	: cut on meson-angle
Set slope	3.	: b-slope of t
Set LMass	1.1	: resonance region: lower mass (GeV)
Set UMass	2.	: resonance region: upper mass (GeV)
Set GenHadrons	YES	: generate hadronic final state
Set AllWeights	YES	: store all 5 DVCS-models in user table

The generation limits for the phase space generator are given by $TMIN < t < TMAX$ (t negative!) and the standard parameters that control the limits in x_B and Q^2. One additional cut is needed to speed up the process of generation considerably: In many cases the meson is far outside the HERMES acceptance. Such events can directly be rejected. The field *cutmeson* contains the maximum allowed opening angle of the meson with respect to the beam.

Sometimes it is not clear if additional tracks/clusters are due to the target fragmentation products or if they are secondaries originating from the lepton. This can be checked by switching off the generation of hadrons using the field *GenHadrons*.

D.2. *gmc_dvcs* as BH/DVCS-Generator

gmc_dvcs behaves very differently if it is being used for the generation of DVCS events instead of simple phase space generation. As the BH-cross-section has a rather complicated 4-dimensional shape, the event weight w_i (that is set to 1 for phase space generation) is filled with the value of $d\sigma/dx_B\,dQ^2\,dt\,d\phi$. Inside the applied cuts the predicted cross-section is then obtained from

$$\sigma = \frac{\Delta x_B\,\Delta Q^2\,\Delta t\,\Delta\phi}{\text{Number of generated events}} \sum_i w_i, \tag{D.1}$$

where the generated events have to be counted before any events are rejected (e.g. because of forbidden kinematics). For some settings additional factors are included into the weight such that the more general statement is: Using the number of generated events from the file gmc.norm.kumac and the value of "extraweight" in this file, the predicted cross-section in microbarn is

$$\sigma = \frac{\text{extraweight}}{\text{Number of generated events}} \sum_i w_i. \tag{D.2}$$

The statistical errors obtained from a weighted Monte Carlo can be calculated as shown in chapter 6. In general the relative error on the cross-section $d\sigma/\sigma$ obtained with N weighted Monte Carlo events is at least as large as $1/\sqrt{N}$ but typically larger. As soon as very different event weights are added up, the error increases and in the limit of one dominating event the estimate of the relative error is $d\sigma/\sigma = 1$. Consequently some time must be spent to find an initial distribution, such that the event weight is approximately constant inside the considered kinematics.

Although this method may appear a bit cumbersome, it is well suited for the case of DVCS in interference with BH as the cross-section is changing very rapidly. Two other methods can be used for the same application:

The DVCS-generator *genDVCS* [Sau99] determines the event weight in a similar way. However, the events are generated according to the hit-and-miss method. This means that first phase-space is scanned for the biggest event-weight w_0 and then each event w_i is only accepted if w_i/w_0 is less then a random number r_i with $0 \leq r_i \leq 1$. The advantage of this is that the statistical error on N events inside some bin is given by $\sqrt{N}$. The disadvantage of this method at HERMES is that the singularities in the BH-cross-section can lead to a very high value of w_0. Since the singularities are outside the HERMES acceptance, the final yield of accepted event would be unnecessarily low.

gmc_dvcs reacts differently to singularities: As the event weights are only considered after the acceptance cuts, the number of good events inside these cuts is independent of singularities that are outside the acceptance. If - by chance - a singularity is inside the final analysis cuts, a few event weights will be very high. These spikes signal that there is a problem with the cuts and not with the generator.

A third method to generate exclusive photon events is used in the program *polrad* [AIS+97]: Since this code is designed for radiative corrections, the total radiative cross-section for each event kinematics is calculated. If the event is chosen to be a radiative instead of a DIS event, the photon is generated according to the numerically integrated cross-section. Although there is nothing wrong with this method, it is unnecessarily complicated for the case of DVCS. It has been checked that a good agreement of *polrad* and *gmc_dvcs* is obtained for the elastic BH-cross section.

gmc_dvcs can simulate BH and DVCS on a proton target as well as on various nuclear targets. In order to select this functionality, Mode must be set to 0. In the case of a proton target the following options are available: If the elastic process is chosen ($DMODE = 0$), the parameter *Spectrum* controls the cross-section model. $Spectrum = 2$ means that the events are generated flat in x_B, Q^2, t and ϕ and that the BH/DVCS-cross-section is calculated using the code supplied by V. Korotkov ($GPDtype > 0$), or the BH cross-section only is calculated based on the internal code derived from reference [MT69] ($GPDtype = 0$). The same cross section can be generated in an optimised way if $Spectrum = 5$ is chosen: In this case the initial event distribution is flat in x_B, $1/Q^4$, $\exp(bt)$ and ϕ. The parameter b is again given by the value of *slope*. In this case the slope has no direct impact on the generated cross-section. Instead it optimises the speed of statistical convergence; consequently a value of about 3 GeV^{-2} should be used here, which is different from the slope discussed before. $Spectrum = 5$ generates much faster good results and should be preferred with respect to $Spectrum = 2$. For debugging reasons, $Spectrum = 3$ allows to study the BH cross-section supplied by V. Korotkov and $Spectrum = 4$ selects the DVCS-cross-section (in both cases optimised generation). In general it is more efficient to set the field *AllWeights* to 'true' such that all 5 MC-models are evaluated at the same time and the results are stored in the user table (cf. explanation below). The obtained cross-section depends on the selected beam charge and beam polarisation.

The code has also an interface to read the look-up tables that have been provided by J. Volmer using the code according to [VGG99]. For $2 \leq Spectrum \leq 5$ this routine can calculate the target polarisation dependent DVCS+BH cross-section. If $GPDtype = -1$ a linear interpolation of $\log d\sigma_{BH/DVCS}$ is made, while $GPDtype = -2$ selects a linear interpolation of $d\sigma_{BH/DVCS}/d\sigma_{BH}$ which is subsequently multiplied by σ_{BH} according to the internal BH-code. Both methods try to reduce the error of the interpolation which can be substantial if a linear interpolation of $d\sigma$ is directly attempted. The result depends on the selected beam charge as well as on the beam polarisation and the target polarisation.

Settings of $DMode \neq 0$ indicate that target fragmentation is selected. In this case the parameter $Spectrum$ must be set to 3 as only the BH-process is available. If $DMode = 1$ the mass and decay of the $\Delta(1232)$ are generated as in the case of the phase-space generator. The cross-section is calculated according to the Δ transition formfactors from reference [DT68]. It has been checked that the finite width of the generated Δ-mass in the Monte Carlo does not change the results, although the formfactors of reference [DT68] assumes a Δ-width of zero (cf. section 4.4).

An improved approach to the resonance region is possible by using the differential cross-section in W for the electromagnetic excitation of resonances. This is achieved by setting *DMode* to 3. The mass range can be selected by the limits *LMass* and *UMass*, with a maximum range of 1.1 GeV … 2 GeV. The cross-section type can be selected using the field *XType*. In general the Brasse-parametrisation number one [B+76] should be the best. It is known to work well inside the full region in W and also for large values of Q^2 (which correspond to large values of $|t|$ in the case of BH). For the region delimited by the experimental acceptance of reference [E6175], very good agreement is found between the parametrisation $XType = 1$ and $XType = 4$. For $XType \leq 4$ the 2 contributions σ_L and σ_T are not separated. Consequently an additional parametrisation of $R = \sigma_L/\sigma_T$ is needed.

$Rtype = 0$ selects $R = 0$, while $Rtype = 1$ gives a fixed value of $R = 0.18$. $Rtype = 2$ selects the W^2 and Q^2 dependent parametrisation of R that is obtained by combining the results of the first and the third parametrisation by Brasse. Due to inconsistencies in the datasets the quality of this parametrisation is unclear. Under the assumption that R is the same for resonances and DIS at the same values of x_B and Q^2, the parametrisation by L.W. Whitlow can be used. Due to the typically low values of t the application of this parametrisation is questionable. $Rtype = 5$ selects an extreme ratio of $R = 0.5$, while for $Rtype = 6$ R is taken from the MAID2000-model. As the model only includes resonant single meson production, the true value for R can be very different, especially for large values of Q^2 and W^2. The default setting is $R = 0$.

If $DMode = 4$ *gmc_dvcs* generates exclusive events (using $Spectrum = 5$ and the corresponding *GPDtype*) and semi-exclusive BH in parallel. In this case *gmc_dvcs* is designed to work as a supplement to *gmc_disng* and replaces the routines for elastic BH as well as for BH with resonance excitation in this generator. Apart from the missing DVCS-contribution, this is necessary as *gmc_disng* extrapolates parametrisations of F_2 [AL97] and R [WRB+90] from the DIS to the resonance region. Consequently the predicted cross-section in the resonance region is slightly wrong. It is suggested to combine the results of *gmc_dvcs* and *gmc_disng* in the following way:

$$\begin{aligned}\sigma = {} & \frac{\text{extraweight}_{\text{gmc\_dvcs}}}{\text{Number of generated gmc\_dvcs}-\text{events}} \sum_i w_{i,GMC\_DVCS} + \\ & \frac{\text{extraweight}_{\text{gmc\_disng}}}{\text{Number of generated gmc\_disng}-\text{events}} \sum_i w_{i,GMC\_DISNG},\end{aligned} \tag{D.3}$$

where only semi-inclusive events and radiative events with $trueW2 > 4$ GeV^2 are selected from the *gmc_disng* sample.

D.3. *gmc_dvcs* and Nuclear Targets

gmc_dvcs can also be used for a deuterium target. In this case the cross-section is by definition the cross-section per nucleon and 5 processes are generated in parallel: Elastic coherent BH/DVCS, elastic incoherent BH/DVCS on the proton and the neutron and incoherent BH on the proton and the neutron with excitation of a resonance. Almost all settings that are available for the proton are also available for the neutron inside the deuteron. One exception is that only $GPDType \geq 0$ is allowed.

Two special options can be set for the deuteron: The flag *DeutEMode* selects the way in which the coherent process is treated. For $DeutEMode = 0$ it is completely switched off. For

$DeutEMode = 1$ coherent BH events are simulated in addition to the incoherent processes. $DeutEMode = 2$ selects the parametrisation of the A_{LU} given in reference [KM02], which is simply multiplied to the BH-cross-section. Finally $DeutEMode = 3$ selects a constant asymmetry of -0.25 that is treated in the same way.

The variable *DeutSMode* selects the treatment of the incoherent process. Apart from straight forward assumptions about its disappearance at low values of t [GS03] no strict model calculations exist at the moment. As the binding effects at low $|t|$ are essential to explain the experimentally observed t-distribution, several very basic models have been implemented: $DeutSMode = 0$ switches off the process. $DeutSMode = 1$ selects the suppression as discussed in reference [E6175], while $DeutSMode = 2$ follows the prescription from reference [AW73]. If the recoil detector can be used in combination with deuterium gas, the second model will generate a realistic distribution of spectator nucleons, while the first model will be better in explaining the cross-section at low values of t. $DeutSMode = 3$ generates incoherent BH/DVCS under the assumption of free nucleons. This model fails to reproduce the t-dependence of the measured data. $DeutSMode = 4$ is based on reference [DFW66] and is not very well motivated for the deuteron.

Two heavier nuclei can also be selected as targets: Neon ($TarZ = 10$, $TarA = 20$) and Krypton ($TarZ = 36$, $TarA = 84$). In these cases the parameters *DeutSMode* and *DeutEMode* are also used, but the available options are only $DeutEMode = 0, 1, 2$ and $DeutSMode = 0, 3, 4$. The default settings are $DeutSMode = 4$ and $DeutEMode = 1$, since an additional model-dependent A_{LU} can still be added during event analysis by reweighting the coherent events.

Some additional information about each event is available in the output tables. The structure of "g1mcUser" is shown in table D.2. The table "g1MEvents" contains the original event kinematics. In the case that exclusive photon-production is generated, the value of "Q2True" is by definition set to t and "XTrue" is set to the number of nucleons A in the target particle ($A = 1$ for incoherent process). The weight in this table is the one that has to be used, when the results of the simulation are analysed.

Table D.2.: Contents of the table g1mcUser from *gmc_dvcs*.

ID	Name	comment
1	t	for $Mode = 1$ identical to g1MEvent.Q2True
2	ppr	momentum of generated (decay) proton
3	thetapr	θ of proton with respect to beam
4	px_meson	p_x of exclusive meson
5	py_meson	p_y of exclusive meson
6	pz_meson	p_z of exclusive meson
7	mass_meson	mass of meson; fixed except for ρ-production
8	Ipn	target particle: 1(proton), 2(neutron), 3(deuteron), 4(neon), 5(krypton)
9	m(N)	mass of target particle
10	EBEAM	beam energy, recalculated for $DeutSMode = 2$
11	phi_e	azimuthal angle of lepton
12	phi_g	azimuthal angle of photon in rest frame of target particle
13	x-BH	event weight due to BH-cross-section
		Onlyif$AllWeight = .TRUE.$ and elastic, incoherent process:
14	x-DVCS	DVCS-cross-section weight (model 1)
15	x-DVCS	DVCS-cross-section weight (model 2)
16	x-DVCS	DVCS-cross-section weight (model 3)
17	x-DVCS	DVCS-cross-section weight (model 4)
18	x-DVCS	DVCS-cross-section weight (model 5)
19	x-INT	interference term cross-section weight (model 1)
20	x-INT	interference term cross-section weight (model 2)
21	x-INT	interference term cross-section weight (model 3)
22	x-INT	interference term cross-section weight (model 4)
23	x-INT	interference term cross-section weight (model 5)

List of Figures

List of Tables

Bibliography

[A199] A. Liesenfeld et al. (A1 Collaboration), *A measurement of the axial form-factor of the nucleon by the $p(e, e'\pi^+)n$ reaction at $W = 1125$ MeV*, Phys. Lett. **B468**, 20 (1999).

[A+72a] J. C. Alder et al., *Separation of σ_l and σ_t at q^2 nearly 1 (GeV/c)^2 in the resonance region*, Nucl. Phys. **B48**, 487 (1972).

[A+72b] T. A. Armstrong et al., *Total hadronic cross-section of gamma rays in hydrogen in the energy range 0.265-GeV to 4.215-GeV*, Phys. Rev. **D5**, 1640 (1972).

[A+87] L. A. Ahrens et al., *Measurement of neutrino - proton and anti-neutrino - proton elastic scattering*, Phys. Rev. **D35**, 785 (1987).

[A+98] H. Avakian et al., *Performance of the electromagnetic calorimeter of the HERMES experiment*, Nucl. Instrum. Meth. **A417**, 69 (1998).

[A+04] J. Arrington et al., *Pre-Conceptual Design Report for the Science and Experimental Equipment for the 12 GeV Upgrade of CEBAF*, http://www.jlab.org/div_dept/physics_division/GeV.html, 2004.

[ABBHHM66] H. G. Hilpert et al. (ABBHHM Collaboration), *The reaction $\gamma p \to N^{*++}\pi^-$ at energies up to 5.8 GeV*, Phys. Lett. **23**, 707 (1966).

[ABBHHM68] R. Erbe et al. (ABBHHM Collaboration), *Photoproduction of meson and baryon resonances at energies up to 5.8-GeV*, Phys. Rev. **175**, 1669 (1968).

[AH89] I. J. R. Aitchison and A. J. G. Hey, *Gauge Theories in Particle Physics, second edition*, Institute of Physics Publishing, 1989.

[AIS+97] I. Akushevich, A. Ilichev, N. Shumeiko, A. Soroko and A. Tolkachev, *POLRAD 2.0: FORTRAN code for the radiative corrections calculation to deep inelastic scattering of polarized particles*, Comput. Phys. Commun. **104**, 201 (1997).

[AKP01] T. W. Allen, W. H. Klink and W. N. Polyzou, *Point-Form Analysis of Elastic Deuteron Form Factors*, Phys. Rev. **C63**, 034002 (2001).

[AL97] H. Abramowicz and A. Levy, *The ALLM parameterization of $\sigma_{tot}(\gamma^* p)$: An update*, hep-ph/9712415, 1997.

[ALR97] M. Arneodo, L. Lamberti and M. Ryskin, *DIPSI: A Monte Carlo generator for elastic vector meson production in charged lepton proton scattering*, Comput. Phys. Commun. **100**, 195 (1997).

[AP77] G. Altarelli and G. Parisi, *Asymptotic freedom in parton language*, Nucl. Phys. **B126**, 298 (1977).

[AW73] W. B. Atwood and G. B. West, *The extraction of asymptotic nucleon cross-sections from deuterium data*, Phys. Rev. **D7**, 773 (1973).

[B+72] K. Baetzner et al., *Separation of σ_s and σ_t in the region of the Δ(1236) resonance and determination of the magnetic dipole transition form-factor*, Phys. Lett. **B39**, 575 (1972).

[B+76] F. W. Brasse et al., *Parametrization of the q^2 dependence of virtual γp total cross-sections in the resonance region*, Nucl. Phys. **B110**, 413 (1976).

[B+78a] C. J. Bebek et al., *Electroproduction of single pions at low ϵ and a measurement of the pion form-factor up to $Q^2 = 10$ GeV^2*, Phys. Rev. **D17**, 1693 (1978).

[B+78b] F. W. Brasse et al., *Separation of σ_L and σ_T in eta - electroproduction at the resonance S_{11} (1535)*, Nucl. Phys. **B139**, 37 (1978).

[B+81] A. Bussiere et al., *Momentum distribution of nucleons in the deuteron from the $d(e, e'p)n$ reaction*, Nucl. Phys. **A365**, 349 (1981).

[B+94] R. Brun et al., *GEANT detector description and simulation tool (long writeup W5013)* , CERN-CN Application Software Group, Geneva, 1994.

[B+02] M. Beckmann et al., *The longitudinal polarimeter at HERA*, Nucl. Instrum. Meth. **A479**, 334 (2002).

[B+03] P. Bertin et al., *Deeply Virtual Compton Scattering On The Neutron*, Proposal to Jefferson Lab PAC 24, 2003.

[BBKT98] P. Ball, V. M. Braun, Y. Koike and K. Tanaka, *Higher twist distribution amplitudes of vector mesons in QCD: Formalism and twist three distributions*, Nucl. Phys. **B529**, 323–382 (1998).

[BCVZ89] R. Brun, O. Couet, C. E. Vandoni and P. Zanarini, *PAW: A general purpose portable software tool for data analysis and presentation*, Comput. Phys. Commun. **57**, 432 (1989).

[BDH01] S. J. Brodsky, M. Diehl and D. S. Hwang, *Light-cone wavefunction representation of deeply virtual Compton scattering*, Nucl. Phys. **B596**, 99 (2001).

[BDS+75] V. G. Bagrov, O. F. Dorofeev, A. A. Sokolov, I. M. Ternov and V. R. Khalilov, *On the Radiation Selfpolarization of Electrons Moving in a Magnetic Field. (in Russian)*, Dokl. Akad. Nauk Ser. Fiz. **221**, 312 (1975).

[Bec03] M. Beckmann, *Target polarisation values and their uncertainties used by the Delta-q analysis group for the 1996 to 2000 running periods*, HERMES internal note 03-005, 2003.

[Ber72] J. Bernabeu, *Quasielastic electron and neutrino interactions and the exclusion effects*, Nucl. Phys. **B49**, 186 (1972).

[BFM00] A. V. Belitsky, A. Freund and D. Müller, *Evolution kernels of skewed parton distributions: Method and two-loop results*, Nucl. Phys. **B574**, 347 (2000).

[BH34] H. Bethe and W. Heitler, *On the Stopping of fast particles and on the creation of positive electrons*, Proc. Roy. Soc. Lond. **A146**, 83 (1934).

[BK03] V. V. Bytev and E. A. Kuraev, *Radiative corrections to DVCS electron tensor*, hep-ph/0310226, 2003.

[BL87] R. Brun and D. Lienart, *HBOOK user guide: CERN computer center program library long write-up: Version 4*, 1987, CERN-Y250.

[BLAST98] R. Alarcon (BLAST Collaboration), *The BLAST scientific program*, 1998, Prepared for 2nd Workshop on Electronuclear Physics with Internal Targets and the BLAST Detector, Cambridge, Massachusetts, 28-30 May 1998.

[BM01] A. V. Belitsky and D. Müller, *Hard exclusive meson production at next-to-leading order*, Phys. Lett. **B513**, 349–360 (2001).

[BM02] A. V. Belitsky and D. Müller, *Nucleon hologram with exclusive leptoproduction*, Nucl. Phys. **A711**, 118 (2002).

[BMK02] A. V. Belitsky, D. Müller and A. Kirchner, *Theory of deeply virtual Compton scattering on the nucleon*, Nucl. Phys. **B629**, 323 (2002).

[Bor02] A. Borisenko, private communication, 2002.

[BR97] I. I. Balitsky and A. V. Radyushkin, *Light-ray evolution equations and leading-twist parton helicity-dependent nonforward distributions*, Phys. Lett. **B413**, 114 (1997).

[Bur03] M. Burkardt, *Impact parameter space interpretation for generalized parton distributions*, Int. J. Mod. Phys. **A18**, 173 (2003).

[C$^+$93] S. Choi et al., *Axial and pseudoscalar nucleon form-factors from low-energy pion electroproduction*, Phys. Rev. Lett. **71**, 3927 (1993).

[CF99] J. C. Collins and A. Freund, *Proof of factorization for deeply virtual Compton scattering in QCD*, Phys. Rev. **D59**, 074009 (1999).

[Cha80] C. Chahine, *Nonperturbative method for radiative corrections applied to lepton - proton scattering*, Phys. Rev. **D22**, 1062 (1980).

[CLAS01] S. Stepanyan et al. (CLAS Collaboration), *First observation of exclusive deeply virtual Compton scattering in polarized electron beam asymmetry measurements*, Phys. Rev. Lett. **87**, 182002 (2001).

[Col98] J. C. Collins, *Proof of factorization for diffractive hard scattering*, Phys. Rev. **D57**, 3051 (1998).

[COSY-TOF98] P. Michel et al. (COSY-TOF Collaboration), *MARS: A start detector system for the COSY time-of-flight spectrometer TOF,* Nucl. Instrum. Meth. **A408**, 453 (1998).

[CP04] F. Cano and B. Pire, *Deep electroproduction of photons and mesons on the deuteron*, Eur. Phys. J. **A19**, 423 (2004).

[DFW66] J. De Forest, T. and J. D. Walecka, *Electron scattering and nuclear structure*, Adv. Phys. **15**, 1 (1966).

[DHKT99] D. Drechsel, O. Hanstein, S. S. Kamalov and L. Tiator, *A unitary isobar model for pion photo- and electroproduction on the proton up to 1-GeV*, Nucl. Phys. **A645**, 145 (1999).

[DMR$^+$88] F. M. Dittes, D. Müller, D. Robaschik, B. Geyer and J. Horejsi, *The Altarelli-Parisi kernel as asymptotic limit of an extended Brodsky-Lepage kernel*, Phys. Lett. **B209**, 325–329 (1988).

[dN01] L. de Nardo, *Trigger Efficiencies for 98 and 99 Data*, HERMES internal note 01-005, 2001.

[dN02] L. de Nardo, *Measurement of the Structure Function g_1^d at HERMES and Extraction of Polarized Parton Distributions*, Dissertation, University of Alberta, 2002.

[DP00] D. Diakonov and V. Y. Petrov, *Nucleons as chiral solitons*, hep-ph/0009006, 2000.

[DT68] A. J. Dufner and Y.-S. Tsai, *Phenomenological analysis of the $\gamma N N^*$ form-factors*, Phys. Rev. **168**, 1801 (1968).

[Dür98] M. Düren, *Protecting the* HERMES *Experiment from Synchrotron Radiation*, HERMES internal note 98-004, 1998.

[E15503] P. L. Anthony et al. (E155 Collaboration), *Precision measurement of the proton and deuteron spin structure functions g_2 and asymmetries A_2*, Phys. Lett. **B553**, 18 (2003).

[E$^+$97] W. Eick et al., *Development of the H1 backward silicon strip detector*, Nucl. Instrum. Meth. **A386**, 81 (1997).

[E$^+$01] R. Ent et al., *Radiative corrections for $(e, e'p)$ reactions at GeV energies*, Phys. Rev. **C64**, 054610 (2001).

[E6175] S. Stein et al. (E61 Collaboration), *Electron scattering at 4-degrees with energies of 4.5-GeV - 20-GeV*, Phys. Rev. **D12**, 1884 (1975).

[E66597] M. Adams et al. (E665 Collaboration), *Diffractive production of $\rho^0(770)$ mesons in muon-proton interactions at 470 GeV*, Z. Phys. **C74**, 237 (1997).

[Ell03] F. Ellinghaus, *Beam-Charge and Beam-Spin Azimuthal Asymmetries in Deeply-Virtual Compton Scattering*, Dissertation, Humboldt University of Berlin, 2003.

[Els01] U. Elschenbroich, *Bhabha-Streuung und Luminositätsmessungen im* HERMES*-Experiment*, Diplomarbeit, Universität Düsseldorf, 2001.

[Els02] U. Elschenbroich, *Analysis of Luminosity Monitor Data for Different Years*, HERMES internal note 02-013, 2002.

[Ely02] J. Ely, *Measurement of the single spin azimuthal asymmetry in the predominantly exclusive electroproduction of photons from the proton*, Dissertation, University of Colorado, 2002.

[ENVY04] F. Ellinghaus, W.-D. Nowak, A. Vinnikov and Z. Ye, *Prospects for Measuring the Transverse Target Spin Asymmetry in DVCS and ρ^0 Production at HERMES*, HERMES internal note 04-008, 2004.

[F$^+$96] J. L. Forest et al., *Femtometer Toroidal Structures in Nuclei*, Phys. Rev. **C54**, 646 (1996).

[FA79] W. Fabian and H. Arenhovel, *Electrodisintegration of deuterium including nucleon detection in coincidence*, Nucl. Phys. **A314**, 253 (1979).

[FB99] W. Fallot-Burkhardt, *HELIX128-x User Manual* , HD-ASIC-33-0697, 1999.

[FB00] K. Foehl and D. Branford, *A high resolution germanium detector telescope*, Prog. Part. Nucl. Phys. **44**, 465 (2000).

[Fie00] K. Fiedler, *Nachweis von Zuschauernukleonen im HERMES-Experiment*, Dissertation, Universität Erlangen-Nürnberg, 2000.

[FKS96] L. Frankfurt, W. Koepf and M. Strikman, *Hard diffractive electroproduction of vector mesons in QCD*, Phys. Rev. **D54**, 3194 (1996).

[FMS03] A. Freund, M. McDermott and M. Strikman, *Modelling generalized parton distributions to describe deeply virtual Compton scattering data*, Phys. Rev. **D67**, 036001 (2003).

[FPPS99] L. L. Frankfurt, P. V. Pobylitsa, M. V. Polyakov and M. Strikman, *Hard exclusive pseudoscalar meson electroproduction and spin structure of a nucleon*, Phys. Rev. **D60**, 014010 (1999).

[FPS98] L. L. Frankfurt, M. V. Polyakov and M. Strikman, *N to Δ DVCS, exclusive DIS processes and skewed quark distributions in large N_c limit* , hep-ph/9808449, 1998.

[Fre99] A. Freund, *Extraction of skewed parton distributions from experiment*, Nucl. Phys. Proc. Suppl. **79**, 368 (1999).

[FS04] A. Freund and M. Strikman, *DVCS on nuclei: Observability and consequences*, Eur. Phys. J. **C33**, 53 (2004).

[G+04] I. Gregor et al., *Study of the First Prototype for the HERMES Silicon Recoil Detector with the ZEUS Beam Telescope*, HERMES internal note 04-019, 2004.

[GBMR99] K. J. Golec-Biernat, A. D. Martin and M. G. Ryskin, *Diagonal input for the evolution of off-diagonal partons*, Phys. Lett. **B456**, 232 (1999).

[GMV03] P. A. M. Guichon, L. Mosse and M. Vanderhaeghen, *Pion production in deeply virtual Compton scattering*, Phys. Rev. **D68**, 034018 (2003).

[GPV01] K. Goeke, M. V. Polyakov and M. Vanderhaeghen, *Hard exclusive reactions and the structure of hadrons*, Prog. Part. Nucl. Phys. **47**, 401 (2001).

[Group01] M. Anselmino et al. (TESLA-N Study Group Collaboration), *TESLA: The superconducting electron positron linear collider with an integrated X-ray laser laboratory. Technical design report. Pt. 6: Appendices. Chapter 4: ELFE: The electron laboratory for Europe*, 2001, DESY-01-011.

[GS03] V. Guzey and M. Strikman, *DVCS on spinless nuclear targets in impulse approximation*, Phys. Rev. **C68**, 015204 (2003).

[H100] C. Adloff et al. (H1 Collaboration), *Elastic electroproduction of rho mesons at HERA*, Eur. Phys. J. **C13**, 371 (2000).

[H101] C. Adloff et al. (H1 Collaboration), *Measurement of deeply virtual Compton scattering at HERA*, Phys. Lett. **B517**, 47 (2001).

[Har04a] M. Hartig, Private Communication, 2004.

[Har04b] M. Hartig, *Proposal for a TDC readout of the 12th dynode for the SciFi Detector*, HERMES recoil detector note, 2004.

[Has03] D. Hasch, private communication, 2003.

[HER97] HERMES, *New silicon-detector systems for the HERMES front region* , HERMES Internal Report 97-032, 1997.

[HER02] HERMES, *The HERMES Recoil Detector*, HERMES internal note 02-003, 2002.

[HER04] HERMES, *Shift Primer*, HERMES internal note, 2004.

[HERMES] M. Contalbrigo (HERMES Collaboration), *A first measurement of the tensor structure function $b_1(d)$*, Prepared for 17th Les Rencontres de Physique de la Vallee d'Aoste: Results and Perspectives in Particle Physics, La Thuile, Aosta Valley, Italy, 9-15 Mar 2003.

[HERMES98] K. Ackerstaff et al. (HERMES Collaboration), *The HERMES Spectrometer*, Nucl. Instr. Meth. **A417**, 230 (1998).

[HERMES99] K. Ackerstaff et al. (HERMES Collaboration), *Flavor decomposition of the polarized quark distributions in the nucleon from inclusive and semi-inclusive deep- inelastic scattering*, Phys. Lett. **B464**, 123 (1999).

[HERMES00] A. Airapetian et al. (HERMES Collaboration), *Exclusive leptoproduction of ρ^0 mesons from hydrogen at intermediate virtual photon energies*, Eur. Phys. J. **C17**, 389 (2000).

[HERMES01a] A. Airapetian et al. (HERMES Collaboration), *Measurement of the beam spin azimuthal asymmetry associated with deeply-virtual Compton scattering*, Phys. Rev. Lett. **87**, 182001 (2001).

[HERMES01b] R. Kaiser (HERMES Collaboration), *A large acceptance recoil detector for HERMES*, 2001, DESY-PRC-97-06-ADD.

[HERMES02] F. Ellinghaus (HERMES Collaboration), *Beam-charge asymmetry associated with DVCS at HERMES*, Nucl. Phys. **A711**, 171 (2002).

[HERMES03a] A. Airapetian et al. (HERMES Collaboration), *Measurement of single-spin azimuthal asymmetries in semi- inclusive electroproduction of pions and kaons on a longitudinally polarised deuterium target*, Phys. Lett. **B562**, 182 (2003).

[HERMES03b] F. Ellinghaus, R. Shanidze and J. Volmer (HERMES Collaboration), *Deeply-virtual Compton scattering on deuterium and neon at HERMES*, AIP Conf. Proc. **675**, 303 (2003).

[HERMES04a] E. Avetisyan, A. Rostomyan and A. Ivanilov (By HERMES Collaboration), *Beam-spin azimuthal asymmetries in pion electroproduction at HERMES*, hep-ex/0408002, 2004.

[HERMES04b] U. Elschenbroich, G. Schnell and R. Seidl (HERMES Collaboration), *Transverse spin physics at HERMES*, hep-ex/0405017, 2004.

[HJ62] T. Hamada and I. D. Johnston, *A Potential model representation of two nucleon data below 315-MeV*, Nucl. Phys. **34**, 382 (1962).

[Hoe04] M. Hoek, *A Gain Monitoring System for the Recoil SciFi Detector*, HERMES recoil detector note, 2004.

[Hoy02] P. Hoyer, *Probing QCD at medium Q^2*, Nucl. Phys. **A711**, 3 (2002).

[HP93] R. Horisberger and D. Pitzl, *A Novel readout chip for silicon strip detectors with analog pipeline and digitally controlled analog signal processing*, Nucl. Instrum. Meth. **A326**, 92 (1993).

[HT04] Y. V. Haarlem and M. Tytgat, *The Recoil Detector PMT Test Stand*, HERMES recoil detector note, 2004.

[IIM04] I.Gregor, I.Hristova and M.Kopytin, *HELIX128-3.0 Parameter Test for the HERMES Silicon Recoil Detector*, HERMES recoil detector note, 2004.

[Ji97] X.-D. Ji, *Deeply-virtual Compton scattering*, Phys. Rev. **D55**, 7114–7125 (1997).

[Ji98] X. Ji, *Off-forward parton distributions*, J. Phys. **G24**, 1181 (1998).

[JMS97] X. Ji, W. Melnitchouk and X. Song, *A study of off-forward parton distributions*, Phys. Rev. **D56**, 5511 (1997).

[JS73] H. F. Jones and M. D. Scadron, *Multipole $\gamma N \Delta$ form-factors and resonant photoproduction and electroproduction*, Ann. Phys. **81**, 1 (1973).

[K+99] A. Kastenmuller et al., *Fast detector readout for the HADES-RICH*, Nucl. Instrum. Meth. **A433**, 438 (1999).

[K+02] M. Kopytin et al., *Decision on the readout chip for the new Hermes silicon recoil detector*, HERMES internal note 02-020, 2002.

[Kai97] R. Kaiser, *Particle identification at HERMES*, HERMES Internal Note 97-025, 1997.

[Kis03] A. Kisselev, private communication, 2003.

[KM02] A. Kirchner and D. Müller, *Predictions for deeply virtual Compton scattering on a spin-one target*, hep-ph/0202279, 2002.

[KM03] A. Kirchner and D. Müller, *Deeply virtual Compton scattering off nuclei*, Eur. Phys. J. **C32**, 347 (2003).

[KN02a] V. A. Korotkov and W. D. Nowak, *Extraction of the generalized parton distribution $H(\xi, \xi, t)$ from DVCS*, Nucl. Phys. **A711**, 175 (2002).

[KN02b] V. A. Korotkov and W. D. Nowak, *Future measurements of deeply virtual Compton scattering at HERMES*, Eur. Phys. J. **C23**, 455 (2002).

[Kol98] H. Kolster, *The HERMES gaseous internal polarized proton target and its use in the HERA positron storage ring*, Dissertation, Ludwig-Maximilians-Universität München, 1998.

[Kop04] M. Kopytin, private communication, 2004.

[Kra76] F. Krautschneider, *Photoproduction of negative π - mesons between 900-MeV and 1800-MeV*, 1976, BONN-IR-76-37.

[Kra00] B. Krauss, *Ein Silizium-Detektor für das* HERMES*-Experiment* , Diplomarbeit, Universität Erlangen-Nürnberg, 2000.

[Kra03] B. Krauss, *Optimisation of the Flex-Foil Layering for the HERMES Recoil Detector*, HERMES recoil detector note, 2003.

[Kro01] K. Kroeninger, *Digitization of Signals from a Scintillating Fiber Detector*, HERMES summer student report, 2001.

[Kro02] K. Kroeninger, *Private Communication*, 2002.

[KS95] A. P. Kobushkin and A. I. Syamtomov, *Deuteron electromagnetic form factors in the transitional region between nucleon-meson and quark-gluon pictures*, Phys. Atom. Nucl. **58**, 1477 (1995).

[L+02] J. Lu et al., *Target-Spin Asymmetry from Deeply Virtual Compton Scattering on the Deuteron*, HERMES analysis report, 2002.

[Lut99] G. Lutz, *Semiconductor Radiation Detectors*, Springer Verlag, 1999.

[Lyo86] L. Lyons, *Statistics for nuclear and particle physicists*, Camebridge University Press, 1986.

[MS94] B. Martin and G. Shaw, *Particle Physics*, John Wiley & Sons, 1994.

[MT69] L. W. Mo and Y.-S. Tsai, *Radiative corrections to elastic and inelastic ep and μp scattering*, Rev. Mod. Phys. **41**, 205 (1969).

[Mül03] D. Müller, private communication, 2003.

[Muon84] J. J. Aubert et al. (European Muon Collaboration), *The measurement of Bethe-Heitler bremsstrahlung in muon - hydrogen interactions at 200-GeV*, Z. Phys. **C22**, 341 (1984).

[N+03] A. Nass et al., *The HERMES polarized atomic beam source*, Nucl. Instrum. Meth. **A505**, 633 (2003).

[O'N03] T. O'Neill, *Development of the TIGRE Compton Telescope for Intermediate-Energy Gamma-Ray Astronomy*, IEEE Trans. Nucl. Sci. **50,2**, 251 (2003).

[Par00] Particle Data Group, *The European Physical Journal C: Review of Particle Physics*, Springer, 2000.

[PB93] H. Plothow-Besch, *PDFLIB: A Library of all available parton density functions of the nucleon, the pion and the photon and the corresponding alpha-s calculations*, Comput. Phys. Commun. **75**, 396 (1993).

[Pei92] A. Peisert, *Silicon microstrip detectors*, Adv. Ser. Direct. High Energy Phys. **9**, 1 (1992).

[Pic03] N. Pickert, *Vorbereitende Untersuchungen an Silizium-Streifenzählern für den HERMES-Rückstoß-Detektor*, Diplomarbeit, Universität Erlangen-Nürnberg, 2003.

[Pol03] M. V. Polyakov, *Generalized parton distributions and strong forces inside nucleons and nuclei*, Phys. Lett. **B555**, 57 (2003).

[PTG94] Programming-Techniques-Group, *ADAMO – Entity-Relationship programming system, Version 3.3*, ECP Division, CERN, Geneva, 1994.

[R+75] E. M. Riordan et al., *Extraction of the structure functions and $R = \sigma_l/\sigma_t$ from deep inelastic ep and ed cross-sections*, 1975, Contributed paper to Int. Symposium on Lepton and Photon Interactions, Stanford, Calif., Aug 21-27, 1975.

[R+96] R. H. Richter et al., *Strip detector design for ATLAS and HERA-B using two-dimensional device simulation*, Nucl. Instrum. Meth. **A377**, 412 (1996).

[Rad99] A. V. Radyushkin, *Symmetries and structure of skewed and double distributions*, Phys. Lett. **B449**, 81–88 (1999).

[Rei68] J. Reid, Roderick V., *Local phenomenological nucleon-nucleon potentials*, Ann. Phys. **50**, 411 (1968).

[Ryc02] D. Ryckbosch, *The ELFE project*, Nucl. Phys. **A699**, 392 (2002).

[Sau99] P. Saull, *GenDVCS, a Monte Carlo generator for DVCS at HERA*, http://www-zeus.desy.de/physics/diff/pub/MC/, 1999.

[She04] C. Shearer, *Integration of the Recoil Detector into the HERMES Monte Carlo Simulation*, HERMES internal note 04-007, 2004.

[SLM01] T. Sjostrand, L. Lonnblad and S. Mrenna, *PYTHIA 6.2: Physics and manual*, hep-ph/0108264, 2001.

[SS04] W. Sommer and H. Stenzel, *Alignment of the SciFi Detector at the DESY22 electron testbeam*, HERMES recoil detector note, 2004.

[Sur98] B. Surrow, *Measurement of the Proton Structure Function F_2 at Low Q^2 and Very Low x with the ZEUS Beam Pipe Calorimeter at HERA*, Dissertation, Universität Hamburg, 1998.

[T$^+$03] T.Chen et al., *Report on Monte Carlo Studies for a HERMES C3 Collimator*, HERMES recoil detector note, 2003.

[The02] The Hermes target group, *The polarization of Hermes target and its error for the deuterium running in 2000* , HERMES internal note 02-010, 2002.

[TVFS00] J. A. Templon, C. E. Vellidis, R. E. J. Florizone and A. J. Sarty, *The radiation tail in $(e, e'p)$ reactions and corrections to experimental data*, Phys. Rev. **C61**, 014607 (2000).

[Tyt01] M. Tytgat, *Diffractive Production of ρ^0 and ω Vector Mesons at HERMES*, Dissertation, Universiteit Gent, 2001.

[V$^+$00] M. Vanderhaeghen et al., *QED radiative corrections to virtual Compton scattering*, Phys. Rev. **C62**, 025501 (2000).

[vB$^+$98] M. van Beuzekom et al., *Technical Design Report of the new Silicon-Detector System* , HERMES Internal Report 98-014, 1998.

[vB$^+$03] M. G. van Beuzekom et al., *The HERMES silicon project: The radiation protection system*, Nucl. Instrum. Meth. **A512**, 44 (2003).

[VCS00] J. Roche et al. (VCS Collaboration), *The first determination of generalized polarizabilities of the proton by a virtual Compton scattering experiment*, Phys. Rev. Lett. **85**, 708 (2000).

[Vel02] J. Velthuis, *Results of ^{60}Co irratiation of the ZEUS-MVD frontend chips, the HELIX 3.0*, ZEUS internal note 02-005, 2002.

[VES02] J. Volmer, M. Ehrenfried and A. Schwind, *Results from rate measurements inside the transverse magnet chamber,* HERMES internal note 02-002, 2002.

[VGG99] M. Vanderhaeghen, P. A. M. Guichon and M. Guidal, *Deeply virtual electroproduction of photons and mesons on the nucleon: Leading order amplitudes and power corrections*, Phys. Rev. **D60**, 094017 (1999).

[VGG00] M. Vanderhaeghen, P. A. M. Guichon and M. Guidal, *Deeply virtual electroproduction of photons and mesons on the nucleon,* Nucl. Phys. **A663**, 324 (2000).

[Vog03] C. Vogel, *Auslese eines Silizium-Testdetektors für das HERMES-Experiment,* Diplomarbeit, Universität Erlangen-Nürnberg, 2003.

[Wan96] W. Wander, *Rekonstruktion hochenergetischer Streuereignisse im HERMES-Experiment,* Dissertation, Universität Erlangen-Nürnberg, 1996.

[Wen03] J. Wendland, *Polarized Parton Distributions Measured at the HERMES Experiment,* Dissertation, Simon Fraser University, 2003.

[Whi90] L. W. Whitlow, *Deep inelastic structure functions from electron scattering on Hydrogen, Deuterium, and Iron at* 0.6 *GeV*^{2} $\leq Q^2 \leq 30$ *GeV*^{2}, 1990, SLAC-0357.

[Wie98] M. Wiesmann, *Messungen an einem Siliziumdetektor für das HERMES-Experiment,* Diplomarbeit, Universität Erlangen-Nürnberg, 1998.

[WMF96] D. Widmann, H. Mader and H. Friedrich, *Technologie hochintegrierter Schaltungen*, Springer-Verlag, 1996.

[WRB$^+$90] L. W. Whitlow, S. Rock, A. Bodek, E. M. Riordan and S. Dasu, *A Precise extraction of* $R = \sigma_L/\sigma_T$ *from a global analysis of the SLAC deep inelastic e-p and e-d scattering cross-sections*, Phys. Lett. **B250**, 193 (1990).

[ZEUS03] S. Chekanov et al. (ZEUS Collaboration), *Measurement of deeply virtual Compton scattering at HERA*, Phys. Lett. **B573**, 46 (2003).

Lebenslauf

Name:		Bernhard Krauß
Geburtstag:		12.12.1974
Geburtsort:		Nürnberg
Nationalität:		deutsch
Familienstand:		ledig
Schulausbildung:	09/81 - 07/85	Grundschule Altdorf bei Nürnberg
	09/85 - 07/94	Leibniz-Gymnasium Altdorf, mathematisch–naturwissenschaftlicher Zweig
	07/94	Abitur; Prüfungsfächer: Physik, Mathematik, Englisch, Erdkunde;
Zivildienst:	08/94 - 10/95	Zivildienst im Schullandheim Vorra
Studium:	11/95 - 02/01	Studium an der Friedrich–Alexander Universität Erlangen–Nürnberg; Fach: Physik Diplom, Wahlfach: Werkstoffwissenschaften Glas/Keramik; Stipendium der Bayerischen Hochbegabtenförderung; Studienbegleitende Fremdsprachenausbildung: Französisch: Unicert I, Spanisch: Elementarkurs I
	07/97	Diplom–Vorprüfung
	09/97 - 03/98	Auslandssemester an der Universität Glasgow
	08/98 - 09/98	Teilnahme am DESY-Sommerstudenten-Programm
	09/98 - 02/01	Stipendium der Studienstiftung des Deutschen Volkes
	02/01	Diplom–Hauptprüfung
	seit 03/01	Wissenschaftlicher Mitarbeiter am Physikalischen Institut der Universität Erlangen–Nürnberg

Zusammenfassung

Die vorliegende Arbeit beschäftigt sich mit der Beobachtung von Tiefvirtueller Compton-Streuung im HERMES-Experiment am HERA Beschleuniger (DESY/Hamburg) und einer dafür geplanten Erweiterung des HERMES-Experimentes, dem Rückstoßdetektor.

Tiefvirtuelle Compton-Streuung (DVCS) bezeichnet den Prozeß, bei dem ein einlaufendes Lepton ein virtuelles Photon emittiert, welches mit einem Quark im Inneren eines Protons wechselwirkt und dabei in ein reelles Photon umgewandelt wird. Das Quark fällt daraufhin in das Proton zurück, sodaß der Endzustand der Reaktion nur aus zwei geladenen Teilchen und einem hochenergetischen Photon besteht.

Tiefvirtuelle Compton-Streuung zählt zur Kategorie der harten exklusiven Prozesse, die mit Hilfe der sogenannten Generalisierten Partonverteilungen (GPDs) beschrieben werden können. Diese Objekte beinhalten die konventionellen Parton-Verteilungen des Nukleons ebenso wie seine Formfaktoren, können darüber hinaus aber auch mit anderen Größen, wie dem Gesamtdrehimpuls der Quarks im Nukleon in Zusammenhang gebracht werden.

Auf Grund des gleichen Endzustandes kommt es im realen Experiment zu einer quantenmechanischen Interferenz zwischen DVCS und Bremsstrahlung (Bethe-Heitler/BH), wobei im Fall von BH das reelle Photon vom Lepton abgestrahlt wird. Diese Interferenz führt dazu, daß der Wirkungsquerschnitt von Strahlladung, Strahlpolarisation und Targetpolarisation abhängig wird, was sich durch die Bildung geeigneter Asymmetrien quantitativ überprüfen läßt. Speziell die Asymmetrie bezüglich der Strahlhelizität wurde am HERMES-Experiment weltweit zum ersten Mal gemessen [HERMES01a].

In der vorliegenden Arbeit werden nun alle Asymmetrien untersucht, die mit einem longitudinal polarisierten Deuteriumtarget beobachtet werden können. Dafür werden Daten verwendet, die mit dem HERMES-Experiment in den Jahren 1998-2000 genommen wurden. Auch im Falle von Deuterium kann das Konzept der GPDs angewendet werden; allerdings werden zur Beschreibung des exklusiven Prozesses $ed \rightarrow e'd'\gamma$ neun anstelle von vier GPDs benötigt.

Experimentell wird der Fall des Deuteriums dadurch komplizierter, daß zusätzlich zum kohärenten Prozeß auch der quasielastische Prozeß möglich ist: $ed \rightarrow e'pn\gamma$. Darüberhinaus treten innerhalb des beobachteten Datensatzes auch weitere Hintergrundprozesse auf. Um einen konsistenten Vergleich zwischen Daten und Theorie zu ermöglichen, wurde ein Monte-Carlo-Ereignis-Generator entwickelt, der alle dominanten Prozesse simuliert. Eine gute quantitative Übereinstimmung zwischen Realität und Simulation wurde in Bezug auf die beobachteten Ereignisraten erreicht. Die Simulation erlaubt damit auch Rückschlüsse auf die erwartete kinematische Verschmierung im Experiment und die Auswirkung von Akzeptanz-Effekten.

Da die Anforderungen an das Experiment z.B. in Bezug auf die Auflösung und Kalibration des Kalorimeters weit über die ursprünglichen Spezifikationen des HERMES-Spektrometers hinausgehen, war eine systematische Überprüfung von apparativen Fehlerquellen notwendig. Im Rahmen der erforderlichen Genauigkeit wurden keine grundsätzlichen Probleme entdeckt und verbleibende systematische Fehler abgeschätzt.

Ein wesentlicher Teil der Arbeit bestand daraufhin aus der Wahl und Überprüfung einer geeigneten Extraktionsmethode für die erwarteten Asymmetrien. Auf Grund der beschränkten verfügbaren Ereignis-Zahl waren Unterschiede zwischen der neu entwickelten sukzessiven Anpassung der Simulation und der traditionellen Fit-Methode gering, weshalb schließlich trotz ihrer Nachteile diese etwas transparentere Methode zum Einsatz kam. Der Einfluß sowohl der endlichen Intervall-Größe in den verschiedenen kinematischen Variablen als auch der beschränkten Ereignisstatistik auf die Resultate wurde überprüft und die erwarteten Fehler abgeschätzt. Ebenso wurde der Effekt der nicht vollständigen Target-Polarisation studiert. Hintergrundprozesse wurden identifiziert und ihr Beitrag soweit wie möglich aus den Ergebnissen entfernt.

Auf diese Weise wurden Resultate für die Strahlspin- und Strahlladungsasymmetrie mit unpolarisiertem und tensorpolarisiertem Targetgas betimmt. In beiden Fällen wurde eine Asymmetrie gefunden, die mit den bereits erhaltenen Ergebnissen am Wasserstoff verträglich ist. Die Target-Spin Asymmetrie am Deuterium ist im Rahmen der Fehlerbalken Null, allerdings sagen theoretische Modelle voraus, daß diese Asymmetrie stark von der Kinematik abhängt. Die beobachteten Tensor-Asymmetrien sind im Rahmen der deutlich größeren Fehlerbalken ebenfalls verträglich mit Null.

Als wesentliches Problem stellte sich - wie bei der Analyse von DVCS am Wasserstoff - die mangelnde Identifikation des Hadronischen Endzustandes heraus. Mit der Lösung dieses Problems beschäftigte sich der experimentelle Teil dieser Arbeit: Der Entwurf des Rückstoßdetektors. Um den erwarteten Impuls- und Winkelbereich der Rückstoßprotonen von DVCS am Wasserstoff abdecken zu können, muß der Rückstoßdetektor Impulse ab etwa 100 MeV/c und Winkel von mehr als 0.4 rad relativ zum Strahl nachweisen können. Zu diesem Zweck wurde ein Aufbau aus drei verschiedenen faßförmigen Detektor-Komponenten entworfen: ein Siliziumstreifen-Detektor im Vakuum der Streukammer, ein umgebender Faserdetektor und ein Photonenzähler aus Szintillator-Paneelen als äußerste Lage. Außerdem wird zur Impulsbestimmung geladener Teilchen ein supraleitender Solenoid-Magnet benötigt.

Die erwarteten Einsatzmöglichkeiten eines solchen Detektors wurden simuliert und eine signifikante Unterdrückung der verschiedenen Hintergrund-Prozesse erreicht. Außerdem wurde die Unterdrückung von unkorreliertem Hintergrund (z.B. Møller-Streuung) optimiert. Verschiedene Teststrahl-Experimente wurden durchgeführt, um sicherzustellen, daß die festgelegten Spezifikationen in der Realität erfüllt werden.

Da die Erlanger HERMES-Gruppe für Einkauf und Überprüfung der Silizium-Detektoren zuständig war, wurden im Rahmen der Arbeit daneben auch systematische Tests der schließlich verwendeten Sensoren durchgeführt. Dabei wurde die Funktionalität der Oberflächenstrukturen ebenso wie das Langzeitverhalten überprüft.

Die einzelnen Komponenten des HERMES-Rückstoßdetektors existieren bereits und werden nach dem Zusammenbau und einem Testbetrieb mit kosmischer Strahlung voraussichtlich im Sommer 2005 in HERMES eingebaut. Der Betrieb bis zum Jahr 2007 soll eine weitere Eingrenzung der GPDs des Protons ermöglichen.

Acknowledgements

Many people have contributed to the successful completion of this thesis and I would like to thank all of them for their cooperation and support. This includes all members of the HERMES-collaboration and especially all people working on DVCS analysis and the HERMES Recoil Detector.

In particular I would like to thank Prof. Dr. K. Rith for the opportunity to take part in the complete redesign of the HERMES recoil detector which started about five years ago. This project has accompanied me through my diploma thesis as well as through this PHD thesis and I am glad to see that due to the combined efforts of all members of the recoil group the construction of the detector is almost finished by now. I hope that it will allow for a significant contribution to our understanding of DVCS and the GPDs.

I am also grateful for the support and the good and productive working atmosphere that I have enjoyed in our Erlangen group. Without this help several results presented in this thesis would have been impossible to obtain. In addition I am thankful for the important work that was carried out in the workshops of the Physics Institute in Erlangen as well as for the bonding that was done at the Institute of Applied Physics; also the admission to a probe station at the Fraunhofer Institute of Integrated Systems and Device Technology was very valuable for the progress of the recoil detector project.

Finally I would like to thank my friends, my family and my favourite pharmacist for the special and never-ending support that has carried me through this project.